LOW TEMPERATURE MECHANICAL PROPERTIES AND FRACTURE TOUGHNESS (*J*-INTEGRAL) OF SA.738 GR.B AND TWO NICKEL STEELS

by

YUNPENG GAO

A thesis submitted to the University of Birmingham for the degree of
DOCTOR OF PHILOSOPHY

School of Metallurgy and Materials
College of Engineering and Physical Sciences
University of Birmingham
May 2025

ACKNOWLEDGEMENTS

I am extremely grateful to my supervisor Prof. P. Bowen, for giving me the opportunity to pursue my PhD and for his generous sponsorship. His kind support and patience gave me the encouragement to complete my PhD study. The study in his group has made a total difference of my life.

I would also like to thank Baowu Steel for their financial support and for providing the materials used in this project.

My sincere thanks go to my second supervisor, Dr. M. Novovic, for his support with the experimental work, and for his insightful and patient discussions.

Appreciation is also extended to Mr. D. Price and Mr. T. Doel for their valuable assistance with the preparation of the experimental work.

Thanks are due to Weichen Xu and Huize Fan for their assistance with the experimental work, particularly with the SEM fractography.

Special thanks are due to Jiayun (George) Jiang for generously offering me a place to stay in his apartment and for his support during daily life throughout the pandemic.

I would like to thank Dou for the laughter and joy she brought into my life. I cherish the memories of the time we spent together.

Finally, I would like to express my heartfelt gratitude to my parents for their unwavering support, both financial and emotional, throughout the course of my studies. Their encouragement has been a constant source of strength in completing this thesis.

ABSTRACT

This thesis presents a comprehensive evaluation of SA738 Gr.B steel and 9 wt% and 7 wt% Nickel steels, focusing on their low-temperature mechanical properties and fracture mechanisms. SA738 Gr.B steel, a high-strength low-alloy steel, is widely used in pressure vessels and nuclear reactor components due to its resistance to brittle fracture. In contrast, high-nickel steels offer exceptional toughness at cryogenic temperatures, making them ideal for LNG storage tanks and other low-temperature applications. Mechanical testing included hardness testing, tensile testing, Charpy impact testing, blunt-notch fracture stress testing, and sharp-crack fracture toughness testing, conducted across temperatures ranging from -196 °C to -60 °C.

For SA738 Gr.B steel, two heat treatment conditions (HT1 and HT2) were assessed. Tensile testing revealed that both conditions exhibited splitting fracture behaviour, likely caused by the development of a high triaxial stress state within the necked region during tensile deformation. A pronounced temperature dependence of yield stress was also observed: the yield stress decreased systematically as the test temperature increased. The ductile-to-brittle transition behaviour was similar for HT1 and HT2, showing a range of -100 °C to -80 °C. Their transition temperatures were estimated as -90 °C and -86 °C, respectively, from tanh curve fitting. Strong linear correlations were observed between Charpy impact energy and fracture surface parameters, including lateral expansion, ductile thumbnail extension, and cleavage area fraction.

Fracture stress testing with blunt-notched specimens tested at -196 °C showed cleavage initiation stresses between 1803 and 2071 MPa, while fracture toughness testing with sharp-cracked specimens produced similar local fracture stress values, independent of temperature.

Inclusions are found at all initiation sites and considered to be the primary reason triggering cleavage fracture in these fracture stress tests. Inclusion analysis identified calcium-, aluminium-, and titanium-bearing inclusions at crack initiation sites; however, no clear relationship between inclusion size and fracture stress was observed. The effective surface energies for cleavage fracture ranged between 5.9 and 21.1 J/m², with cleavage behaviour predominantly controlled by local tensile stress.

In Charpy impact testing, the 7 wt% Nickel steel shows a ductile-to-brittle transition region of -180 °C to -140 °C, with a ductile-to-brittle transition temperature of around -165 °C. The 9 wt% Nickel steel demonstrated superior ductility and fracture toughness, with no ductile-to-brittle transition observed down to -196 °C.

Fracture toughness testing of 9 wt% and 7 wt% Nickel steels was conducted using single-edge notched bending (SENB) specimens at -163 °C. The unloading compliance technique proved reliable for pre-crack length estimation. *J*-resistance curves indicated higher fracture toughness and higher local cleavage stress thresholds for the 9 wt% Nickel steel compared to the 7 wt% Nickel steel, consistent with microstructural observations, as fractography revealed a mixed mode of transgranular cleavage fracture and micro-void coalescence on the fracture surfaces of both Nickel steels.

TABLE OF CONTENTS

LIST OF SYMBOLS

Symbol	Description	Unit
a_0	Initial crack size	mm
a_i	Crack size at force *P(i)*	mm
A_0	Original cross-sectional area before deformation	mm²
C_i	Uncorrected specimen elastic compliance	mm/N
CVN(T)	Fitted absorbed energy at different temperatures	J
D	Half the initial distance between displacement points	mm
E	Young's modulus	GPa
*H**	Initial half-span of load points	mm
J	*J*-integral, a measure of energy release rate per unit crack extension	kJ/m²
J_c	Critical *J*-integral at fracture instability	kJ/m²
J_{Ic}	Critical *J*-integral under plane strain conditions (elastic–plastic fracture toughness)	kJ/m²
K	Stress intensity factor	$MPam^{-1/2}$
K_C	Critical stress intensity factor (general)	$MPam^{-1/2}$
K_{Ic}	Plane strain fracture toughness (Mode I)	$MPam^{-1/2}$
K_{Jc}	Equivalent fracture toughness derived from J_c	$MPam^{-1/2}$
K_{JIc}	Equivalent fracture toughness derived from J_{Ic}	$MPam^{-1/2}$
l	Loading half span	mm
L_0	Original gauge length	mm
ΔL	Extension of gauge length during testing	mm
M	Bending moment	N·mm

n	Work hardening exponent	–
$P(i)$	Force at point i	N
P_Q	Qualified force for fracture toughness calculation	N
R	Fracture distance ahead of the precrack tip	–
SIF	Stress intensification factor	–
T_0	Location parameter	°C
γ_P	Effective surface energy	J/m²
ε	Engineering strain	–
ν	Poisson's ratio	–
σ	Engineering stress	MPa
$\sigma(X_0)$	Stress at cleavage initiation site	MPa
σ_f	Local cleavage fracture stress	MPa
σ_{TS}	Ultimate tensile strength	MPa
σ_Y	Effective yield strength	MPa
σ_{YS}	Yield stress	MPa
σ_{yymax}	Local maximum tensile stress	MPa
σ_{nom}	Nominal bending stress	MPa

CHAPTER 1 – INTRODUCTION

The critical role of steels in the advancement of technology and industry cannot be overstated, particularly in the context of their mechanical properties and resilience under extreme conditions. This thesis focuses on two specific types of steels: SA.738 Gr.B, 9 and 7 %Nickel Steels (all compositional percentages are given in weight percent unless otherwise stated), both of which are renowned for their performance in low-temperature applications.

SA.738 Gr.B, a low alloy steel with high strength and toughness, is widely utilized in the fabrication of pressure vessels and nuclear reactor components, where resistance to brittle fracture is critical. In contrast, Nickel Steels, with its high nickel content, exhibits extraordinary resilience at cryogenic temperatures, making it an ideal candidate for constructing storage tanks for liquefied natural gas (LNG) and other low-temperature applications.

1.1 OBJECTIVES

The primary objectives of this thesis are:

1. To characterize the low-temperature mechanical properties of SA738 Gr.B steel and 9% and 7% Nickel steels, including tensile strength and impact energy.
2. To establish and compare ductile-to-brittle transition behaviour through Charpy impact testing for the selected steels.
3. To evaluate fracture toughness properties by performing blunt-notch fracture stress testing and sharp-crack fracture toughness testing, and to understand cleavage fracture mechanisms.

4. To validate the application of the unloading compliance technique for estimating crack growth in compact tension and single-edge notched bending specimens at cryogenic temperatures.
5. To develop *J*-resistance curves for Nickel steels to better understand their crack growth resistance behaviour. And to compare the mechanical performance of 9% and 7% Nickel steels and evaluate their suitability for cryogenic applications.

1.2 THESIS STRUCTURES

This thesis is organized into three parts. Part 1 provides a review of SA738 Gr.B, 9% Nickel, and 7% Nickel steel, along with a discussion of the microscopic features of steels and the development and understanding of fracture micromechanisms across the ductile, ductile-to-brittle transition, and brittle fracture regions as defined by Charpy impact testing.

Part 2 focuses on the study of SA738 Gr.B steel and includes four chapters. Chapter 3 introduces the material characterization and experimental procedures. Chapters 4 and 5 present the results and discussion of material characterization, tensile testing, Charpy impact testing, microscopic cleavage fracture stress analysis, and fracture toughness testing. Ductile-to-brittle transition curves were established, and transition temperatures were estimated. The unloading compliance method was applied to estimate pre-crack lengths in compact tension (CT) specimens. Detailed investigations were carried out within the transition region for fracture toughness behaviour, and correlations between Charpy impact energy and fracture toughness were discussed using several empirical relationships. Results from blunt-notched and sharp-cracked specimens were compared and analysed. Chapter 6 presents the conclusions drawn from the evaluation of SA738 Gr.B steel at low temperatures and suggests potential future research directions for this material.

Part 3, comprising Chapters 7 and 8, presents the work on 9% and 7% Nickel steels. Chapter 7 details the results and discussion of material characterization, tensile properties, Charpy impact testing, microscopic cleavage fracture stress testing, and fracture toughness evaluation. Comparisons between the 9% and 7% Nickel steels were made. Due to their excellent low-temperature mechanical properties, *J*-resistance curves were developed to better characterize their crack growth resistance. The unloading compliance technique was employed on single-edge notched bending specimens to estimate crack growth during testing. Chapter 8 concludes the findings by evaluating and comparing the low-temperature mechanical performance of 9% and 7% Nickel steels and proposing potential future research directions for these materials.

CHAPTER 2 – A REVIEW OF PREVIOUS WORK ON THE SA.738 GR.B AND TWO NICKEL STEELS AND THE MICROSCOPIC FEATURES AND MICROMECHANISM OF FRACTURE

This chapter provides an in-depth review of the current understanding of the microstructure, mechanical properties, and fracture behaviour of SA738 Gr.B steel and 9% and 7% Nickel steels, with particular emphasis on their performance at low temperatures, as relevant to their critical industrial applications. A review of previous work on the microscopic features and micromechanism of fracture is also provided.

2.1 A BRIEF REVIEW OF SA.738 GR.B STEEL AND ITS APPLICATION

2.1.1 Development of Containment Steels in Nuclear Power Plants

The safety of nuclear power plants relies heavily on the integrity of critical components such as reactor pressure vessels and containment vessels. The containment vessel serves as the final barrier preventing the release of radioactive materials during severe accidents. In early nuclear designs, steels such as SA285 and SA516 Gr.70 were widely employed for containment construction due to their good weldability and availability [1][2]. SA516 Gr.70, a carbon-manganese steel, offers moderate strength (around 485 MPa ultimate tensile strength) and acceptable fabrication characteristics; however, its fracture toughness at subzero temperatures is limited, and thick sections generally require mandatory post-weld heat treatment (PWHT) to ensure adequate performance [2].

More advanced alloy steels such as SA508 Gr.3 were introduced later. SA508 Gr.3 steel is a quenched and tempered Mn-Mo-Ni alloy steel that offers higher tensile strength (approximate 620 MPa) and excellent toughness [3]. However, SA508 Gr.3 steel is generally more sensitive to irradiation embrittlement over time and requires stricter quality control, making it less ideal for large, thick-walled containment vessels where long-term structural integrity under both operational and accident conditions is important [4].

In response to these challenges, SA738 Gr.B was developed to provide a superior balance of strength, low-temperature toughness, weldability, and fabrication flexibility. This steel, specified under ASTM A738/A738M, combines a tempered martensitic microstructure with stringent cleanliness requirements to achieve both high strength and exceptional fracture resistance [5].

These improvements have enabled SA738 Gr.B to be adopted in Generation III and III+ nuclear reactor designs, such as the Westinghouse AP1000 and the APR1400, where safety margins against brittle fracture must be conservatively maintained [6][7]. The material's excellent mechanical properties, combined with its robust performance in fracture toughness testing, ensure that it can resist crack initiation and propagation even under the severe conditions associated with design-basis accidents. As a result, SA738 Gr.B has emerged as a well-balanced and reliable material for modern containment vessels, addressing both historical shortcomings and the evolving safety standards of the nuclear industry.

2.1.2 Chemical Composition and Typical Heat Treatment

SA738 Gr.B steel's remarkable mechanical attributes arise from a meticulously controlled chemical composition featuring carbon (C), manganese (Mn), nickel (Ni), molybdenum (Mo), chromium (Cr), vanadium (V), and niobium (Nb) [5]. Carbon content is carefully restricted

(typically below 0.20%) to prevent excessive brittleness, while Mn, Ni, Mo, and Cr substantially improve toughness, strength, and hardenability.

The heat treatment applied to SA738 Gr.B typically involves quenching and tempering processes, designed to achieve an optimized tempered martensitic microstructure. The steel is commonly austenitized at approximately 900 °C, followed by water quenching to form martensite. In the as-quenched state, SA738 Gr.B exhibits a fine lath martensitic microstructure. After tempering, the matrix consists of fine ferrite laths with uniformly dispersed carbides, typically Fe_3C and vanadium-rich MC carbides, which act to pin dislocations and grain boundaries [8]. Subsequent tempering at temperatures between 600-670 °C refines this martensitic structure, precipitates fine carbides, and thus significantly enhances toughness and ductility while retaining high strength levels [6]. Li et al. emphasized that tempering at approximately 630-670 °C provides the ideal balance between strength and toughness, beyond which brittleness may become pronounced due to formation of coarse carbides or martensitic islands [8]. A more detailed review of the influence of chemical compositions and heat treatment on the mechanical properties will be discussed in section 2.3.

2.1.3 Low Temperature Mechanical Properties

The specified minimum mechanical properties for SA738 Gr.B include a yield strength of 345 MPa, tensile strength between 485-620 MPa, and a minimum Charpy V-notch impact energy of 27 J at -45 °C [5]. However, actual values often significantly exceed these requirements. According to Liu et al. [6] and Ohtsubo et al. [7], Charpy impact energies exceeding 200 J were achieved at temperatures between -60 °C and -40 °C, ensuring ductile behaviour under normal and accident conditions. Furthermore, the material can be exempted from post-weld

heat treatment (PWHT) for thicknesses up to 44.5 mm under ASME Code Case N-841, offering fabrication and cost advantages [7].

Fracture toughness measurements further confirm these it's superior mechanical properties under cryogenic environment. Liu et al. [6] investigated the fracture behaviour of SA738 Gr.B plates and reported plane-strain fracture toughness (K_{Ic}) values in the range of 100-300 $MPam^{-1/2}$ at temperatures between -60 and -45 °C, depending on thickness. These high K_{Ic} values reflect the material's strong resistance to cleavage fracture initiation even within the ductile-to-brittle transition region.

2.2 A BRIEF REVIEW OF NI STEELS AND THEIR APPLICATION

2.2.1 Historical Development, Motivation and LNG Applications

The development of nickel steels, particularly those containing 9% Nickel, has been historically motivated by the need to ensure structural integrity at cryogenic temperatures. The beneficial effects of nickel in enhancing low-temperature toughness were recognized early in the 20th century, with systematic studies establishing its ability to refine ferrite grains, lower the ductile-to-brittle transition temperature, and stabilize retained austenite phases [9]. In the 1940s, the International Nickel Company developed a 9% Nickel steel capable of maintaining notch toughness at liquid nitrogen temperatures, eliminating the need for post-weld heat treatment and enabling practical fabrication of cryogenic pressure vessels [9].

The emergence of liquefied natural gas (LNG) storage and transportation technologies in the 1960s accelerated the adoption of 9% Nickel steel, as conventional carbon steels were inadequate for service temperatures around -162 °C [10]. To ensure safety against brittle fracture under such extreme conditions, nickel steels were incorporated into critical structures

such as LNG storage tanks, with 9% Nickel alloys offering superior fracture resistance, even in large welded constructions [11].

The excellent combination of strength, toughness, and reliability provided by 9% Nickel steel was further demonstrated during “Operation Cryogenics”, a landmark experimental campaign conducted in 1960 to validate the safety of cryogenic storage vessels fabricated without post-weld heat treatment [9]. The vessels, pressurized and impacted at liquid nitrogen temperatures, exhibited highly ductile behaviour and remarkable crack arrest capabilities, laying the foundation for wide acceptance of 9% Nickel steel in LNG infrastructure.

More recently, the reliability and performance of 9% Nickel steel have been validated through long-term service experience, exceeding 28 years without major incidents [12]. Over 189 large-scale LNG tanks worldwide were constructed using 9% Nickel steel by the late 1980s, providing empirical evidence that the alloy system can deliver highly dependable performance under severe thermal and mechanical conditions [12]. Their role in enabling the safe and economic storage and handling of LNG has become increasingly important in the context of global energy demands, leading to their designation as a standard material in modern cryogenic applications [10].

Beyond LNG tanks, 9% Nickel steel have been increasingly deployed in spherical LNG ship tanks, aboveground and in-ground storage tanks, and double containment tank designs, offering versatility and compliance with evolving international codes such as API 620, BS 7777, and EEMUA 147 [10].

2.2.2 Classification and Influence of Nickel Content on Microstructure and Properties

Nickel steels are classified according to their nickel content, typically ranging from 3% to 9%. As the nickel content increases, significant microstructural changes are observed. In steels

with 3-5% nickel, bainitic or martensitic structures predominate, but as nickel exceeds 7%, stabilization of retained austenite becomes a critical feature [13].

Nickel plays a critical role in maintaining and enhancing the strength and toughness of the steels, particularly at low temperatures. Acting as a potent austenite stabilizer, nickel promotes and stabilizes the austenitic phase even at room temperature and below, where the face-centred cubic (FCC) crystal structure provides higher ductility due to its greater number of slip systems [13]. Unlike many alloying elements, nickel dissolves uniformly in the iron matrix without forming brittle intermetallic phases, thereby preserving ductility while simultaneously strengthening the steel. The presence of nickel atoms induces lattice distortions that impede dislocation motion, contributing to enhanced strength without a corresponding loss in toughness. As a result, nickel-alloyed steels retain excellent plastic deformability at cryogenic temperatures, making them particularly suited for applications such as LNG storage and transportation where extreme low-temperature resistance is essential.

For electron beam welding, studies revealed that once nickel content exceeded 4%, weld metals exhibited rapid coarsening of prior austenite grains, and the formation of cellular dendritic structures enriched with retained austenite along boundaries [13]. Further increases in nickel content resulted in a morphological transition of retained austenite from discontinuous films to continuous networks, significantly improving impact toughness [13]. This retained austenite contributes to enhanced crack arrest behaviour by promoting energy absorption during fracture processes.

The heat treatment process also plays a crucial role. For 9% Nickel steel, double normalization and tempering treatments are typically applied to refine microstructures and enhance toughness. Nickel's strong influence in suppressing proeutectoid ferrite formation, delaying

martensitic transformation, and promoting fine retained austenite dispersion collectively results in steels with excellent mechanical performance at cryogenic temperatures [9-11].

Furthermore, the reduction of silicon content and the microalloying with elements such as niobium have been reported to substantially improve the heat-affected zone (HAZ) toughness in welded 9% Nickel steel without sacrificing base metal strength [11]. This design innovation enhances the weldability and structural integrity of heavy-section LNG tank plates up to 50 mm thick, even under severe service conditions.

The impact of nickel content on toughness is nuanced. While moderate additions improve toughness by grain refinement and austenite stabilization, excessive amounts, especially combined with improper cooling rates, can lead to undesirable coarse bainite formation and reduced impact resistance [13]. Nevertheless, carefully controlled compositions and thermal treatments have enabled 9% Nickel steels to achieve a remarkable balance of strength, toughness, and weldability essential for LNG applications.

In addition, the retained austenite in 9% Nickel steel acts as a beneficial phase during crack propagation, blunting crack tips and delaying unstable crack growth, thereby enhancing the overall fracture resistance under both static and dynamic loading conditions [13]. X-ray diffraction and electron back-scattered diffraction studies have confirmed that the volume fraction of retained austenite increases progressively with nickel content, contributing significantly to cryogenic toughness [13].

2.2.3 Low Temperature Mechanical Properties

The low-temperature mechanical behaviour of 9% Nickel steel is characterized by excellent strength retention, high fracture toughness, and stable ductile fracture mechanisms. Tensile tests performed at -196 °C demonstrated that the yield strength increased by approximately

20% relative to room temperature conditions, with the elongation to failure remaining relatively stable even under high strain rates [14].

Dynamic tensile testing confirmed that 9% Nickel steel exhibits strong strain-rate hardening behaviour. Shin et al. [14] reported that yield strength increased by up to 33% when the strain rate was raised to 500 s^{-1} at room temperature, and approximately 20% at -196 °C, with minimal loss of ductility. The material's ability to maintain high elongation values at cryogenic temperatures is critical to preventing brittle fracture during impact or accident conditions.

Du et al. [15] observed that at -196 °C, specimens initially fractured along longitudinal planes due to stress triaxiality, followed by a transition to ductile transverse cracking, reflecting significant energy absorption. The fracture surfaces exhibited mixed quasi-cleavage and ductile dimple morphologies, suggesting strong resistance to cleavage initiation even under cryogenic service conditions.

Moreover, impact toughness values in Charpy V-notch testing consistently exceeded the minimum requirements, with absorbed energies well above 27 J at -196 °C. It has been reported that values greater than 50 J are common for properly heat-treated 9% Nickel steels, providing substantial safety margins [9-13]. Studies also indicate that the lateral expansion measured during Charpy testing remains sufficiently high even at subzero temperatures, supporting ductile failure modes under impact conditions.

Fatigue crack growth behaviour at cryogenic temperatures has also been investigated. Studies indicate that fatigue crack growth rates are either similar to or slower than those at room temperature, implying that cyclic loading under service conditions does not significantly accelerate damage progression [9]. For example, wide plate and compact tension specimens

tested at -196 °C displayed crack arrest behaviour and low da/dN rates even at high stress intensity ranges, confirming the outstanding fatigue resistance of 9% Nickel steels [9].

Fracture toughness values are likewise impressive. Plane-strain fracture toughness (K_{IC}) measurements revealed values typically exceeding 300 $MPam^{-1/2}$ at -196 °C in optimized materials [11]. These results demonstrate the material's ability to resist crack propagation even within the ductile-to-brittle transition regime, satisfying strict leak-before-failure criteria specified for LNG tanks.

Welding processes, when properly controlled, do not significantly degrade low-temperature mechanical properties. Electron beam welded joints, for instance, were shown to retain excellent impact and fracture toughness due to minimized heat input and microstructural refinement in the weld metal and heat-affected zones [13]. Welding trials using Ni-based filler metals and controlled heat input parameters have produced joints that exceed minimum toughness requirements for LNG applications, providing further confidence in the suitability of welded 9% Nickel steel structures.

2.3 A REVIEW OF PREVIOUS WORK ON THE MICROSCOPIC FEATURES AND MICROMECHANISM OF FRACTURE

The foundation of steel's diverse utility lies in its microstructure, which is a complex combination of various phases such as ferrite, martensite, bainite and austenite. These phases emerge from the steel's composition and the thermal and mechanical treatments applied during its processing, fundamentally influencing its mechanical behaviours. The alloying effect in steels is another critical area of focus, revealing how the addition of elements such as carbon, manganese, chromium, nickel, and others can manipulate the steel's microstructure and, by extension, its mechanical properties. These alloying elements can alter the transformation

temperatures of the steel phases, adjust the strength and hardness, improve corrosion resistance, and impact the steel's response to heat treatment processes. The intricate balance between enhancing desired properties while mitigating undesirable effects requires a deep understanding of the alloying mechanisms and their impacts on the microstructural evolution of steel.

Furthermore, this chapter also focused on the material behaviours exhibited by steel across different regions of ductility, ductile-to-brittle, and into the brittle fracture region. Fracture mechanics has evolved into an indispensable tool for predicting material failures at the macroscopic level, thus facilitating the creation of engineering design principles. This methodology is distinctively advantageous due to its autonomy from comprehending the microscopic aspects of materials. Such independence is perceived as both an asset and a limitation. On the positive side, the method of fracture mechanics is beneficial as it relies exclusively on the evaluation of material parameters. These parameters can be accurately measured via small-scale experiments conducted in a laboratory environment, thereby simplifying the process of forecasting design parameters for large-scale engineering projects. Conversely, the drawbacks of this approach become apparent through its inability to analyse post-failure scenarios or consider complexities such as the impact of strain rates on failure mechanisms.

Moreover, the inconsistency observed in the results of fracture mechanics experiments, especially in materials characterized by heterogeneous structures, like steels infused with hard second-phase particles or weldments, has sparked a growing interest in the microscopic foundations of fracture. This interest specifically targets the relationship between microscopic fracture mechanisms and macroscopic parameters, such as the critical stress intensity factor

(K_{IC}). The importance of this exploration is shown by the behaviour of materials with body-centred cubic (BCC) structures, which exhibit a wide range of properties. These materials can range from having high toughness and demonstrating slow crack growth, described as "ductile", to displaying low fracture energy and experiencing rapid failure through "brittle cleavage fracture". Such behaviours are influenced by variables including temperature, strain rate, and specimen geometry (stress state), which dictate the transition between ductile and brittle fracture modes. This understanding highlights the complex interplay between macroscopic fracture mechanics and microscopic material behaviour.

2.3.1 Microscopic Features of Steels

2.3.1.1 Martensite

Martensite represents a metastable phase within steel, notable for its diffusionless transformation mechanism. This process involves a shift from the crystal structure of austenite to that of martensite through homogeneous deformation, bypassing the need for atomic diffusion. Its microstructure, characterized by needle-like or plate-like morphology, plays a pivotal role in enhancing the hardness and strength of steel [16]. However, this increase in mechanical properties comes at the cost of reduced ductility.

The formation of martensite is attributed to a shear transformation, which is inherently crystallographic, occurring without the necessity for atoms to diffuse large distances. This transformation is predominantly athermal, capable of taking place at exceedingly low temperatures where atomic diffusion is impractical within the transformation's duration. In the context of steel, martensite is essentially a supersaturated solid solution of carbon within body-centred tetragonal (BCT) ferrite [17]. The diffusionless characteristic of this phase transformation entraps carbon atoms within the iron lattice, engendering considerable internal

stresses. Consequently, while the resulting structure is notably hard, it is also inherently brittle, reflecting the complex interplay between the microstructural characteristics and mechanical properties of martensite.

2.3.1.2 Bainite

Discovered by Davenport and Bain in 1929 [18], bainite is a microstructure that can develop in steels across a broad range of temperatures, either through the isothermal transformation of austenite or during continuous cooling processes. Its formation mechanism, which is displacive much like martensite, aids in reducing the strain energy, facilitating the growth of bainite into thin plates.

Bainite formation typically occurs within a temperature range that lies between the start of Martensite transformation (Ms) and the onset temperature for ferrite formation. This transformation process to bainite takes place as steel cools from its austenite phase region under meticulously controlled conditions. The exact temperature window conducive to bainite formation is significantly influenced by the steel's chemical composition, with elements like carbon, manganese, and silicon playing pivotal roles in adjusting the transformation temperatures.

Bainite can be further differentiated into two distinct categories: upper bainite, which crystallizes at the higher end of the bainite transformation temperature spectrum, and lower bainite, emerging at temperatures nearer to the Ms temperature. Although the precise temperature boundaries for bainite development may vary, they typically appear above the Ms temperature yet beneath the threshold at which pearlite begins to form. This temperature range is characterized by a cooling rate that is insufficiently rapid to allow for martensite formation but is expedited enough to avert the crystallization of pearlite.

Upper bainite, distinguished by its formation at the higher spectrum of the bainitic temperature range, exhibits a needle-like or lath-like morphology. In this formation, cementite typically precipitates between the plates of bainitic ferrite, resulting in a microstructure where carbon-enriched austenite may persist in an untransformed state amidst these plates. This configuration contributes to the unique mechanical properties and microstructural characteristics of upper bainite [19]. Lower bainite develops at the cooler end of the bainitic temperature spectrum and is uniquely characterized by the internal precipitation of cementite within the bainitic ferrite plates, rather than interspersed between them. This microstructural pattern forms due to a quicker diffusion rate of carbon out of the ferrite, which in turn precipitates cementite directly within the plates. The morphological and physical attributes of lower bainite are markedly distinct, showcasing a finer structure attributed to its formation at these reduced temperatures [20].

2.3.1.3 Retained Austenite

Retained austenite, as a result of incomplete transition from austenite to martensite during quenching process, presents in various morphologies such as film-like and blocky appearances. The appearances are significantly influenced by the cooling rate, the alloy's chemical composition, and the heat treatment protocols applied. The research by Matsumura in 1992 [21] showed the positive impact that an optimal volume fraction of retained austenite has on the press formability of high-strength sheet steels, indicating a delicate correlation between the stability of austenite and its morphological features.

The stability of retained austenite, along with its ability to transform into martensite under strain, a phenomenon known as the transformation-induced plasticity (TRIP effect), plays a crucial role in enhancing both the ductility and strength of steels. According to findings by

Chen et al. [22], film-like retained austenite contributes to improved low-temperature impact toughness, while blocky retained austenite boosts the ultimate tensile strength and the capacity for strain hardening. This TRIP effect is instrumental in elevating the mechanical properties of advanced high-strength steels, facilitating an advantageous amalgamation of strength and ductility.

In high nickel steels, such as those (9 % and 7% Nickel steel) considered later in this thesis, the role of retained austenite becomes even more critical due to nickel's austenite-stabilizing effect. The work of Cock et al. [23] emphasizes the role of external factors in dictating the quantity of retained austenite in alloyed steels, underscoring the notion that the mechanical and thermal stability of retained austenite can be meticulously adjusted through specific alloying techniques and heat treatment procedures. This adjustment process influences the steel's overall toughness, strength, and ductility. A high nickel content not only facilitates the formation of retained austenite but also affects its stability during mechanical deformation, potentially amplifying the TRIP effect and thereby improving the material's comprehensive performance characteristics. In general, the higher content of nickel leads to a greater amount of retained austenite which results in the better mechanical performance at low temperatures.

2.3.1.4 Martensite-Austenite Constituents

The toughness of steel can be significantly affected by the presence of "local brittle zones", which often comprise a mix of untempered martensite and retained austenite, collectively referred to as "martensite-austenite (M-A) constituents". These M-A constituents are prevalently identified within welded joints, as the heat generated by welding promotes their formation. The existence of M-A phases in various contexts is considered a critical factor adversely impacting the toughness of steel [24].

The formation of M-A constituents within granular bainite has been thoroughly investigated by researchers [25]. During the formation of sub-unit grains in granular bainite, excess carbon is expelled into the surrounding retained austenite. This gradual accumulation of carbon in the retained austenite reaches a tipping point, rendering the austenite-to-bainite transformation thermodynamically unfavourable. When the carbon-enriched austenite cools to temperatures below the martensite transformation temperature, it transforms into martensite. Should any austenite remain untransformed, it evolves into martensite-austenite constituents. The extent of martensite formation is dictated by the critical carbon content of the residual austenite at the cessation of the bainite transformation.

Research findings [26][27][28] indicate that the volume of M-A constituents is a principal factor diminishing material toughness, with additional studies suggesting that the volume fraction of these constituents also plays a significant role in adversely affecting toughness [28][29]. Further investigations into M-A constituents reveal that not only the size but also the shape of M-A constituents crucially influences steel's toughness. Specifically, elongated M-A constituents have been associated with the lowest toughness levels compared to other shapes like "round dot" and massive M-A constituents [30].

Moreover, the reduction in steel toughness is not solely determined by the size, distribution, and morphology of M-A constituents but also by their interaction with the surrounding matrix [24]. Crack initiation is predominantly observed at the interface between coarse M-A constituents and the matrix, highlighting the complex interplay between microstructural features and the mechanical properties of steel [31][32]. This understanding marks the importance of controlling the formation and characteristics of M-A constituents to enhance the

overall toughness of steel, particularly in welded structures where these constituents are commonly formed.

2.3.1.5 Effects of Alloying Elements

Carbon stands as the paramount alloying element in steel, exerting a direct influence on its hardness and strength. By forming iron carbide, carbon enhances the steel's hardness and tensile strength, effectively transforming its mechanical properties. Generally, an increase in carbon content correlates with a steel that is harder and possesses greater strength. However, this enhancement in hardness and strength is often offset by a reduction in ductility and toughness, presenting a trade-off that is critical in the material selection and engineering design processes.

Molybdenum plays an important role in steel alloying by effectively hindering the transformation processes that lead to pearlite and bainite formation. Moreover, the introduction of molybdenum into the alloy composition notably decreases the rate at which dislocations are annihilated. It also decelerates the coarsening of nanometre-scale (Nb,M)C carbides during prolonged tempering at high temperatures. This action contributes significantly to the material's enhanced resilience against softening that typically follows peak hardening, thereby increasing the steel's hardness and strength. Similar to molybdenum, cobalt is also used to improve strength and hardness, especially at high temperatures.

Titanium, vanadium and niobium are effective in refining the grain size of steel as they can form stable compounds, such as nitrides and carbides in steel. These compounds are usually formed early in the steel solidification process or during controlled heat treatments. Their efficacy in pinning grain boundaries is instrumental in inhibiting excessive grain enlargement throughout the heat treatment stages. Owing to their remarkable stability and minimal

solubility in the steel matrix, these particles retain their integrity at elevated temperatures. Consequently, they persist in a dispersed state within the steel, contributing to the uniformity and refinement of the material's microstructure, which, in turn, enhances the mechanical properties of the steel.

Manganese is a critical alloying element in steel, contributing significantly to the modification of steel's structure and its mechanical and physical properties. Its multifaceted role is pivotal in steelmaking due to its deoxidizing, desulfurizing, and alloying properties. Manganese acts as a powerful deoxidizer, reacting with oxygen in the molten steel to form manganese oxides, which then float to the slag. This process is crucial because oxygen in steel can lead to unwanted reactions that weaken the steel's structural integrity. In addition to its deoxidizing capabilities, manganese also plays a role in desulphurization. It binds with sulphur present in the molten steel to form manganese sulphide (MnS), which, unlike iron sulphide, does not cause brittleness at high temperatures. It is worth noting that calcium can also works as deoxidiser and desulphurizer. By forming solid solutions in ferrite, strengthening the steel through solution hardening, manganese also improves the steel's strength, hardness, and wear resistance while maintaining its ductility.

2.3.1.6 Effect of Tempering

Tempering is a crucial heat treatment process for steel, aimed at reducing the brittleness induced by quenching and enhancing mechanical properties such as ductility, toughness, and wear resistance. By heating quenched steel to a sub-critical temperature (150 to 700 °C) and then cooling it, typically in air, tempering transforms some of the hard but brittle martensite into tempered martensite, achieving a more balanced microstructure. This process significantly increases the steel's toughness and ductility, making it more resistant to impacts

and enabling it to deform more before fracturing. It also relieves internal stresses to prevent distortion or cracking, allowing for precise adjustment of hardness to tailor the steel for specific applications.

The tempering temperature directly influences the final properties; lower temperatures maintain higher hardness and strength, ideal for tools, while higher temperatures improve toughness and ductility, suitable for high-stress structural components. Through tempering, steel achieves an optimized balance between hardness, strength, and ductility, making it versatile for a wide range of applications, from engineering components to machinery parts.

2.3.2 Ductile Fracture

Ductile fracture in steels involves a complex interplay of micro-mechanisms that can be comprehensively understood through a detailed examination of the material's microstructure and the applied loading conditions. The process of ductile fracture is typically identified by the presence of a dimpled texture on the fracture surface. This process is typically characterized by three key stages: void nucleation, where microscopic cavities form within the material due to stresses; void growth, where these cavities enlarge as the material continues to deform under stress; and void coalescence, where these enlarged cavities merge to form a crack, leading to the eventual failure of the material [33].

2.3.2.1 Void Nucleation

Void nucleation is the initial stage of ductile fracture, where microscopic voids form within the material. This process is predominantly initiated at the sites of microstructural heterogeneities such as inclusions, second-phase particles, or grain boundaries under stress. Pineau et al. documented the development of the studies of void nucleation [34]. In 1949,

Tipper firstly identified the premature fracture of metals due to the formation of voids at second-phase particles [35]. An early comprehensive examination of this phenomenon by Goods and Brown [36] considered both homogeneous and heterogeneous nucleation, with a special emphasis on the latter's association with second-phase particles and grain boundaries. The initiation of nucleation from large inclusions has been explored in model materials [37] and has been documented using high-resolution X-ray tomography [38]. Within a soft matrix, such as pure aluminium, nucleation primarily occurs through particle decohesion. Conversely, in a harder matrix, exemplified by a structural aluminium alloy, the fracturing of particles is predominantly observed. These mechanisms manifest to varying degrees within engineering materials [39][40].

The critical void nucleation stress (σ_{crit}), which is the minimum stress required to initiate the formation of voids within a material in a ductile material, especially in the vicinity of a second phase particle or inclusion, is a key parameter in understanding the onset of ductile fracture. This critical stress is influenced by both the mean hydrostatic stress and the additional local stress that arises due to strain hardening around the inclusions. The overall critical stress (σ_{crit}) for void nucleation can be conceptually represented by the sum of these stress components [41-44]:

$$\sigma_{crit} = \sigma_{hydro} + \sigma_{local} \tag{2-1}$$

where:

σ_{crit} is the critical void nucleation stress,

σ_{hydro} is the mean hydrostatic stress, and

σ_{local} is the local stress increase due to strain hardening around inclusions.

The mean hydrostatic stress (σ_{hydro}) is a measure of the volumetric stress state and is defined as one-third of the trace of the stress tensor:

$$\sigma_{hydro} = \frac{\sigma_1 + \sigma_2 + \sigma_3}{3} \tag{2-2}$$

where σ_1, σ_2 and σ_3 are the principal stresses.

The local stress (σ_{local}) increases due to strain hardening around inclusions can be more complex to quantify precisely, as it depends on the material's strain hardening behaviour, the geometry and distribution of inclusions, and the overall deformation history. However, it reflects the additional resistance to deformation in regions of the material that have been work-hardened, particularly around stiff inclusions where the local deformation is constrained.

This combined stress criterion acknowledges that void nucleation is not solely a function of the overall stress state but also significantly influenced by the microstructural heterogeneities that can concentrate stress and promote localized plastic deformation leading to void nucleation.

2.3.2.2 Void Growth

Following nucleation, voids grow in response to the applied load, with their growth driven by plastic deformation in the material surrounding the voids. The void growth rate depends on the applied stress and the material's plastic flow properties. The Rice and Tracey model focuses on the ductile growth of voids under triaxial stress states, considering the void growth as a continuum plasticity problem [45]. They derived a formula for the growth rate of an isolated spherical void in a material subjected to triaxial stress states, emphasizing the significant effect

of mean stress or hydrostatic tension on the growth rate. The key equation derived from their analysis is as follows:

$$D = 0.283exp\frac{3\sigma_m}{2\sigma_0} \quad (2\text{-}3)$$

where:

D is the dilatational amplification factor,

σ_m is the mean normal stress, and

σ_o is the yield stress in shear.

This equation reveals that the rate of void growth is exponentially amplified by the ratio of mean stress to yield stress. In essence, this indicates that under higher triaxial tension (higher mean stress), voids in ductile materials grow significantly faster, which could lead to early failure due to the coalescence of these growing voids. It is worth noting that this model is primarily applicable to non-hardening materials, limiting its generalizability to materials that exhibit strain hardening.

2.3.2.3 Void Coalescence

The final stage leading to ductile fracture is void coalescence, where neighbouring voids merge to form a crack that propagates, culminating in material failure. This stage is critically dependent on the void spacing and the material's strain-hardening behaviour. The critical microvoid volume fraction at which coalescence becomes significant can be approached through the McClintock criterion or the Thomason model.

The McClintock criterion focuses on the growth and coalescence of voids based on critical conditions under which the material between the voids fails, leading to coalescence [46]. It emphasizes the role of the material's stress state and the geometric arrangement of voids.

The Thomason model introduces an innovative viewpoint by considering the void volume fraction at which coalescence begins and incorporating this aspect into damage models such as the Gurson–Tvergaard–Needleman (GTN) model [44, 47-49]. This model is especially recognized for its ability to predict the commencement of void coalescence, relying on the critical void volume fraction that signifies the shift to the coalescence phase. Its reliability has been affirmed through experimental comparisons and numerical analyses, showcasing its capability in accurately predicting material failure under various conditions. This includes considering the influence of material strain hardening and stress triaxiality on ductile fracture outcomes. For instance, incorporating Thomason's criterion within the GTN damage model has been proven to precisely identify the critical void volume fraction necessary for coalescence initiation, thus enhancing the accuracy of failure predictions in materials [50].

2.3.3 The Ductile-to-Brittle Transition Region

The ductile-to-brittle transition (DBT) in steels represents a critical shift in the failure mechanism from ductile, characterized by significant plastic deformation, to brittle fracture, which occurs with little to no prior plastic deformation. Steels that exhibit a DBT can fail catastrophically under certain conditions, especially at low temperatures. Understanding the DBT helps in predicting and preventing sudden, brittle failure in steels that are otherwise ductile and tough at higher temperatures. This is crucial for the safe operation of structures and machinery in environments where they might be exposed to low temperatures.

Understanding the mechanisms behind DBT is essential for optimizing the design, processing to modify the steel's composition and heat-treatment in ways that lower the DBT temperature.

This transition is influenced by specimen geometry, strain rate, and the material's microstructural characteristics. In the DBT region, the competition between ductile and brittle mechanisms is closely related to the microstructural barriers to crack propagation and the activation of dislocations.

One seminal model that helps in understanding the propagation of cleavage cracks, particularly in the DBT region, is Cottrell's theory. His studies on the interactions between dislocations and solute atoms, provided a foundational understanding of how impurities can affect the mechanical properties of metals.

2.3.3.1 Limiting Condition for Cleavage Crack Propagation

According to Cottrell, the stress required for a cleavage crack to propagate is influenced by the presence of dislocations, which can blunt crack tips and impede crack growth. Assuming the cleavage is growth controlled, the critical stress can be express as follows [34]:

$$\sigma_f = \frac{2\mu\gamma_s}{\pi(1-\nu)k_y \cdot \sqrt{d}} \tag{2-4}$$

where:

μ is the macroscopic shear modulus,

γ_s is the free energy of a surface exposed by cleavage,

υ is the Poisson’s ratio,

d is the grain size, and

k_y is the coefficient of the Hall-Petch equation predicting the variation of yield strength σ_y with different grain sizes:

$$\sigma_y = \sigma_i + \frac{k_y}{\sqrt{d}} \tag{2-5}$$

where σ_i is the lattice friction stress.

2.3.3.2 Factors Influencing the DBT

Specimen geometry can significantly affect the stress distribution within the material. Sharp corners, notches, and other geometrical discontinuities can cause stress concentration, where stress levels are significantly higher than the average stress in the material. This localized stress can promote brittle fracture, especially at lower temperatures where materials are less ductile. The size and shape of specimens also affect the level of constraint during deformation. In thicker specimens, there is a higher triaxial state of stress, which increases the level of constraint on the material. This higher constraint promotes brittle fracture and results in a higher DBTT. In contrast, in thinner specimens or those with less constraint, the stress state shifts from plane strain to plane stress, which promotes more ductile behaviour. As a result, thinner specimens exhibit a lower DBTT because the material appears more ductile at a given temperature. Furthermore, findings from references [51] and [52] indicated that reducing the size of Charpy specimens leads to a decrease in normalized upper shelf energy due to the smaller volume involved in the fracture process. Given that neither the loading rate nor the notch geometry were adjusted accordingly, these outcomes highlight a clear influence of specimen geometry, rather than purely size, on the impact energy. The observed “size effect”

on ductile fracture documented in these studies warrants further examination due to its significant practical implications.

Several studies have investigated the impact of strain rate on the DBT. For instance, research on ferritic steels has shown that the DBT temperature increases with strain rate. This is attributed to the reduced time available for dislocation movement and creep processes at higher strain rates [53].

Theoretical models, such as the Cottrell-Petch model, have been developed to describe the relationship between yield strength, grain size, and strain rate, providing insight into how these factors influence the DBT. These models support the experimental findings that higher strain rates lead to increased resistance to dislocation motion, thus raising the DBT temperature.

The grain size of steel significantly affects its DBT behaviour. According to the Hall-Petch relationship, finer grains improve the toughness of steel by increasing the yield strength, thereby requiring higher stresses for crack propagation. This shifts the DBT to lower temperatures.

As previous section discussed, elements such as Ni, Mn, and Mo are known to refine the grain size and influence the distribution of inclusions, which can improve toughness and modify the DBT range. Non-metallic inclusions can act as crack initiation sites. Control over the size, distribution, and type of inclusions through steelmaking practices can improve the DBT behaviour. The thermal history of steel, including tempering and cooling rates, influences the dislocation structure and precipitate formation, impacting the DBT region.

The complex interplay of these microstructural factors determines the material's behaviour in the DBT region. Advanced modelling and experimental techniques, including the finite

element method incorporating damage mechanics and micromechanical models, are utilized to predict the DBT behaviour of steels under different conditions, aiding in the design of materials with superior fracture toughness.

2.3.4 Cleavage Fracture

2.3.4.1 Griffith Theory and its Extension

A.A. Griffith's seminal work in the 1920s on the theory of brittle fracture marked the beginning of modern fracture mechanics.

Griffith proposed that materials contain inherent flaws or cracks and that the stress concentration at the tip of these flaws could lead to fracture if it exceeded a critical value. His work introduced the concept of fracture toughness and showed that the energy required to create new surface area could predict the failure of brittle materials [54].

Griffith developed an equation relating the critical stress for a crack to propagate to the size of an inherent crack and the material's surface energy, laying the groundwork for later developments in the field. For a pre-existing crack, the concept of Griffith fracture stress in different states is presented by following equations:

For plain stress state:

$$\sigma_f = \sqrt{\frac{2E \cdot \gamma}{\pi a}} \tag{2-6}$$

For plain strain state:

$$\sigma_f = \sqrt{\frac{2E \cdot \gamma}{\pi(1-\upsilon^2)a}} \tag{2-7}$$

where:

E is the Young's modulus,

γ is the surface energy of unit crack area, and

a is half the length of the pre-existing crack.

Griffith also found that in plain stress state, as one of three stresses equals to zero, the following relationship can be derived from Equation 2-6:

$$\sigma_f \sqrt{\pi a} = \sqrt{2E \cdot \gamma} \tag{2-8}$$

It was noticed by Griffith that the right-hand side of the above equation represented a constant value which was strictly controlled by the material's intrinsic property. This constant value indicates the material's resistance to further crack propagation. Conversely, composed of parameters related to the fracture stress and the geometry of the specimen, the left-hand side of the equation should remain constant as well, emphasizing the driving force behind the propagation of a crack [55]. Consequently, the Griffith theory establishes a foundational criterion for the occurrence of fractures within a body containing a crack, serving as a cornerstone for the field of fracture mechanics.

Following Griffith's work, which was established on an ideal brittle body with a crack, further research in the 1940s and 1950s by scientists like Irwin and Orowan expanded the understanding of fracture mechanics to include the behaviour of more ductile materials, which could undergo plastic deformation before fracturing [56][57].

Irwin and Orowan found that it is often necessary for plastic strain to occur locally as a precursor to initiating cleavage fracture for quasi-brittle material like ferrite steels in low temperature environments. Should plastic strain concentrate near the tip of the crack, and if the majority of energy released during crack propagation is consumed by plastic work before instability occurs, then the Griffith theory can be expanded to apply to engineering quasi-brittle materials as follows [58-60]:

For plain stress state:

$$\sigma_f = \sqrt{\frac{2E \cdot (2\gamma + \gamma_p)}{\pi a}} \tag{2-9}$$

For plain strain state:

$$\sigma_f = \sqrt{\frac{2E \cdot (2\gamma + \gamma_p)}{\pi(1 - \upsilon^2)a}} \tag{2-10}$$

where γ_p represents the amount of plastic energy expended per unit length of crack extension.

As the value of 2γ is much smaller than γ_p, the above equations were rewritten by Knott as follows:

For plain stress state:

$$\sigma_f = \sqrt{\frac{2E \cdot \gamma_p}{\pi a}} \tag{2-11}$$

For plain strain state:

$$\sigma_f = \sqrt{\frac{2E \cdot \gamma_p}{\pi(1-\upsilon^2)a}} \tag{2-12}$$

2.3.4.2 Development of Cleavage Fracture

Cleavage fracture is a critical failure mode in materials, particularly in steel, where it occurs through the propagation of cracks along specific crystallographic planes, leading to a brittle fracture. This phenomenon has been the subject of extensive research, leading to the development of various theoretical models that aim to explain the mechanisms and conditions under which cleavage fracture occurs.

Stroh, in 1954, introduced a theory, as schematically illustrated in Figure 2.1 [58], addressing that dislocations at the tip of the slip-band are compressed, thereby generating a normal stress $\sigma_{\theta\theta}$. This stress is responsible for creating a crack nucleus within a second phase particle. Dislocation pile-up leads to increased stress level, and eventually triggers the crack to initiate:

$$\tau_{eff} = \tau_y - \tau_i \geq \sqrt{\frac{E\pi\gamma}{4(1-\upsilon^2)d}} \tag{2-13}$$

where:

τ_{eff} represents the required shear energy,

τ_y is the shear stress,

τ_i is lattice stress,

γ is the effective surface energy of ferrite,

and d is the half-length of slip band.

According to above Equation 2-13, the equilibrium of energy necessary for further crack propagation is considered to be already achieved, assuming that the surface energy is maintained at a constant level. Consequently, the initiation phase of a crack is anticipated to be the most challenging aspect in the process of cleavage, leading to the conclusion that cleavage fracture is predominantly controlled by nucleation [61].

Building upon Stroh's seminal contributions, A.H. Cottrell further refined the understanding of cleavage fractures. His model, developed in the 1950s, underlines the influence of impurities and their interaction with dislocations, introducing the concept known as "cleavage after yielding".

Cottrell's theory suggests that impurities, like carbon in steel, tend to segregate to dislocation lines, thereby hindering plastic deformation of the metal by pinning dislocations. This segregation amplifies the local stress needed to mobilize dislocations, thus increasing the propensity for cleavage fractures under conditions typically conducive to plastic deformation. His model marks the critical role of chemical composition and microstructural integrity in dictating steel's brittleness or ductility, offering guidance for alloy design and thermal treatment strategies to curtail cleavage fractures. A simplified expression showing the interaction between impurities and dislocations is given as follow:

$$\tau = \tau_0 + \frac{Gb}{l} \tag{2-14}$$

where:

τ is the total resolved shear stress required to move a dislocation,

τ_0 is the intrinsic lattice resistance to dislocation movement,

G is the shear modulus of the material,

b is the magnitude of the Burgers vector,

l is the effective distance between pinning points (impurities).

The theoretical landscape of cleavage fracture was further enriched by Smith, who concentrated on the role played by microstructural barriers, such as grain boundaries and second-phase particles, in hindering crack propagation. Introduced in the 1960s, Smith's theory proposes that the resistance to crack advancement significantly relies on these microstructural constituents, serving as obstacles to dislocation movement and crack growth. Smith introduced the concept of "microcleavage", positing that crack propagation navigates a path of least resistance, often bypassing more resistant phases or grain boundaries. His theory accentuates the impact of grain size, shape, and orientation, along with the distribution of second-phase particles, on the cleavage fracture toughness of materials, contributing to the development of steel variants with optimized microstructures for superior fracture resistance. A schematic illustration is shown in Figure 2.2 to describe his theory [62]. Figure 2.2 depicts the formation of a dislocation pile-up within a ferrite grain, which is facilitated by the effective shear stress τ_e and obstructed by a carbide layer at the grain boundary. The application of tensile stress σ_{yy} generates a tensile stress from this pile-up, leading to the initiation of a microcrack within the carbide layer. This microcrack then extends across the particle/grain boundary into the adjacent matrix grain.

In the early 1980s, the Beremin model emerged as a groundbreaking work that provided a statistical approach for forecasting cleavage fractures in steel, focusing on micro-mechanical factors such as the dispersion of microstructural impediments including carbides and

inclusions. This model employs the Weibull statistical distribution to consider the variability in microstructural elements and their effect on fracture toughness. The equation is shown as:

$$P_f = 1 - \exp\left(-\left(\frac{\sigma}{\sigma_u}\right)^m \cdot V\right) \quad (2\text{-}15)$$

where:

σ is the applied stress,

σ_u is the scale parameter related to the critical stress for fracture,

m is the shape parameter reflecting material's sensitivity to stress and microstructural variability,

V is the volume under consideration.

This model marks the statistical aspect of cleavage fracture, acknowledging the inherent variations in microstructural defects that act as nucleation points for cracks.

2.3.4.3 Ritchie, Knott, and Rice (RKR) Model

The foundational connection between the microscopic parameter of cleavage fracture stress (σ_F) and the macroscopic parameter of fracture toughness was established by Ritchie, Knott, and Rice [63]. Following this, Rice and Johnson [64] published a finite element analysis on the stress field preceding a blunting crack, which bore similarities to the analysis of a blunt notch conducted by Griffith and Owen [65]. It was theorized that unstable fracture would occur when stress intensification at the crack tip escalated the maximum principal tensile stress (σ_{yymax}) beyond the microscopic cleavage fracture stress. However, for dimensional accuracy within the model, the existence of a specific distance was necessary. This led to the

introduction of a characteristic distance (x_c), considered to be a microstructurally influenced metric, and estimated to be roughly equivalent to two grain diameters. The RKR model is then expressed as follow [63]:

$$K_{IC} = \frac{1}{\beta^{\frac{n+1}{2}}} \sqrt{x_c \cdot \frac{\sigma_y^{\frac{n+1}{2}}}{\sigma_F^{\frac{n-1}{2}}}} \tag{2-16}$$

The above Equation 2-16 proposed that both the characteristic distance and the microscopic cleavage fracture stress remain unaffected by variations in test temperature. This implies that the temperature dependency of K_{IC} could be anticipated based on an understanding of the material's yield stress (σ_y) and work hardening exponent (n) variations with test temperature. This groundbreaking analysis offered a nuanced perspective on the interplay between microstructural attributes and macroscopic material properties, enhancing our ability to predict material behaviour under different conditions.

2.3.4.4 Linear Elastic Fracture Mechanics (LEFM)

While Griffith's work was focused on brittle fracture, Irwin extended his concepts to ductile materials. Irwin introduced the stress intensity factor (K), which quantifies the stress state at the tip of a crack and linked it to the fracture toughness of materials. The stress intensity factor became a critical parameter in understanding the conditions under which a crack in a material would begin to propagate. Following equations were developed by Irwin using Westergaard's solution, in the linear-elastic condition [66]:

$$\sigma_{xx} = \frac{K_I}{\sqrt{2\pi r}} \left\{ \cos\left(\frac{\theta}{2}\right) \left[1 - \sin\left(\frac{\theta}{2}\right) \sin\left(\frac{3\theta}{2}\right) \right] \right\} \tag{2-17}$$

$$\sigma_{yy} = \frac{K_I}{\sqrt{2\pi r}}\left\{\cos(\frac{\theta}{2})\left[1 + \sin(\frac{\theta}{2})\sin(\frac{3\theta}{2})\right]\right\} \quad (2\text{-}18)$$

$$\sigma_{zz} = \upsilon(\sigma_{xx} + \sigma_{yy}) \quad (2\text{-}19)$$

$$\tau_{xy} = \frac{K_I}{\sqrt{2\pi r}}\left[\sin(\frac{\theta}{2})\cos(\frac{\theta}{2})\sin(\frac{3\theta}{2})\right] \quad (2\text{-}20)$$

$$\tau_{xz} = \tau_{yz} = 0 \quad (2\text{-}21)$$

where:

r is the distance from the crack tip,

θ is the angle relative to the crack plane,

σ_{xx}, σ_{xy} and σ_{yz}, τ_{xx}, τ_{xy} and τ_{yz} are defined in Figure 2.3.

The stress intensity factor K_I under Mode I loading conditions is defined as:

$$K_I = \sigma\sqrt{\pi a} \quad (2\text{-}22)$$

where σ is the remote applied stress and a is the half length of the crack.

Through the analysis of above equations at a designated point (specified by r and θ), it was observed that the stresses are exclusively determined by K_I. Subsequent research has revealed that under Mode I loading conditions, the distributions of stress and strain, along with the crack-tip opening displacement in the regime of small-scale yielding, are predominantly governed by the K_I stress intensity factor.

Consequently, it has been established that the fields surrounding the crack tip in materials under Mode I loading, whether in elastic conditions or small-scale yielding scenarios, are

defined or influenced by K_I. This singular parameter's ability to characterize the stress and strain fields lays the foundation for the principles of linear-elastic fracture mechanics, as outlined by Bates in 1987 [67].

The criterion for a cleavage fracture to be triggered is presented as:

$$K_I \geq K_{IC} \tag{2-23}$$

This equation demonstrates that when the crack-tip field, regulated by K_I, initiates a cleavage fracture when it escalates to a critical field defined by K_{IC}.

2.3.4.5 Elastic-Plastic Fracture Mechanics (EPFM)

While the stress intensity factor K_I, serving as a solitary parameter, dictates the field around the crack tip under Mode I loading, its applicability is restricted to conditions of linear-elasticity and small-scale yielding, as researchers explored materials that did not behave purely elastically at the point of fracture, especially metals that undergo significant plastic deformation [68]. The field of EPFM was then developed.

In the context of elastic-plastic conditions, two parameters have been introduced, functioning similarly to the role of K_I in linear-elastic fracture mechanics.

The first parameter, known as the *J*-integral (referred to simply as *J*), was developed by Rice in 1968 [69]. It is defined as a line integral over a curve Γ that encircles a notch tip, executed in a counterclockwise direction, commencing from the notch's lower surface and concluding on its upper surface, as illustrated by curves $\Gamma 1$ or $\Gamma 2$ in Figure 2.4 [70], given by:

$$J = \int_{\Gamma} \left[w\, dy - T_i \left(\frac{\partial u_i}{\partial x} \right) ds \right] \tag{2-24}$$

where:

Γ is any curve surrounding the notch tip traversing in the anticlockwise direction,

w is the strain energy density, which is defined as $w = \int_0^{\varepsilon_{ij}} \sigma_{ij}\, d\varepsilon_{ij}$,

σ_{ij} and ε_{ij} are the stress and strain tensor,

$T_i = \sigma_{ij}\, n_j$ is the traction vector,

u_i is the are the displacement vector components, and

ds is a length increment along the contour Γ.

In the scenario where a material exhibits elastic-plastic behaviour, the J-integral corresponds to the decrease in potential energy due to an extension in crack length. Thus, it effectively serves as an equivalent to the energy release rate G. The J-integral under Mode I loading condition for a linear elastic body can then be presented as:

$$J_I = G = \frac{(1 - \nu^2) K_I^2}{E} \tag{2-25}$$

A fracture criterion is also developed for stable crack growth:

$$J_I \geq J_{IC} \tag{2-26}$$

The K_{IC} can then be derived from a measured J_{IC}, as:

$$K_{IC} = \sqrt{\frac{E \cdot J_{IC}}{1 - \nu^2}} \tag{2-27}$$

The second parameter, known as crack opening displacement (COD), was proposed by Wells in 1963 as a method to quantify the resistance against ductile cracking, particularly in scenarios of general yielding and beyond [71].

The fundamental criterion for the initiation of a crack is the achievement of a critical strain at the crack tip. Given the challenges in directly measuring the plastic strain at the crack tip, the measurement was instead focused on the opening displacement at the original crack tip, as shown in Figure 2.5 (a) and (b) [72]. This measurement was defined as COD and represented by the symbol δ_{COD}. As shown in Figure 2.5 (c), a 45° COD was also defined [64]. Wells [71] discovered that the COD obtained under different loading conditions could serve as indicators for the prevailing crack-tip field under specific circumstances. In the context of the small-scale yielding regime, the stress and strain within the plastic zones are determined by the ratio R/δ_{COD} (where R represents the original distance from a point to the initially sharp crack tip), applicable to both hardening and non-hardening materials. As a result, by scaling stresses and strains with R/δ_{COD}, their distribution can be graphically represented in relation to COD values.

A failure criterion necessitating a particular mix of stress and/or strain across a microstructural distance suggests failure at a critical δ_{COD} value, which can be expressed as follows:

$$\delta_{COD} \geq \delta_{COD,C} \tag{2-28}$$

In conditions of full plasticity, stress does not scale uniformly with R/δ_{COD} across all geometries. Nevertheless, scaling the stress and strain fields by R/δ_{COD} remains a viable

approach for examining cleavage fracture behaviour. For elastic-plastic condition, the critical value of COD is presented as:

$$\delta_{COD,C} = (\frac{8\sigma_y a}{\pi E}) \ln[\sec \frac{\pi \sigma_F}{2\sigma_y}] \quad (2\text{-}29)$$

where σ_F is the fracture stress at the crack initiation point.

The $\delta_{COD,C}$ value obtained from measurements and the fracture stress σ_F, as predicted by above Equation 2-29 can be employed to assess the fracture toughness of materials that fracture both before and after reaching general yield.

The J_{IC} can also be converted from the fracture toughness and critical COD values in plain strain state, as:

$$J_{IC} = K\sigma_y \delta_{COD,C} \quad (2\text{-}30)$$

It is important to note that unlike a K_{IC} value, the critical COD value applies solely to the initiation of crack growth and does not characterise the moment of complete instability.

CHAPTER 3 – MATERIAL CHARACTERIZATION AND EXPERIMENTAL PROCEDURES OF SA.738 GR.B STEEL

3.1 MATERIAL AND MICROSTRUCTURE

3.1.1 Material and Heat Treatment

The steels studied in this research are SA.738 Gr.B steel, 9% and 7% Nickel steels. The SA.738 Gr.B steel follows the SA-738/SA-738M specification in ASME Boiler and Pressure Vessel Code, Section II, Part A [73]. The 9% and 7% Nickel steels were developed by Baowu Steel for Liquified Natural Gas (LNG) storage applications. Chemical compositions are presented in Tables 3.1, 3.2, and 3.3.

The SA.738 Gr.B steel was supplied in the form of 55 mm thick plate. Two heat treatments (HT1 and HT2) were applied, both consisting of austenization at 900 °C for two hours followed by water quenching and tempering at 630 °C for three hours. The HT2 condition included an additional tempering at 620 °C for 15 hours.

Both 9% and 7% Nickel steels specimens were supplied in the form of 20 mm thick plate. The 9% Nickel steel plate underwent heat treatment involving heating at 820 °C for 51 minutes, followed by water quenching to room temperature, and subsequent tempering at 590 °C for 34 minutes. The 7% Nickel steel underwent a more complex sequence: heating at 820 °C for 60 minutes, water quenching, reheating at 675 °C for 60 minutes, another water quenching, and finally tempering at 590 °C for 60 minutes.

Specimen sampling schemes and orientations for all steel types are detailed in Figures 3.1 and 3.2.

3.1.2 Microstructure

The specimens for microstructure analysis were prepared from T-L (Transverse-Longitudinal) sections of tested Charpy specimens. Specimens were mounted in Bakelite, ground progressively from 120 to 1200 grit SiC papers, polished with diamond solutions (6, 3, and 1 μm), and etched with 2% Nital.

A Keyence VHX-7000 Digital Microscope was used to photograph their microstructures at different magnifications. Appropriate magnifications were selected to make sure their microstructures were clearly visible, and linear intercept method was then used to determine their average grain sizes according to ASTM E112-13 standard [73]. The etched microstructure specimens were also analysed under a JEOL 7000 Field Emission Scanning Electron Microscope (FE SEM) using its Electron Backscatter Diffraction (EBSD) function for grain size and phase area percentage.

3.2 INCLUSION ANALYSIS

Inclusion analysis was carried out on samples which were cut from tested Charpy specimens for all steel types. Images were captured using an XL30-ESEM with INCA EDX at 1000X magnification. Backscatter mode was used to highlight the background of the surfaces, and the inclusions are considered as dark areas. The size and number of the inclusions was measured using the ImageJ software.

3.3 HARDNESS TESTING

Hardness tests was carried out using a Struers DuraScan-5 Microhardness tester with a 5kg load. Specimens were ground and polished before the analysis, starting with 120, 400, 800, 1200 grit SiC papers, and ending with 3 and 1 μm diamond lubricants. Hardness measurements

were taken at 1 mm intervals across the plate thickness, from 2 mm from the top edge toward the centre.

3.4 TENSILE TESTING

3.4.1 Tensile Specimens and Test Procedures

Tensile testing specimens were machined at quarter thickness of the 55 mm thick plate with longitudinal direction of the tensile specimen parallel to the plate transverse direction. The geometry of the specimens follows the ASTM standard E8/E8M-16a: Section 6.4 Round Specimens [74], as shown in Figure 3.3. The specimens used in this study have diameter of 10 mm and gauge length of 50 mm.

Tensile testing was performed to evaluate the mechanical behaviour of the studied steels under varying low-temperature conditions, in accordance with ASTM E8/E8M-16a standard procedures. All tests were conducted in displacement control mode with a constant crosshead displacement rate of 0.5 mm/min.

Prior to testing, specimens were threaded at both ends and mounted into high-strength steel pull rods with matching internal threads. These pull rods formed part of a self-aligning tensile fixture, which incorporated spherical-seated grips retained within hardened steel cages. The spherical interface permitted limited angular adjustment, allowing the specimen to self-align during loading and thereby minimizing bending or eccentric stresses. Specimens were manually screwed into the pull rods until securely seated. Manual tightening was employed to achieve firm engagement without overloading the threads or introducing unwanted pre-stress.

For tests at -196 °C, a Zwick hydraulic testing machine equipped with a 200 kN load cell was used, as shown in Figure 3.4. The specimen was fully submerged in a liquid nitrogen bath

contained within a thermally insulated stainless steel tank mounted to the lower crosshead. The test was initiated while the specimen remained submerged to ensure uniform temperature conditions. Due to the limitations of extensometer operation at this temperature, strain was estimated from crosshead displacement data.

For tests conducted at temperatures equal to or above -170 °C, an Instron low-temperature chamber integrated into a Denson-Mayes (DMG) screw-driven testing machine with a 100 kN load capacity was used, as shown in Figure 3.5. The temperature within the chamber was regulated via the controlled discharge of liquid nitrogen and monitored continuously using a calibrated type T thermocouple affixed at the midpoint of the specimen gauge length. A low-temperature-compatible external extensometer was attached to the specimen to record strain throughout the test.

All specimens were held at the target test temperature for at least 20 minutes prior to loading to ensure thermal equilibrium. Load and displacement data were continuously recorded during each test using the respective machine's data acquisition system.

Following fracture, specimens were immediately submerged in acetone to preserve the fracture surfaces and to minimize oxidation or moisture absorption. Once the specimens returned to room temperature, they were gently dried using a low-temperature air stream. Fractographic analysis was subsequently performed using a Philips XL30 scanning electron microscope to examine the fracture mechanisms.

Tensile testing was carried out over temperature ranges representative of the steels' service environments. For SA.738 Gr.B steel, testing was conducted from -196 to -60 °C. For 9% and 7% Nickel steels, tensile tests were performed at -196, -170, -150, and -130 °C, reflecting their use in cryogenic applications such as LNG storage.

3.4.2 Data Analysis Procedures

The engineering stress σ and engineering strain ε can be calculated using the following equations:

$$\sigma = \frac{F}{A_0} \tag{3-1}$$

and,

$$\varepsilon = \frac{L - L_0}{L_0} = \frac{\Delta L}{L_0} \tag{3-2}$$

where:

F is the force applied on the specimen

A_0 is the original cross-sectional area of the specimen before deformation has taken place

L is the successive values of the gauge length during the testing

L_0 is the original value of the gauge length

ΔL is the extension of the gauge length during the testing.

The engineering stress-strain curves can then be plotted using the σ and ε calculated from the equations above. Once the engineering stress-strain curve is plotted, the yield stress σ_y can be obtained from the lower yield point, the uniform (elongation to fracture) and total strain (total elongation) of the specimen can be calculated by drawing lines parallel to the elastic part of the curve across the ultimate tensile strength and fracture point.

Due to elastic and plastic deformation during the testing, the cross-sectional area of the specimens keeps decreasing. The true stress σ_t and true strain ε_t can then be expressed by the following expressions:

$$\sigma_t = \frac{F}{A} \tag{3-3}$$

And,

$$\varepsilon_t = \int \frac{\delta L}{L} \tag{3-4}$$

The true stress and true strain can then be defined by engineering stress and engineering strain as follow:

$$\sigma_t = \frac{F}{A} = \frac{F}{A_0} \cdot \frac{A_0}{F} = \frac{F}{A_0} \cdot \frac{L}{L_0} = \sigma(1 + \varepsilon) \tag{3-5}$$

And,

$$\delta\varepsilon_t = \frac{\delta L}{L} \tag{3-6}$$

Integrate both sides and apply the boundary conditions,

$$\varepsilon_t = \ln\left(\frac{L}{L_0}\right) = \ln(1 + \varepsilon) \tag{3-7}$$

where ln is the natural log.

In the region of uniform plastic deformation, the flow curve can be defined by the Hollomon equation [75]:

$$\sigma_t = k \cdot {\varepsilon_t}^n \tag{3-8}$$

where:

k is the strength coefficient,

n is the work hardening exponent.

To determine the work hardening exponent n, a ln-ln plot of true stress and true strain curve in the region between the yield stress and the ultimate tensile strength can be plotted logarithmically:

$$n = \frac{\ln \sigma_t - \ln k}{\ln \varepsilon_t} \tag{3-9}$$

As the equation above shown, the work hardening exponent n can be calculated as the slope of the true stress and true strain curve.

3.5 CHARPY IMPACT TESTING

3.5.1 Charpy Impact Specimens and Test Procedures

Charpy impact testing complied with ASTM E23-16b standards, with tests conducted on an Instron-Wolpert impact tester (300 J capacity). Specimens have the standard geometry with 10×10 mm^2 cross section, 55 mm length and an accurately machined 2 mm deep V-notch of 0.25 mm root radius in the centre of the specimen, as shown in Figure 3.6 [76]. The tests were carried out on a calibrated Instron-Wolpert Charpy impact testing machine with a 300 J capacity as shown in Figure 3.7.

For SA.738 Gr.B steel, tests were conducted from -196 to -40 °C, whereas tests for the 9% Nickel steel were performed only at -196 °C, and tests for the 7% Nickel steel were carried out from -196 to -80 °C.

For tests performed at -196 °C, temperature was achieved by immersing the specimens into liquid nitrogen. For tests carried out at -100 °C and above, mixtures of ethanol and liquid nitrogen were used as the cooling medium. By controlling the amount of ethanol and liquid nitrogen added into the mixtures, different desired temperatures were achieved within ±1 °C of the desired test temperature. The mixtures' temperature was monitored using a calibrated type T thermocouple. At every testing temperature, the specimens were all submerged into the cooling mixture for 20 minutes (2 minutes per 1 mm of the specimen thickness) and transferred onto the anvils of the impact machine for impact within 5 seconds after being taken out of the mixture according to the ASTM standard [76].

For test temperatures between -196 to -100 °C, the tests were achieved by cooling specimens in liquid nitrogen for 20 minutes and then placed onto a set of spare specimen support anvils for different certain amount of time, which was estimated by temperature-time calibration curves, before transferring onto the Charpy machine for impact. To develop the temperature-time curves, a setup similar to the Charpy testing machine was used as shown in Figure 3.8. This setup has a set of specimen support anvils with the same size as the machine's anvils and it was used to rest the specimen after the specimen was transferred from the liquid nitrogen. The temperature of the calibration specimen was recorded using a set of type T thermocouples inserted in the 5 mm-deep small holes drilled at a location around the notch area as shown in Figure 3.9. An average calibration curve was then established from 5 calibration curves which were obtained based on the same calibration procedure. Five calibration curves and the

average calibration curve are shown in Figure 3.10 and Figure 3.11. The averaged calibration curve was used to estimate the specimen temperature during the tests. For example, to achieve a test temperature of -120 °C, the specimens were transferred to the impact machine for testing 28 seconds after removal from the liquid nitrogen bath.

After testing, the tested specimens were immediately submerged into acetone and removed once reached room temperature, dried using hair dryer for fractographic examination. Fracture surfaces were measured and photographed using a Keyence VHX-7000 Digital Microscope and a Philips XL30 scanning electron microscope. The lateral expansion, ductile thumbnail extension, shear lip size and cleavage area were measured for all broken halves of the Charpy impact specimens. Schematic illustration of the measurement procedures are shown in Figure 3.12. For lateral expansion measurements, the expansion of both sides of the broken halves need to be measured and the maximum expansions of both sides need to be included, as shown in Figure 3.12 (a).

3.5.2 Data Analysis Procedures

Impact data were analysed using Excel with a tanh regression function to generate ductile-to-brittle transition curves, characterizing the transition temperatures from the fitted curves. The tanh function is of the form:

$$CVN(T) = A + B \cdot \tanh\left(\frac{T - T_0}{C}\right) \tag{3-10}$$

where,

CVN(T) is the fitted absorbed energy at different temperatures,

A, *B* are constants used to scale the curve,

(A-B) stands for the lower shelf energy,

(A+B) stands for the upper shelf energy,

T_0 is the location parameter,

C is the gradient parameter of the curves.

The transition temperatures of both conditions were determined as the average of the upper and lower shelf temperatures from the tanh fitting.

3.6 MICROSCOPIC CLEAVAGE FRACTURE STRESS TESTING

3.6.1 Fracture Stress Specimens and Test Procedures

The fracture stress testing was carried out over the temperature range of -196 to -160 °C for the SA.738Gr. B steel, and at -196 °C only for the 9% Nickel steel. The blunt-notched (fracture stress) specimens have a thickness (*B*) of 12.7 mm, width (*W*) of 12.7 mm and length (*L*) of 80 mm. The notch root with radius of 0.25 mm, were carefully machined using diamond grinding process to minimise the residual stress. Two more locating notches, which have a distance of 63.5 mm between them, were also machined centred about the midline of specimen to locate the rollers. The specimen geometry as well as the notch profile is as shown in Figure 3.13. The specimens have the same transverse longitudinal (TL) notch orientation as for the Charpy impact specimens, Figure 3.1. Keyence digital optical microscope was used to examine the notch profiles of the specimens to make sure the notches were precisely machined.

Fracture stress tests were conducted using the four-point bending method at target temperatures of -196 °C, -170 °C and -160 °C. Testing at temperatures above -160 °C was not performed, as it would exceed the temperature range validated by the FEM simulations.

For tests performed at -196 °C, an ESH hydraulic testing machine equipped with a calibrated 100 kN load cell was used. Prior to testing, specimens were fully immersed in a liquid nitrogen bath contained within a custom-built, thermally insulated steel tank positioned directly beneath the loading fixture. The bath level was maintained to ensure complete submersion of the specimens throughout the loading process. Once the specimen was fixed onto the four-point bending supports, the load was applied without removing the specimen from the liquid nitrogen, ensuring the specimen temperature remained at -196 °C throughout the test. Load and crosshead displacement data were recorded in real-time using LabVIEW software. The ESH hydraulic machine setup, including the submersion bath and data acquisition system, is shown in Figure 3.14.

For tests conducted at -170 °C and -160 °C, testing was carried out using a DMG screw-driven testing machine equipped with a low-temperature environmental chamber. Specimens were first cooled to the target temperature inside the chamber, which followed the same protocol as described previously for tensile testing, where temperature stabilization was confirmed by monitoring the specimen surface temperature using a type T thermocouple. Once the target temperature was reached and stabilized within ±1 °C, the four-point bending test was initiated.

Both the ESH and DMG testing machines were operated under displacement (stroke) control mode at a constant crosshead speed of 0.5 mm/min. Tests were stopped immediately upon specimen fracture, which was identified by a sudden load drop in the recorded load-displacement curve, often accompanied by an audible noise indicative of unstable crack propagation. Throughout each test, specimen temperature was continuously monitored by attaching a type T thermocouple to specimen surface. Displacement and load data were

synchronized with temperature measurements to allow accurate analysis of fracture conditions. The DMG test setup and low-temperature chamber arrangement are shown in Figure 3.15.

Fractured halves of the specimens were immediately put into acetone to preserve the fracture surfaces and avoid oxidation after testing. After the fractured halves have reached room temperature, they were dried using a hair dryer. Their fracture surfaces were then photographed using a Keyence VHX-7000 Digital Optical Microscope. The fracture surfaces were also examined using an XL30-ESEM with a build-in INCA EDX analysis system, the positions of the cleavage fracture initiation sites, the size and their chemical compositions of inclusions at the initiation sites were analysed while applicable.

3.6.3 Griffith-Owen FEM Analysis

According to the stress analysis conducted by Griffiths and Owen [65], the stress and strain fields surrounding a blunt notch can be determined using finite element method (FEM) analysis. Young's modulus of 2.1×10^5 MPa and Poisson's ratio of 0.28 are obtained from tensile test results and used in the analysis.

The nominal bending stress σ_{nom} at the fracture force P of the test is calculated from the following equation [63]:

$$\sigma_{nom} = \frac{6M}{B(W-a)^2} \tag{3-11}$$

where:

$M = Pl/2$, is the bending moment,

l is the loading half span, which is the distance between the inner and outer rollers,

a is the depth of the notch.

Figure 3.16 depicts the linear relationship between the applied load L and nominal bending stress. As the applied load is linearly proportional to the nominal stress, the relationship estimated from the study can be expressed as:

$$\frac{L}{L_{GY}} = 0.465 \cdot \frac{\sigma_{nom}}{\sigma_{YS}} \tag{3-12}$$

where:

L_{GY} is the general yield load,

σ_{YS} is the yield stress.

Due to the limitation of the present study, the maximum L_{GY}/L is limited to 1.065 for specimen with a geometry of 12.7 × 12.7 × 80 mm^3.

A schematic illustration between the stress intensification factor *SIF* and nominal bending stress is shown in Figure 3.17, which derives from a mathematical expression of the regression:

$$SIF = 0.0615 + 1.8464\left(\frac{\sigma_{nom}}{\sigma_{YS}}\right)^{0.4017} \tag{3-13}$$

The local maximum tensile stress (σ_{yymax}) below the notch root at various loads can then be obtained using the following equation:

$$\sigma_{yymax} = SIF \cdot \sigma_{YS} \tag{3-14}$$

Figure 3.18 depicts the finite element analysis for relationship between *SIF* and the distance below the notch root as a multiple of notch root radius 0.25 mm [65].

Once the distances X_0 between the notch root and initiation location of cleavage is measured from the fracture surfaces, the value of local stress intensification *SIF* can be determined at specific loading conditions from the FEM analysis in Figure 3.18. $\sigma(X_0)$, which is the stress at the cleavage initiation site, can now be calculated using the local *SIF* value.

If an inclusion is present at the initiation site, the local cleavage fracture stress σ_f derived from $\sigma(X_0)$, under the assumption that the critical event involves a penny-shaped crack propagating from the inclusion into the surrounding matrix, can be calculated using the following modified Griffith equation [54]:

$$\sigma_f = \sqrt{\frac{\pi \cdot E \cdot \gamma_P}{(1 - v^2) \cdot 2c}} \tag{3-15}$$

where:

E is the Young's modulus,

γ_P is the effective surface energy,

v is the Poisson's ratio,

$2c$ is the equivalent diameter of the inclusion found at initiation site.

The effective surface energy γ_P can then be estimated from above equation, as follow:

$$\gamma_P = \frac{{\sigma_f}^2 \cdot (1 - v^2) \cdot 2c}{\pi \cdot E \cdot \gamma_P} \tag{3-16}$$

3.7 FRACUTURE TOUGHNESS TESTING

3.7.1 Introduction

Fracture toughness testing was conducted following the procedures outlined in ASTM E1820-17: Section 8 [77], using the unloading compliance method and *J-R* curve evaluation. All tests were performed on a calibrated DMG servo-hydraulic testing machine equipped with a 100 kN load cell and an Instron low-temperature environmental chamber capable of maintaining testing temperatures down to -170 °C within ±1 °C.

For SA738 Gr.B steel, tests were carried out over the temperature range of -120 to -80 °C, to study their fracture toughness property in the ductile-to-brittle transition region. The specimens used were compact tension (CT) specimens in accordance with ASTM E1820-17: Annex A2 [77]. Each CT specimen had a thickness (B) of 25 mm, a width (W) of 50 mm, and pin holes with a diameter of 12.5 mm. Internal knife edges were machined at the top of the notches to accommodate the clip gauge used for recording the notch mouth opening displacement (which also served as the load-line displacement during this testing). The specimen geometry is shown in Figure 3.19.

For 9% and 7% Nickel steels, fracture toughness testing was carried out at a single temperature of -163 °C. The same DMG testing machine and environmental chamber setup were used. The specimens followed the single-edge notched bend (SENB) configuration, as specified in ASTM E1820-17: Annex A1 [77]. The SENB specimens had a width (W) of 32 mm, thickness (B) of 16 mm, and total length of 144 mm, with a centrally machined 12 mm-deep notch having a root radius of 0.08 mm. Internal knife edges were machined at the top of the notches to facilitate accurate placement of the clip gauge. The geometry of the SENB specimens is shown in Figure 3.20.

3.7.2 Fatigue Pre-cracking

All specimens were fatigue pre-cracked at room temperature on an Amsler Vibrophore machine. A maximum stress intensity factor of 25 $MPam^{1/2}$ was applied to limit the fatigue force during the final 1.5 mm of the fatigue crack extension. The total length of the notch and fatigue pre-crack a_0 is approximately 0.45 of the width W of specimen. The fatigue force ratio used for the fatigue pre-cracking was 0.1 which means the minimum load is 1/10 of the maximum load applied on the specimens over the cycles respectively.

Direct current potential drop technique was used to monitor the fatigue pre-cracking. Thin nickel-chromium alloy wires named Brightray were spot welded diagonally on both side of the notch and a current was applied through wires attached to either end of the specimens via screws. The current was adjusted so that the voltage across the notch was set to 200 μV before the fatigue pre-cracking starts. As the current was applied, the temperatures of the specimens would increase which would results in the changes of the voltage readouts. Therefore, the current was applied 20 minutes prior to the fatigue pre-cracking in order to stabilise the sample temperature and the voltage readouts of the specimens. The change in voltage was then utilised as an indication of the fatigue crack extension as the increase of voltage across the notch indicating the decrease of cross-section due to crack extension. The replica method was also used to check the physical crack extension on the surfaces of both sides of the specimens. A cellulose acetate replica slice was softened using acetone and then pressed onto the crack extension area at the notch root for 1 minute. After the acetone dried and the slice became hardened, the crack extension was then replicated on the slice. The slice was examined under an optical microscope and the crack length on the surface was measured.

3.7.3 Test Procedures

Fracture toughness testing for SA738 Gr.B and 9%/7% Nickel steels was performed using the resistance curve method with the elastic compliance technique, following ASTM E1820-17: Section 8.6 [77].

For SA738 Gr.B, Compact Tension (CT) specimens were used, while for 9% and 7% Nickel steels, Single Edge Notch Bend (SENB) specimens were tested in three-point bending with a support span (S) of 128 mm (4W).

After fatigue pre-cracking, initial pre-crack lengths were estimated by conducting at least five unloading/reloading cycles in load control mode at room temperature and test temperatures. For SA738 Gr.B, cycles were performed within a load range of 4-8 kN, and for 9% and 7% Nickel steels, within 3.5-7.0 kN. The applied loading rate was 100 N/s, with a 5-second hold at maximum load during each cycle to minimize load relaxation effects. This procedure generated compliance data necessary for crack length estimation prior to fracture testing.

Cryogenic-compatible type T thermocouples were inserted into the side surfaces of specimens to monitor internal temperatures: 5 mm-deep holes for SA738 Gr.B and 10 mm-deep holes for Nickel steels. After the environmental chamber reached the target temperatures, specimens were held for an additional 20 minutes to ensure stable core temperatures. The temperature difference between specimen cores and chamber control readings was maintained within ±1 °C.

Fracture toughness testing was conducted in clip gauge-controlled displacement mode, with a DG-40 clip gauge applied between the knife edges to monitor both notch mouth opening displacement and load-line displacement. A loading rate of 4 μm/s and an unloading rate of 3 μm/s were used throughout. For SA738 Gr.B steel, loading corresponded to tensile opening

and unloading to partial crack closure, while for Nickel steels, loading corresponded to bending (opening) and unloading to elastic recovery. A 5-second hold was maintained between loading and unloading sequences to further eliminate relaxation effects.

During testing, both clip gauge displacement and load were continuously recorded to establish load-displacement curves. These curves were used to calculate crack extensions and J-integral values at various stages, ultimately constructing the *J-R* curves.

Following fracture toughness testing, specimens were immediately submerged in acetone to prevent oxidation and preserve the fracture surfaces. Fracture surfaces were examined using a Keyence VHX-7000 Digital Optical Microscope. To quantify stable crack extension, nine equally spaced measurement lines were drawn across the fracture surface, with the two outer lines positioned 0.005W from each edge (0.25 mm for SA738 Gr.B and 0.16 mm for Nickel steels). The average crack extension was determined by averaging the central seven measurements with the average of the two near-surface measurements, as illustrated in Figure 3.22.

For additional verification, estimated initial and final crack extensions from compliance data were compared with actual measured values. The differences were used to correct the crack growth estimates at each loading sequence, improving the reliability of crack extension data used to establish the final *J-R* curves.

Additionally, fracture surfaces were examined under an XL30-ESEM equipped with an INCA EDX analysis system to identify the chemical composition of inclusions at crack initiation sites, where applicable.

3.7.4 Result Analysis

3.7.4.1 SA738 Gr.B Steel CT Specimens

3.7.4.1.1 Determination of Stress Intensity Factor *K* and *J* integral

Following the ASTM standard E1820-170: Annex A2 [77], for compact tension (CT) specimens at a force $P_{(i)}$, the value of the stress intensity factor $K_{(i)}$ can be calculated as follows:

$$K_{(i)} = \frac{P_{(i)}}{B \cdot W^{1/2}} f(\frac{a_i}{W}) \tag{3-17}$$

where a_i is the crack size at force $P_{(i)}$ and

$$f\left(\frac{a_i}{W}\right) = \frac{(2+\frac{a_i}{W}) \cdot [0.886 + 4.64\left(\frac{a_i}{W}\right) - 13.32\left(\frac{a_i}{W}\right)^2 + 14.72\left(\frac{a_i}{W}\right)^3 - 5.6\left(\frac{a_i}{W}\right)^4]}{(1-\frac{a_i}{W})^{3/2}} \tag{3-18}$$

Based on the load versus clip gauge displacement curves, the crack size can be calculated using the following equations:

$$\frac{a_i}{W} = 1.000196 - 4.06139u + 11.242u^2 - 106.043u^3 + 464.335u^4 - 650.677u^5 \tag{3-19}$$

where:

$$u = \frac{1}{[BEC_{c(i)}]^{1/2} + 1} \tag{3-20}$$

$C_{c(i)}$ is the specimen load-line crack opening elastic compliance $(\Delta v/\Delta P)_{(i)}$ on an unloading/reloading sequence corrected for rotation.

Due to the rotation of the pins during tests, the crack size needs to be corrected from the uncorrected crack size values. The uncorrected crack size values a_i calculated from the above equations 3-19 and 3-20 are then used to obtain the corresponding corrected elastic compliances:

$$C_{c(i)} = \frac{C_i}{(\frac{H^*}{R_i}\sin\theta_i - \cos\theta_i)(\frac{D}{R_i}\sin\theta_i - \cos\theta_i)} \tag{3-21}$$

where:

C_i is the measured uncorrected specimen elastic compliance, $(\Delta v/\Delta P)_{(i)}$,

$H^*$is the initial half-span of the load points (centre of the pin holes),

R_i is the radius of rotation of the crack centreline, $(W + a_i)/2$,

D is one half of the initial distance between the displacement measurement points,

$$\theta_i = \sin^{-1}\left(\frac{D + \frac{V_{m(i)}}{2}}{(D^2 + R_i^2)^{1/2}}\right) - \tan^{-1}(\frac{D}{R_i}) \tag{3-22}$$

Where,

$V_{m(i)}$ is the total measured load-line displacement at the beginning of the i-th unloading/reloading sequence.

To consider a result of K as a valid linear-elastic plane strain fracture toughness value of K_{Ic} according to the ASTM standard E399 [78], the value of the specimen ligament size (W-a) needs to satisfy the following expression:

$$W - a \geq 2.5(K/\sigma_{YS})^2 \tag{3-23}$$

where:

σ_{YS} is the 0.2% offset or lower yield stress at corresponding testing temperature.

Otherwise, the results can only be designated as the critical stress intensity factor K_Q at the force P_Q, which is the qualified force obtained from a load-displacement curve.

The plastic zone size ahead of the crack tip of the specimen can then be calculated from the Irwin's approach as follow:

$$r_I = \frac{1}{2\pi}(\frac{K_I}{\sigma_{YS}})^2 \tag{3-24}$$

where r_I is the radius of the plastic zone, K_I is the fracture toughness.

With the calculated stress intensity factor $K_{(i)}$, the J integral at a point corresponding to $a_{(i)}$, $P_{(i)}$ and displacement $v_{(i)}$ on the specimen load versus clip gauge displacement curves can be obtained using follow equations:

$$J_{(i)} = \frac{(K_{(i)})^2(1-v^2)}{E} + J_{pl_{(i)}} \tag{3-25}$$

where:

$$J_{pl_{(i)}} = \left[J_{pl_{(i-1)}} + \left(\frac{\eta_{pl_{(i-1)}}}{b_{(i-1)}}\right)\left(\frac{A_{pl_{(i)}} - A_{pl_{(i-1)}}}{B_N}\right)\right] \cdot [1 - \gamma_{pl_{(i-1)}}\left(\frac{a_{(i)} - a_{(i-1)}}{b_{(i-1)}}\right)]$$

(3-26)

where:

$\eta_{pl_{(i-1)}} = 2.0 + 0.522b_{(i-1)}/W$, and

$\gamma_{pl_{(i-1)}} = 1.0 + 0.76b_{(i-1)}/W$.

The quantity of $A_{pl(i)}$ can be calculated using the following equation:

$$A_{pl_{(i)}} = A_{pl_{(i-1)}} + \frac{\left[P_{(i)} + P_{(i-1)}\right] \cdot \left[v_{pl_{(i)}} - v_{pl_{(i-1)}}\right]}{2} \tag{3-27}$$

where:

$v_{pl_{(i)}}$ is the plastic part of the loading/unloading sequences which equals to $v_{(i)} - P_{(i)}C_{(i)}$.

The elastic-plastic stress intensity factor K_{Jc} value is determined by J_c according to the following equation:

$$K_{Jc} = \left(\frac{E \cdot J_c}{1 - v^2}\right)^{1/2} \tag{3-28}$$

where E is the Young's modulus of the steel, v is the Poisson's ratio.

3.7.4.1.2 Measurement of Crack-tip Opening Displacement

Crack-tip opening displacement (CTOD) at any point on the load-displacement curve can be calculated as follows:

$$\delta_i = \frac{J_i}{m\sigma_Y} \tag{3-29}$$

where:

$$m = 3.62 - 4.21\left(\frac{\sigma_{YS}}{\sigma_{TS}}\right) + 4.33\left(\frac{\sigma_{YS}}{\sigma_{TS}}\right)^2 - 2\left(\frac{\sigma_{YS}}{\sigma_{TS}}\right)^3$$

σ_Y = effective yield strength, $(\sigma_{YS} + \sigma_{TS})/2$

σ_{TS} = ultimate tensile strength.

3.7.4.1.3 Correlations Between the Absorbed Impact Energy and Fracture Toughness

Different correlation methods were developed and used for fracture toughness K_{Ic} estimation at the upper, transition and lower shelf of the ductile-to-brittle transition curve. For the upper shelf region, fracture toughness can be converted using the following equation proposed by Rolfe, Novak and Barsom [79][80] :

$$(\frac{K_{Ic}}{\sigma_{YS}})^2 = 0.64\left(\frac{CVN}{\sigma_{YS}}\right) - 0.0064 \quad (3\text{-}30)$$

This equation was firstly developed for steels with yield stress in the range of 760 to 1700 MPa but was later proved to be applicable to steels with lower yield stress.

Because of the rapid change and scattering of absorbed impact energy in the ductile-to brittle transition region, different methods are used in this study to estimate the fracture toughness for better comparison.

The first method, which is applicable to *CVN* between 3 to 82 J, was proposed by Barsom and Rolfe [80] :

$$K_{Ic} = \sqrt{0.22\, E \cdot CVN^{3/2}} \quad (3\text{-}31)$$

where E is the Young's modulus of the steel in GPa.

Based on the study by Barsom and Rolfe, an empirical formula with relatively smaller acceptable range (7 J < CVN < 68 J) was proposed Corten and Sailors [81] as follow:

$$K_{Ic} = 14.6\sqrt{CVN} \tag{3-32}$$

Similar to what Corten and Sailors developed above but without eliminating of extreme CVN values, Marandet and Sanz developed a correlation for materials with yield stress in the range of 215 to 1100 MPa shown as follow:

$$K_{Ic} = 19\sqrt{CVN} \tag{3-33}$$

Lower bound correlation method, proposed by Roberts and Newton [82], providing a conservative estimation of fracture toughness at both transition region and lower shelf region, is also included:

$$K_{Ic} = 8.47CVN^{0.63} \tag{3-34}$$

These studies also suggest that the T_{28J} and T_{41J}, which are the corresponding temperatures while the absorbed impact energies are at 28 and 41 J respectively, could provide a reliable method of predicting the reference temperature T_0, which is defined as the temperature with the fracture toughness value of 100 MPam$^{-1/2}$.

3.7.4.1.4 McMeeking Stress Distribution Analysis

McMeeking's finite element analysis [83] is used in this study to analyse the stress distribution near the tip of the cracks under different situation. The FEM analysis models of McMeeking for different work hardening exponents, n = 0 and n = 0.1, are used in this study as shown in

Figure 3.23. As shown in these figures, $\sigma_{\theta\theta}$ is the true stress, σ_o is the yield stress from tensile test. R, as mentioned in previous section 2.3.4.5, equals to the fracture distance ahead of the precrack tip, as mode I type tensile opening is subjected in this study. δ is the CTOD.

3.7.4.2 9% and 7% Nickel Steels SENB Specimens

For Single-edge Notched Bending (SENB) specimens, the whole calculation process of J follows the ASTM standard E1820-170: Annex A1 [77]. Before the calculation of J, the value of the stress intensity factor $K_{(i)}$ at a force $P_{(i)}$ needs to be calculated first as follows:

$$K_{(i)} = [\frac{P_{(i)} \cdot S}{(BB_N)^{1/2} \cdot W^{3/2}}] f(\frac{a_i}{W}) \tag{7-11}$$

where B_N is the minimum thickness measured at the roots of the side grooves, and in this case $B_N = B$; a_i is the crack size at force $P_{(i)}$ and

$$f\left(\frac{a_i}{W}\right) = \frac{3(\frac{a_i}{W})^{1/2} \cdot [1.99 - (\frac{a_i}{W})(1 - \frac{a_i}{W})(2.15 - 3.93\left(\frac{a_i}{W}\right) + 2.7\left(\frac{a_i}{W}\right)^2]}{2[1 + 2\left(\frac{a_i}{W}\right)](1 - \frac{a_i}{W})^{3/2}} \tag{7-12}$$

Then calculate J integral at a point corresponding to $a_{(i)}$, $P_{(i)}$ and displacement $v_{(i)}$ on the specimen load versus clip gauge displacement curves, as follows:

$$J_{(i)} = \frac{(K_{(i)})^2(1 - v^2)}{E} + J_{pl_{(i)}} \tag{7-13}$$

where:

$$J_{pl_{(i)}} = \left[J_{pl_{(i-1)}} + \left(\frac{\eta_{pl_{(i-1)}}}{b_{(i-1)}}\right)\left(\frac{A_{pl_{(i)}} - A_{pl_{(i-1)}}}{B_N}\right)\right] \cdot [1 - \gamma_{pl_{(i-1)}}\left(\frac{a_{(i)} - a_{(i-1)}}{b_{(i-1)}}\right)] \tag{7-14}$$

where:

$\eta_{pl_{(i-1)}} = 1.9$, and

$\gamma_{pl_{(i-1)}} = 0.9$.

The quantity of $A_{pl(i)}$ can be calculated using the following equation:

$$A_{pl_{(i)}} = A_{pl_{(i-1)}} + \frac{\left[P_{(i)} + P_{(i-1)}\right] \cdot \left[v_{pl_{(i)}} - v_{pl_{(i-1)}}\right]}{2} \tag{7-15}$$

where:

$v_{pl_{(i)}}$ is the plastic part of the loading/unloading sequences which equals to $v_{(i)} - P_{(i)}C_{(i)}$, and

$C_{(i)}$ is the experimental compliance of corresponding unloading sequence, $(\Delta v/\Delta P)_{(i)}$, corresponding to the current crack size a_i.

The crack size can be calculated from the following equation:

$$\frac{a_i}{W} = 0.0999748 - 3.9504u + 2.9821u^2 - 3.21408u^3 + 51.51564u^4 - 113.031u^5 \tag{7-16}$$

where:

$$u = \frac{1}{\left[\frac{4 \cdot BWEC_i}{S}\right]^{1/2} + 1} \tag{7-17}$$

Therefore, the crack extension Δa during testing can be calculated as follows:

$\Delta a = a_i - a_0$

where:

a_0 is the initial crack size calculated using the compliance obtained from the unloading/reloading compliance prior to the fracture toughness testing.

Once both the J integral and crack extension Δa are calculated, the J-R curves can be established using the least squares fitting method. A linear regression line can be determined in the following form:

$$\ln J = \ln C_1 + C_2 \ln(\frac{\Delta a}{k}) \tag{7-18}$$

where k = 1.0 mm.

J_Q was defined as the intersection of the linear regression line established from above with the 0.2-mm offset line. J_Q can then be qualified as J_{Ic} if the following criteria are met:

Thickness, $B > 10\, J_Q / \sigma_Y$,

Initial ligament, $b_0 > 10\, J_Q / \sigma_Y$.

Where σ_Y is the uniaxial yield strength which equals to the average of the yield stress σ_{YS} and the ultimate tensile strength, σ_{TS}.

With the qualified J_{Ic}, K_{JIc} can be calculated using the following equation:

$$K_{JIc} = \sqrt{\frac{E \cdot J_{Ic}}{1 - v^2}} \tag{7-19}$$

The calculation of the crack-tip opening displacement (CTOD) δ at the point where the specimen failed on the load-displacement curve requires the σ_{YS} must be equal to or larger than

half of σ_{TS}, and in this case all specimens meet this requirement. To calculation the δ_i, the following equation is needed:

$$\delta_i = \frac{J_i}{m_i \sigma_Y} \tag{7-20}$$

where:

$$m = A_0 - A_1\left(\frac{\sigma_{YS}}{\sigma_{TS}}\right) + A_2\left(\frac{\sigma_{YS}}{\sigma_{TS}}\right)^2 - A_3\left(\frac{\sigma_{YS}}{\sigma_{TS}}\right)^3 \tag{7-21}$$

with:

$A_0 = 3.18 - 0.22(a_i/W)$,

$A_1 = 4.32 - 2.23(a_i/W)$,

$A_2 = 4.44 - 2.29(a_i/W)$, and $A_3 = 2.05 - 1.06(a_i/W)$.

CHAPTER 4 – RESULTS FOR SA.738 GR.B STEEL

4.1 MICROSTRUCTURE

Optical microscope and scanning electron microscope (SEM) images of the microstructures for the HT1 and HT2 conditions of SA738 Gr.B steel are presented in Figures 4.1 and 4.2, respectively. The Electron Backscatter Diffraction (EBSD) analysis results are shown in Figure 4.3. In both conditions, the microstructures exhibit a distinct layered morphology, characterized by visible bands of different phases. The majority of the microstructure consists of granular bainite, with a smaller fraction of lath bainite. Additionally, lath-like and blocky clusters of carbides, appearing as lighter contrast features, are observed near the grain boundaries in both conditions.

Based on the linear intercept method according to ASTM Standard E112-13, the average grain size for both conditions were calculated. For HT1 condition, the average grain size is 7.90 μm while the average size of HT2 condition is 9.27 μm. Their grain sizes were also measured using the build-in application from EBSD analysis on the JEOL 7000 FE SEM. For HT1 condition, the average grain size is 7.78 μm with a standard deviation of 1.45 μm. For HT2 condition, the average grain size is 9.11 μm with a standard deviation of 2.15 μm.

4.2 INCLUSION ANALYSIS

4.2.1 Inclusion Size

Figure 4.4 shows the polished surfaces of both HT1 and HT2 conditions under backscattered mode. The results of the inclusion analysis are shown in Figure 4.5 and Figure 4.6 for HT1 and HT2 conditions. In the HT1 condition, more than 80 % of inclusions lie in the 0-1 μm size

range, while roughly 10 % exceed 3 μm. The HT2 condition exhibits a comparable profile: nearly 80 % of inclusions measure 0-1 μm, and about 10 % are larger than 3 μm. The results are summarised from a measurement of 4491 inclusions with a limit of detection of 450 inclusions/mm^2 for HT1 condition and a measurement of 4496 inclusions with a limit of detection of 480 inclusions/mm^2 for HT2 condition. The average equivalent diameters are 0.51 and 0.54 μm for HT1 and HT2 conditions respectively. Both conditions have the inclusion diameters lying in the range of 0.2 to 5 μm. However, the inclusions which have a diameter below 0.2 μm for both conditions were probably not counted as they were not recognizable by the ImageJ software due to resolution limitation.

4.2.2 Chemical Composition of the inclusions

The inclusions were found to have similar chemical compositions for both HT1 and HT2 conditions and two typical examples of inclusions of each condition are shown in Figure 4.7 and Figure 4.8. Most compositions of the inclusions appear to be Calcium, but Aluminium and Titanium were also found for both conditions. Based on Liu and Webler's findings [84][85], the inclusions are likely to be primarily calcium aluminates ($CaO \cdot Al_2O_3$). Where titanium is present, literature also shows a possible progression toward complex Ca-Al-Ti oxides without altering the dominant Ca fraction [86]. Inclusions of varying sizes were analysed in both conditions, showing little variation in their overall chemical composition.

Because HT2 condition underwent only an additional tempering step at 620 °C for 15 h relative to HT1 condition, no appreciable change in inclusion size, morphology, or number density was anticipated. The results of quantitative and compositional inclusion analyses confirmed this assumption, showing that inclusion characteristics remained unchanged.

4.3 HARDNESS TESTS

10 indents with 1 mm intervals of 9 mm long traces were applied on both HT1 and HT2 conditions of the SA738Gr.B steel. Table 4.1 shows hardness results for the HT1 and HT2 conditions. It can be seen that HT1 condition has an average hardness of 191 kg/mm^2 within the region of 187 to 197 kg/mm^2 while the HT2 condition has an average hardness of 184 kg/mm^2 within the region of 178 to 187 kg/mm^2.

4.4 TENSILE TESTS

For the HT1 and HT2 conditions of the SA738 Gr.B steel, tensile tests were carried out between -196 and -60 °C with various specimens tested at each temperature. A total of 15 specimens was tested for each condition. Three specimens were tested at -196 °C, one specimen was tested at -170 and -160 °C respectively for each condition. Two specimens from each condition were tested at temperatures of -140, -120, -100, -80, and -60 °C respectively.

Among early tests, splitting along the longitudinal direction was found at the centre of the specimens prior to final fracture. Therefore, some selective tests, which were performed at -100, -80 and -60 °C, were terminated once the splits were observed during the final stages of the tests. It was noticed that these splitting happened after the achievement of the maximum load plateau and before final fracture. Necking could also be found on these two specimens. The rest of the specimens all fractured after achieving the maximum load plateau and necking.

Some typical specimens tested at different temperatures are shown in Figure 4.09. Fractured specimens and specimens which appeared splitting before final fracture. Different modes of fracture can be found in these figures: HT1-02 and HT2-01 tested at -196 °C, HT1-15 and HT2-16 tested at -60 °C fractured in the middle of the necking region; HT1-06 tested at -

140 °C fractured near the necking region; HT1-04 and HT2-04 tested at -170 °C, HT2-06 tested at -160 °C fractured along the loading direction and perpendicular to the loading direction at the same time. The splitting prior to final fracture can be found on specimen HT1-16 and HT2-15 tested at -60 °C. Although few of these specimens fractured perpendicular to the loading direction after necking, it is still worth noting that most of the specimens tested at and below -140 °C have the appearance of splitting along the loading direction.

4.4.1 Lower Yield Stress and Ultimate Tensile Strength

The gauge cross-section diameters and the area were measured and calculated as shown in Table 4.2 and Table 4.3. Figure 4.10 to Figure 4.11 show the engineering stress-strain curves for HT1 and HT2 conditions of SA738Gr.B steel at different temperatures. The tensile results including the yield stress, ultimate tensile strength, uniform and total plastic elongation are summarized in Table 4.4, Table 4.5 and Figure 4.12 for better comparison.

It can be seen from Table 4.4, Table 4.5 and Figure 4.12 that both HT1 and HT2 conditions show little differences in terms of yield stress and ultimate tensile strength across the temperature range of -196 to -140 °C and the differences become slightly larger when the temperature increase from -140 to -60 °C. However, it can still be noticed that the values of both yield stress and ultimate tensile strength of HT1 condition are slightly higher than HT2 condition at all testing temperatures. Their yield stress and ultimate tensile strength both have the trends of decreasing as the temperature increases while their rate of decreasing also decreases slightly.

For both HT1 and HT2 conditions, their engineering stress appears to decrease to lower yield points after reaching the upper yield points, before climbing up to the ultimate tensile strength

points. Therefore, stress values at the lower yield points of their engineering stress-strain curves are quoted as the yield stress here.

The yield stress decrease from an average of 928 MPa at -196 °C, to 562 MPa at -60 °C for HT1 condition while these values of HT2 condition decrease from 927 MPa at -196 °C to 533 MPa at -60 °C. The ultimate tensile strength decreases from an average of 952 MPa and 947 MPa at -196 °C to 654 MPa and 640 MPa at -60 °C for HT1 and HT2 conditions respectively.

Figure 4.13 shows the comparisons of the uniform and total plastic elongations of HT1 and HT2 conditions. The values of uniform elongation vary from 15.7 to 20.0% for the HT1 condition and from 14.8 to 21.3% for the HT2 condition. Values of total plastic elongation are in the range of 33.3 to 40.1% for the HT1 condition and in the range of 28.5 to 44.8% for the HT2 condition. The HT1 condition has narrower uniform and total plastic elongation ranges than the HT2 condition. The figure also suggests that the testing temperature has very little influence on both of these values.

4.4.2 Work Hardening Exponent

The results of the work hardening exponent *n* for all testing temperatures are summarised as shown in Table 4.4 and Table 4.5 based on Huize's calculation [87]. The work hardening exponent *n* varies between 0.01 to 0.09 for the HT1 condition while the HT2 condition has n values in the range of 0.01 to 0.11.

4.4.3 Fractography of Tensile Specimens

Fracture surfaces of selected specimens were examined using a Keyence digital optical microscope, and representative images are shown in Figure 4.14. For specimens tested at -196 °C, the fracture surfaces exhibit predominantly cleavage features, consistent with brittle

fracture mechanisms. At -120 °C, small regions of matted surface texture, indicative of limited plastic deformation, were observed; however, cleavage fracture remained the dominant mode. As the temperature increased above -80 °C, ductile fracture features, such as microvoid coalescence and fibrous surfaces, became increasingly dominant across the fracture surfaces. It is noteworthy that splitting across the cross-section of the specimens was observed at various temperatures, irrespective of whether the overall fracture mode was cleavage-dominated or ductile-dominated.

The fracture surface of a tensile specimen tested at -196 °C is shown in Figure 4.15. Figure 4.16 shows the fractography of HT2-04 tested at -170 °C. The fracture surface perpendicular to the loading direction shows a cleavage fracture mode. The general appearance of the fracture pattern can be characterized as a “star-shaped” fracture which indicates the dominance of cleavage fracture combining with a small amount of ductile microvoid coalescence. A more in-depth discussion is provided in Section 5.2.

4.5 CHARPY TESTS

4.5.1 Charpy Impact Results

For the HT1 and HT2 conditions of the SA738 Gr.B steel, Charpy impact test results, which include the absorbed impact energy, lateral expansion, ductile thumbnail extension, shear lip size and cleavage area percentage of the tests are presented in Table 4.6 and Table 4.7 and the impact energy values for both HT1 and HT2 conditions are plotted in Figure 4.17 and Figure 4.18 respectively. A combination of the impact energy values for both conditions is plotted in Figure 4.19.

The lowest impact energy was found as low as 2.0 J at -196 °C for both conditions. And as the temperature increasing to -90 °C, the impact energy started to vary from 12.0 to 299.0 J for HT1 condition and vary from 8.5 to 247.5 J for HT2 condition. For tests carried out at and above -60 °C, the impact energy for both conditions appear to reach the maximum capacity (300 J) of the Charpy impact testing machine. A total of 30 specimens were tested between -90 and -60 °C for each condition in order to estimate their ductile-to-brittle transition temperature (DBTT).

Ductile-to-brittle transition curves were fitted using the tanh fitting method mentioned in previous section and the tanh function for HT1 condition is calculated as follow:

$$CVN(T) = 150.5 + 148.5 \cdot \tanh\left(\frac{T + 89.9}{9.4}\right)$$

While the tanh function for HT2 condition is calculated as:

$$CVN(T) = 150.5 + 148.5 \cdot \tanh\left(\frac{T + 85.9}{11.2}\right)$$

Following the above fitting functions, Figure 4.20 and Figure 4.21 depict the tanh fitting of both conditions respectively.

The lower shelf and upper shelf energies are considered to be approximately 2 and 299 J respectively for both conditions. Their estimated DBTT, which is the temperature where the absorbed energy reached the average of the lower shelf and upper shelf energies, as the tanh curves suggested, are -90 °C for HT1 condition and -86 °C for HT2 condition.

A comparison of the ductile-to-brittle transition curves for both conditions is shown in Figure 4.22. Similar lower shelf and upper shelf behaviour, and narrow ductile-to-brittle transition

regions were found based on the fitting curves for both conditions. HT1 condition shows a transition region ranging from -100 to -80 °C while HT2 condition shows a transition region ranging from -96 to -76 °C. Figure 4.22 also shows a ductile-to-brittle transition curve estimated from the combined results from both HT1 and HT2 conditions. Its DBTT was estimated to be -88 °C. It is also worth noting that for both conditions, obvious gaps can be found between impact energy of 50 to 200 J which is in the transition region. Only two and three out of 60 tested specimens were found located in this region for HT1 and HT2 condition respectively.

4.5.2 Charpy Impact Specimen Fracture Surface Overview

Figure 4.23 shows the fracture surfaces for both conditions examined by optical microscope. Fully microvoid coalescence fracture mode can be observed from the specimens tested at temperatures locating in the upper shelf region (above -60 °C) with high impact energy values. Pure cleavage fracture mode can be found at temperatures locating in the lower shelf region (below -110 °C) with low impact energy values. For specimens tested in the transition region, both fracture mechanisms can be found on the fracture surface of the same specimen while the proportion of the brittle fracture area increases with the decrease of testing temperature.

Figure 4.24 to Figure 4.33 shows the scatter plots of temperature and impact energy versus lateral expansion, ductile thumbnail extension, shear lip size and cleavage area percentage for the HT1 and HT2 conditions. As the Instron-Wolpert Charpy impact testing machine only has a capacity of 300 J, the plots with more than 280 J impact energy were removed from these figures to have better estimations.

Figure 4.24 to Figure 4.27 and Figure 4.29 to Figure 4.32 indicate that impact energy has consistent linear relationships with their lateral expansion, ductile thumbnail extension, and

shear lip sizes for both conditions. Separations for these three features in the transition regions similar to the impact energy gaps were also found.

Figure 4.28 and Figure 4.33 depict similar trends for the cleavage area percentage of the fracture surfaces versus temperature and impact energy. 100% cleavage which indicates the lower shelf behaviour was firstly observed at -100 °C for both conditions. Meanwhile, the 0% crystallinity, indicating the upper shelf behaviour, was first observed at -90 °C for the HT1 condition and -80 °C for the HT2 condition.

4.5.3 Charpy Impact Specimen Fractography

Figure 4.34 to Figure 4.38 show some typical fractographies from different specimens tested at various temperatures. Clear river patterns can be observed converging toward locations as the arrows indicate while rectangular frames indicate the possible initiation sites. Inclusion related initiation, matrix cracking and potential martensite-austenite constituents caused matrix cracking were found from these possible initiation sites. Figure 4.38 shows a matrix cracking within cleavage fracture area below the ductile thumbnail region at -90 °C.

Table 4.8 summarised the information of the fracture initiation sites including the fracture initiation reason, fracture distance X_0 (the distance from the end of ductile thumbnail to the cleavage initiation), ductile crack growth, initiator diameter and facet diameter at various temperatures for both HT1 and HT2 conditions, based on the fractography taken by Weichen [88].

Figure 4.39 depicts the ductile crack growth measured from fracture surfaces versus absorbed impact energy for HT1 and HT2 conditions combined. Strong linear relationship between the

ductile crack growth and absorbed energy can be observed, as longer ductile crack growth required higher energy.

Among these fractographies of specimens tested from -196 to -90 °C, their fracture distance X_0 varies from 229 to 693 μm, ductile crack growth ranges from 23 to 3830 μm. The longest ductile crack growth, which is almost 3000 μm longer than the second longest growth, was found on specimen HT2-04 tested at -90 °C with an absorbed impact energy of 192J. However, the fracture distance of this specimen is only 312 μm. The initiator diameter located at the possible initiation sites is in the range of 1.6 to 2.7 μm, while no initiators were found on five of the examined 14 specimens. The facet diameter was measured and varies from 24 to 54 μm.

4.6 MICROSCOPIC CLEAVAGE FRACTURE STRESS TESTING

4.6.1 Test Results

Figure 4.40 to Figure 4.42 show the load-displacement curves of the fracture stress tests for HT1 and HT2 conditions of SA738Gr.B steel at different temperatures. The testing temperatures include -196, -170 and -160 °C for both HT1 and HT2 conditions. The load-displacement curves of specimens tested at -196 °C exhibit significant linear tendency while the curves at -160 °C have relatively less linearity.

The test results including the maximum load, nominal stress and the σ_{nom}/σ_{YS} ratio at -170 and -160 °C for both HT1 and HT2 conditions are given in Table 4.9. All tested specimens fractured at the maximum load which ranges from 50.1 to 57.0 kN for the HT1 condition and ranges from 43.9 to 58.7 kN for the HT2 condition. The nominal stress varies from 2095 to 2384 MPa for the HT1 condition while it is in the range of 1836 to 2455 MPa for the HT2 condition. However, it is found that the σ_{nom}/σ_{YS} ratios have the smallest value of 2.339 and

increase to 3.273 which exceed the validity of finite element analysis model's predictions for both conditions. A maximum σ_{nom}/σ_{YS} ratio of 2.292 and a stress intensification factor of 2.62 predicted by Griffith and Owen is used in this study to produce the predicted maximum principal stress σ_{yymax}.

Based on the results of tests carried out at -170 and -160 °C, three tests were performed for each condition at -196 °C to ensure cleavage fracture before general yield and to obtain valid ratios of σ_{nom}/σ_{YS} for the FEM analysis. The results including the maximum fracture load, calculated nominal stress σ_{nom}, σ_{nom}/σ_{YS} ratios, L/L_{GY} ratios, stress intensification factors and the predicted maximum principal stress σ_{yymax} at -196 °C are summarised in Table 4.10.

All specimens tested at -196 °C fractured at the maximum load which ranges from 29.0 to 33.2 kN for the HT1 condition and ranges from 23.3 to 29.7 kN for the HT2 condition. The nominal stress varies from 1213 to 1388 MPa for the HT1 condition while it is in the range of 974 to 1242 MPa for the HT2 condition.

The maximum values of the σ_{nom}/σ_{YS} ratios are 1.496 and 1.340 for HT1 and HT2 conditions respectively. Therefore, all values of the σ_{nom}/σ_{YS} ratios of both conditions at -196 °C are within the validity of the FEM analysis model.

The stress intensification factor *SIF*, which is derived from the σ_{nom}/σ_{YS} ratio, has ranges of 2.12 to 2.23 and 1.94 to 2.14 for the HT1 and HT2 condition respectively. The σ_{yymax} values for the HT1 condition are in the range of 1965 to 2071 MPa, with a mean value of 2002 MPa and a standard deviation of 49 MPa, while the values of HT2 condition are in the range of 1083 to 1982 MPa, showing a mean value of σ_{yymax} of 1914 MPa and a standard deviation of 79 MPa. The large standard deviation is mainly caused by specimen HT2-07 which has the

lowest maximum fracture load value of 23.3 kN and σ_{yymax} value of 1803 MPa for the HT2 condition.

4.6.2 Fractography

Figure 4.43 and Figure 4.44 show the fracture surfaces of all tested specimens examined under optical microscope. Clean, flat appearance of cleavage fracture can be observed from the fracture surfaces of the specimens tested at -196 °C for both conditions. But more ductile failure is observed with the increasing of test temperature.

The fracture surfaces of the specimens tested at -196 °C were thoroughly examined under the XL30-ESEM with a build-in INCA EDX analysis system. Fractography and corresponding EDX composition analysis of these specimens are shown in Figure 4.45 to Figure 4.56.

The locations of the cleavage fracture initiation sites and their chemical compositions of inclusions at the initiation sites were analysed while applicable. The distance X_0 between these fracture initiation sites and the notch root, the size of inclusion and the cleavage facet size were measured using the ImageJ image processing software.

The initiation sites were managed to locate on all specimens tested at -196 °C as the river patterns converging toward the sites. The information of the initiation sites and the inclusions is summarised as shown in Table 4.11.

The initiation sites were found to be all metallic inclusions. Calcium was found in all inclusions, while aluminium and titanium were also found in some of the inclusions. Calcium and aluminium inclusions have the appearance of spherical shape, while titanium inclusions have the appearance of cuboidal shape as shown in Figure 4.49 and Figure 4.55. It appears that all brittle cleavage fractures were initiated by inclusion cracking for both conditions.

The sizes (diameters) of the inclusions range from 1.8 to 3.2 μm with the fracture distance X_0 varies from 227 to 333 mm for specimens of HT1 condition, while all inclusions have the same diameter of 2.3 μm and X_0 varies from 221 to 365 μm for specimens of HT2 condition. For specimens of HT1 condition, the facet areas where the inclusions located range from 320 to 538 μm^2 and the equivalent diameters range from 20.2 to 26.2 μm. The specimens of HT2 condition have much larger facet areas which range from 970 to 1347 μm^2 and the equivalent diameters range from 35.2 to 41.4 μm.

4.6.3 Cleavage Fracture Stress at Initiation Site

The distance below the notch root as a multiple of notch root radius is calculated based on the fracture distance measure above. The locations of the cleavage fracture initiation sites located within the specimens are plotted on the Griffith-Owen FEM analysis, with the help of corresponding levels derived from the values of σ_{nom}/σ_{YS} ratio.

Figure 4.57 depicts the FEM analysis of stress intensification factor *SIF* versus the ratio of distance below the notch root as a multiple of notch root radius. As shown in the figure, five specimens fall between 0.965 and 1.448 of the σ_{nom}/σ_{YS} levels, while only one specimen locates slight above the largest value of the 1.448 of the σ_{nom}/σ_{YS} level.

The stress intensification factor $SIF(X_0)$ is derived from the FEM analysis shown in Figure 4.57 and used to calculate the cleavage fracture stress $\sigma(X_0)$ at the initiation site. The estimations of stress intensification factor and cleavage fracture stress at the initiation site, comparison with maximum principal stress, are summarised in Table 4.12. The $SIF(X_0)$ was found to be in the range of 2.02 to 2.19 for sites located within HT1 condition, and 1.65 to 2.08 within HT2 condition. The corresponding cleavage fracture stress $\sigma(X_0)$ ranges from 1874 to 2032 MPa with a mean value of 1927 MPa, and 1530 to 1929 MPa with a mean value of

1765 MPa, for HT1 and HT2 conditions respectively. The ratios of $\sigma(X_0)/\ \sigma_{yymax}$ vary from 0.95 to 0.98 for HT1 condition, and 0.85 to 0.97 for HT2 condition.

The effective surface energy is calculated from the local cleavage fracture stress σ_f, which is derived from $\sigma(X_0)$, using the Griffith equation mentioned in previous section (equation 3-15). Table 4.13 summarised the results of inclusion diameter, local cleavage fracture stress and the corresponding effective surface energy calculated from inclusion. The effective surface energy of HT1 condition is found to be in the range of 10.3 to 15.5 J/m^2, and 7.4 to 11.8 J/m^2 for HT2 condition.

Plots of σ_{yymax}, $\sigma(X_0)$ versus the reciprocal square root of the inclusion diameter and equivalent facet diameter at the initiation site are depicted as shown in Figure 4.58. Weak linear correlations are observed due to the limitation of test specimens.

4.7 FRACTURE TOUGHNESS TESTING

4.7.1 Evaluation of Fracture Toughness

Fracture toughness tests were carried out on Compact Tension (CT) specimen for both HT1 and HT2 conditions. A total of 27 fracture toughness tests were performed, with six specimens tested at -120 and -100 °C for each condition at corresponding temperatures. One and two were tested at -80 °C for HT1 and HT2 conditions respectively.

Their load-displacement curves are given in Figure 4.59 to Figure 4.61. As the curves shown, only few unloading/reloading sequences were performed at -120 and -100 °C, while relatively more unloading/reloading sequences were performed at -80 °C before final fracture occurs for both conditions.

The results, including the original crack size a_0, load P_Q and P_{max} during testing, values of K, of the fracture toughness tests at -120, -100 and -80 °C are given in Table 4.14 and Table 4.15. Summary of the K and J values for both HT1 and HT2 conditions are given in Table 4.16.

The measurements of crack lengths show that all specimens have a_0 values within the standard required range 0.45 to 0.7 W with the longest value of 25.97 mm and the shortest value of 24.65 mm. The elastic compliance estimated a_0 and the actual a_0 measured from the fracture surface are listed in the table, and the differences between them range from -0.61 to 0.67 mm. All differences are within the acceptable range according to the standard.

At -120 °C, the J_C values for HT1 and HT2 conditions were measured to be in the ranges of 13.3-48.5 kJ/m^2 and 19.0-32.8 kJ/m^2, respectively. These relatively low J_C values are consistent with brittle cleavage-dominated fracture, where limited energy absorption occurs prior to failure. The low energy values reflect the material's limited capacity for plastic deformation and crack growth at this low temperature.

For tests carried out at -100 °C, the J_C values for the HT1 condition were measured in the range of 33.8-53.0 kJ/m^2, while for the HT2 condition, the J_C values ranged from 15.4-77.0 kJ/m^2.

At -80 °C, a noticeable increase in J_C values was observed, with 63 kJ/m^2 for HT1 condition and 94.4-139.2 kJ/m^2 for HT2 condition. The higher J_C values at -80 °C indicate a greater energy absorption capability before fracture, suggesting increased ductility and more significant plastic deformation ahead of the crack tip. This behaviour is consistent with the expected ductile-to-brittle transition, where fracture resistance improves with increasing temperature. The large scatter in values for HT2 condition at -80 °C also reflects more

variation in local fracture behaviour as the material moves closer to fully ductile tearing mechanisms.

The values of K_Q were estimated to be in the range of 54.9-95.1, 64.7-82.8 and 72.0 MPam$^{-1/2}$ for HT1 condition tested at -120, -100 and -80 °C, respectively. For HT2 condition in the same temperature range, the values are in the range of 66.3-84.8, 58.6-84.6, and 83.0-96.0 MPam$^{-1/2}$, respectively.

For values of K_Q to be qualified as valid linear-elastic plane strain K_{Ic} as the standard required, the values of P_{max}/P_Q need to be smaller than 1.1 and the values of $2.5(K/\sigma_{YS})^2$ need to be smaller than the ligament sizes of specimen. As shown in Table 4.14 and Table 4.15, only three specimens tested at -120 °C and one specimen tested at -100 °C meet the requirements and therefore have the valid values of K_{Ic}. The K_{Ic} has average values of 58.8 and 58.6 MPam$^{-1/2}$ at -120 and -100 °C respectively.

Figure 4.62 shows the plots of K_Q and K_{Jc} values at various testing temperatures. Similar results K_Q and K_{Jc} values are found at the same temperature between HT1 and HT2 condition. At -120 °C, the K_Q and K_{Jc} values are considered to be similar with average values of 72.9 and 75.6 MPam$^{-1/2}$ for HT1 condition and 75.8 and 76.3 MPam$^{-1/2}$ for HT2 condition respectively. However, there are scatters across the test temperatures, due to the variation of the micro-mechanism of fracture in the ductile-to-transition region. At-100 °C, the K_Q and K_{Jc} values have larger differences, with average values of 76.8 and 117.0 MPam$^{-1/2}$ for HT1 condition and 75.6 and 96.5 MPam$^{-1/2}$ for HT2 condition. More distinct differences can be found between the K_Q and K_{Jc} values at -100 and -80 °C, comparing to the difference at -120 °C because more ductile fracture and plasticity is formed during the tests at higher temperatures.

Figure 4.63 and Figure 4.64 show the comparisons of J_C and CTOD for the HT1 and HT2 conditions. Similar J_C values and amount of CTOD can be found while at the same test temperatures. The values of both variables tend to increase as the temperature increases.

4.7.2 Fractography

Figure 4.65 and Figure 4.66 are the fracture surfaces examined under optical microscope for both HT1 and HT2 conditions. More brittle cleavage fracture, with flat, clean appearances, can be found on the surfaces of specimens tested at -120 °C, while relatively larger amount of ductile fracture behaviour is observed as the temperature increases to -100 and -80 °C as the figures show. Fractography examined under SEM of typical specimens are shown in Figure 4.67 to Figure 4.86.

Table 4.17 shows the summary of the fracture initiation sites, including initiation reason, inclusion composition, fracture distance, ductile crack length, inclusion diameter at the initiation site and facet diameter, based on Weichen Xu's fractography and EDX analysis [88].

The initiation reason of 16 examined specimens is inclusion cracking and decohesion at the initiation sites, while the rest 10 specimens initiated with matrix related reasons. The major compositions of those identified inclusions are Calcium and Aluminium, while Titanium, Niobium and Manganese are also found in some of the inclusions.

Figure 4.87 plots the fracture distance X_0 versus initiation reasons of fractures. The fracture distance ranges from 22 to 660 μm for inclusion related initiation while ranges from 49 to 639 μm for matrix related initiation. The figure shows no clear pattern whether the fracture distance is related to the composition of inclusions at the initiation sites. But it seems to have a

significant shorter fracture distance with initiation caused by matrix related reason, as most of the distance is below 121 μm except one specimen fracture at 639 μm.

The ductile crack growth is found to be in similar range for both conditions. At -120 °C, the crack growth is in the range of 3-15 μm, and 5-10 μm for HT1 and HT2 conditions respectively. The crack growth increases as the temperature reaching -100 and -80 °C, with values in the range of 8-70 μm and 3-54 μm for HT1 and HT2 conditions. More scatter of the values is found as the temperatures reaching the transition temperatures.

The equivalent diameter of the inclusion found at the initiation site is in the range of 0.8 to 3.3 μm, and the equivalent diameter of the facet is in the range of 20 to 45 μm. 11 inclusions are found to have the appearance of spherical shape with calcium as major composition. The equivalent diameter of these inclusions ranges from 0.8 to 3.3 μm. The rest five inclusions are found to have sharp-edged cuboidal shape majorly composited of titanium, with diameters between 1.2 to 1.8 μm.

4.7.3 Correlations Between Charpy Impact Energy and Fracture Toughness

Four different empirical correlations with different applied ranges are used for the estimation of the fracture toughness and the reference temperature T_0 for HT1 and HT2 conditions. The results including the T_0 (test) calculated using the master curve procedure from the fracture toughness test results and other empirical estimations are given in Table 4.18. The T_0 (test) values for HT1, HT2 and combination of HT1+2 conditions are from Huize Fan's research [87], with values of -99.9, -100.5 and -100.1 °C respectively, while the estimated reference temperatures are in the range of 95.1 to 101.3 °C.

As the correlation developed by Corten and Sailors only applies for absorbed impact energy within the range of 7-68 J, the data from the tanh fittings and corresponding temperatures are used to establish the correlation between the Charpy impact energy and fracture toughness.

Similar procedures are used on the other three correlations while applied range is required. The curves of four different correlations for HT1, HT2 and combination of HT1+2 conditions and fracture toughness results calculated from tests are shown in Figure 4.88.

4.7.4 Results of McMeeking's FEM Analysis

As the work hardening exponents of both HT1 and HT1 conditions are close to 0.1 according to the tensile results from previous section, the FEM analysis of McMeeking with $n = 0.1$and $\theta = 0$, as shown in Figure 4.89, is used for the calculation of local cleavage fracture stress. As the original FEM stress distribution curve was only estimated to the R/δ ratio of 10, further estimation was done based on the trend of the original curve and extended to a R/δ ratio of 20.

With the fracture distance X_0 measured from the fractographies and the CTOD, the values of R/δ can be calculated as the ratio of X_0/CTOD. The corresponding σ_f/σ_{YS} values can then be estimated from the FEM analysis. Figure 4.90 shows the plots of both conditions located on the McMeeking's FEM analysis. Two specimens from HT2 condition are located before the maximum plateau of the stress distribution curve, which suggests that these two specimens fractured before reaching the maximum principal stress. Four specimens are found exceeding the R/δ ratio of 10, while the rest 20 specimens are located within the range of 2-7.

Table 4.19 and Table 4.20 summarised the fracture distance, CTOD, values of R/δ and σ_f/σ_{YS}, corresponding local cleavage fracture stress σ_f, and the ratios of σ_f/σ_{max}. At -120 °C, the σ_f/σ_{YS} values are in the range of 3.05-3.82 with corresponding σ_f values in the range of 2004-2510

MPa for HT1 condition, while the σ_f/σ_{YS} values are in the range of 2.97-3.74 with corresponding σ_f values in the range of 1892-2382 MPa for HT2 condition. With the σ_{max} estimated from the peak location of the stress distribution curve, the ratios of σ_f/σ_{max} are calculated to be in the range of 0.8-1.0 and 0.78-0.98 at 120 °C for HT1 and HT2 conditions respectively. At -100 °C, the σ_f/σ_{YS} values of most specimens are in the range of 3.60-3.78 with corresponding σ_f values in the range of 2246-2359 MPa for HT1 condition, while one specimen is found to have a σ_f/σ_{YS} value of 2.97 and σ_f value of 1853 MPa. For HT2 condition, the σ_f/σ_{YS} values are in the range of 3.05-3.82 with corresponding σ_f values in the range of 1839-2303 MPa. The ratios of σ_f/σ_{max} are in the range of 0.78-0.99 and 0.8-1.0 at 100 °C for HT1 and HT2 conditions respectively. At -80 °C, the σ_f/σ_{YS} and σ_f values are 3.45, 3.35 and 1998, 1903 MPa for HT1 and HT2 conditions respectively.

By assuming a penny shaped crack at the initiation sites, the effective surface energy can be calculated using the modified Griffith equation stated in previous section. The effective surface energy is only estimated from initiation site with inclusion identified. The results of the effective surface energy with corresponding inclusion diameter and σ_f values are summarised in Table 4.21.

CHAPTER 5 – DISCUSSION FOR SA.738 GR.B STEEL

5.1 INFLUENCE OF MICROSTRUCTURE ON BRITTLE FRACTURE

Fractographic and metallographic analyses show that both HT1 and HT2 are dominated by granular bainite with a minor fraction of lath bainite. Lath-like and blocky carbide clusters with brighter SEM contrast are concentrated along prior-austenite grain and packet boundaries in both conditions. Linear-intercept measurements give average grain sizes of 7.90 μm for HT1 and 9.27 μm for HT2.

Although tensile and Charpy impact data indicate that HT1 and HT2 conditions have similar mechanical properties, subtle differences in microstructure could still influence the intrinsic propensity for brittle fracture.

Granular bainite is intrinsically more prone to cleavage than lath bainite because its ferrite sub-units are equiaxed rather than elongated; the lack of a pronounced lath/packet hierarchy reduces the number of high-angle packet and block boundaries that can arrest an advancing cleavage crack [89]. In both HT1 and HT2 conditions the microstructure is granular-bainite-dominated, so the primary crack-arrest capability must come from grain/packet boundaries rather than lath interfaces. The presence of a minor lath-bainite constituent will locally improve resistance, yet its volume fraction is too small to dominate overall fracture behaviour.

The lath-like and blocky carbides observed at grain and packet boundaries act as double-edged swords. According to the literature, irregular carbide clusters accentuate stress concentration and serve as preferred cleavage-crack nucleation sites, especially at low temperatures [90]. Conversely, a fine, continuous dispersion of carbides inside ferrite laths can impede dislocation motion and raise the effective cleavage strength. The clustered morphology seen

here therefore favours brittle initiation, offsetting any beneficial effect expected from refinement.

The finer grain size of HT1 condition compared with HT2 condition raises the critical cleavage stress according to the Hall–Petch relationship, which can be illustrated by the follow equation:

$$\sigma_y = \sigma_0 + kd^{-1/2} \quad (5\text{-}1)$$

Where:

σ_y is the yield strength of the material,

σ_0 is the inherent or lattice fraction yield strength,

k is a constant which the Hall-Petch coefficient,

d is the average grain diameter.

As both σ_0 and k are material specific constants, the yield stress and tensile strength would be higher if the grain size of the material is smaller.

5.2 TENSILE TESTING

Tensile test results show that the yield stress and tensile strength of both HT1 and HT2 heat treatment conditions decrease gradually while the testing temperature is increasing. The difference in yield stress and tensile strength of these two heat treatment conditions is very limited. At -196 °C, the difference can barely be noticed. The difference in yield stress become more distinct as the temperature become higher. But the same trend is not noticed in tensile strength as the difference maintains a small amount. In general, very similar results are found among the HT1 and HT2 conditions. Their small differences can be attributed to their grain

size difference as the grain size of HT1 condition is smaller than the HT2 condition based on the observations from previous section.

Total elongation (total strain) and elongation to fracture (uniform strain) of both conditions show little change with increasing of the testing temperature. Little difference and no obvious trend can be observed from the plastic strain results of both conditions. The plastic strain was estimated using the measurements of crosshead displacement which could be less accurate than using an extensometer. However, it is still hard to obtain an accurate plastic strain because the failure occurred randomly within the specimen's gauge length as the fracture profiles showed in Figure 4.09. These factors resulted in some scatter in the plastic strain results.

The work hardening exponent *n* was determined by analysing the plastic deformation that takes place between the lower yield point and the point of reaching ultimate tensile strength. As the stress-strain curves of both conditions show typical mild steel behaviour, it is easy to distinguish those two points. Some scatters were found in the work hardening exponent results but in general, similar *n* are found among the two conditions.

5.2.1 Physical Processing During Tensile Tests

During a uniaxial tensile test, the material experiences a progression of deformation stages: initial elastic behaviour, uniform plastic deformation, localized necking, and final fracture. As the material enters the necking stage, the stress state becomes increasingly triaxial due to the geometric constraint in the necked region. This elevated triaxiality raises the hydrostatic component of stress, promoting conditions that may suppress ductile void growth and instead favour brittle fracture modes such as cleavage [91]. Cleavage fracture typically occurs by crack propagation along specific crystallographic planes and is often associated with low temperature, high strain rate, or microstructural embrittlement [91]. In steels such as SA738

Gr.B or 9%Ni steel, cleavage fracture may still occur even after substantial plastic deformation, particularly within the necked zone. This is because the combination of local strain hardening, stress triaxiality, and the presence of microstructural stress concentrators (e.g., inclusions or coarse carbides) can raise the local stress beyond the critical cleavage stress needed to initiate crack propagation [93].

In contrast, other mechanical tests such as the Charpy impact test and fracture toughness test introduce very different loading conditions. The Charpy impact test, for instance, applies a high strain rate load at a notched location, leading to minimal time for plastic deformation to develop before fracture occurs. The notch creates a localized region of high triaxial stress, and the rapid loading suppresses dislocation movement, promoting cleavage fracture in susceptible materials, especially at temperatures below the ductile-to-brittle transition [94]. Similarly, fracture toughness tests, such as those measuring the *J*-integral or CTOD, use pre-cracked specimens subjected to quasi-static loading. In these tests, the sharp crack tip creates a high constraint and localized plasticity zone. Cleavage fracture in such tests typically initiates directly at the crack tip without the development of a necked region, as the global plasticity is limited and the local stress concentration is extremely high [92].

5.2.2 “Star-Shaped” Fracture Pattern

Fractography presented in Figure 4.15 reveals the characteristic “star-shaped” fracture pattern commonly observed on the fracture surfaces of heavily processed high-strength bainitic steels subjected to tensile loading at low temperatures. Cleavage fracture is identified as the primary failure mode, accompanied by limited regions exhibiting microvoid coalescence. According to Li et al. [95], the distinctive "star" shape primarily originates from splitting fractures occurring parallel to the applied tensile load direction. This behaviour is closely associated

with the complex multi-axial stress state developed within the necked region of tensile specimens. Finite element analysis simulations reported in the literature indicate that while the principal tensile stress dominates deformation, lateral tensile stresses, although lower, play a crucial role in initiating and propagating cracks perpendicular to the principal loading axis [95].

Furthermore, Li et al. [95] propose that the occurrence of the star-shaped split fracture pattern is not simply due to inferior mechanical properties in the thickness direction, but rather a consequence of the interplay between texture evolution, grain boundary redistribution, and the localized three-dimensional stress state during deformation. Bainitic steels, characterized by their ferrite-carbide microstructure, exhibit distinct anisotropy due to the alignment of grain boundaries and crystallographic textures under deformation. These microstructural features enhance the susceptibility to cleavage fracture under the multi-axial stress conditions typical in necked tensile regions, particularly at low temperatures where ductility is inherently reduced [95][96].

5.3 CHARPY IMPACT TESTING

5.3.1 Transition Region Behaviour

Both HT1 and HT2 heat treatment conditions show narrow and sharp transition ductile-to-brittle transition region. HT1 condition shows a transition region within the temperature range of -80 to -100 °C and an interval of 20 °C, while the HT2 condition has a less steep slope ranging from -74 to -98 °C with an interval of 24 °C. The ductile-to-brittle transition temperature are -90 and -86 °C for HT1 and HT2 condition respectively. HT1 condition exhibits a lower DBTT than the HT2 condition, but there is only 4 °C difference. The small difference between these two conditions could be ignored as there are some uncertainties

associated to the tanh method used for the estimation of DBTT. Research has found that the scatter of test data in the transition region could affect the accuracy of estimation, which could also be influenced by the presumption of the lower and upper shelf energy [97] [98].

Scatters are observed in the transition region for both conditions. The absorbed impact energy tends to converge toward the borders of the transition region, and the upper and lower shelves. Only a small amount of data is observed between impact energy of 50 to 200 J although 30 specimens were test in the transition region for the best DBTT estimation. This separation in the transition region is possibly attributed to the BCC crystallographic structure, as limited number of slip system makes it less ductile and more prone to cleavage fracture.

According to the fractography results, matrix cracking, inclusion-initiated fracture and matrix cracking with possible M-A-C are the main reasons of failure in transition regions for both conditions. Strong linear relationship between the ductile crack growth and absorbed energy can be observed, as longer ductile crack growth required higher energy as depicts in Figure 4.39.

5.3.2 Lower Shelf and Upper Shelf Behaviour

Figure 4.27 (HT1 condition) and Figure 4.32 (HT2 condition) show that the percentage of cleavage area on the fracture surfaces versus impact energy follows the similar trend to impact energy versus test temperature. 100% cleavage failure is observed on lower shelf and 100% ductile failure is observed on upper shelf. Both conditions have the lowest impact energy of 2 J and the highest impact energy of 299 J, which indicates their similar lower shelf and upper shelf behaviours. Figure 4.24 and Figure 4.29 show that in the lower shelf regions, it seems to have more obvious trends for the lateral expansion to absorbed. Similar trends can also be found in Figures of ductile thumbnail and shear lip size relationships with absorbed energy.

5.3.3 Correlations Between the Impact Energy with Lateral Expansion, Ductile Thumbnail Extension, Shear Lip Size and Cleavage Area Percentage

By measuring the lateral expansion, ductile thumbnail extension and shear lip size, the specimen's absorbed energy and its plastic deformation before fracturing can be estimated. Strong linear relationships are shown between the impact energy with these three features. Larger lateral expansion size and shear lip size indicates the specimens experienced higher impact energy. While the absorbed impact energy is less than 50 J, all specimens have lateral expansion size and shear lip size smaller than 0.5 mm.

As an indication of plastic deformation prior to fracture, the ductile thumbnail extension could show the ability of resisting brittle failure of the specimens. Similar to the correlation between impact energy and lateral expansion and shear lip size, the ductile thumbnail extensions are less than 0.4 mm while the impact energy is lower than 25 J. Higher impact energy results in larger ductile thumbnail extension, reflecting that the specimens underwent substantial ductile deformation, which is also consistent with the correlation between impact energy and cleavage area percentage.

The cleavage area percentage is a measure to quantify the amount of cleavage fracture observed on cross section below the notch root of the specimen. Cleavage fracture surface often exhibits flat and shiny appearance with "river pattern" propagating towards the possible initiation locations. As less cleavage area is observed, more ductile fracture will appear, and the absorbed impact energy will increase. Good correlation is shown between the cleavage area percentage with impact energy and temperature for both conditions.

No identical differences are found between these correlations for both HT1 and HT2 conditions.

5.4 MICROSCOPIC CLEAVAGE FRACTURE STRESS TESTING

5.4.1 The Relationship Between $\sigma(X_0)$ and the Griffith-Owen FEM Analysis

Figure 4.57 depicts the plots of measured initiation sites on the FEM analysis regressions of the ratio of stress versus the distance below notch root. All initiation sites were found to be located within the region of 85 to 100% of the maximum stress, and it even located above 95% of the stress for HT1 condition. This provides compelling proof in favour of the critical stress-controlled conditions necessary for the initiation of cleavage fractures, as a strain-controlled site would be much closer to notch root. Specimen HT2-07 was found to be located very close to the elastic-plastic zone, while the other five specimens were all found to be located close to the elastic-plastic interface. The reason for specimen HT2-07 located close to the elastic-plastic zone could be cause by its lowest fracture load of 23.3 kN, which is plausibly the consequence of the shorted distance from the notch root to inclusion or, the stress concentration caused by the presence of inclusion.

5.4.2 Inclusion Size Relationship with σ_{yymax}, $\sigma(X_0)$ and σ_f

The modified Griffith equation mentioned in previous section (Equation 3-15) suggests a linear relationship between local cleavage fracture stress σ_f and the inclusion size, which is in the form of a reciprocal square root of its diameter. This relationship allows the effective surface energy to be estimated from the slope of the fitting regression, as the rest variables are material related. The reciprocal square roots of inclusion diameter and equivalent facet diameter are plotted as shown in Figure 4.58. There is no strong evidence showing that these variables have strong linear correlation as only limited number of test results were obtained at -196 °C. Different results of γ_P from above plots suggests that other factors could also influence

cleavage fracture as well as the propagation of a microcrack from an inclusion into the matrix [99].

Table 4.13 summarised the values of effective surface energy γ_P calculated from inclusion size for both conditions such that $\sigma(X_0)$ equals to the local cleavage fracture stress σ_f. Figure 4.49 shows the initiation site of fracture stress specimen HT1-09, possibly combined with two different inclusions, spherical calcium inside a cuboidal shape titanium inclusion. In this case, the presence of two different shaped metallic inclusions may result in more complicated microcrack propagating behaviour than the Griffith model could take into consider.

In another example, a lowest cleavage fracture stress σ_f with a value of 1530 MPa, was estimated by the Griffith model for specimen HT2-07 among all results. According to its fractography of Figure 4.51, the cracked inclusion located at the initiation site has a diameter of 2.3 μm, within a cleavage facet with an equivalent diameter of 39 μm. However, a cracked inclusion within HT2-08 with same diameter and chemical composition as HT2-07, but inside a slightly smaller facet (equivalent diameter of 35 μm), which normally has the tendency to reduce the potency, has a much larger σ_f with a value of 1929 MPa as shown in Figure 4.53.

5.4.3 Microstructure Influence on Surface Energy

The effective surface energy measured for the HT1 condition (10.3-15.5 J/m²) was higher than that of the HT2 condition (7.4-11.8 J/m²). This disparity can primarily be attributed to the differences in carbide precipitation and distribution resulting from the distinct tempering processes. The shorter tempering time of the HT1 condition results in finer, more homogeneously dispersed carbides, which enhance crack propagation resistance, thus positively influencing the fracture toughness and associated effective surface energy [89][100]. Conversely, the prolonged tempering in the HT2 condition causes carbide coarsening,

particularly at prior austenite grain boundaries. Coarse carbides are well-known stress concentrators that readily facilitate crack initiation and propagation, thereby reducing the effective surface energy [100][101].

The correlation between microstructural morphology and effective surface energy is widely recognized in the literature. Martensitic microstructures typically exhibit high resistance to crack propagation due to their refined lath structure and high-density grain boundaries that effectively deflect and impede crack paths, thus increasing effective surface energy [89][102]. Bainitic structures, particularly lower bainite, can similarly provide significant crack resistance due to fine carbide dispersions within the ferritic matrix; however, upper bainite, which features coarser carbides at grain boundaries or within ferrite laths, tends to reduce effective surface energy by facilitating easier crack propagation [101][102]. Ferritic microstructures, due to their relatively coarser and softer nature, generally display lower resistance to crack propagation, and thus lower effective surface energies are often observed when compared with tempered martensitic or refined bainitic structures [102][103].

5.4.4 Effect of Test Temperature

Due to the limitations of the FEM analysis, fracture stress values were only calculated for tests carried out at -196 °C. The load-displacement curves for tests performed from -196 to -160 °C, as shown in Figure 4.40 to Figure 4.42, suggest that less linear behaviour is exhibited as the test temperature increases. However, it is assumed that the cleavage fracture is temperature independent, as it follows a critical tensile stress mechanism. A more comprehensive comparison will be discussed in the fracture toughness test section.

5.4.5 Effect of Loading Rate

According to the Charpy impact tests, the lower shelves range below -100 °C for both conditions. The test temperatures involved in the fracture stress tests are significantly away from the transition regions. Based on the fracture surfaces observation, flat, clean brittle cleavage fracture can be found on specimens tested at -196 °C for both Charpy impact and fracture stress tests. But for specimens tested at -170 and -160 °C for fracture stress tests, obvious ductility behaviours are found on their fracture surfaces. This ductility behaviour is even more distinct than the fracture surfaces of specimens tested at -120 °C in Charpy impact tests.

The primary distinction between the two different tests is the loading rate, as Charpy tests involve rapid loading and fracture stress tests undergo quasi-static loading conditions at a much slower rate. Fast loading rate tends to promote brittle fracture because specimens may not have sufficient time for more significant plastic deformation. Conversely, specimens undergo slower loading rate have more time to redistribute dislocations and accommodate the applied load through plastic deformation which lead to ductile behaviour even at the lower shelf of the material.

5.5 FRACTURE TOUGHNESS TESTING

5.5.1 Discussion of Fracture Toughness, *J* integral and CTOD Results

5.5.1.1 Fracture Toughness and *J* integral

The load-displacement curves of specimens tested at -120, -100 and -80 °C show that most curves exhibit a predominantly linear response, with only minor non-linearity prior to catastrophic brittle cleavage fracture. At -120 °C, all specimens failed before reaching a

maximum load plateau, whereas at -100 and -80 °C, a few specimens fractured catastrophically after reaching or slightly beyond the load plateau.

Although J_C was directly measured in this study, fracture toughness is primarily discussed in terms of K_{Jc} to allow easier comparison with conventional K_{Ic} data and to facilitate engineering interpretation, following ASTM E1820 recommendations.

To be qualify as a valid K_{Ic}, several requirements must be satisfied for a conditional fracture toughness value K_Q, according to ASTM E1820. Due to specimen size limitations, only four valid K_{Ic} values were obtained in this study. For most specimens, the remaining ligament sizes (W-a_0) were smaller than the $2.5(K_Q/\sigma_{YL})^2$ criterion required for K_{Ic} validity. Additionally, many specimens exhibited a maximum load (P_{max}) greater than 1.1 times the qualified load (P_Q) at -100 and -80 °C, further limiting the number of valid K_{Ic} values.

Reducing the original crack size, a_0, would increase the ligament size and thus expand the validation range for K_{Ic}. However, the a_0 values must remain within 0.45-0.70W according to ASTM E1820 and achieving the required P_{max}/P_Q ratio remains challenging. The limited number of valid K_{Ic} values is likely due to the ductile-to-brittle transition behaviour exhibited by the steels between -120 and -80 °C. The valid K_{Ic} values obtained were 66.0, 54.9, and 55.4 $MPam^{-1/2}$ for the HT1 condition at -120 °C, and 58.6 $MPam^{-1/2}$ for the HT2 condition at -100 °C.

The K_Q values were also used to calculate the equivalent plastic zone size around the crack tip using Equation (3-24). The equivalent diameters of the plastic zone, summarised in Table 4.22, ranged from 278 to 850 μm across the different test temperatures. Cleavage initiation sites were consistently found within the calculated plastic zone ahead of the crack tip, consistent with brittle fracture initiation behaviour.

Small amounts of ductile crack growth prior to cleavage fracture were observed, supporting the use of the critical *J*-integral, J_C, to characterise fracture toughness under conditions of limited plasticity. As detailed in Section 4.7.2, the measured ductile crack extensions were 3-15 μm for HT1 condition and 5-10 μm for HT2 condition at -120 °C, increasing to 8-70 μm for HT1 condition and 3-54 μm for HT2 condition as the temperature rose to -100 and -80 °C. These small extensions indicate that fracture generally occurred at instability, with only minor stable tearing preceding cleavage.

According to ASTM E1820, J_C represents the critical *J*-integral at fracture instability prior to significant stable crack growth, whereas J_{Ic} characterises the fracture resistance at the onset of stable tearing under plane-strain conditions. In the present study, most specimens exhibited crack extensions much smaller than the 0.2 mm required for a valid J_{Ic} determination. Therefore, the fracture toughness values derived here are more accurately described as J_C and the corresponding K_{Jc} and should not be interpreted as valid J_{Ic} or K_{JIc} values.

The calculated K_{Jc} values, obtained from the corresponding J_C values, represent the local effective stress intensity at cleavage initiation. A comparison between K_Q and K_{Jc}, as shown in Figure 4.62, demonstrates that the difference between K_Q and K_{Jc} becomes more pronounced at higher temperatures, indicating increased plasticity development prior to fracture.

Figure 4.91 illustrates the relationship between J_C and ductile crack growth, revealing a strong positive linear correlation: greater ductile crack growth corresponds to larger J_C values. A similar trend is observed in Figure 4.92, where J_C values are plotted against fracture distances. These results are consistent with the expected behaviour where increased ductile extension provides greater energy absorption before fracture. The cracks initiated when the local stress concentration exceeded the material's local strength, leading to cleavage propagation. Longer

ductile extensions reflect higher energy absorption capability, corresponding to higher J_C values.

As K_{Jc} values are derived from J_C, similar correlations are observed between K_{Jc} and ductile crack growth and fracture distance, as shown in Figures 4.93 and 4.94. Most specimens exhibited fracture distances within 200 μm and corresponding K_{Jc} values below 100 MPam$^{1/2}$. This suggests that fracture is often triggered by microstructural defects, such as inclusions, that are unable to withstand the accumulation of local stress. Local variations in material microstructure or properties may also influence the location and resistance to fracture initiation, as discussed further in the following fractographic analysis section.

5.5.1.2 CTOD

Figure 4.95 shows the values of CTOD versus the stable ductile crack growth length for both conditions. It can be seen that strong linear relationships are shown between these two variables for both HT1 and HT2 conditions. This suggests that more opening of the crack surfaces is triggered as the ductile crack growth occurs. Figure 4.96 shows the plots of the fracture distance versus the values of CTOD. The linear relationship between them can also be found in Figure 4.97, but most of the opening of the crack tip is found within 80 μm. The specimens normally fractured within this limit and no more opening of the crack tip is triggered.

5.5.2 Fractography

5.5.2.1 Ductile crack growth and fracture distance

All specimens failed with cleavage fracture or with catastrophic cleavage fracture after stable ductile crack growth. A small amount of plasticity and ductile crack growth within 20 μm are

found on most of the specimens, While only one specimen, HT1-CT-01, tested at -100 °C showed a ductile crack length of 70 μm. Increments are found for the ductile crack growth length for both conditions, but the increments tend to be small and scattered.

For most of the specimens, initiation locations are found to be within the 200 μm range below the fatigue pre-crack tip. The fractographies and the corresponding EDX analysis of those which have fracture distances exceeding 200 μm are shown in Figure 4.67 to Figure 4.86. The initiation sites of two specimens at -120 and -80 °C, four at -100 °C are located beyond the 200 μm range. Although there is a 100% possibility for the specimens tested at -80 °C, but due to the very limited number of tests, it is still hard to make the conclusion in this study that the specimens are least likely to be found fracturing beyond 200 μm with the increasing of test temperature.

Among the eight specimens which have fracture distances exceeding 200 μm, only one specimen is found to initiate with matrix cracking. Figure 4.67 and Figure 4.68 shows the initiation site of specimen HT1-CT-21, with a fracture distance of 639 μm. Both sides of the fractured halves of the specimen was examined, with the river pattern converging solely towards this located site, no possible inclusions are found at this location. The initiation reason is identified as matrix cracking with fine lines propagating from the centre of the matrix. The chemical composition of this matrix is analysed using the EDX, but no different composition was found compared to other matrix of the specimen.

HT1-CT-01 and HT2-CT-01 are two specimens fractured with distances of 660 and 631 μm respectively. Their fractographies and EDX analysis are shown in Figure 4.72 to Figure 4.74, Figure 4.78 to Figure 4.80. The EDX analysis of initiation site from one half of the HT1-CT-01 suggests the composition of inclusion is mainly calcium and aluminium, while only matrix

composition was found from the hole located at the initiation site on the other fractured half. This suggests that the reason of initiation is decohesion of inclusion for HT1-CT-01. Cuboidal shape inclusion was found at the initiation site of HT2-CT-01 with titanium and niobium found from both halves of the fractured specimen, as Figure 4.80 shown. The finding of same chemical compositions on both halves of the specimen suggests inclusion cracking as the initiation reason.

For specimen HT1-CT-17 and HT2-CT-25 with fracture distance of 289 and 490 μm, inclusion cracking and same chemical compositions with calcium, titanium and aluminium are found from the initiation sites, as shown in Figure 4.83 and Figure 4.86.

With different initiation reasons and inclusion compositions found at different temperatures, it is hard to say whether the longer fracture distance is related to these variables from this study due to limited number of tests.

5.5.2.2 Effects of Inclusions

5.5.2.2.1 Inclusion behaviour

Among 16 located initiation sites with inclusions found as the initiation reason, only one inclusion has decohered, while the other 15 inclusions cracked regarding various shapes and compositions. With the higher probability of finding a cracking rather than decohesion of inclusion, it also suggests that it takes less energy to crack an inclusion than separating it from its surrounding matrix.

The finding of the phenomenon indicates that an inclusion is most likely to crack instead of decohering, as the stress tends to build up on the inclusion itself at a potent initiation site.

5.5.2.2.2 Inclusion size

In the fracture toughness tests, the average equivalent diameters of inclusions found at cleavage initiation sites were measured as 1.6 μm and 1.8 μm for the HT1 and HT2 conditions, respectively. The similarity in average inclusion sizes between the HT1 and HT2 conditions suggests that the heat treatment process did not significantly alter the underlying inclusion population. However, the inclusions identified at cleavage initiation sites were consistently larger than the average inclusion sizes measured on as-received specimens, reflecting the tendency for cleavage fracture to preferentially initiate at larger inclusions.

The variation of inclusion size and fracture distance could be caused by the statistical effect of sampling potent inclusions. Ritchie and Knott [100] demonstrated that cleavage fracture is highly sensitive to microstructural defects such as inclusions and second-phase particles, with larger defects significantly lowering the critical stress required for crack initiation. Their work showed that the presence of larger inclusions increases the likelihood of early cleavage initiation. Therefore, the slightly larger average inclusion sizes measured at initiation sites reflect the inherent statistical effects associated with defect-controlled brittle fracture, rather than differences in the overall material quality between the HT1 and HT2 conditions.

Further comparison of inclusion sizes between sharp-cracked (fracture toughness) specimens and blunt-notched (fracture stress) specimens reveals that the average equivalent inclusion size is larger in the blunt-notched specimens. Specifically, the average equivalent inclusion size was measured as 2.5 μm in fracture stress tests, compared to 1.7 μm in fracture toughness tests.

This trend reflects the different fracture initiation mechanisms governed by the local stress states in each testing configuration. In sharp-cracked specimens, the high local stresses at the crack tip allow smaller inclusions to act as effective cleavage initiation sites, whereas in blunt-

notched specimens, where the stress concentration is lower due to the larger notch root radius, larger inclusions are required to initiate fracture. This observation is consistent with the findings of Lin et al. [104], who demonstrated that the abundance of finer particles has a stronger influence on cleavage initiation under sharp-crack conditions where local stresses are substantially higher. Similarly, Wenman [103] noted that in blunt-notched specimens, lower stress magnitudes ahead of the notch favour fracture initiation at larger inclusions, aided by the larger process zone that increases the probability of encountering such defects.

5.5.3 Estimation of Reference Temperature using Charpy Impact Results

Many researchers have proved that the master curve procedure is one of the most reliable methods to estimate the reference temperatures T_0 for steels [105-109].

It is worth noting that the reference temperatures T_0 and T_{28J} or T_{41J} are influenced by both the loading rate and notch acuity [105-107]. The higher loading rate associated with Charpy impact testing tends to shift these characteristic temperatures to higher values, promoting brittle behaviour. In contrast, the use of a blunted notch tends to shift the transition temperatures to lower values, due to the reduced local stress concentration and increased apparent toughness. Compared to the Charpy impact test, the fracture toughness test is conducted at a much slower loading rate but with a significantly sharper notch (i.e., a fatigue-precracked tip). Their combined effect on the estimation can be considerably small, with the opposite effects of these two factors, thus the correlations between T_0 and T_{28J} or T_{41J} is relatively more reliable. This is possibly why the master curve method holds an advantage when it comes to achieving agreement between predicted results from direct empirical estimation and test data from fracture toughness results. Therefore, the reference temperature

calculated from the fracture toughness test are used as a reference value for the four empirical correlations used in this study.

As the Corten and Sailors' procedure is only applicable for energy between 7 to 68 J, the estimated curves are limited within the temperature ranges of -96 to -109, -93 to -108 and -95 to -109 °C, for HT1, HT2 and combination of HT1+2 conditions respectively, as shown in Figure 4.97 (a). Due to the limited temperature range of this correlation, the fracture toughness values of HT1 and HT2 conditions cannot be estimated at either -120 or -80 °C, but it seems to have good correlation with the test results calculated at -100 °C.

Similar behaviour can also be found in the Barsom and Rolfe's correlation, whereas this correlation has a relatively wider applicable energy range of 3-82 J, as shown in Figure 4.97 (b). Consequently, wider temperature ranges can be estimated, with ranges of -95 to -116, -92 to -117 and -94 to -118 °C, for HT1, HT2 and combination of HT1+2 conditions respectively. But still, this correlation can only be used to compare with fracture toughness results at -100 °C. Good estimation with the test results calculated at -100 °C is also found in this correlation.

As shown in Figures 4.97(c) and (d), the Marandet & Sanz and Roberts & Newton correlations are applicable across the full transition region, without energy restrictions, allowing estimations from -120 to -80 °C. However, the experimental K_{Jc} data show considerable scatter relative to these empirical predictions. The Marandet & Sanz method tends to produce slightly higher fracture toughness estimations, whereas the Roberts & Newton method generally provides a lower-bound estimation. Although both models capture the general temperature dependence, no strict point-by-point correlation with experimental data is observed, particularly at temperatures approaching the lower and upper shelves.

Comparisons of the correlation curves and test results are summarised in Figures 4.88 and 4.98. As shown in Figure 4.88, all four empirical correlations yield reasonable estimations of fracture toughness from Charpy results when temperatures are close to the transition range. However, systematic deviations are observed: all methods tend to underestimate fracture toughness values as temperatures approach the lower shelf, and to overestimate them as temperatures approach the upper shelf. This behaviour is likely related to the sharp transition regions exhibited by the HT1 and HT2 conditions, combined with reduced ductility in Charpy tests due to higher loading rates.

Overall, the four empirical correlations and the associated T_{28J} and T_{41J} values provide reasonable estimations of the reference temperatures for the steels investigated in this study. As shown in Figure 4.98, only three out of 12 estimations are out of the ±3 °C range, and most estimations slightly overpredict the reference temperatures relative to direct master curve analysis. These results suggest that while empirical correlations provide useful rough estimations of fracture toughness near the transition temperature, they must be applied with caution at temperatures approaching the lower or upper shelves.

5.5.4 Local Cleavage Fracture Stress

5.5.4.1 McMeeking FEM Analysis

The local cleavage fracture stress calculation for the sharp-crack fracture toughness tests is based on the McMeeking's FEM analysis, which depicted the stress distribution and plain strain state of the specimens at various distances. According to McMeeking's estimation, the local cleavage fracture stress has the trend of reaching a maximum principal stress value and declining gradually to a certain plateau with increasing distance. Whereas the plain strain of the specimen just keeps decreasing to near zero as the distance increases. Much greater value

of strain in specimens with short distances can be found comparing to the specimens exceeding the maximum principal stress location.

With the help of fractography, the x-axis R/δ value can be derived from the ratios of the measured fracture distance and calculated CTOD. However, four specimens are found having R/δ values in the range of 10-16, while the original stress distribution curve in FEM analysis only estimated the stress within the R/δ value of 10. Therefore, the stress distribution and plain strain curves are extended from the original estimation with minimal errors, as the curves have already tended to the plateau regions, as shown in Figure 4.89.

Among 26 examined specimens, two specimens HT2-CT-03 and HT2-CT-07 with R/δ values of 1.3 are found to failed catastrophically before reaching the maximum principal stress with R/δ value of 2.0, while the rest of the specimens fractured at or after the maximum principal stress, based on the results given in Table 4.19, Table 4.20 and Figure 4.90. These two specimens are also found to have the largest local principal strain values of 0.05 while the other specimens have the values in the range of near zero to 0.02. Therefore, these two specimens could be considered as mixed stress and strain controlled, while all others as tensile stress controlled.

It is of interest to note that the maximum principal stress from the stress distribution curve maintains constant even if the applied load (represented as the CTOD, or in this case b) increases [110]. Therefore, failure of these two specimens should have occurred at a lower CTOD value because the stresses at this position were already at a value which exceeded the stress when failure occurred.

The R/δ value of the maximum principal stress location is around 2.0, depicted from the FEM stress distribution curve in Figure 4.88, which indicates that the distance X_{max} of the maximum

principal stress location is two times the CTOD value. The strain value at this location is around 0.16. The negative and positive values, ranging from -24 to 525 μm, of X_0-X_{max} shown in Table 4.22 also indicates that the cleavage fracture is not necessarily initiated at the location of maximum principal stress. As estimated by Lin et al. [104], all fracture initiation sites should be beyond the distance of X_{max}, if the criterion of the critical plastic strain is necessarily satisfied in the high stress area, and the critical tensile stress equalling to or larger than the σ_f, is the unique criterion for cleavage fracture propagation.

5.5.4.2 Local Cleavage Fracture Stress Compared with Maximum Principal Stress

Table 4.19 and Table 4.20 summarised the relationship between the local cleavage fracture stress and the maximum principal stress, represented as the ratio of σ_f/σ_{max}.

With the σ_{max} estimated from the peak location of the stress distribution curve, the ratios of σ_f/σ_{max} are calculated to be in the range of 0.8-1.0 and 0.78-1.0 for HT1 and HT2 conditions respectively. Whereas the cleavage fracture locations of all specimens are located within the plastic zone ahead of the crack tip.

It is of interest for researchers to discuss the conditions for fracture to initiate and cracks to propagate. Among 26 examined specimens, if the 0.90 ratio of σ_f/σ_{max} is considered to be the criterion for prediction of cleavage fracture in both conditions, 17 specimens, as in 65% of the total specimens will meet this criterion. With the same criterion of 0.90 of the maximum principal stress, similar results were found by Wenman [103] in a MnMoNi steel, as 24 of 32 specimens meet this criterion.

If the criterion of 0.80 of the maximum principal stress is considered, 24 of 26 specimens will meet this criterion (these 24 specimens are all located beyond the peak value), as in 92% of

total specimens, while 38 of the total 49 specimens have the ratio of σ_f/σ_{max} greater than this criterion, in blunt-notched specimens of a HSLA steel in Bose's study [111].

5.5.4.3 Comparison to Fracture Stress Results

5.5.4.3.1 Effect of Temperature

Figure 4.99 shows the plots of the local cleavage fracture stress in both blunt-notched (fracture stress) specimens and sharp-cracked (fracture toughness) specimens at various test temperatures.

At -196 °C, the local cleavage fracture stress derived from McMeeking's FEM analysis of blunt-notched specimens has an average value of 1846 MPa, within the range of 1530 to 2032 MPa.

For sharp-cracked specimens test at -120 °C, the local cleavage fracture stress estimated from Griffith-Owen FEM analysis has an average value of 2287 MPa, with a lower bound value of 1892 MPa. While at -100 °C, the average and lower bound values of local cleavage fracture stress are 2165 and 1839 MPa. At -80 °C, the average value decreases to 1950 MPa.

Therefore, as shown in Figure 4.99 and by comparing the average values of the local cleavage fracture stress values at -196, -120, -100 and -80 °C, no obvious evidence suggests that temperature has any effect on the lower bound local cleavage fracture stress.

5.5.4.3.2 Fracture Distance Comparison

Comparison between the blunt-notched (fracture stress) specimens and sharp-cracked (fracture toughness) specimens are given in Figure 4.100. The measured fracture distance of blunt-notched specimens is in the range of 221 to 365 μm, while the fracture distance ranges

from 22 to 660 μm, with the majority of them located within 200 μm, for the sharp-cracked specimens.

Below 200 μm, the local cleavage fracture stress of the sharp-cracked specimens tends to have higher values, while the stresses are more scattered with fracture distance exceeding 200 μm. Similar stress conditions are found in both blunt-notched and sharp-cracked specimens while the fracture distance exceeds 200 μm, as the values of local cleavage fracture stress suggest. The combination results of both specimen geometries are consistent with the FEM analysis estimated, as their stress conditions decrease and reach relatively stable region with increasing fracture distance.

Figure 4.101 and Figure 4.102 show the relationships between the inclusion size, facet size and the fracture distance of both specimen geometries. The figures depict complex relationships between these variables with no obvious correlations found. However, it seems that the inclusion sizes for sharp-cracked specimens, which are generally below 2 μm, are smaller than those found in blunt-notched specimens, but the relationship tends to be more complex in terms of facet sizes.

5.5.4.3.3 Surface Energy Estimations

Table 4.23 gives the comparison of effective surface energy calculated for specimens with inclusion cracking for both blunt-notched fracture stress and sharp-cracked fracture toughness specimens. As the modified Griffith equation is assumed for a penny shaped crack, it is of interest to compare the results for specimens with inclusion cracking for better accuracy. While 5 blunt-notched specimens have cracked inclusions as critical event, there are 15 cracked inclusions found among 26 examined sharp-cracked specimens.

The effective surface energy values (based on inclusion sizes) are in the range of 7.4 to 15.5 J/m^2 for blunt-notched specimens, and in the range of 5.9 to 19.6 J/m^2 for sharp-cracked specimens.

For 6 specimens containing titanium with cuboidal shaped appearance, the effective surface energy values are in the range of 7.0-13.8 J/m^2 with an average value of 11.7 J/m^2. For the rest of the specimen, spherical shaped appearances are found, and the effective surface energy values are in the range of 5.9-15.6 J/m^2 with an average value of 10.3 J/m^2. With observed small differences between shapes of inclusions, it is still hard to say whether the effective surface energy is related to the geometry of inclusions.

Different microcrack propagating modes, such as initiating directly from a cracked inclusion or decohered before propagating into the matrix, could also potentially lead to different results, as one inclusion within HT1-CT-01 was found to be decohered with an effective surface energy value of 8.4 J/m^2, which is below the average value (11.1 J/m^2) of cracked inclusions.

CHAPTER 6 – CONCLUSIONS AND FUTURE WORK OF SA.738 GR.B STEEL

6.1 CONCLUSIONS

1. Based on the results of the tensile, Charpy impact, microscopic fracture stress and fracture toughness tests, these HT1 and HT2 heat treatment conditions are considered to be identical.
2. Splitting fracture behaviour was observed in tensile specimens tested at various temperatures for both heat-treated conditions. This cracking, occurring parallel to the load application direction, is attributed to the development of a high triaxial stress state within the necked region during tensile deformation. The elevated hydrostatic stress promotes cleavage fracture initiation even after substantial plastic deformation, with the multi-axial stress condition enhancing susceptibility to splitting fractures at low temperatures.
3. Ductile-to-brittle transition curves of Charpy impact tests show similar behaviours in the transition regions for both HT1 and HT2 conditions. Similar lower and upper shelf behaviours are exhibited according to macroscopic fracture surface observation and detailed fractography. The ductile-to-brittle transition regions are considered to be within the range of -100 to -80 °C, for both HT1 and HT2 conditions. The tanh curves suggested the DBTT for HT1 and HT2 conditions are -90 and -86 °C, respectively.
4. Impact energy versus lateral expansion, ductile thumbnail extension, shear lip size and cleavage area percentage, show strong linear correlations for both conditions. The absorbed impact energy per unit of crack growth is also found to be identical.

5. In fracture stress tests carried out at -196 °C, σ_{yymax} values for both HT1 and HT2 conditions are in the range of 1803 to 2071 MPa, while the $\sigma(X_0)$ values derived from the FEM analysis are in the range of 1530 to 2032 MPa. The $\sigma(X_0)$ values are found to be very close to the maximum principal stress, with the ratios of $\sigma(X_0)/\sigma_{yymax}$ varying from 0.94 to 0.98, except the one specimen with $\sigma(X_0)$ value of 1530 MPa, has the value of 0.85.
6. Inclusions are found at all initiation sites and considered to be the primary reason triggering cleavage fracture in these fracture stress tests. The compositions of the inclusions contain calcium, but with aluminium and occasionally titanium (in cuboidal shaped inclusions) also found in some of inclusions. The inclusion sizes range from 1.8 to 3.2 μm, while no obvious relationship between the size and composition or shape of the inclusions was found.
7. The effective surface energy γ_P of is found to be in the range of 7.4 to 15.5 J/m^2 for both conditions, assuming that the critical event is a penny shaped crack propagating from the inclusion into the surrounding matrix. The smallest γ_P value of 7.4 J/m^2 came from the specimen with $\sigma(X_0)$ value of 1530 MPa. The weak linear correlations observed in the plots of σ_{yymax}, $\sigma(X_0)$ versus the reciprocal square root of the inclusion diameter suggests that the inclusion triggers the fracture, but that the value of fracture stress measured cannot be predicted from their absolute size.
8. Unloading compliance method was used for the estimation of pre-crack length of the CT specimens, and the estimations were compared with actual crack length measured under optical microscope. The difference between the estimation and actual length was proved to be in the ASTM standard's acceptable range. However, estimation of stable crack growth was not applicable to SA.738 Gr.B steel, due to its early brittle fracture

with the maximum length of 70 μm during tests. The good estimation of pre-crack length from unloading compliance method suggests the promising potential of this method for establishing crack growth resistance curves where more substantial stable ductile crack growth is observed.

9. Four empirical correlations were applied in this study to estimate fracture toughness values from Charpy impact energy results. While some scatter was observed between the estimated and measured toughness values, particularly outside the transition region, the correlations provided reasonable predictions near the ductile-to-brittle transition temperatures. The reference temperatures could also be reliably estimated using T_{28J} and T_{41J}, as well as the temperatures corresponding to 100 $MPam^{-1/2}$ calculated from Charpy energy values. Among the 12 estimations of reference temperature (95.1 to 101.3 °C), only three differed by approximately 5 °C from the master curve-derived T_0 values (99.9 to 100.5 °C), while the remaining estimations showed differences within ±3 °C. These results confirm that the empirical methods can provide a useful first approximation of fracture toughness in the transition regime, though some caution is required when interpreting values outside this range.
10. For most of the sharp-crack fracture toughness specimens, the initiation sites are found within 200 μm from the crack tip. No evidence has been found that the inclusion type has influence on the fracture distance. Inclusions found at the cleavage initiation sites of the specimens show chemical compositions of calcium, aluminium and titanium, with equivalent diameter in the range of 0.8-3.3 μm. No significant micromechanism of cleavage difference is found between the spherical shaped calcium inclusions and cuboidal shaped inclusions. The inclusions found in the blunt-notched specimens were larger than those found in the sharp-cracked specimens, consistent with the lower stress

concentration ahead of a blunt notch requiring larger defects to initiate cleavage fracture.

11. Two of 26 tested fracture toughness specimens fractured catastrophically before reaching the maximum principal stress location, while 24 specimens are found located at or beyond the maximum principal stress location. According the McMeeking's FEM analysis, the ratios of σ_f/σ_{max} are calculated to be in the range of 0.78-1.0 for both conditions.
12. The combined results of blunt-notch fracture stress and sharp-crack fracture toughness testing across the temperature range of -196 to -80 °C suggest that the local cleavage fracture stress in this steel is temperature independent.
13. The effective surface energies of fracture toughness specimens are in the range of 5.9-21.1 J/m^2. The large variation is caused by the inclusion sizes (0.8-3.3 μm) which contributes to the calculation of effective surface energy. No significant differences between the blunt-notched and sharp-cracked specimens are found by comparing the cracked inclusion sizes and the related surface energy.
14. The overall results of two different test piece geometries from blunt-notch fracture stress and sharp-crack fracture toughness testing suggest that cleavage fracture is tensile stress controlled in this steel. This reinforces the well-established understanding of the micro-mechanism of cleavage fracture seen in much previous research.

6.2 FUTURE WORK

The empirical formulas used in this study for the conversion of Charpy impact energy to fracture toughness showed reliable results, but due to the validation of K_{IC} values no direct comparisons were made between the Charpy impact energy converted fracture toughness

values and fracture toughness tests calculated values. More fracture toughness tests with different specimen geometry are suggested so that there would be more valid K_{IC} values for better comparison.

A more specific modern FEM analysis made specifically for this steel is suggested for a more comprehensive analysis as the Griffth-Owen and McMeeking's analysis are limited with work hardening exponents n=0, 0.1 and 0.2. Actual stress-strain curves with appropriate work hardening estimation need to be made for this steel.

CHAPTER 7 – RESULTS AND DISCUSSION OF 9% AND 7% NICKEL STEELS

7.1 MICROSTRUCTURE

Optical microscope and scanning electron microscope (SEM) images of the microstructures of 9% and 7% Nickel steels are displayed in Figure 7.1 and Figure 7.2. The results from the electron backscatter diffraction analysis are as shown in Figure 7.3. It can be observed that the primary component of both 9% and 7% Nickel steels microstructure is tempered martensite. For 9% Nickel steel, lath-like retained austenite and carbides which exhibit a lighter contrast compared to the tempered martensite are visible at grain boundaries. Phase distribution result from the EBSD result in Figure 7.3 also proves this theory as the phase were found at the grain boundaries are mainly FCC (face-centred cubic) rather than BCC (body-centred cubic) crystal structure. The phase distribution results also suggest that approximately 3% of FCC content was found in 9% Nickel steel and none was found in 7% Nickel steel.

The mean grain size of 9% Nickel steel, as determined by the linear intercept method according to ASTM Standard E112-13, is 9.6 µm while the average of 7% Nickel steel is 18.1 µm. Their grain sizes were also measured using the build-in application from the EBSD analysis. For 9% Nickel steel, the average grain size is 9.3 µm with a median size of 6.8 µm. For 7% Nickel steel, the average grain size is 16.6 µm with a median size of 12.8 µm.

7.2 INCLUSION ANALYSIS

Figure 7.4 shows the polished surfaces of both 9% and 7% Nickel steels under backscattered mode. The results of the inclusion analysis are shown in Figure 7.5 and Figure 7.6 for 9% and 7% Nickel steels. Around 90% of the inclusions per mm^2 have a diameter between 0 to 1.0

μm, and nearly 10% of the inclusions per mm^2 have a diameter between 1.0 to 2.0 μm for 9% Nickel steel. Around 87% of the inclusions per mm^2 have a diameter between 0 to 1.0 μm, and around 10% of the inclusions per mm^2 have a diameter larger between 1.0 to 2.0 μm for 7% Nickel steel.

The results are summarised from a measurement of 6402 inclusions with a limit of detection of 648 inclusions/mm^2 for 9% Nickel steel and a measurement of 6673 inclusions with a limit of detection of 606 inclusions/mm^2 for 7% Nickel steel. Both conditions have the inclusion diameters lying in the range of 0.2 to 4 μm. However, the inclusions which have a diameter below 0.2 μm for both conditions were probably not counted as they were not recognizable by the ImageJ software due to resolution limitation.

The inclusions were found to have similar chemical composition for both 9% and 7% Nickel steels and two typical examples of inclusions of each condition are shown in Figure 7.7 and Figure 7.8. Most compositions of the inclusions appear to be aluminium and magnesium, but small amount of manganese were also found for both steels. Inclusions with different sizes were analysed from both conditions and showing little difference in chemical composition.

7.3 HARDNESS

Ten indents of 9 mm long traces were applied on both 9% and 7% Nickel steels. The hardness results of both 9% and 7% Nickel steels are shown in Table 7.1. For 9% Nickel steel, it has a hardness in the region of 242 to 257 HV with an average hardness of 251 HV while the 7% Nickel steel has a hardness in the region of 243 to 265 HV with an average hardness of 253 HV. It can be seen that there were only an overall hardness differences of 2 HV with 7% Nickel steel slightly higher than the 9% Nickel steel.

7.4 TENSILE TESTING

7.4.1 Yield Stress and Ultimate Tensile Strength

Engineering stress-strain curves for the 9% and 7% Nickel steels at different temperatures are shown in Figure 7.9 and Figure 7.10. A summary of the tensile results including the yield stress, ultimate tensile strength, uniform and total plastic elongation are presented in Table 7.2 and Table 7.3. The tensile testing temperatures of the results are -196, -170, -150 and -130 °C.

For 9% Nickel steel tested between -170 and -130 °C, as shown in Figure 7.11, the engineering stresses only decrease slightly after reaching the linear elastic stage and the upper yield points, then they start the strain hardening process and reach the ultimate tensile strength. And for tests carried out at -196 °C, there were no decreases or discontinuous yield points observed after the curves reaching the linear elastic stage and the upper yield points. Therefore, the 0.2% offset stress (0.2% proof stress) was quoted here as the yield stress. The 0.2% offset stress was calculated by the intersection of the engineering stress-strain curve and the 0.2% offset line of the linear elastic stage of the curve.

For 7% Nickel steel, the curves of all tested temperatures appear to decrease to lower yield points after reaching the linear elastic stage and the upper yield points, before climbing up to the ultimate tensile strength points. For better comparison with the 9% Nickel steel, both 0.2% offset stress and the lower yield stress are calculated for the 7% Nickel steel. However, it is worth noting that for the 7% Nickel steel, the 0.2% offset yield stress tend to be close to the upper yield points.

Table 7.2, Table 7.3 and Figure 7.11 show that both the yield stress and ultimate tensile strength of 9% and 7% Nickel steels increase as the testing temperature decreases. It appears

that the differences between the yield stress and ultimate tensile strength of 7% Nickel steel are smaller than the differences of the yield stress and ultimate tensile strength the 9% Nickel steel.

The 0.2% offset yield stress of 9% Nickel steel increases from an average of 812 MPa at -130 °C to an average of 968 MPa at -196 °C. The ultimate tensile strength increases from an average of 1009 MPa at -130 °C to an average of 1176 MPa at -196 °C. The uniform and total plastic elongations show similar results of approximately 32% as the testing temperature decreases from -130 to -196 °C.

As for 7% Nickel steel, the 0.2% offset yield stress increases from an average of 900 MPa at -130 °C to an average of 1077 MPa at -196 °C. The lower yield stress increases from an average of 879 MPa at -130 °C to an average of 1051 MPa at -196 °C. The ultimate tensile strength increases from an average of 932 MPa at -130 °C to an average of 1093 MPa at -196 °C. The uniform and total plastic elongations show similar results of approximately 30% as the testing temperature decreases from -130 to -196 °C. However, 7% Nickel steel tends to have smaller uniform and total plastic elongations than the 9% Nickel steel as shown in Figure 7.12. The figure also suggests that both of these values have little relation to testing temperatures.

7.4.2 Work Hardening Exponent

True stress-strain curves of both 9% and 7% Nickel steels were plotted logarithmically between the region of the 0.2% offset yield stress and ultimate tensile strength as shown in Figure 7.13 and Figure 7.14 to determine the work hardening exponent *n* for all testing temperatures. The results are summarised with the yield stress and tensile strength calculated from the engineering stress-strain curve above in Table 7.2 and Table 7.3. Figure 7.15 shows

the comparison of the work hardening exponent *n* between 9% and 7% Nickel steels. The work hardening exponent *n* varies between 0.12 to 0.17 for the 9% Nickel steel while the 7% Nickel steel has a relatively more consistent *n* value of 0.08 to 0.09. For both materials, the *n* values are consistent against different temperatures between -196 to -130 °C.

7.4.3 Fractography

Figure 7.16 shows a typical fractography of 9% steel tensile specimen 9Ni-09 tested at -130 °C. Three different locations of the fracture surface were examined using SEM. Fully ductile failure dominated by micro-void coalescence mechanism can be observed.

7.5 CHARPY TESTING

7.5.1 Charpy Impact Results

The results of the Charpy impact tests, including the absorbed impact energy, lateral expansion, and cleavage area percentage for the 9% and 7% Nickel steel are presented in Table 7.4 and Table 7.5 respectively, The absorbed impact energy for the 7% Nickel steel is plotted in Figure 7.17.

For the 9% Nickel steel, tests were only carried out at -196 °C as all of the 6 tested specimens showing fully ductile behaviour and did not fracture into halves. With the highest absorbed impact energy of 278 J, the lowest of 242 J and an average of 260 J of the 6 tested specimens.

In order to make an accurate estimation of the ductile-to-brittle transition temperature (DBTT) for the 7% Nickel steel, 15 Charpy impact tests were carried out over the temperature range of -196 to -80 °C with 7 of them tested in the transition region. As shown by the absorbed

impact energy plots in Figure 7.17, the upper shelf energy is around 238 J while the lower shelf energy is 45 J.

Ductile-to-brittle transition curves were fitted using the tanh fitting method mentioned in previous section and the tanh function for 7% Nickel steel is calculated as follow:

$$CVN(T) = 136.7 + 91.6 \cdot \tanh\left(\frac{T + 164.8}{10.9}\right)$$

The tanh fitted ductile-to-brittle transition curve of 7% Nickel steel is shown in Figure 7.18.The estimated DBTT for the 7% Nickel steel is -165 °C, which is the temperature where the absorbed energy reached the average of the upper and lower shelf energies, as the tanh curve suggested.

7.5.2 Charpy Impact Specimen Fracture Surface Overview

Figure 7.19 and Figure 7.20 shows the fracture surfaces of the 9% and 7% Nickel steel examined by optical microscope. The 9% Nickel steel specimens were not fully broken during the tests at -196 °C. Therefore, they were separated by force after tests for better surface observation. Fully microvoid coalescence fracture mode can be observed under the notch root, and no cleavage fracture can be found from the 9% Nickel steel specimens.

For specimens of 7% Nickel steel tested at upper shelf with high impact energy values, fully microvoid coalescence fracture can also be found, while pure cleavage fracture mode can be found at lower shelf with low impact energy values. For specimens tested in the transition region, both fracture mechanisms can be found in the same specimen while the proportion of the brittle fracture increases with the decrease of test temperature.

The lateral expansion and cleavage area from fracture surfaces of 7% Nickel steel specimens are carefully measured. Figure 7.21 to Figure 7.23 show the scatter plots of temperature and impact energy versus lateral expansion and cleavage area percentage for the 7% Nickel steel.

Figure 7.21 show that lateral expansion has consistent linear relationships with the impact energy. With the increasing absorbed energy and test temperature, the among of lateral expansion tends to increase.

Figure 7.22 and Figure 7.23 depict similar trend for the cleavage area percentage of the fracture surfaces versus impact energy and temperature. The lower shelf behaviour which has roughly 80% crystallinity, was firstly noticed at -180 °C, while near 0% crystallinity which indicates the upper shelf behaviour was firstly noticed at -130 °C.

7.5.3 Fractography

Figure 7.24 to Figure 7.29 show the fractography of 9% Nickel steel Charpy specimens. Fully ductile failure, dominated by micro-void coalescence mechanism in accordance with high values of impact energy obtained for these Charpy specimens can be observed.

The size of the inclusions located inside the micro-voids have been measured using SEM images, while their composition has been obtained using EDX analysis. The observed inclusions were primarily cuboidal shape with sharp edges. The size of most inclusions is found below 6 μm in equivalent diameter. Majority of inclusions are aluminium-rich in composition, while manganese is also found in some of the inclusions.

7.6 MICROSCOPIC CLEAVAGE FRACTURE STRESS TESTING

Two fracture stress tests of 9% Nickel steel were carried out as four-point bending at -196 °C in liquid nitrogen bath and the maximum load reached 79kN. Figure 7.30 shows the load-displacement curves for the tests. However, similar to the Charpy testing results of 9% Nickel steel, the fracture stress specimens also exhibit large plastic deformation which indicates the 9% Nickel steel has an excellent resistance to cleavage fracture.

Table 7.6 gives the results of 9% Nickel steel including the maximum fracture load, nominal stress, the ratios of σ_{nom}/σ_{YS} and L/L_{GY}, and stress intensification factor. The results of 7% Nickel steel from Huize Fan's tests were also included in the table for comparison [87].

With the same sample geometries and same ligament sizes of 9% and 7% Nickel steels' specimens, the 7% Nickel steel tends to have higher nominal stress than 9% Nickel steel due to the higher yield stress. However, as the ratios of σ_{nom}/σ_{YS} and L/L_{GY} both exceed the FEM analysis limits, both 9% and 7% Nickel steels are too ductile for valid microscopic cleavage fracture stress analysis within the testing temperature limitation of -196 °C. The maximum principal stress is at the limit of the original Griffiths-Owen analysis. If the maximum stress intensification factor 2.62 is considered, the maximum principal stress can be calculated as 2536 MPa. It can be deduced that local values of tensile stress of 2536 MPa (estimated within the notch plastic zone) did not trigger cleavage fracture in this steel.

7.7 FRACTURE TOUGHNESS TESTING

Fracture toughness tests were carried out on Single-edge Notched Bending (SENB) specimen. A total of six fracture toughness tests were performed at -163 °C including five 9% Nickel steel specimens and one 7% Nickel steel specimen. Their load-displacement curves are given

in Figure 7.31. As the curves shown, several unloading/reloading sequences were performed, and the specimens were having stable crack growth during the tests. All specimens exhibited brittle cleavage failure after the attainment of a maximum load plateau and stable crack growth is observed before the failure.

7.7.1 Compliance Estimated Crack Length

Table 7.7 shows the measurements of crack lengths including the optical microscope measured lengths and the compliance method estimated lengths. Figures 7.32 shows the unloading/reloading sequences of the elastic compliance technique for the estimation of initial crack lengths. The average slope of five sequences in each test was calculated and then used as $1/C$ to calculate the compliance estimated crack lengths.

The actual initial and final crack lengths are measured from the fracture surfaces shown in Figure 7.33. Four different regions with varying contrasts and surface profiles can be observed on the fracture surfaces. The machined notch surface of the specimens is visible at the top of the surfaces, and the pre-crack regions are depicted as the clean, flat parts below the notch. Below the pre-crack regions, the stable ductile crack growth regions are observed, showing a rougher surface with thumbnail shapes. The fourth region consists of the unstable cleavage fracture parts, featuring river patterns that spread from the boundaries and exhibit darker contrasts.

Five of the six specimens have original a_0 values (after pre-cracking) within the standard range of 0.45-0.55 W (14.4-17.6 mm) with the shortest and longest having values of 14.51 and 14.92 mm respectively. Only one specimen has the value of 14.33 mm which is slightly below the standard range. The compliance estimated original crack lengths $a_{0predicted}$ range from 14.57 to

15.17 mm which are all longer than the actual values. The differences between the actual and compliance estimated original crack lengths are within the range of 0.02 to 0.29 mm.

For the final crack lengths after stable crack growth, the actual a_f values vary from 15.54 to 16.55 mm while the compliance estimated $a_{fpredicted}$ values vary from 15.64 to 16.74 mm. The smallest and largest differences between them have the values of 0.11 and 0.39 mm respectively and all of the compliance estimated values are longer than the actual values. It is worth noting that the differences between the actual and compliance estimated values for both original and final crack lengths are within the limits of the standard required maximum values (0.03 b_0) of 0.51 to 0.53 mm for different specimens. The values of ductile stable crack growth Δa before cleavage failure for 9% Nickel steel specimens range from 0.91 to 1.42 mm while the 7% Nickel steel specimen has a value of 1.91 mm.

7.7.2 Fracture Toughness and *J*-integral

The results of the fracture toughness tests at -163 °C are given in Table 7.8, which shows the stable ductile crack growth Δa, the maximum load P_{max} during testing, *J* values, *K* values and the CTOD.

Although five tests were carried out for 9% Nickel steel, valid *J-R* curves were only able to be constructed from three of the tests. This is due to the limited stable crack growth resulting in insufficient plots between the 0.15-mm and 1.5-mm exclusion lines.

For the three tests with sufficient plots, linear regression lines are determined as the *J-R* curves using the method of least squares with the plots located within the 0.15-mm and 1.5-mm exclusion lines. The interim J_Q values are defined as the intersection of the regression line with the 0.2-mm offset line. J_Q values are qualified as the ductile crack initiation critical fracture

toughness J_{Ic} since they have met the requirements on the specimen thickness and ligament size. K_{JIc} values are then calculated using the qualified J_{Ic} values. The J_{Ic} and K_{JIc} values were in the range of 772 to 851 kJ/m^2 and 422 to 443 MPam$^{1/2}$ for 9% Nickel steel.

Figure 7.34 and Figure 7.35 shows the *J-R* curves for 9% and 7% Nickel steels respectively. All specimens showed the critical values of *J*, *K* and their CTOD values were calculated. Their J_{Ic} and the K_{JIc} values, which were converted from the J_{Ic} values, were calculated respectively.

The maximum load of the tests for 9% Nickel steel specimens ranges from 52.1 to 59.9 kN and has an average value of 54.5 kN while the value for 7% Nickel steel specimen is 50.7 kN. For 9% Nickel steel, the J_C values at fracture vary from 816 to 1122 kJ/m^2 with an average of 967 kJ/m^2 and a standard deviation of 123 kJ/m^2. For 7% Nickel steel, the J_C value is 995 kJ/m^2. As of the K_{Jc} values, the number varies from 184 to 204 MPam$^{1/2}$ with an average of 190 MPam$^{1/2}$ for 9% Nickel steel, and the number is 156 MPam$^{1/2}$ for 7% Nickel steel.

Figure 7.36 shows the comparison of *J-R* curves for 9% and 7% Nickel steels. The J_{Ic} and K_{JIc} values were in the range of 772 to 851 kJ/m^2 and 422 to 443 MPam$^{1/2}$ for 9% Nickel steel, and 663 kJ/m^2 and 391 MPam$^{1/2}$ for 7% Nickel steel respectively. CTOD of 9% Nickel steel ranges from 0.46 to 0.64 mm and of 7% Nickel steel the value is 0.62 mm.

7.8 DISCUSSION

7.8.1 Microstructure

Similar hardness profiles of HV5 values of around 253 kg/mm^2 were observed, while significant smaller grain size is found in the 9% Nickel steel (9.6 μm) than the 7% Nickel steel (18.1 μm). This is possibly caused by the different chemical composition of these two steels, as slightly larger amount of Manganese with additional Molybdenum and Chromium added in

7% Nickel steel. Molybdenum and Chromium could form solid solutions with both Nickel and Iron, enhancing the hardenability of steel during heat treatment processes, such as quenching and tempering [112][113].

Approximately 3% of retained austenite in the form of FCC phase from 9% Nickel steel was identified using a Joel 7000 SEM with Oxford EBSD system. For 7% Nickel steel no FCC phase could be identified. Earlier investigations elsewhere have found that 5-15 volume% of retained austenite could be found in 9% Nickel steel depending on their processing [114-117]. The different amount of retained austenite found between this thesis and the literatures is likely due to the limitation of EBSD analysis. X-Ray Diffraction (XRD) provides improved phase identification and quantification of retained austenite. However, due to the lack of availability of suitable XRD equipment at the University of Birmingham, only preliminary examinations were conducted using EBSD rather than XRD. The higher nickel content in 9% Nickel steel is expected to contribute to the larger amount of retained austenite content, as nickel acts as the stabilising element.

7.8.2 Charpy Impact Properties

The superior ductility of the 9% Nickel steel at -196 °C can be attributed to its higher nickel content and associated microstructural characteristics. Nickel acts as a potent austenite stabilizer, enhancing the cryogenic toughness of steels by promoting the formation of ductile face-centred cubic (FCC) phases such as retained austenite or by transforming into a fine-grained tempered martensite upon heat treatment [89]. Recent studies have demonstrated that 9% Nickel steels subjected to quenching and tempering treatments exhibit exceptional Charpy impact toughness values, with absorbed energies of 238 J at -196 °C and 217 J at -253 °C, indicating a low DBTT and superior cryogenic performance [118].

From a fracture mechanics perspective, the ductile-to-brittle transition curve illustrates a steep increase in absorbed energy as the temperature rises, reflecting the shift from brittle cleavage fracture to ductile shear-dominated fracture. For the 9% Nickel steel, -196 °C likely lies entirely within the upper shelf region of the DBTT curve, consistent with the observed high energy absorption and ductile fracture surfaces. These findings align with recent studies that have reported similarly low DBTTs and superior impact performance at subzero temperatures for high-nickel cryogenic steels [118][119].

According to the standard [121], the DBTT requirement for 9% Nickel steel is at or below -195 °C and for 7% Nickel steel, the temperature is -170 °C. In this study, the DBTT of 7% Nickel steel is very close to the ASTM standard's requirement with a temperature of -165 °C.

7.8.3 Tensile Properties

For tensile specimens of 9% Nickel steel carried out at -196 °C, there were no decreases or discontinuous yield points observed after the curves reaching the linear elastic stage and the upper yield points tested, as shown in Figure 7.9. For tests between -170 and -130 °C, the engineering stresses only decrease slightly after reaching the linear elastic stage and the upper yield points, then they start the strain hardening process and reach the ultimate tensile strength. An upper yield point could not be measured, but all curves have indications of an initial plateau region prior to general work hardening. On contrary, the curves of 7% Nickel steel at all tested temperatures appear to decrease to lower yield points after reaching the linear elastic stage and the upper yield points, before climbing to the ultimate tensile strength.

This different behaviour of the engineering stress-strain curve is possibly caused by the different amount of retained austenite, as similar phenomenon was also observed by Strife et al. [120] that pronounced upper yield points of the specimens contained retained austenite

were always greatly diminished or eliminated while the yield points of the specimens with no or less retained austenite could be observed.

Both 9% and 7% Nickel steels show excellent fracture resistance abilities. In terms of tensile properties, 7% still pass the requirements according to ASTM A553/A553M-22 standard [121], with yield stress of 969 MPa, tensile strength of 1014 MPa and total elongation of 26.2% at -170 °C, while the standard's minimum requirements are 585 MPa, 825 MPa and 20%, respectively.

7.8.4 Fracture Toughness

7.8.4.1 Fracture surface behaviour

All specimens fractured after maximum load and general yielding, and large amounts of stable ductile crack growth were found on both 9% and 7% Nickel steels specimens with most of the ductile crack lengths longer than 1 mm before fracture. A mix of unstable cleavage fracture and micro-void coalescence can then be observed below the stable ductile crack region, as shown on the fracture surfaces of the specimens. No cleavage before general yielding (plastic collapse) indicates strong resistance of the propagation of cleavage at low temperatures for both 9% and 7% Nickel steels.

There is an inverse correlation between the original crack length (pre-crack length) and the maximum fracture load of test as shown in Table 7.7 and Table 7.8. It can be seen that higher plastic collapse loads are often found in the specimen with shorter original crack lengths, as longer remaining ligament size could withstand higher applied load.

7.8.4.2 Crack length estimation using compliance method

The compliance estimated original crack lengths $a_{0predicted}$ range from 14.57 to 15.17 mm which are longer than the actual values. The differences between the actual and compliance estimated original crack lengths are within the range of 0.02 to 0.29 mm. For the final crack lengths after stable crack growth, the actual a_f values vary from 15.54 to 16.55 mm while the compliance estimated $a_{fpredicted}$ values vary from 15.64 to 16.74 mm. The smallest and largest differences between them have the values of 0.11 and 0.39 mm, respectively. It is worth noting that the differences between the actual and compliance estimated values for both original and final crack lengths are within the limits of the standard required maximum values (0.03 b_0) of 0.51 to 0.53 mm for different specimens. The good estimation of crack lengths based on the compliance methods indicated the feasibility of the compliance method used in this study.

7.8.4.3 Fracture Toughness and *J*-integral

The results from three 9% Nickel steel *J-R* curves are combined together to form a single regression curve as there are reasonable agreement between their plots. As shown in Figure 7.34, the combined regression curve of 9% Nickel steel shows average J_{Ic} and K_{JIc} values of 798 kJ/m^2 and 429 MPam$^{1/2}$. Comparing to 9% Nickel steel, the *J-R* curve of 7% Nickel steel shows a smaller slope with the corresponding J_{Ic} and K_{JIc} values of 663 kJ/m^2 and 391 MPam$^{1/2}$, as shown in Figure 7.35.

The finding of J_{Ic} values of 798 kJ/m² for 9% Nickel steel in this study is similar to the most recent fracture-mechanics data on similar 9% Ni-alloys, while no specific J_{Ic} values were found for 7% Nickel steels. Afzali et al. [122] reported J_{Ic} values of approximately 802 kJ/m^2 on EN 10028-4 1.5662+QT640 steel from 25 mm plate tested at -160 °C under side-grooved SENB specimens Additionally, another study of 9 % Ni girth-welded pipe recorded J_m values at maximum load around 1200 kJ/m^2 for base-metal (9% Nickel steel ASTM A333 Gr. 8)

SENB specimens [123]. Although there is no formal standard establishing a direct relationship between J_{Ic} and J_m, an engineering practice is applied to estimate J_{Ic} as approximately 70% of J_m. This empirical approximation is based on the typical shape of J-Δa resistance curves, where maximum load occurs after the onset of stable crack growth. Applying this approximation to the reported J_m value yields an estimated J_{Ic} of approximately 840 kJ/m².

However, the absence of side grooves in this study almost certainly inflated the apparent J_{Ic} through crack tunnelling. Without grooves, the constraint at the edges is reduced, allowing plastic deformation to dominate in these regions. This results in the observed crack tunnelling, where crack growth is greater at mid-thickness than at the specimen surfaces. Under low constraint conditions near the edges, the stress intensity at the crack tip is diminished, leading to a blunting effect rather than crack propagation [124][125]. Consequently, crack extension near the specimen edges is delayed or remains incomplete, even while mid-thickness crack growth proceeds. This behaviour introduces additional energy absorption into the J-integral measurement, effectively inflating the J_{Ic} value. While the J_{Ic} measurement is considered non-conservative for design purposes, it still provides valid comparative information within the scope of this study.

Figure 7.36 shows the comparison of both 9% and 7% Nickel steels. As the J-R curves indicate the energy per unit of fracture surface needed to drive crack growth, more energy is needed for a crack to propagate in the 9% Nickel steel than in 7% Nickel steel. Figure 7.36 also suggests that the energy difference tends to decrease as the crack grows. The higher J_{Ic} and K_{JIc} values observed for 9% Nickel steel suggest a significantly enhanced resistance to both crack initiation and ductile crack propagation when compared to 7% Nickel steel. The J_{Ic} value, being a measure of the energy required to initiate crack growth, and the K_{JIc} value, indicative

of the stress intensity factor at which crack propagation becomes critical, both highlight the superior performance of 9% Nickel steel in terms of its ability to absorb and redistribute stress around flaws without succumbing to brittle fracture.

The observed differences in fracture toughness between 9% and 7% Nickel steels can be attributed to their microstructural differences as Nickel enhances the toughness of steel by promoting a face-centred cubic (FCC) crystal structure, which is more ductile and resistant to crack propagation compared to a body-centred cubic (BCC) structure. These results are consistent with their microstructure differences as more austenitic phase are found in the 9% Nickel steel than the 7% Nickel steel. The smaller grain size found in 9% Nickel steel could also contribute to its better cleavage fracture resistance as found in many other ferritic steels, as the Hall-Petch effect suggests that smaller grains increase yield strength and, consequently, its resistance to crack initiation.

With the help of McMeeking's FEM analysis, it is also possible to estimate the maximum available local tensile stress of the specimens. It is perhaps of interest to note that it can be suggested that local tensile stresses of 3581 to 4840 MPa for 9% Nickel steel, calculated from the analysis with n=0.1 and 0.2 (as the work hardening exponent of 9% Nickel steel is in the range of 0.12-0.15, and with yield stress of 901 MPa at -170 °C), will have been present within the crack tip plastic zone and which have not triggered cleavage fracture. For comparison, the maximum local tensile stress of 7% Nickel steel is estimated to be in the range of 3156 to 3892 MPa as its work hardening exponent is 0.08 (using analysis for n=0 and 0.1), with yield stress of 969 MPa at -170 °C. It is another strong evidence of the more superior low temperature fracture resistance property of 9% Nickel steel.

Although as the *J-R* curves shown in Figure 7.36, the larger initial slope of 9% Nickel steel suggests higher energy required for the initiation of a crack, the 7% Nickel steel also cleavages after passing the maximum load, as the 9% Nickel steel. The high J_{Ic} and K_{JIc} values of 7% Nickel steel still indicates its remarkable low temperature cleavage fracture resistance ability.

CHAPTER 8 – CONCLUSIONS AND FUTURE WORK OF 9% AND 7% NICKEL STEELS

8.1 CONCLUSIONS

1. No upper yield points were found on the engineering stress-strain curves of the 9% Nickel steel, while such upper yield points were found for 7% Nickel steel. The smaller yield stress/tensile strength ratio, longer total elongation and higher work hardening exponent suggests better ductility of 9% Nickel steel comparing to 7% Nickel steel over the temperatures (-196 to -130 °C) tested in this thesis.
2. No DBTT was found for 9% Nickel steel. However, for 7% Nickel steel, ductile-to-brittle transition behaviour is observed between -180 to -140 °C and the tanh fitting estimated DBTT is -165 °C, which is close to the envisaged operating temperature for some LNG steels. Therefore, the operating temperature of LNG steels remains on the upper shelf and above the DBTT of 9% Nickel steel.
3. With some difficulties, the good estimation of crack lengths indicated the feasibility of the compliance method on the SENB geometry at low temperatures. The accurate crack length estimation helps evaluate the *J-R* curves. It is worth noting that, in this preliminary work, some important procedures, such as the alignment of the specimen and fixtures, selection of unloading compliance line, were found to have significant influence on the estimation.
4. In addition to its DBTT, the 9% Nickel steel also has better ductile crack growth resistance as demonstrated by analysis of *J-R* curves. The combined *J-R* curve of 9% Nickel steel shows average J_{Ic} and K_{JIc} values of 798 kJ/m^2 and 429 MPam$^{1/2}$, while the 7% Nickel steel has the corresponding values of 624 kJ/m^2 and 379 MPam$^{1/2}$.

Although the J_{Ic} and K_{JIc} values were found to be consistent with some recent research, it is still worth noting that the absence of side grooves in this study almost certainly inflated the apparent J_{Ic} through crack tunnelling.

5. Based on McMeeking's FEM analysis, it can be suggested that local tensile stresses of between 3581 to 4840 MPa for 9% Nickel steel will have been present within the crack tip plastic zone and which have not triggered cleavage fracture. The maximum local tensile stress of 7% Nickel steel is between 3156 to 3892 MPa. This suggests that the cleavage fracture stress will be higher for the 9% Nickel steel is consistent with the absence of a ductile-brittle transition in Charpy impact tests even at -196 °C in the present work.
6. In general, the 9% Nickel steel has a lower DBTT, implying enhanced resistance to cleavage fracture, and features a steeper *J-R* curve, indicating improved ductile crack growth resistance. Thus, it demonstrates superior resistance to both cleavage and ductile crack growth to the 7% Nickel steel.

8.2 FUTURE WORK

The percentage of retained austenite was only analysed crudely by EBSD analysis, further analysis such as X-ray diffraction analysis (XRD) and transmission electron microscopy (TEM) is necessary for more accurate and comprehensive analysis.

The microscopic cleavage fracture stress testing results exceeded the limit of current FEM analysis as only n=0, 0.1 and 0.2 available. In order to get the microscopic cleavage fracture stress, further tests can be carried out on sharp-cracked test pieces at -196 °C with initiation site identified on fracture surface.

Specimens with side grooves and different specimen geometry such as compact tension specimens could be used as additional tests for more comprehensive study of fracture toughness and *J-R* curves.

REFERENCES

1. International Atomic Energy Agency (IAEA). Assessment and Management of. Ageing of Major Nuclear Power Plant Components Important to Safety: PWR Vessel. IAEA-TECDOC-1361. Vienna; 2003.
2. Isozaki T, Soda K, Miyazono S. Structural analysis of Japanese PWR steel containment vessel under internal pressure loading. Nucl Eng Des. 1991;126(3):387-393.
3. Lee BS, Kim MC, Yoon JH, Hong JH. Characterization of high strength and high toughness Ni–Mo–Cr low alloy steels for nuclear application. Int J Press Vessel Pip. 2010;87(1):74-80.
4. Berggren RG, Stelzman WJ. Radiation strengthening and embrittlement in heavy section plate and welds. Nucl Eng Des. 1971;17(1):103-115.
5. American Society of Mechanical Engineers. Boiler and Pressure Vessel Code. Section II, Part A, SA-738/SA-738M Specification for Pressure Vessel Plates, Heat-Treated, Carbon-Manganese-Silicon Steel, for Moderate and Lower Temperature Service. New York, NY: ASME; 2001.
6. Liu HB, Zhang HQ, Li JF. Toughness of SA738Gr.B steel used for nuclear containment vessel. Int J Press Vessel Pip. 2018;168:200-209.
7. Ohtsubo H, Araki K, Moriya Y. Development of SA-738 Gr. B high strength steel plate with excellent toughness for power generating plants. JFE Tech Rep. 2013;(18):48-55.
8. Li Y, Zhang S, Zhao C, Song M, Jiang Z. Effects of high-temperature tempering on mechanical properties and microstructure of SA738 Gr.B steel. Metals. 2020;10(9):1207.
9. Pense AW, Stout RD. Fracture toughness and related characteristics of the cryogenic nickel steels. Nickel Institute; 2021.
10. Kern A, Schriever U, Stumpfe J. Development of 9% nickel steel for LNG applications. Steel Res Int. 2007;78(3):189-194.
11. Kubo T, Ohmori A, Tanigawa O. Properties of high toughness 9% Ni heavy section steel plate and its applicability to 200,000 kl LNG storage tanks. Kawasaki Steel Technical Report. 1999;(40):72-79.
12. Mounce WS. Nine percent nickel – 28 years of reliable service in LNG containment. Nickel Development Institute; 1988.

13. Khodir S, Shibayanagi T, Takahashi M, Abdel-Aleem H, Ikeuchi K. Microstructural evolution and mechanical properties of high strength 3–9% Ni-steel alloys weld metals produced by electron beam welding. Mater Des. 2014;60:391-400.
14. Shin HS, Lee HM, Kim MS. Impact tensile behavior of 9% nickel steel at low temperature. Int J Impact Eng. 2000;24(6):571-581.
15. Du WS, Cao R, Yan YJ, Tian ZL, Peng Y, Chen JH. Fracture behavior of 9% nickel high-strength steel at various temperatures: Part I. Tensile tests. Mater Sci Eng A. 2008;486(1-2):611-625.
16. Honda K, Sekito S. Two kinds of martensite. Nature. 1928;121:744.
17. Ron M, Kidron A, Schechter H, Niedźwiedź S. Structure of martensite. J Appl Phys. 1967;38(2):590-4.
18. Davenport ES, Bain EC. Transformation of austenite at constant subcritical temperatures. Metall Trans A. 1970;1(12):3503-30.
19. Furuhara T, Kawata H, Morito S, Maki T. Crystallography of upper bainite in Fe-Ni-C alloys. Mater Sci Eng A. 2006;431:228-36.
20. Takahashi M, Bhadeshia H. Model for transition from upper to lower bainite. Mater Sci Technol. 1990;6(7):592-603.
21. Matsumura O, Sakuma Y, Ishii Y, Zhao J. Effect of retained austenite on formability of high strength sheet steels. ISIJ Int. 1992;32:1110-6.
22. Chen J, Lv M, Tang S, Liu Z, Wang G-d. Correlation between mechanical properties and retained austenite characteristics in a low-carbon medium manganese alloyed steel plate. Mater Charact. 2015;106:108-11.
23. Cock T, Ferrer JP, Capdevila C, Caballero F, López V, Andrés C. Austenite retention in low Al/Si multiphase steels. Scripta Mater. 2006;55:441-3.
24. Lan L, Qiu C, Zhao D, Gao X, Du L. Analysis of microstructural variation and mechanical behaviors in submerged arc welded joint of high strength low carbon bainitic steel. Mater Sci Eng A. 2012;558:592-601.
25. Wang SC, Yang JR. Effects of chemical composition, rolling and cooling conditions on the amount of martensite/austenite (M/A) constituent formation in low carbon bainitic steels. Mater Sci Eng A. 1992;154: 43-49.

26. Davis CL, King JE. Cleavage initiation in the intercritically reheated coarse-grained heat-affected zone: Part I. Fractographic evidence. Metall Mater Trans A. 1994;25(3):563-73.
27. Lambert A, Drillet J, Gourgues AF, Sturel T, Pineau A. Microstructure of martensite-austenite constituents in heat affected zones of high strength low alloy steel welds in relation to toughness properties. Sci Technol Weld Join. 2000;5(3):168-73.
28. Li Y, Baker TN. Effect of morphology of martensite-austenite phase on fracture of weld heat affected zone in vanadium and niobium microalloyed steels. Mater Sci Technol. 2010;26(9):1029-40.
29. Li BZ, Li CS, Jin X, Zhang J. Effect of M–A constituents formed in thermo-mechanical controlled process on toughness of 20CrNi2MoV steel. J Iron Steel Res Int. 2019;26(12):1340-9.
30. Luo X, Chen X, Wang T, Pan S, Wang Z. Effect of morphologies of martensite–austenite constituents on impact toughness in intercritically reheated coarse-grained heat-affected zone of HSLA steel. Mater Sci Eng A. 2018;710:192-9.
31. Caballero FG et al. Influence of bainite morphology on impact toughness of continuously cooled cementite free bainitic steels. Mater Sci Technol. 2012;28(1):95-102.
32. Chen J, Tang S, Liu ZY, Wang GD. Microstructural characteristics with various cooling paths and the mechanism of embrittlement and toughening in low-carbon high performance bridge steel. Mater Sci Eng A. 2013;559:241-9.
33. Thomason PF. Ductile fracture of metals. Oxford: Pergamon Press; 1993.
34. Pineau A, Benzerga AA, Pardoen T. Failure of metals I: Brittle and ductile fracture. Acta Mater. 2016;107:424-83.
35. Tipper CF. The fracture of metals. Metallurgia. 1949;39:133-7.
36. Goods SH, Brown LM. The nucleation of cavities by plastic deformation. Acta Metall. 1979;27:1-15.
37. Marini B, Mudry F, Pineau A. Experimental study of cavity growth in ductile rupture. Eng Fract Mech. 1985;22:989-96.
38. Babout L, Brechet Y, Maire E, Fougeres R. On the competition between particle fracture and particle decohesion in metal matrix composites. Acta Mater. 2004;52:4517-25.

39. Argon AS, Im J. Separation of second phase particles in spheroidized 1045 steel, Cu-0.6pct Cr alloy, and maraging steel in plastic straining. Met Trans A. 1975;6A:839-51.
40. Le Roy G, Embury JD, Edward G, Ashby MF. A model of ductile fracture based on the nucleation and growth of voids. Acta Metall. 1981;29:1509-22.
41. Argon AS, Im J, Safoglu R. Cavity formation from inclusions in ductile fracture of A508 steel. Metall Trans A. 1975;6A:825-37.
42. Brown LM, Stobbs WM. The work-hardening of copper-silica V. Equilibrium plastic relaxation by secondary dislocations. Philos Mag. 1976;34:351-72.
43. Iricibar R, Le Roy G, Embury JD. Relationship of strain hardening and damage in ductile fracture. Metal Sci. 1980;14:337-43.
44. Tvergaard V, Needleman A. Analysis of the cup-cone fracture in a round tensile bar. Acta Metall. 1984;32(1):157-69.
45. Rice JR, Tracey DM. On the ductile enlargement of voids in triaxial stress fields. J Mech Phys Solids. 1969;17(3):201-17.
46. McClintock FA. A criterion for ductile fracture by the growth of holes. J Appl Mech. 1968;35(2):363-71.
47. Gurson AL. Continuum theory of ductile rupture by void nucleation and growth: Part I—Yield criteria and flow rules for porous ductile media. ASME J Eng Mater Technol. 1977;99(1):2-15.
48. Thomason PF. A theory for ductile fracture by internal necking of cavities. J Mech Phys Solids. 1985;33(5):43-58.
49. Springmann M, Kuna M. Identification of material parameters of the Gurson–Tvergaard–Needleman model by combined experimental and numerical techniques. Comput Mater Sci. 2005 Jun;33(4):501-9.
50. Msolli S, Bettaieb M, Abed-Meraim F. Modelling of void coalescence initiation and its impact on the prediction of material failure. AIP Conf Proc. 2016.
51. Louden BS, Kumar AS, Garner FA, Hamilton ML, Hu WL. The influence of specimen size on Charpy impact testing of unirradiated HT-9. J Nucl Mater. 1988;155-157:662-7.
52. Benzerga AA, Tvergaard V, Needleman A. Size effects in the Charpy V-notch test. Int J Fract. 2002;116:275-96.
53. Porter DA, Easterling KE, Sherif MY. Phase transformations in metals and alloys. 4th ed. CRC Press; 2021.

54. Griffith AA. The phenomena of rupture and flow in solids. Philos Trans R Soc Lond. 1921;A221:163-98.
55. Chen JH, Cao R. Introduction. In: Chen JH, Cao R, editors. Micromechanism of Cleavage Fracture of Metals. Butterworth-Heinemann; 2015. p. 1-54.
56. Irwin GR. Fracture dynamics. In: Fracturing of Materials. Cleveland: American Society Metals; 1948. p. 126-47.
57. Orowan E. Fracture and strength of solids. Rep Prog Phys. 1949;12:185-232.
58. Knott JF. Fundamentals of Fracture Mechanics. London: The Butterworth Group; 1973. p. 150-75.
59. Lawn BR. Fracture of Brittle Solids. 2nd ed. Cambridge: Cambridge University Press; 1993.
60. Broek D. Elementary Engineering Fracture Mechanics. 4th ed. Martinus Nijhoff Publishers; 1986.
61. Curry DA. Cleavage micromechanisms of crack extension in steels. Metal Sci. 1980;14:319-26.
62. Smith E. The nucleation and growth of cleavage microcracks in mild steel. In: Physical Basis of Yield and Fracture. Oxford: Institute of Physics and Physical Society; 1966. p. 36-46.
63. Ritchie RO, Knott JF, Rice JR. On the relationship between critical tensile stress and fracture toughness in mild steel. J Mech Phys Solids. 1973;21:395-410.
64. Rice JR, Johnson MA. The role of large crack tip geometry changes in plane strain fracture. In: Kanninen MF, et al., editors. Inelastic Behaviour of Solids. New York: McGraw Hill; 1970. p. 641-72.
65. Griffiths JR, Owen DRJ. An elastic-plastic stress analysis for a notched bar in plane strain bending. J Mech Phys Solids. 1971;19:419-31.
66. Irwin GR. Analyses of stress and strain near the end of a crack traversing a plate. J Appl Mech. 1957;24:364-81.
67. Bates RC. Micromechanical modelling for prediction of lower shelf, transition region, and upper shelf fracture properties. In: Nair SV, Tien JK, Bates RC, Buck O, editors. Fracture Mechanics: Microstructure and Micromechanics. Metal Park, Ohio: ASM International; 1987. p. 131-68.

68. Hutchinson JW. Plastic stress and strain field at a crack tip. J Mech Phys Solids. 1968;16:13-31.
69. Rice JR, Rosengren GR. Plane strain deformation near a crack tip in a power-law hardening material. J Mech Phys Solids. 1968;16:1-12.
70. Shu DL. Mechanical properties of engineering materials. Beijing: China Machine Press; 2007.
71. Wells AA. Application of fracture mechanics at and beyond general yielding. Br Weld J. 1963;11:563-70.
72. Yang W. Macro and Micro Fracture Mechanics. Beijing: Defence Press; 1995.
73. American Society for Testing and Materials. Standard Test Methods for Determining Average Grain Size: E112-13. West Conshohocken, PA: ASTM International; 2013.
74. American Society for Testing and Materials. Standard Test Methods for Tension Testing of Metallic Materials: E8/E8M-16a. West Conshohocken, PA: ASTM International; 2016.
75. Hollomon JH. Tensile deformation. Aime Trans. 1945 Jun;12(4):1-22.
76. American Society for Testing and Materials. Standard Test Methods for Notched Bar Impact Testing of Metallic Materials: E23-16b. West Conshohocken, PA: ASTM International; 2016.
77. American Society for Testing and Materials. Standard Test Method for Measurement of Fracture Toughness: E1820-17. West Conshohocken, PA: ASTM International; 2017.
78. American Society for Testing and Materials. Standard Test Method for Linear-Elastic Plane-Strain Fracture Toughness KIc of Metallic Materials: E399-17. West Conshohocken, PA: ASTM International; 2017.
79. Rolfe ST, Novak SR. Slow-bend KIc Testing of Medium-strength High-toughness Steels. In: Review of Developments in Plane Strain Fracture Toughness Testing. ASTM STP 463. West Conshohocken, PA: ASTM; 1970. p. 124–159.
80. Barsom JM, Rolfe ST. Correlations Between KIc and Charpy V-notch Test Results in the Transition-temperature Range. In: Impact Testing of Metals Symp. ASTM STP 466. West Conshohocken, PA: ASTM; 1970. p. 281–302.
81. Corten HT, Sailors RH. Relationship Between Material Fracture Toughness Using Fracture Mechanics and Transition Temperature Tests. T. & A.M. Rep. No. 346, Tech.

Rep. No. 15. Urbana, IL: Heavy Section Steel Technology Program, University of Illinois; 1971.

82. Roberts R, Newton C. Interpretive Report on Small-scale Test Correlations with KIc Data. WRC Bull. 1981;(265):1-18.
83. McMeeking RM. Finite Deformation Analysis of Crack-tip Opening in Elastic-plastic Materials and Implications for Fracture. J Mech Phys Solids. 1977;25(5):357–381.
84. Liu C, Webler B. Evolution of non-metallic inclusions during heat treatment. Metall Res Technol. 2020;117(4):408.
85. Li Y, Zhang T, Duan H. Influence of Al on evolution of the inclusions in Ti-bearing steel with Ca treatment. Metals. 2019;9(1):104.
86. Zhang T, Liu C, Qiu J, Li X, Jiang M. Effect of Ti content on the characteristics of inclusions in Al–Ti–Ca complex deoxidized steel. ISIJ Int. 2017;57(2):314-321. doi:10.2355/isijinternational.ISIJINT-2016-417.
87. Fan H. Micromechanisms of Cleavage Fracture at Cryogenic Temperatures of SA. 738 Gr. B Steel and 7% Nickel Steel [PhD thesis]. Birmingham: University of Birmingham; 2023.
88. Xu W. Characterisation of Micro-Mechanisms of Cleavage Fracture in SA738Gr.B Steel [PhD thesis]. Birmingham: University of Birmingham; 2023.
89. Bhadeshia HKDH, Honeycombe RWK. Steels: Microstructure and Properties. 3rd ed. Oxford: Butterworth-Heinemann; 2006.
90. Ritchie RO, Knott JF. Micro-mechanisms of cleavage fracture and grain size effects in low-strength steel. Acta Metall. 1973;21(5):639-649.
91. Hancock JW, Mackenzie AC. On the mechanisms of ductile failure in high-strength steels subjected to multi-axial stress-states. J Mech Phys Solids. 1976;24(2–3):147–69.
92. Anderson TL. Fracture mechanics: fundamentals and applications. 4th ed. Boca Raton (FL): CRC Press; 2017.
93. Ritchie RO. The influence of microstructure on fracture toughness. Metall Trans A. 1977;8(4):613–23.
94. Barsom JM, Rolfe ST. Fracture and fatigue control in structures: applications of fracture mechanics. 3rd ed. West Conshohocken (PA): ASTM International; 1999.

95. Li X, Xie Z, Wang X, Wang X, Shang C. Split fracture phenomenon and mechanism in tensile tests of high strength low carbon bainitic steel. Acta Metallurgica Sinica. 2013;49(2):167-174.
96. Bhadeshia HKDH. Bainite in Steels: Transformations, Microstructure, and Properties. 2nd ed. London: IOM Communications Ltd; 2001.
97. Cao L, Wu S, Flewitt P. Comparison of Ductile-to-Brittle Transition Curve Fitting Approaches. Int J Pressure Vessels Piping. 2012;93:12-16.
98. Li XJ. Selection of the Mathematical Model on Ductile-brittle Transition Temperature Curve of Impact Test. Phys Test Chem Anal. 2009.
99. Wenman MR. Micromechanisms of Fracture in the Ductile-to-brittle Transition Region of a MnMoNi Steel Weld Metal and a Burn Resistant Beta Titanium Alloy [PhD thesis]. Birmingham: University of Birmingham; 2003.
100. Liu Y, Chen X, Zhang J, Li Q, Wang C. Precipitation Behavior of Carbides and Its Effect on the Mechanical Properties of 15CrNi3MoV Steel. Metals (Basel). 2022;12(10):1758.
101. Qiao LJ, Zhao M, Ma Y, Xiao FR. The Role of Microstructure Morphology on Fracture Mechanisms of Bainitic Steel. Metall Mater Trans A. 2022;53(11):4124–4138.
102. Garrison WM, Moody NR. The Influence of Microstructure on the Cleavage Fracture Toughness of Steel. Metall Trans A. 1987;18(1):43–58.
103. Pickering FB, Gladman T. Metallurgical Developments in Carbon Steels. Ironmaking Steelmaking. 1963;1(1):24–36.
104. Lin T, Evans AG, Ritchie RO. Statistical Analysis of Cleavage Fracture Ahead of Sharp Cracks and Rounded Notches. Acta Metall. 1986;34:2205-16.
105. Gao X, Dodds RH. Loading rate effects on parameters of the Weibull stress model for ferritic steels. Eng Fracture Mech. 2005;72(15):2416–25.
106. Gao X, Joyce JA, Roe C. An investigation of the loading rate dependence of the Weibull stress parameters. Eng Fracture Mech. 2008;75(6):1451–67.
107. Yu M, Luo Z, Chao YJ. Correlations between Charpy V-notch impact energy and fracture toughness of nuclear reactor pressure vessel (RPV) steels. Eng Fracture Mech. 2015;147:187-202.
108. Collins W, Sherman R, Leon R, Connor R. State-of-the-Art Fracture Characterization. II: Correlations between Charpy V-Notch and the Master Curve Reference Temperature. J Bridge Eng. 2016;21.

109. Li HF, Duan QQ, Zhang P, Zhou XH, Wang B, Zhang ZF. The quantitative relationship between fracture toughness and impact toughness in high-strength steels. Eng Fracture Mech. 2019;211:362-70.
110. Chen JH, Cao R. Criteria for Cleavage Fracture. In: Chen JH, Cao R, editors. Micromechanism of Cleavage Fracture of Metals. Oxford: Butterworth-Heinemann; 2015. p. 181-238.
111. Bose Filho WW, Carvalho ALM, Bowen P. Micromechanisms of cleavage fracture initiation from inclusions in ferritic welds. Part I. Quantification of local fracture behaviour observed in notched testpieces. Mater Sci Eng A. 2007;460–461:436–52.
112. Ohmura T, Hara T, Tsuzaki K, Nakatsu H, Tamura Y. Mechanical characterization of secondary-hardening martensitic steel using nanoindentation. J Mater Res. 2004;19(1):79–84.
113. Chen X, Zhai Q, Dong H, Dai B, Mohrbacher H. Molybdenum alloying in cast iron and steel. Adv Manufact. 2019;8:3-14.
114. Syn CK, Fultz B, Morris Jr. JW. Mechanical stability of retained austenite in tempered 9Ni steel. Metall Trans A. 1978;9A(11):1635-40.
115. Nippes EF, Balaguer JP. A study of the weld heat-affected zone toughness of 9% nickel steel. Weld Res (Miami). 1986:237S-243S.
116. ArcelorMittal USA. Plate- 9% Nickel Steel: For use at cryogenic temperatures. ArcelorMittal; 2010.
117. Jahrsengene G, Wenn M, Karlsen M, Westermann I, Akselsen OM, Hjelen J. EBSD Quantification of Retained Austenite in 9% Ni Steel Related to Thermal Treatments. Paper presented at the Twenty-fifth International Ocean and Polar Engineering Conference, Kona, Hawaii, USA; June 2015.
118. Lee J, Kim S, Park J, et al. Enhanced ultra-cryogenic impact toughness in 9 wt% Ni steel via QLT treatment. Mater Sci Eng A. 2024;862:145097.
119. Zhou Y, Wang X, Liu H, et al. Fracture behavior of 9% nickel high-strength steel at various temperatures. Mater Sci Eng A. 2023;858:144528.
120. Strife JR, Passoja DE. The effect of heat treatment on microstructure and cryogenic fracture properties in 5Ni and 9Ni steel. Metall Trans A. 1980;11:1341–50.

121. American Society for Testing and Materials. ASTM A553/A553M-22 Standard Specification for Pressure Vessel Plates, Alloy Steel, Quenched and Tempered 7%, 8%, and 9% Nickel. West Conshohocken, PA: ASTM International; 2022.
122. Afzali N, Stranghöner N, Langenberg P. Fracture Toughness Behaviour of Nickel Alloy Steel 1.5662+QT640. Materials. 2024;17:6117.
123. Fernandes VS, Farias CWF, Payão Filho JC. Fracture toughness of a 9 % Ni steel pipe girth welded with Ni-based superalloy 625 filler metal operating in a sour environment. J Mater. Res. Technol. 2020;9(3):6305–6321.
124. Shih CF, German MD. Requirements for a one-parameter characterization of crack-tip fields by the HRR singularity. Int J Fract. 1981;17:27–43.
125. Zuo J, Deng X, Sutton MA, Cheng C. Three-dimensional crack growth in ductile materials: effect of stress constraint on crack tunneling. J Press Vessel Technol. 2008 Aug;130(3):031401.

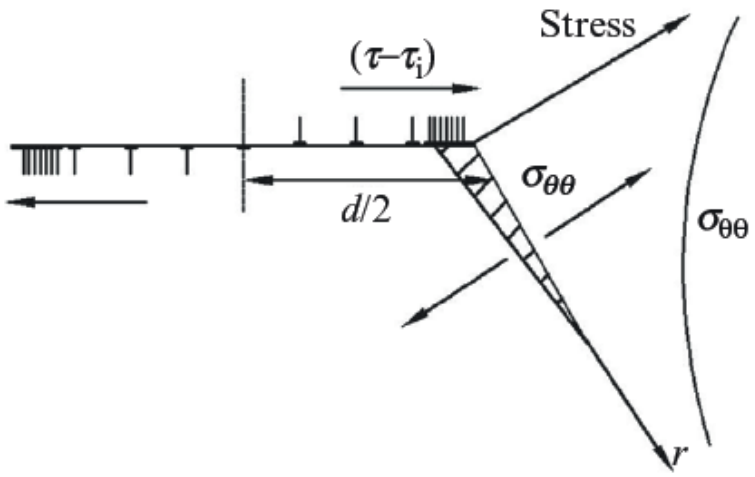

Figure 2.1 Schematic illustration of the dislocations at the crack tip of slip-band [43].

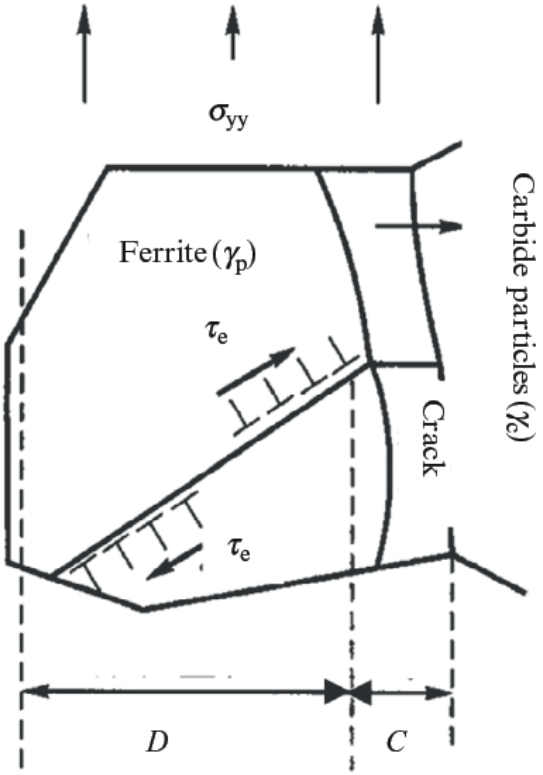

Figure 2.2 Schematic illustration of formation of a dislocation pile-up within a ferrite grain [47].

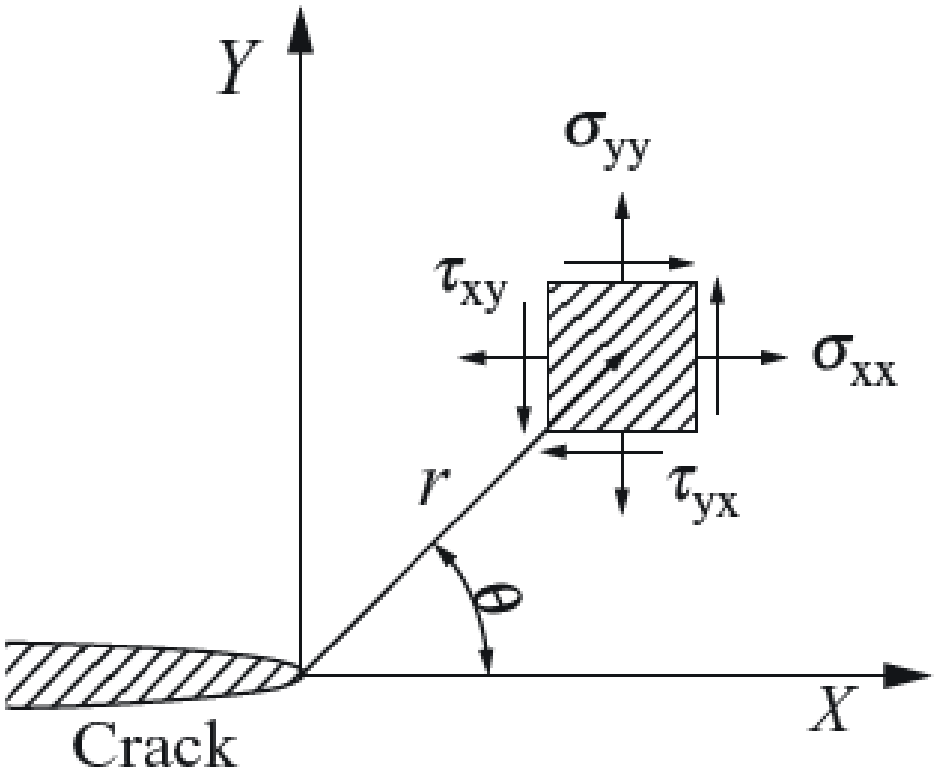

Figure 2.3 Schematic definition of the coordinate axis ahead of the crack tip, the X and Y directions are parallel and perpendicular to the crack surface, the Z direction aligns with the crack tip [51].

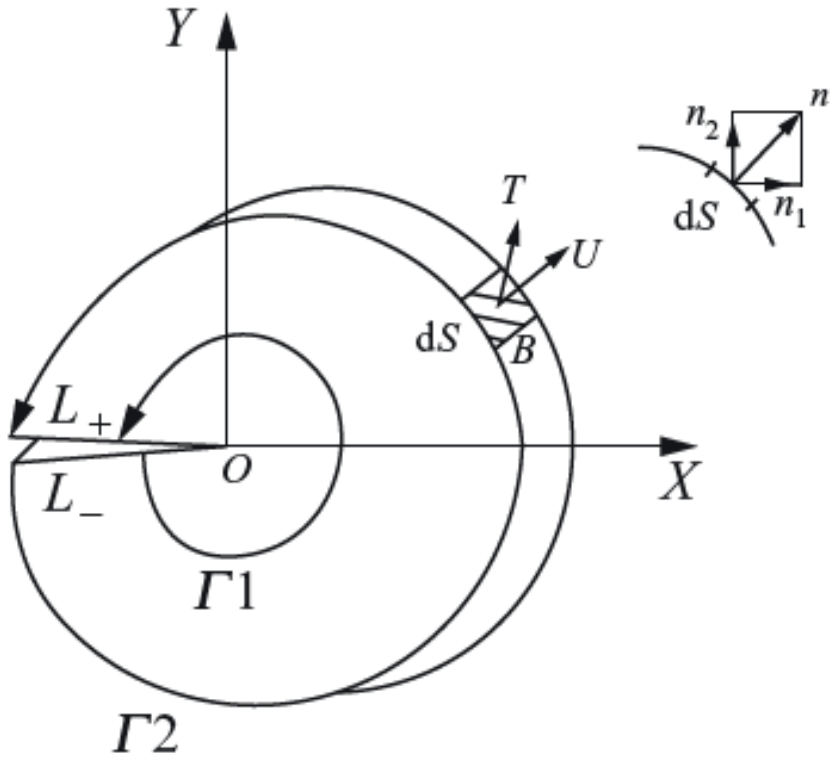

Figure 2.4 Schematic definition of the line integral *J* [55].

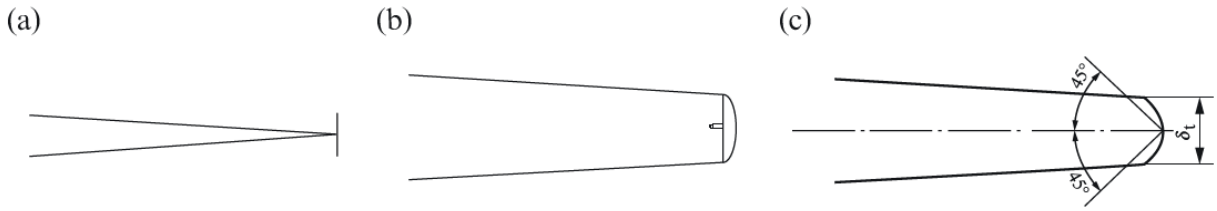

Figure 2.5 Definition of COD (a) original crack, (b) crack tip opening to δ_{COD}, (c) crack tip opening 45° COD ($\delta_{COD,t}$) [57].

Table 3.1 Chemical composition of SA738Gr.B from Baosteel 55m thick plate.

Element [wt%]	C	Si	Mn	P	S	Cr + Ni + Cu	Mo	V + Nb	CE*
Baowu Steel	**0.088**	**0.18**	**1.47**	**0.003**	**0.0002**	**0.37**	**0.19**	**0.063**	**0.4**
ASME Requirement	**≤ 0.20**	**0.15 - 0.55**	**0.90 - 1.50**	**≤ 0.030**	**≤ 0.030**	**≤ 1.25**	**≤ 0.30**	**≤ 0.080**	**≤ 0.48**

*Note: CE (carbon equivalent) = C + Mn/6 + (Cr + Mo +V)/5 + (Ni + Cu)/15

Table 3.2 Chemical Composition of 9% Nickel steel.

Element [wt%]	C	Si	Mn	P	S	Al	Ni
9% Nickel	**0.037**	**0.205**	**0.599**	**0.0036**	**0.0002**	**0.032**	**9.688**

Table 3.3 Chemical Composition of 7% Nickel steel.

Element [wt%]	C	Si	Mn	P	S	Al	Ni	Mo	Cr	N*
7% Nickel	**0.051**	**0.01**	**0.65**	**0.004**	**0.0035**	**0.029**	**7.14**	**0.064**	**0.39**	**37**

*Note: The composition of N is counted by part per million (ppm).

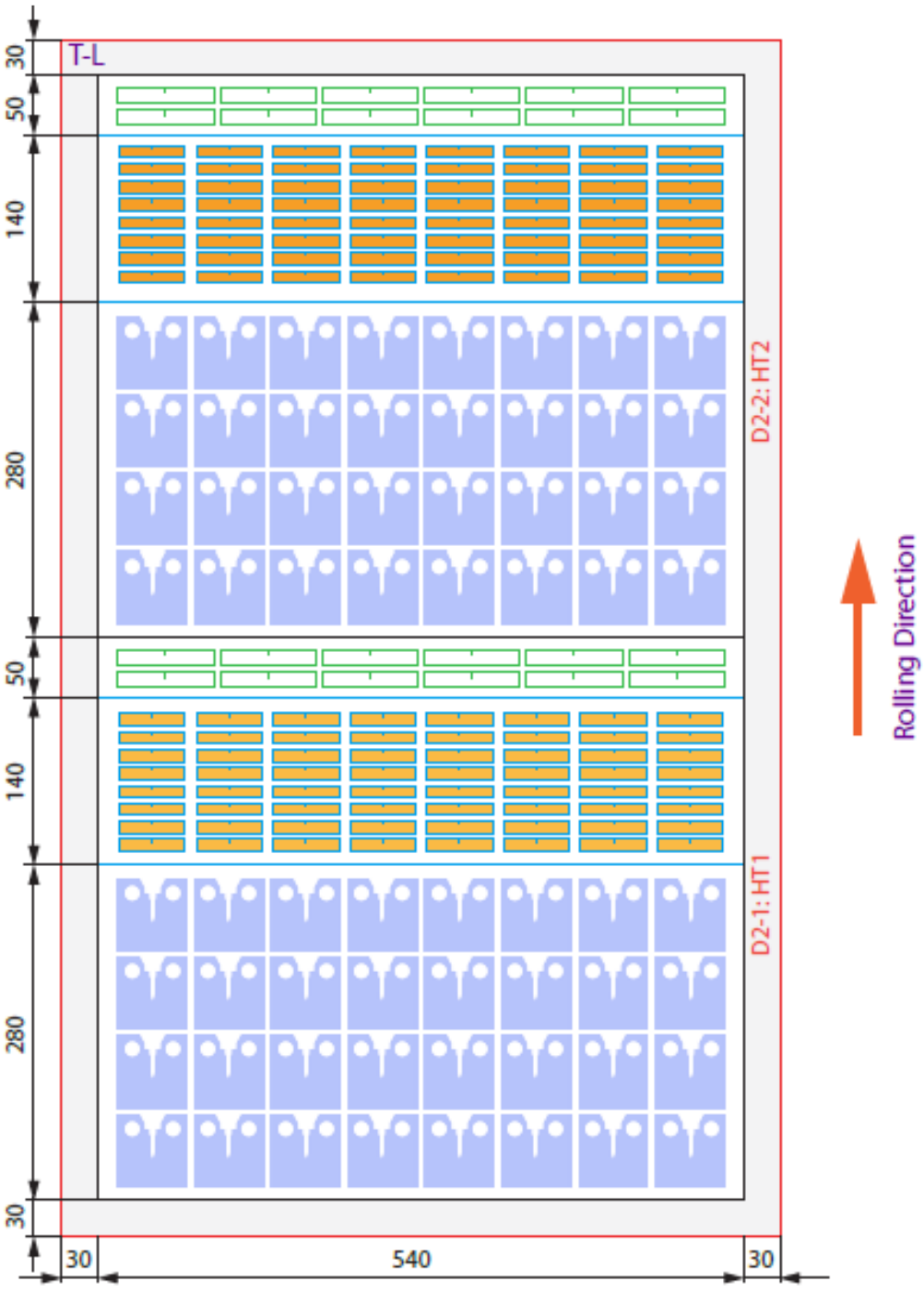

Figure 3.1 Schematic illustration of the steel plate orientation and the specimen sampling scheme for SA.738Gr.B steel.

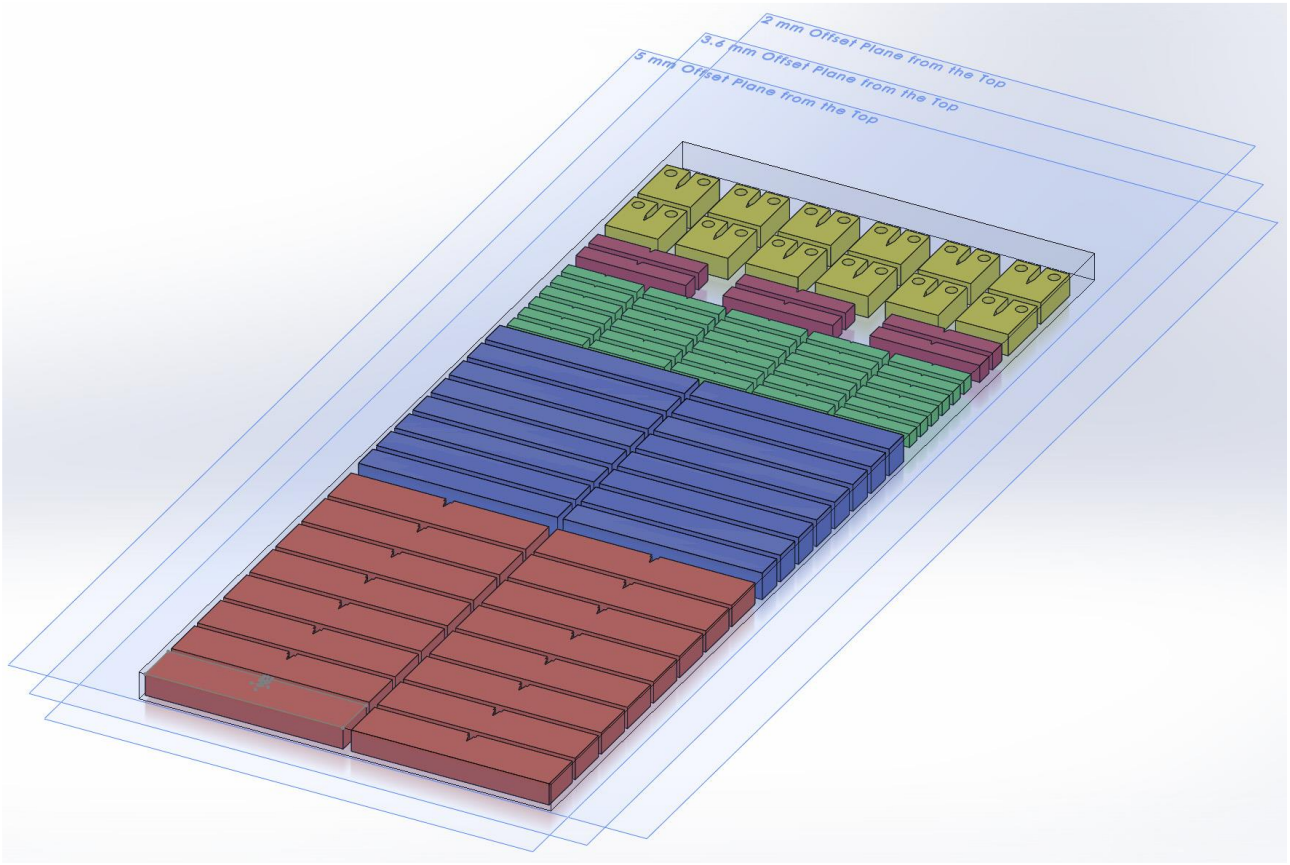

Figure 3.2 Schematic illustration of the specimen sampling scheme for both 9% and 7% Nickel steels.

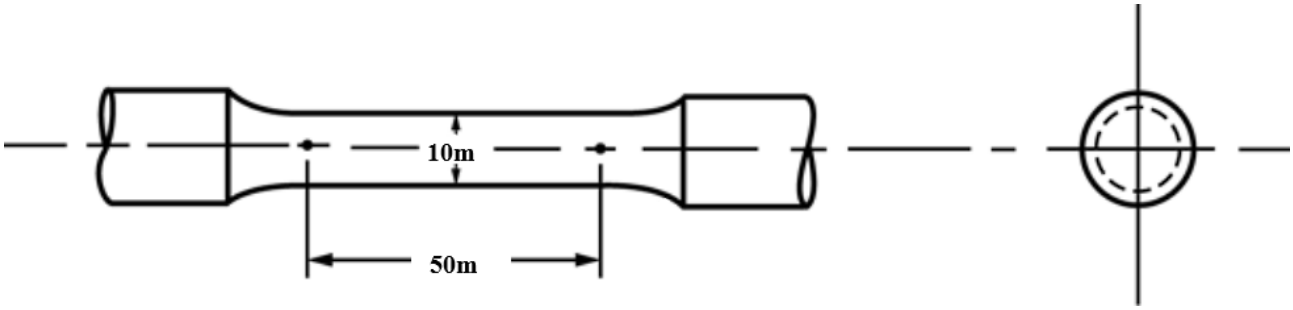

Figure 3.3 Tensile specimen geometry.

Figure 3.4 Tensile testing set-up for tests carried out at -196 °C.

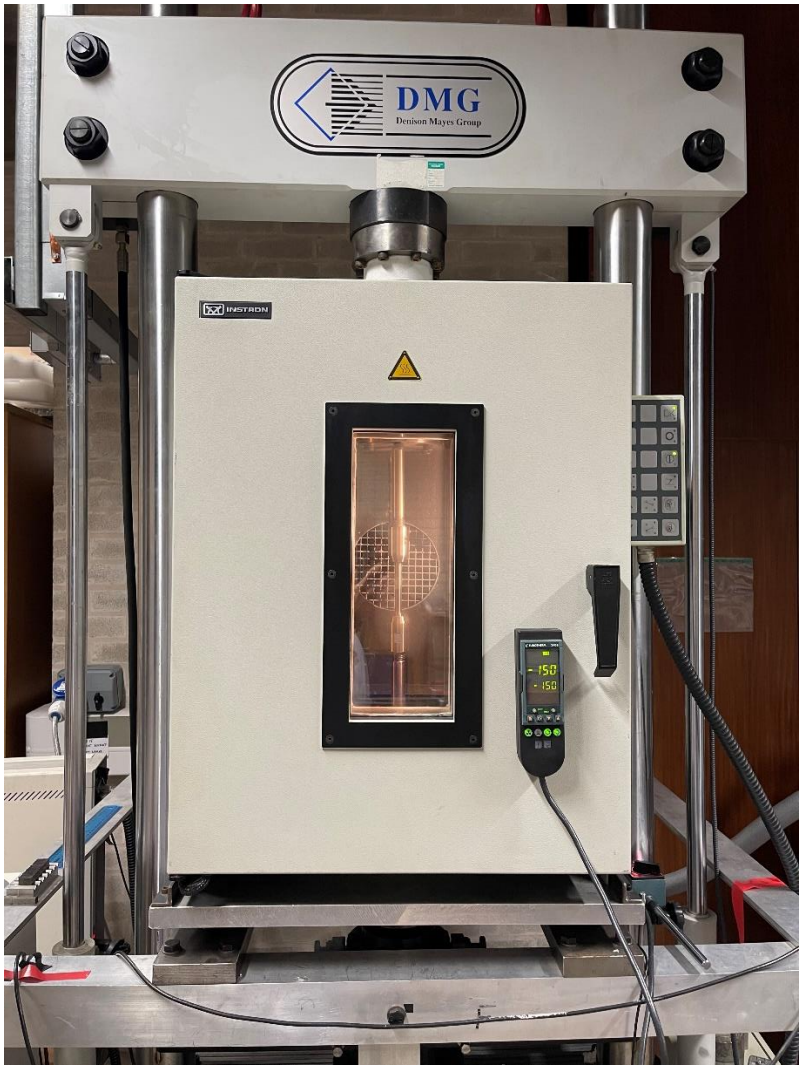

Figure 3.5 Tensile testing set-up for tests carried out at -170 °C and above temperatures.

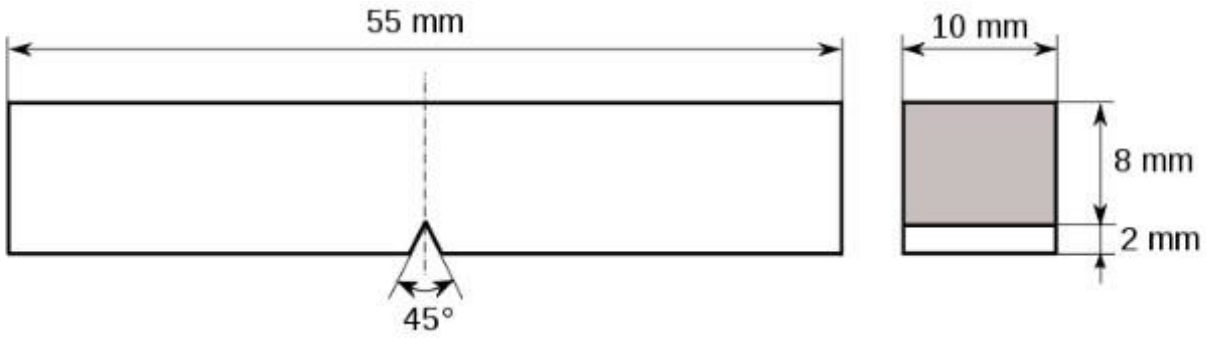

Figure 3.6 Charpy impact specimen geometry.

Figure 3.7 Instron-Wolpert Charpy impact testing machine with a 300 J capacity.

Figure 3.8 Set-up for the development of the temperature-time curves.

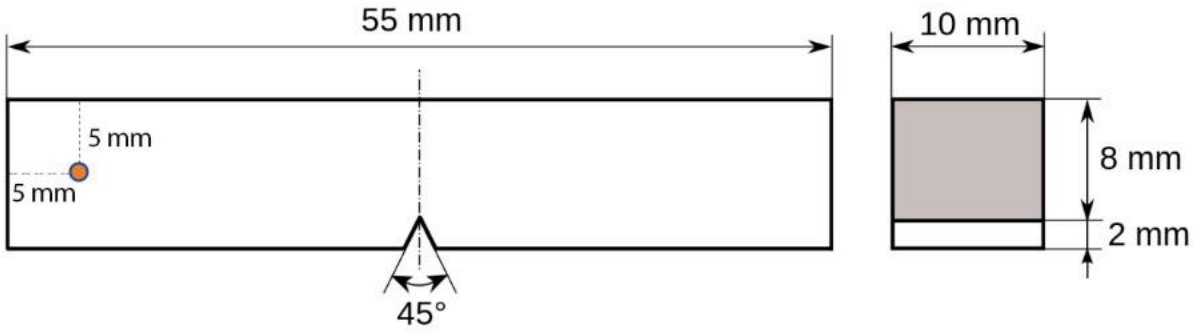

Figure 3.9 Location for thermocouple insertion on Charpy impact specimen.

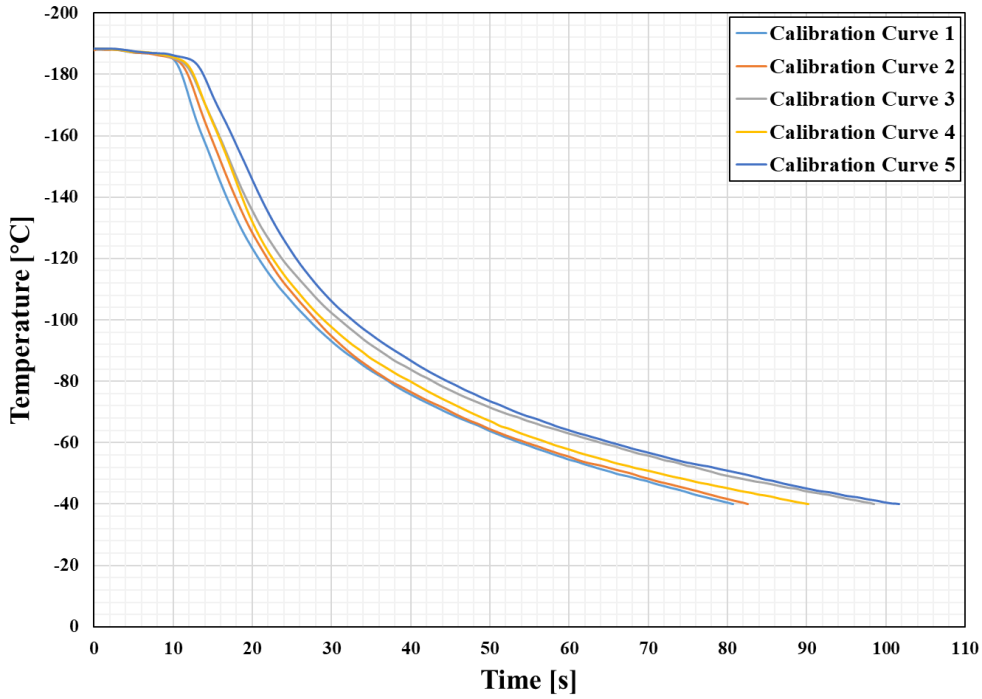

Figure 3.10 Five temperature calibration curves.

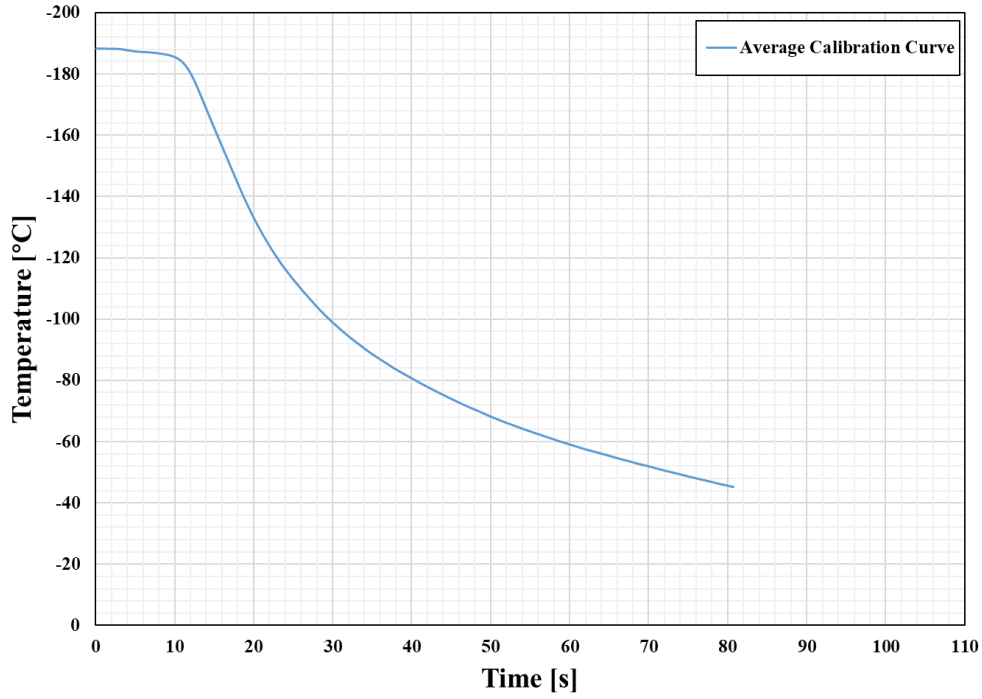

Figure 3.11 Average temperature calibration curve.

(a)

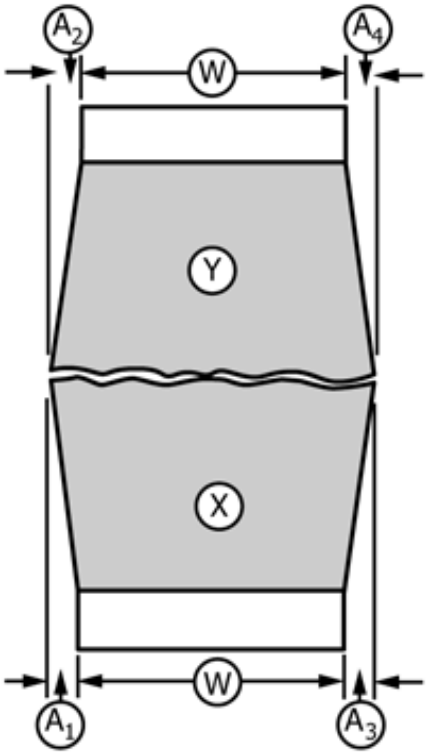

(b)

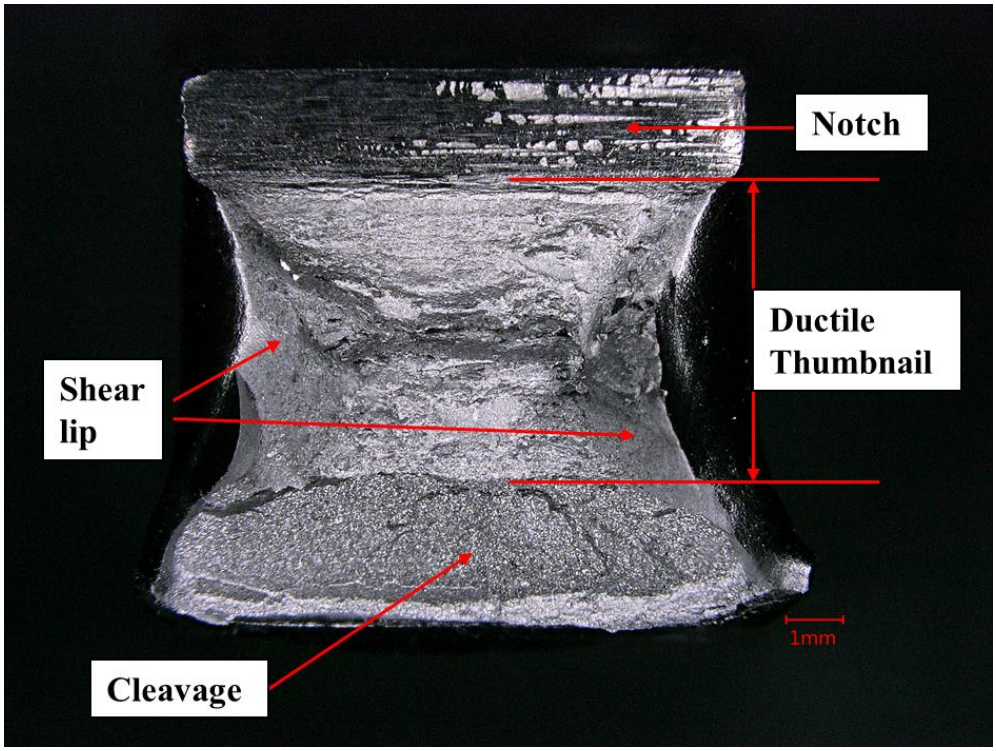

Figure 3.12 Schematic illustration of the measurements of (a)lateral expansion, (b) ductile thumbnail extension, shear lip size and cleavage area.

(a)

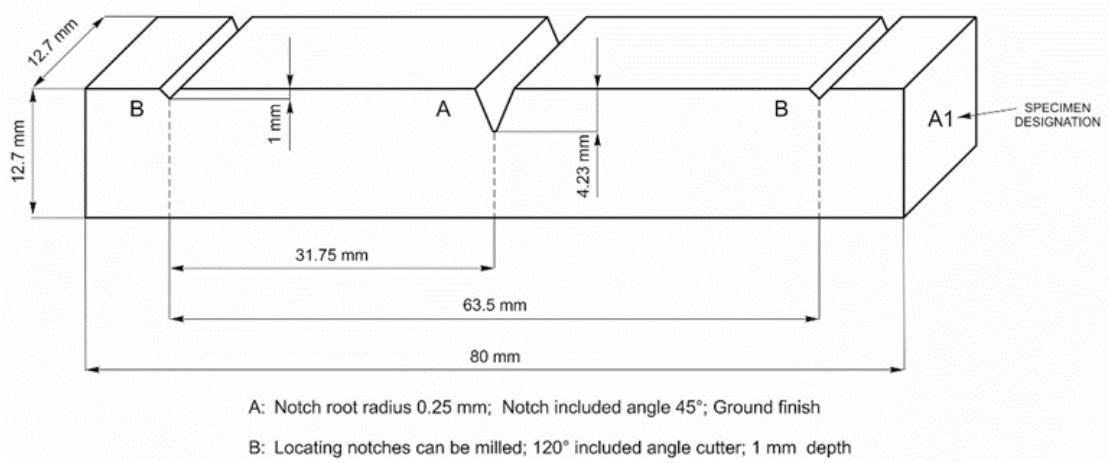

(b)

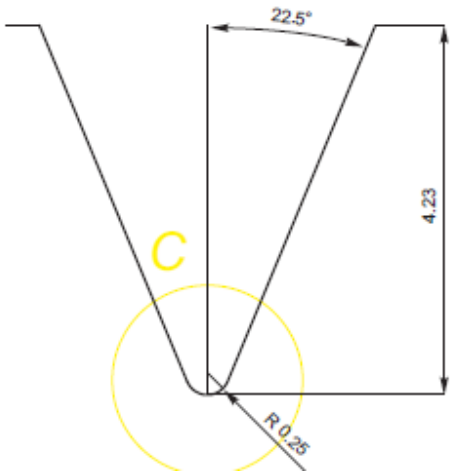

Figure 3.13 Fracture stress (a) specimen geometry, (b) notch profile.

Figure 3.14 The ESH hydraulic testing machine set-up for test at -196°C.

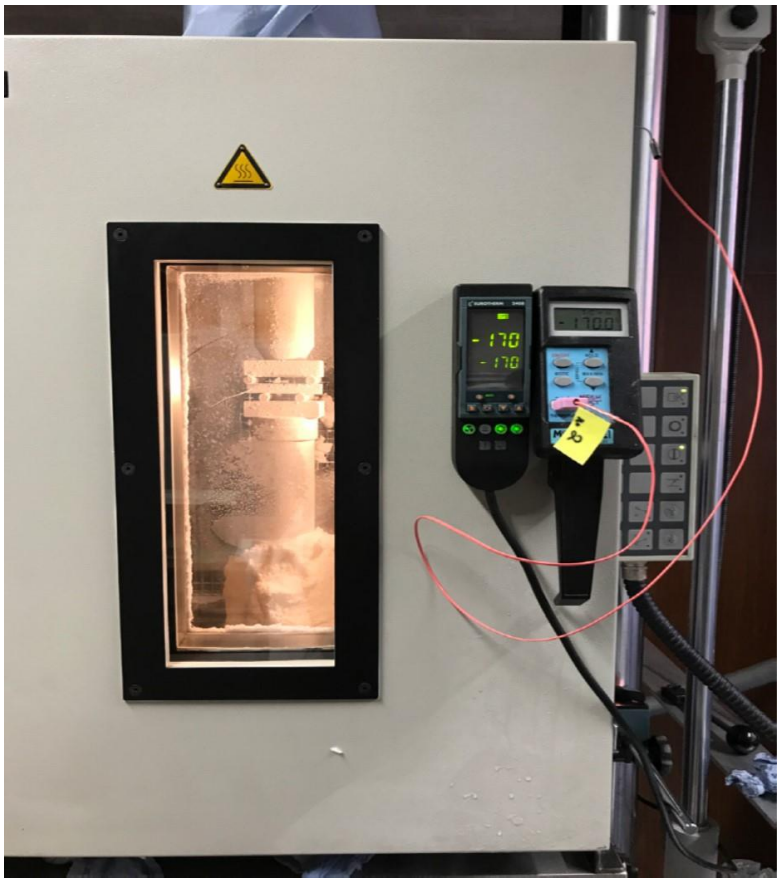

Figure 3.15 The DMG screw driven machine for test at -170 and -160°C.

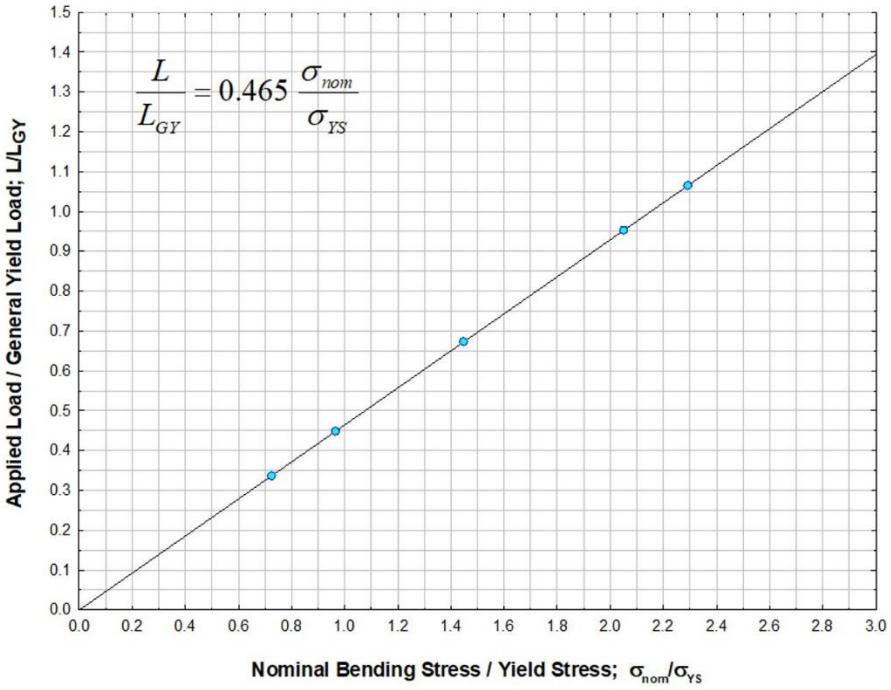

Figure 3.16 Relationship between the applied load and nominal bending stress.

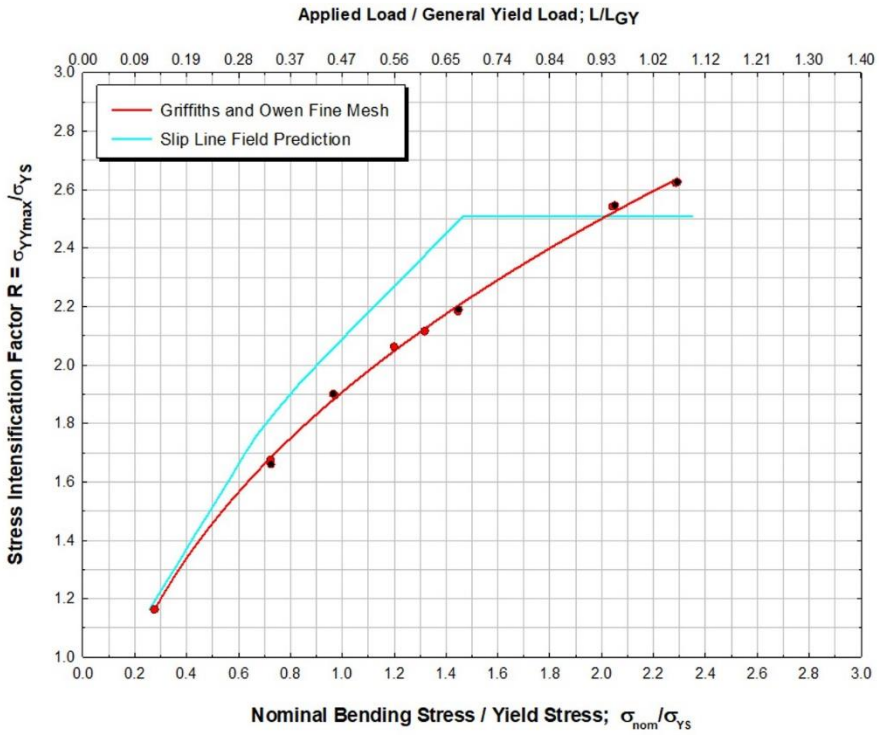

Figure 3.17 Relationship between the stress intensification factor and nominal bending stress.

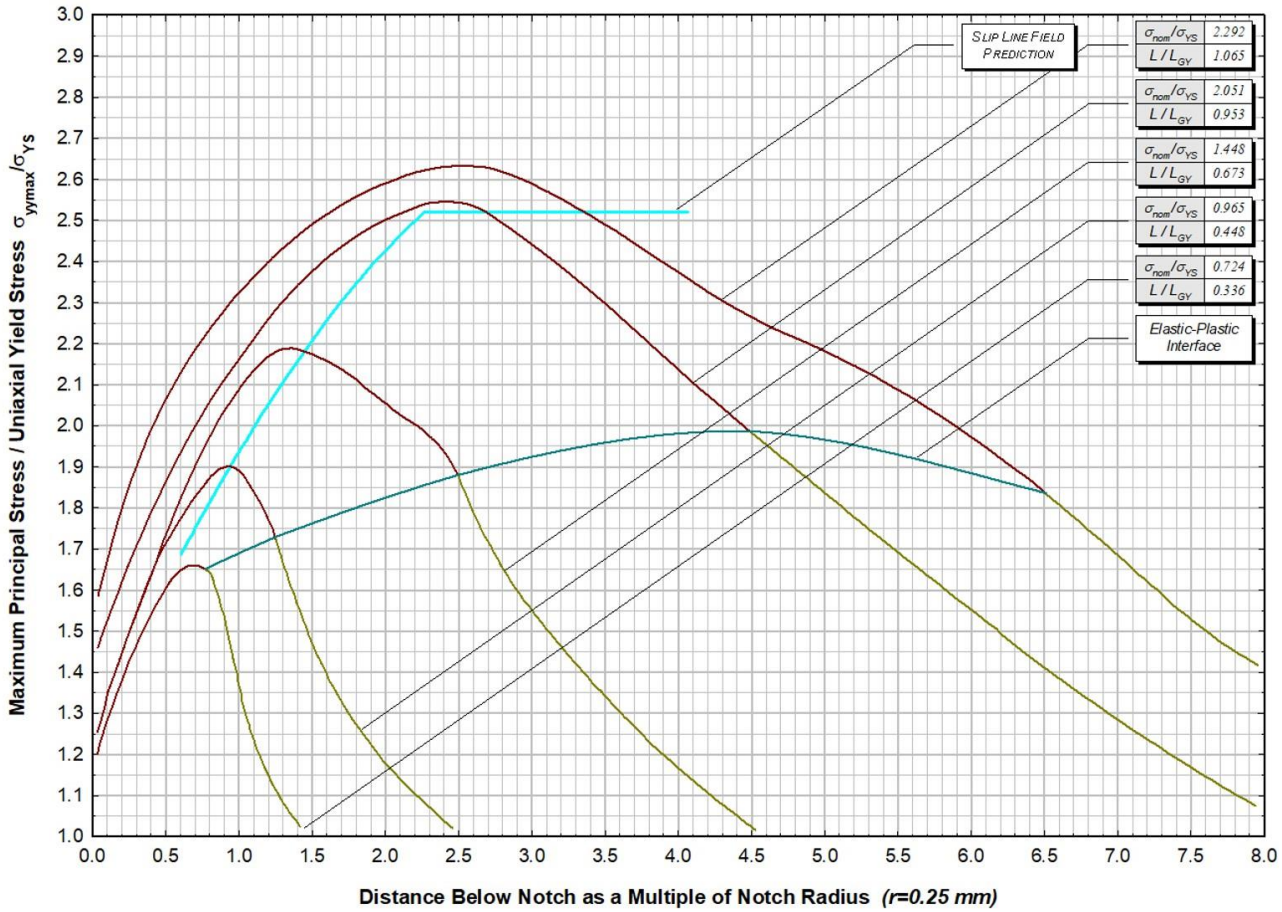

Figure 3.18 Finite element analysis for relationship between stress intensification factor *SIF* and the distance below the notch root as a multiple of notch root radius 0.25 mm.

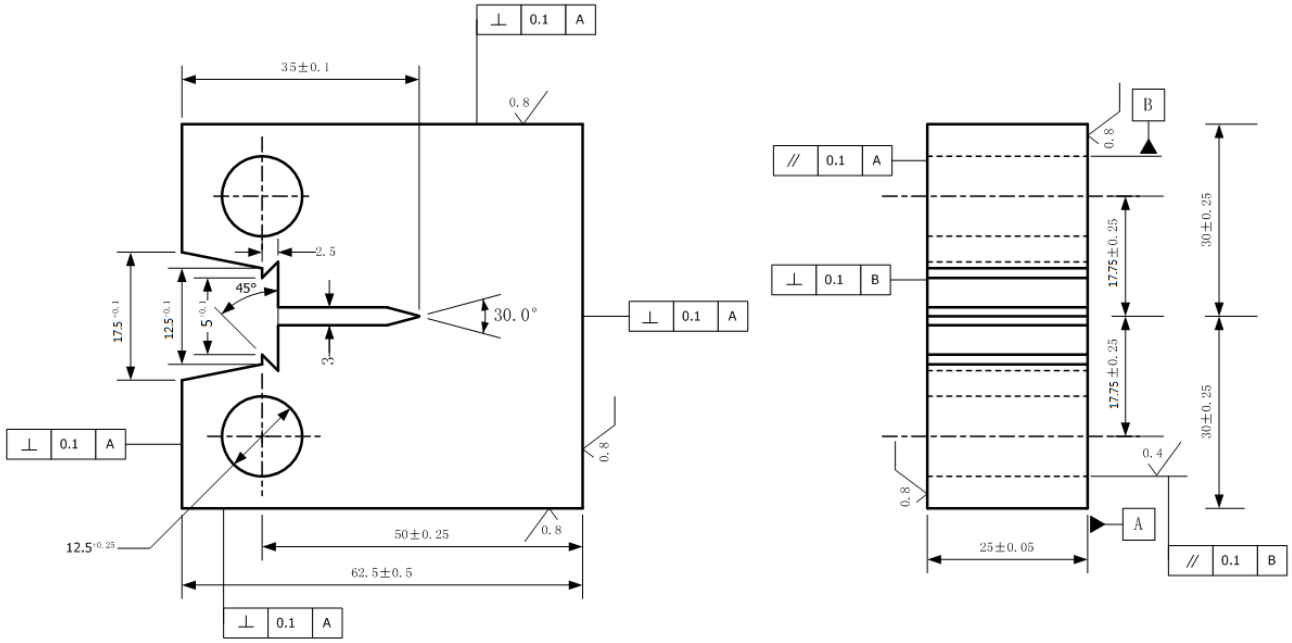

Figure 3.19 Geometry of the Compact Tension (CT) specimen used in Fracture Toughness tests.

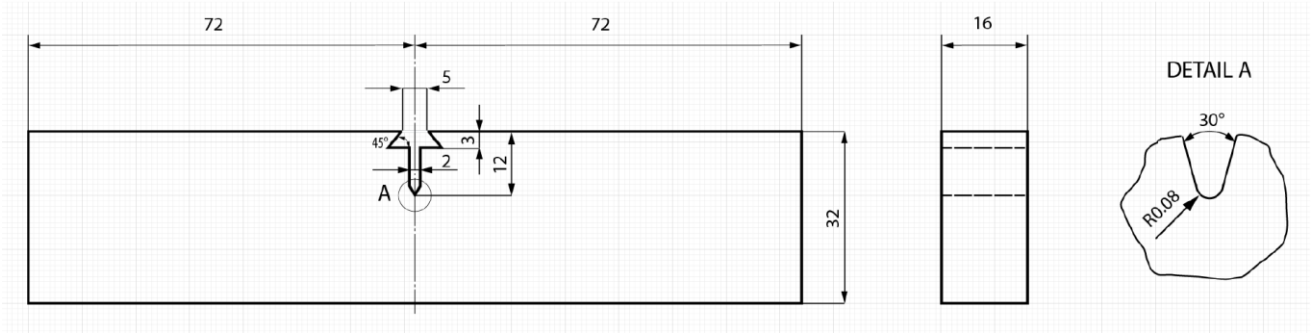

Figure 3.20 Geometry of the Single-Edge Notched Bend (SENB) specimen used in Fracture Toughness tests.

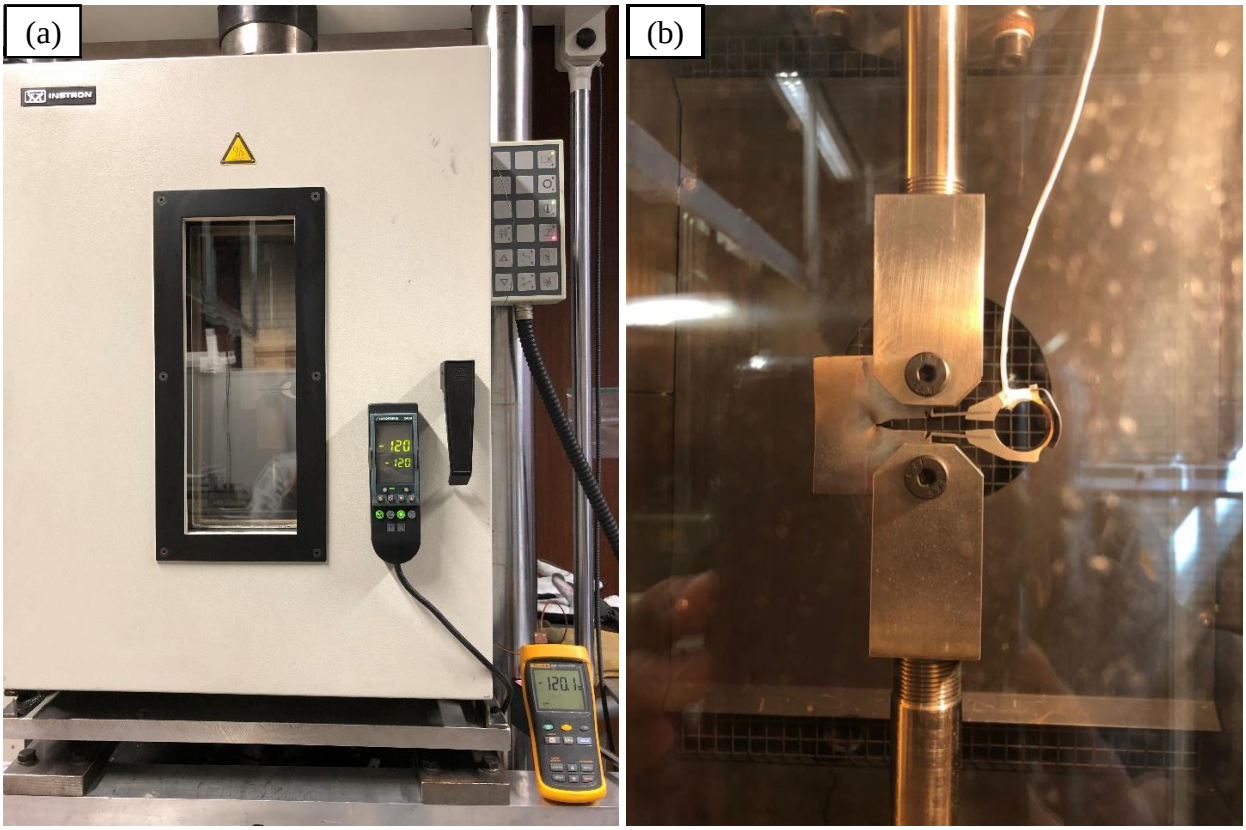

Figure 3.21 Test set-up for Fracture Toughness tests, (a) temperature chamber, (b) specimen loaded inside the chamber.

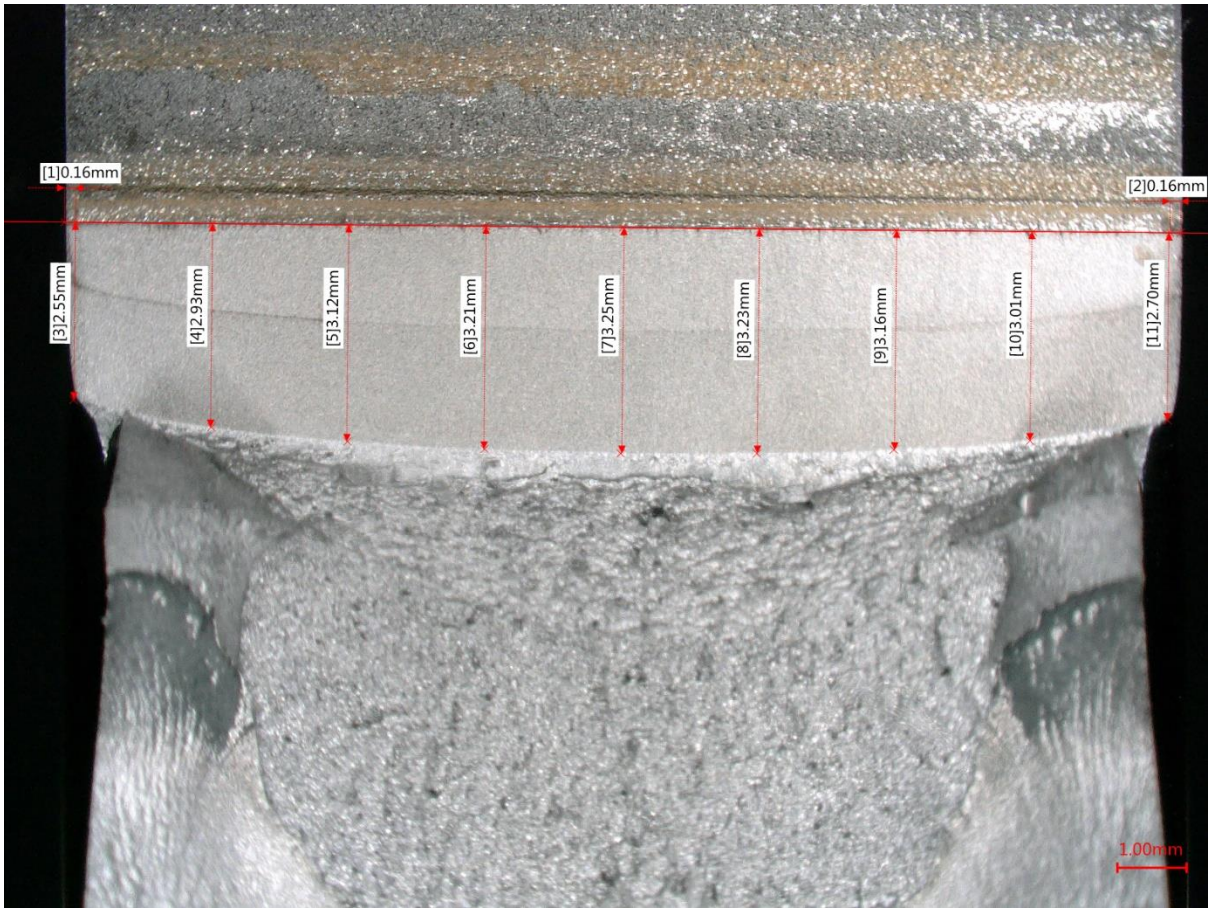

Figure 3.22 Schematic illustration of the measurements of crack length.

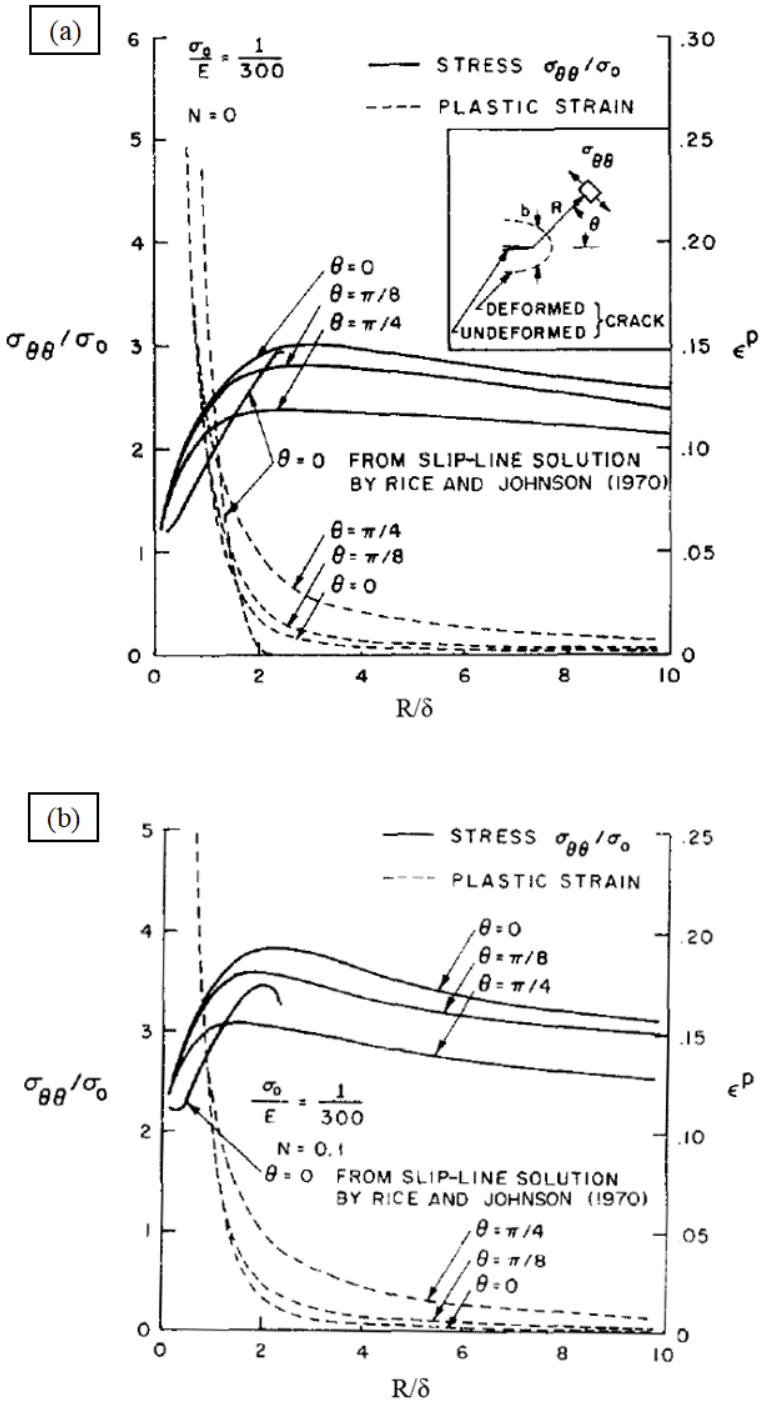

Figure 3.23 FEM analysis models of McMeeking for different work hardening exponents,

(a) $n = 0$, (b) $n = 0.1$ and (c) $n = 0.2$ [69].

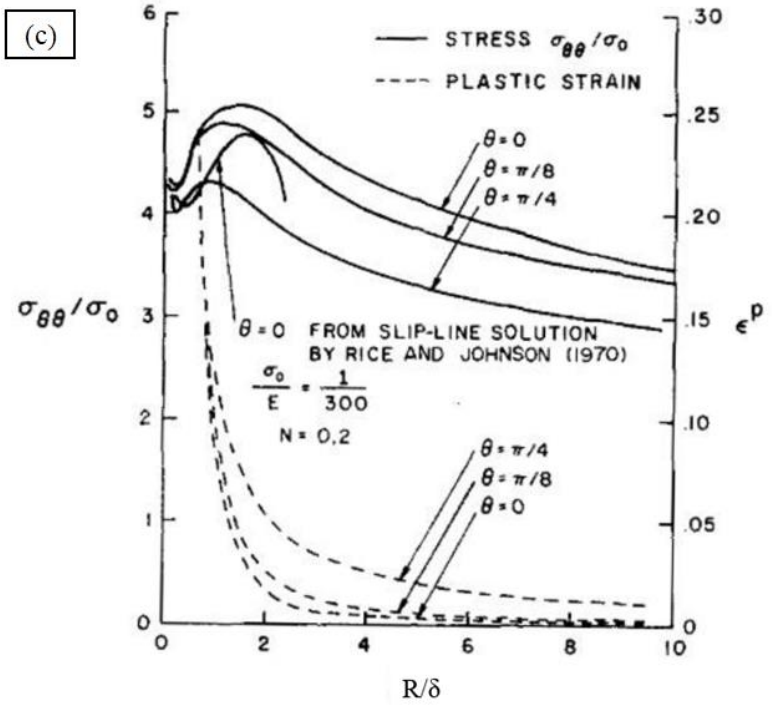
(c)
STRESS $\sigma_{\theta\theta}/\sigma_0$
PLASTIC STRAIN
$\theta = 0$
$\theta = \pi/8$
$\theta = \pi/4$
$\theta = 0$ FROM SLIP-LINE SOLUTION
BY RICE AND JOHNSON (1970)
$\frac{\sigma_0}{E} = \frac{1}{300}$
N = 0.2
$\theta = \pi/4$
$\theta = \pi/8$
$\theta = 0$
$\sigma_{\theta\theta}/\sigma_0$
ϵ^p
R/δ

(c) $n = 0.2$.

Table 4.1 Hardness results for HT1 and HT2 conditions.

Distance to start point [mm]	HT1			HT2		
	Diagonal 1 [µm]	Diagonal 2 [µm]	HV 5	Diagonal 1 [µm]	Diagonal 2 [µm]	HV 5 [kg/mm^2]
0.0	221.42	221.42	189	223.50	224.13	185
1.0	221.94	220.87	189	221.94	225.59	185
2.0	222.98	222.96	187	224.54	224.53	184
3.0	221.91	222.46	188	224.00	225.07	184
4.0	219.85	220.37	191	221.42	225.56	186
5.0	218.81	219.83	193	227.16	229.73	178
6.0	216.21	217.25	197	223.51	224.55	185
7.0	219.33	220.37	192	226.12	228.16	180
8.0	220.37	218.27	193	222.44	222.98	187
9.0	220.37	220.35	191	223.50	222.98	186
Average	220.32	220.42	191	223.81	225.33	184

Table 4.2 Measured gauge diameters and average cross-section areas of HT1 tensile specimens.

Specimen Number	Test Temperature	Gauge Diameter				Area
		d_1	d_2	d_3	$d_{average}$	$S_{average}$
	[°C]	[mm]	[mm]	[mm]	[mm]	[mm^2]
HT1-06	**-140**	9.95	9.93	9.93	9.94	77.55
HT1-08		9.95	9.95	9.95	9.95	77.76
HT1-09	**-120**	10.03	9.98	9.99	10.00	78.54
HT1-10		9.95	9.95	9.95	9.95	77.76
HT1-11	**-100**	9.95	9.95	9.96	9.95	77.76
HT1-12		9.93	9.92	9.93	9.93	77.44
HT1-13	**-80**	9.93	9.93	9.93	9.93	77.44
HT1-14		9.91	9.91	9.91	9.91	77.13
HT1-15	**-60**	9.93	9.93	9.93	9.93	77.44
HT1-16		9.93	9.91	9.92	9.92	77.29

Table 4.3 Measured gauge diameters and average cross-section areas of HT2 tensile specimens.

Specimen Number	Test Temperature	Gauge Diameter				Area
		d_1	d_2	d_3	$d_{average}$	$S_{average}$
	[°C]	[mm]	[mm]	[mm]	[mm]	[mm^2]
HT2-06	**-140**	9.99	10.01	10.00	10.00	78.54
HT2-08		9.98	9.98	9.99	9.98	78.28
HT2-09	**-120**	9.99	10.01	9.99	10.00	78.54
HT2-10		9.98	9.99	9.98	9.98	78.28
HT2-11	**-100**	9.99	9.99	10.00	9.99	78.44
HT2-12		10.01	10.03	9.99	10.01	78.70
HT2-13	**-80**	9.98	9.98	9.98	9.98	78.23
HT2-14		9.98	9.98	9.98	9.98	78.23
HT2-15	**-60**	10.01	10.02	10.02	10.02	78.80
HT2-16		10.01	10.00	9.99	10.00	78.54

Table 4.4 Tensile testing results summary of HT1 specimens at different temperatures.

Specimen Number	Test Temperature	Lower Yield Stress	Ultimate Tensile Strength	Strain		Work Hardening Exponent n
				Uniform	Total	
	[°C]	[MPa]	[MPa]	[%]		
HT1-01	-196	921	952	20.0	39.9	0.02
HT1-02		932	954	19.1	35.5	0.01
HT1-03		931	949	19.5	41	0.01
HT1-04	-170	791	844	19.7	38.0	0.04
HT1-07	-160	767	823	21.0	38.4	0.04
HT1-06	-140	717	772	17.2	35.0	0.04
HT1-08		711	782	15.7		0.05
HT1-09	-120	677	732	17.2	35.6	0.06
HT1-10		636	736	21.3	40.1	0.08
HT1-11	-100	633	702	18.0	37.3	0.08
HT1-12		614	703	20.0		0.09
HT1-13	-80	577	678	16.2	33.3	0.08
HT1-14		581	677	19.1	35.3	0.08
HT1-15	-60	566	652	17.1	34.7	0.08
HT1-16		558	655	17.0	39.1	0.09

Table 4.5 Tensile testing results summary of HT2 specimens at different temperatures.

Specimen Number	Test Temperature	Lower Yield Stress	Ultimate Tensile Strength	Strain		Work Hardening Exponent n
				Uniform	Total	
	[°C]	[MPa]	[MPa]	[%]		
HT2-01	-196	934	951	14.8	28.5	0.01
HT2-02		926	941	17.8	33.1	0.01
HT2-03		921	950	18.1	41.3	0.03
HT2-04	-170	785	829	14.9	38.2	0.04
HT2-07	-160	750	814	19.0	39.0	0.04
HT2-06	-140	707	765	21.3	44.8	0.04
HT2-08		696	768	18.3	44.8	0.06
HT2-09	-120	646	722	19.1	43.9	0.06
HT2-10		628	721	21.0	44.8	0.08
HT2-11	-100	607	693	18.9	36.3	0.06
HT2-12		598	692	18.0	41.0	0.09
HT2-13	-80	567	663	17.3	36.6	0.08
HT2-14		568	662	17.5	38.6	0.08
HT2-15	-60	529	640	16.2	39.0	0.11
HT2-16		536	639	16.9	35.8	0.08

Table 4.6 Charpy impact test results of HT1 condition.

Specimen Number	Test Temperature	Absorbed Impact Energy	Lateral Expansion	Ductile Thumbnail Extension	Shear Lip Size	Cleavage Area Percentage
	[°C]	[J]	[mm]	[mm]	[mm]	%
1	-196	2.4	0.14	0.00	0.00	100.00
2		2.9	0.12	0.00	0.00	100.00
3		2.0	0.14	0.00	0.00	100.00
7	-120	5.0	0.12	0.06	0.00	99.10
8		5.0	0.12	0.00	0.00	99.29
9		5.0	0.14	0.06	0.00	98.37
52		7.5	0.23	0.01	0.00	98.69
53		7.5	0.15	0.00	0.00	99.22
54		5.0	0.17	0.04	0.00	98.05
10	-100	26.0	0.37	0.09	0.19	92.95
11		15.0	0.25	0.12	0.20	94.80
12		10.5	0.35	0.28	0.13	97.01
16		8.5	0.16	0.19	0.18	95.07
17		15.0	0.27	0.19	0.22	95.90
18		8.0	0.17	0.09	0.17	96.50
37		13.0	0.26	0.20	0.31	90.40
38		19.5	0.31	0.27	0.19	91.92
39		11.5	0.22	0.16	0.00	94.85
46		6.0	0.14	0.01	0.00	99.92
47		3.0	0.08	0.00	0.00	98.12
48		7.5	0.20	0.00	0.00	98.69
4	-90	298.0	2.54	2.86	2.49	0.00
5		56.5	0.52	0.43	0.49	83.48
6		25.0	0.27	0.16	0.22	91.52
28		12.0	0.23	0.09	0.00	91.93
29		12.0	0.25	0.14	0.00	91.79
30		267.0	2.23	2.18	2.31	18.21

Specimen Number	Test Temperature	Absorbed Impact Energy	Lateral Expansion	Ductile Thumbnail Extension	Shear Lip Size	Cleavage Area Percentage
	[°C]	[J]	[mm]	[mm]	[mm]	%
40	-90	299.0	2.15	5.25	3.06	0.00
41		298.5	1.98	3.44	3.19	0.00
42		63.0	0.65	0.86	0.35	86.02
13	-80	299.0	2.30	2.88	2.66	0.00
14		236.0	2.34	2.16	2.02	0.00
15		298.5	2.20	2.67	3.35	0.00
19		297.0	2.50	1.64	2.98	0.00
20		297.0	2.26	1.65	3.23	0.00
21		246.0	2.32	1.53	2.09	23.60
25		299.0	2.28	2.63	2.91	0.00
26		273.0	2.04	2.30	2.11	15.39
27		282.0	1.87	1.65	2.72	0.00
34	-70	298.5	1.79	3.53	2.91	0.00
35		298.5	2.28	3.64	2.79	0.00
36		283.5	2.19	3.01	1.95	14.76
43		298.5	2.25	3.40	3.61	0.00
44		278.0	1.92	2.82	1.91	20.09
45		272.5	2.04	2.61	2.12	19.62
22	-60	297.5	2.28	3.24	2.95	0.00
23		297.0	2.36	2.24	2.96	0.00
24		297.0	2.53	3.19	3.14	0.00
31		299.0	2.35	1.98	3.34	0.00
32		299.0	2.44	4.24	3.26	0.00
33		298.5	2.21	3.66	3.12	0.00
49	-40	298.5	2.25	4.07	3.46	0.00
50		298.5	2.39	3.06	3.45	0.00
51		298.5	2.36	3.61	3.66	0.00

Table 4.7 Charpy impact test results of HT2 condition.

Specimen Number	Test Temperature	Absorbed Impact Energy	Lateral Expansion	Ductile Thumbnail Extension	Shear Lip Size	Cleavage Area Percentage
	[°C]	[J]	[mm]	[mm]	[mm]	%
1	-196	2.2	0.15	0.00	0.00	100.00
2		2.4	0.08	0.00	0.00	100.00
3		2.0	0.18	0.00	0.00	100.00
7	-120	5.0	0.10	0.00	0.00	100.00
8		5.5	0.10	0.00	0.00	100.00
9		6.0	0.13	0.06	0.00	100.00
52		8.5	0.13	0.01	0.00	97.54
53		5.0	0.15	0.00	0.00	100.00
54		5.0	0.17	0.00	0.00	100.00
10	-100	12.5	0.27	0.09	0.21	94.60
11		7.5	0.22	0.00	0.16	95.63
12		19.0	0.47	0.00	0.29	93.35
16		36.0	0.18	0.19	0.41	96.91
17		12.2	0.15	0.02	0.22	96.90
18		23.0	0.18	0.09	0.14	95.36
37		14.0	0.15	0.05	0.17	96.59
38		9.5	0.32	0.00	0.21	97.33
39		20.0	0.25	0.07	0.23	95.24
46		8.0	0.17	0.00	0.00	99.44
47		10.0	0.27	0.00	0.16	96.21
48		6.0	0.11	0.00	0.00	99.83
4	-90	192.0	1.74	1.86	2.30	44.47
5		159.0	1.32	1.43	1.89	62.52
6		8.5	0.09	0.16	0.00	94.77
28		12.0	0.10	0.09	0.00	93.47
29		9.5	0.09	0.14	0.00	90.98
30		32.0	0.16	0.14	0.31	92.27

Specimen Number	Test Temperature	Absorbed Impact Energy	Lateral Expansion	Ductile Thumbnail Extension	Shear Lip Size	Cleavage Area Percentage
	[°C]	[J]	[mm]	[mm]	[mm]	%
40	-90	247.5	2.42	2.25	2.59	23.37
41		25.0	0.14	0.12	0.22	94.82
42		89.7	1.02	0.86	0.68	78.96
13	-80	23.0	0.12	0.08	0.25	94.10
14		258.5	2.08	2.16	2.33	19.03
15		250.0	2.21	2.07	2.73	20.63
19		241.0	2.26	1.98	2.49	25.15
20		203.0	2.01	1.65	2.30	35.02
21		212.0	2.15	1.73	2.38	30.29
25		261.0	2.13	2.13	2.43	11.38
26		278.0	2.22	2.58	2.53	6.01
27		298.5	2.35	3.20	3.37	0.00
34	-70	298.5	2.24	3.53	2.91	0.00
35		240.0	2.40	2.34	2.67	0.00
36		233.0	2.21	2.31	2.21	0.00
43		229.5	2.33	2.25	2.26	0.00
44		298.5	2.12	3.62	3.23	0.00
45		298.5	2.47	2.61	3.38	0.00
22	-60	297.0	2.33	3.24	2.73	0.00
23		297.0	2.36	2.94	2.87	0.00
24		297.0	2.44	3.19	2.70	0.00
31		299.0	2.33	2.98	2.63	0.00
32		267.0	2.43	2.24	2.63	6.51
33		299.0	2.10	3.66	2.86	0.00
49	-40	299.0	2.46	3.85	3.05	0.00
50		299.0	2.36	3.06	3.22	0.00
51		299.0	2.30	3.61	3.29	0.00

Table 4.8 Information of the fracture initiation sites of Charpy impact test specimens for both HT1 and HT2 conditions, initiation sites observation from Weichen Xu [71].

Specimen Number	Test Temperature	Absorbed Impact Energy	Initiation Reason	Fracture distance X_0	Ductile Crack Growth	Initiator Diameter	Facet Diameter
	[°C]	[J]		[µm]	[µm]	[µm]	[µm]
HT2-01	-196	2	Inclusion	229	23	1.9	38
HT1-07	-120	5	Matrix cracking	229	63	N/A	38
HT1-10	-100	26	Matrix cracking	365	88	N/A	46
HT1-18		8	Inclusion	390	90	1.7	24
HT2-11		7.5	Inclusion	428	76	2.3	51
HT2-12		19	Matrix cracking	636	154	N/A	44
HT2-16		36	M-A-C	545	224	1.6	30
HT2-18		23	M-A-C	530	197	2.7	54
HT1-05	-90	56.5	Inclusion	693	427	1.6	42
HT1-06		25	Inclusion	596	157	2.2	52
HT2-04		192	Matrix cracking	312	3803	N/A	40
HT2-30		32	Matrix cracking	413	273	N/A	33
HT2-41		18	M-A-C	619	184	1.9	32
HT2-42		90	Inclusion	300	1074	1.8	34

Note: M-A-C indicates the potential martensite-austenite constituents.

Table 4.9 Test results including the maximum load, nominal stress and the σ_{nom}/σ_{YS} ratio at -170 and -160°C for both HT1 and HT2 conditions.

Specimen Number	Temperature	Yield Stress	Maximum Load	Nominal Stress	σ_{nom}/σ_{YS}
	T [°C]	σ_{YS} [MPa]	P [kN]	σ_{nom} [MPa]	(max 2.292)
HT1-FS-01	-160	767	56.2	2350	3.064
HT1-FS-02			50.8	2124	2.769
HT1-FS-03			52.5	2195	2.862
HT2-FS-01		750	55.1	2304	3.072
HT2-FS-02			51.4	2149	2.865
HT2-FS-03			58.7	2455	3.273
HT1-FS-04	-170	791	50.1	2095	2.649
HT1-FS-05			57.0	2384	3.014
HT1-FS-06			51.0	2133	2.697
HT2-FS-04		785	43.9	1836	2.339
HT2-FS-05			45.0	1882	2.397
HT2-FS-06			56.5	2363	3.010

Table 4.10 Summary of the maximum fracture load, nominal stress σ_{nom}, σ_{nom}/σ_{YS} ratios, L/L_{GY} ratios, stress intensification factors and predicted maximum principal stress σ_{yymax} at -196°C for both conditions.

Specimen Number	Temperature	Yield Stress	Maximum Load	Nominal Stress	σ_{nom}/σ_{YS}	L/L_{GY}	Stress Intensification	Maximum Principal Stress	Mean Value
	T [°C]	σ_{YS} [MPa]	P [kN]	σ_{nom} [MPa]	(max 2.292)	(max 1.065)	SIF (max 2.62)	σ_{yymax} [MPa]	σ_{yymax} [MPa]
HT1-FS-07	-196	928	29.0	1213	1.308	0.608	2.12	1965	2002
HT1-FS-08			33.2	1388	1.496	0.696	2.23	2071	
HT1-FS-09			29.2	1221	1.316	0.612	2.12	1970	
HT2-FS-07		927	23.3	974	1.050	0.489	1.94	1803	1914
HT2-FS-08			29.7	1242	1.340	0.623	2.14	1982	
HT2-FS-09			28.7	1200	1.294	0.602	2.11	1956	

Table 4.11 Summary of initiation reason, chemical composition of the initiator and information of the initiation sites at -196°C for both HT1 and HT2 conditions.

Specimen Number	Temperature	Initiation Reason	Chemical Composition	Fracture distance X_0	Inclusion Diameter	Facet Area	Equivalent Facet Diameter
	[°C]			[µm]	[µm]	[µm^2]	[µm]
HT1-FS-07	-196	Inclusion	Ca, Al	333	3.2	418	23.1
HT1-FS-08		Inclusion	Ca	320	1.8	320	20.2
HT1-FS-09		Inclusion	Ca, Ti	227	2.8	538	26.2
HT2-FS-07		Inclusion	Ca, Al	365	2.3	1172	38.6
HT2-FS-08		Inclusion	Ca, Al	274	2.3	970	35.2
HT2-FS-09		Inclusion	Ca, Ti, Al	221	2.3	1347	41.4

Table 4.12 Summary of estimations of stress intensification factor and cleavage fracture stress at the initiation site, comparison with maximum principal stress.

Specimen Number	Temperature	Fracture Distance	Stress Intensification Factor at Initiation Site	Cleavage Fracture Stress at Initiation Site	Mean Value	Maximum Principal Stress	$\sigma(X_0)/\sigma_{yymax}$
	T [°C]	X_0 [µm]	$SIF(X_0)$	$\sigma(X_0)$ [MPa]	$\sigma(X_0)$ [MPa]	σ_{yymax} [MPa]	
HT1-FS-07	-196	333	2.02	1874	1927	1965	0.95
HT1-FS-08		320	2.19	2032		2071	0.98
HT1-FS-09		227	2.02	1874		1970	0.95
HT2-FS-07		365	1.65	1530	1765	1803	0.85
HT2-FS-08		274	2.08	1929		1982	0.97
HT2-FS-09		221	1.98	1836		1956	0.94

Table 4.13 Results of inclusion diameter, local cleavage fracture stress and the corresponding effective surface energy.

Specimen Number	Temperature	Inclusion Diameter	$(2c)^{-1/2}$	Equivalent Facet Diameter	Local Cleavage Fracture Stress	Effective Surface Energy
	T [°C]	2c [μm]	$[(\mu m)^{-1/2}]$	[μm]	σ_f [MPa]	γ_P $[J/m^2]$
HT1-FS-07	-196	3.2	0.56	23.1	1874	15.5
HT1-FS-08		1.8	0.74	20.2	2032	10.3
HT1-FS-09		2.8	0.60	26.2	1874	13.6
HT2-FS-07		2.3	0.66	38.6	1530	7.4
HT2-FS-08		2.3	0.66	35.2	1929	11.8
HT2-FS-09		2.3	0.66	41.4	1836	10.7

Table 4.14 Summary of the *K* values and validity of Fracture Toughness test at -120°C for both HT1 and HT2 conditions.

Specimen Number	Temperature	B	W	a_0 (compliance)	a_0	W-a_0	P_{max}	P_Q	P_{max}/P_Q	K_Q	Average K_Q	$2.5(K_Q/\sigma_{YL})^2$	Validity for K_{Ic}
	[°C]	[mm]	[mm]	[mm]	[mm]	[mm]	[kN]	[kN]		[MPam$^{1/2}$]	[MPam$^{1/2}$]	[mm]	
HT1CT-16	-120	24.93	49.77	25.32	25.52	24.25	37	37	1.00	66.0	72.9	25.23	valid
HT1CT-20		25.03	49.87	25.26	25.55	24.32	31	31	1.00	54.9		17.48	valid
HT1CT-21		24.94	49.66	25.46	25.91	23.75	66	53	1.25	95.1		52.38	invalid
HT1CT-22		24.97	49.63	25.47	25.87	23.76	48	48	1.00	86.5		43.34	invalid
HT1CT-23		24.98	49.70	25.27	25.73	23.97	31	31	1.00	55.4		17.78	valid
HT1CT-24		24.98	49.70	25.38	25.68	24.02	44	44	1.00	79.6		36.70	invalid
HT2CT-05		24.90	49.73	25.68	25.07	24.66	38	38	1.00	69.6	75.8	29.85	invalid
HT2CT-06		24.90	49.73	24.96	25.42	24.31	45	45	1.00	79.1		38.55	invalid
HT2CT-07		24.90	49.88	25.10	25.46	24.42	45	45	1.00	78.2		37.68	invalid
HT2CT-08		24.92	49.80	25.08	25.55	24.25	49	48	1.02	84.8		44.31	invalid
HT2CT-19		24.92	49.71	25.24	25.58	24.13	43	43	1.00	77.1		36.62	invalid
HT2CT-22		25.01	50.00	24.93	25.60	24.40	43	39	1.12	66.3		27.07	invalid

Table 4.15 Summary the *K* values and validity of Fracture Toughness test at -100 and -80°C for both HT1 and HT2 conditions.

Specimen Number	Temperature	B	W	a_0 (compliance)	a_0	W-a_0	P_{max}	P_Q	P_{max}/P_Q	K_Q	Average K_Q	$2.5(K_Q/\sigma_{YL})^2$	Validity for K_{Ic}
	[°C]	[mm]	[mm]	[mm]	[mm]	[mm]	[kN]	[kN]		[MPam$^{1/2}$]	[MPam$^{1/2}$]	[mm]	
HT1CT-01	-100	24.95	49.59	25.75	25.99	23.60	77	45	1.74	82.2	76.8	43.38	invalid
HT1CT-07		24.97	49.75	25.44	25.74	24.01	67	40	1.69	71.5		32.82	invalid
HT1CT-18		25.02	49.95	25.36	25.66	24.29	63	37	1.73	64.7		26.85	invalid
HT1CT-25		24.97	49.69	25.26	25.43	24.26	52	47	1.12	82.8		44.02	invalid
HT1CT-26		24.96	49.75	25.27	25.58	24.17	68	45	1.50	80.2		41.30	invalid
HT1CT-27		24.94	49.81	25.40	25.40	24.41	54	45	1.21	79.6		40.66	invalid
HT2CT-01		24.95	49.77	25.26	25.50	24.27	69	47	1.47	83.1	75.6	47.48	invalid
HT2CT-02		24.99	49.94	25.02	25.30	24.64	34	34	1.00	58.6		23.62	valid
HT2CT-03		24.96	49.87	25.13	25.30	24.57	55	47	1.16	82.9		47.25	invalid
HT2CT-04		24.90	49.84	25.02	25.18	24.66	56	48	1.15	84.6		49.21	invalid
HT2CT-09		24.94	50.00	25.97	26.10	23.90	46	44	1.04	81.5		45.67	invalid
HT2CT-21		24.95	49.97	25.01	25.76	24.21	75	36	2.06	63.1		27.38	invalid
HT1CT-17	-80	25.02	49.81	25.25	25.86	23.95	70	40	1.75	72.0	72.0	183.82	invalid
HT2CT-24		24.96	49.74	24.65	25.03	24.71	75	58	1.29	96.0	89.5	232.74	invalid
HT2CT-25		24.96	50.08	25.69	25.71	24.37	72	46	1.57	83.0		133.45	invalid

Table 4.16 Summary of the *K* and *J* values of Fracture Toughness test at -120 to -80°C for both HT1 and HT2 conditions.

Specimen Number	Temperature	K_Q	Average K_Q	J_C	K_{Jc}	Average K_{JC}	CTOD
	[°C]	[MPam$^{1/2}$]	[MPam$^{1/2}$]	kJ/m^2	[MPam$^{1/2}$]	[MPam$^{1/2}$]	[mm]
HT1CT-16	-120	66.0	72.9	18.9	66.0	75.6	0.015
HT1CT-20		54.9		13.4	55.7		0.012
HT1CT-21		95.1		49.5	106.9		0.057
HT1CT-22		86.5		34.9	89.7		0.027
HT1CT-23		55.4		13.3	55.4		0.011
HT1CT-24		79.6		27.7	80.0		0.028
HT2CT-05		69.6	75.8	21.0	69.6	76.3	0.017
HT2CT-06		79.1		27.4	79.5		0.023
HT2CT-07		78.2		26.6	78.4		0.022
HT2CT-08		84.8		32.8	87.0		0.028
HT2CT-19		77.1		25.8	77.2		0.021
HT2CT-22		66.3		19.0	66.3		0.026
HT1CT-01	-100	82.2	76.8	194.2	211.7	117.0	0.163
HT1CT-07		71.5		51.6	109.1		0.045
HT1CT-18		64.7		34.5	89.2		0.028
HT1CT-25		82.8		37.3	92.8		0.032
HT1CT-26		80.2		53.0	110.6		0.045
HT1CT-27		79.6		33.8	88.3		0.030
HT2CT-01		83.1	75.6	58.0	115.7	96.5	0.056
HT2CT-02		58.6		15.4	59.6		0.012
HT2CT-03		82.9		36.0	91.1		0.036
HT2CT-04		84.6		37.6	93.2		0.033
HT2CT-09		81.5		32.3	86.3		0.028
HT2CT-21		63.1		77.0	133.3		0.068
HT1CT-17	-80	72.0	72.0	63.0	120.6	120.6	0.056
HT2CT-24		96.0	89.5	94.4	147.6	163.4	0.081
HT2CT-25		83.0		139.2	179.2		0.118

Table 4.17 Summary of the fracture initiation sites, including initiation reason, inclusion composition, fracture distance, ductile crack length, inclusion diameter at the initiation site and facet diameter of Fracture Toughness test, inclusion observation from Weichen Xu [71].

Specimen Number	Temperature	Initiation Reason	Chemical Composition	K_{Jc}	Fracture distance X_0	Ductile Crack Length	Initiator Diameter	Equivalent Facet Diameter
	[°C]			[MPam$^{-1/2}$]	[µm]	[µm]	[µm]	[µm]
HT1-CT-16	-120	Inclusion cracking	Ti, Nb, Al, Mg	66.0	32	3	1.6	23
HT1-CT-20		Matrix related	Matrix composition	55.7	50	4	N/A	32
HT1-CT-21		Matrix cracking	Matrix composition	106.9	639	15	N/A	30
HT1-CT-22		Inclusion cracking	Ca, Al	89.7	168	8	1.6	45
HT1-CT-23		Inclusion cracking	Ti, Nb, Ca	55.4	22	3	1.2	33
HT1-CT-24		Matrix cracking	Matrix composition	80.0	63	4	N/A	35
HT2-CT-05		Inclusion cracking	Ca, Al	69.6	260	10	2.1	36
HT2-CT-06		Matrix related	Matrix composition	79.5	81	6	0.8	22
HT2-CT-07		Inclusion cracking	Ti, Nb	78.4	28	5	1.8	36
HT2-CT-08		Inclusion cracking	Ca, Al, Ti	87.0	90	8	2.5	28
HT2-CT-19		Matrix related (Possible M-A-C)	4wt% Carbon higher than surrounding matrix	77.2	85	5	1.8	29
HT2-CT-22		Inclusion cracking	Ca, Ti, Al	66.3	150	6	1.6	40

continued…

Specimen Number	Temperature	Initiation Reason	Chemical Composition	K_{Jc}	Fracture distance X_0	Ductile Crack Length	Initiator Diameter	Equivalent Facet Diameter
	[°C]			[MPam$^{-1/2}$]	[µm]	[µm]	[µm]	[µm]
HT1-CT-01	-100	Inclusion decohesion	Ca, Al	211.7	660	70	1.2	25
HT1-CT-07		Inclusion cracking	Ti, Nb	109.1	129	21	1.6	27
HT1-CT-18		Inclusion cracking	Ca, Ti	89.2	440	8	1.6	36
HT1-CT-25		Inclusion cracking	Ca, Al, Ti	92.8	112	8	1.5	20
HT1-CT-26		Inclusion cracking	Ca, Al, Ti	110.6	158	19	0.8	27
HT1-CT-27		Matrix related (Possible M-A-C)	11wt% Carbon higher than surrounding matrix	88.3	90	9	1.6	31
HT2-CT-01		Inclusion cracking	Ti, Nb	115.7	631	16	1.5	36
HT2-CT-02		Matrix related	Matrix composition	59.6	68	3	N/A	43
HT2-CT-03		Matrix related (Possible M-A-C)	5wt% Carbon higher than surrounding matrix	91.1	49	9	1.2	25
HT2-CT-04		Matrix cracking	Matrix composition	93.2	80	9	N/A	23
HT2-CT-09		Matrix related	Matrix composition	86.3	121	8	3.3	30
HT2-CT-21		Inclusion cracking	Ca, Ti	133.3	399	32	1.5	36
HT1-CT-17	-80	Inclusion cracking	Ca, Ti, Al	120.6	289	35	2.2	28
HT2-CT-25		Inclusion cracking	Ca, Ti, Al	179.2	490	54	1.6	40

Table 4.18 Comparisons of the reference temperature T_0 from master curve procedure and various empirical estimations from Charpy impact test results, T_0 values calculated by Huize Fan [70].

Heat-Treatment Condition	T_0 (Test)	T_{28J}	T_{41J}	Corten & Sailors	Barsom & Rolfe	Marandet & Sanz	Roberts & Newton
	[°C]						
HT1	-99.9	-101.2	-98.8	-98.0	-99.5	-101.0	-97.6
HT2	-100.5	-99.2	-96.5	-95.6	-97.6	-99.1	-95.1
HT1+2	-99.1	-100.2	-98.0	-97.1	-98.8	-101.3	-96.3

Table 4.19 Summary of the fracture distance, CTOD, values of R/δ and σ_f/σ_{YS}, corresponding local cleavage fracture stress σ_f, and the ratios of σ_f/σ_{max} of fracture toughness test at -120°C for both HT1 and HT2 conditions.

Specimen Number	Temperature	Yield Stress σ_{YS}	σ_{max}	Fracture Distance X_0	CTOD	R/δ	σ_f/σ_{YS}	σ_f	σ_f/σ_{max}
	[°C]	[MPa]	[MPa]	[μm]	[μm]			[MPa]	
HT1-CT-16	-120	657	2510	32	15	2.1	3.81	2503	1.00
HT1-CT-20				50	12	4.2	3.57	2345	0.93
HT1-CT-21				639	57	11.2	3.05	2004	0.80
HT1-CT-22				168	27	6.2	3.33	2188	0.87
HT1-CT-23				22	11	2.1	3.81	2503	1.00
HT1-CT-24				63	28	2.2	3.82	2510	1.00
HT2-CT-05		637	2433	260	17	15.4	2.97	1892	0.78
HT2-CT-06				81	23	3.5	3.69	2351	0.97
HT2-CT-07				28	22	1.3	3.64	2319	0.95
HT2-CT-08				90	28	3.2	3.74	2382	0.98
HT2-CT-19				85	21	4.0	3.60	2293	0.94
HT2-CT-22				150	26	5.7	3.38	2153	0.88

Table 4.20 Summary of the fracture distance, CTOD, values of R/δ and σ_f/σ_{YS}, corresponding local cleavage fracture stress σ_f, and the ratios of σ_f/σ_{max} of fracture toughness test at -100 and -80°C for both HT1 and HT2 conditions.

Specimen Number	Temperature	Yield Stress σ_{YS}	σ_{max}	Fracture distance X_0	CTOD	R/δ	σ_f/σ_{YS}	σ_f	σ_f/σ_{max}
	[°C]	[MPa]	[MPa]	[μm]	[μm]			[MPa]	
HT1-CT-01	-100	624	2384	660	163	4.0	3.60	2246	0.94
HT1-CT-07				129	45	2.9	3.78	2359	0.99
HT1-CT-18				440	29	15.4	2.97	1853	0.78
HT1-CT-25				112	32	3.5	3.69	2303	0.97
HT1-CT-26				158	46	3.5	3.69	2303	0.97
HT1-CT-27				90	31	2.9	3.78	2359	0.99
HT2-CT-01		603	2303	631	57	11.1	3.05	1839	0.80
HT2-CT-02				68	12	5.6	3.39	2044	0.89
HT2-CT-03				49	37	1.3	3.64	2195	0.95
HT2-CT-04				80	34	2.4	3.82	2303	1.00
HT2-CT-09				121	29	4.2	3.57	2153	0.93
HT2-CT-21				399	68	5.9	3.36	2026	0.88
HT1-CT-17	-80	579	2212	289	57	5.1	3.45	1998	0.90
HT2-CT-25		568	2170	490	81	6.0	3.35	1903	0.88

Table 4.21 Local cleavage fracture stress and corresponding effective surface energy of inclusion-initiated specimens for both HT1 and HT2 conditions.

Specimen Number	Temperature	Initiator Diameter	Local Cleavage Fracture Stress σ_f	Effective Surface Energy γ
	[°C]	[μm]	[MPa]	[J/m^2]
HT1-CT-16	-120	1.6	2503	13.8
HT1-CT-20		N/A	2345	N/A
HT1-CT-21		N/A	2004	N/A
HT1-CT-22		1.6	2188	10.6
HT1-CT-23		1.2	2503	10.4
HT1-CT-24		N/A	2510	N/A
HT2-CT-05		2.1	1892	10.4
HT2-CT-06		0.8	2351	6.1
HT2-CT-07		1.8	2319	13.4
HT2-CT-08		2.5	2382	19.6
HT2-CT-19		1.8	2293	13.1
HT2-CT-22		1.6	2153	10.2
HT1-CT-01	-100	1.2	2246	8.4
HT1-CT-07		1.6	2359	12.3
HT1-CT-18		1.6	1853	7.6
HT1-CT-25		1.5	2303	11.0
HT1-CT-26		0.8	2303	5.9
HT1-CT-27		1.6	2359	12.3
HT2-CT-01		1.5	1839	7.0
HT2-CT-02		N/A	2044	N/A
HT2-CT-03		1.2	2195	8.0
HT2-CT-04		N/A	2303	N/A
HT2-CT-09		3.3	2153	21.1
HT2-CT-21		1.5	2026	8.5
HT1-CT-17	-80	2.2	1998	12.1
HT2-CT-25		1.6	1903	8.0

Table 4.22 Comparisons between the fracture distance and the distance between location of the maximum principal stress to notch tip, and plastic zone size of fracture toughness test.

Specimen Number	Temperature	Fracture Distance X_0	X_{max}	X_0-X_{max}	σ_f	Plastic Zone Radius
	[°C]	[μm]	[μm]	[μm]	[MPa]	[μm]
HT1-CT-16	-120	32	30	2	2503	402
HT1-CT-20		50	24	26	2345	278
HT1-CT-21		639	114	525	2004	834
HT1-CT-22		168	55	113	2188	690
HT1-CT-23		22	21	1	2503	283
HT1-CT-24		63	57	6	2510	584
HT2-CT-05		260	34	226	1892	475
HT2-CT-06		81	47	34	2351	614
HT2-CT-07		28	45	-17	2319	600
HT2-CT-08		90	57	33	2382	705
HT2-CT-19		85	43	42	2293	583
HT2-CT-22		150	53	97	2153	431
HT1-CT-01	-100	660	327	333	2246	691
HT1-CT-07		129	90	39	2359	523
HT1-CT-18		440	57	383	1853	428
HT1-CT-25		112	64	48	2303	701
HT1-CT-26		158	91	67	2303	658
HT1-CT-27		90	62	28	2359	647
HT2-CT-01		631	114	517	1839	756
HT2-CT-02		68	24	44	2044	376
HT2-CT-03		49	73	-24	2195	752
HT2-CT-04		80	67	13	2303	784
HT2-CT-09		121	57	64	2153	727
HT2-CT-21		399	136	263	2026	436
HT1-CT-17	-80	289	113	176	1998	616
HT2-CT-25		490	162	328	1903	850

Table 4.23 Comparison of effective surface energy calculated for specimens with inclusion cracking for both blunt-notched fracture stress and sharp-cracked fracture toughness specimens.

Specimen Number	Temperature	Initiator Diameter	Inclusion Composition	Local Cleavage Fracture Stress σ_f	Effective Surface Energy γ
	[°C]	[μm]		[MPa]	[J/m^2]
HT1-FS-07	-196	3.2	Ca, Al	1874	15.5
HT1-FS-08		1.8	Ca	2032	10.3
HT1-FS-09		2.8	Ti, Ca	1874	13.6
HT2-FS-08		2.3	Ca, Al	1929	11.8
HT2-FS-09		2.3	Ca, Ti, Al	1836	10.7
HT1-CT-16	-120	1.6	Ti, Nb, Al, Mg	2503	13.8
HT1-CT-22		1.6	Ca, Al	2188	10.6
HT1-CT-23		1.2	Ti, Nb, Ca	2503	10.4
HT2-CT-05		2.1	Ca, Al	1892	10.4
HT2-CT-07		1.8	Ti, Nb	2319	13.4
HT2-CT-08		2.5	Ca, Al, Ti	2382	19.6
HT2-CT-22		1.6	Ca, Ti, Al	2153	10.2
HT1-CT-07	-100	1.6	Ti, Nb	2359	12.3
HT1-CT-18		1.6	Ca, Ti	1853	7.6
HT1-CT-25		1.5	Ca, Al, Ti	2303	11.0
HT1-CT-26		0.8	Ca, Al, Ti	2303	5.9
HT2-CT-01		1.5	Ti, Nb	1839	7.0
HT2-CT-21		1.5	Ca, Ti	2026	8.5
HT1-CT-17	-80	2.2	Ca, Ti, Al	1998	12.1
HT2-CT-25		1.6	Ca, Ti, Al	1903	8.0

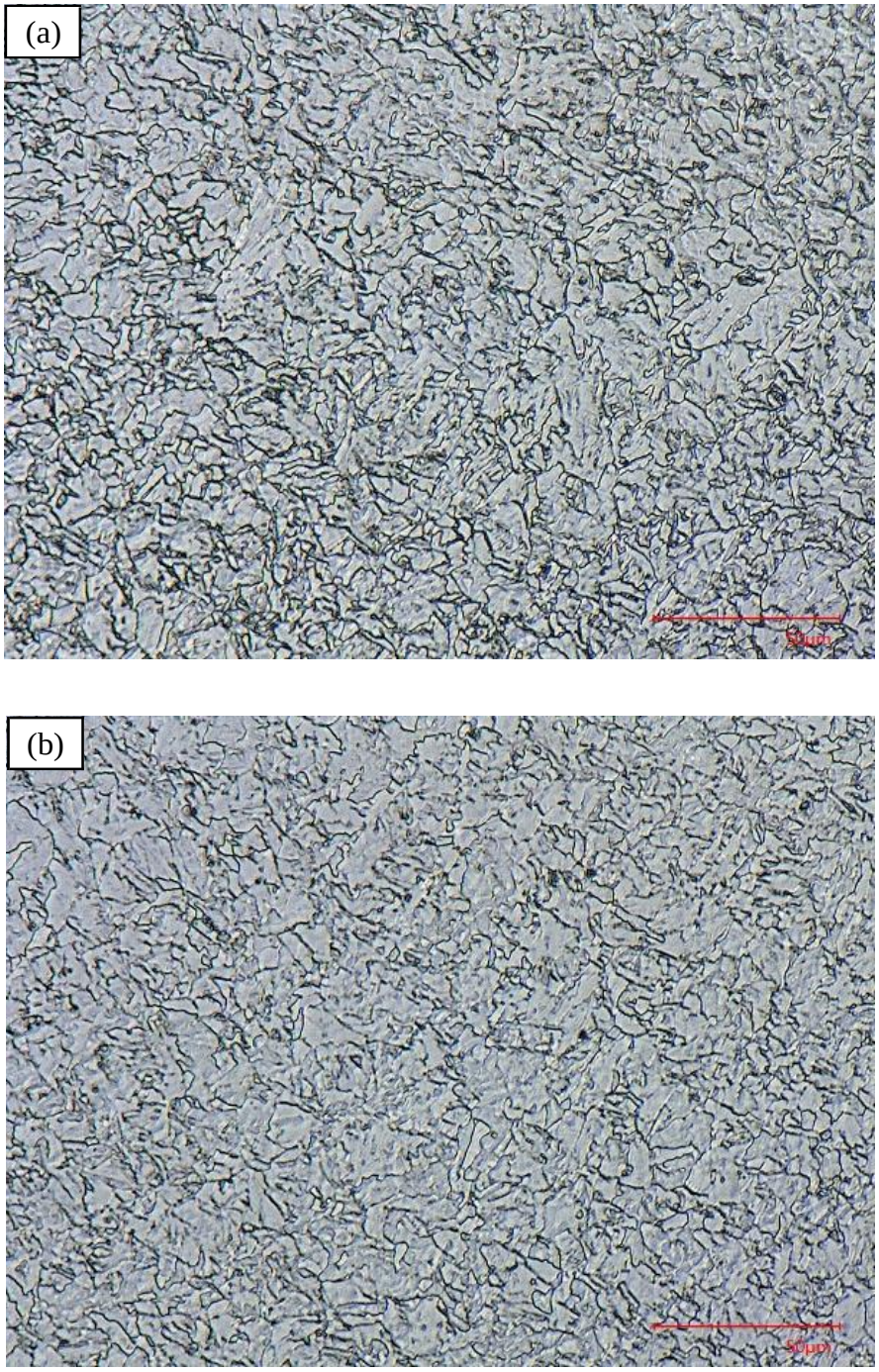

Figure 4.1 Microstructure of (a) HT1 and (b) HT2 conditions of SA738Gr.B steel under optical microscope with magnification of 200×.

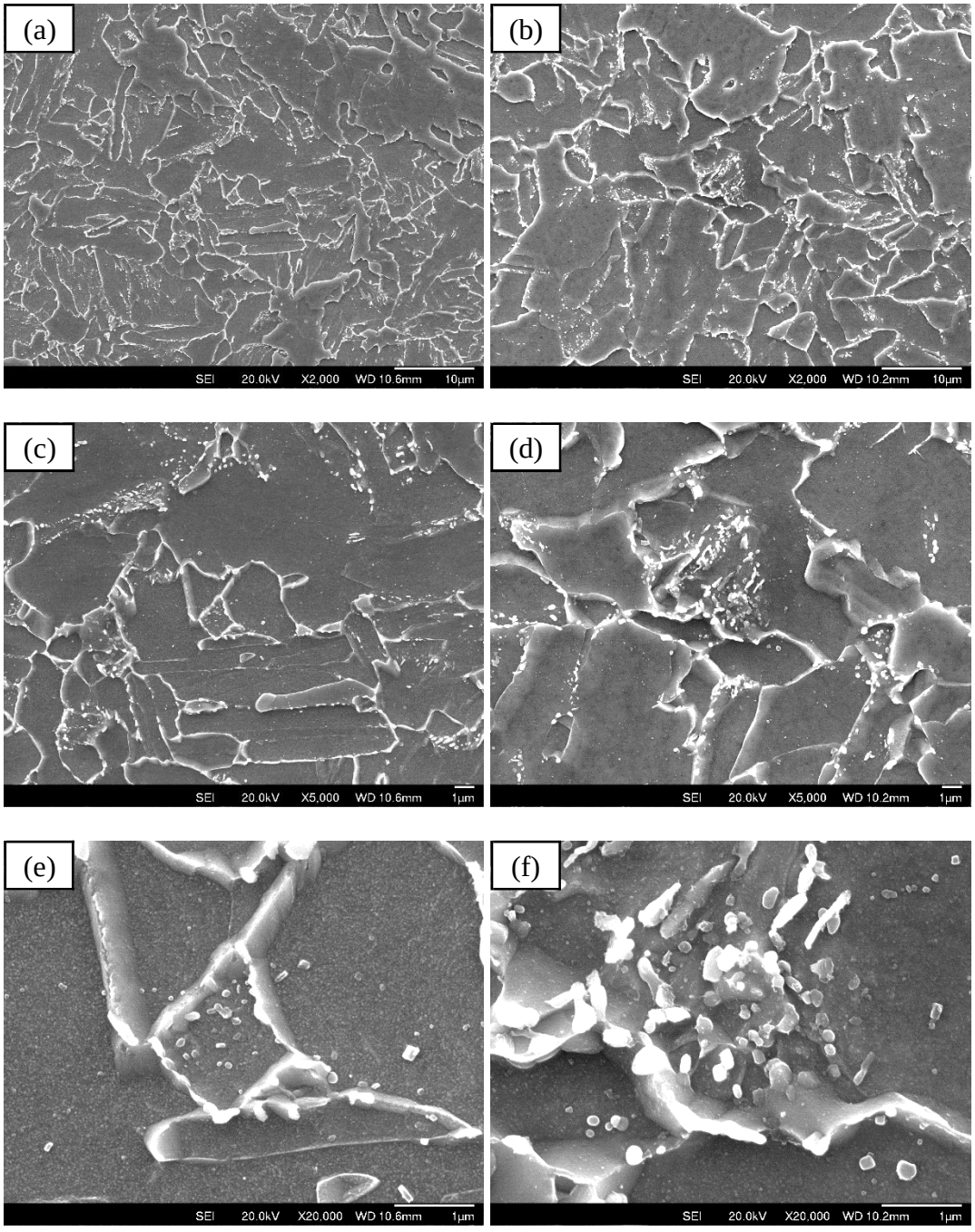

Figure 4.2 A sequence of SEM images of increasing magnification for the microstructure of HT1 (left) and HT2 (right) conditions of SA738Gr.B steel: (a) and (b) 2,000×; (c) and (d) 5,000×; (e) and (f) 20,000×.

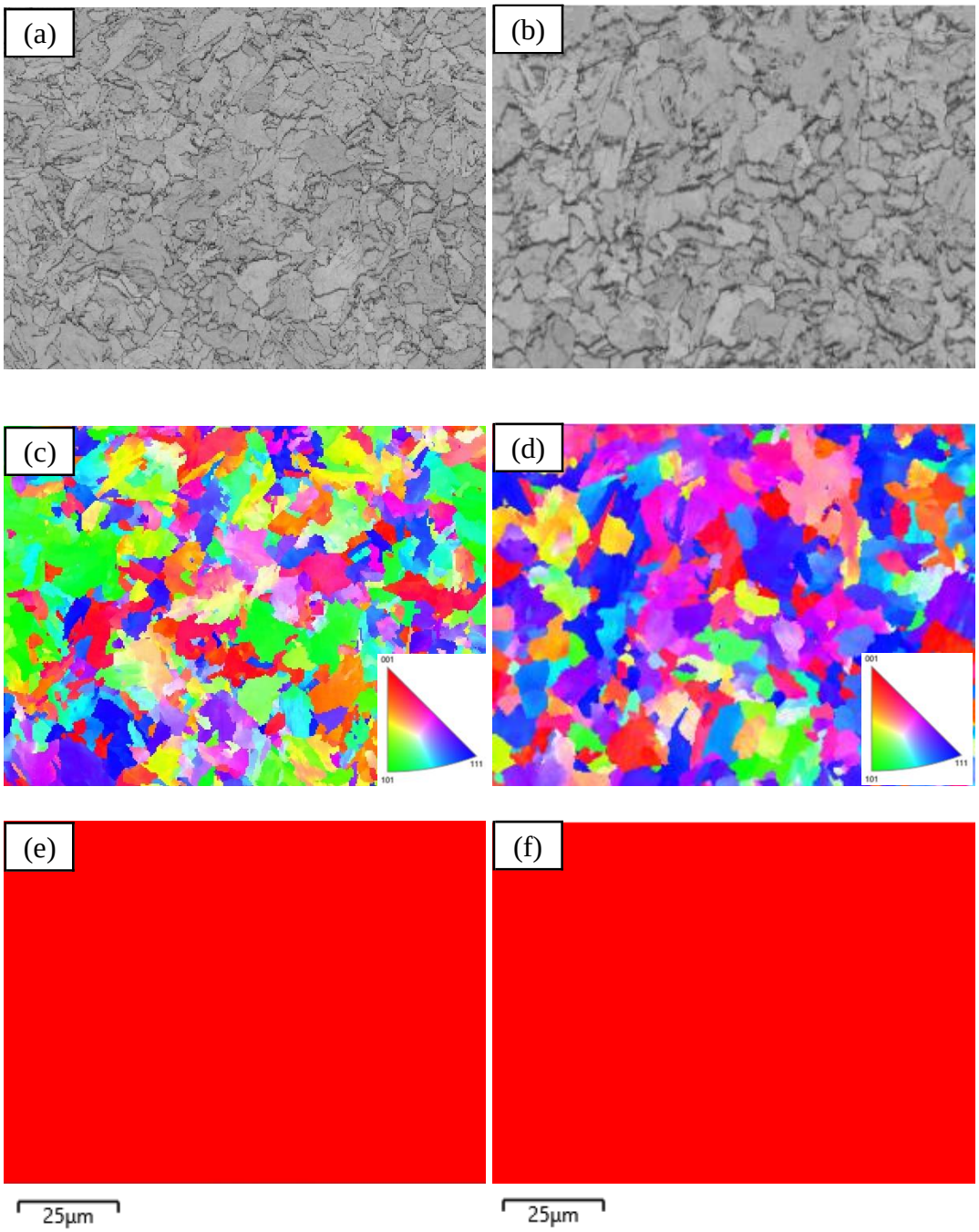

Figure 4.3 EBSD analysis for HT1 (left) and HT2 (right) conditions of SA738Gr.B steel: (a) and (b) are the SEM images; (c) and (d) are the EBSD mappings from the same regions as SEM images; (e) and (f) are their phase distributions in the regions, where only BCC phase was observed (red).

(a)

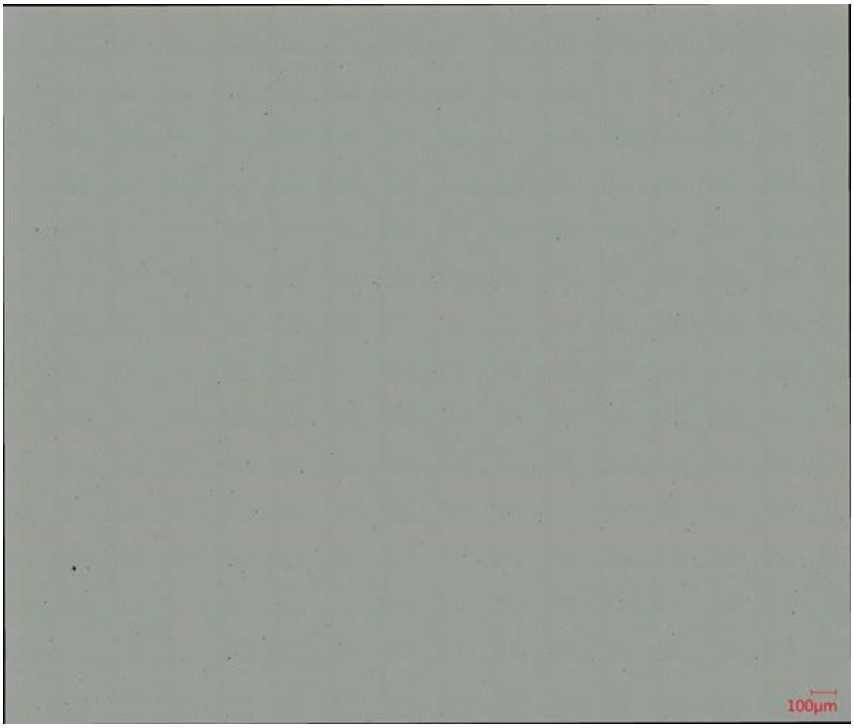

(b)

Figure 4.4 Backscattered mode images of polished surfaces from (a) HT1 and (b) HT2 conditions.

(a)

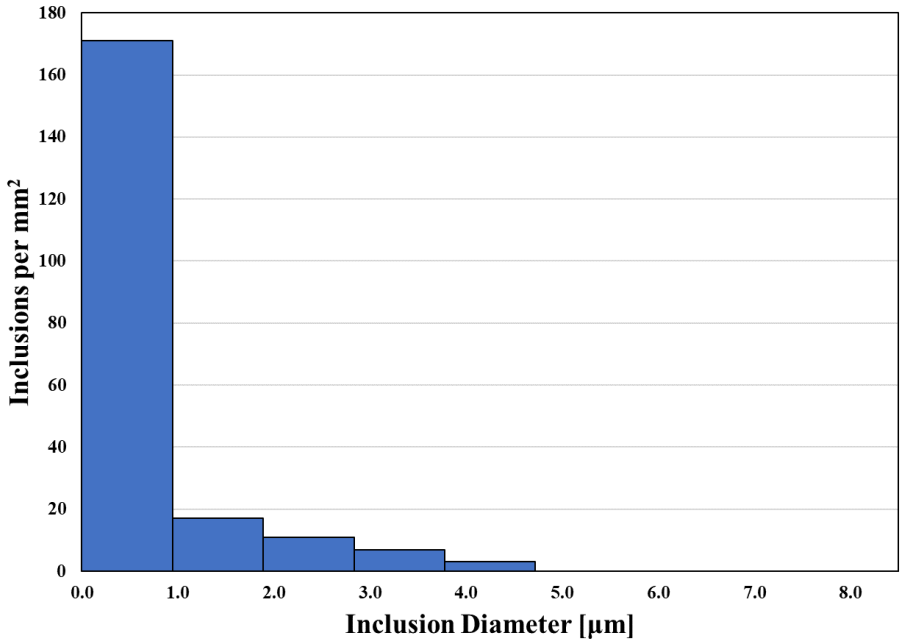

(b)

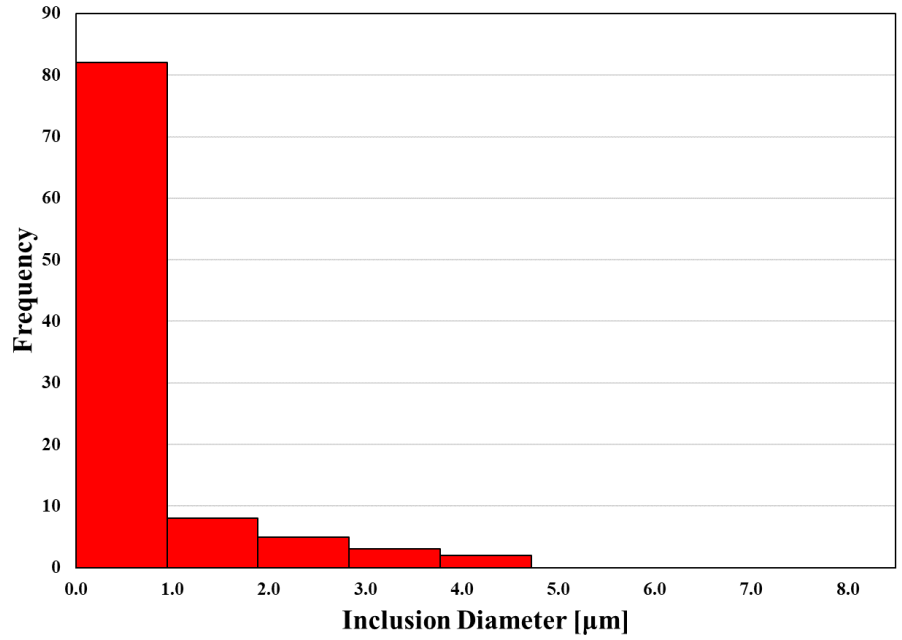

Figure 4.5 Results of inclusion analysis for HT1 condition, (a) inclusion number per mm^2; (b) inclusion frequency.

(a)

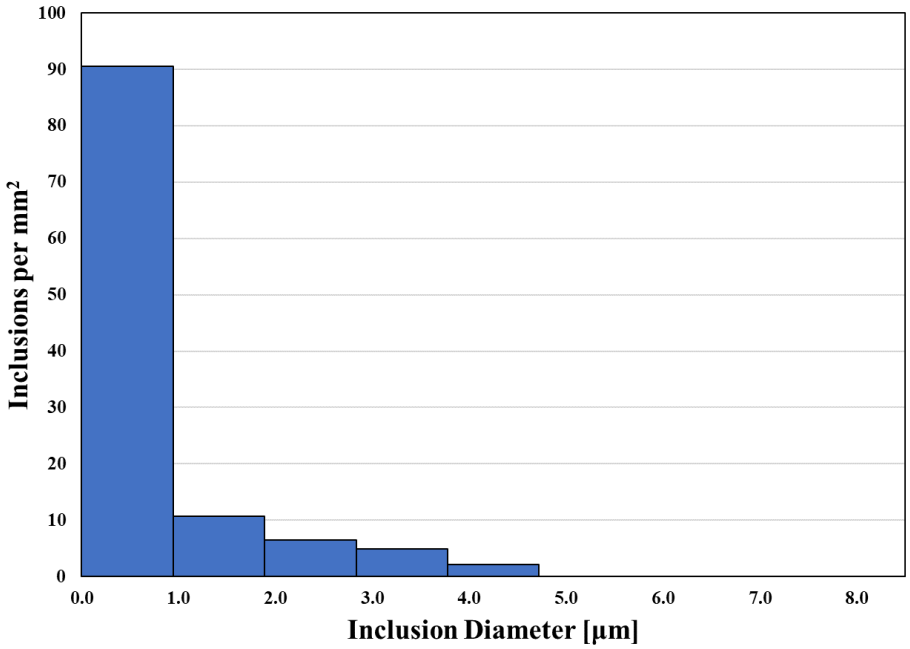

(b)

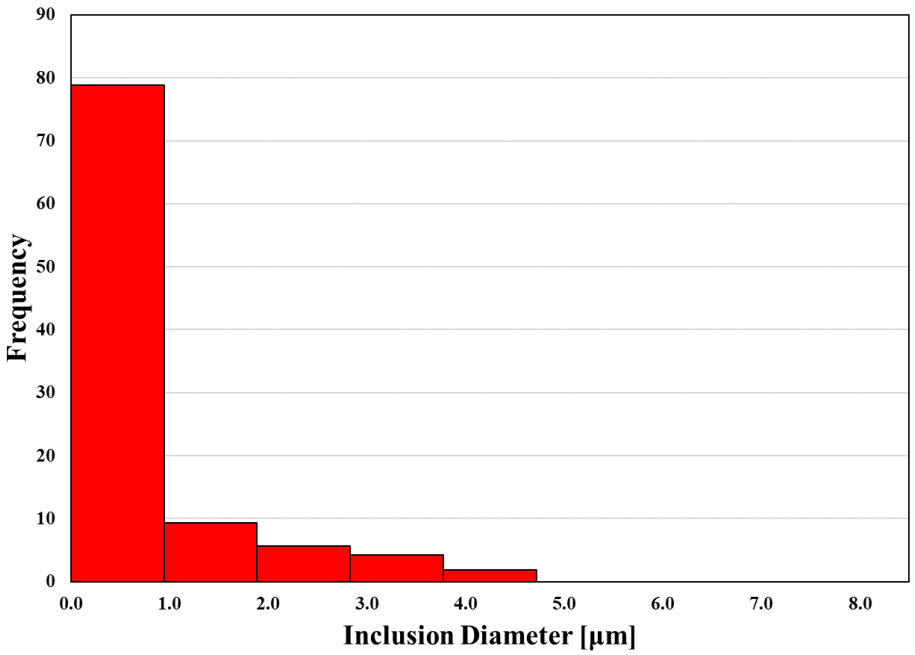

Figure 4.6 Results of inclusion analysis for HT2 condition, (a) inclusion number per mm^2; (b) inclusion frequency.

(a)

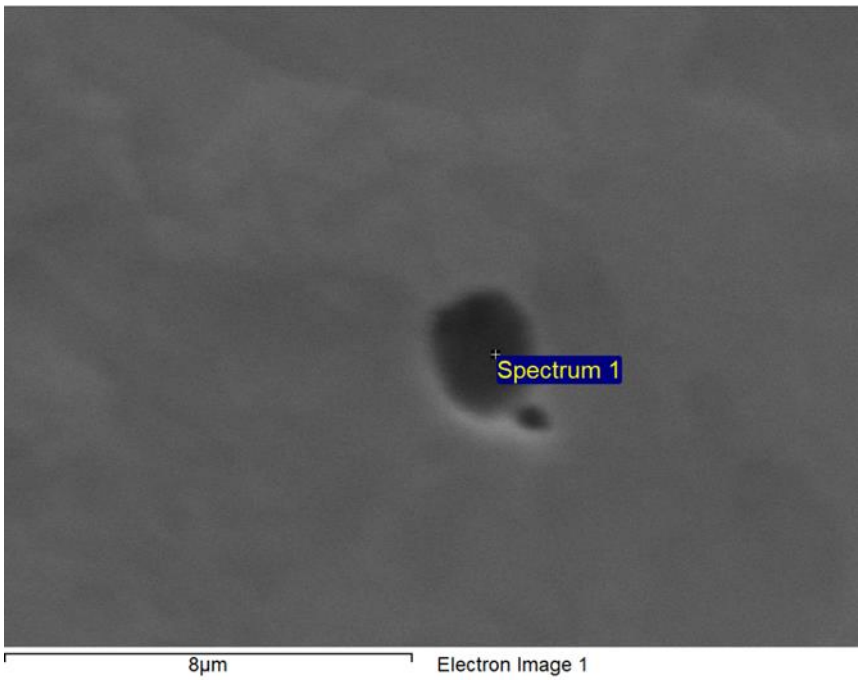

(b)

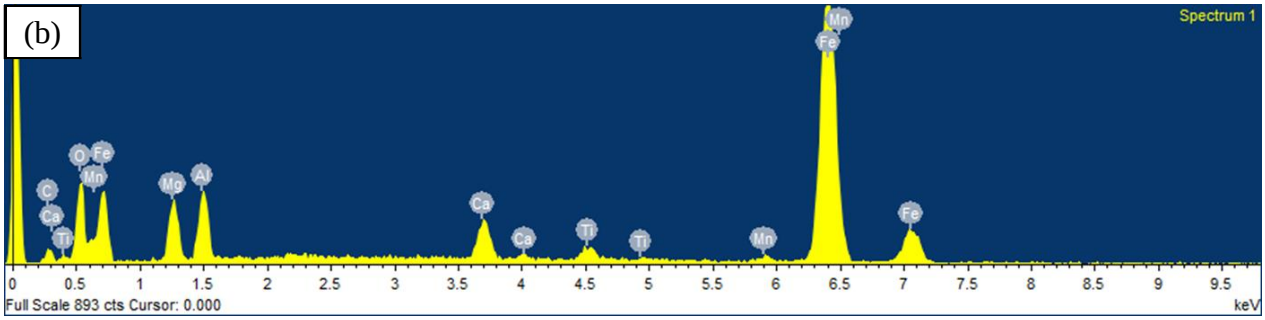

Figure 4.7 Typical inclusion of HT1 condition, (a) SEM image; (b) EDX spectrum.

(a)

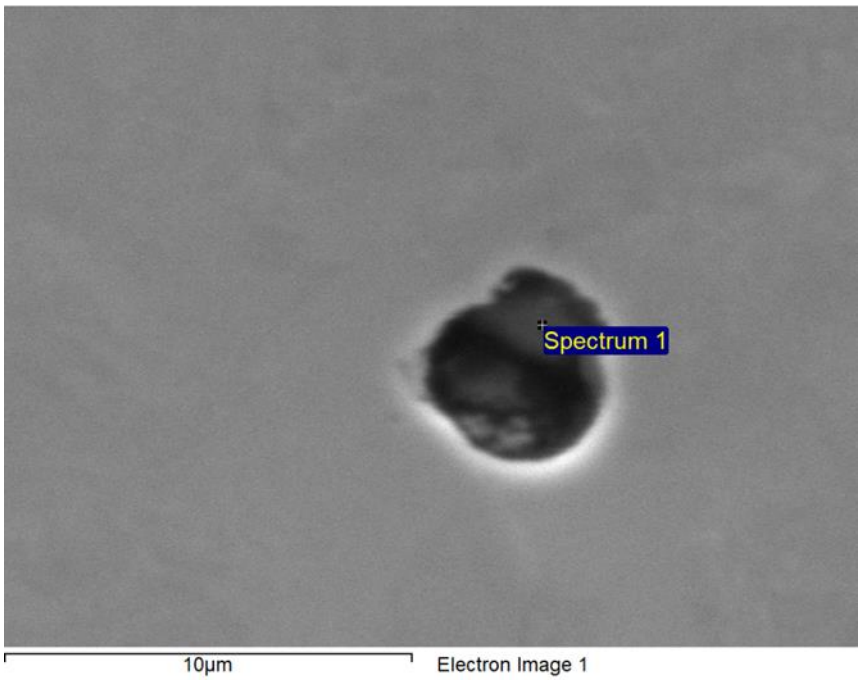

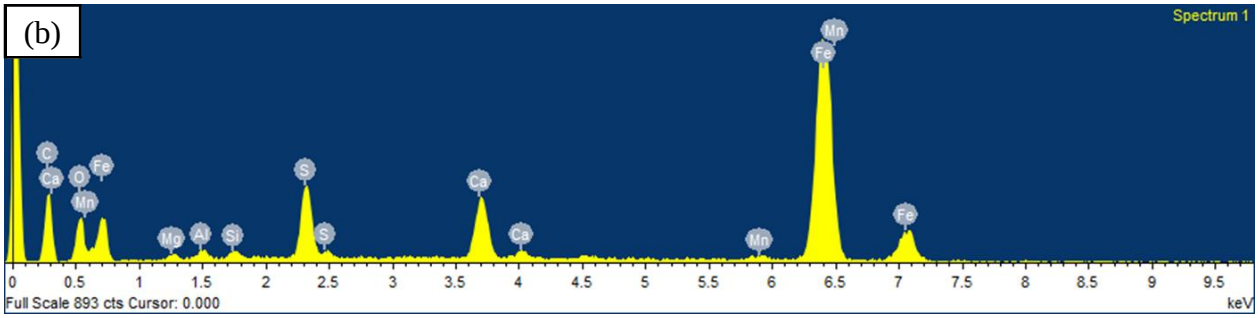

Figure 4.8 Typical inclusion of HT2 condition, (a) SEM image; (b) EDX spectrum.

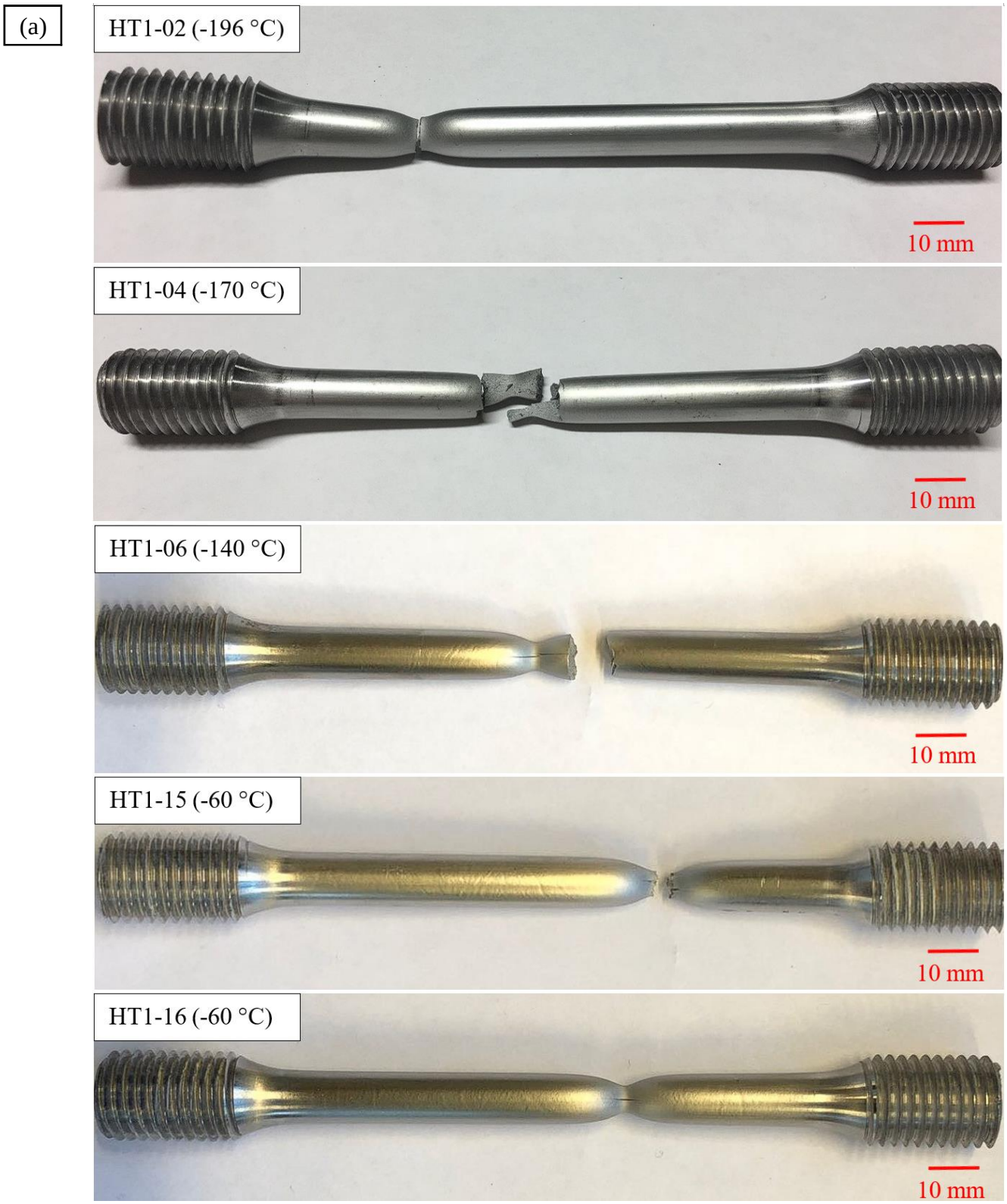

Figure 4.9 Fracture profiles of HT1 and HT2 specimens at different temperatures, (a) HT1 and (b) HT2.

(b)

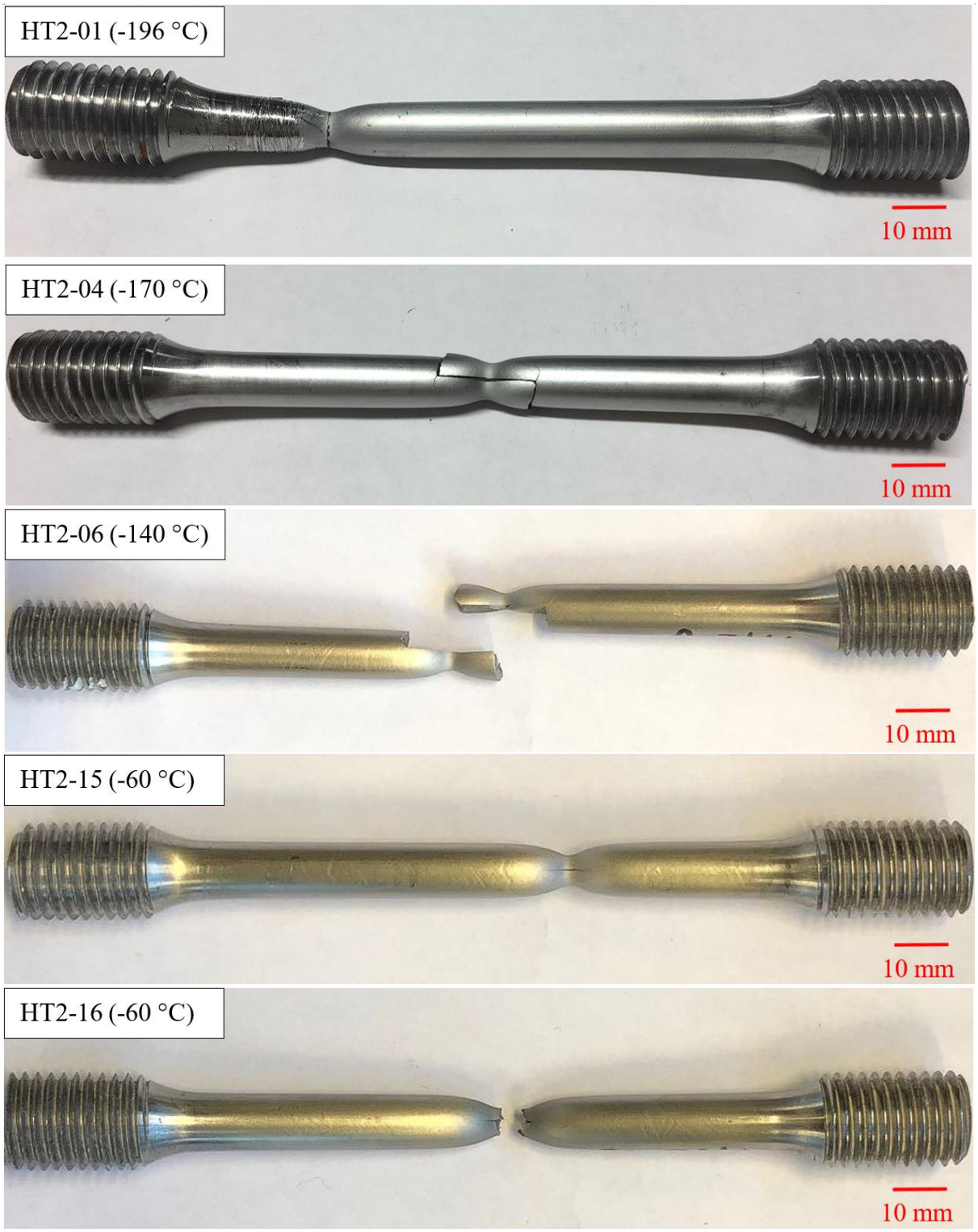
HT2-01 (-196 °C)
10 mm
HT2-04 (-170 °C)
10 mm
HT2-06 (-140 °C)
10 mm
HT2-15 (-60 °C)
10 mm
HT2-16 (-60 °C)
10 mm

(b) HT2.

(a)

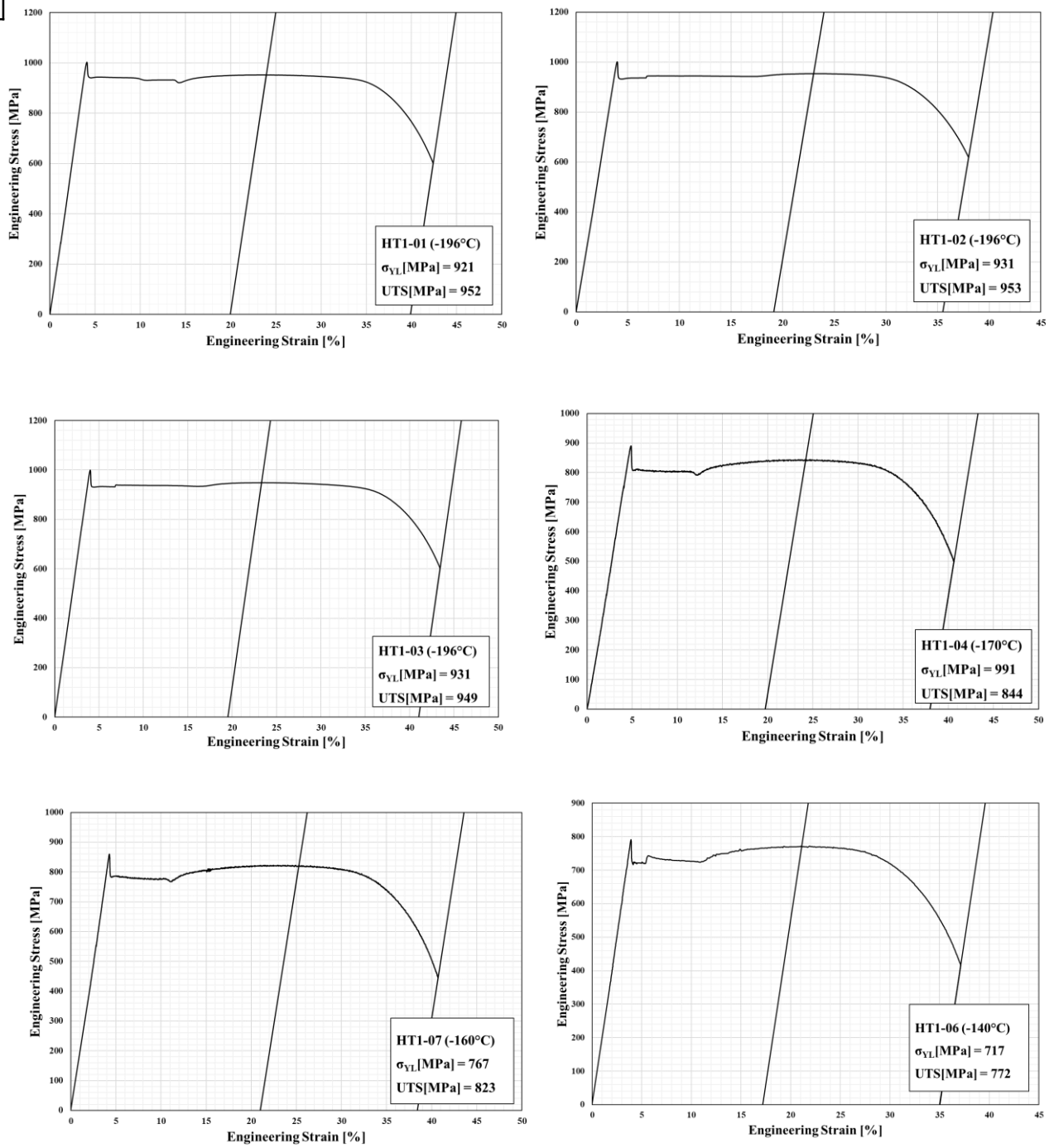

Figure 4.10 Engineering stress-strain curves of HT1 specimens at different temperatures, (a) -196 to -140 °C, (b) -140 to -80 °C and (c) -80 to -60 °C.

(b)

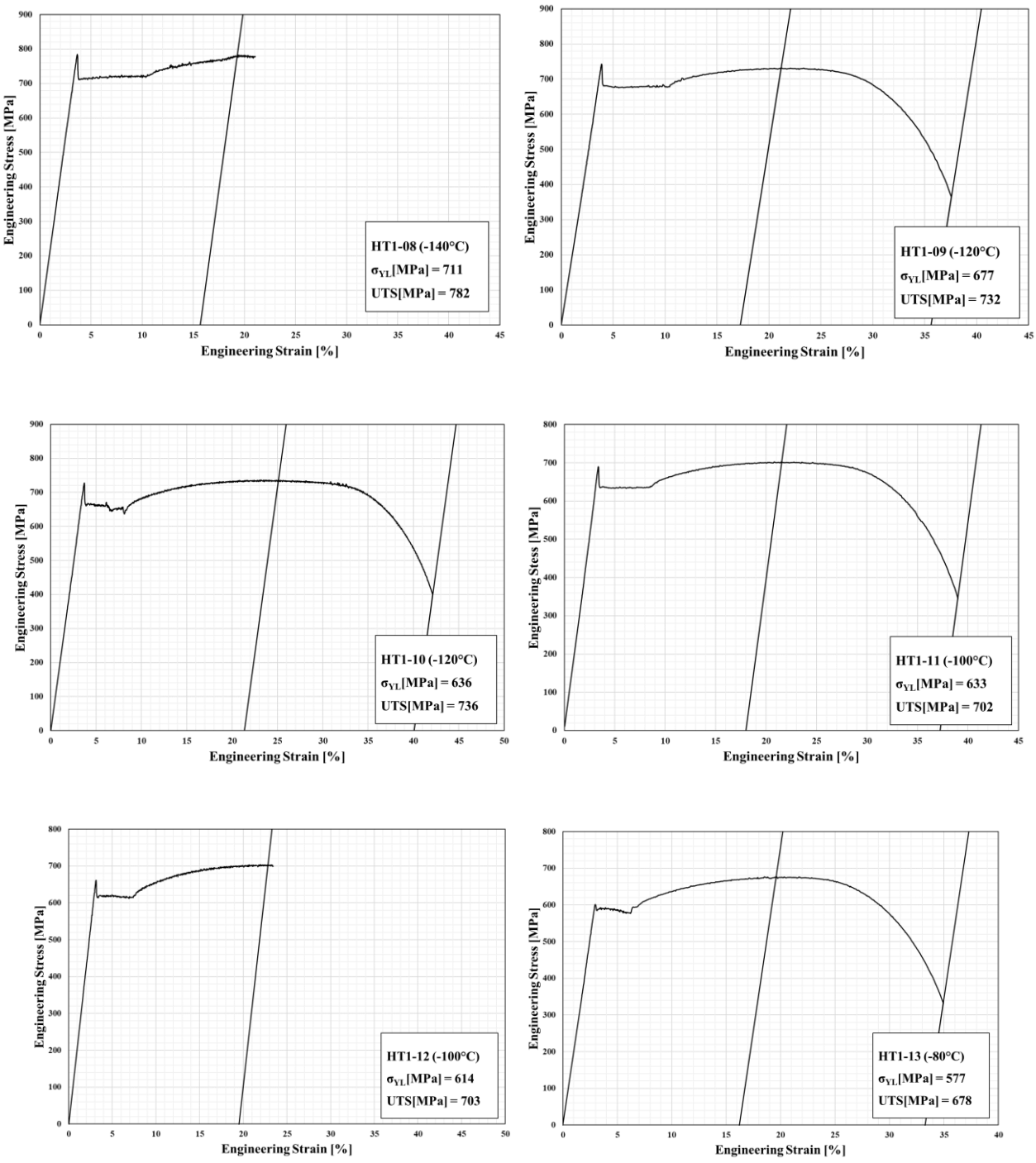
Engineering Stress [MPa]
Engineering Strain [%]
HT1-08 (-140°C)
σYL[MPa] = 711
UTS[MPa] = 782
HT1-09 (-120°C)
σYL[MPa] = 677
UTS[MPa] = 732
HT1-10 (-120°C)
σYL[MPa] = 636
UTS[MPa] = 736
HT1-11 (-100°C)
σYL[MPa] = 633
UTS[MPa] = 702
HT1-12 (-100°C)
σYL[MPa] = 614
UTS[MPa] = 703
HT1-13 (-80°C)
σYL[MPa] = 577
UTS[MPa] = 678

(b) -140 to -80 °C.

(c)

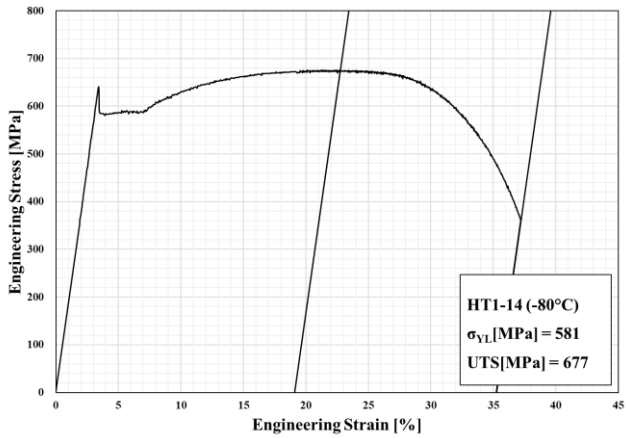
Engineering Stress [MPa]
Engineering Strain [%]
HT1-14 (-80°C)
σYL[MPa] = 581
UTS[MPa] = 677

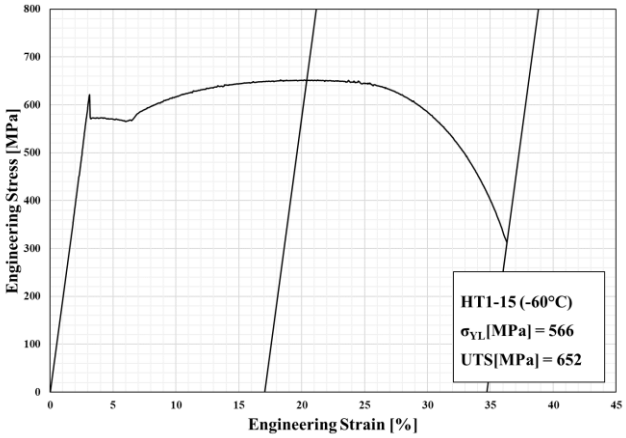
Engineering Stress [MPa]
Engineering Strain [%]
HT1-15 (-60°C)
σYL[MPa] = 566
UTS[MPa] = 652

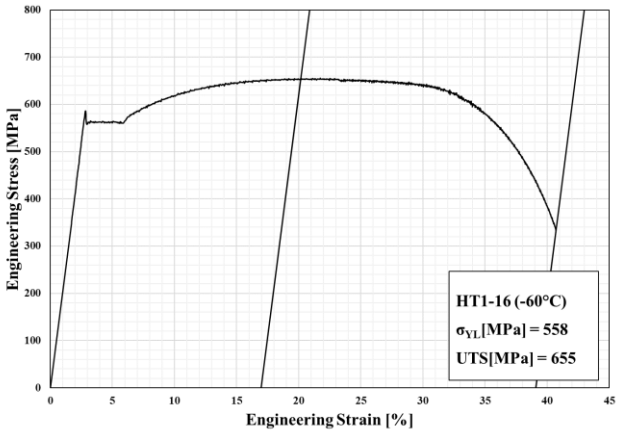
Engineering Stress [MPa]
Engineering Strain [%]
HT1-16 (-60°C)
σYL[MPa] = 558
UTS[MPa] = 655

(c) -80 to -60 °C.

(a)

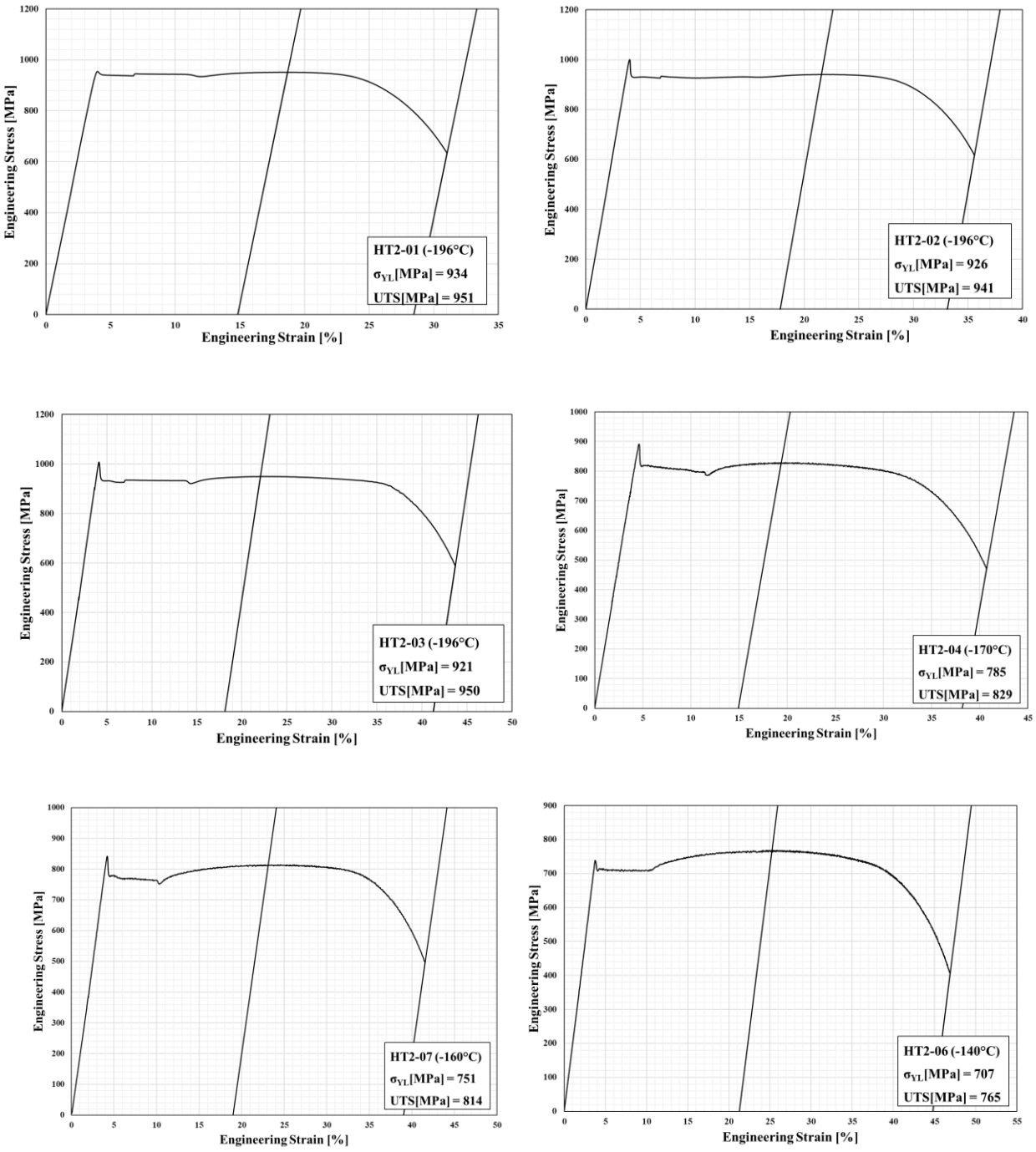

Figure 4.11 Engineering stress-strain curves of HT2 specimens at different temperatures, (a) -196 to -140 °C, (b) -140 to -80 °C and (c) -80 to -60 °C.

(b)

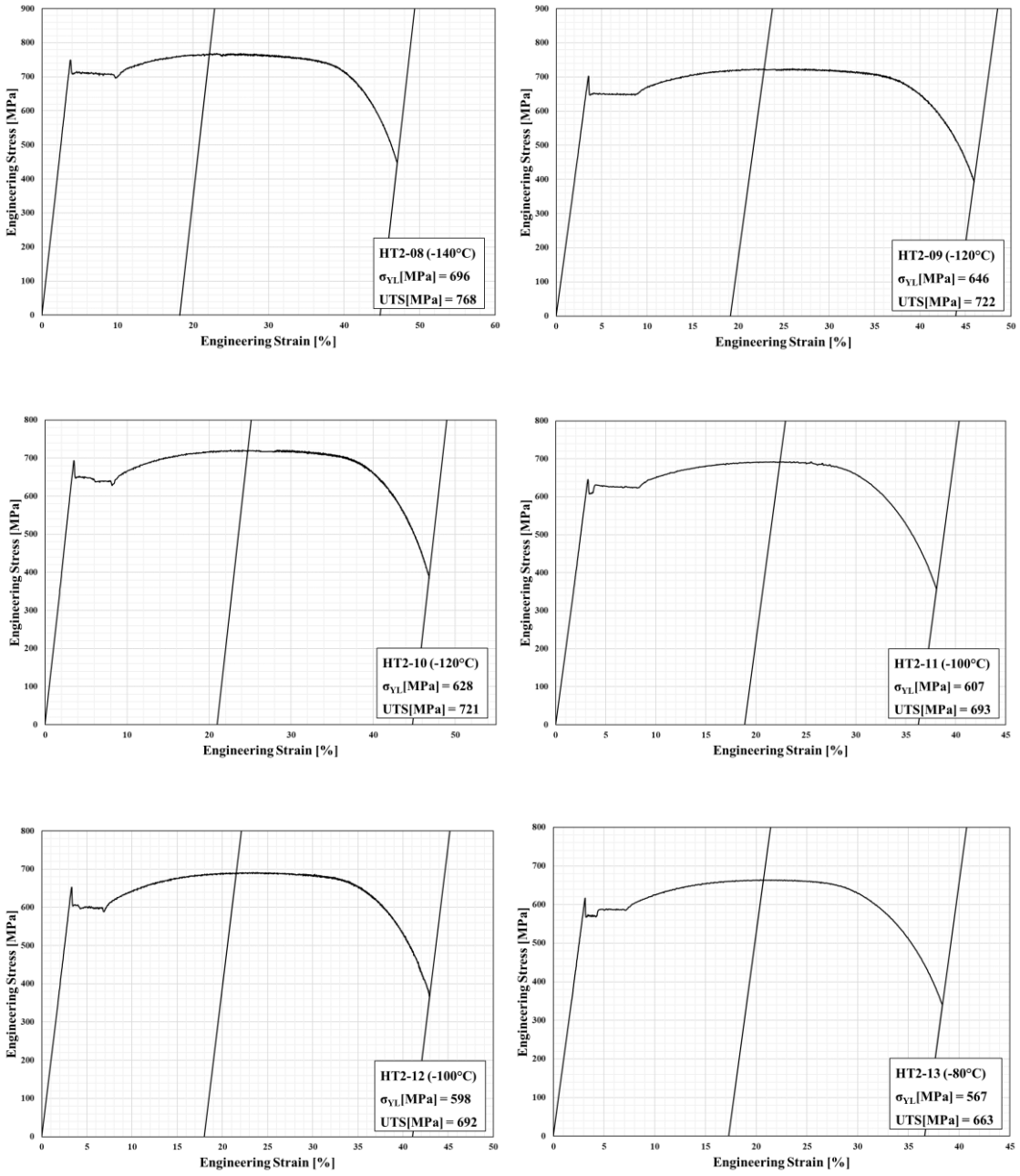
Engineering Stress [MPa]
Engineering Strain [%]
HT2-08 (-140°C)
σYL[MPa] = 696
UTS[MPa] = 768
HT2-09 (-120°C)
σYL[MPa] = 646
UTS[MPa] = 722
HT2-10 (-120°C)
σYL[MPa] = 628
UTS[MPa] = 721
HT2-11 (-100°C)
σYL[MPa] = 607
UTS[MPa] = 693
HT2-12 (-100°C)
σYL[MPa] = 598
UTS[MPa] = 692
HT2-13 (-80°C)
σYL[MPa] = 567
UTS[MPa] = 663

(b) -140 to -80 °C.

(c)

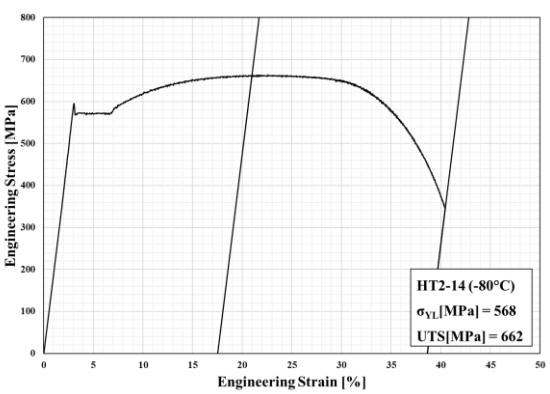
Engineering Stress [MPa]
Engineering Strain [%]
HT2-14 (-80°C)
σYL[MPa] = 568
UTS[MPa] = 662

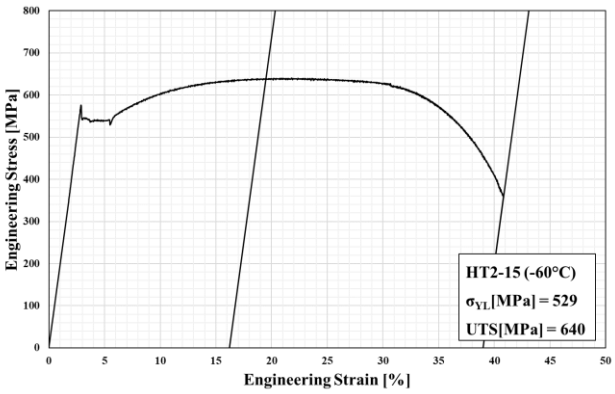
Engineering Stress [MPa]
Engineering Strain [%]
HT2-15 (-60°C)
σYL[MPa] = 529
UTS[MPa] = 640

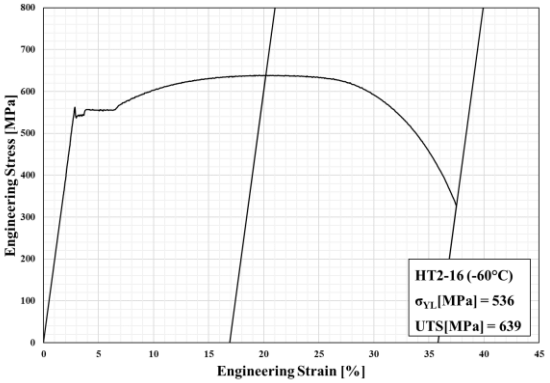
Engineering Stress [MPa]
Engineering Strain [%]
HT2-16 (-60°C)
σYL[MPa] = 536
UTS[MPa] = 639

(c) -80 to -60 °C.

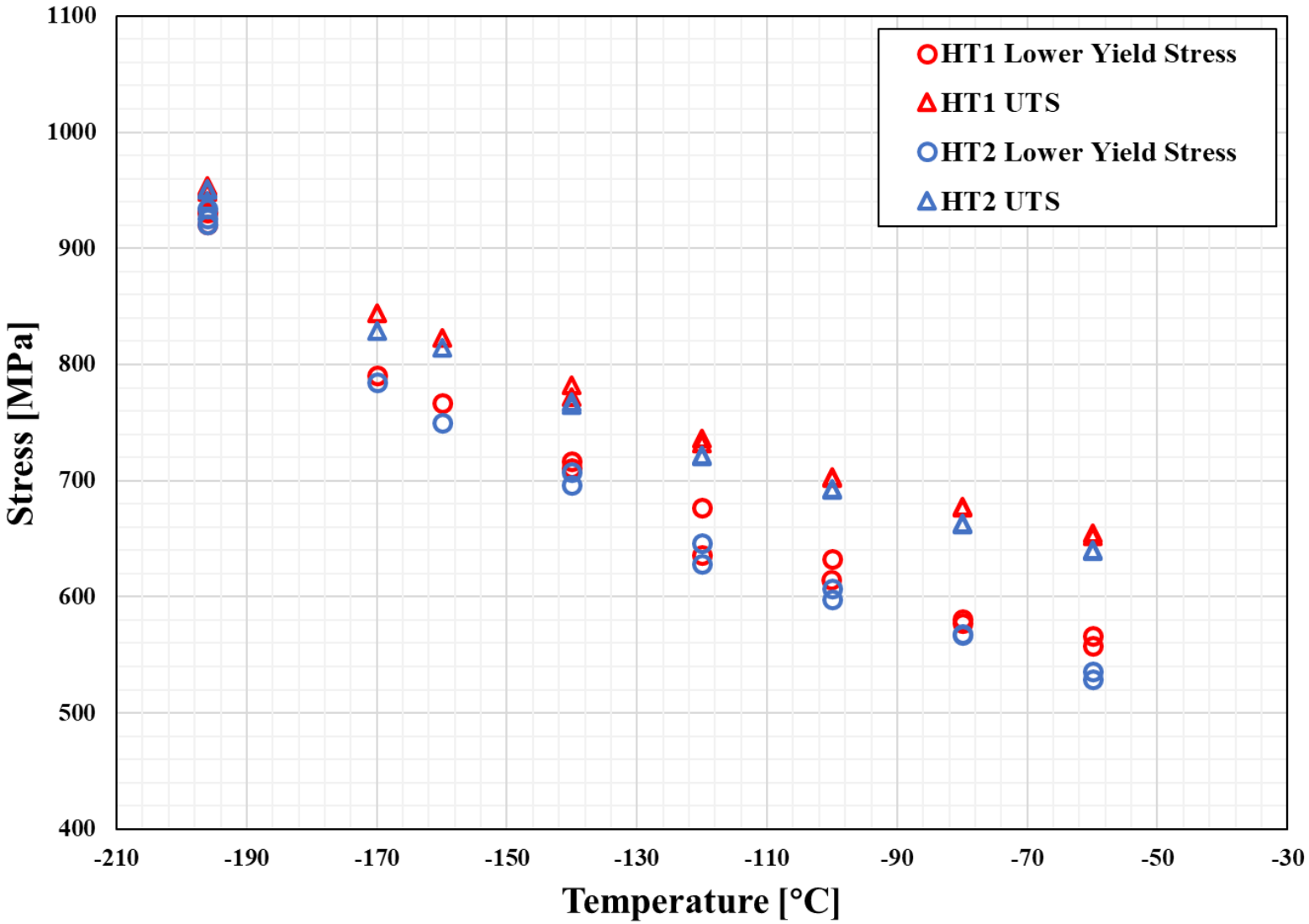

Figure 4.12 Comparisons of lower yield stress and ultimate tensile strength of HT1 and HT2 specimens at different temperatures.

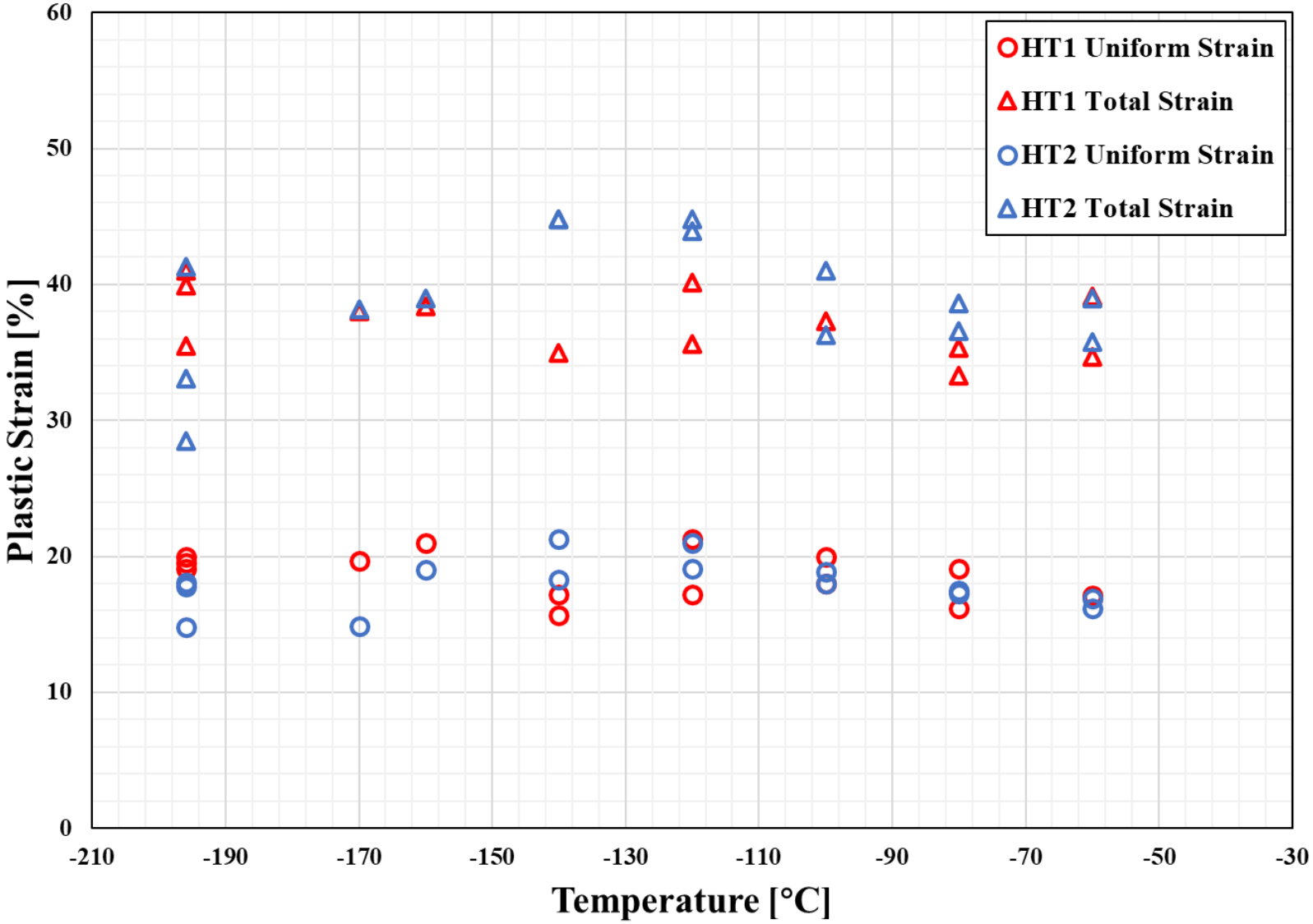

Figure 4.13 Comparisons of uniform strain and total strain of HT1 and HT2 specimens at different temperatures.

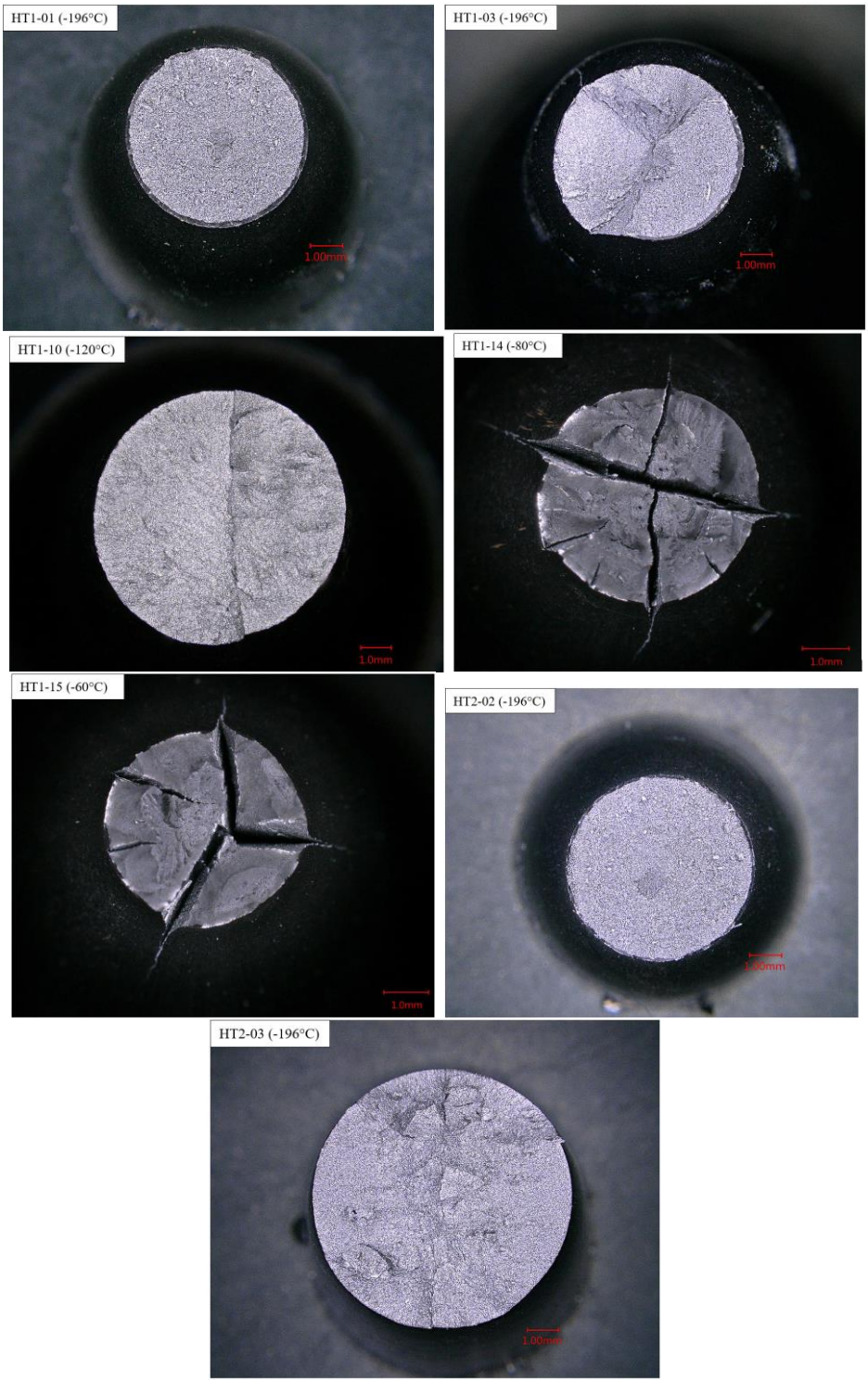

Figure 4.14 Typical fracture surfaces of HT1 and HT2 Tensile specimens at different temperatures observed under optical microscope.

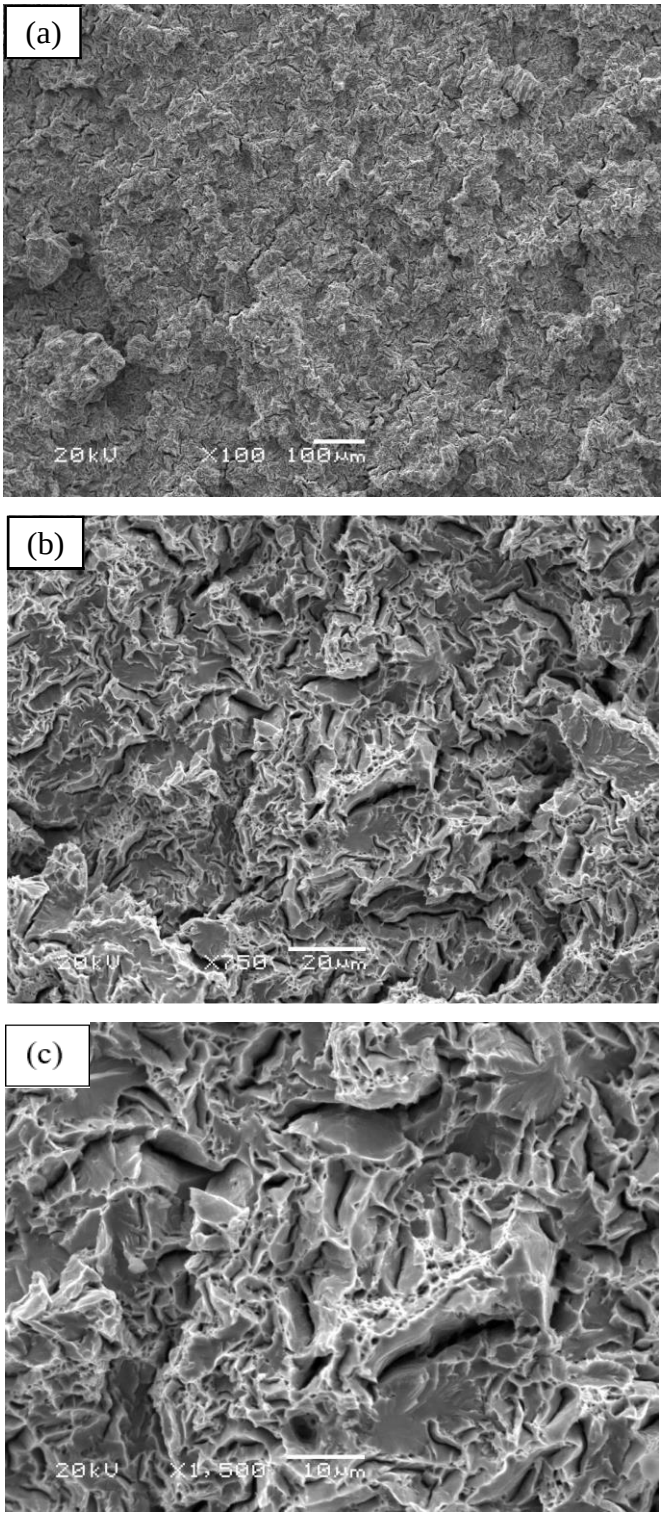

Figure 4.15 Fractography of HT1-01 Tensile specimen tested at -196°C observed under SEM in the sequence of magnification.

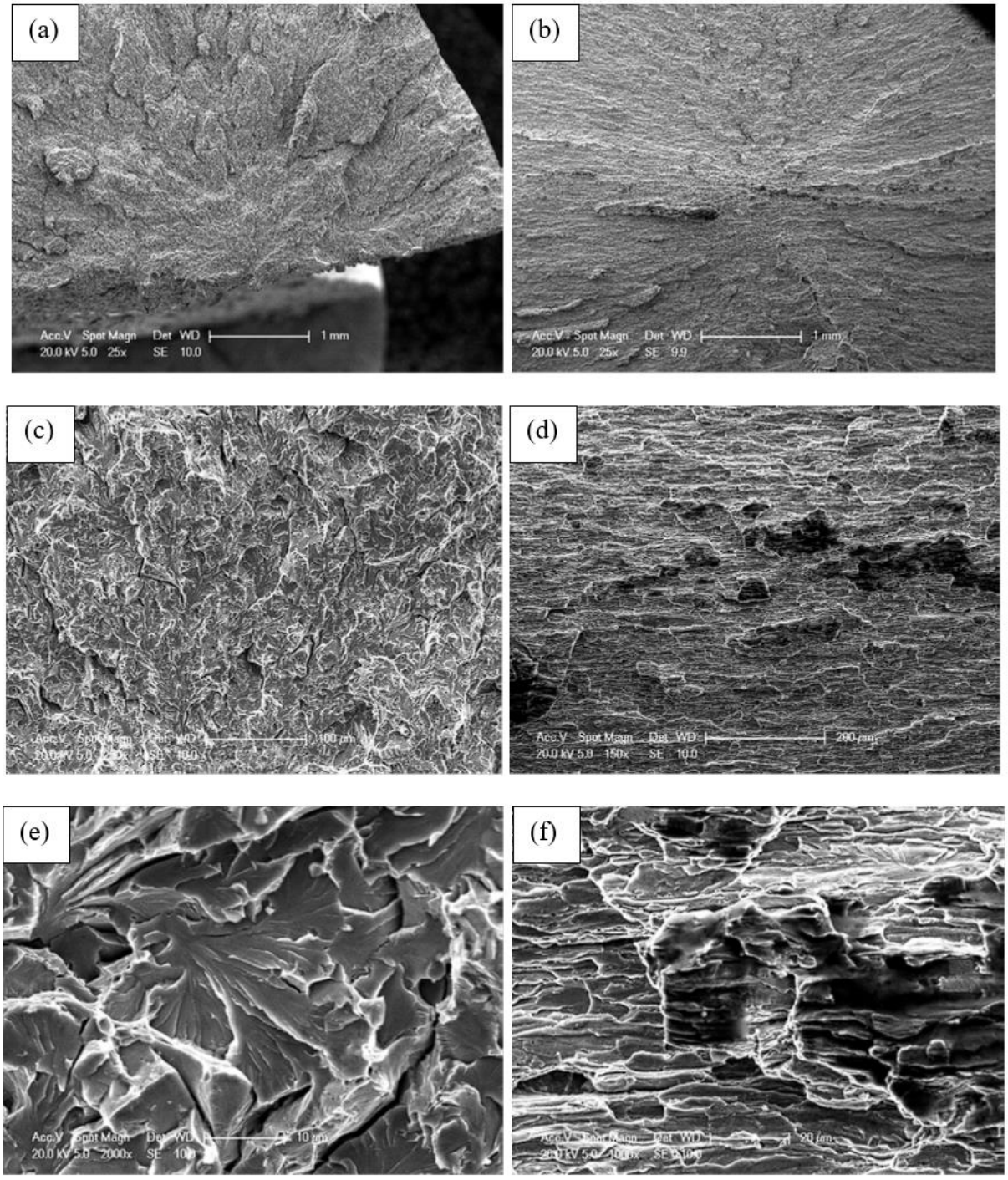

Figure 4.16 Fractography of HT2-04 Tensile specimen tested at -170°C observed under SEM. (a)(c)(e) are the fracture surfaces perpendicular to the loading direction in the sequence of magnification; (b)(d)(f) are the fracture surfaces parallel to the loading direction in the sequence of magnification.

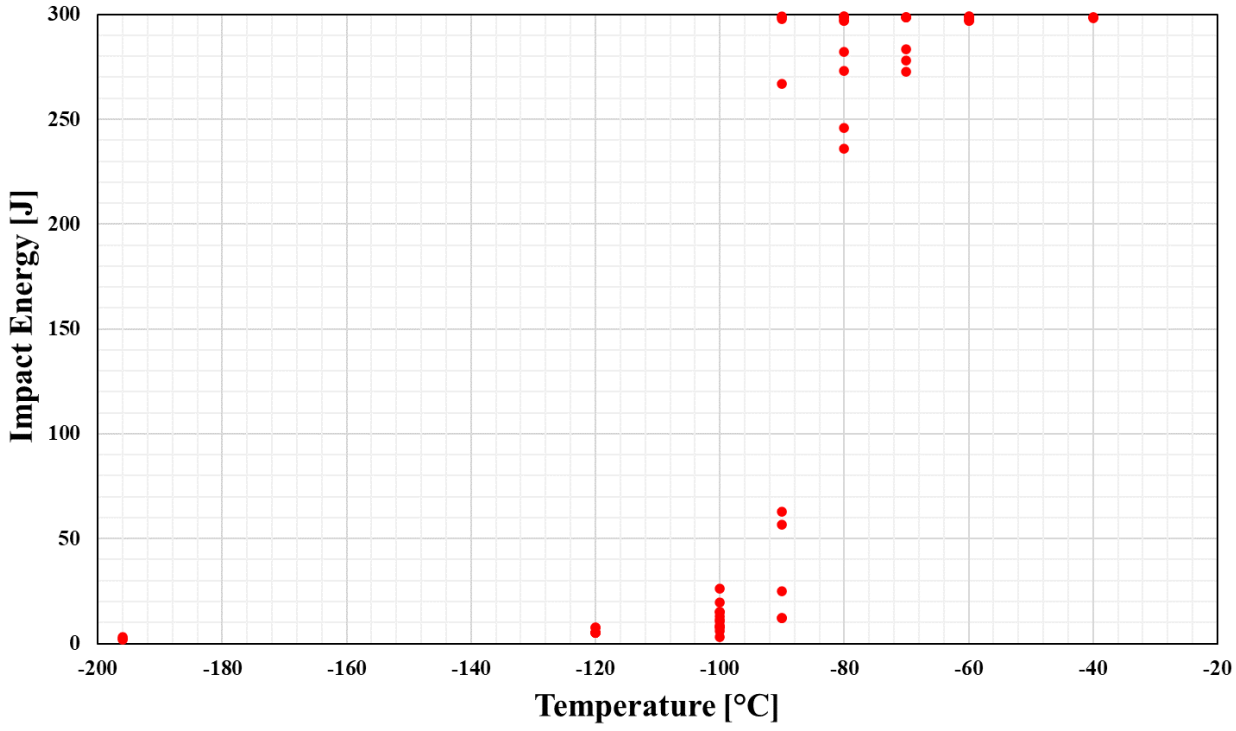

Figure 4.17 Absorbed impact energy for HT1 condition.

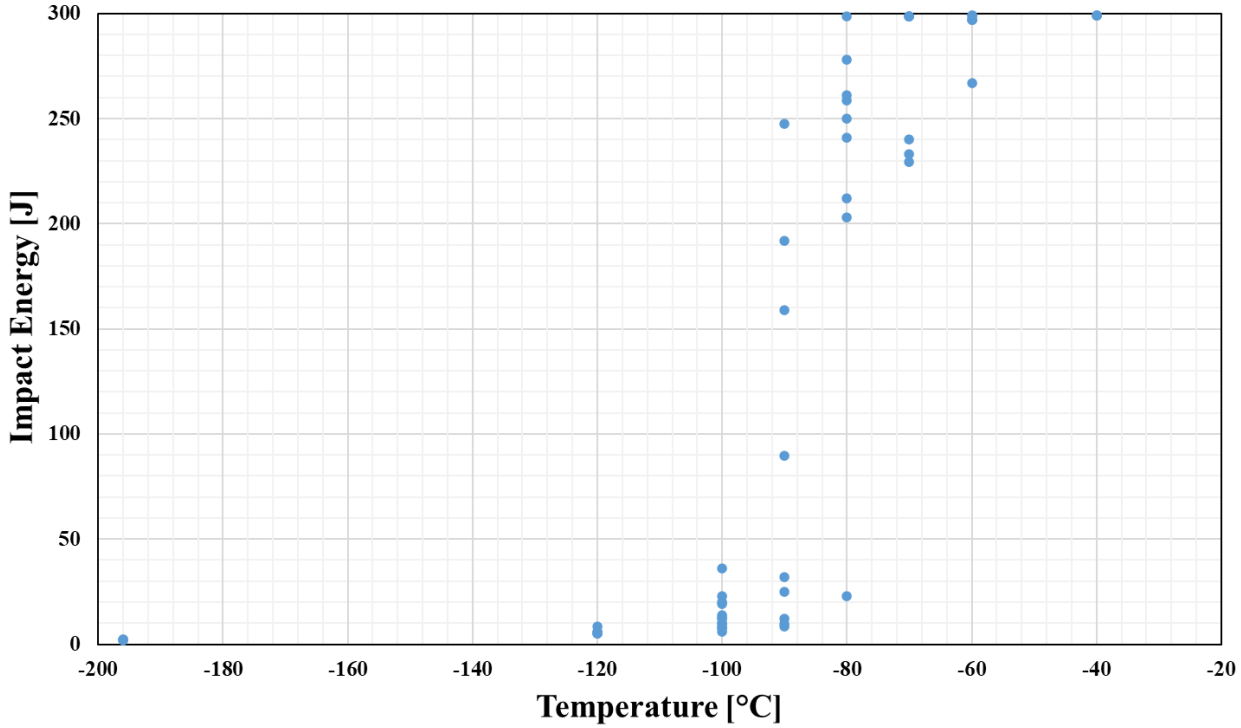

Figure 4.18 Absorbed impact energy for HT2 condition.

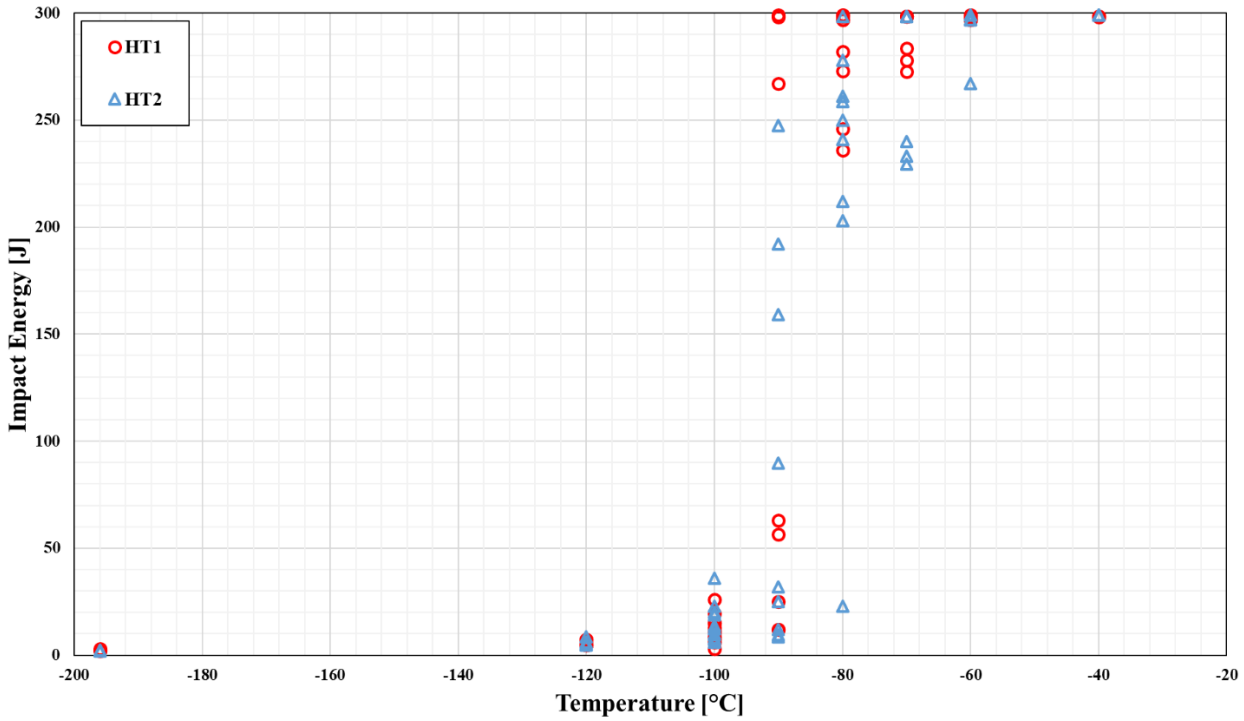

Figure 4.19 Comparison of absorbed impact energy for both HT1 and HT2 conditions.

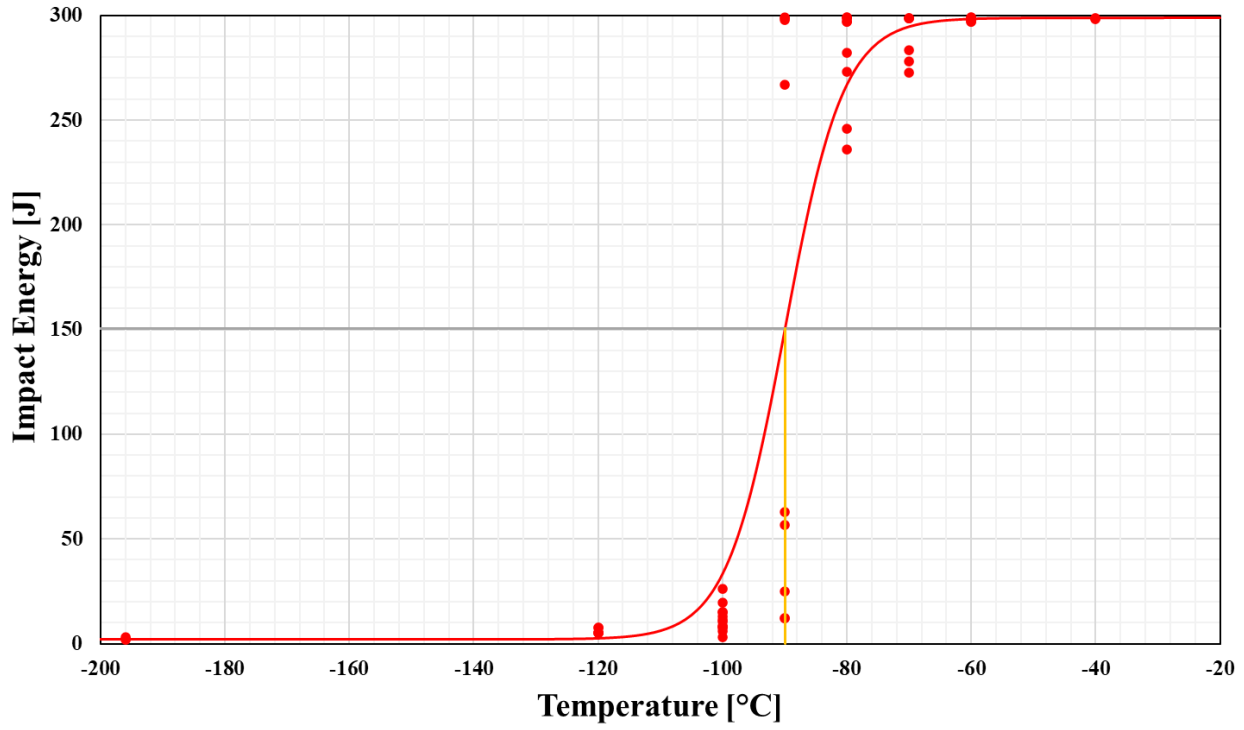

Figure 4.20 Ductile-to-Brittle transition curve for HT1 condition.

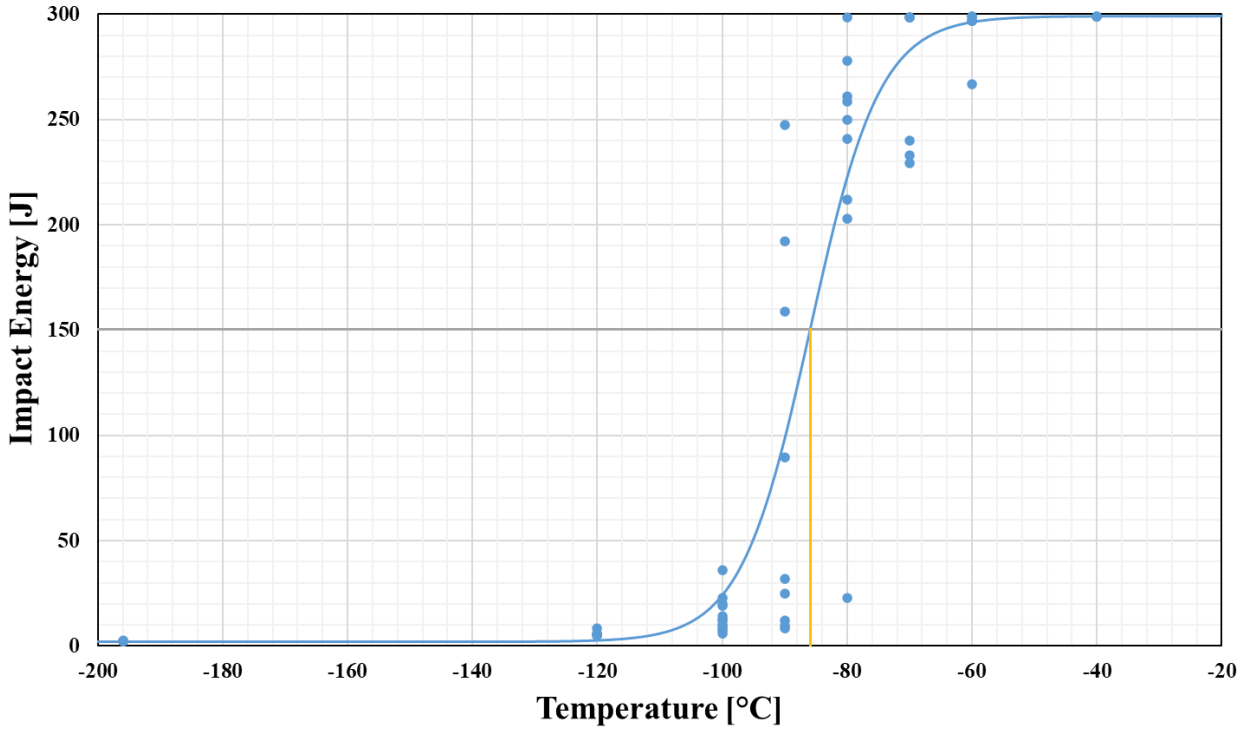

Figure 4.21 Ductile-to-Brittle transition curve for HT2 condition.

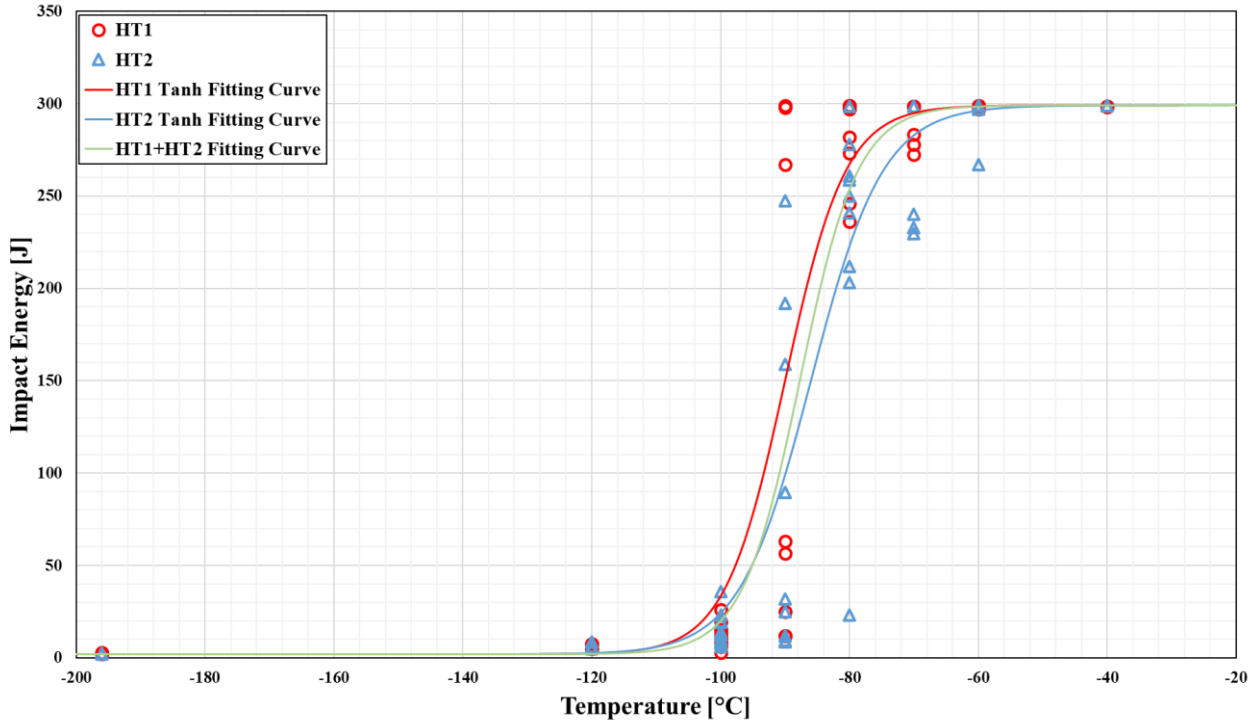

Figure 4.22 Comparison of Ductile-to-Brittle transition curves for both HT1 and HT2 conditions.

(a)

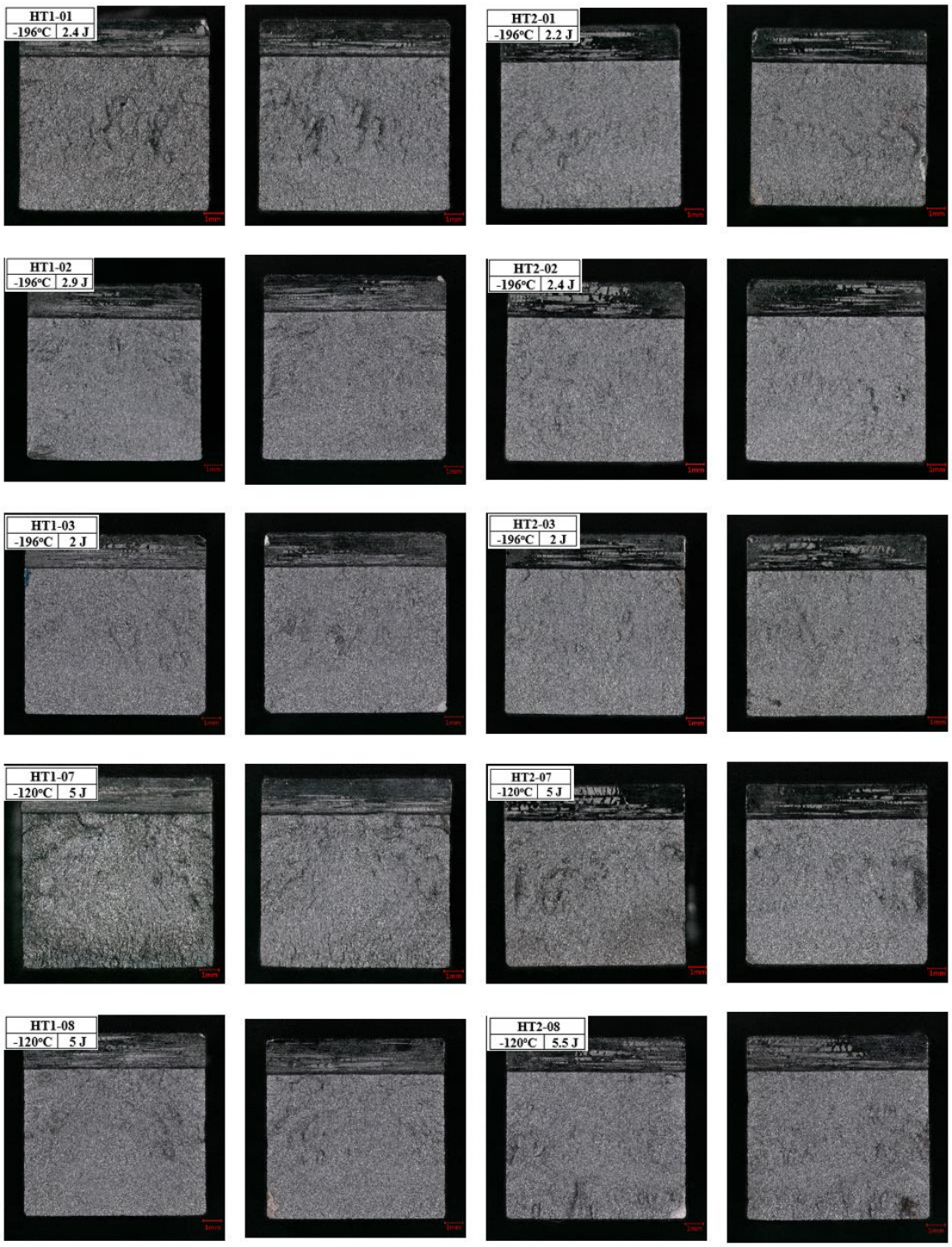

Figure 4.23 Fracture surfaces for both HT1 and HT2 conditions observed under optical microscope, (a) -196 to -120 °C, (b) -120 to -100 °C, (c) -100 °C, (d) -100 °C, (e) -100 to -90 °C, (f) -90 °C, (g) -80 °C, (h) -80 to -70 °C, (i) -70 °C, (j) -60 °C and (k) -60 to -40 °C.

(b)

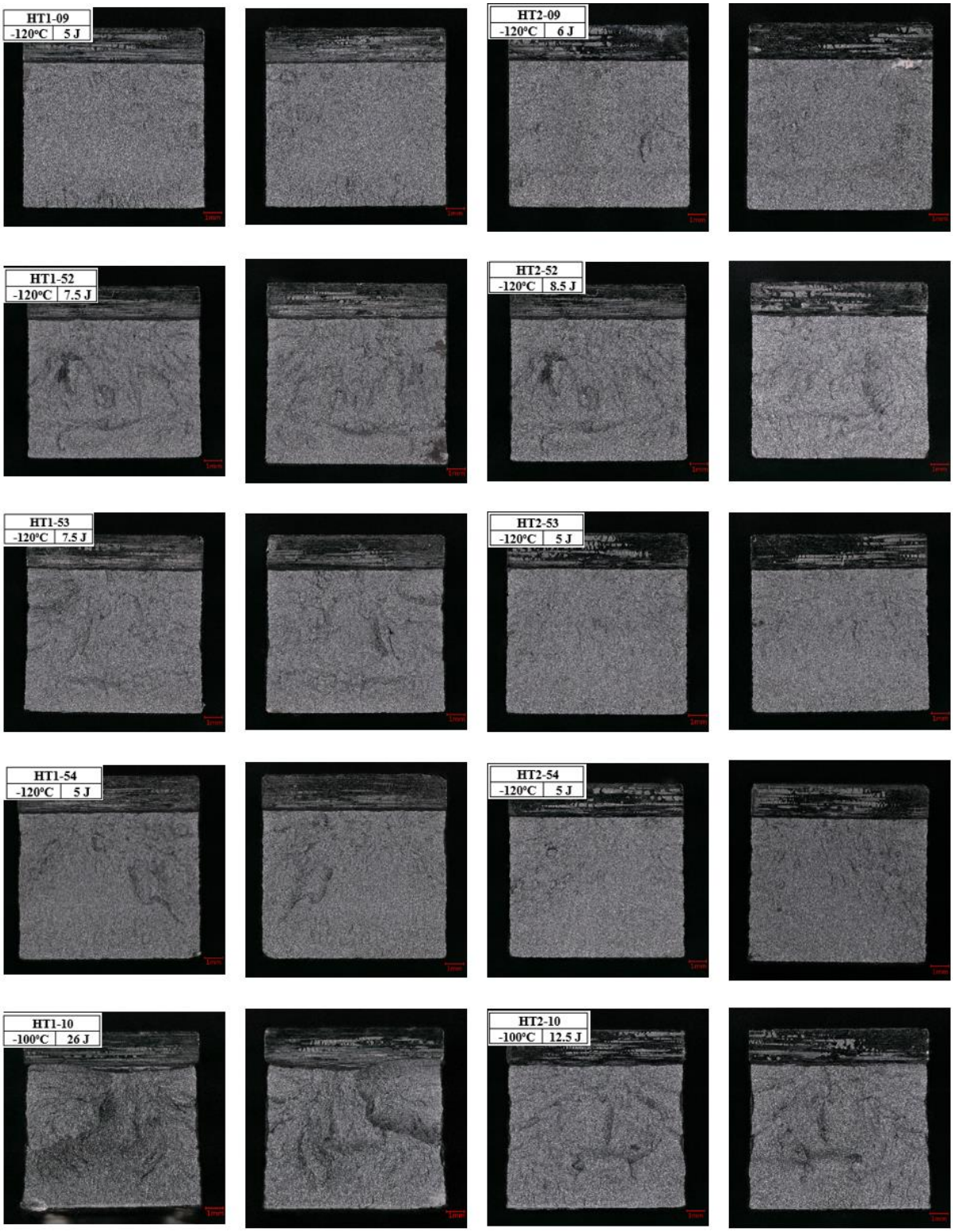

(b) -120 to -100 °C.

(c)

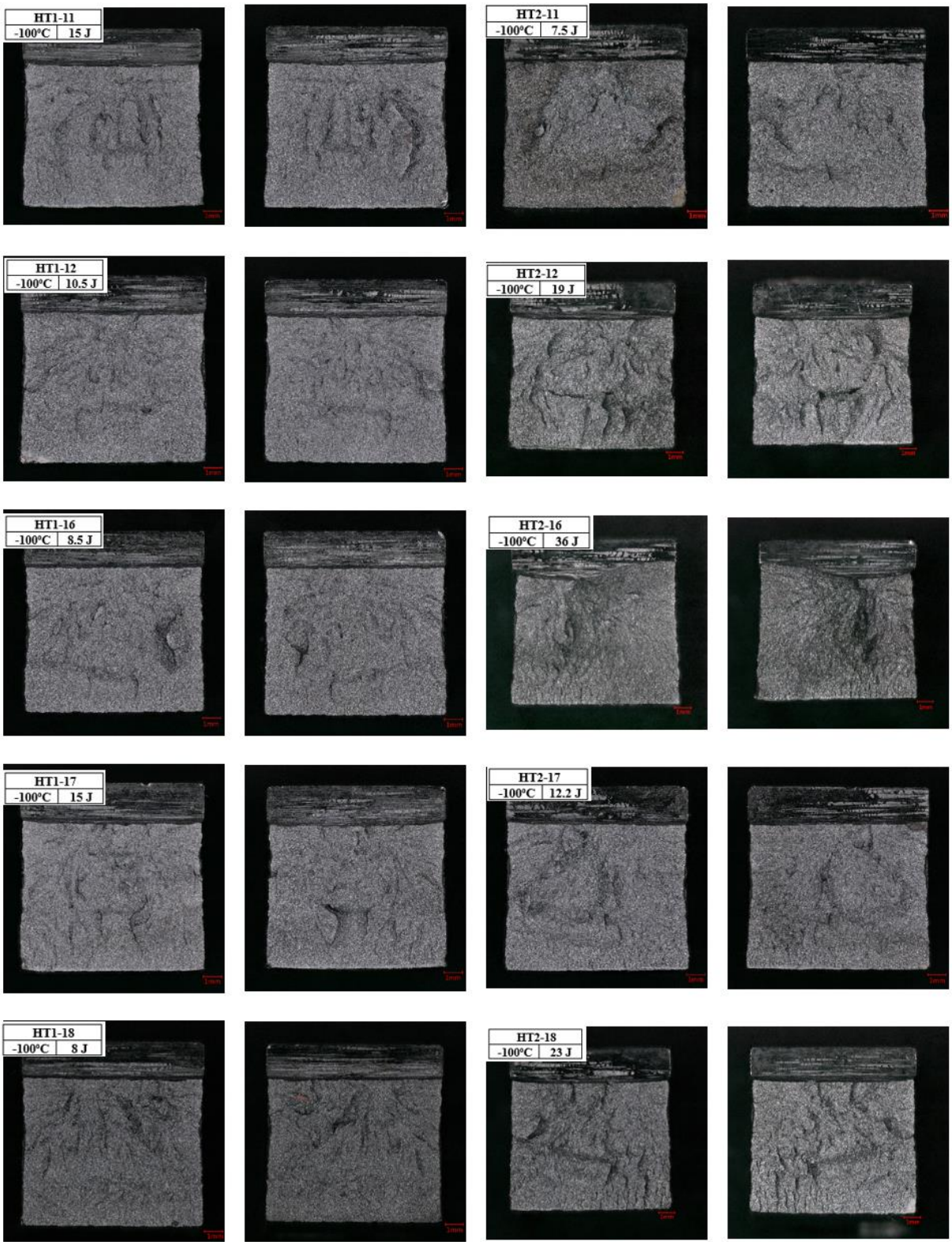
HT1-11
-100°C 15 J
HT2-11
-100°C 7.5 J
HT1-12
-100°C 10.5 J
HT2-12
-100°C 19 J
HT1-16
-100°C 8.5 J
HT2-16
-100°C 36 J
HT1-17
-100°C 15 J
HT2-17
-100°C 12.2 J
HT1-18
-100°C 8 J
HT2-18
-100°C 23 J

(c) -100 °C.

(d)

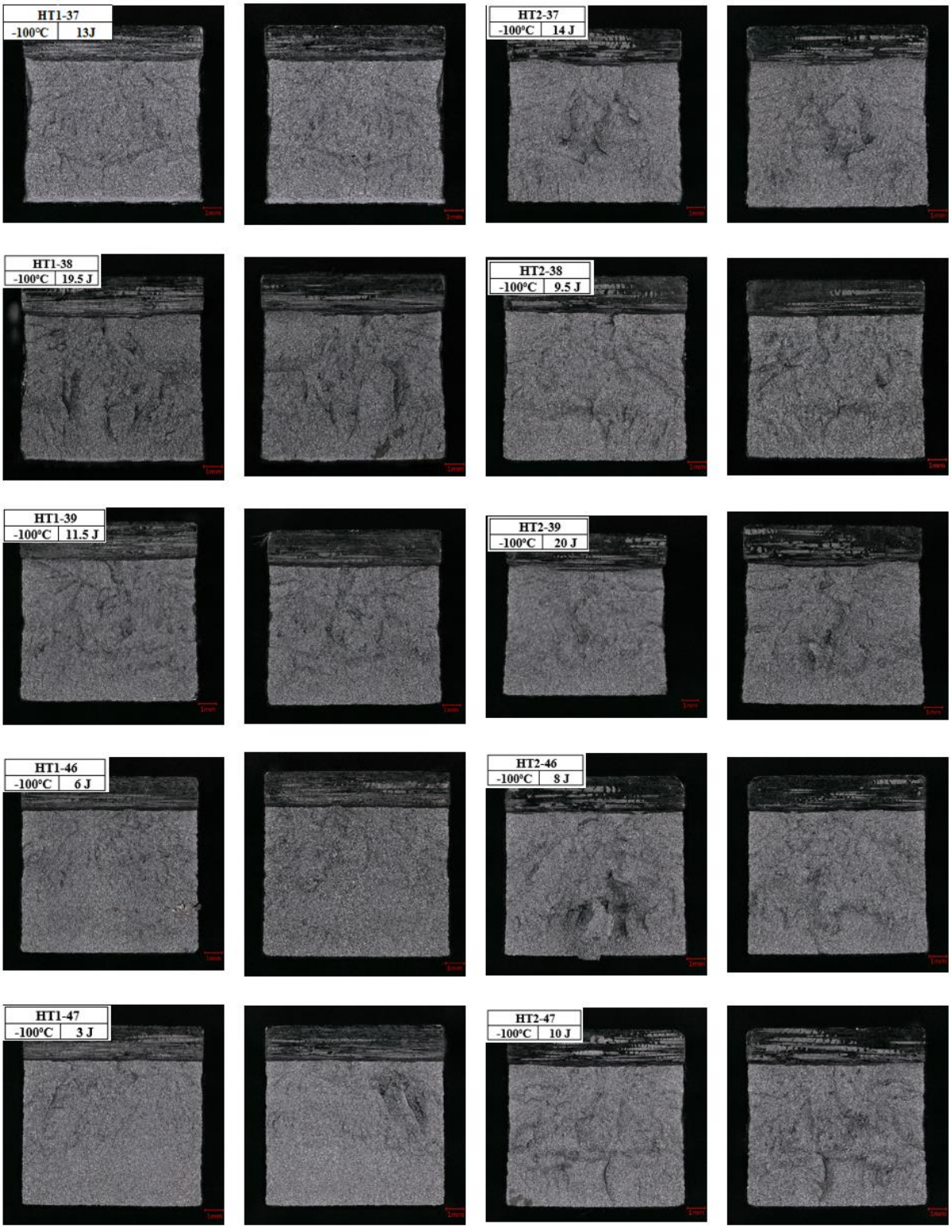
HT1-37
-100°C 13J
HT2-37
-100°C 14 J
HT1-38
-100°C 19.5 J
HT2-38
-100°C 9.5 J
HT1-39
-100°C 11.5 J
HT2-39
-100°C 20 J
HT1-46
-100°C 6 J
HT2-46
-100°C 8 J
HT1-47
-100°C 3 J
HT2-47
-100°C 10 J

(d) -100 °C.

(e)

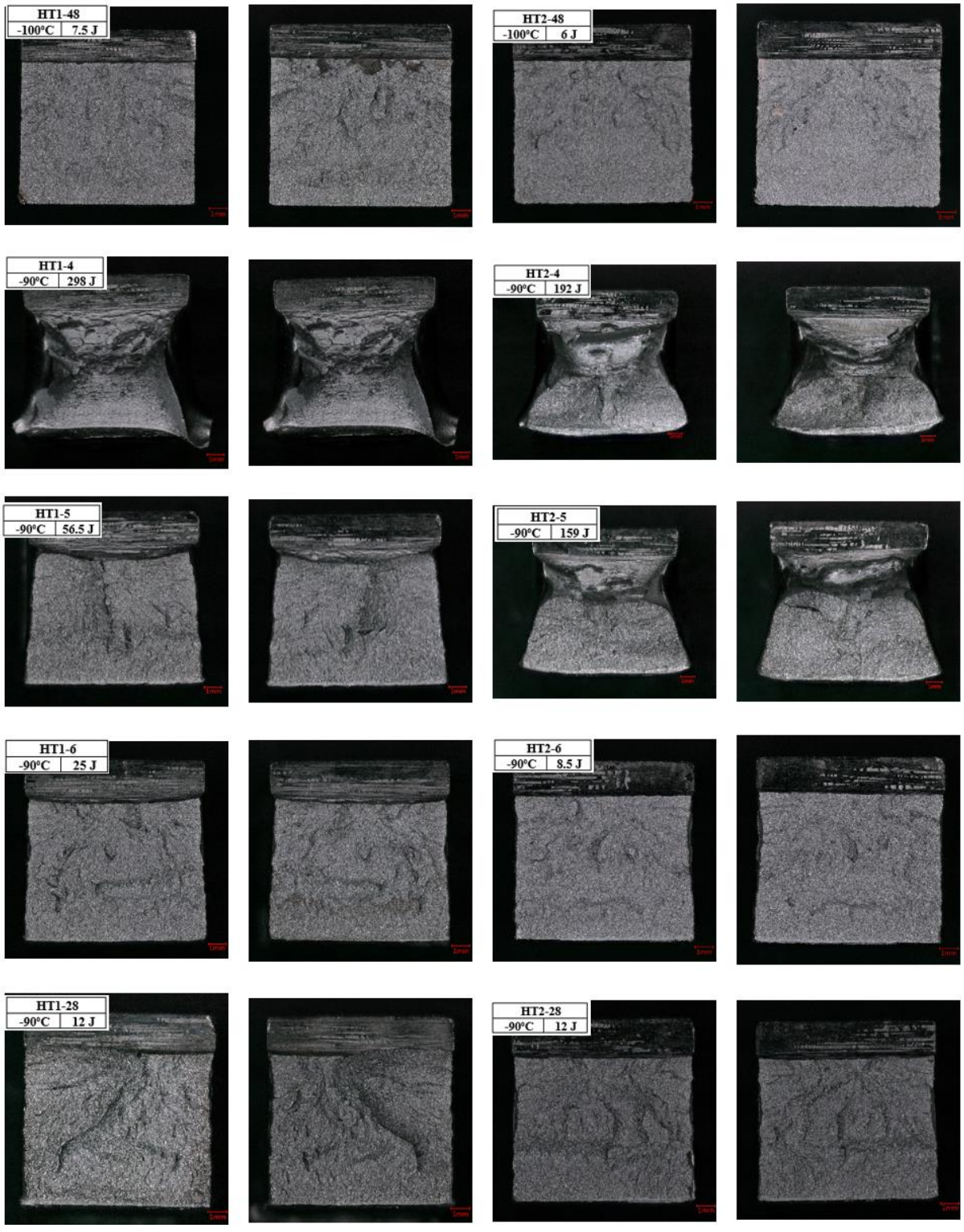
HT1-48
-100°C 7.5 J
HT2-48
-100°C 6 J
HT1-4
-90°C 298 J
HT2-4
-90°C 192 J
HT1-5
-90°C 56.5 J
HT2-5
-90°C 159 J
HT1-6
-90°C 25 J
HT2-6
-90°C 8.5 J
HT1-28
-90°C 12 J
HT2-28
-90°C 12 J

(e) -100 to -90 °C.

(f)

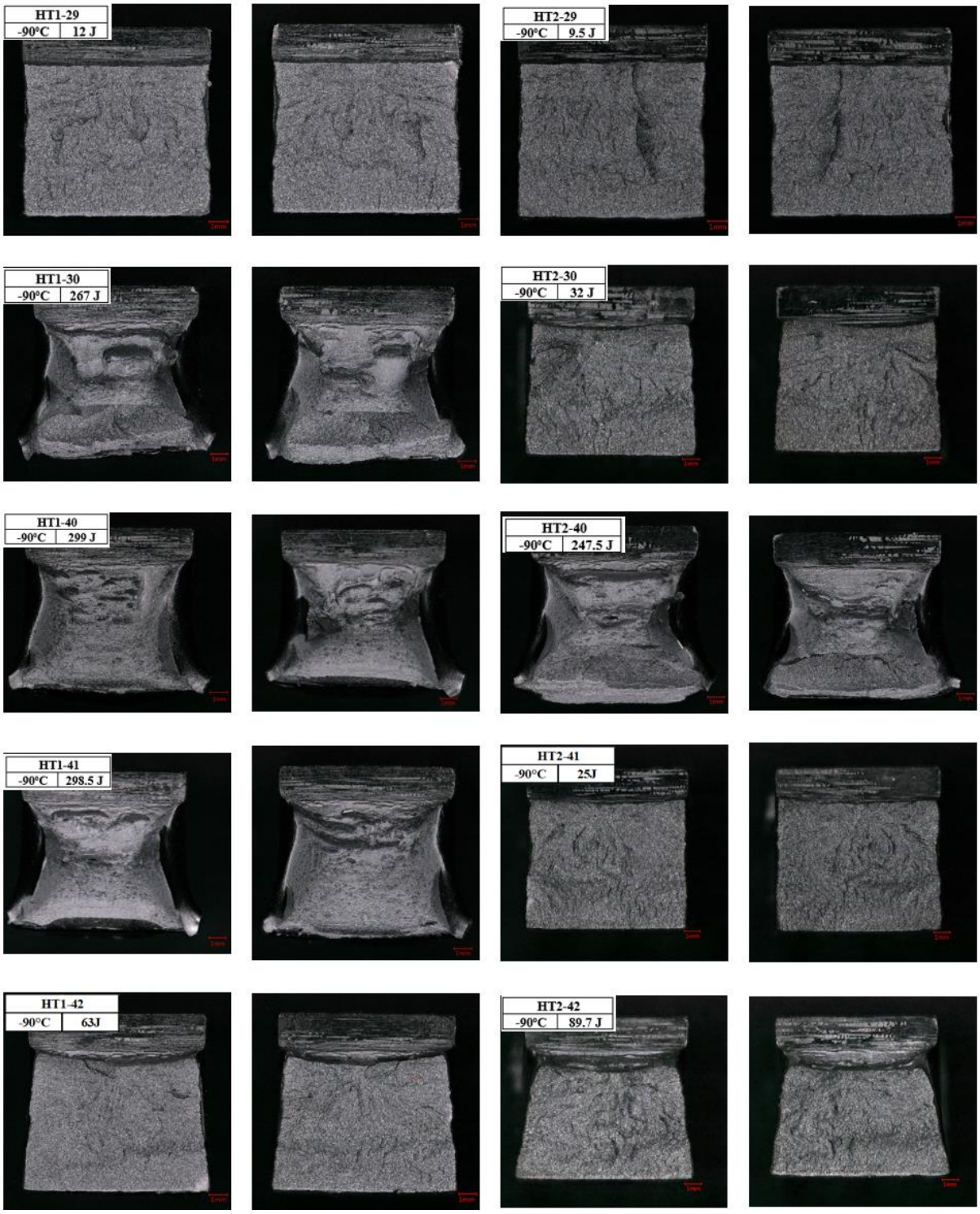
HT1-29
-90°C 12 J
HT2-29
-90°C 9.5 J
HT1-30
-90°C 267 J
HT2-30
-90°C 32 J
HT1-40
-90°C 299 J
HT2-40
-90°C 247.5 J
HT1-41
-90°C 298.5 J
HT2-41
-90°C 25J
HT1-42
-90°C 63J
HT2-42
-90°C 89.7 J

(f) -90 °C.

(g)

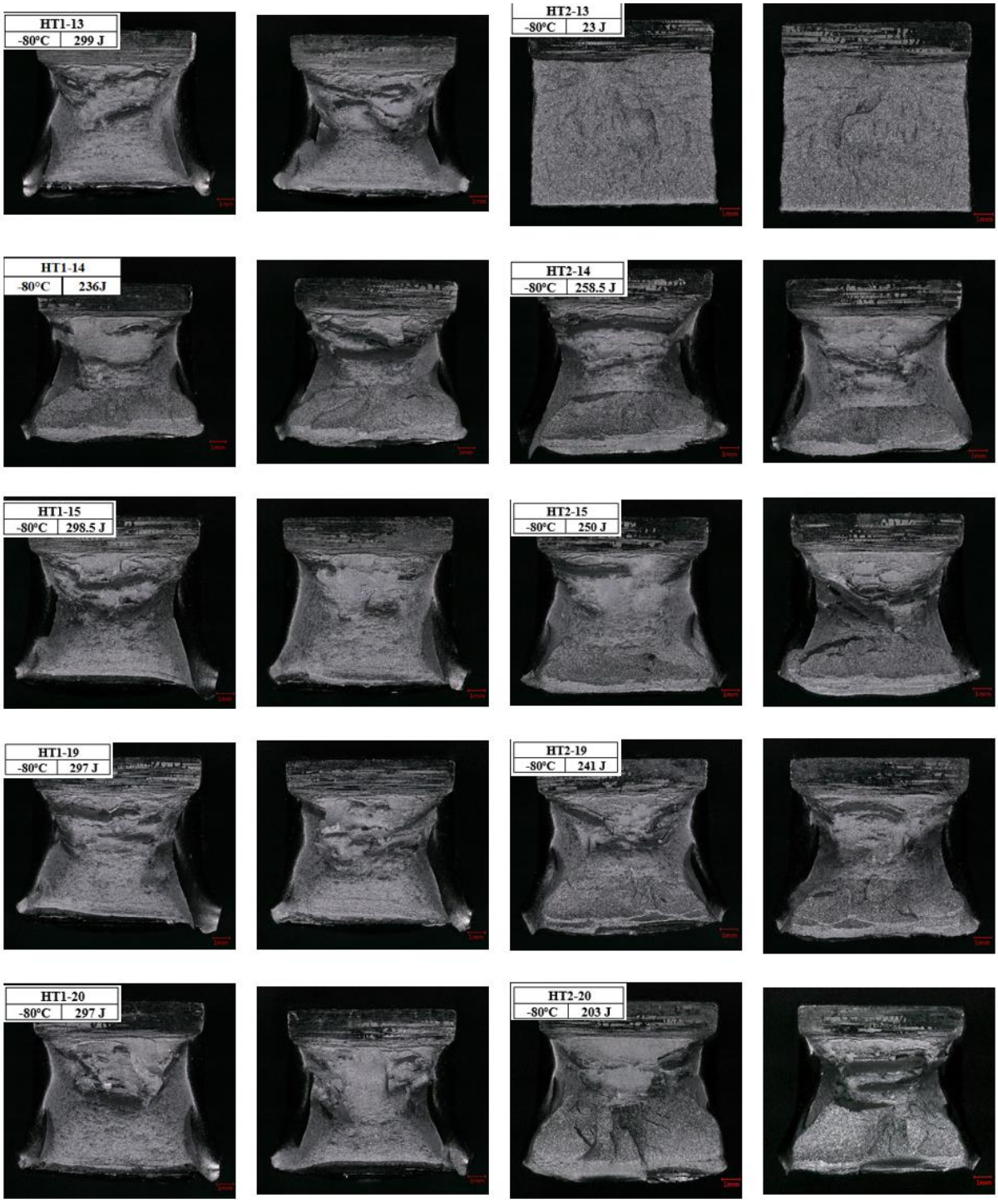
HT1-13
-80°C 299 J
HT2-13
-80°C 23 J
HT1-14
-80°C 236J
HT2-14
-80°C 258.5 J
HT1-15
-80°C 298.5 J
HT2-15
-80°C 250 J
HT1-19
-80°C 297 J
HT2-19
-80°C 241 J
HT1-20
-80°C 297 J
HT2-20
-80°C 203 J

(g) -80 °C.

(h)

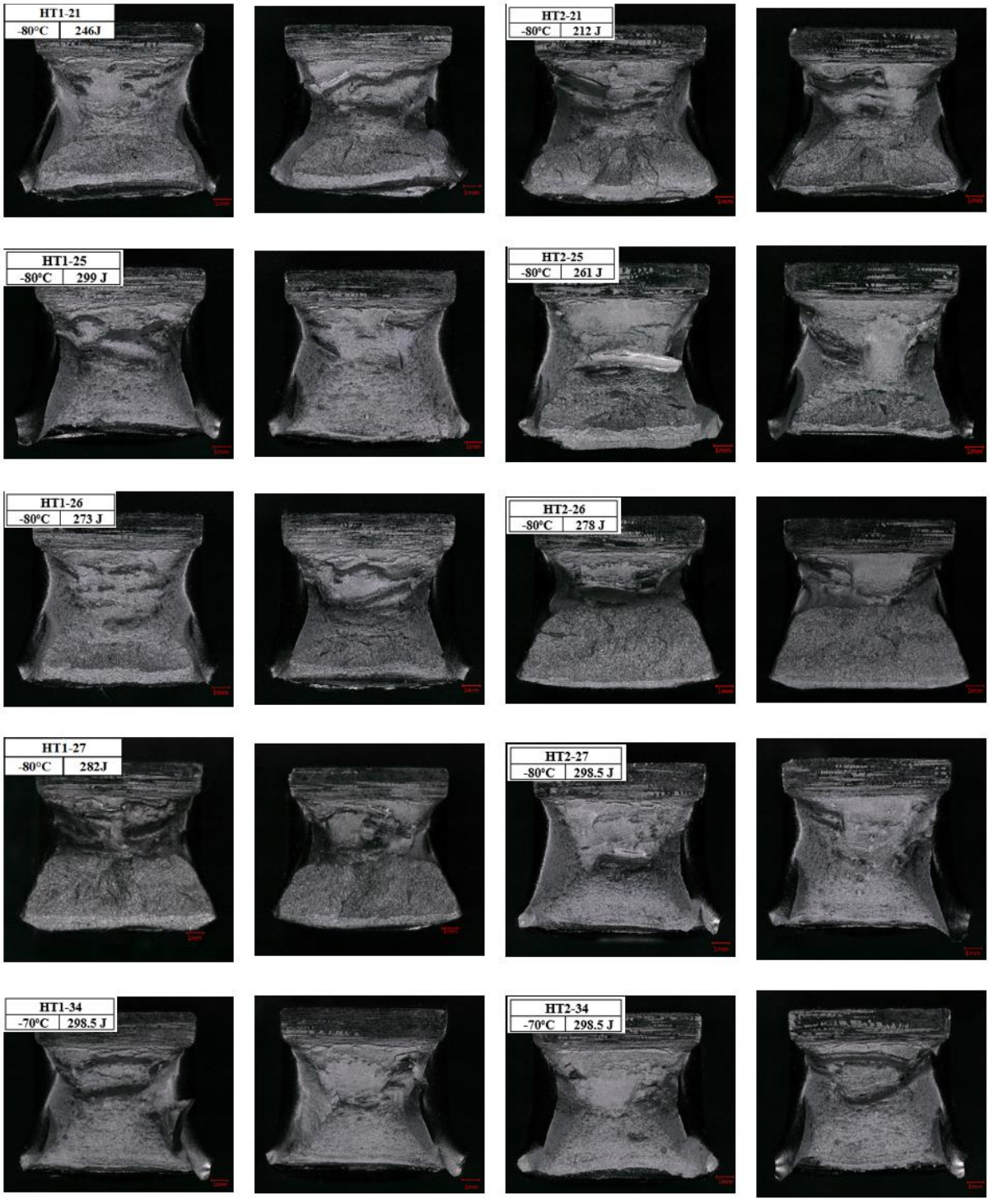
HT1-21
-80°C 246J
HT2-21
-80°C 212 J
HT1-25
-80°C 299 J
HT2-25
-80°C 261 J
HT1-26
-80°C 273 J
HT2-26
-80°C 278 J
HT1-27
-80°C 282J
HT2-27
-80°C 298.5 J
HT1-34
-70°C 298.5 J
HT2-34
-70°C 298.5 J

(h) -80 to -70 °C.

(i)

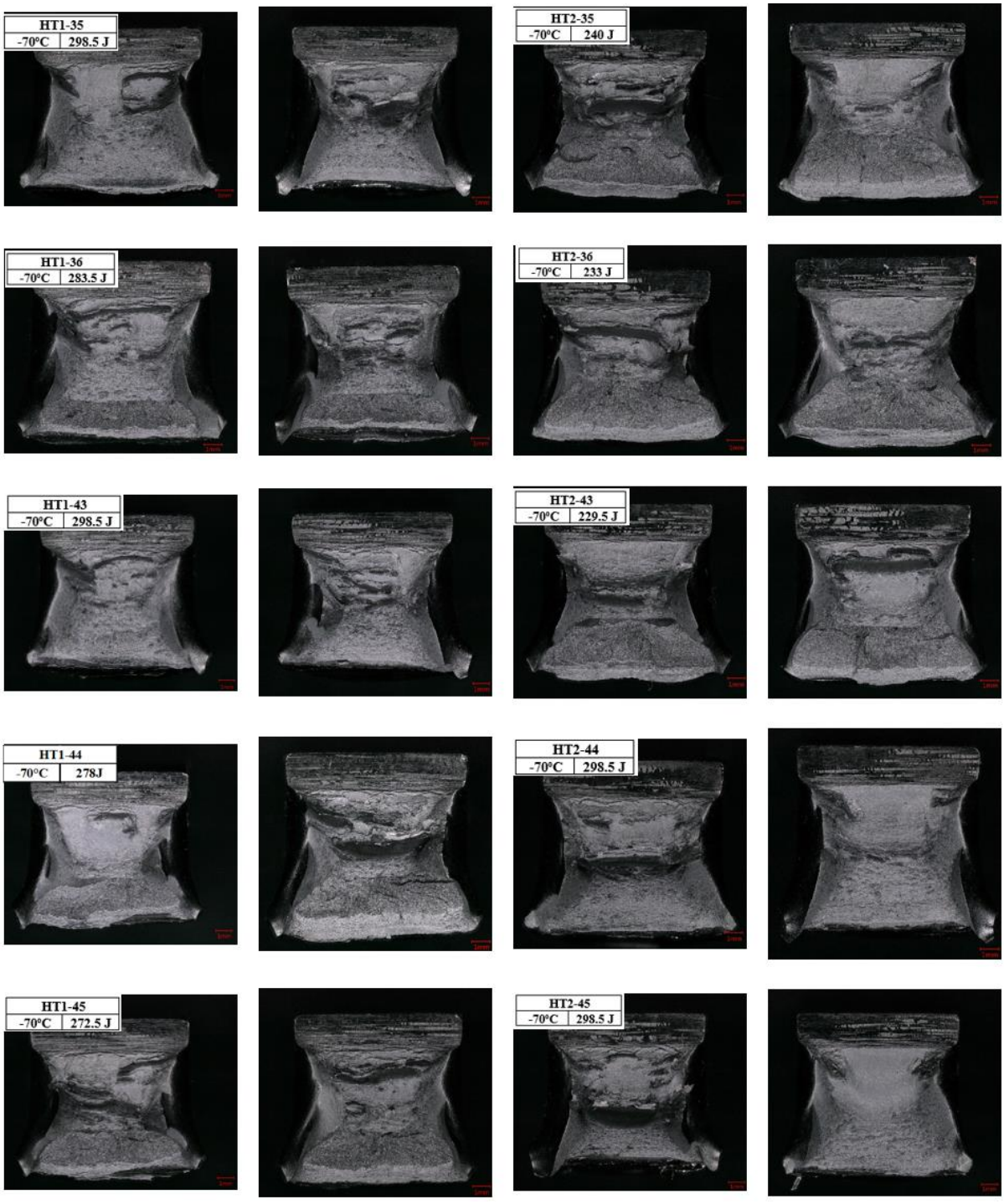
HT1-35
-70°C 298.5 J
HT2-35
-70°C 240 J
HT1-36
-70°C 283.5 J
HT2-36
-70°C 233 J
HT1-43
-70°C 298.5 J
HT2-43
-70°C 229.5 J
HT1-44
-70°C 278J
HT2-44
-70°C 298.5 J
HT1-45
-70°C 272.5 J
HT2-45
-70°C 298.5 J

(i) -70 °C.

(j)

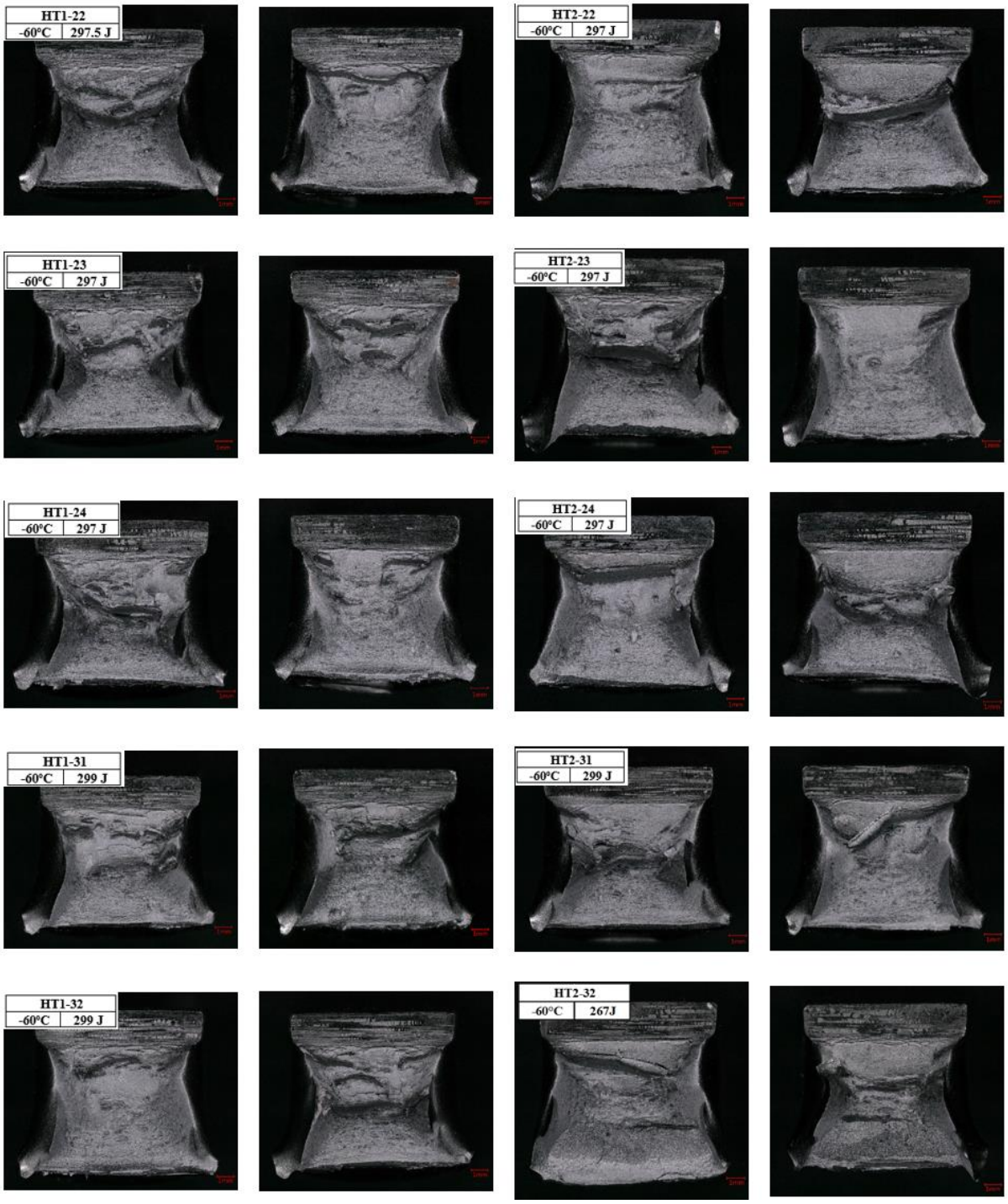
HT1-22
-60°C 297.5 J
HT2-22
-60°C 297 J
HT1-23
-60°C 297 J
HT2-23
-60°C 297 J
HT1-24
-60°C 297 J
HT2-24
-60°C 297 J
HT1-31
-60°C 299 J
HT2-31
-60°C 299 J
HT1-32
-60°C 299 J
HT2-32
-60°C 267J

(j) -60 °C.

(k)

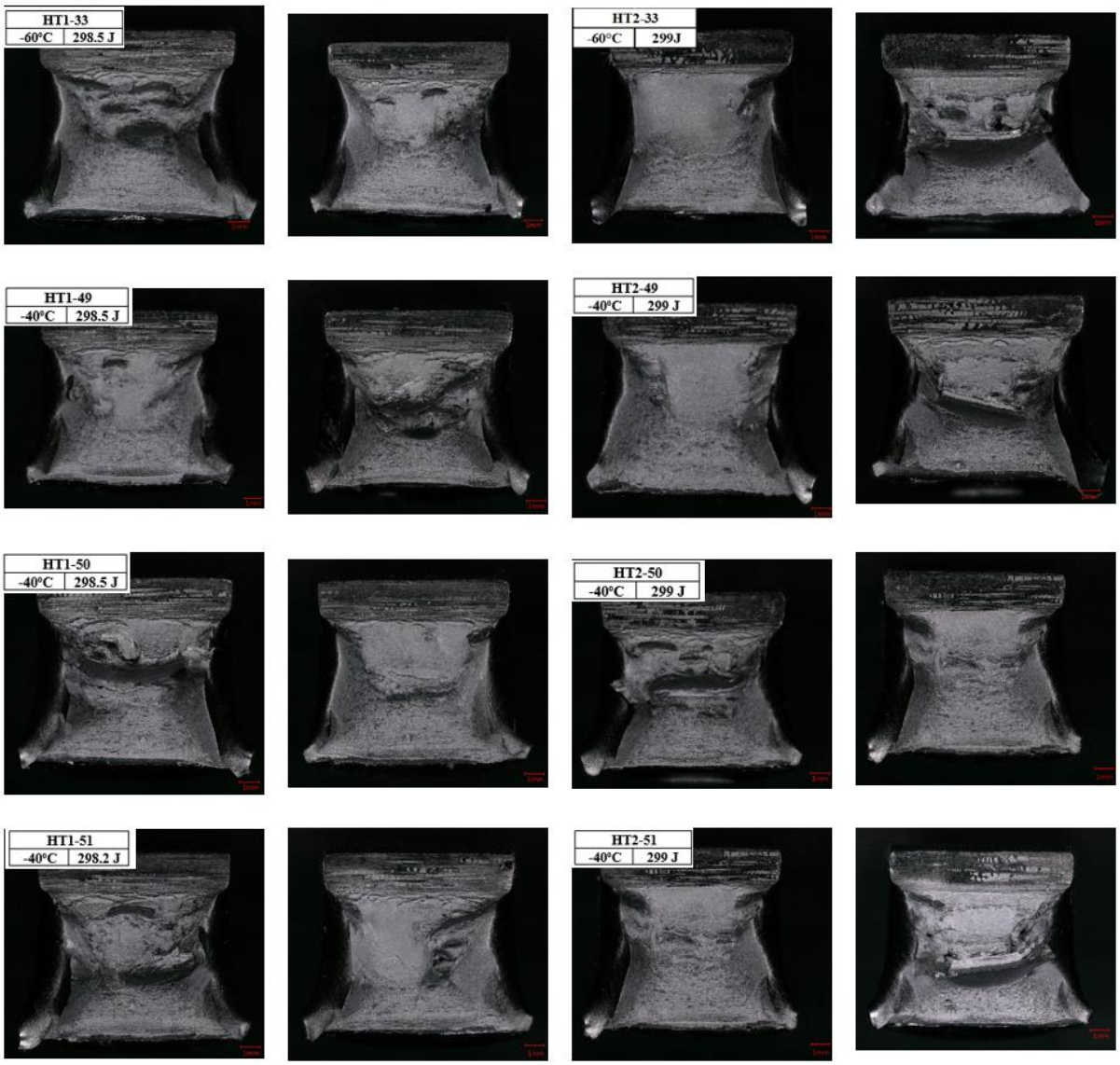
HT1-33
-60°C 298.5 J
HT2-33
-60°C 299J
HT1-49
-40°C 298.5 J
HT2-49
-40°C 299 J
HT1-50
-40°C 298.5 J
HT2-50
-40°C 299 J
HT1-51
-40°C 298.2 J
HT2-51
-40°C 299 J

(k) -60 to -40 °C.

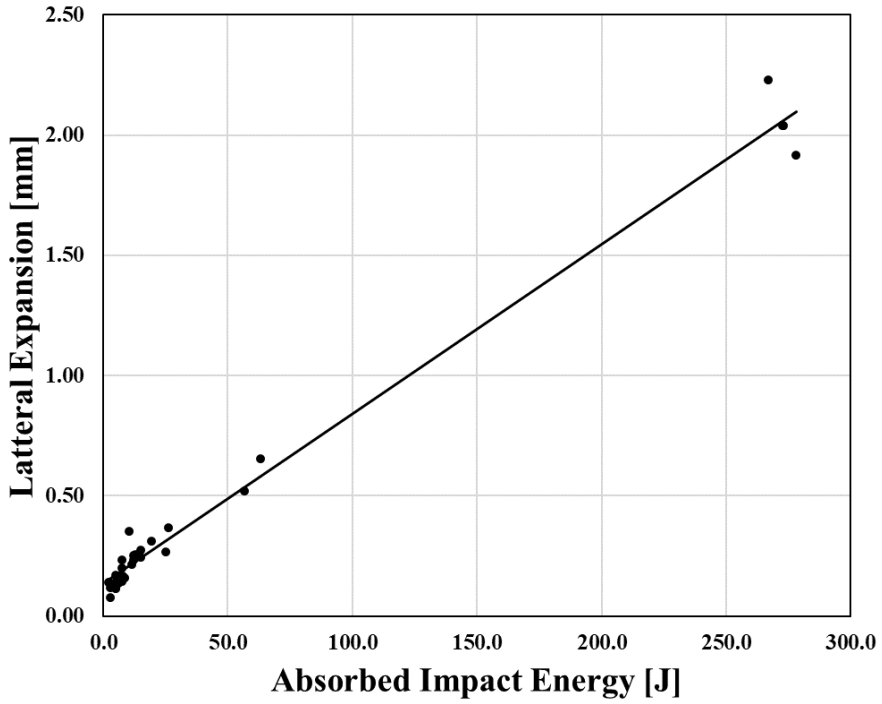

Figure 4.24 Lateral expansion versus absorbed impact energy for HT1 condition.

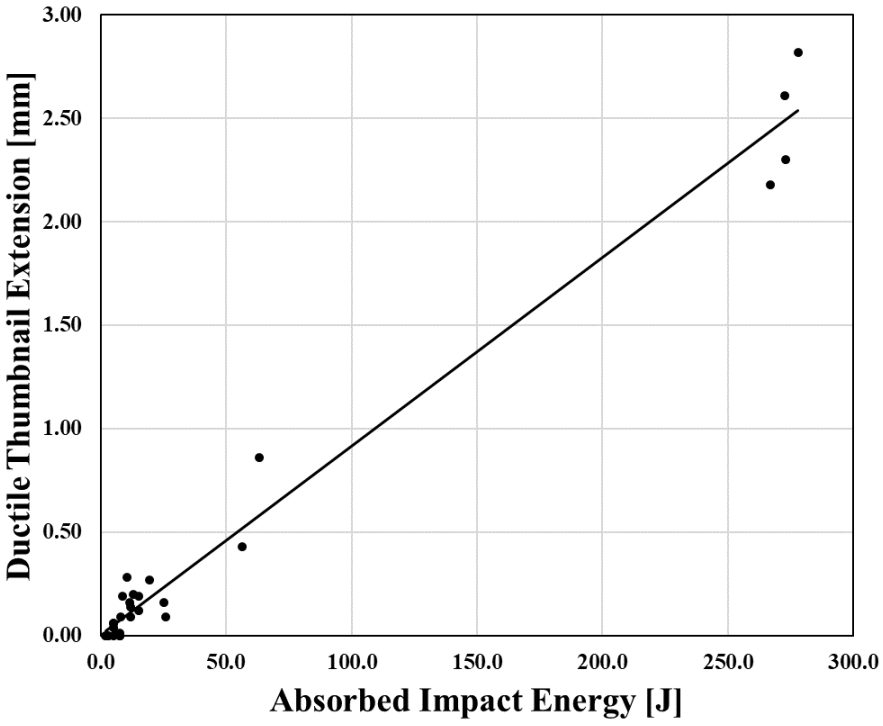

Figure 4.25 Ductile thumbnail extension versus absorbed impact energy for HT1 condition.

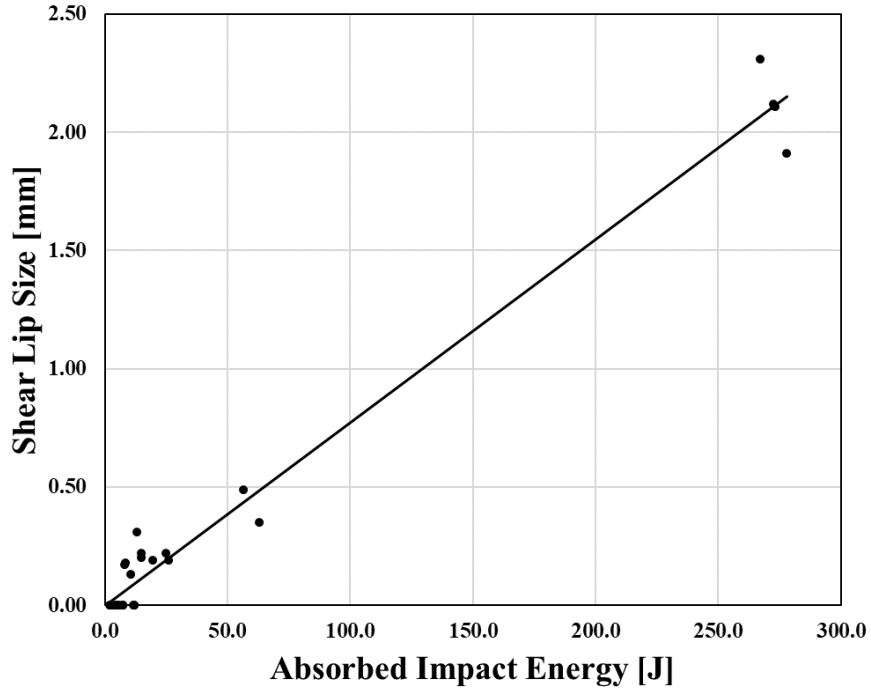

Figure 4.26 Shear lip size versus absorbed impact energy for HT1 condition.

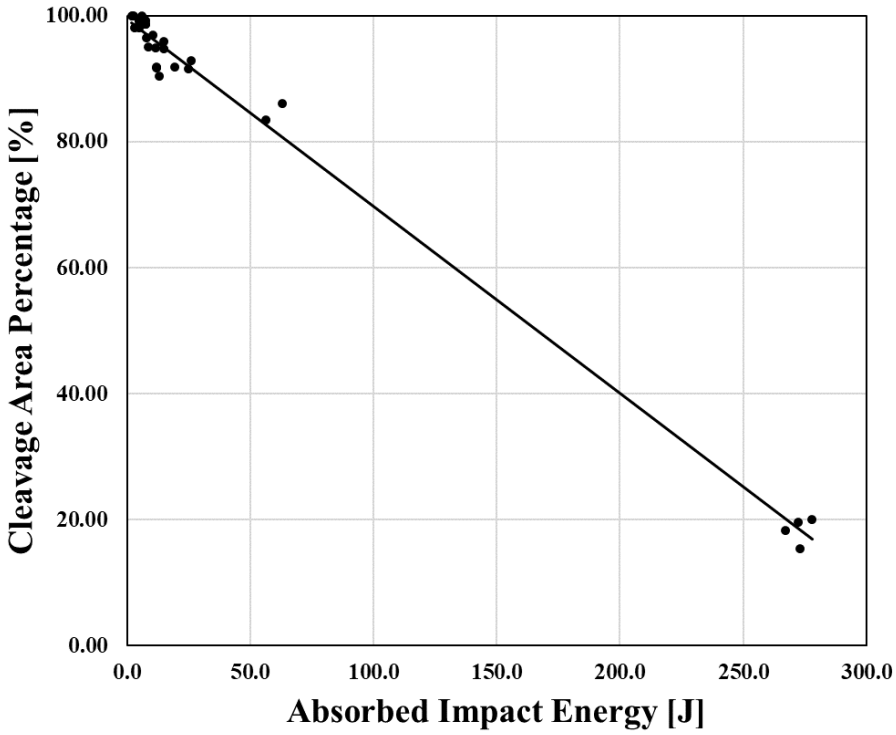

Figure 4.27 Cleavage area percentage versus absorbed impact energy for HT1 condition.

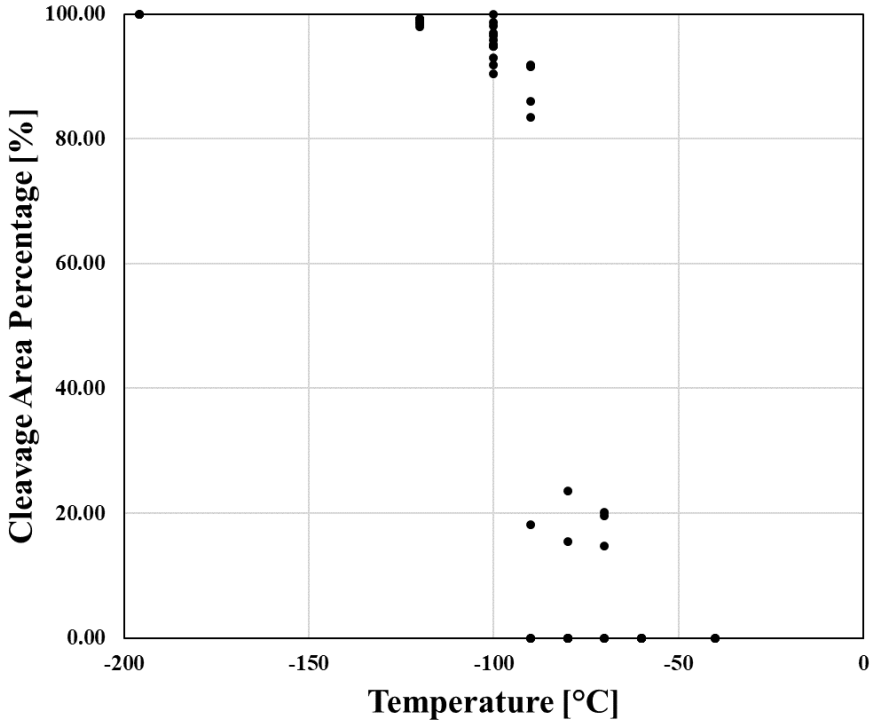

Figure 4.28 Cleavage area percentage versus temperature for HT1 condition.

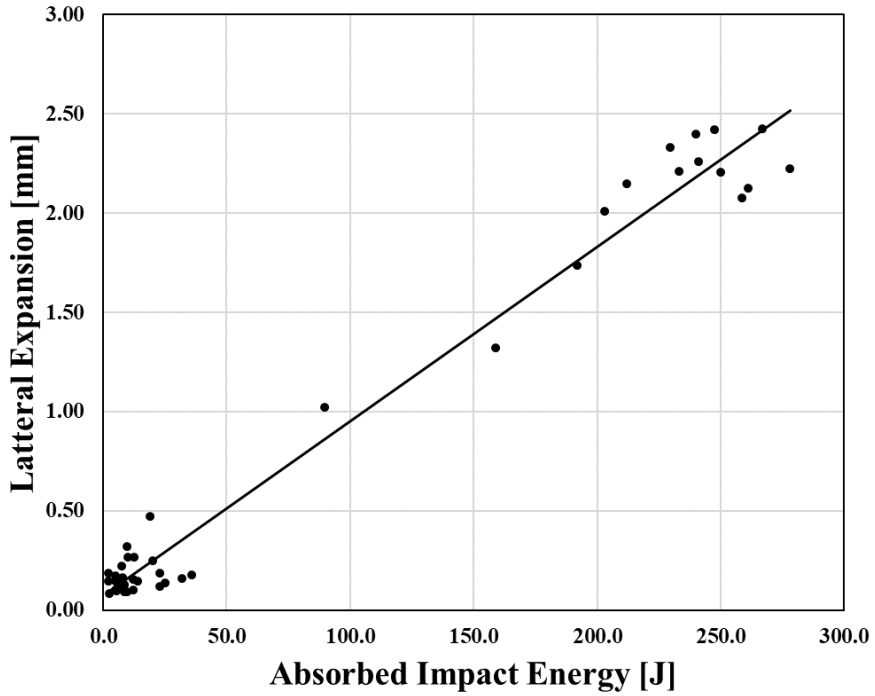

Figure 4.29 Lateral expansion versus absorbed impact energy for HT2 condition.

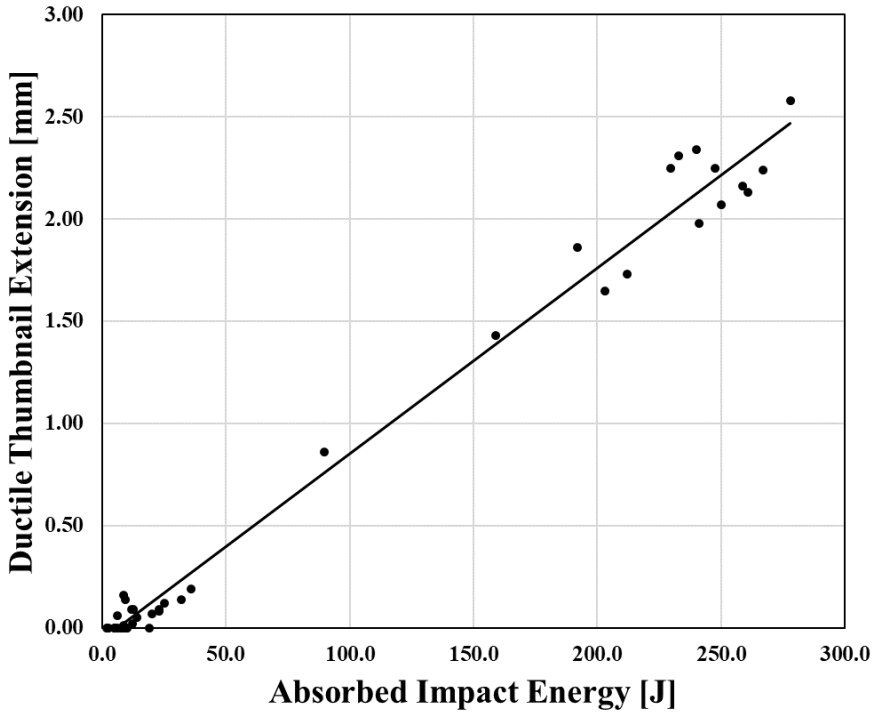

Figure 4.30 Ductile thumbnail extension versus absorbed impact energy for HT2 condition.

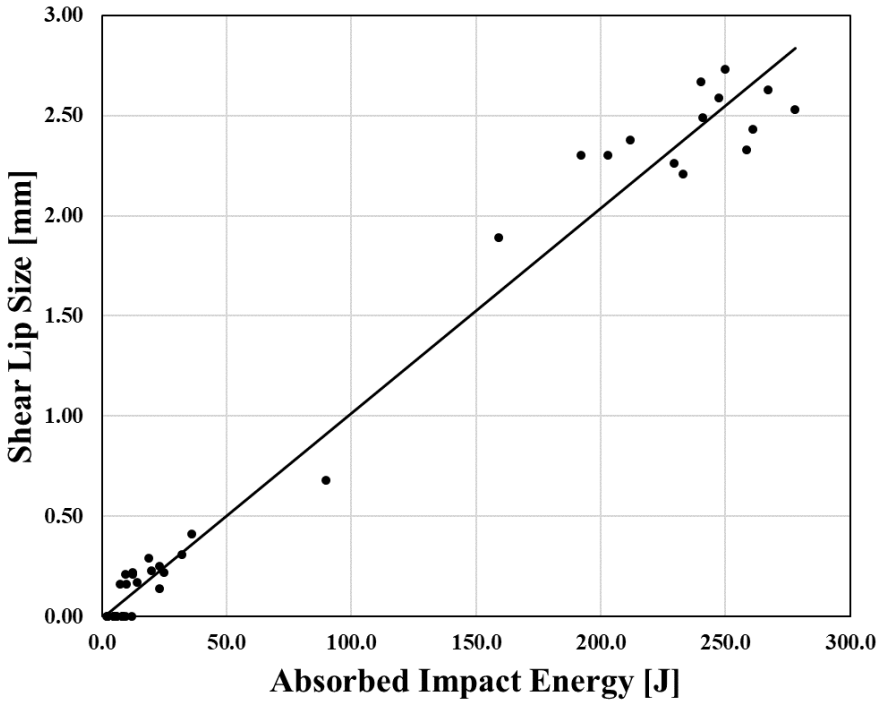

Figure 4.31 Shear lip size versus absorbed impact energy for HT2 condition.

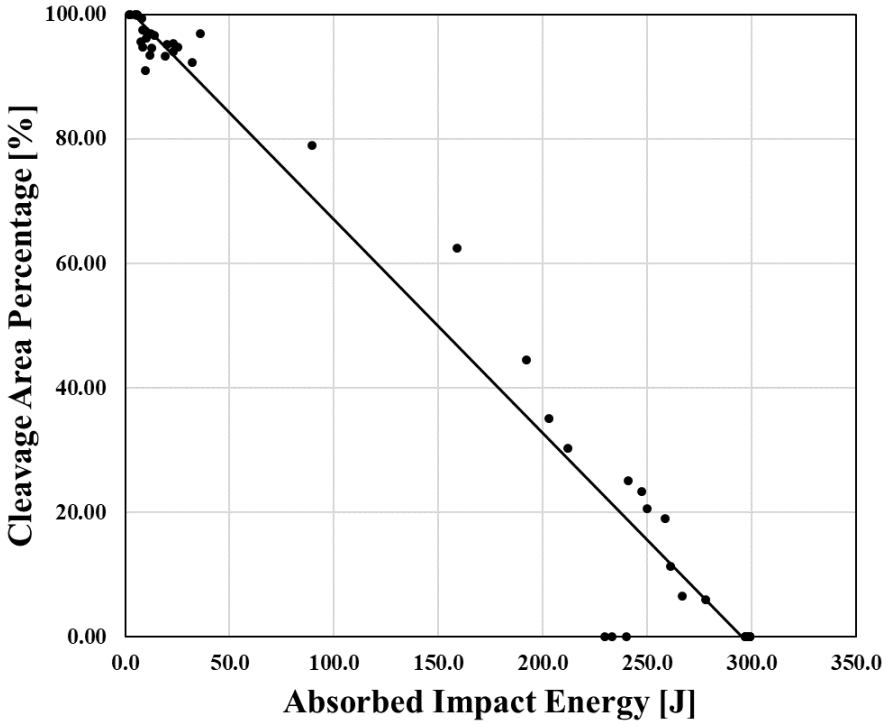

Figure 4.32 Cleavage area percentage versus absorbed impact energy for HT2 condition.

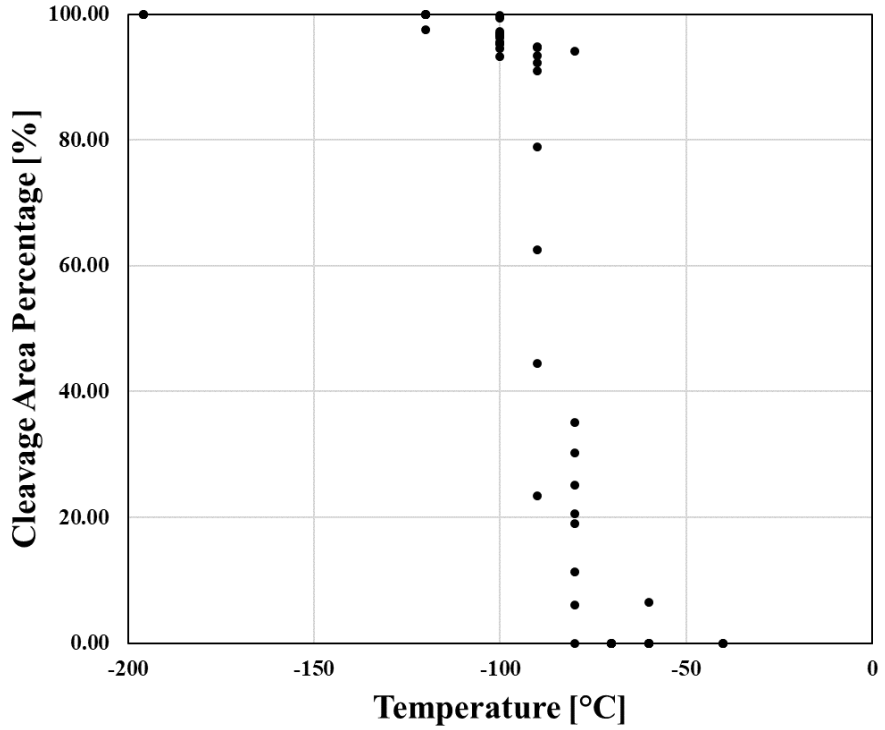

Figure 4.33 Cleavage area percentage versus temperature for HT2 condition.

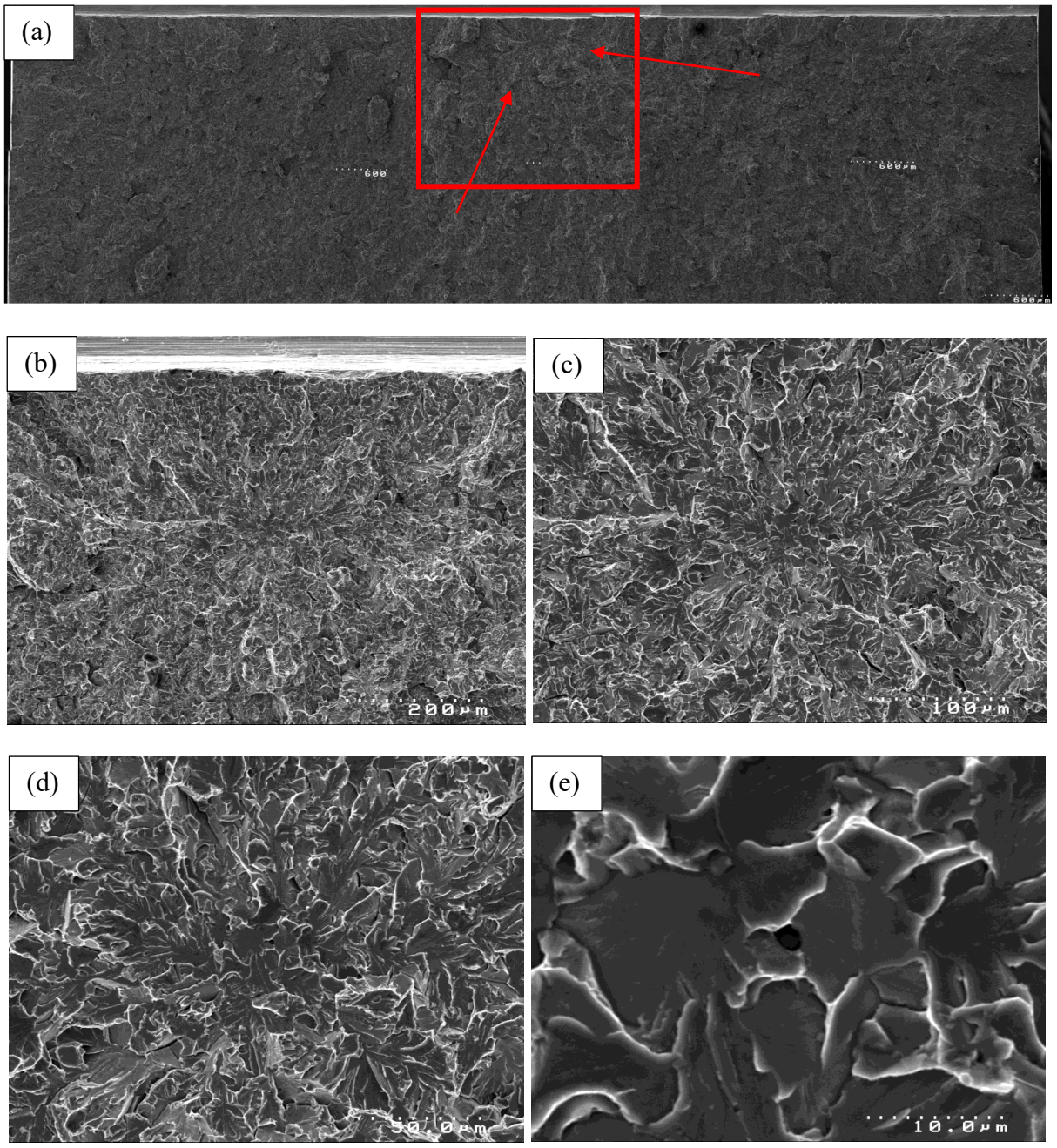

Figure 4.34 Fractography of Charpy specimen HT2-01 tested at -196°C. (a) is the full view across the fracture surface; (b) (c) (d) (e) show the possible initiation site in magnification sequence.

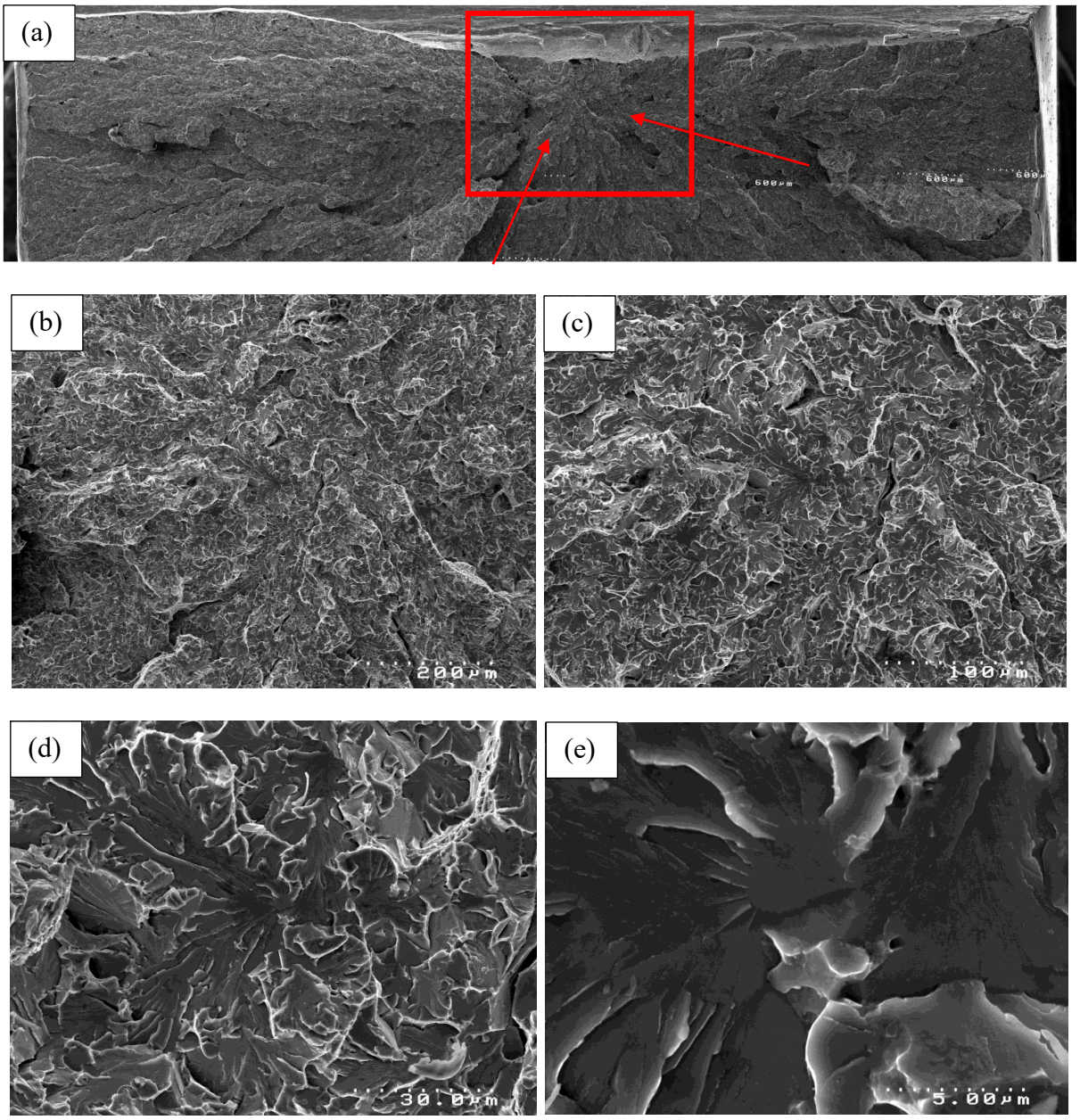

Figure 4.35 Fractography of Charpy specimen HT1-10 tested at -100°C. (a) is the full view across the fracture surface; (b) (c) (d) (e) show the possible initiation site in magnification sequence.

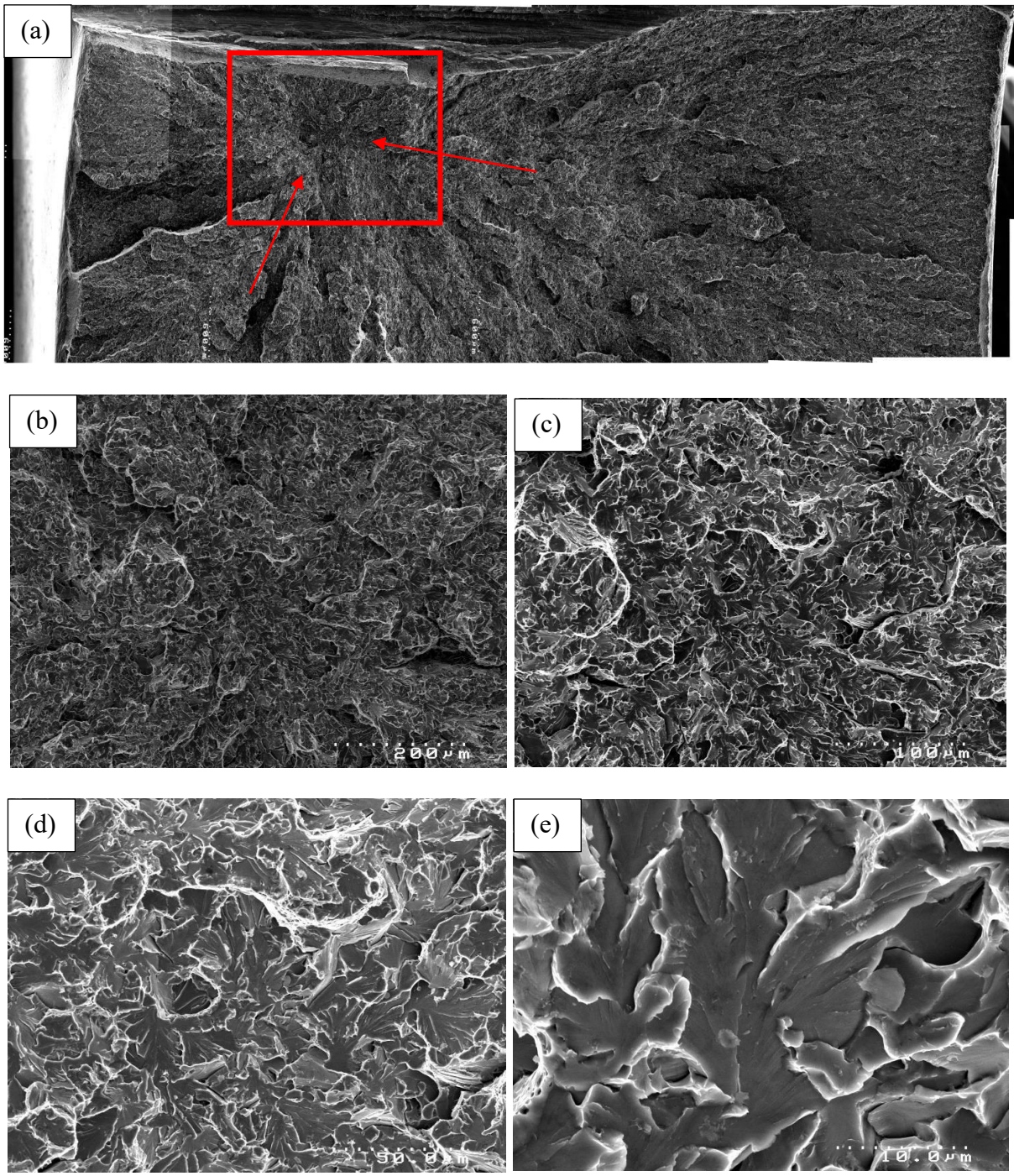

Figure 4.36 Fractography of Charpy specimen HT1-16 tested at -100°C. (a) is the full view across the fracture surface; (b) (c) (d) (e) show the possible initiation site in magnification sequence.

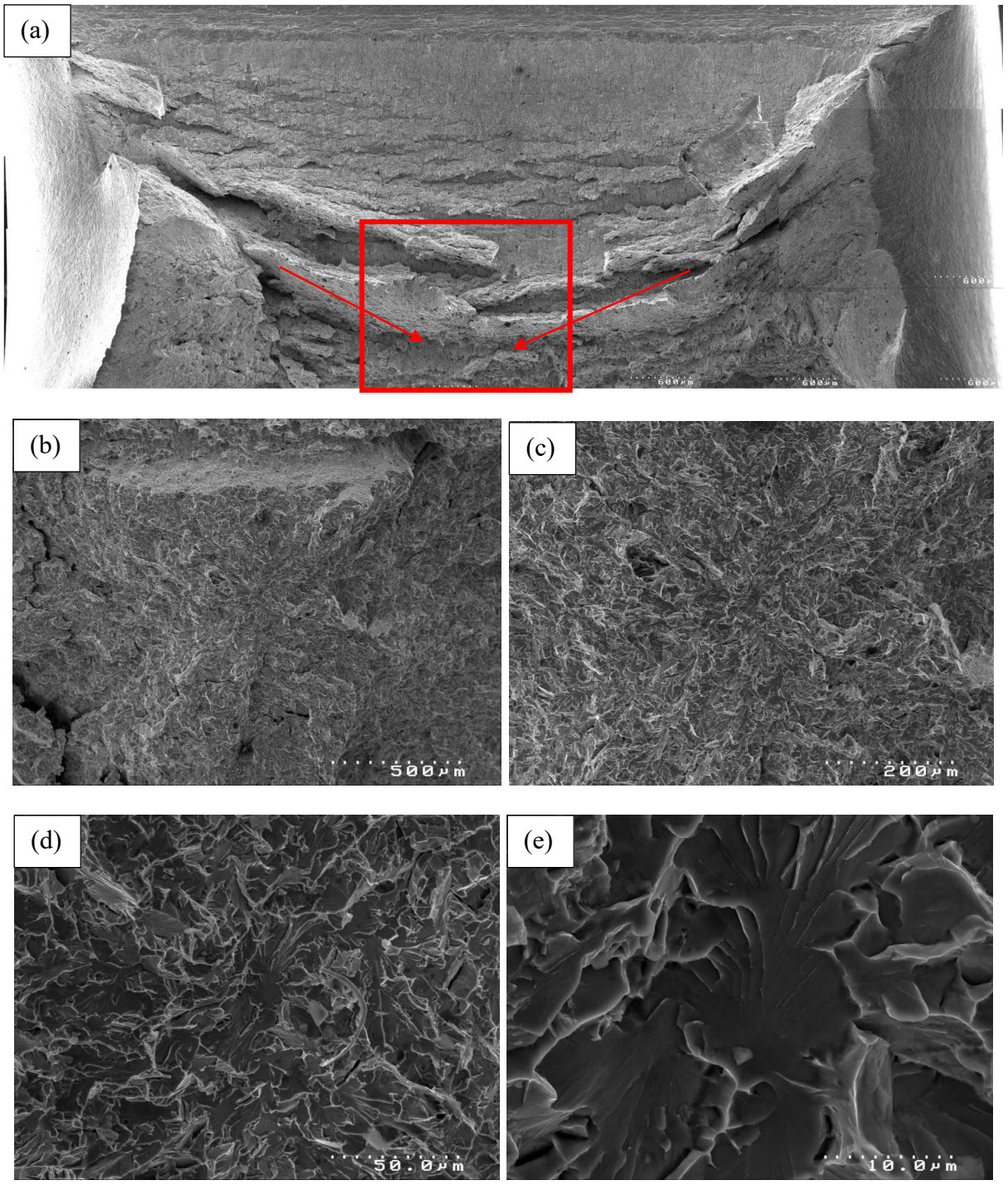

Figure 4.37 Fractography of Charpy specimen HT2-04 tested at -90°C. (a) is the full view across the fracture surface; (b) (c) (d) (e) show the possible initiation site in magnification sequence.

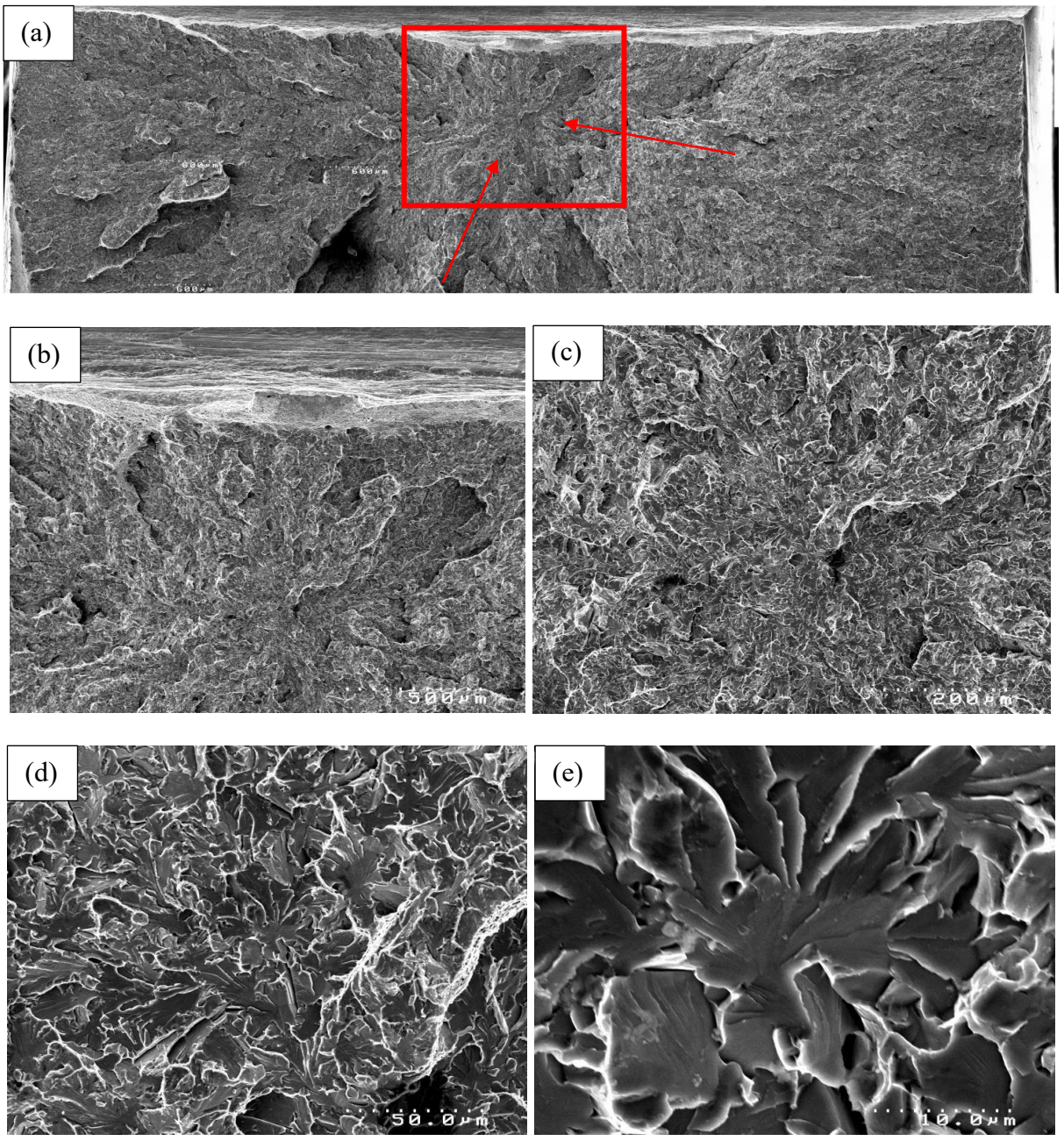

Figure 4.38 Fractography of Charpy specimen HT2-41 tested at -90°C. (a) is the full view across the fracture surface; (b) (c) (d) (e) show the possible initiation site in magnification sequence.

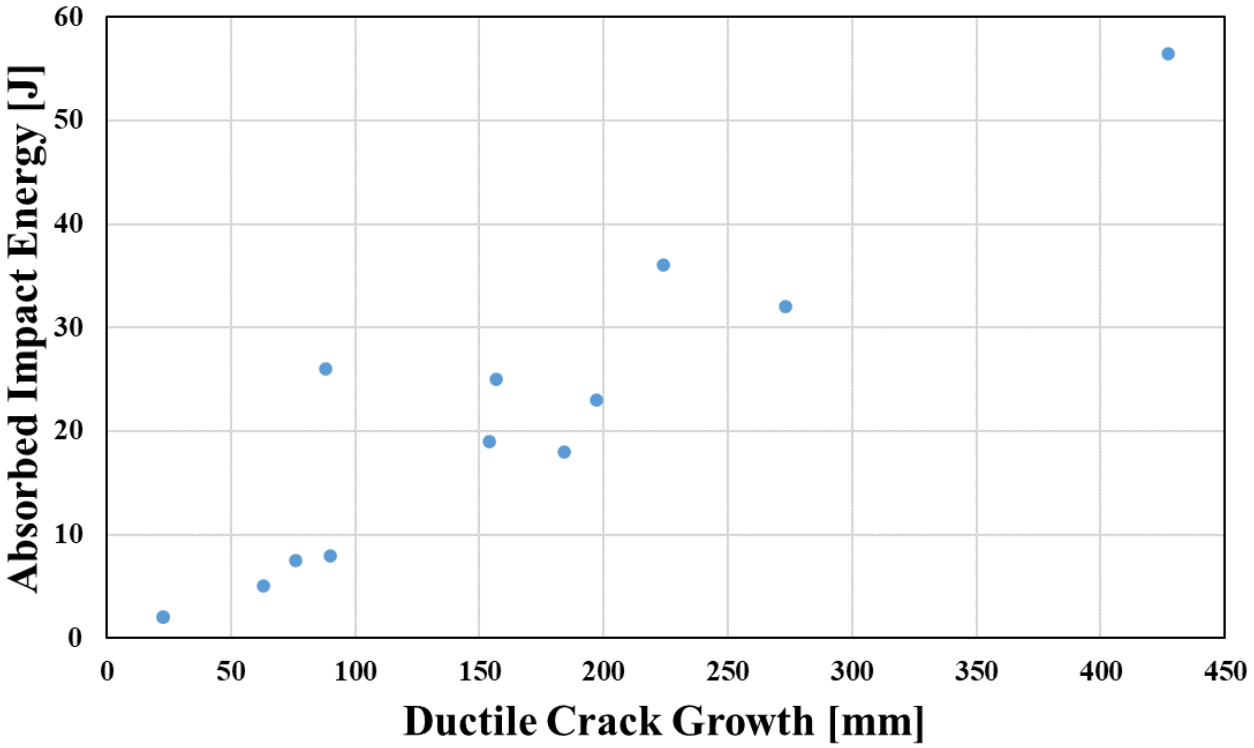

Figure 4.39 Ductile crack growth measured from fracture surfaces versus absorbed impact energy for HT1 and HT2 conditions combined.

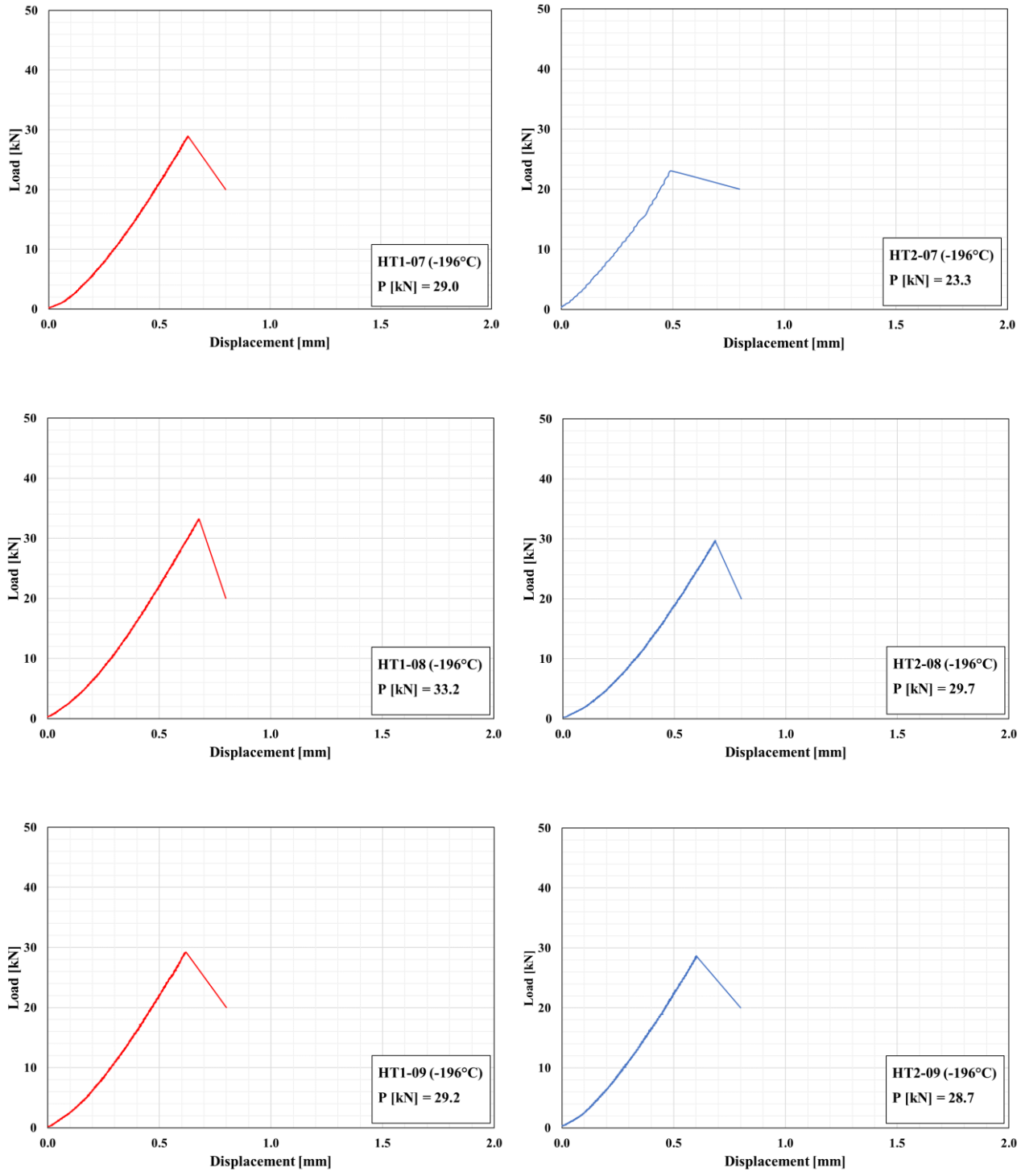

Figure 4.40 Load-displacement curves of Fracture Stress tests for HT1 and HT2 conditions tested at -196°C.

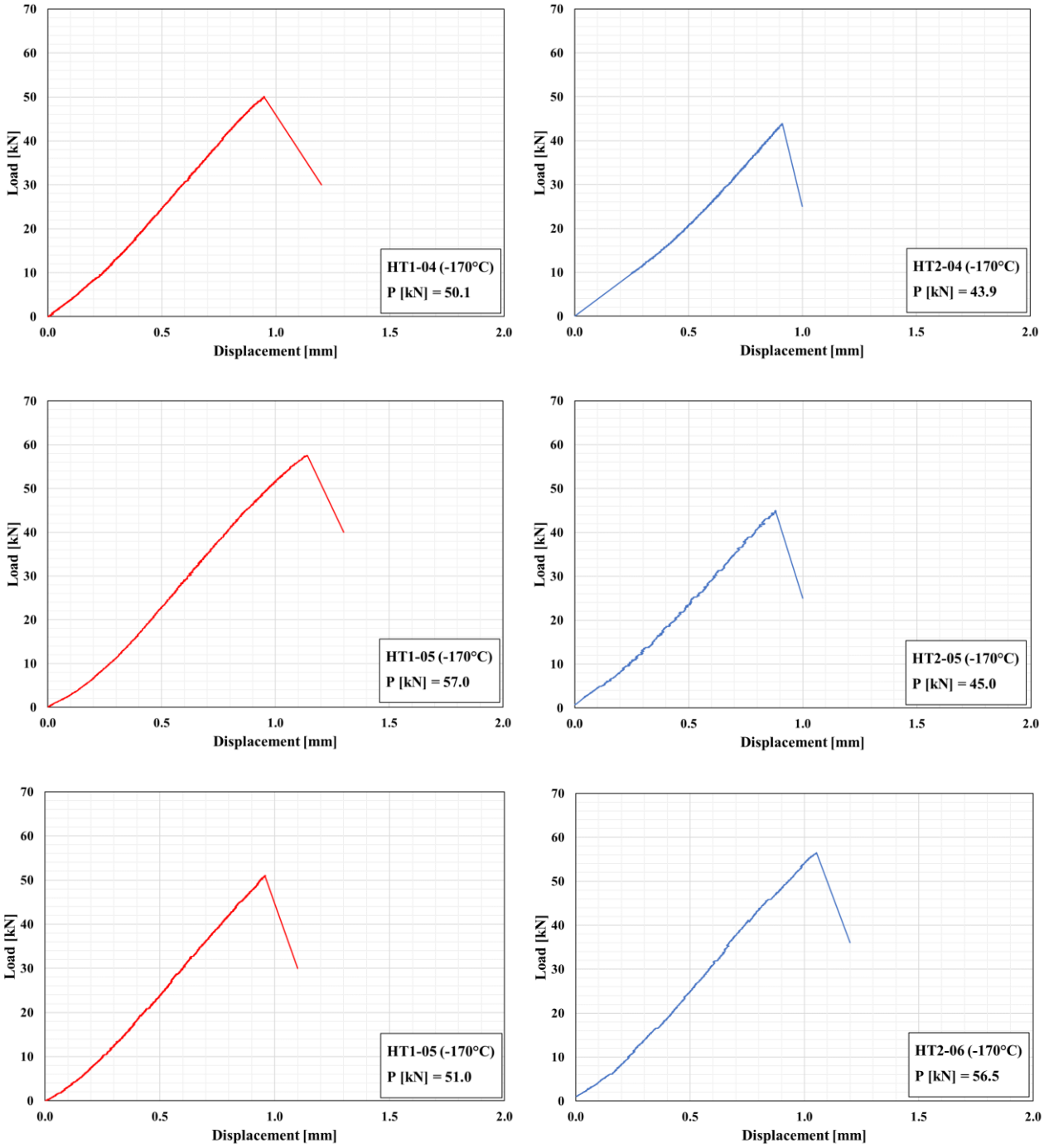

Figure 4.41 Load-displacement curves of Fracture Stress tests for HT1 and HT2 conditions tested at -170°C.

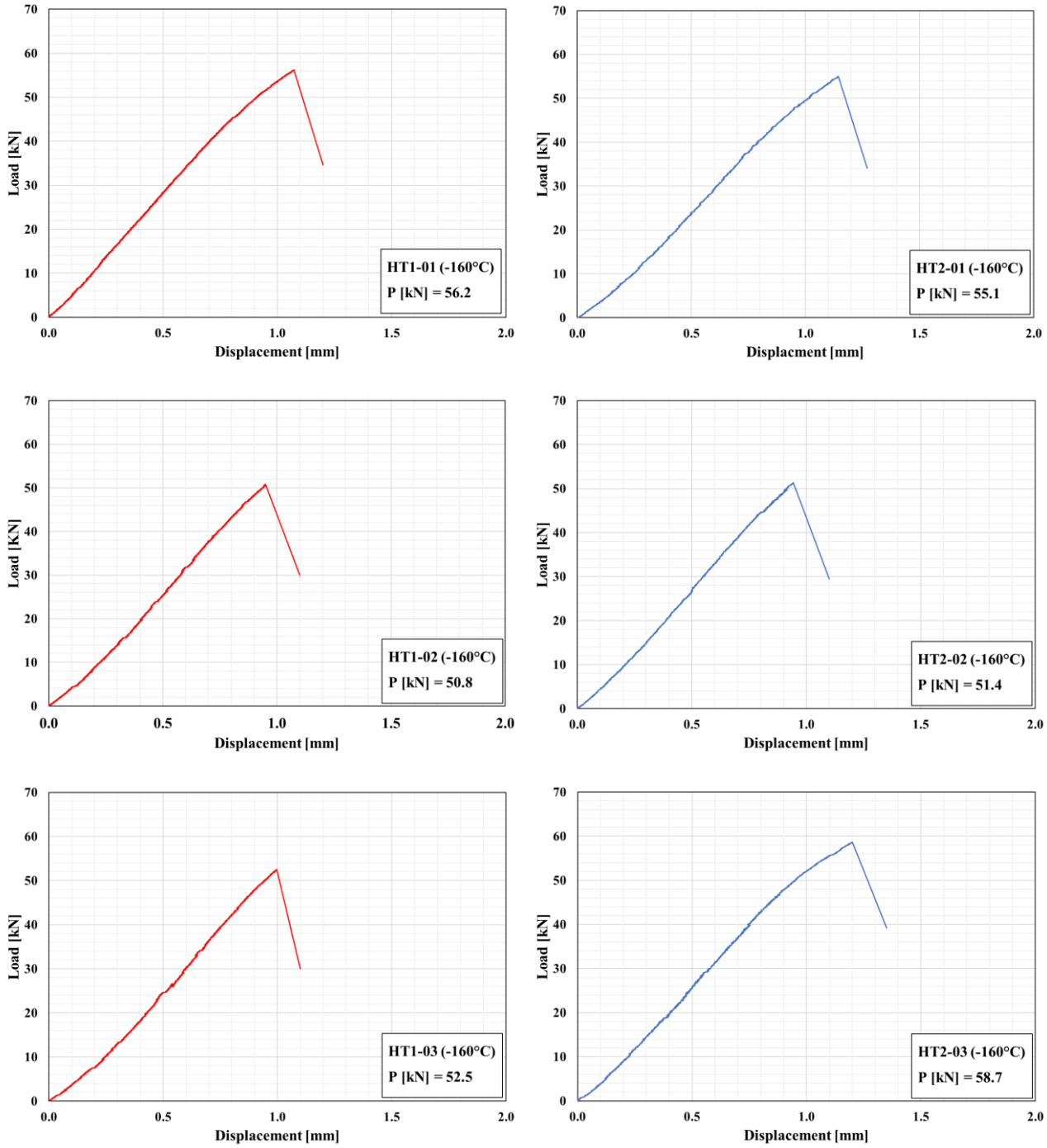

Figure 4.42 Load-displacement curves of Fracture Stress tests for HT1 and HT2 conditions tested at -160°C.

(a)

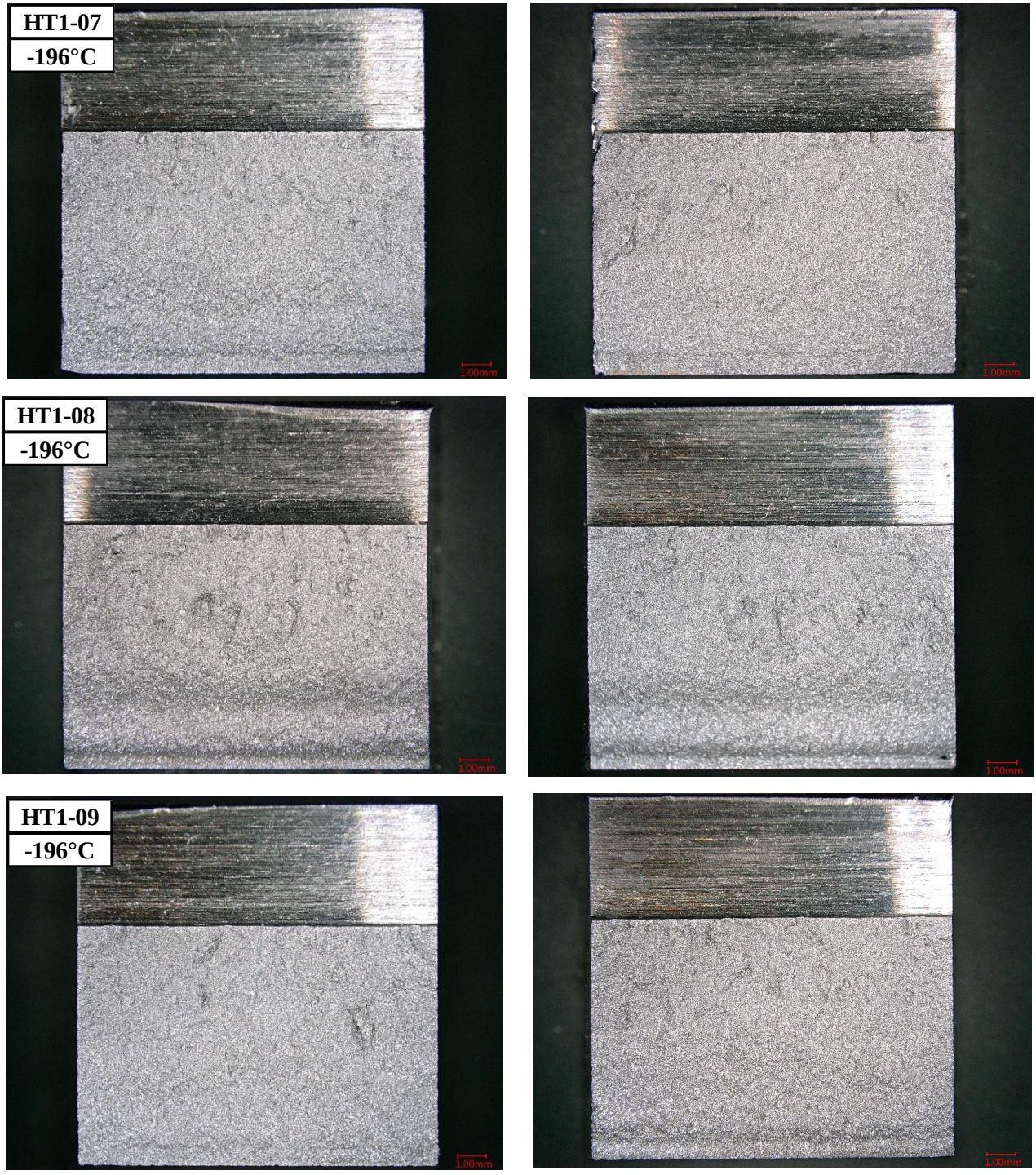

Figure 4.43 Fracture surfaces of Fracture Stress tests for HT1 condition under optical microscope, (a) -196 °C, (b) -170 °C and (c) -160 °C.

(b)

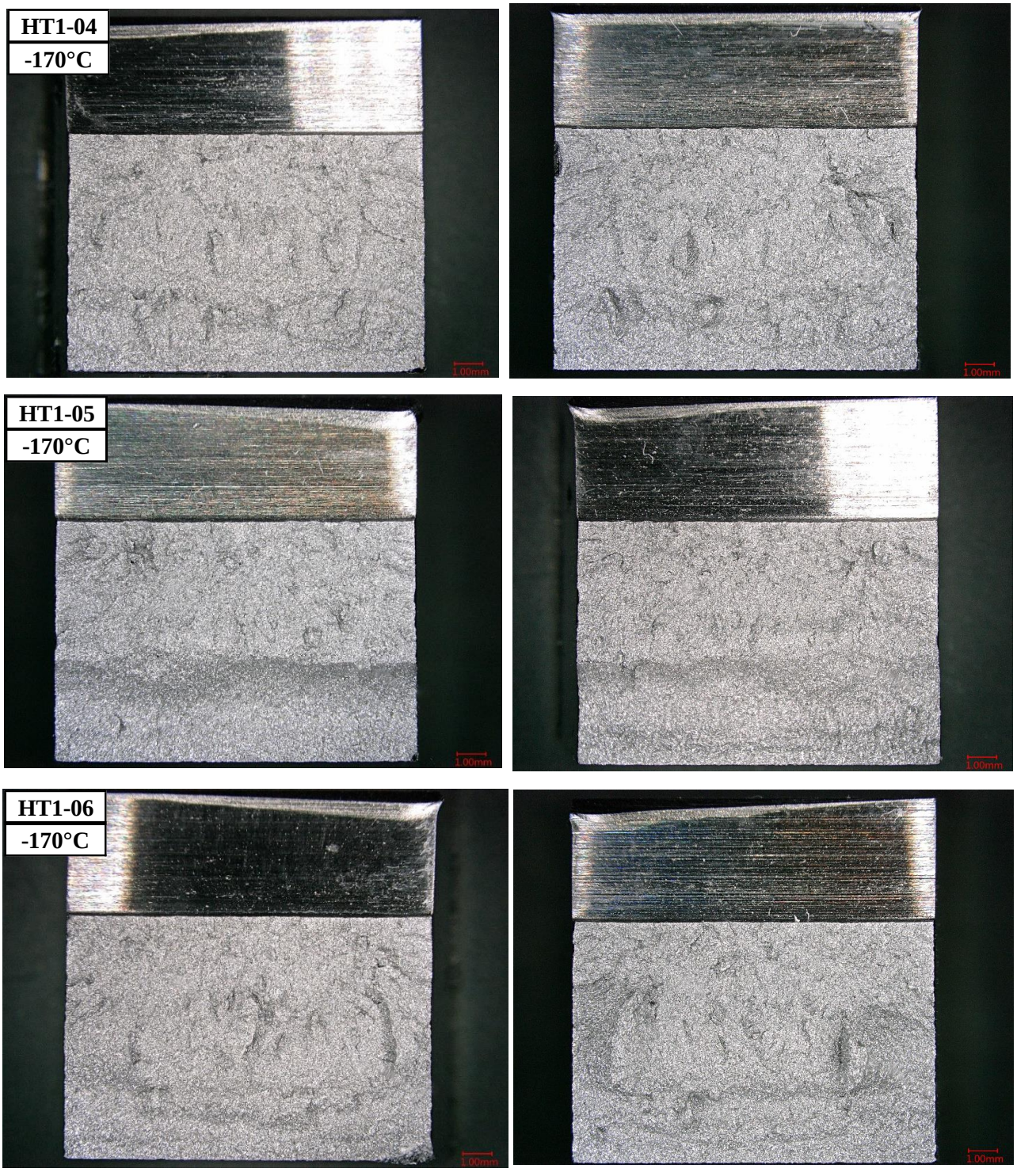

(b) -170 °C.

(c)

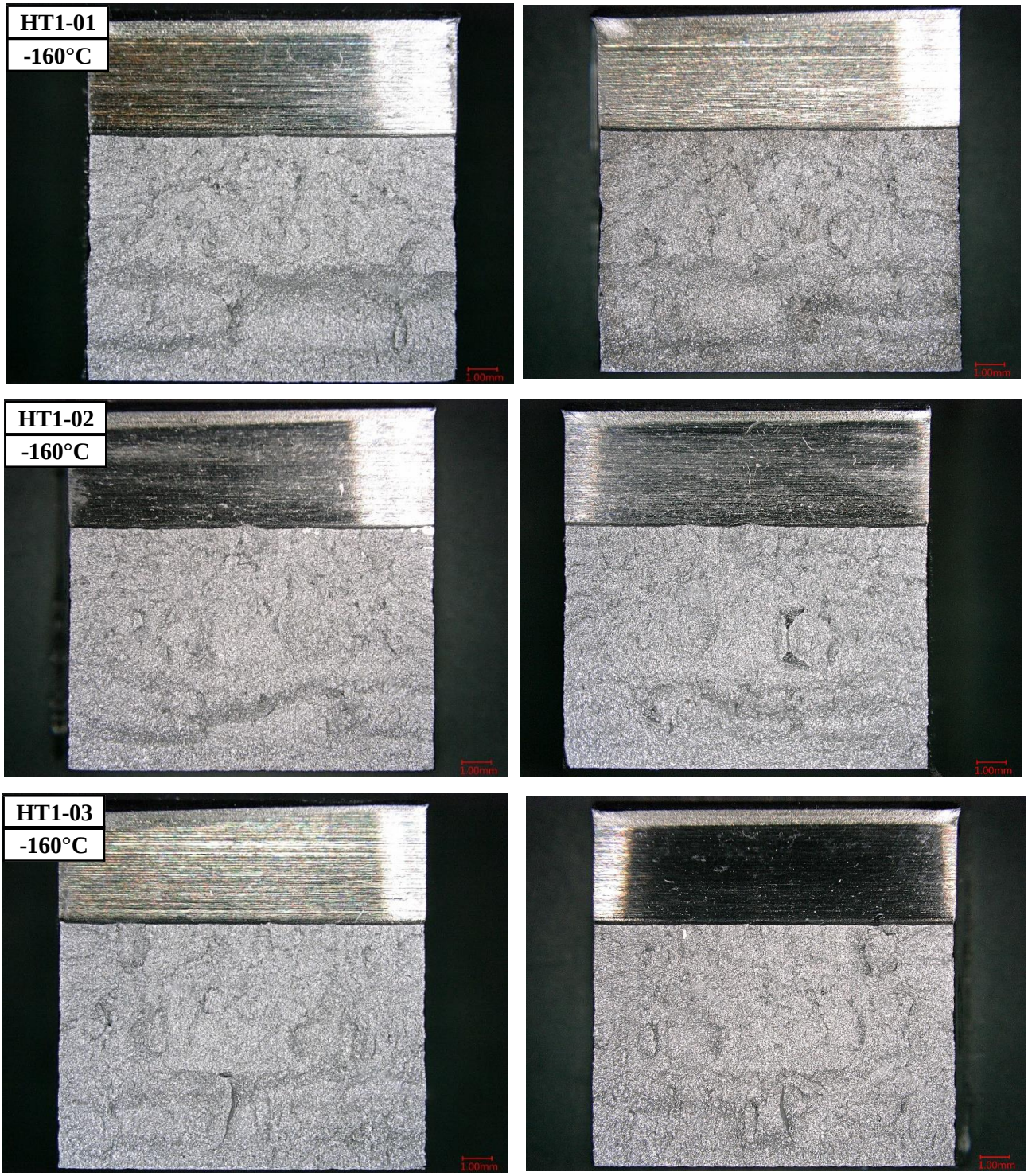

(c) -160 °C.

(a)

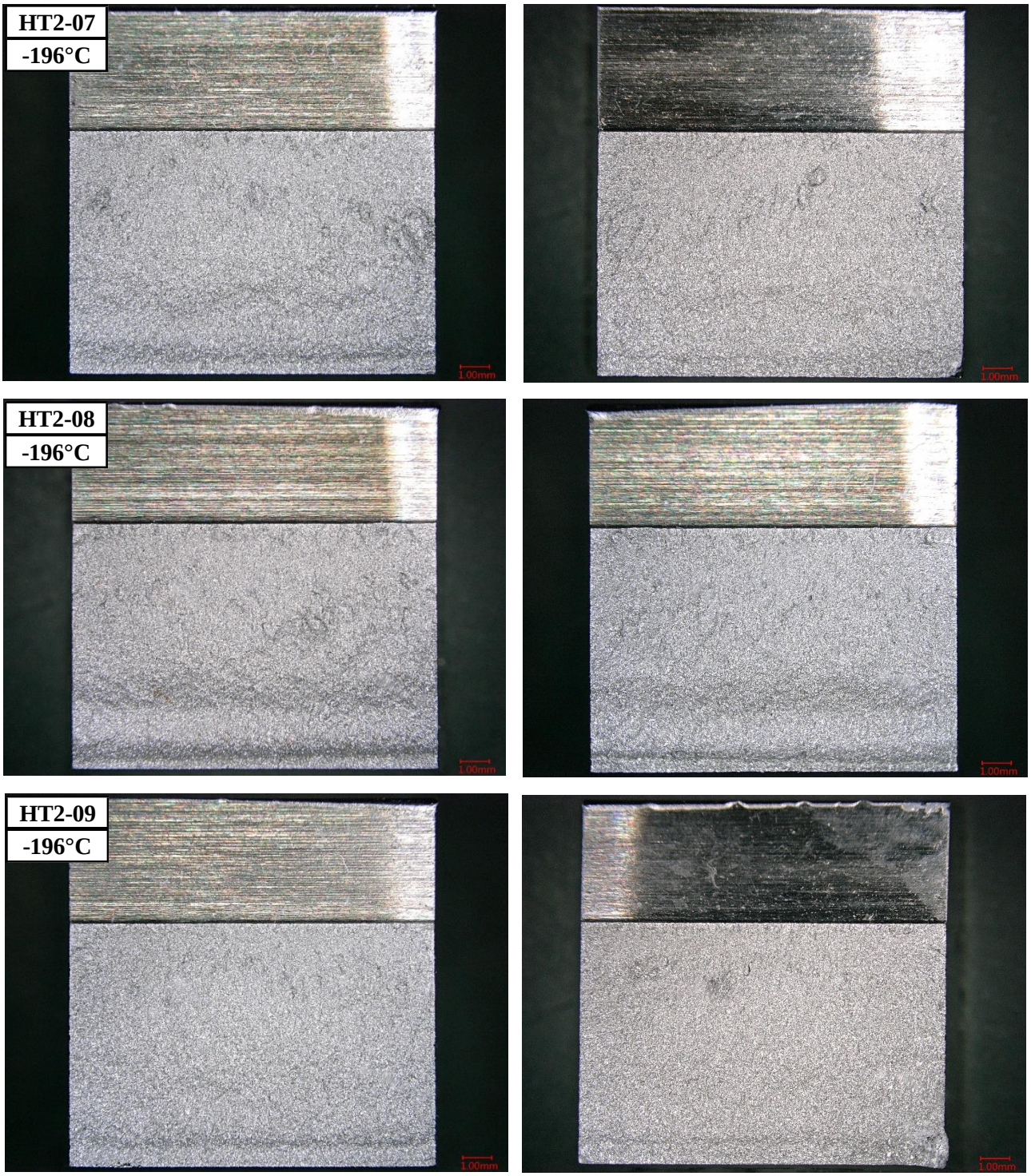

Figure 4.44 Fracture surfaces of Fracture Stress tests for HT2 condition under optical microscope, (a) -196 °C, (b) -170 °C and (c) -160 °C.

(b)

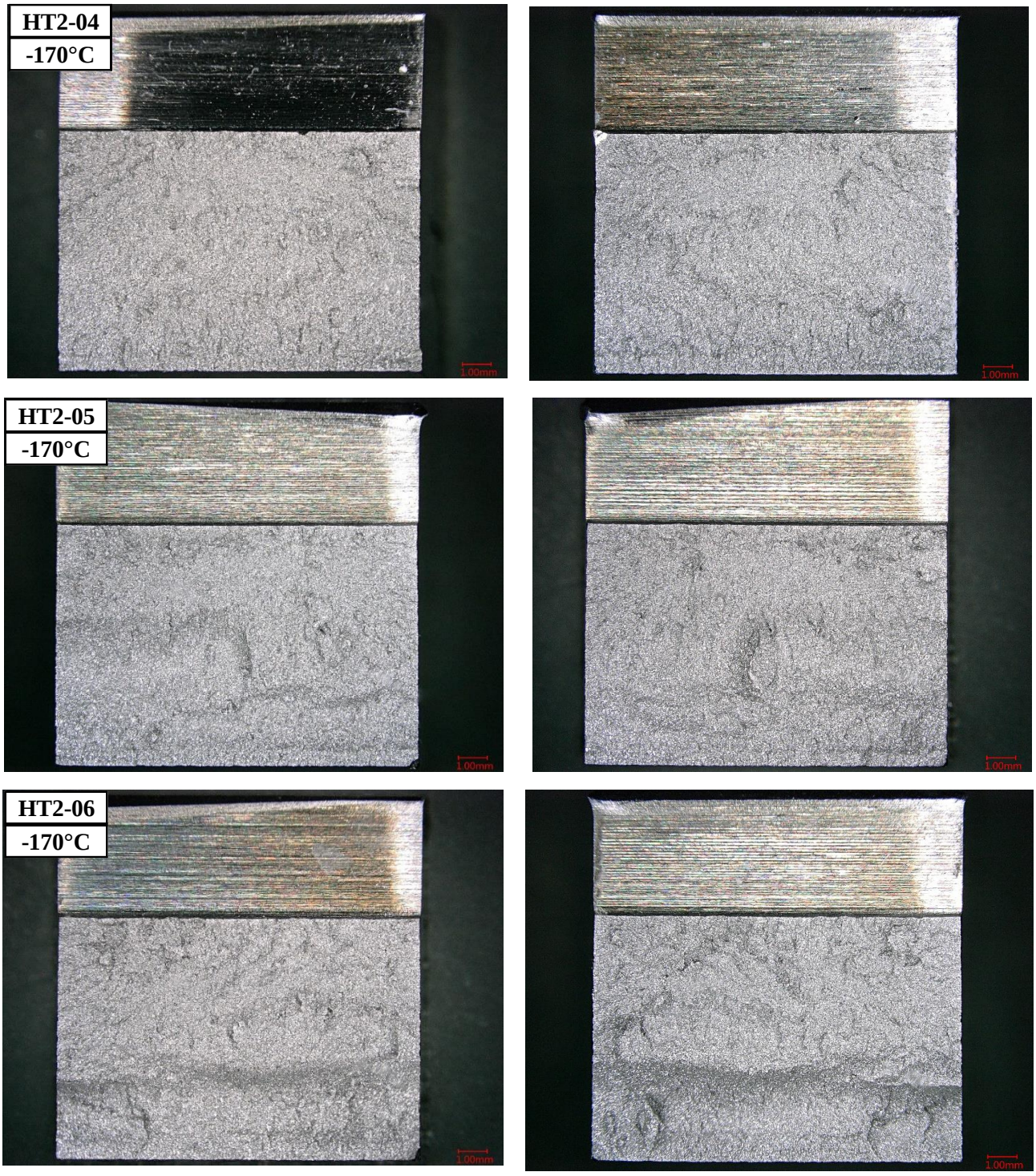

(b) -170 °C.

(c)

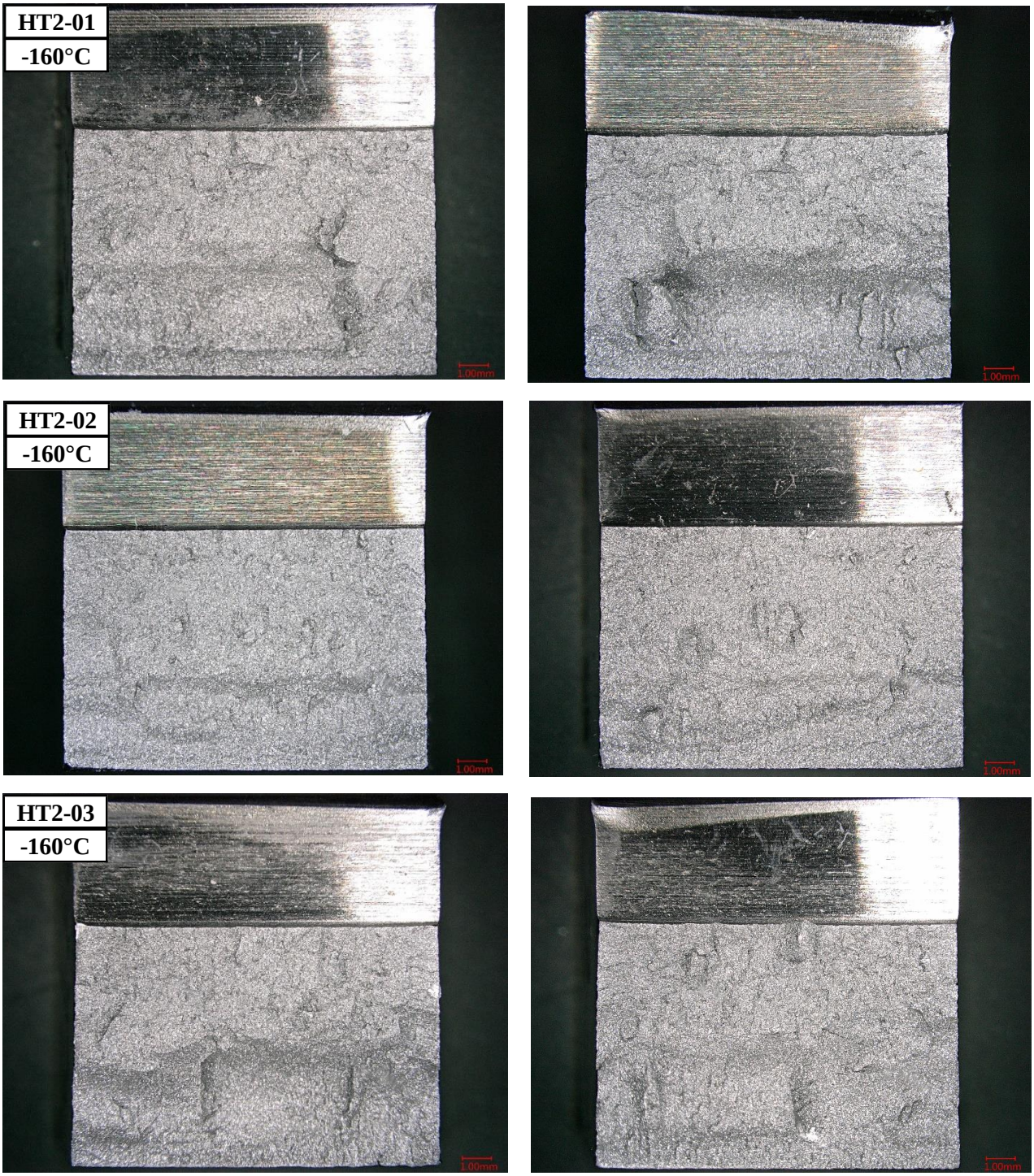

(c) -160 °C.

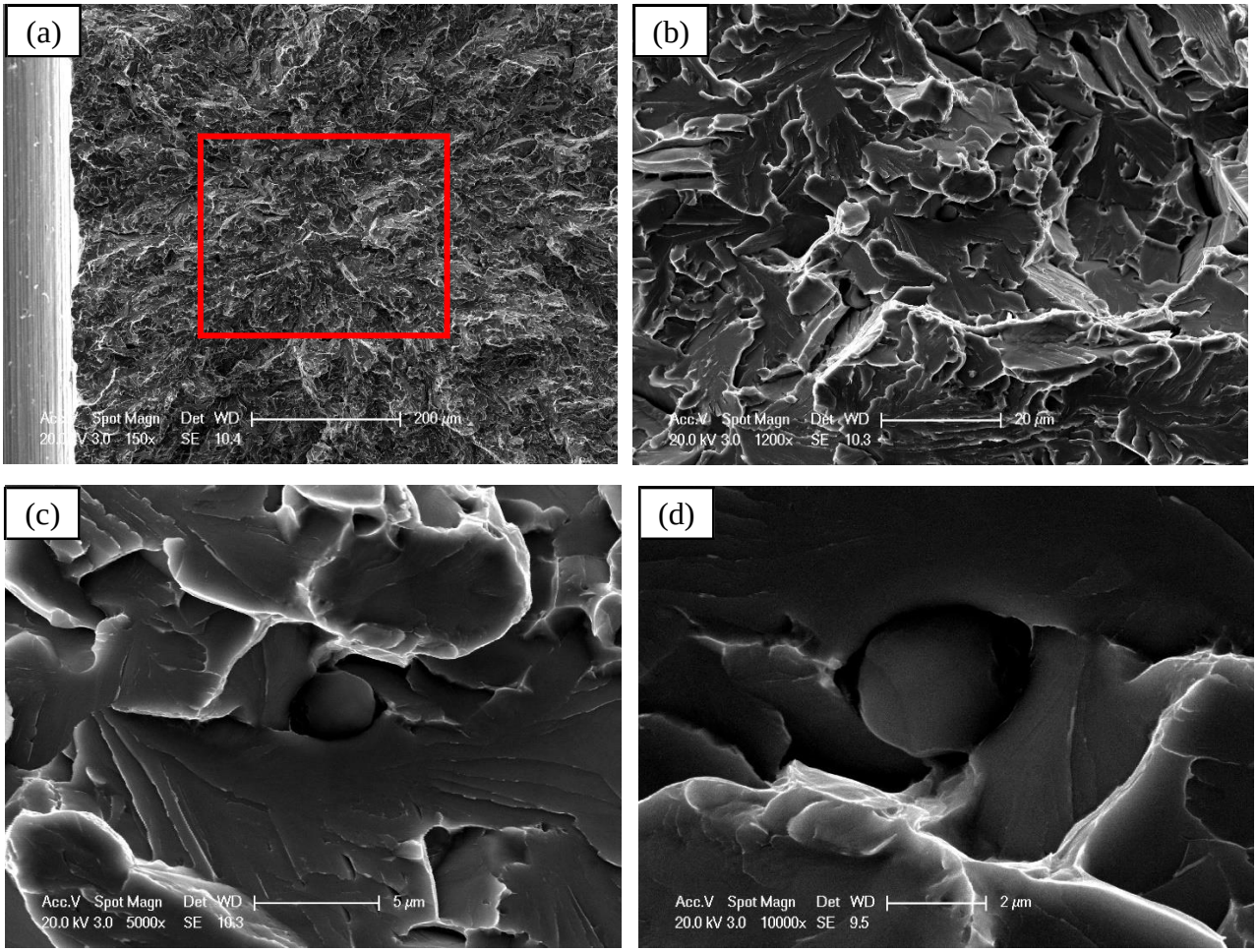

Figure 4.45 Fracture initiation site of Fracture Stress specimen HT1-FS-07 tested at -196 °C, (a) (b) (c) (d) in the sequence of magnification.

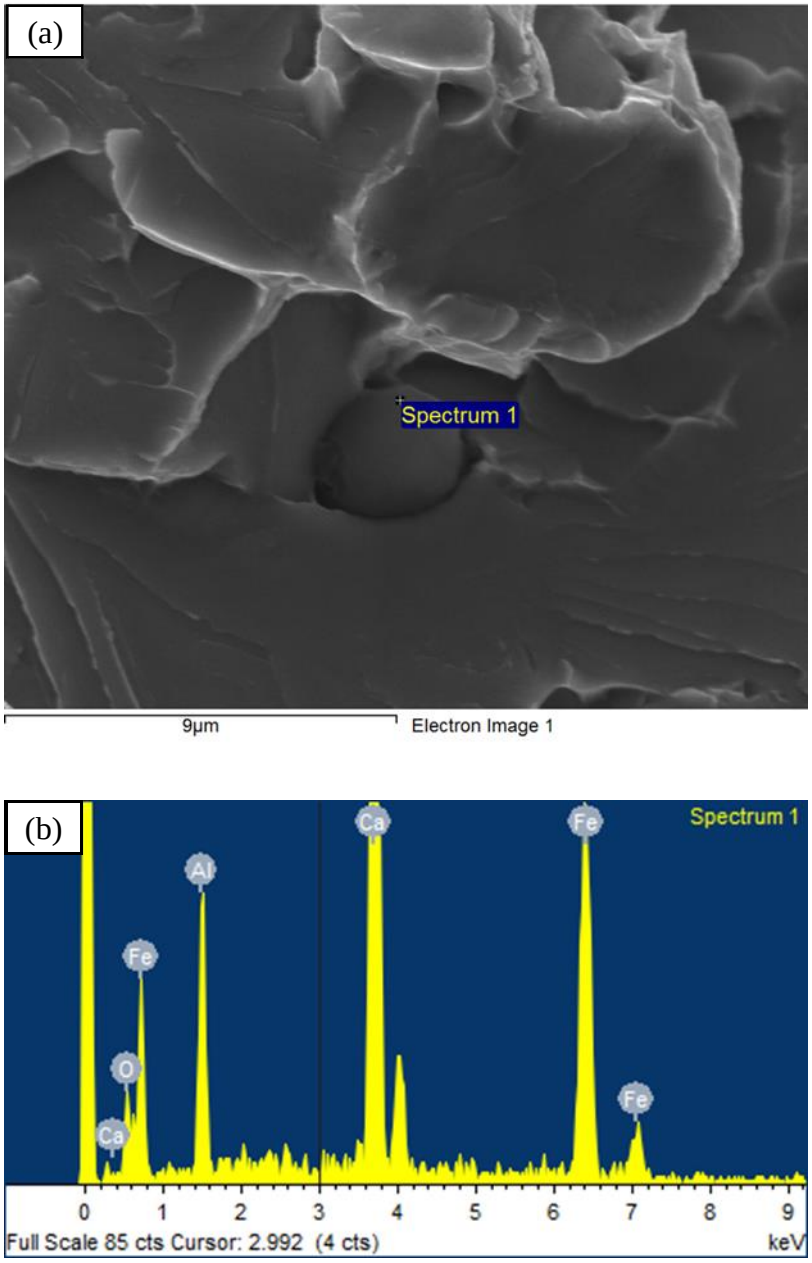

Figure 4.46 Cleavage initiation (a) site of Fracture Stress specimen HT1-FS -07 tested at -196 °C with (b) the corresponding EDX spectrum.

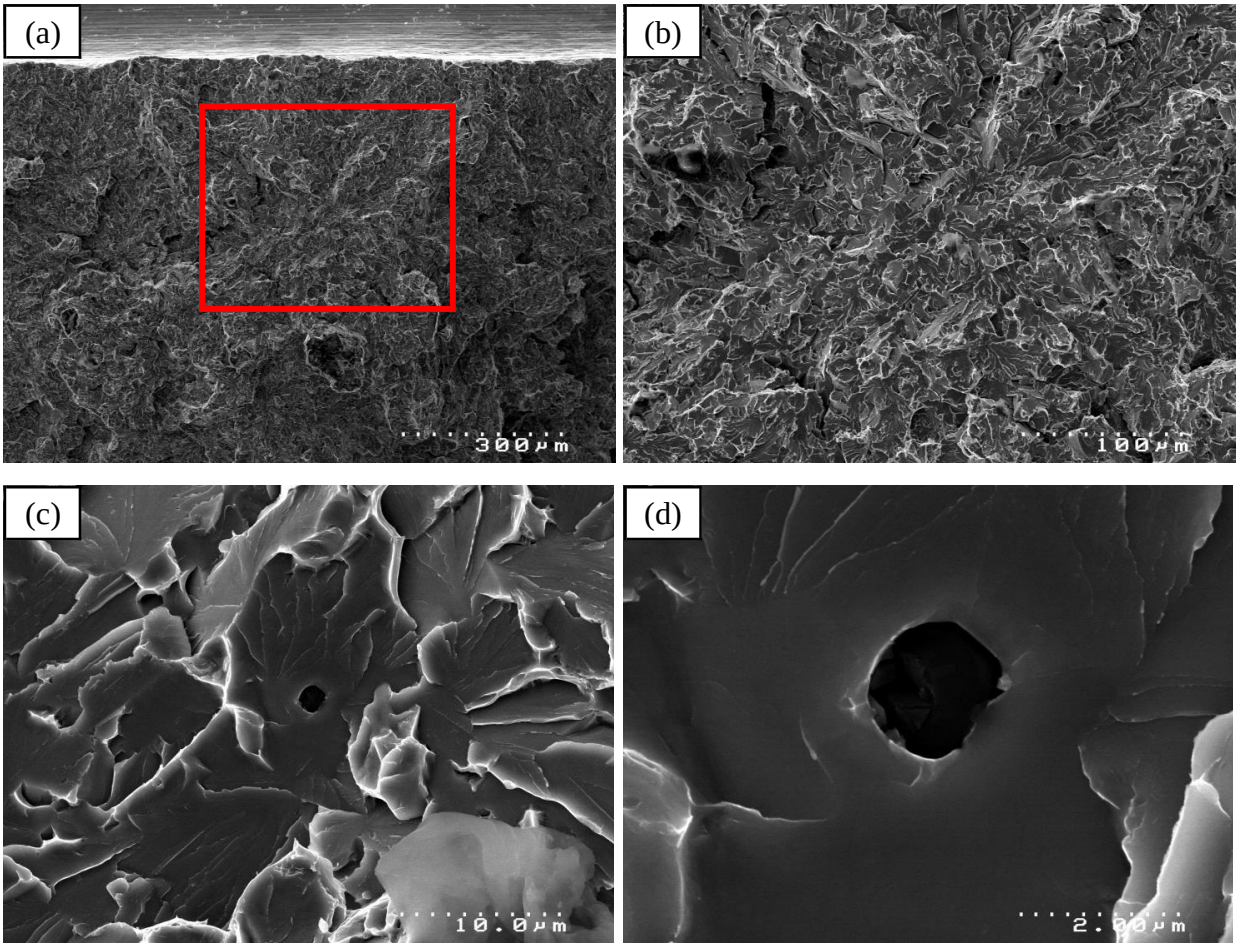

Figure 4.47 Fracture initiation site of Fracture Stress specimen HT1-FS -08 tested at -196 °C, (a) (b) (c) (d) in the sequence of magnification.

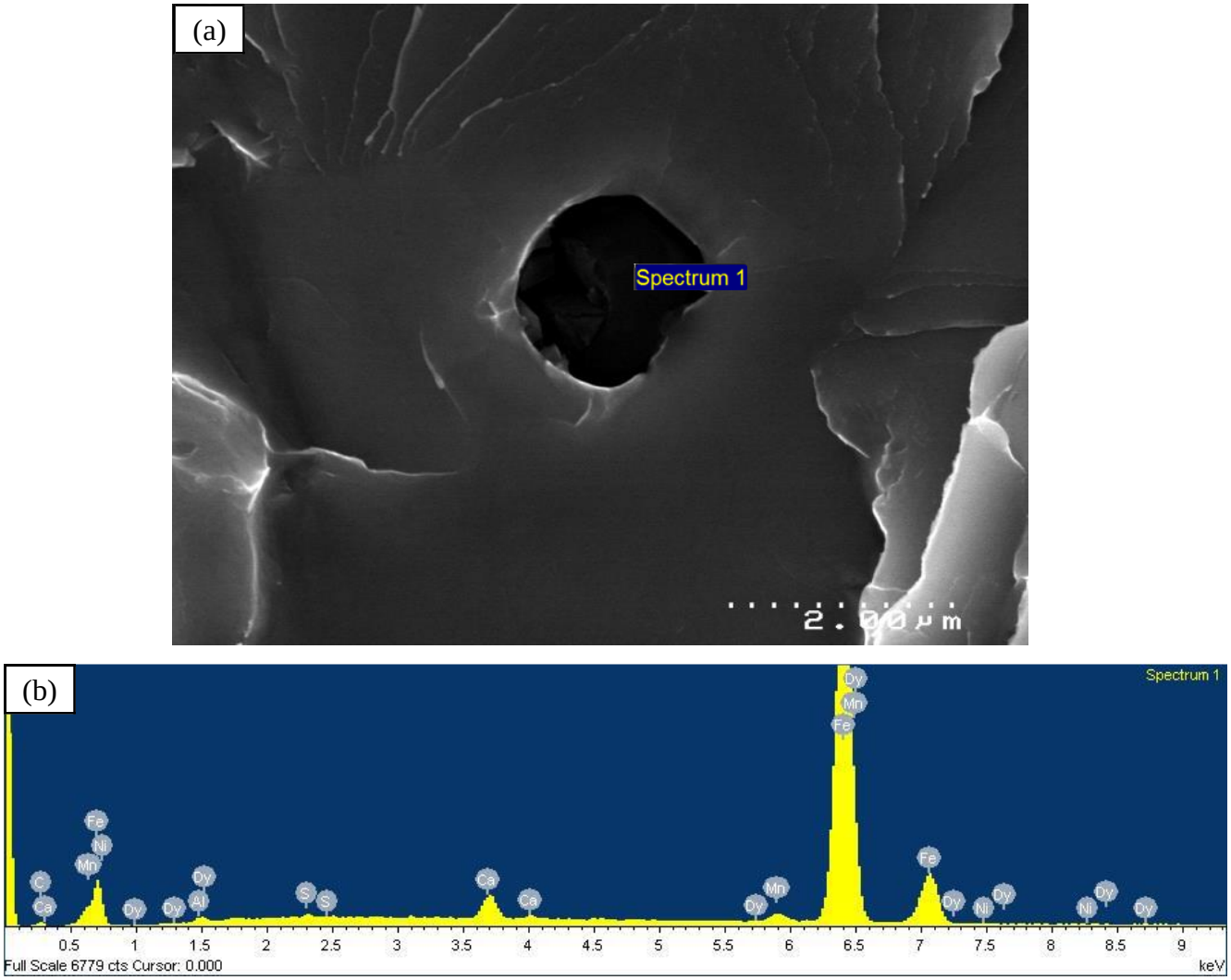

Figure 4.48 Cleavage initiation (a) site of Fracture Stress specimen HT1-FS -08 tested at -196 °C with (b) the corresponding EDX spectrum.

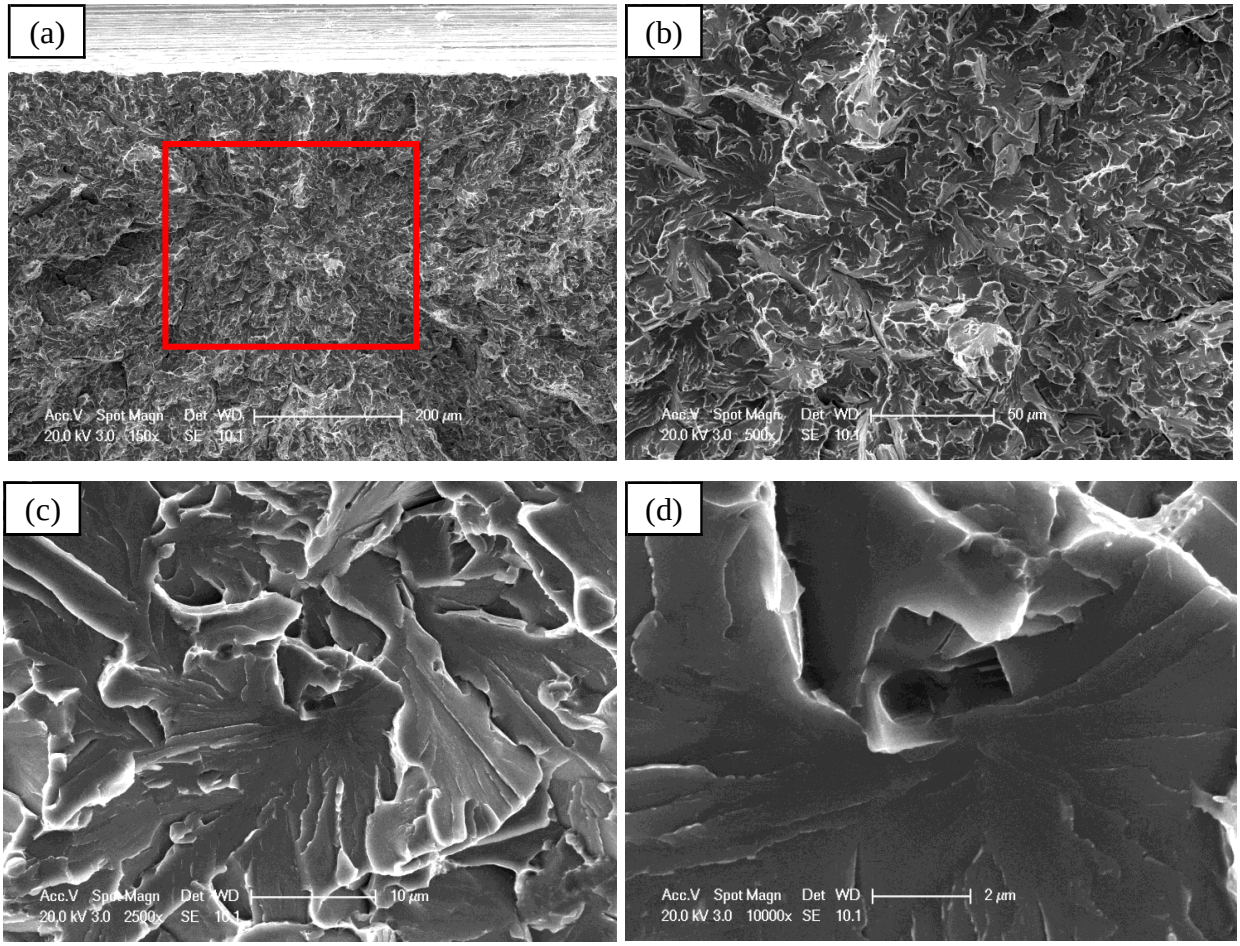

Figure 4.49 Fracture initiation site of Fracture Stress specimen HT1-FS -09 tested at -196 °C, (a) (b) (c) (d) in the sequence of magnification.

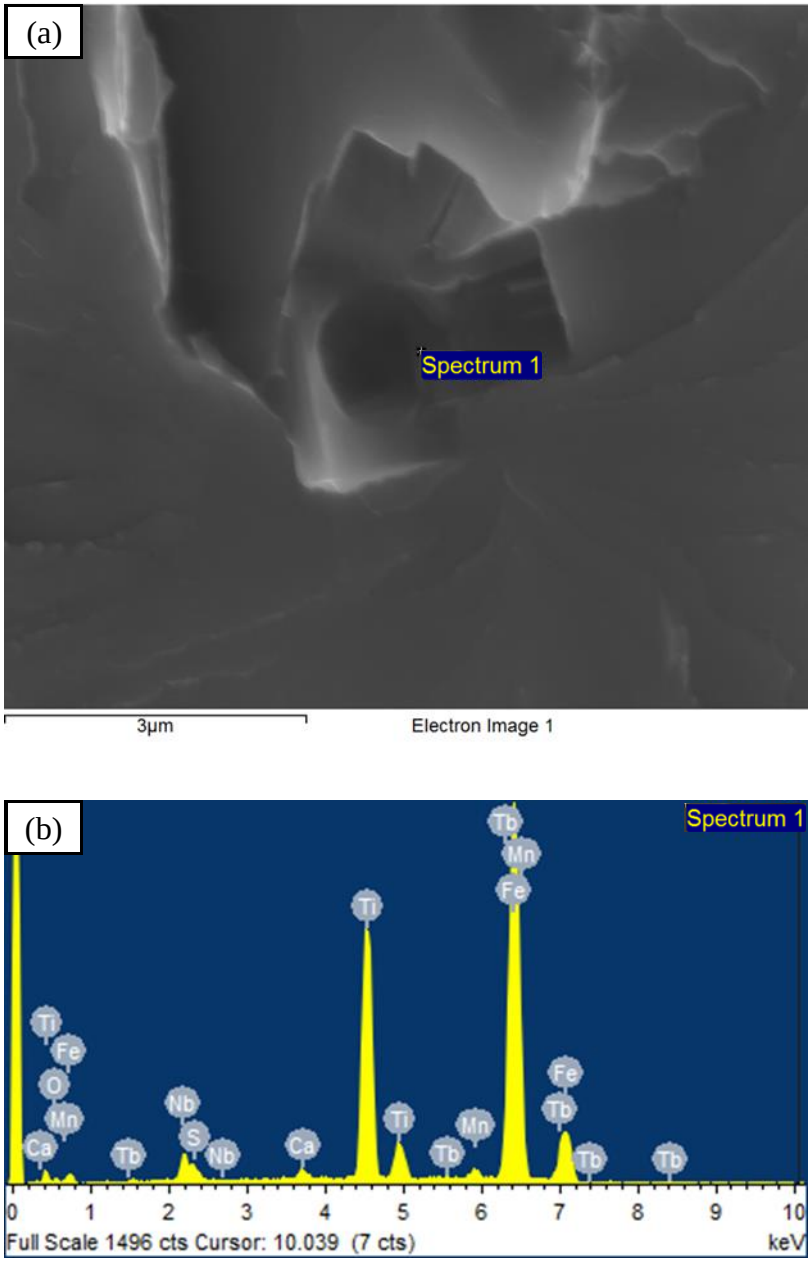

Figure 4.50 Cleavage initiation (a) site of Fracture Stress specimen HT1-FS -09 tested at -196 °C with (b) the corresponding EDX spectrum.

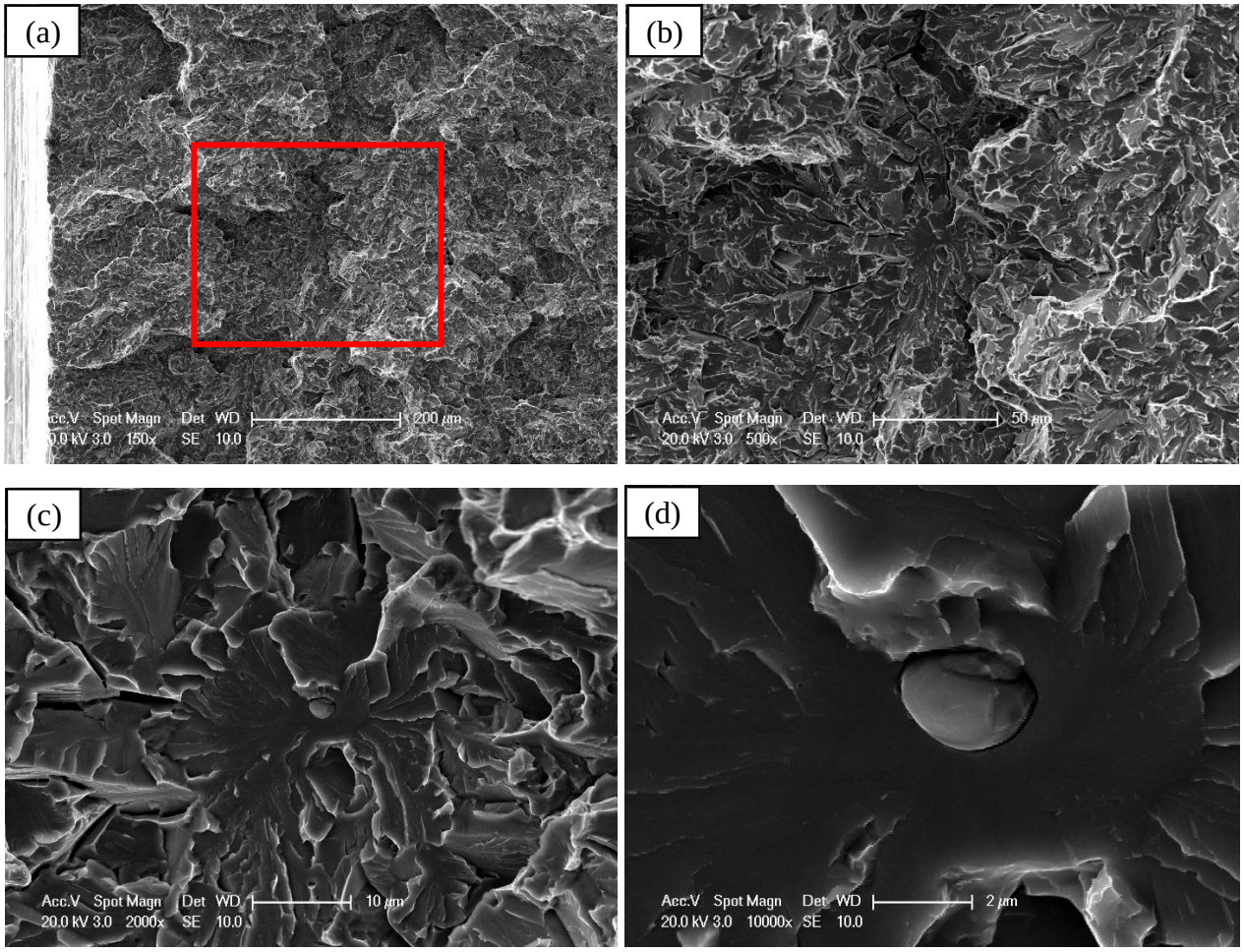

Figure 4.51 Fracture initiation site of Fracture Stress specimen HT2-FS -07 tested at -196 °C, (a) (b) (c) (d) in the sequence of magnification.

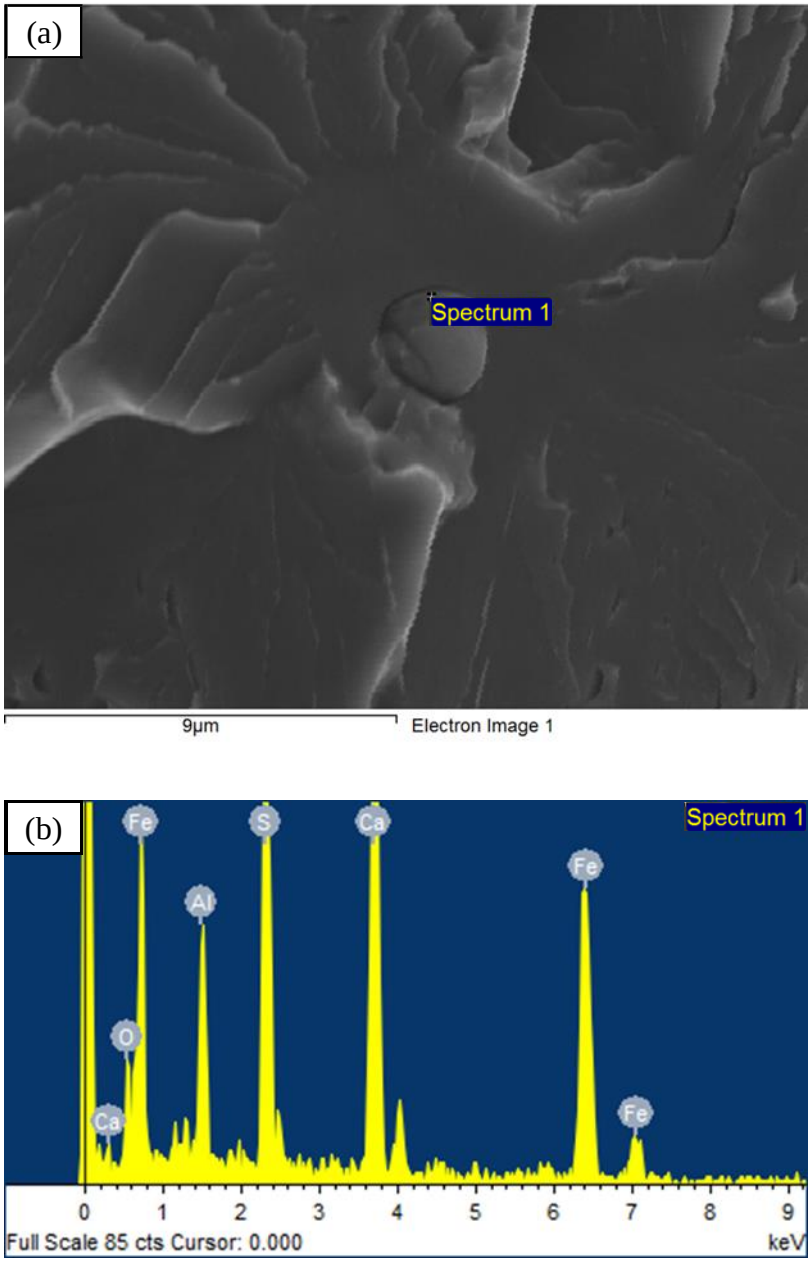

Figure 4.52 Cleavage initiation (a) site of Fracture Stress specimen HT2-FS -07 tested at -196 °C with (b) the corresponding EDX spectrum.

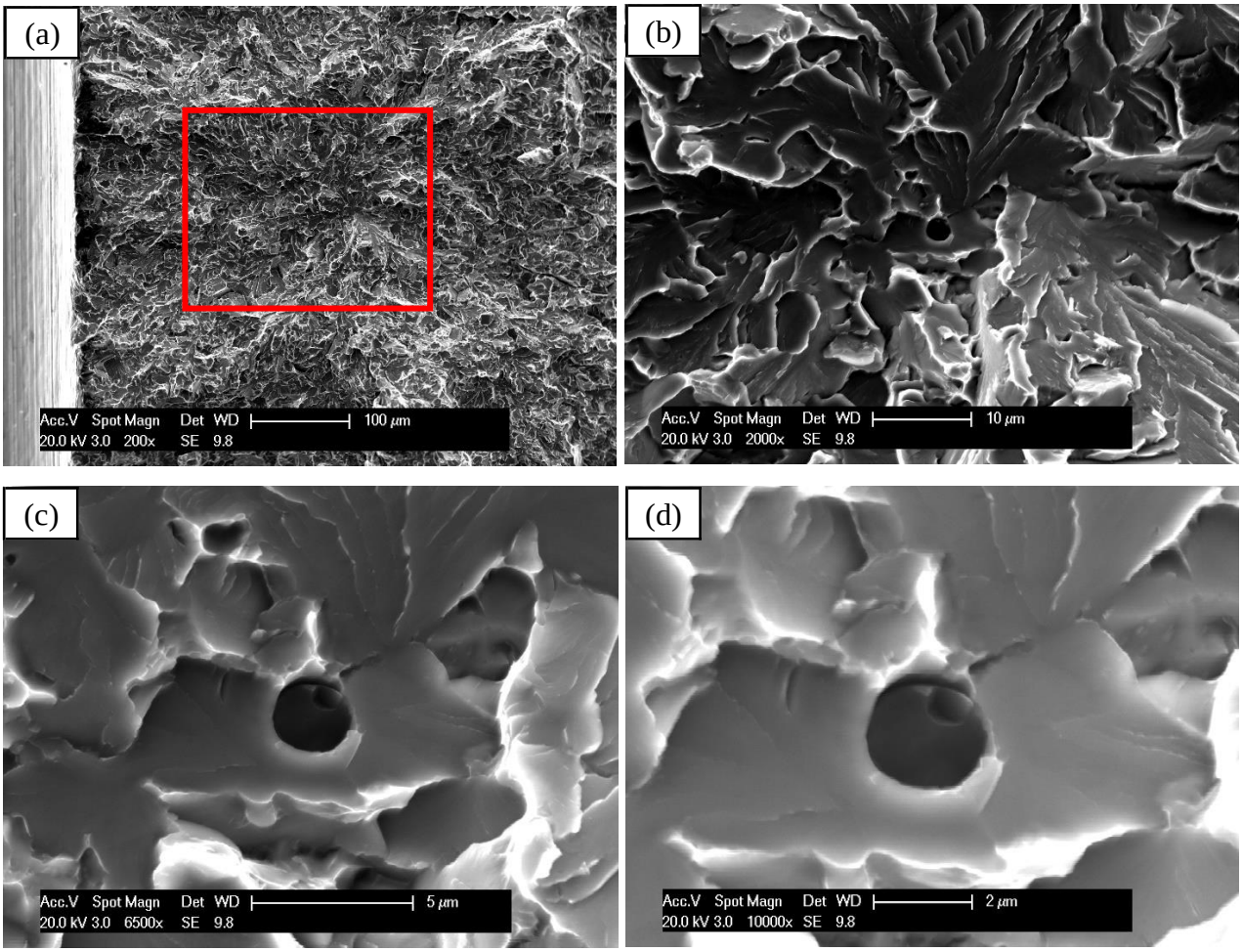

Figure 4.53 Fracture initiation site of Fracture Stress specimen HT2-FS -08 tested at -196 °C, (a) (b) (c) (d) in the sequence of magnification.

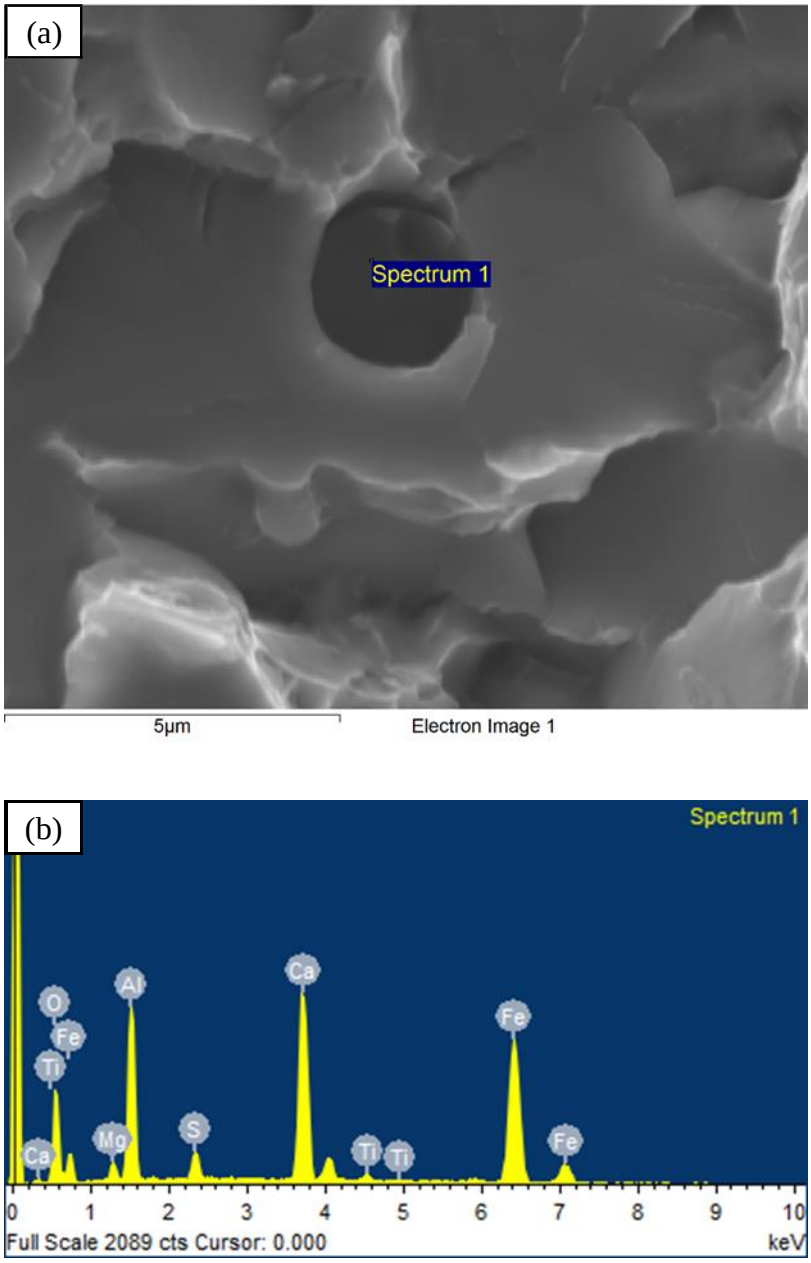

Figure 4.54 Cleavage initiation (a) site of Fracture Stress specimen HT2-FS -08 tested at -196 °C with (b) the corresponding EDX spectrum.

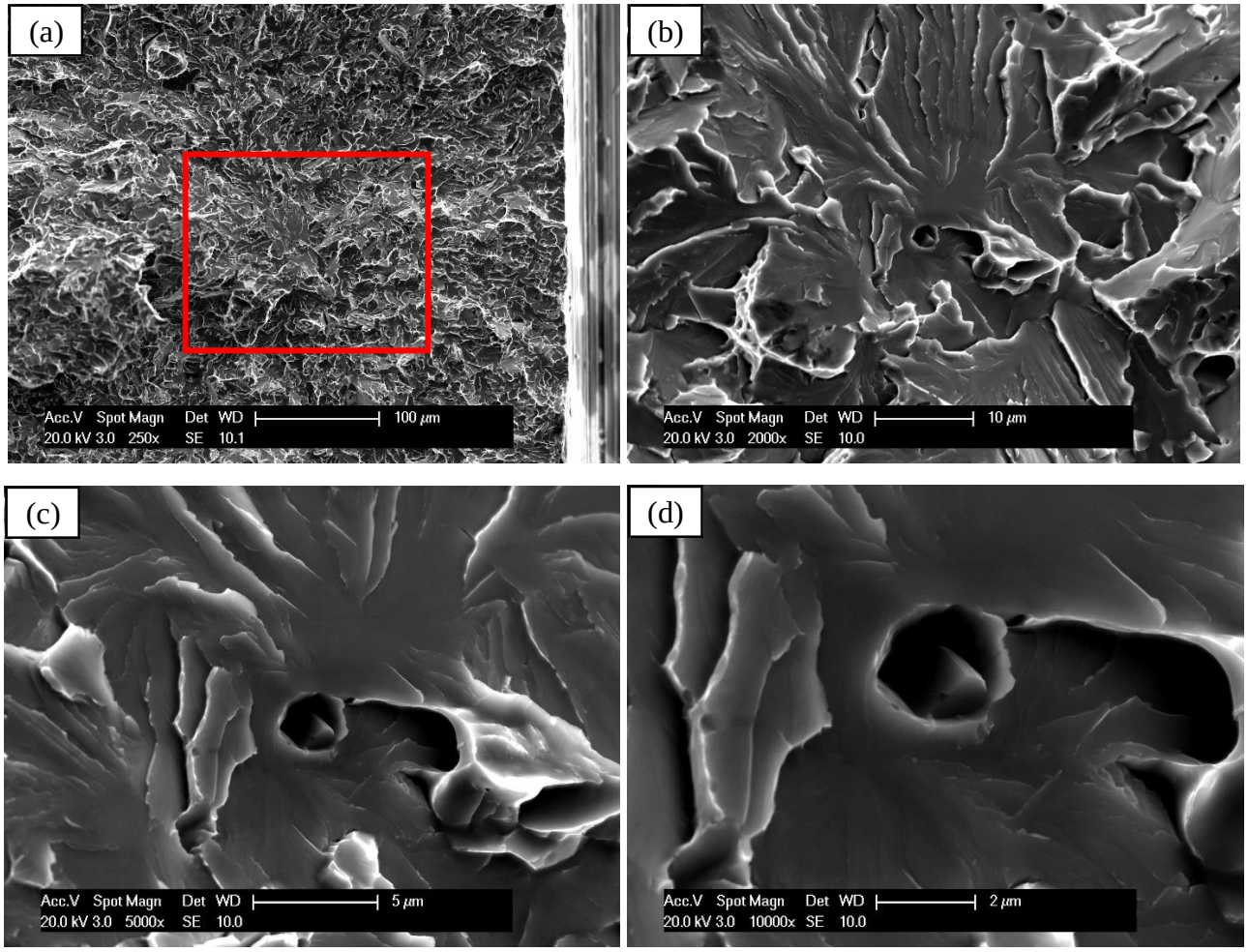

Figure 4.55 Fracture initiation site of Fracture Stress specimen HT2-FS -09 tested at -196 °C, (a) (b) (c) (d) in the sequence of magnification.

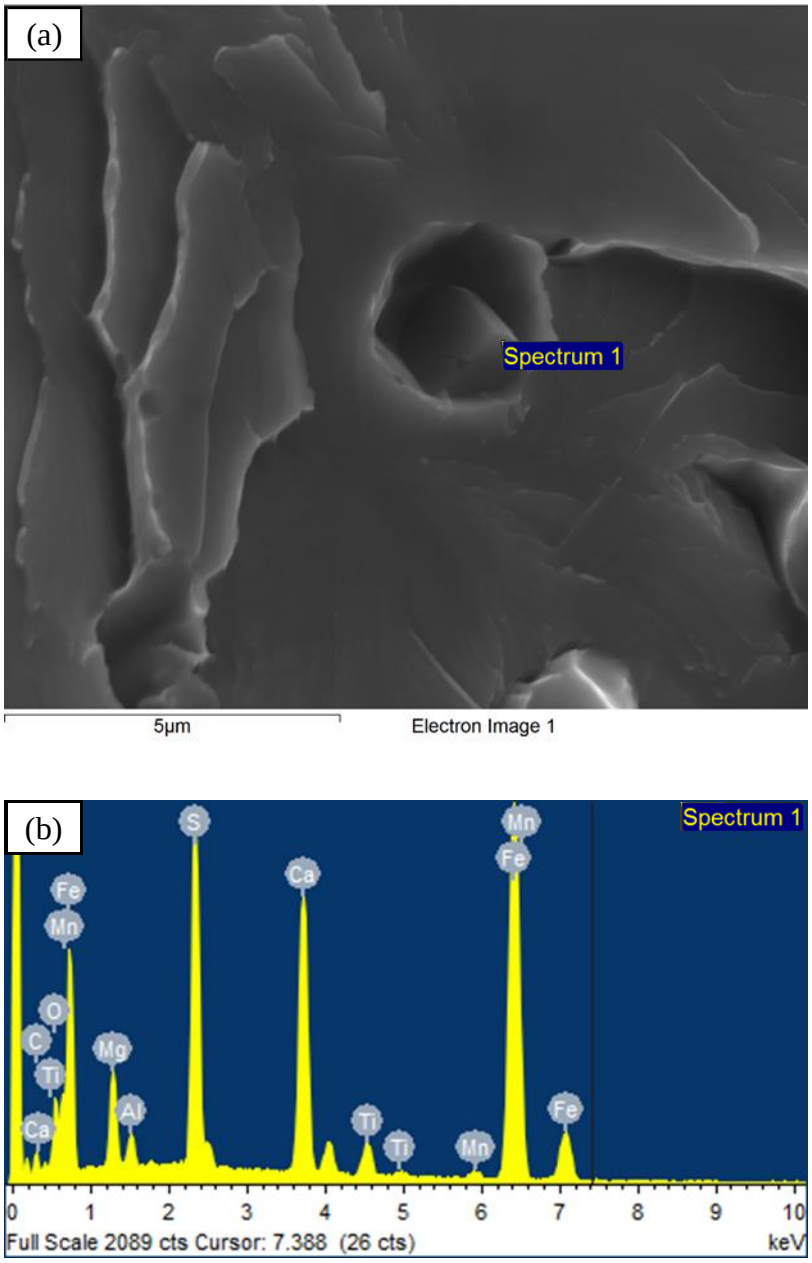

Figure 4.56 Cleavage initiation (a) site of Fracture Stress specimen HT2-FS -09 tested at -196 °C with (b) the corresponding EDX spectrum.

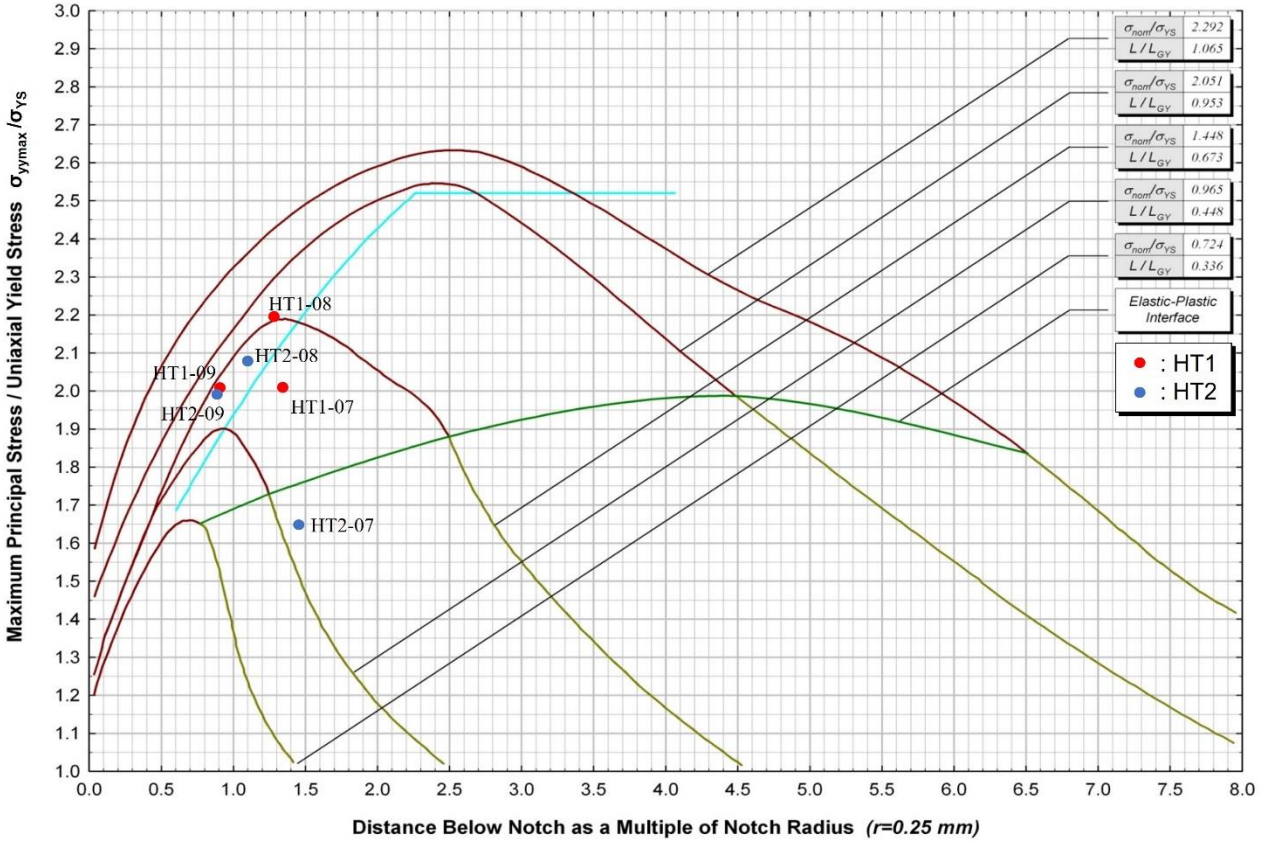

Figure 4.57 The Griffith-Owen FEM analysis of stress intensification factor *SIF* versus the ratio of distance below the notch root as a multiple of notch root radius.

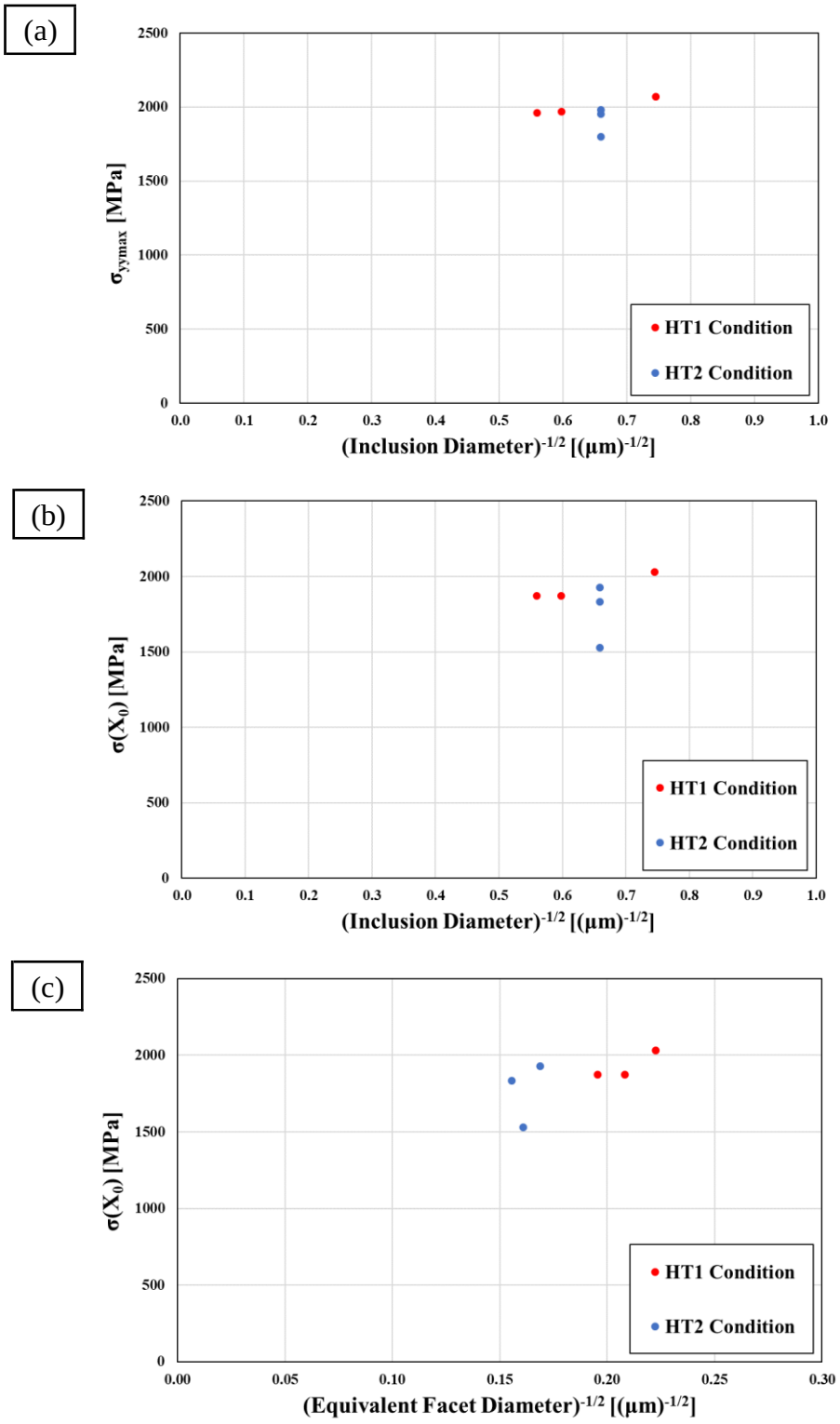

Figure 4.58 Plots and regressions of σ_{yymax}, $\sigma(X_0)$ versus the reciprocal square root of the inclusion diameter and equivalent facet diameter at the initiation site.

(a)

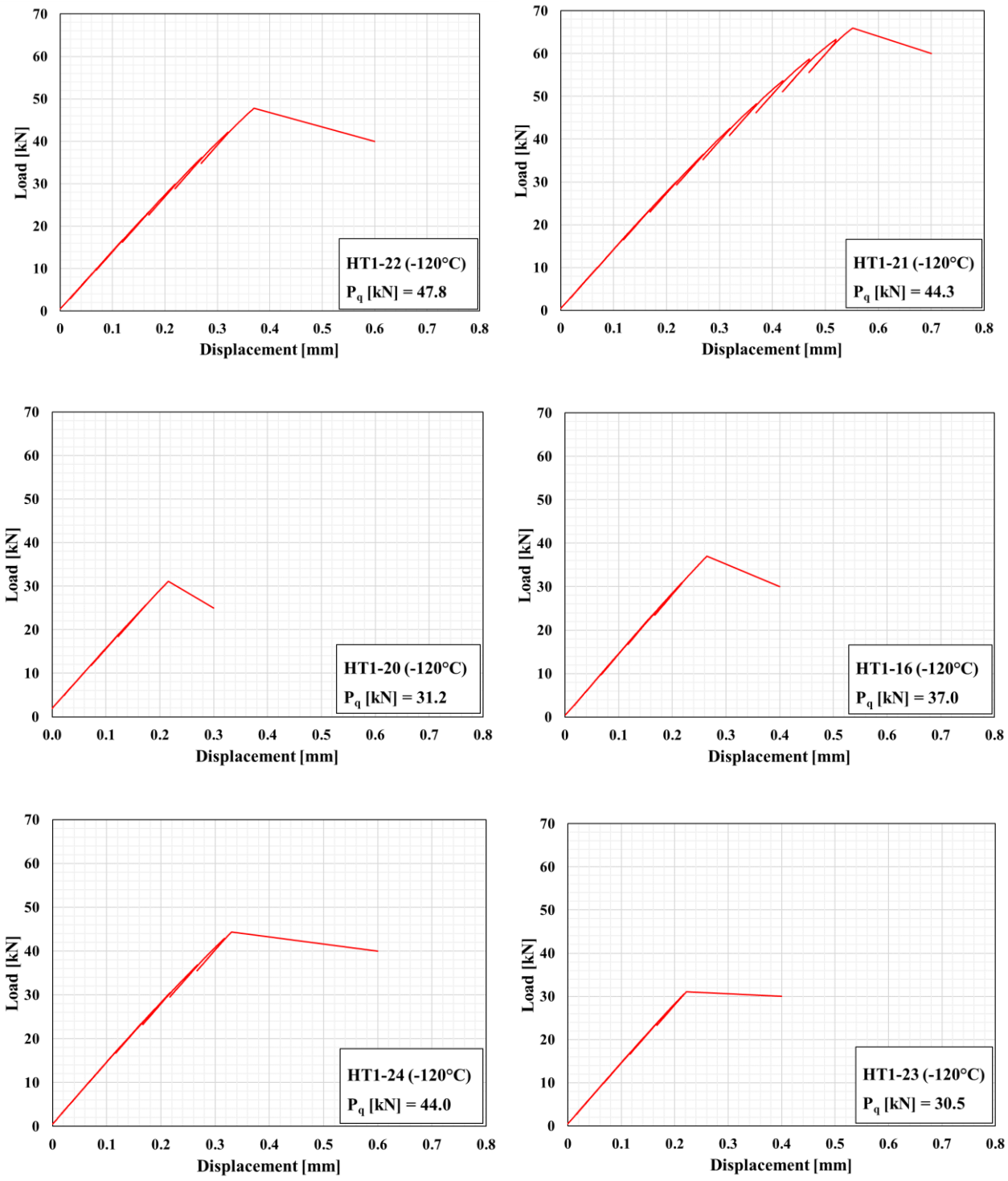

Figure 4.59 Load-displacement curves of Fracture Toughness tests for HT1 and HT2 conditions tested at -120°C, (a) HT1 and (b) HT2.

(b)

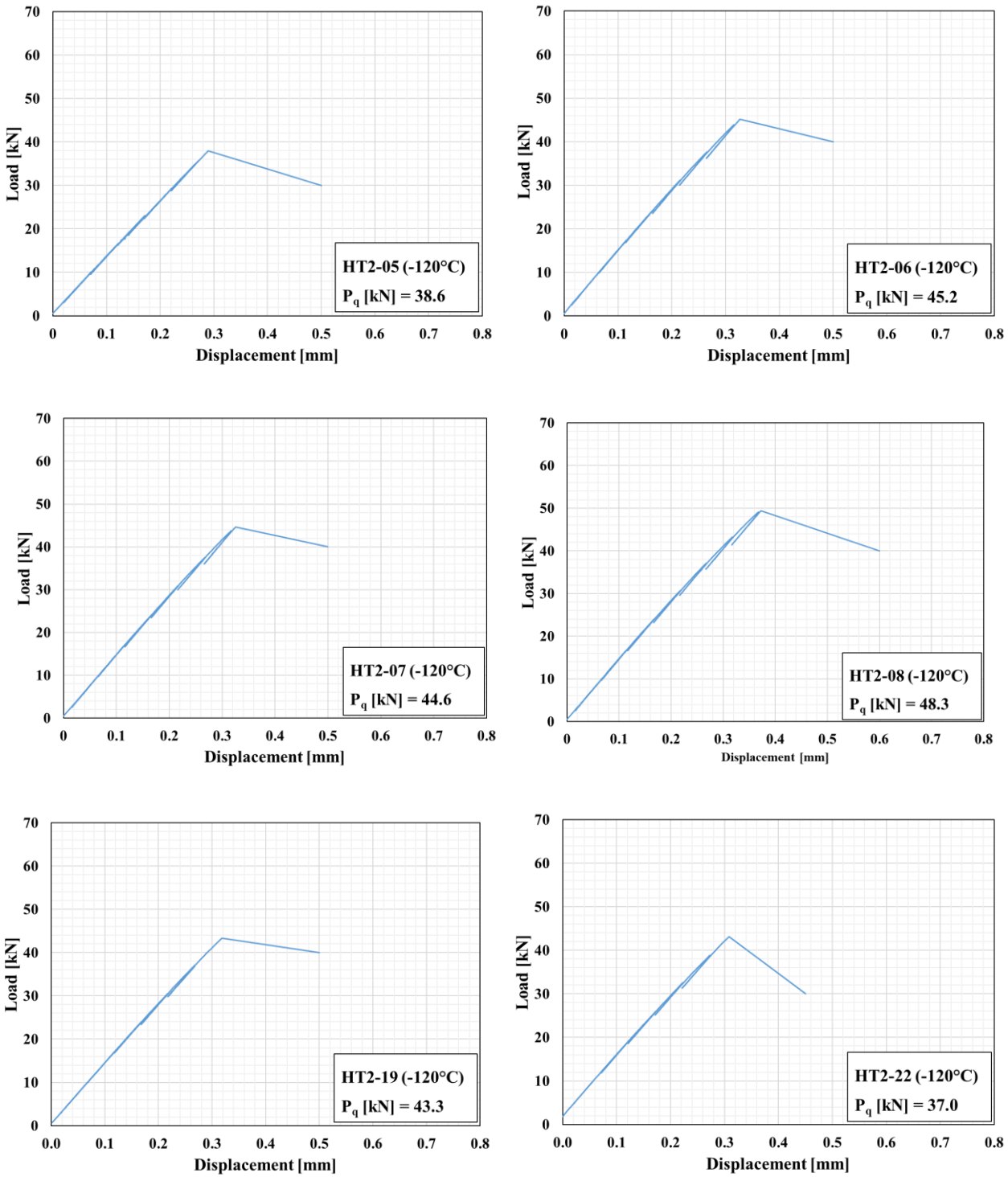
Load [kN]
Displacement [mm]
HT2-05 (-120°C)
P_q [kN] = 38.6
HT2-06 (-120°C)
P_q [kN] = 45.2
HT2-07 (-120°C)
P_q [kN] = 44.6
HT2-08 (-120°C)
P_q [kN] = 48.3
HT2-19 (-120°C)
P_q [kN] = 43.3
HT2-22 (-120°C)
P_q [kN] = 37.0

(b) HT2.

(a)

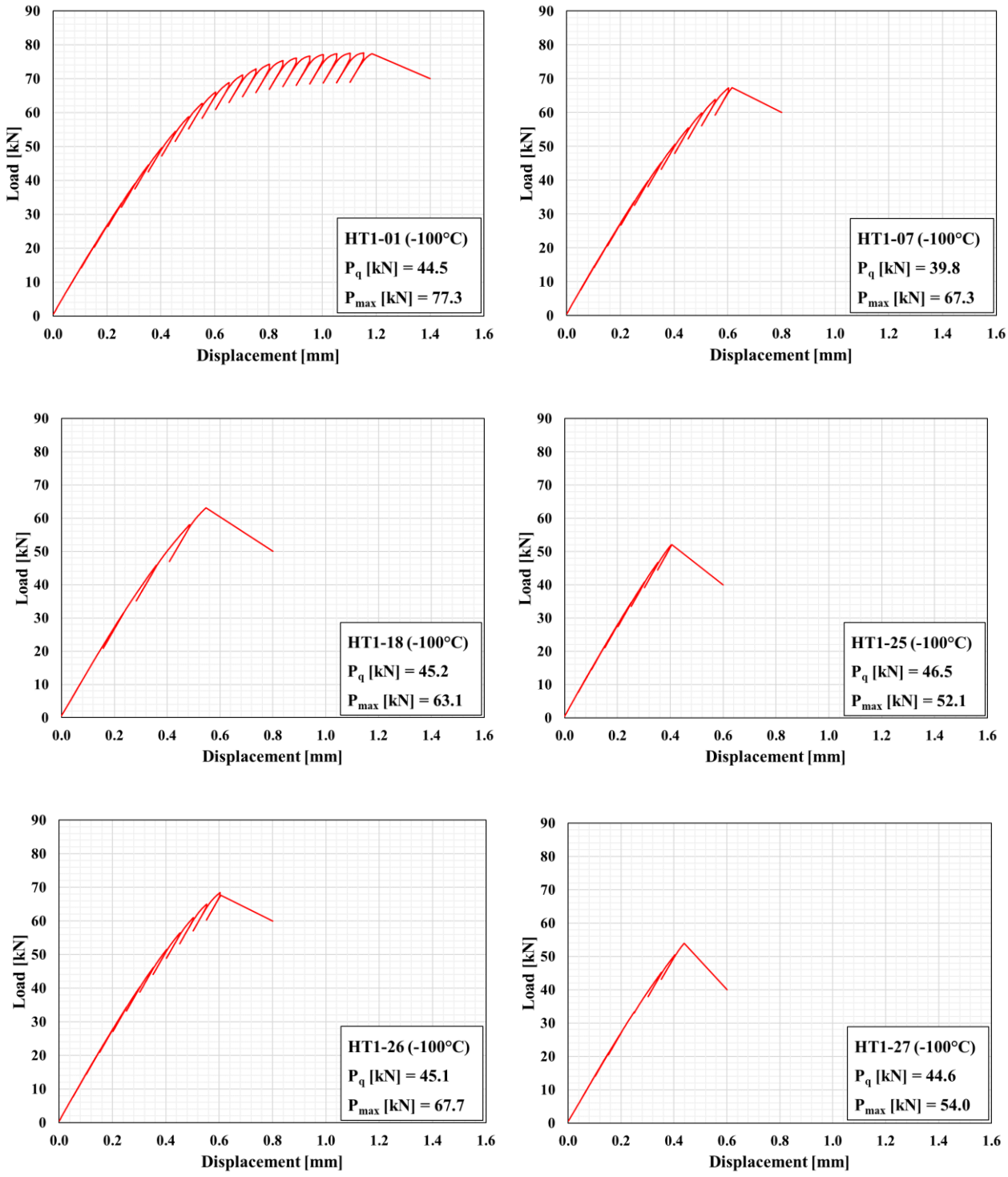

Figure 4.60 Load-displacement curves of Fracture Toughness tests for HT1 and HT2 conditions tested at -100°C, (a) HT1 and (b) HT2.

(b)

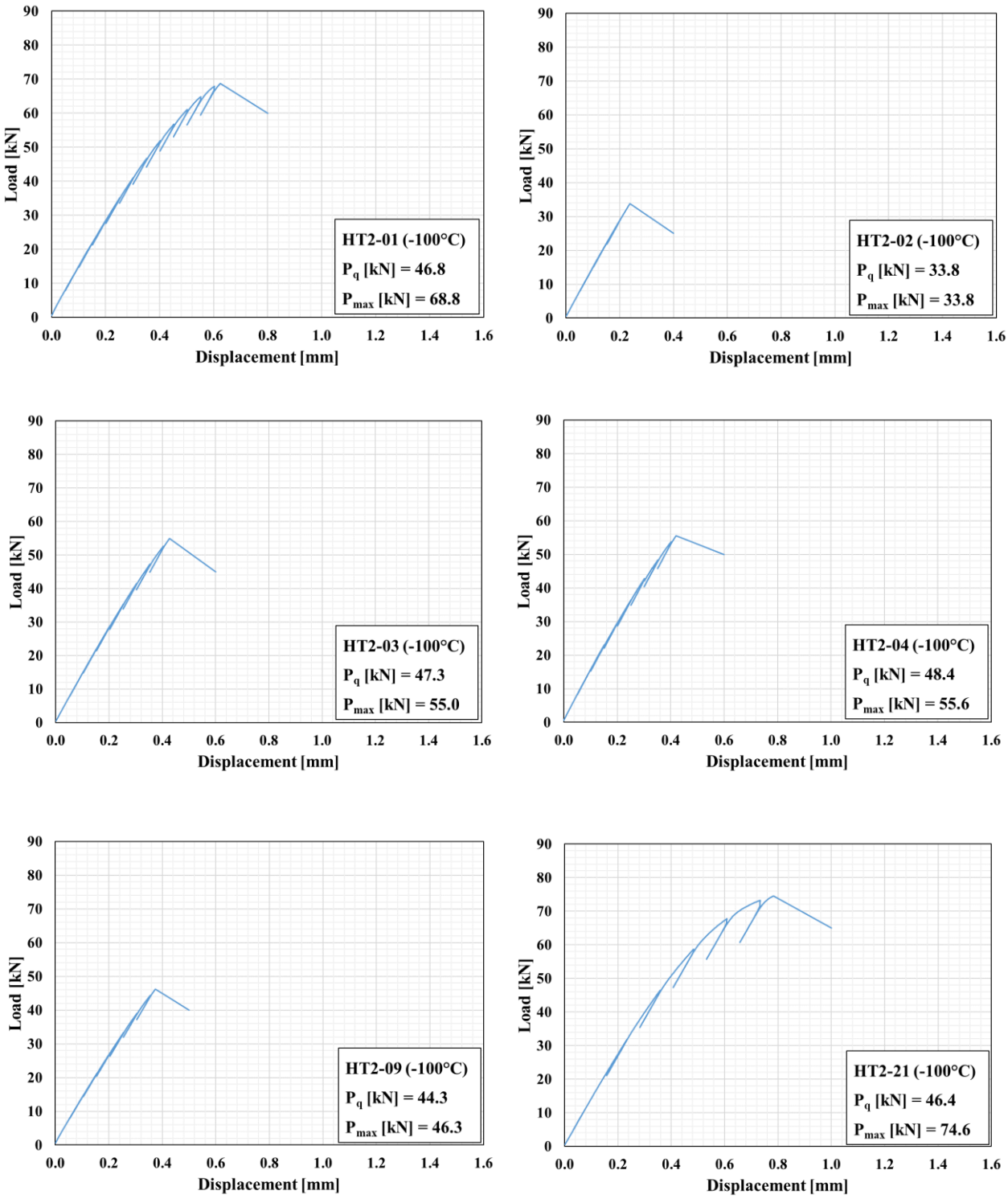
Load [kN]
Displacement [mm]
HT2-01 (-100°C)
P_q [kN] = 46.8
P_{max} [kN] = 68.8
HT2-02 (-100°C)
P_q [kN] = 33.8
P_{max} [kN] = 33.8
HT2-03 (-100°C)
P_q [kN] = 47.3
P_{max} [kN] = 55.0
HT2-04 (-100°C)
P_q [kN] = 48.4
P_{max} [kN] = 55.6
HT2-09 (-100°C)
P_q [kN] = 44.3
P_{max} [kN] = 46.3
HT2-21 (-100°C)
P_q [kN] = 46.4
P_{max} [kN] = 74.6

(b) HT2.

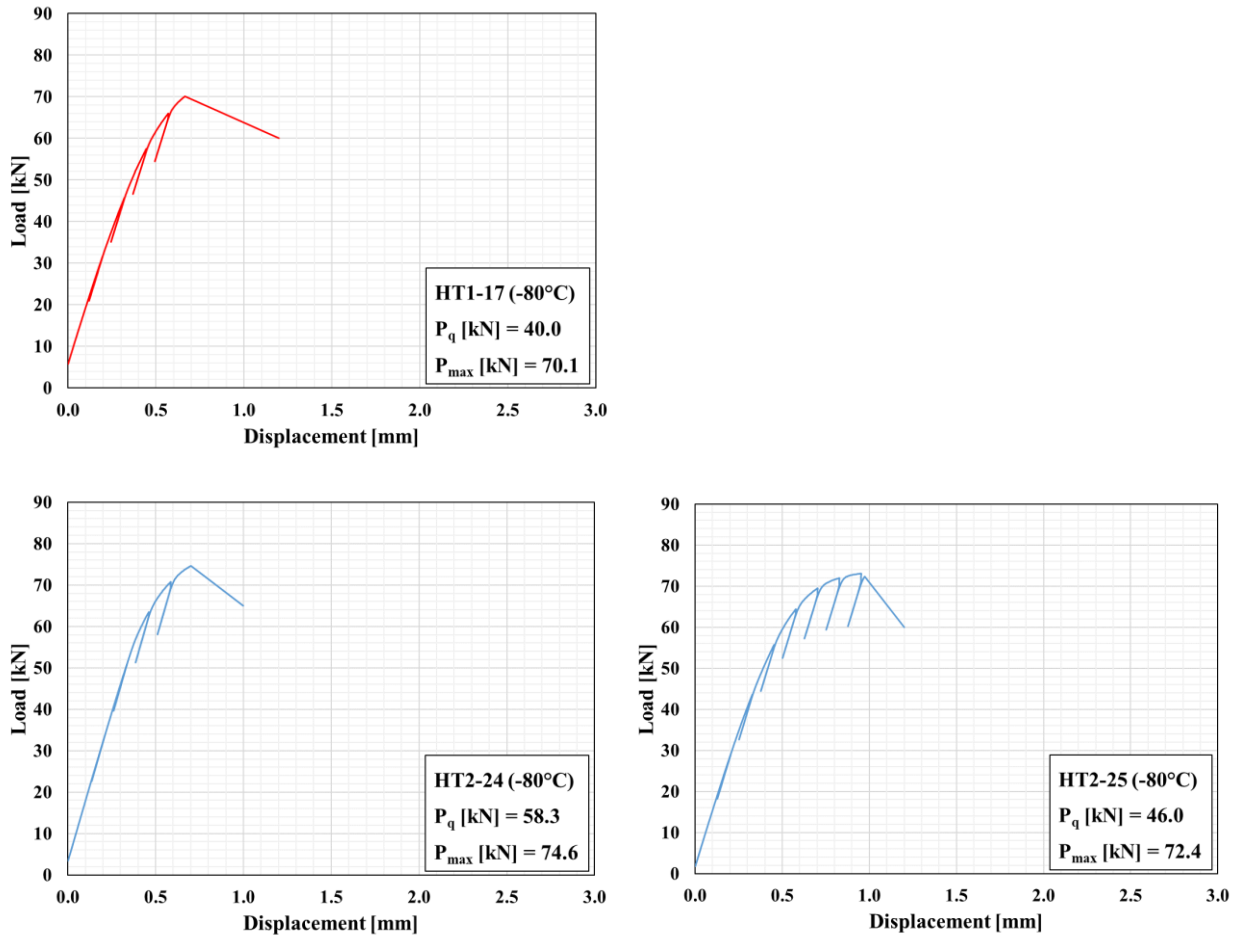

Figure 4.61 Load-displacement curves of Fracture Toughness tests for HT1 and HT2 conditions tested at -80°C.

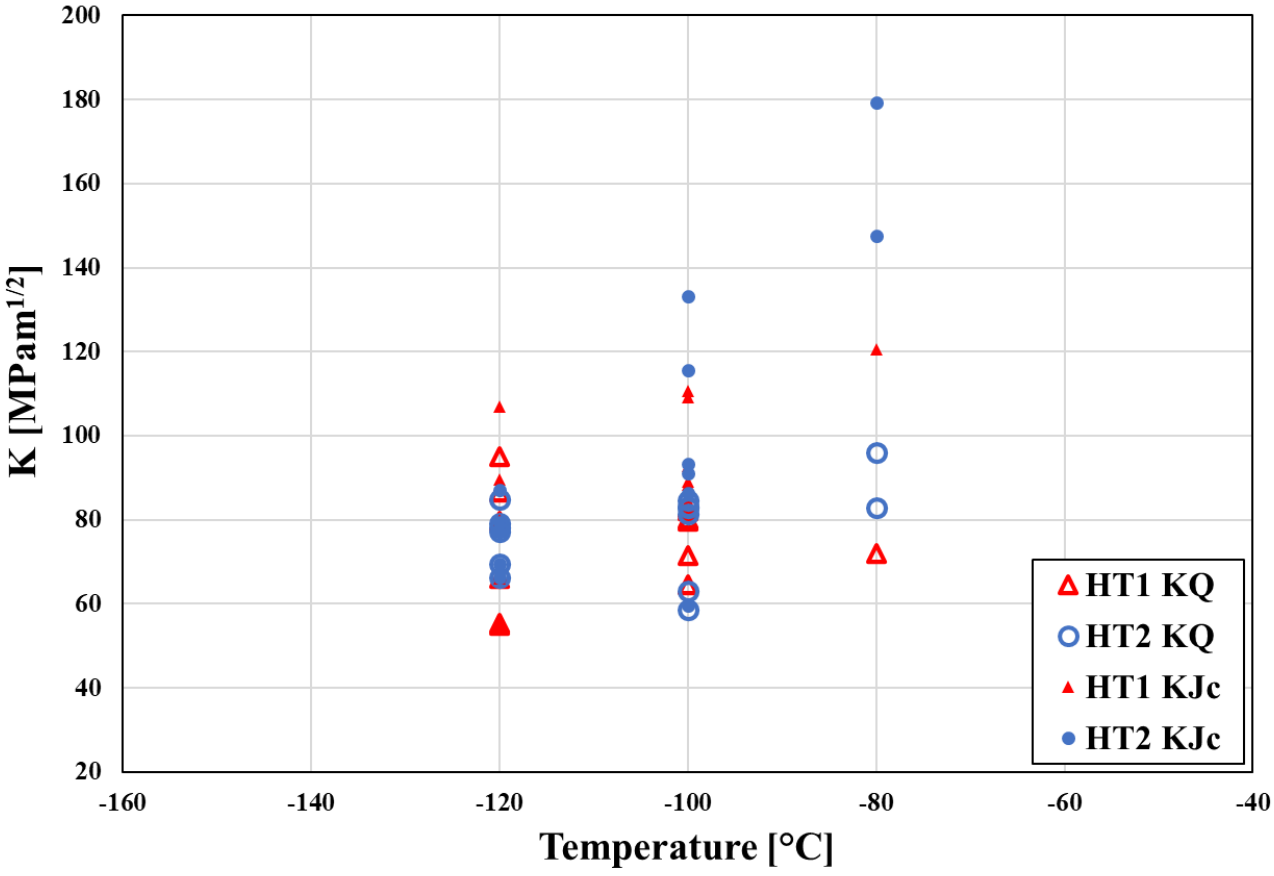

Figure 4.62 Plots of K_Q and K_{Jc} values of Fracture Toughness tests for HT1 and HT2 conditions at various temperatures.

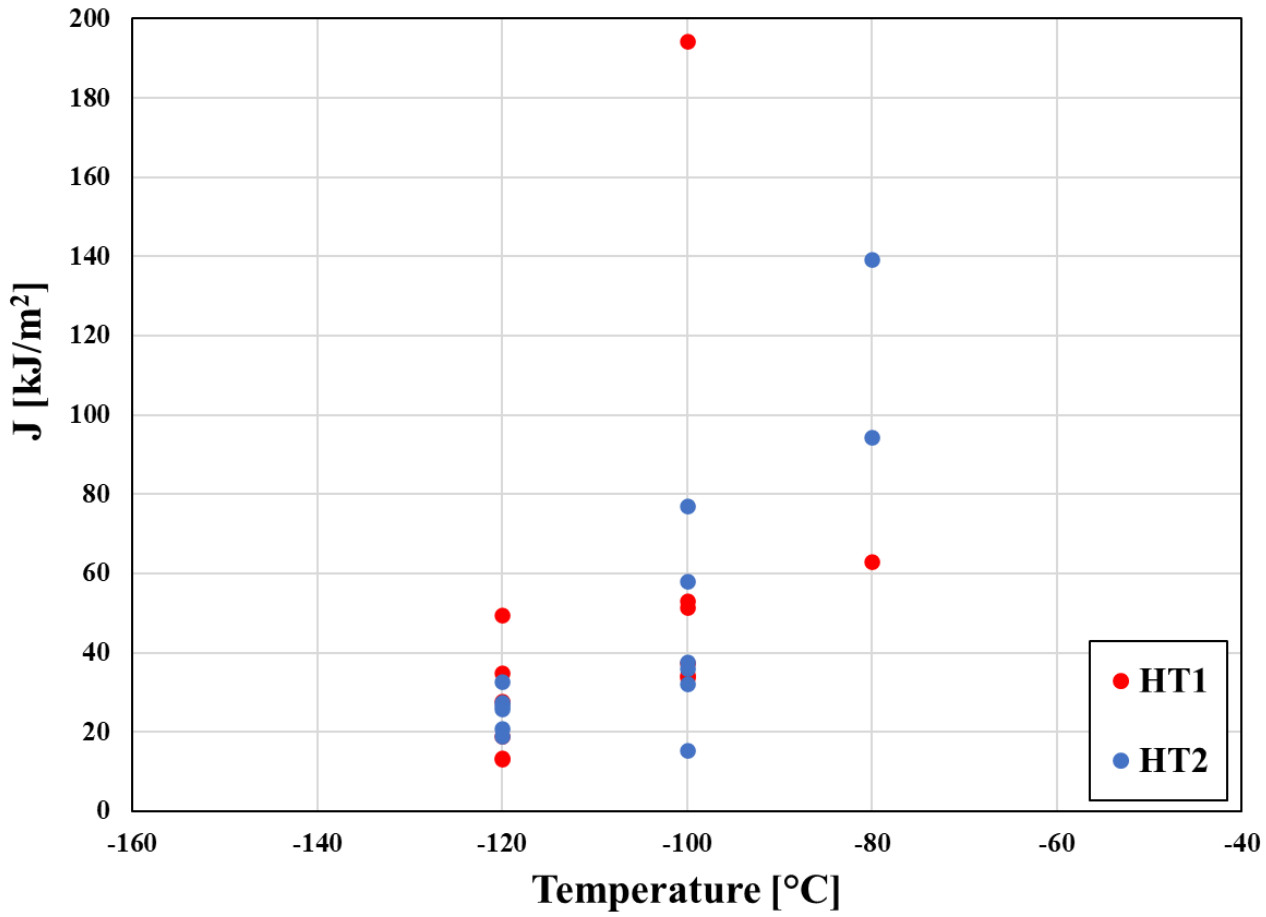

Figure 4.63 Plots of J_c values of Fracture Toughness tests for HT1 and HT2 conditions at various temperatures.

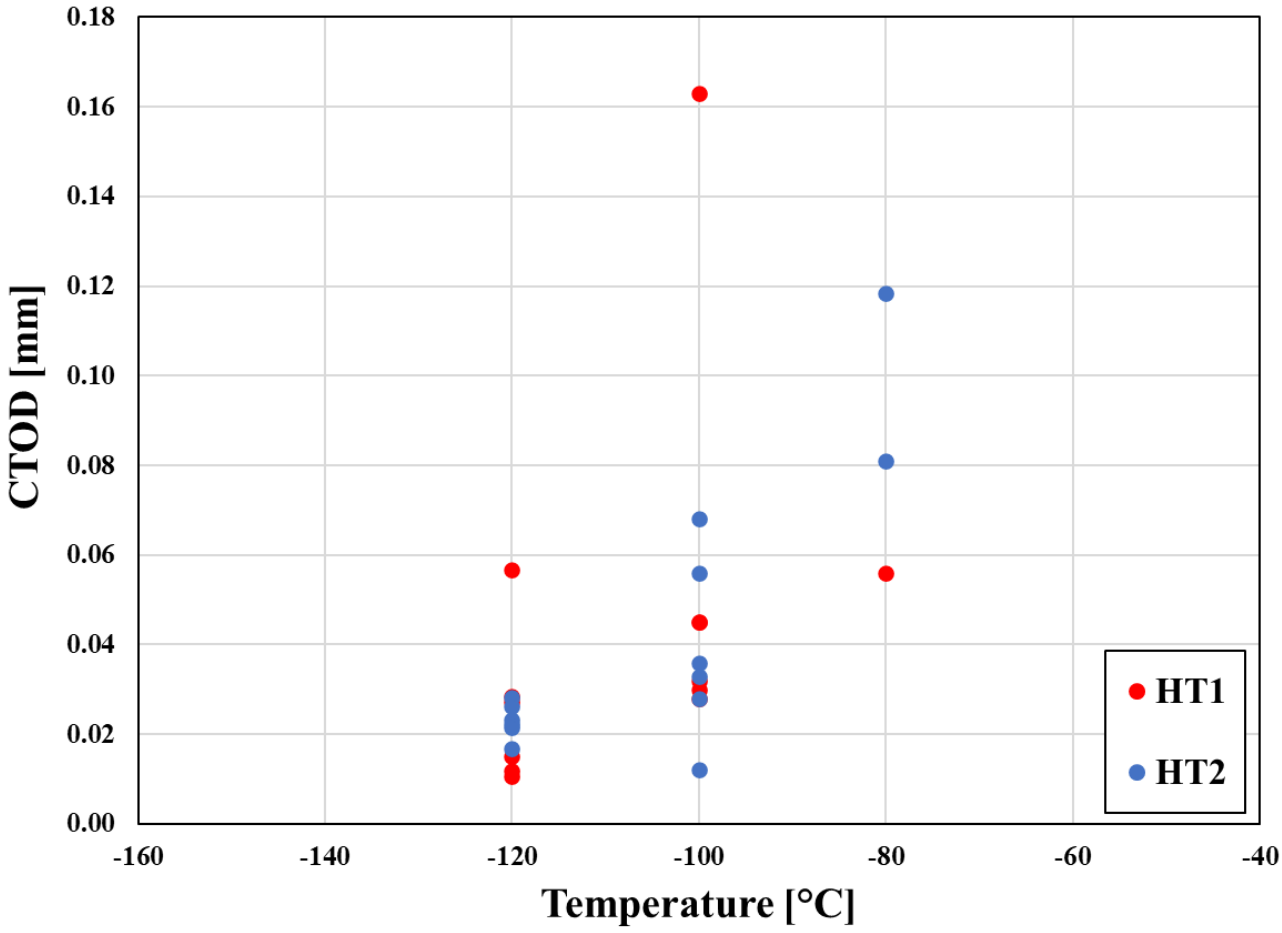

Figure 4.64 Plots of CTOD values of Fracture Toughness tests for HT1 and HT2 conditions at various temperatures.

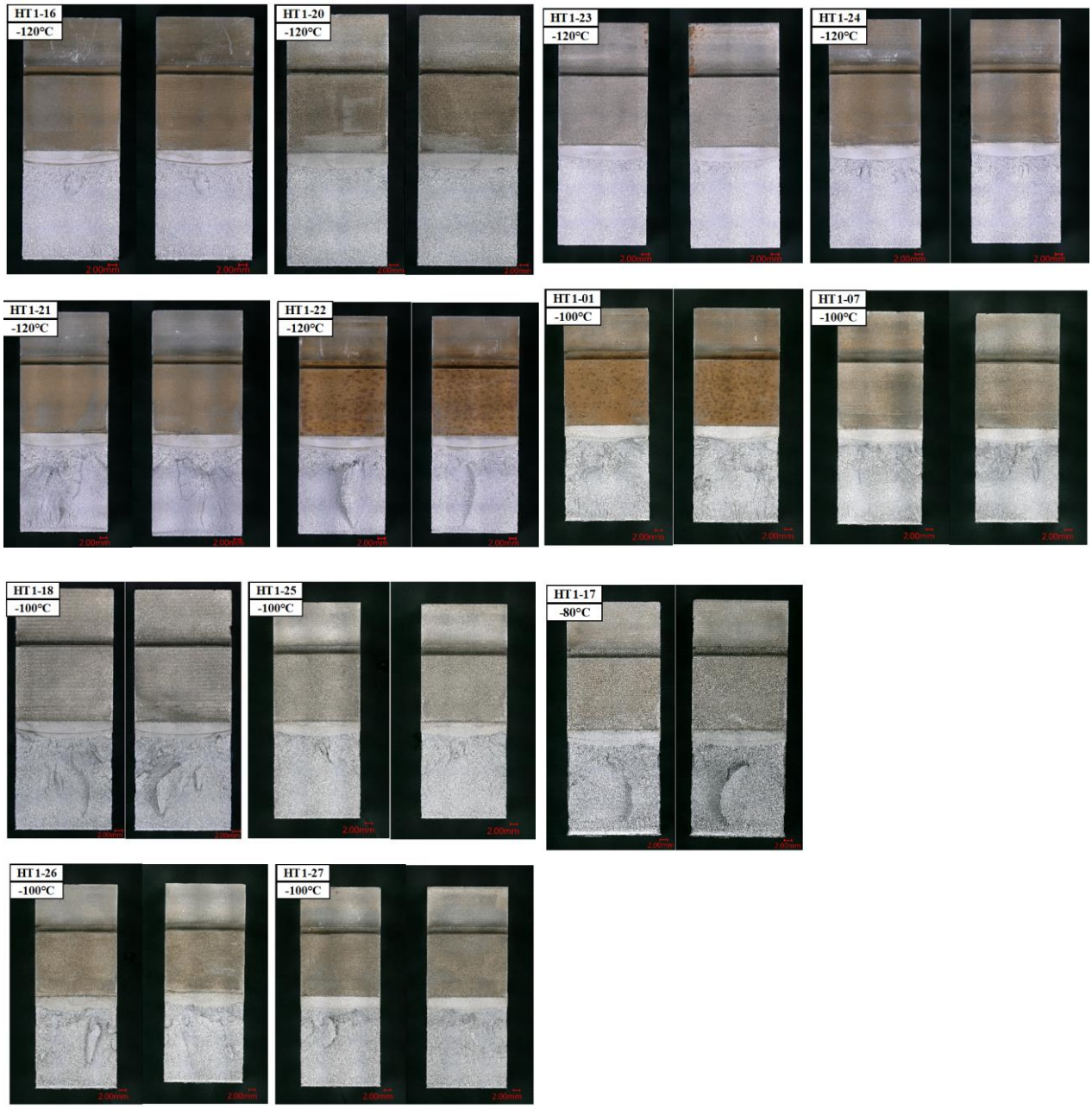

Figure 4.65 Fracture surfaces of Fracture Toughness tests for HT1 condition under optical microscope.

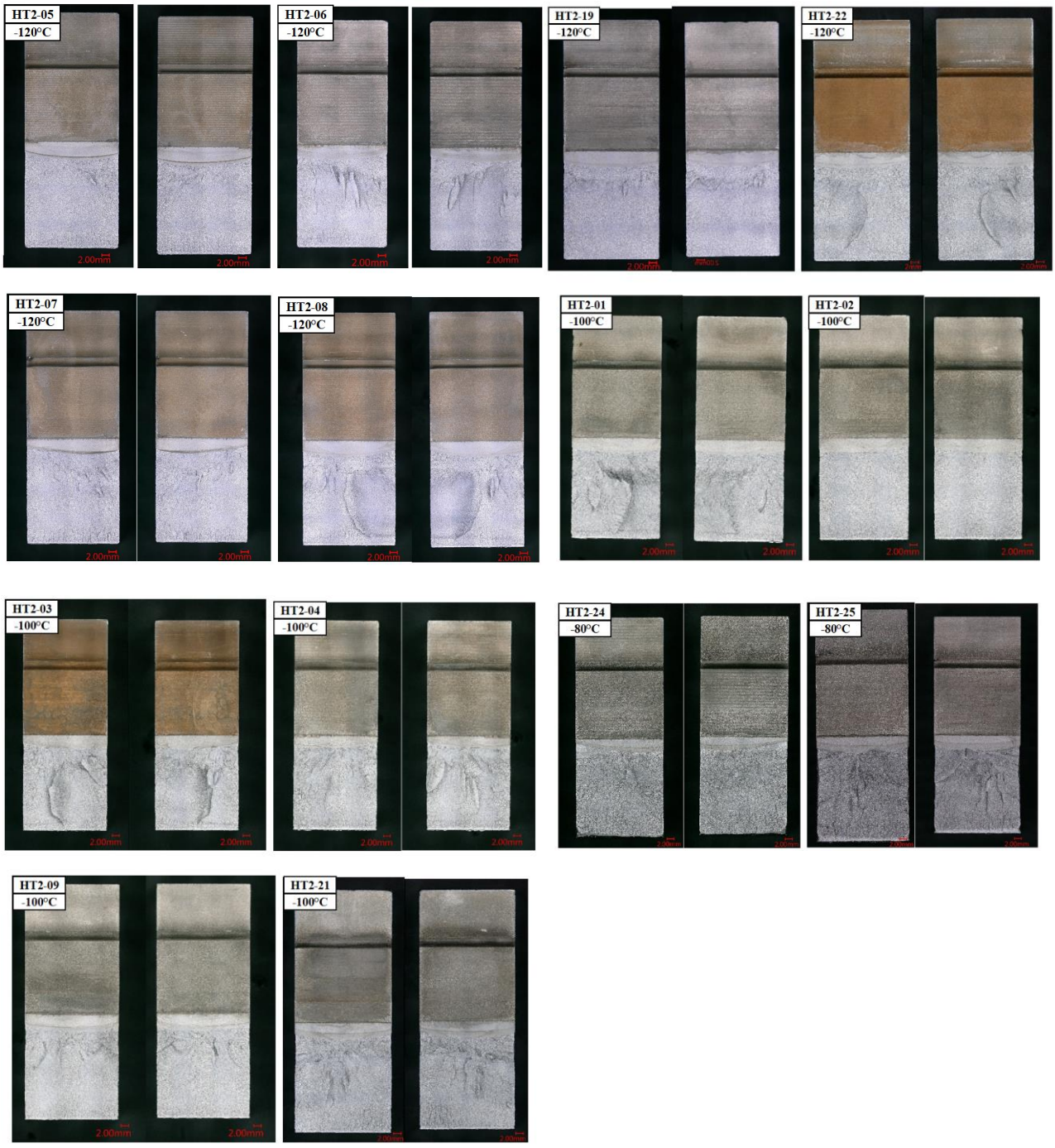

Figure 4.66 Fracture surfaces of Fracture Toughness tests for HT2 condition under optical microscope.

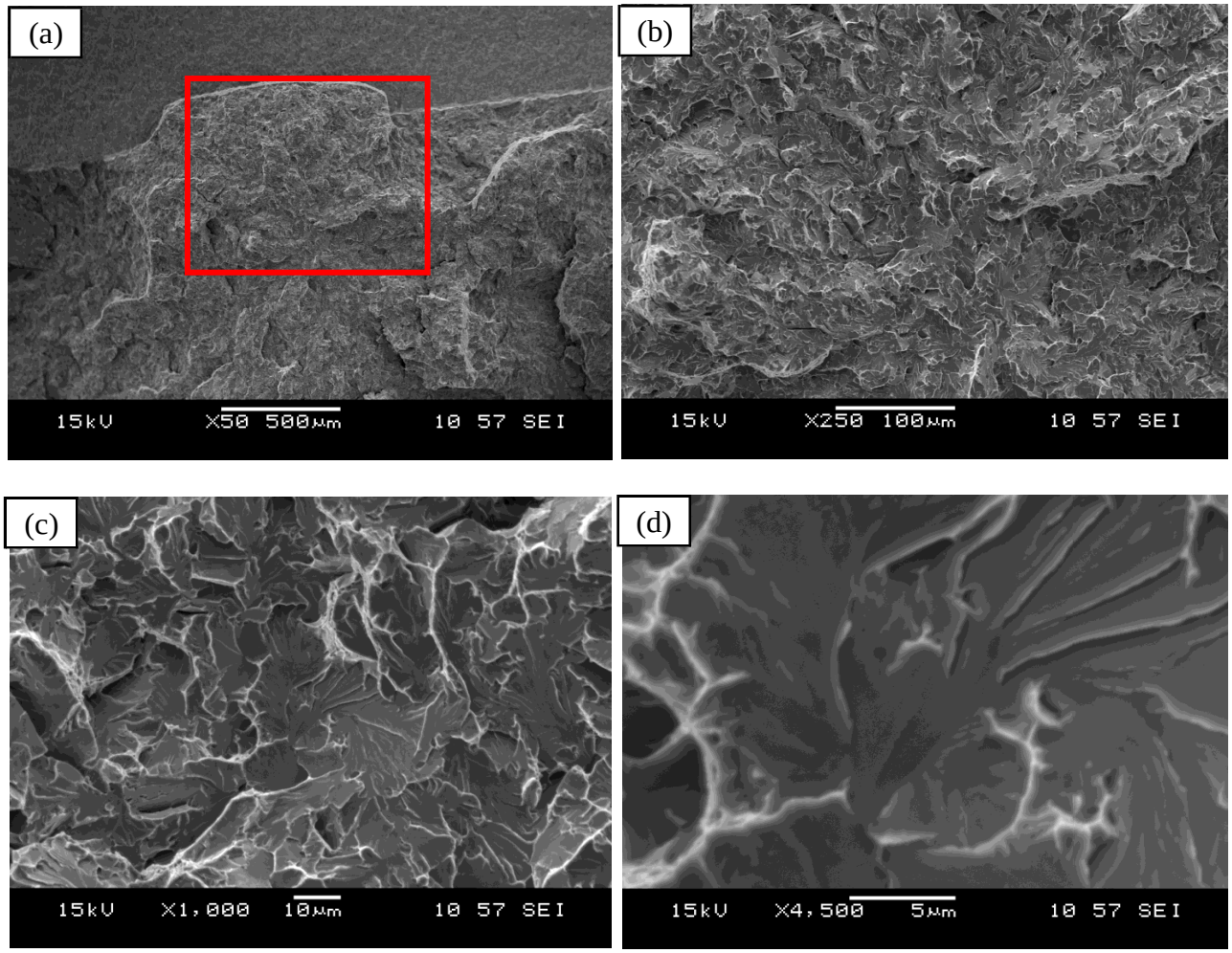

Figure 4.67 Fracture initiation site from one fractured half (A) of fracture toughness specimen HT1-CT-21 tested at -120 °C, (a) (b) (c) (d) in the sequence of magnification.

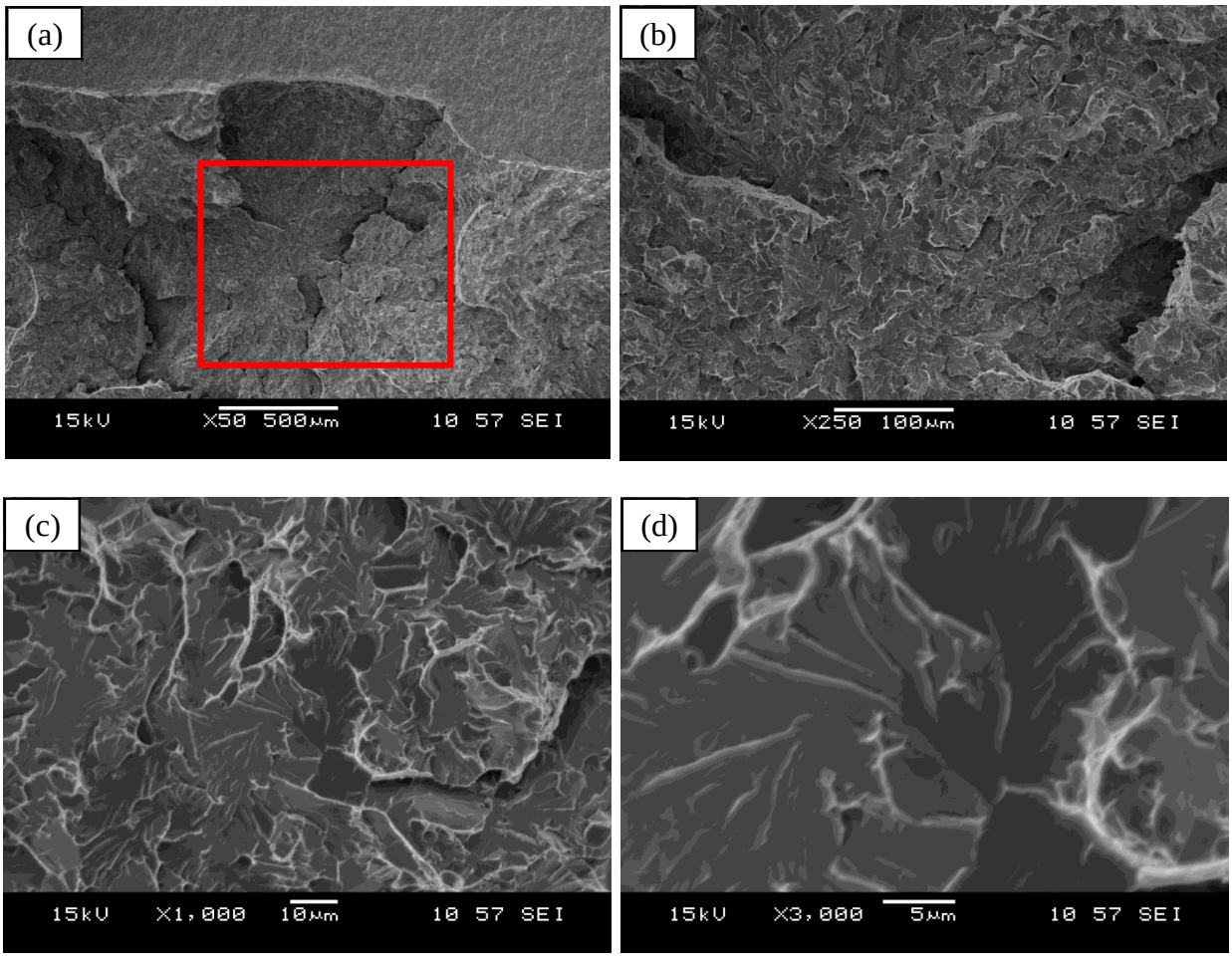

Figure 4.68 Fracture initiation site from the opposite fractured half (B) of fracture toughness specimen HT1-CT-21 tested at -120 °C, (a) (b) (c) (d) in the sequence of magnification.

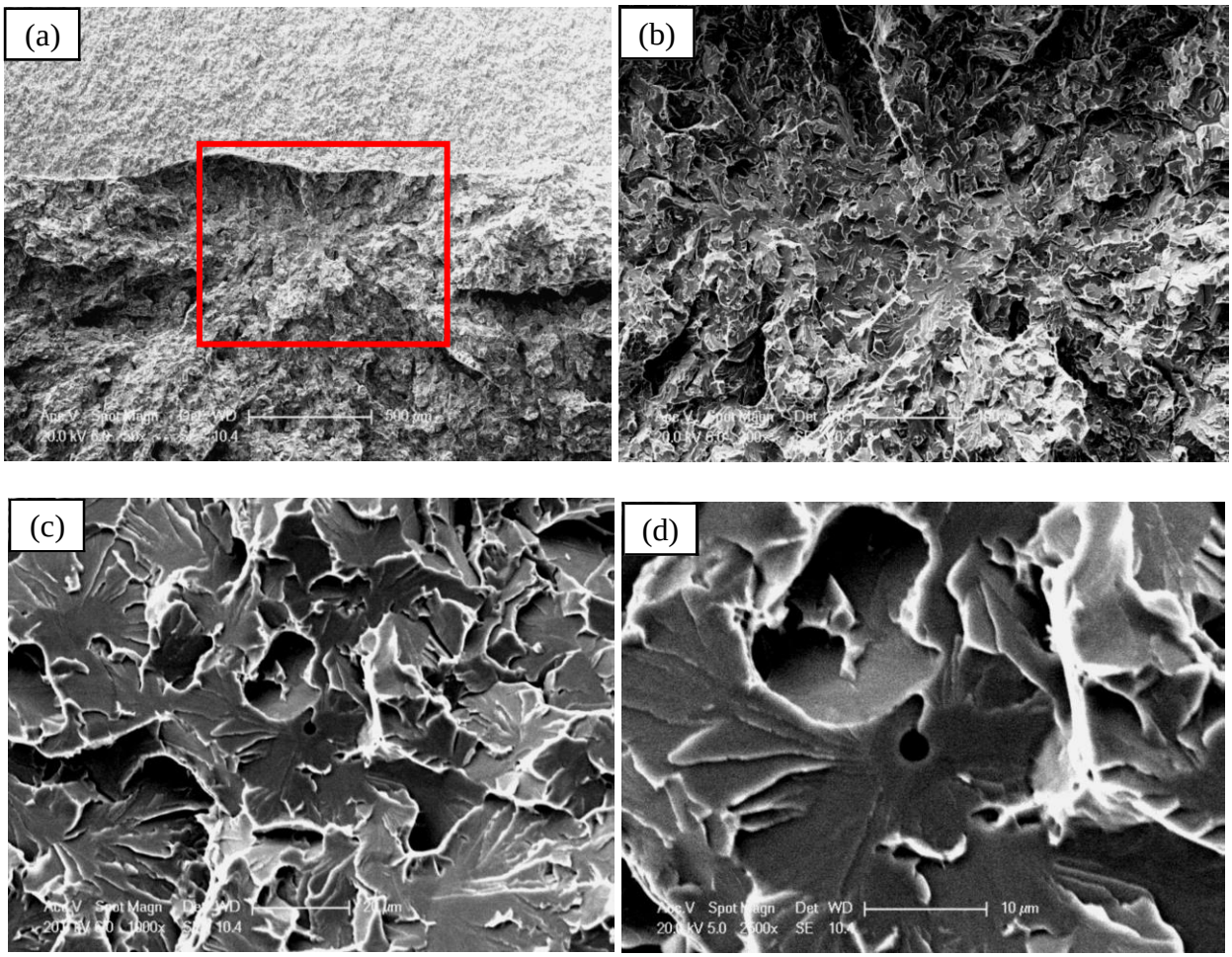

Figure 4.69 Fracture initiation site from one fractured half (A) of fracture toughness specimen HT2-CT-05 tested at -120 °C, (a) (b) (c) (d) in the sequence of magnification.

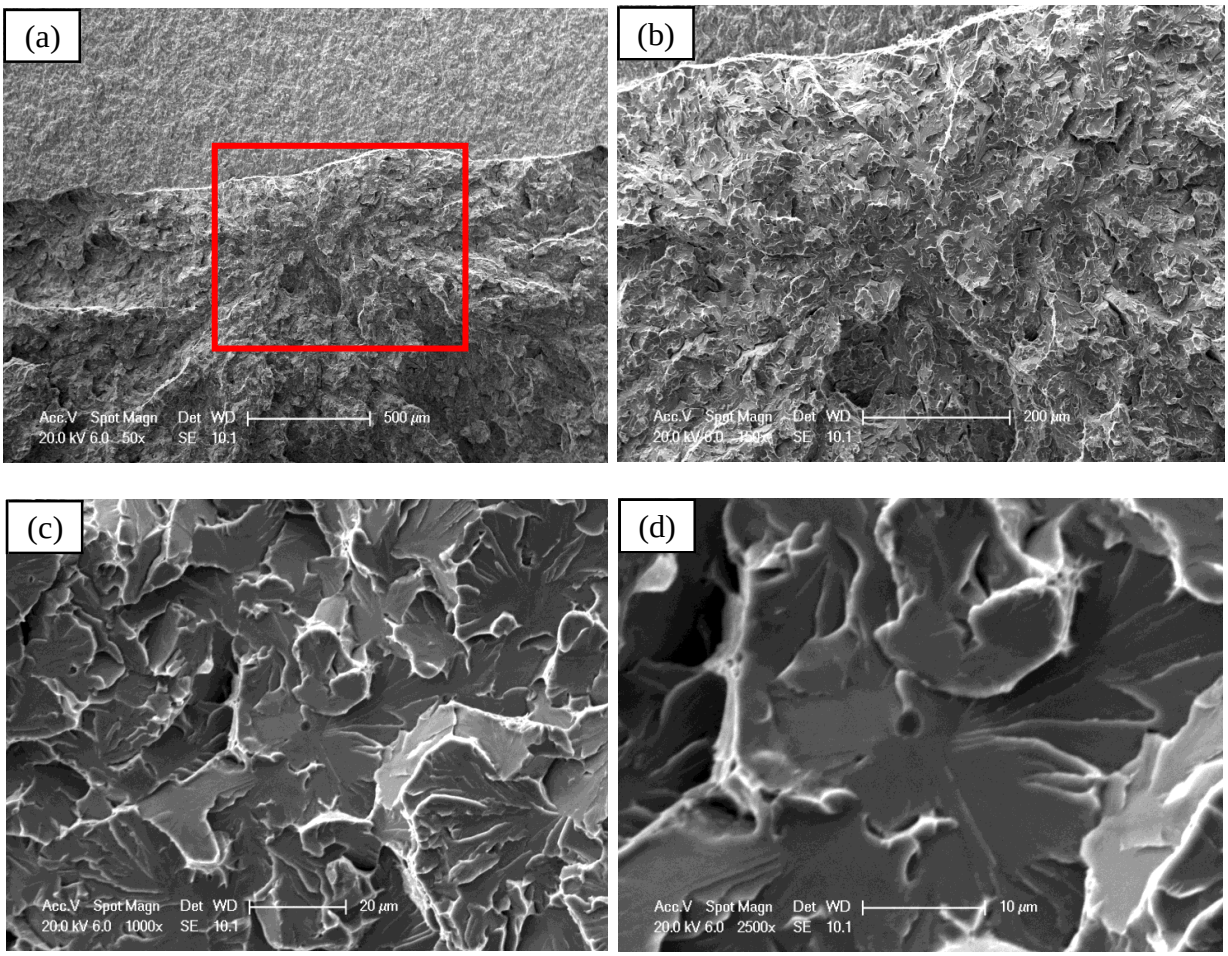

Figure 4.70 Fracture initiation site from the opposite fractured half (B) of fracture toughness specimen HT2-CT-05 tested at -120 °C, (a) (b) (c) (d) in the sequence of magnification.

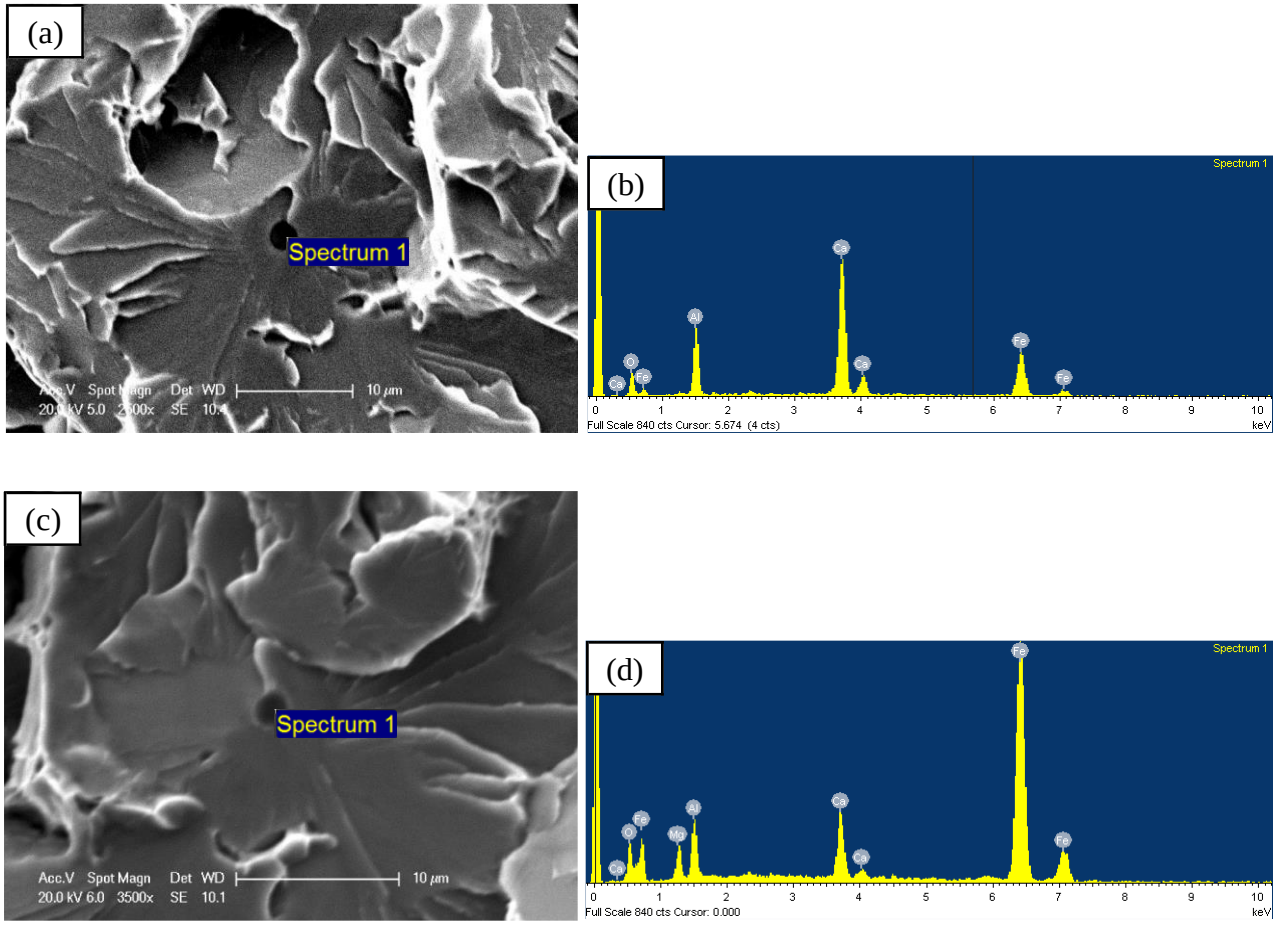

Figure 4.71 Cleavage initiation (a) (c) site of fracture stress specimen HT2-CT-05 tested at -120 °C with (b) (d) the corresponding EDX spectrum.

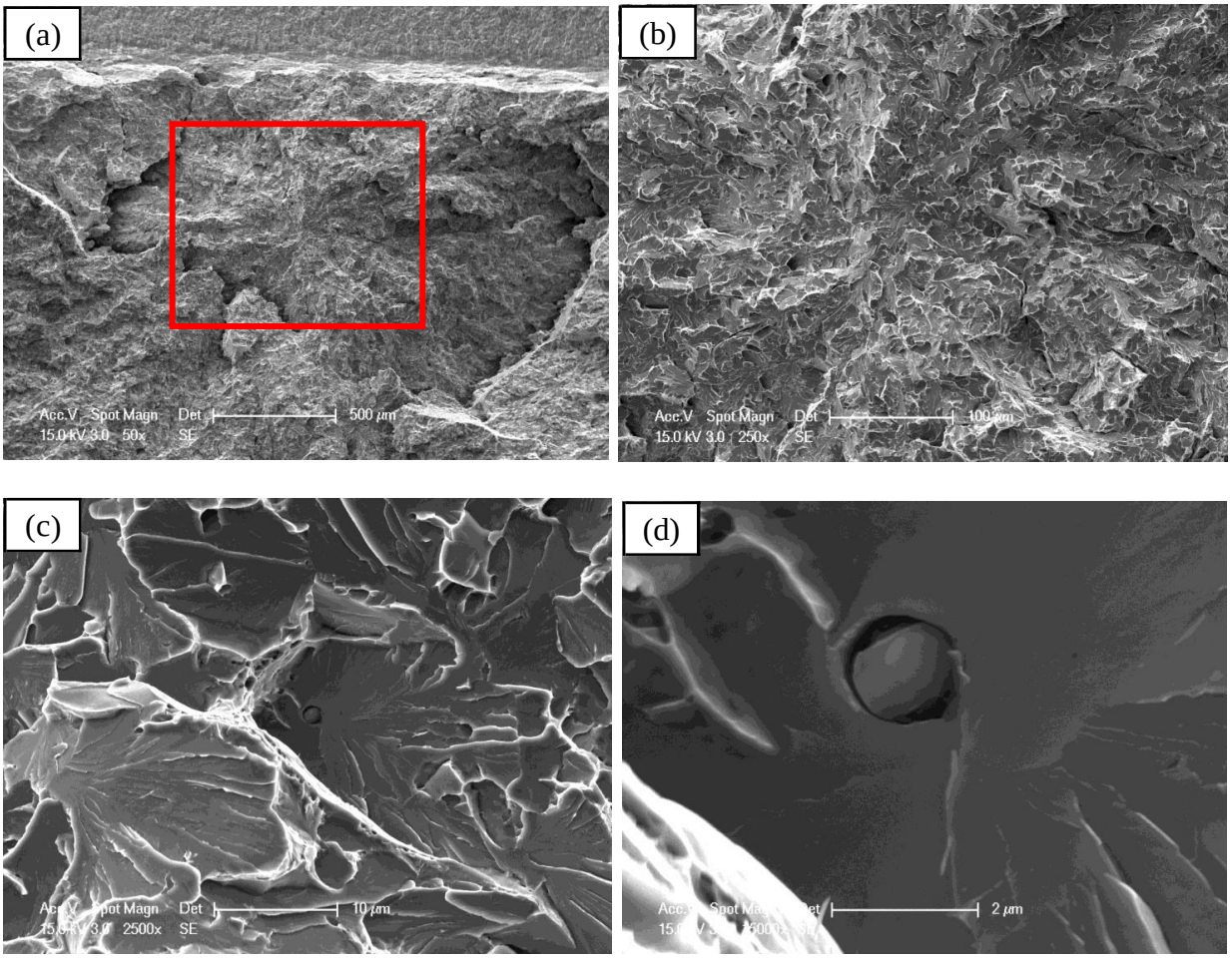

Figure 4.72 Fracture initiation site from one fractured half (A) of fracture toughness specimen HT1-CT-01 tested at -100 °C, (a) (b) (c) (d) in the sequence of magnification.

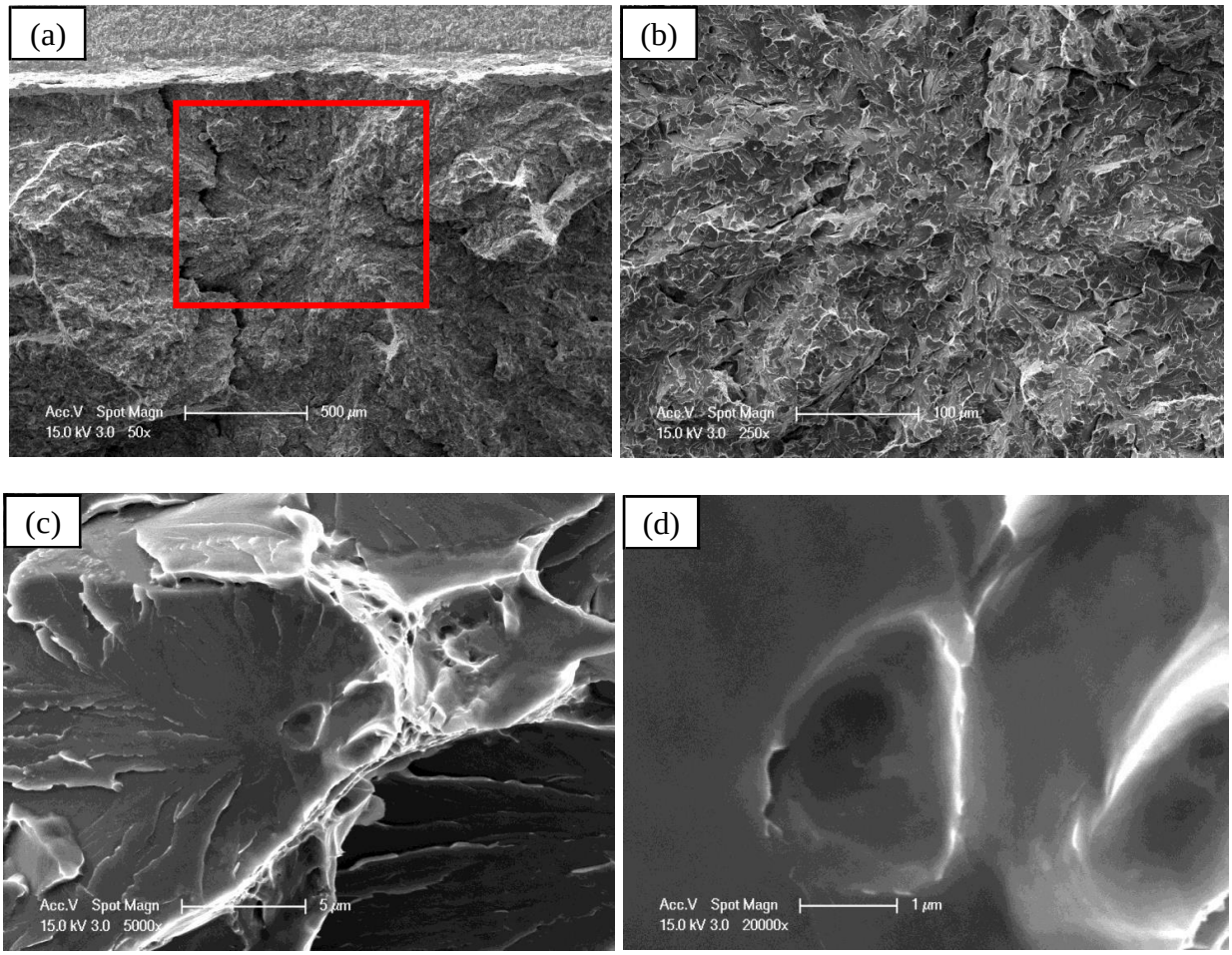

Figure 4.73 Fracture initiation site from the opposite fractured half (B) of fracture toughness specimen HT1-CT-01 tested at -100 °C, (a) (b) (c) (d) in the sequence of magnification.

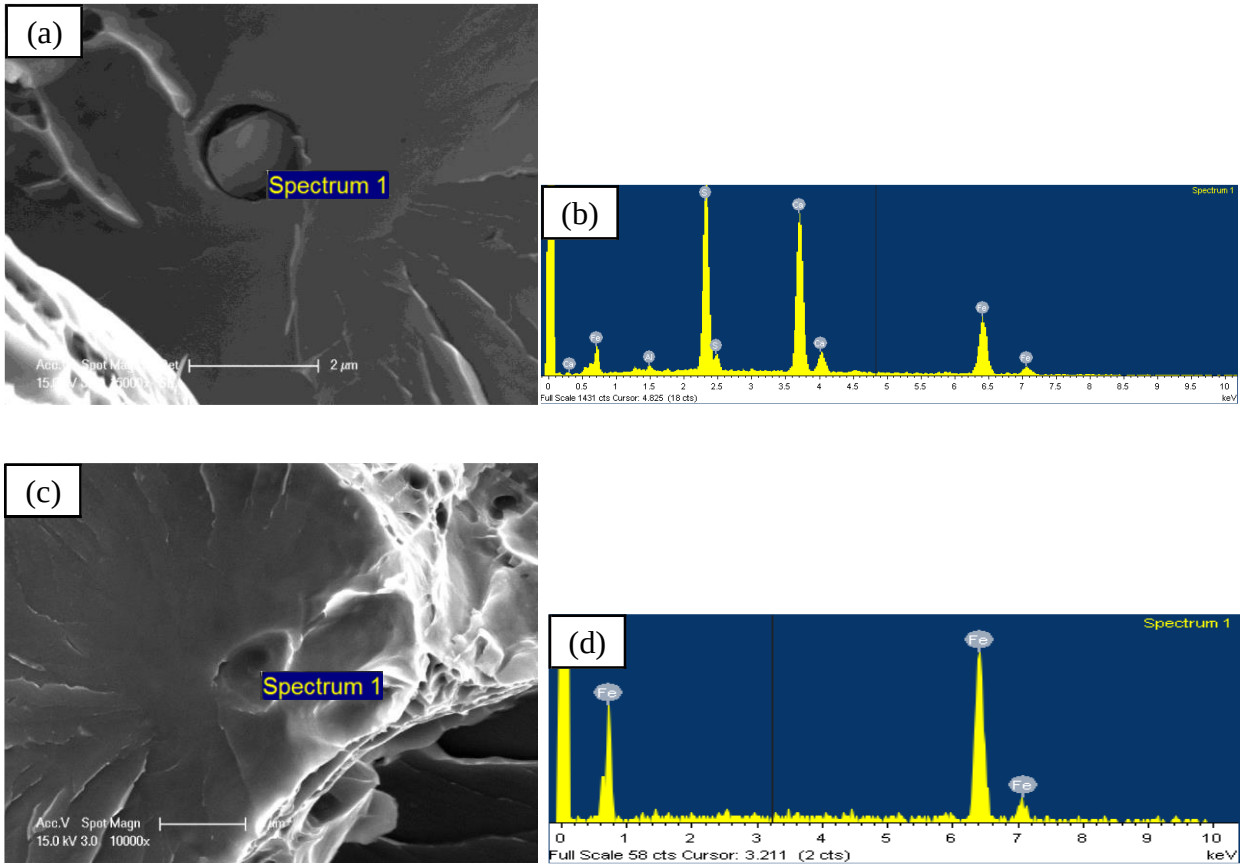

Figure 4.74 Cleavage initiation (a) (c) site of fracture stress specimen HT1-CT-01 tested at -100 °C with (b) (d) the corresponding EDX spectrum.

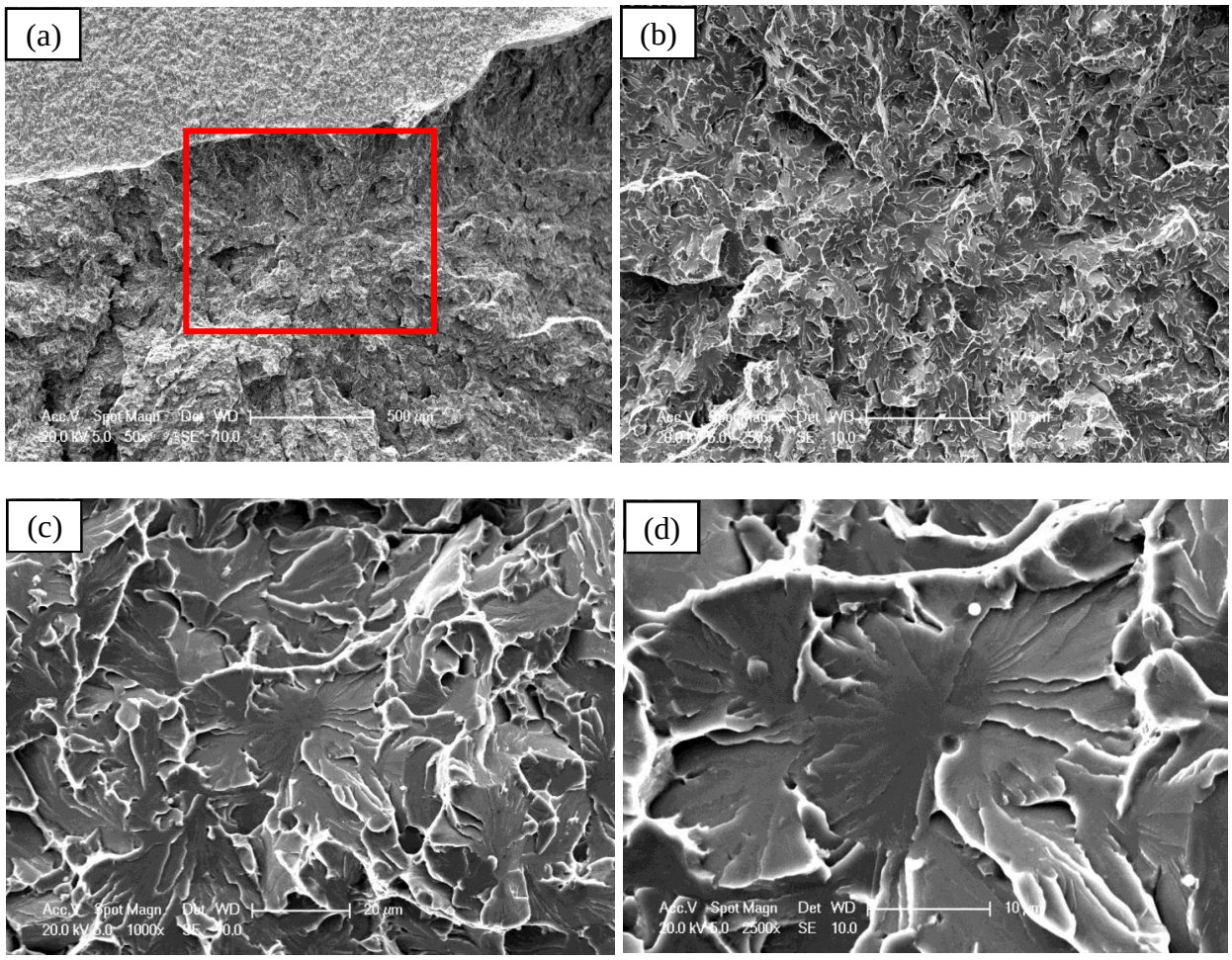

Figure 4.75 Fracture initiation site from one fractured half (A) of fracture toughness specimen HT1-CT-18 tested at -100 °C, (a) (b) (c) (d) in the sequence of magnification.

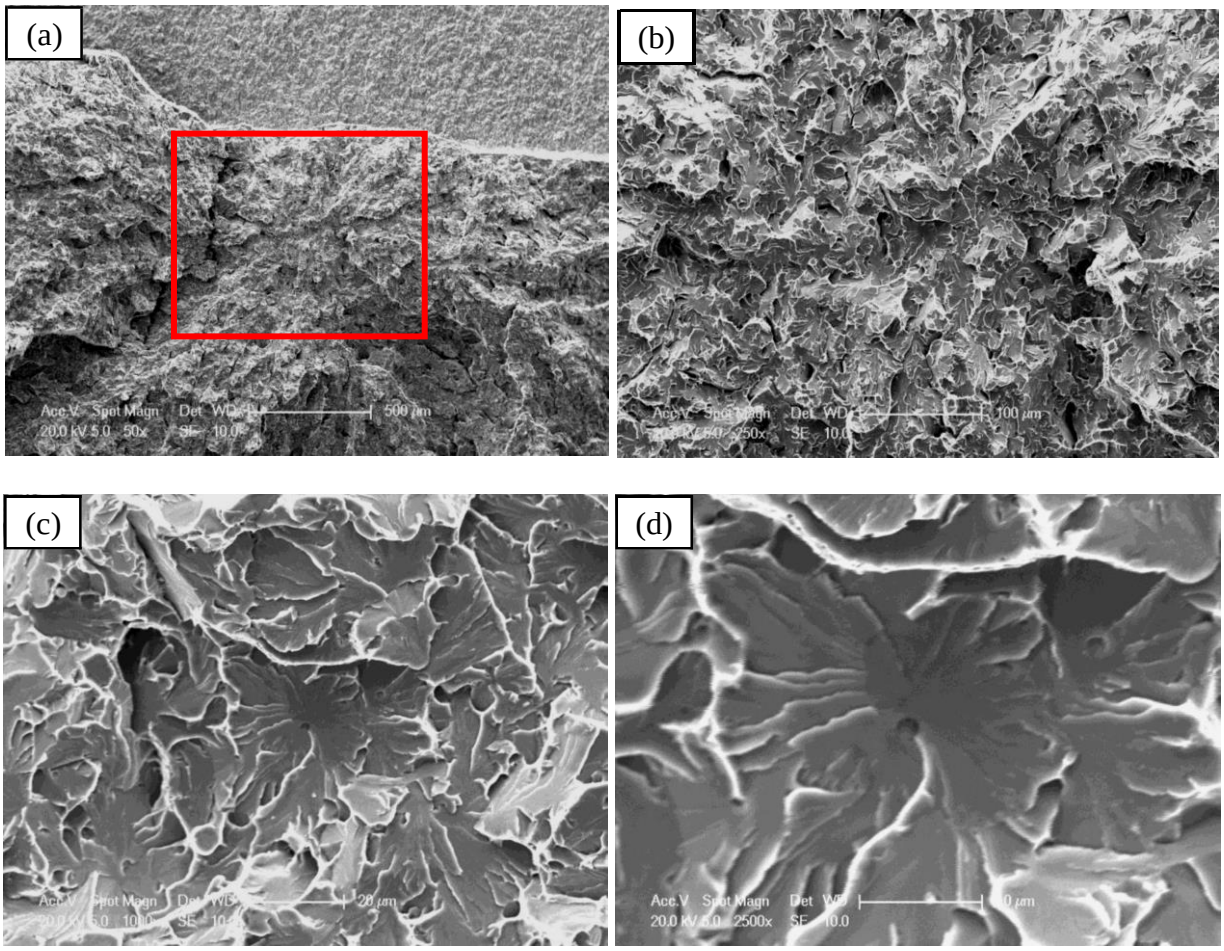

Figure 4.76 Fracture initiation site from the opposite fractured half (B) of fracture toughness specimen HT1-CT-18 tested at -100 °C, (a) (b) (c) (d) in the sequence of magnification.

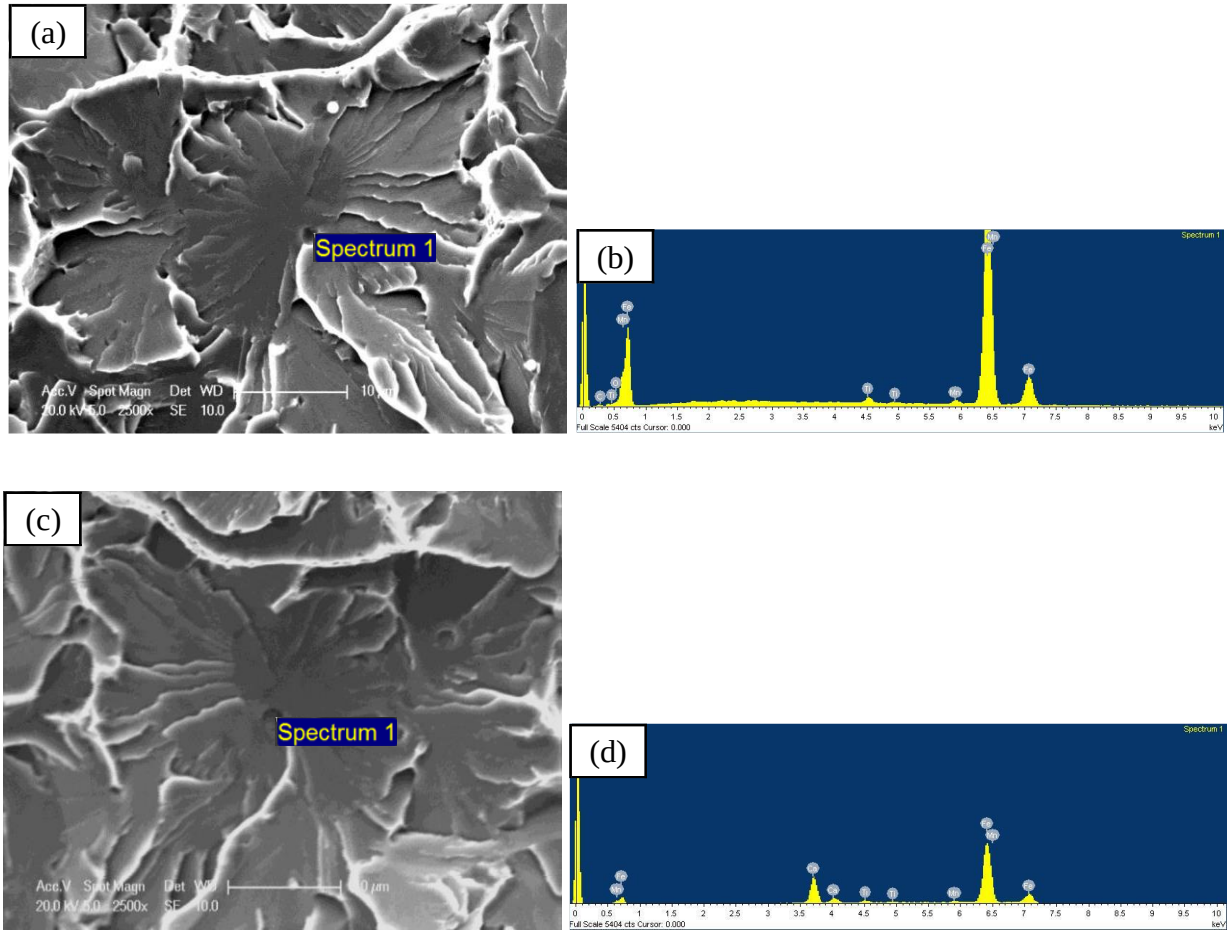

Figure 4.77 Cleavage initiation (a) (c) site of fracture stress specimen HT1-CT-18 tested at -100 °C with (b) (d) the corresponding EDX spectrum.

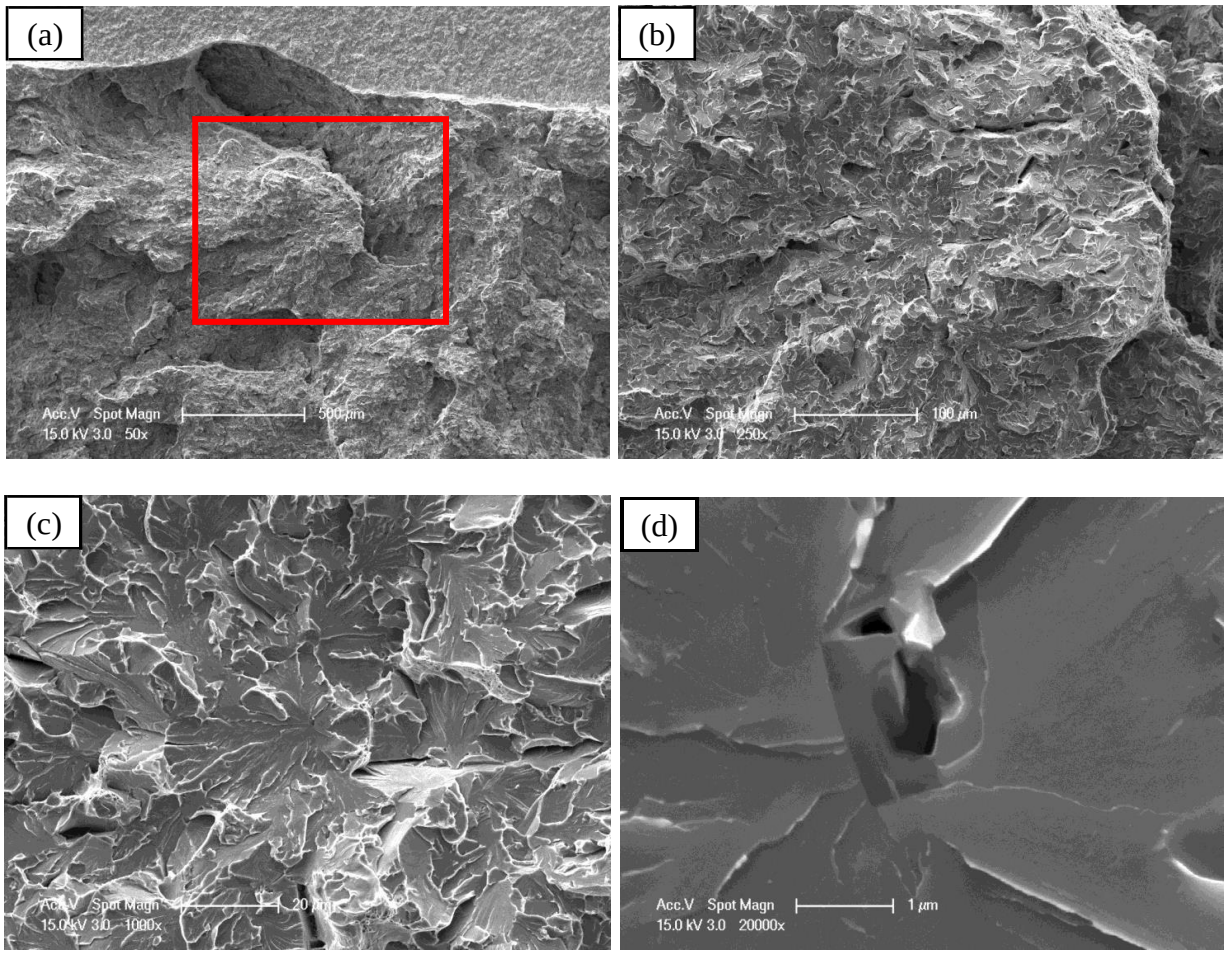

Figure 4.78 Fracture initiation site from one fractured half (A) of fracture toughness specimen HT2-CT-01 tested at -100 °C, (a) (b) (c) (d) in the sequence of magnification.

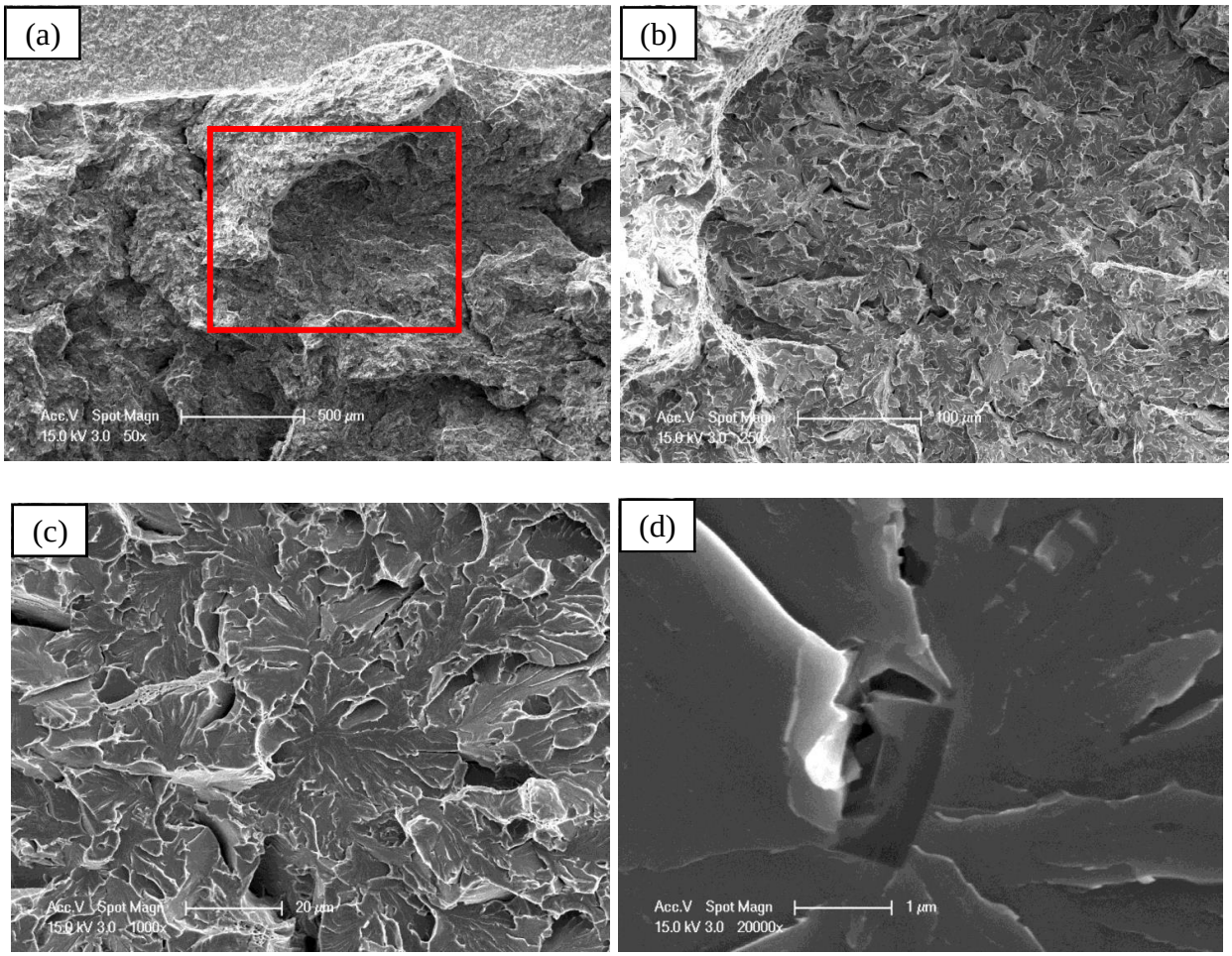

Figure 4.79 Fracture initiation site from the opposite fractured half (B) of fracture toughness specimen HT2-CT-01 tested at -100 °C, (a) (b) (c) (d) in the sequence of magnification.

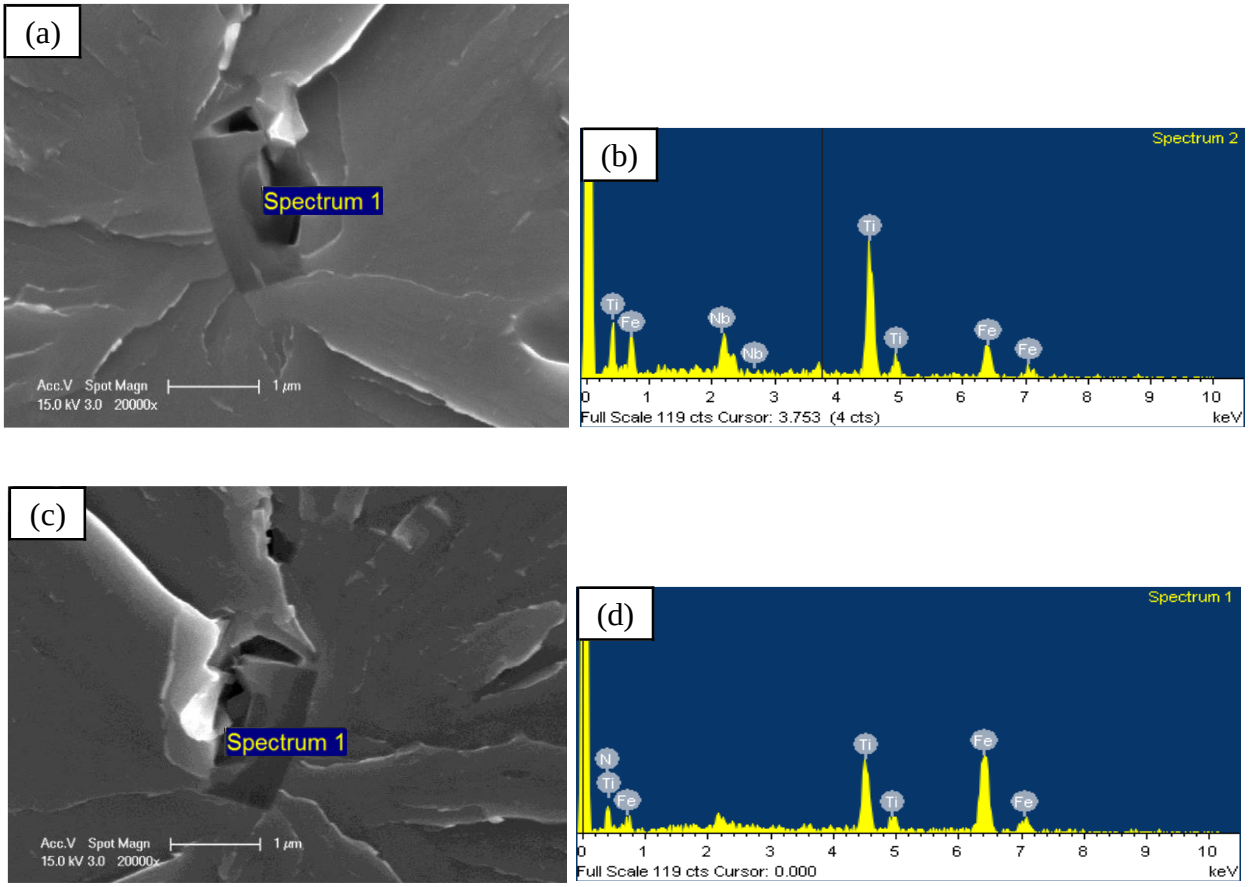

Figure 4.80 Cleavage initiation (a) (c) site of fracture stress specimen HT2-CT-01 tested at -100 °C with (b) (d) the corresponding EDX spectrum.

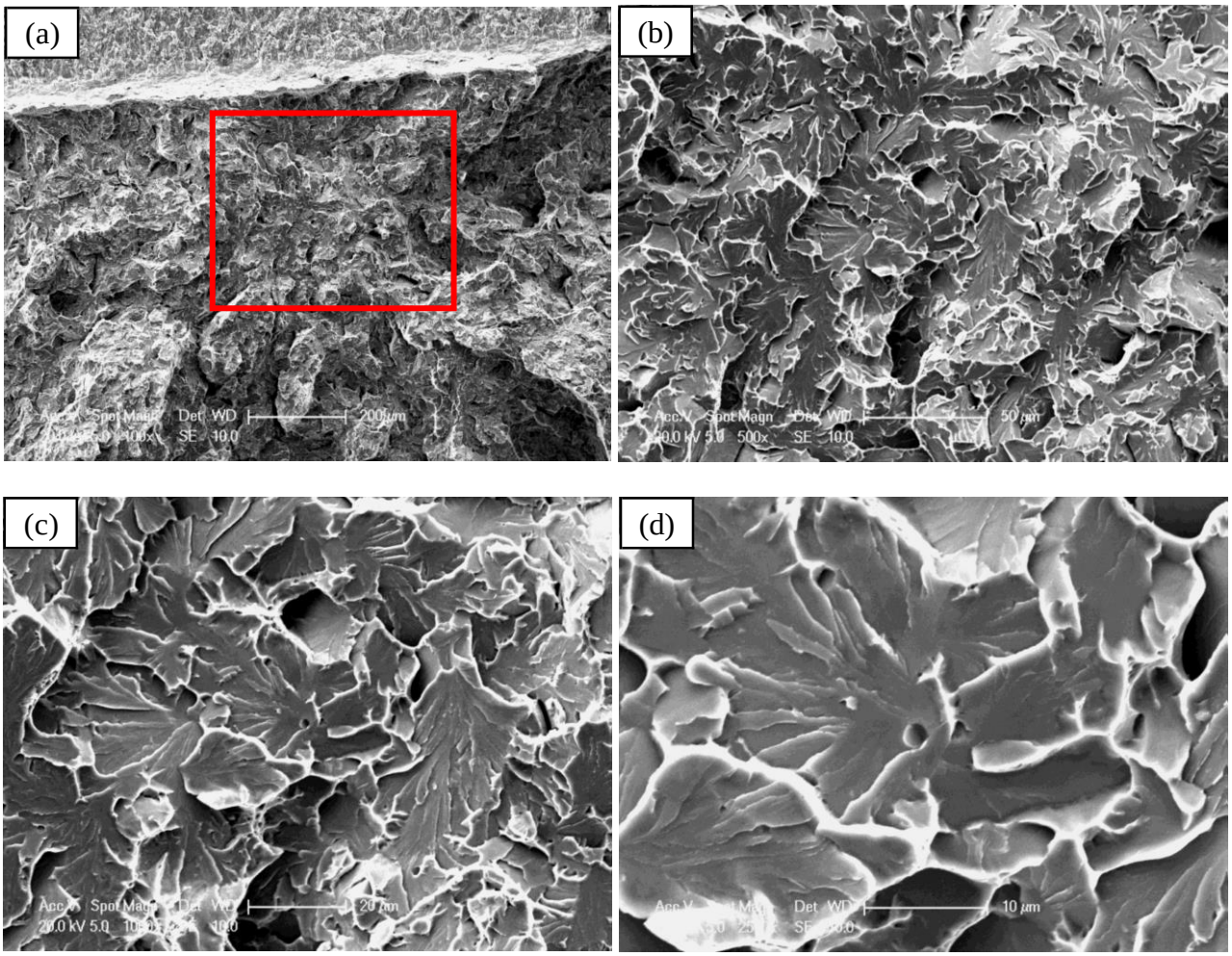

Figure 4.81 Fracture initiation site from one fractured half (A) of fracture toughness specimen HT1-CT-17 tested at -80 °C, (a) (b) (c) (d) in the sequence of magnification.

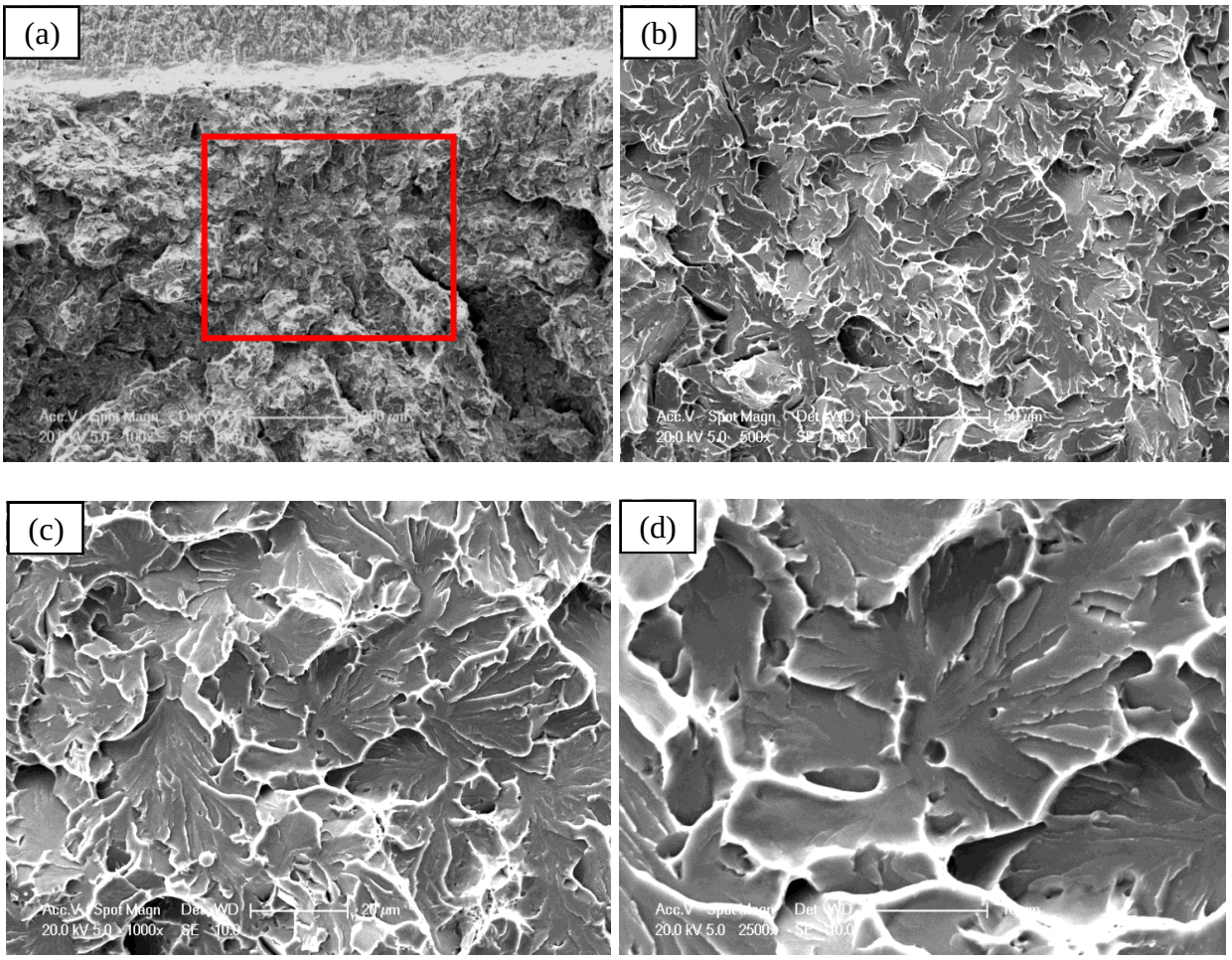

Figure 4.82 Fracture initiation site from the opposite fractured half (B) of fracture toughness specimen HT1-CT-17 tested at -80 °C, (a) (b) (c) (d) in the sequence of magnification.

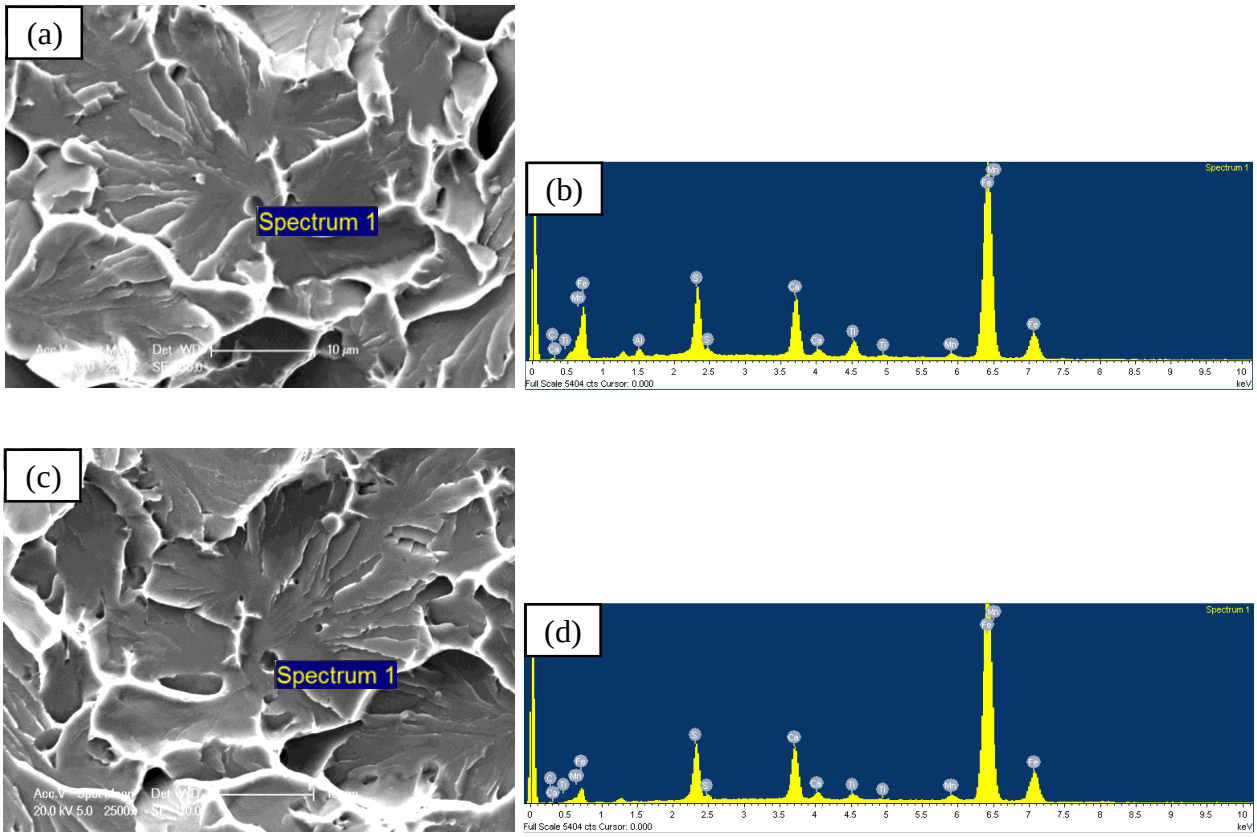

Figure 4.83 Cleavage initiation (a) (c) site of fracture stress specimen HT1-CT-17 tested at -80 °C with (b) (d) the corresponding EDX spectrum.

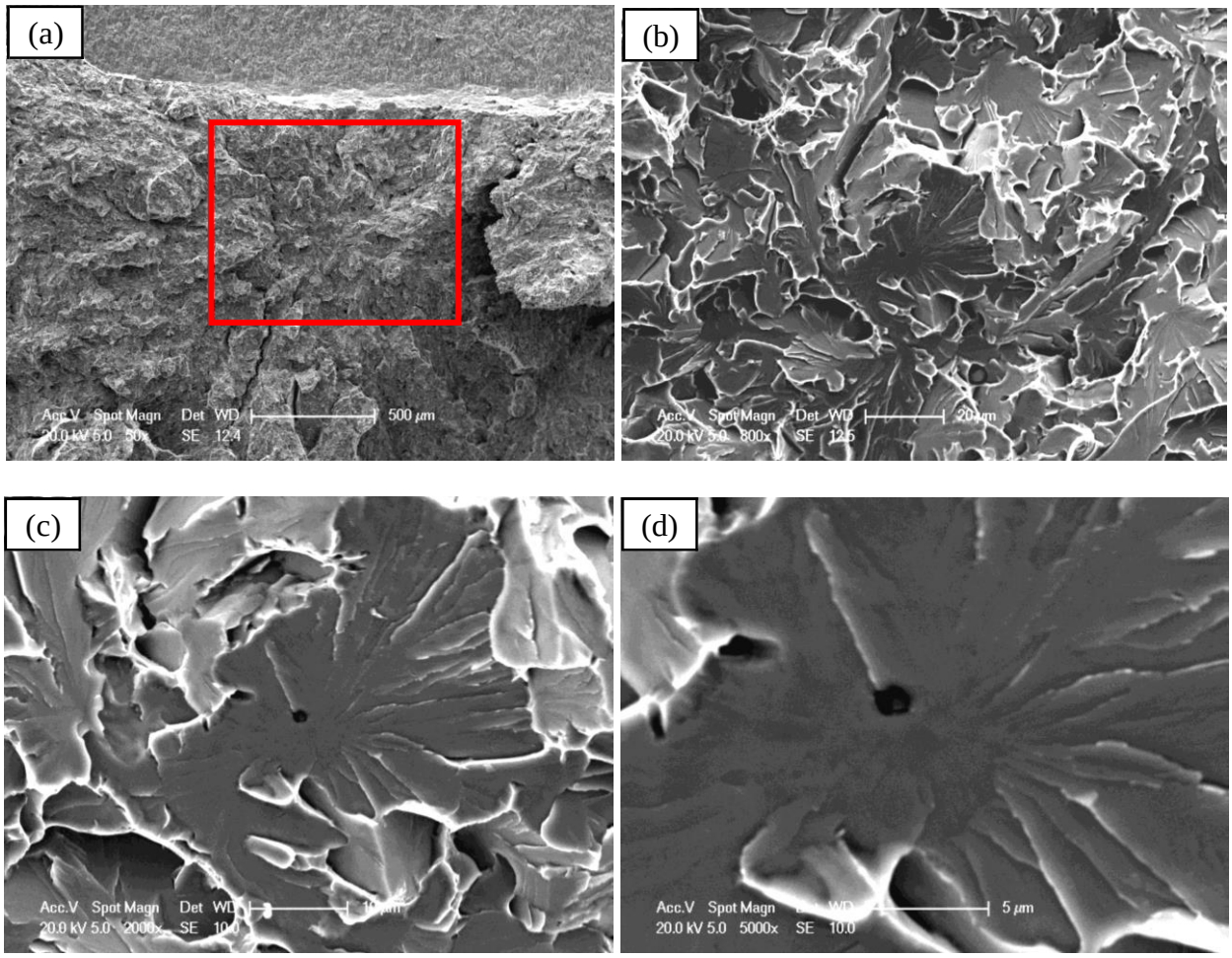

Figure 4.84 Fracture initiation site from one fractured half (A) of fracture toughness specimen HT2-CT-25 tested at -80 °C, (a) (b) (c) (d) in the sequence of magnification.

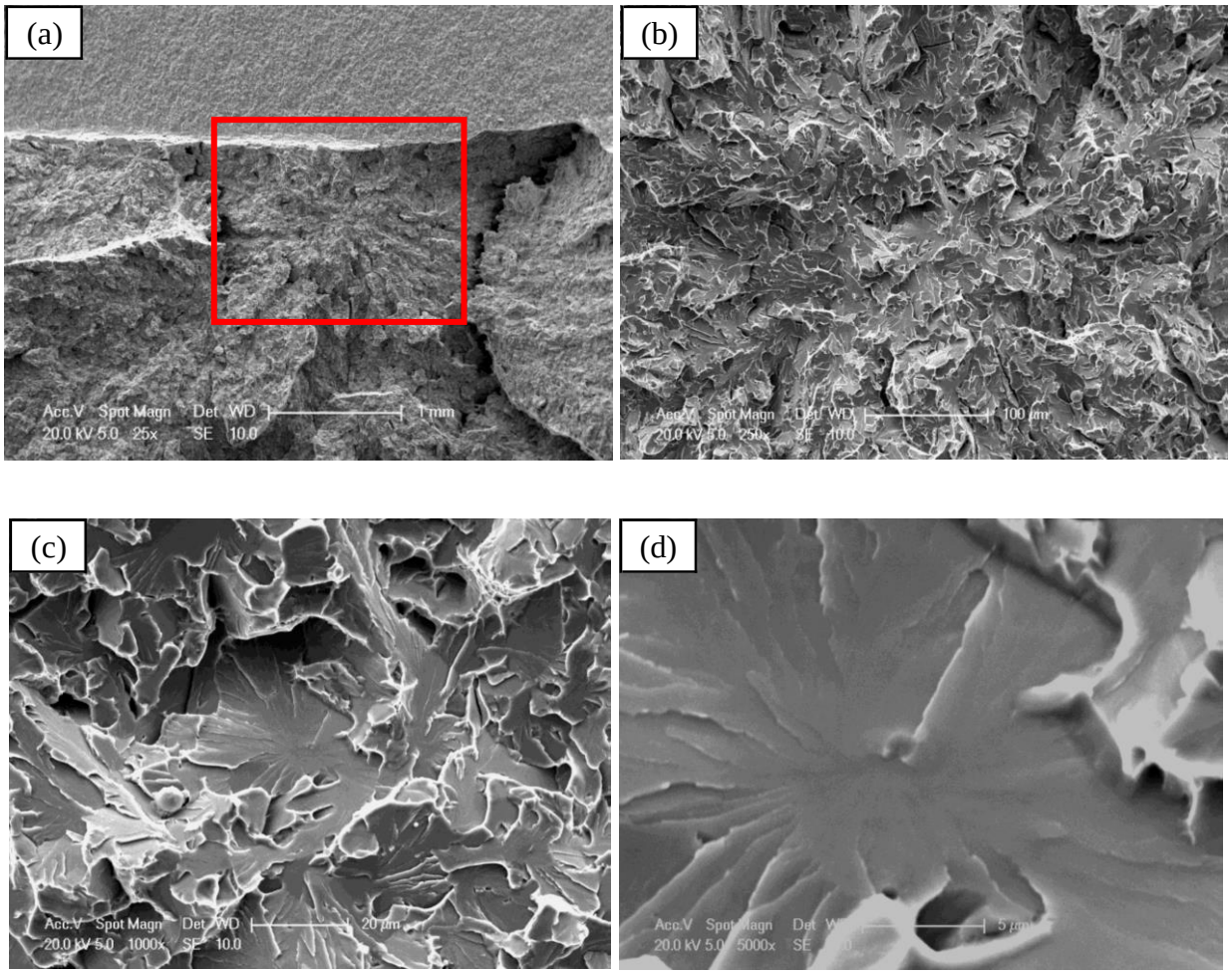

Figure 4.85 Fracture initiation site from the opposite fractured half (B) of fracture toughness specimen HT2-CT-25 tested at -80 °C, (a) (b) (c) (d) in the sequence of magnification.

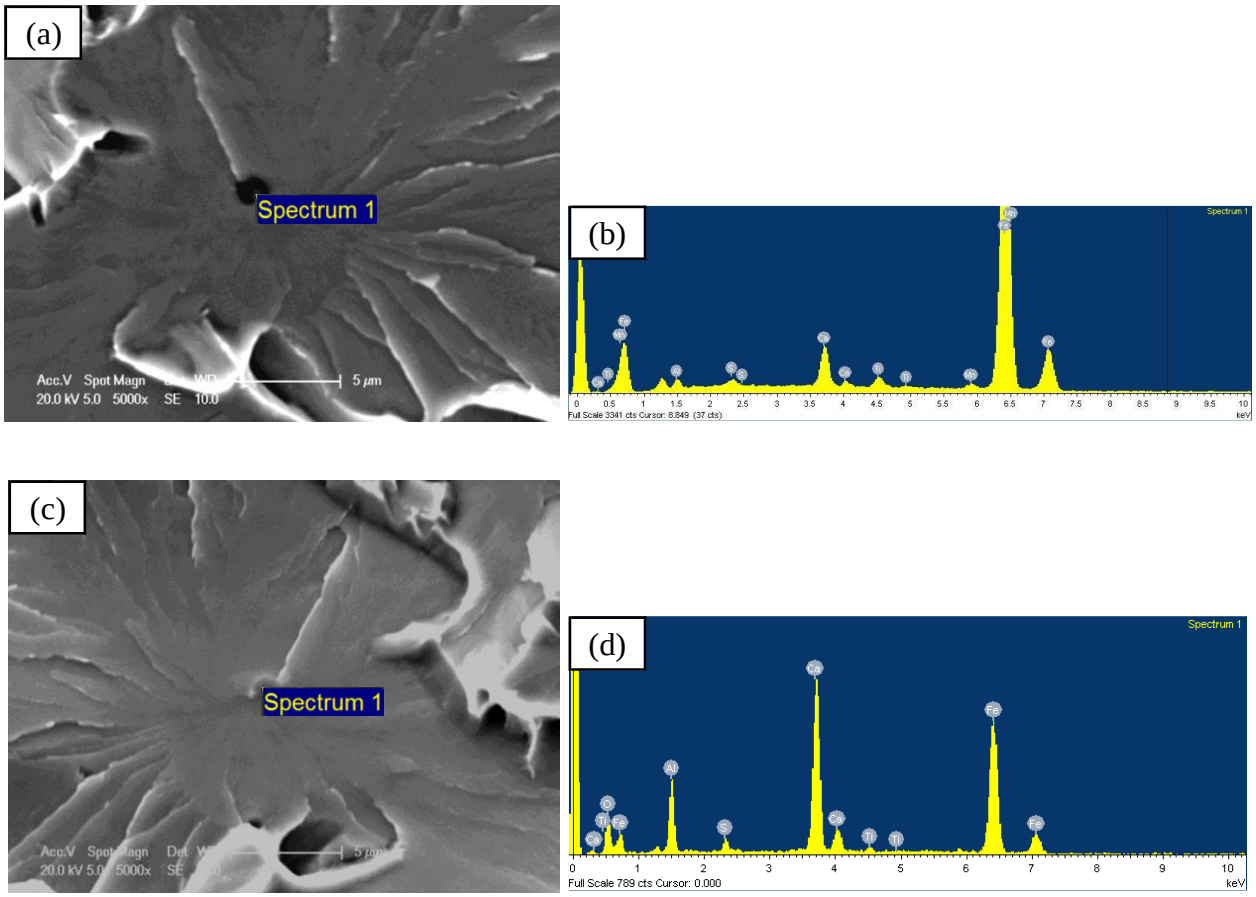

Figure 4.86 Cleavage initiation (a) (c) site of fracture stress specimen HT2-CT-25 tested at -80 °C with (b) (d) the corresponding EDX spectrum.

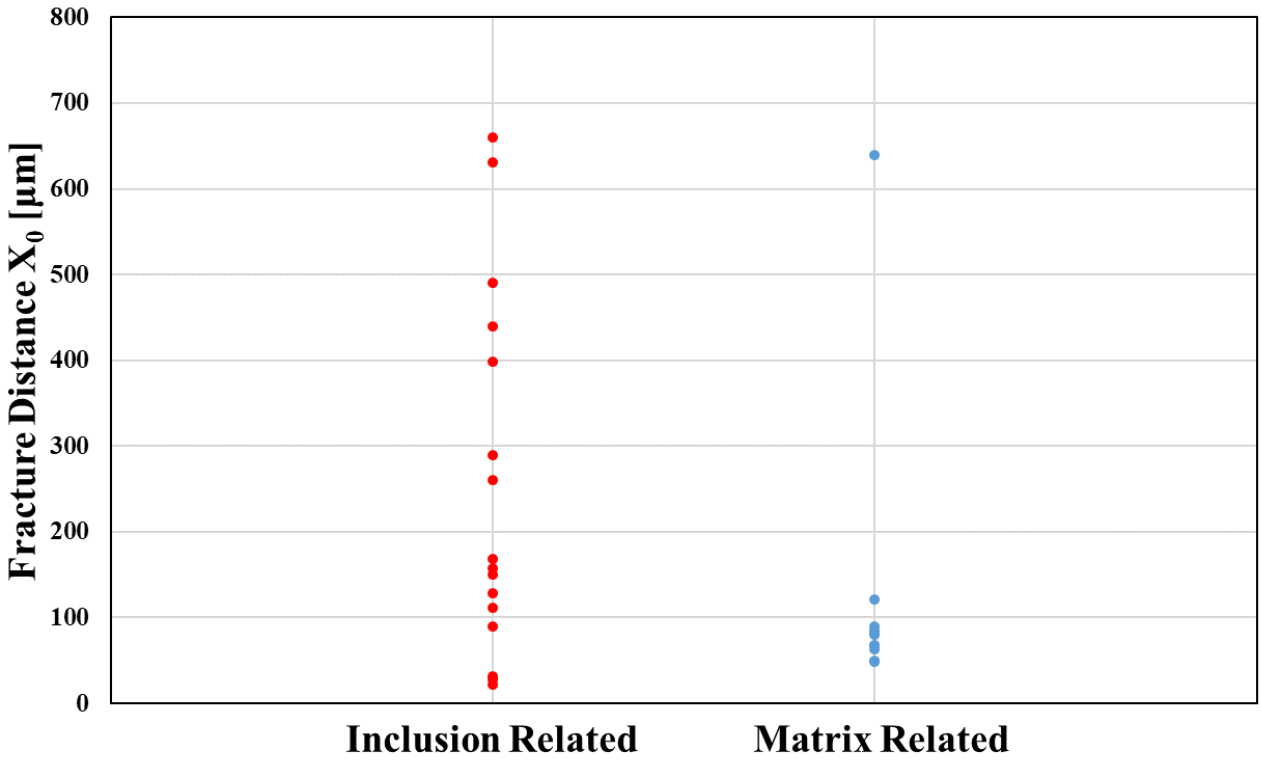

Figure 4.87 Plots of the fracture distance X_0 versus initiation reasons of fractures.

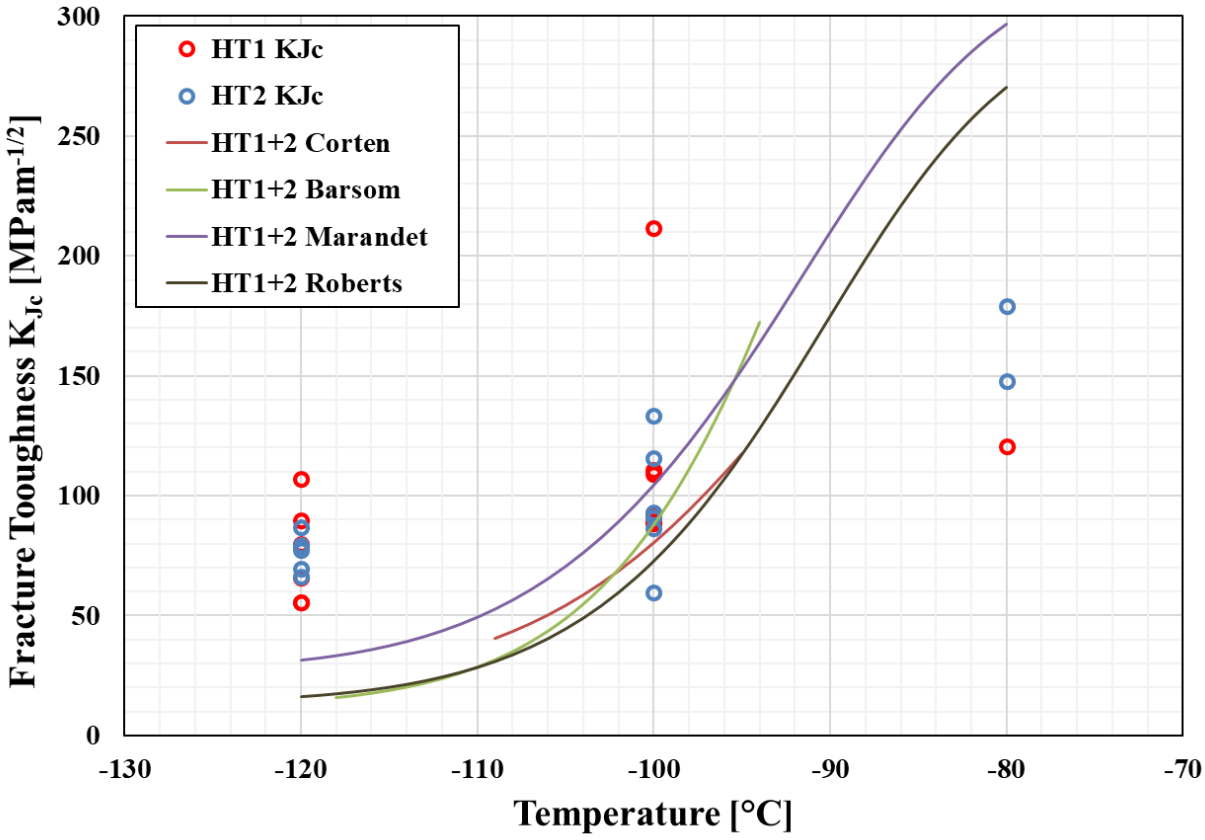

Figure 4.88 Comparisons of the curves of four different correlations for combination of HT1+2 conditions and fracture toughness results calculated from tests.

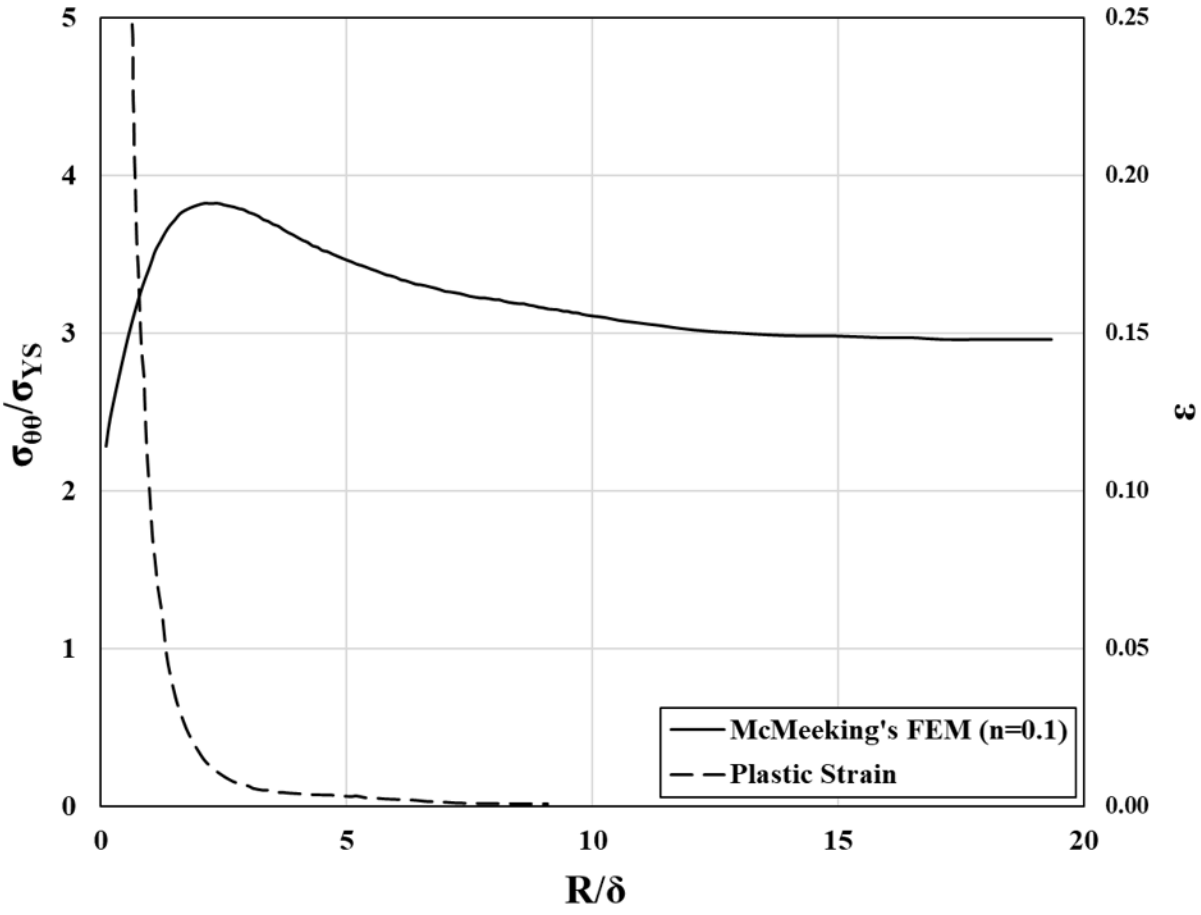

Figure 4.89 FEM analysis of McMeeking with $n = 0.1$and $\theta = 0$.

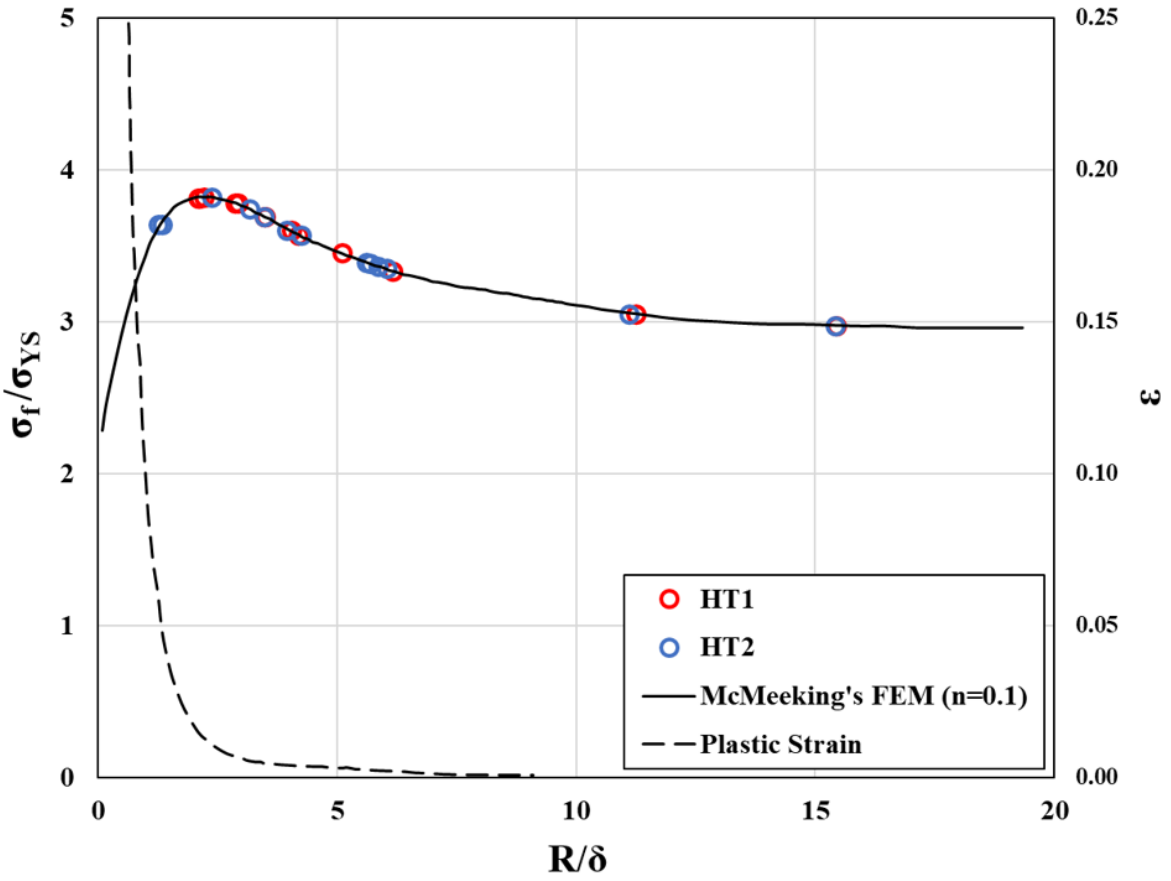

Figure 4.90 FEM analysis of McMeeking with plots of Fracture Toughness test results for HT1 and HT2 conditions located on the curve.

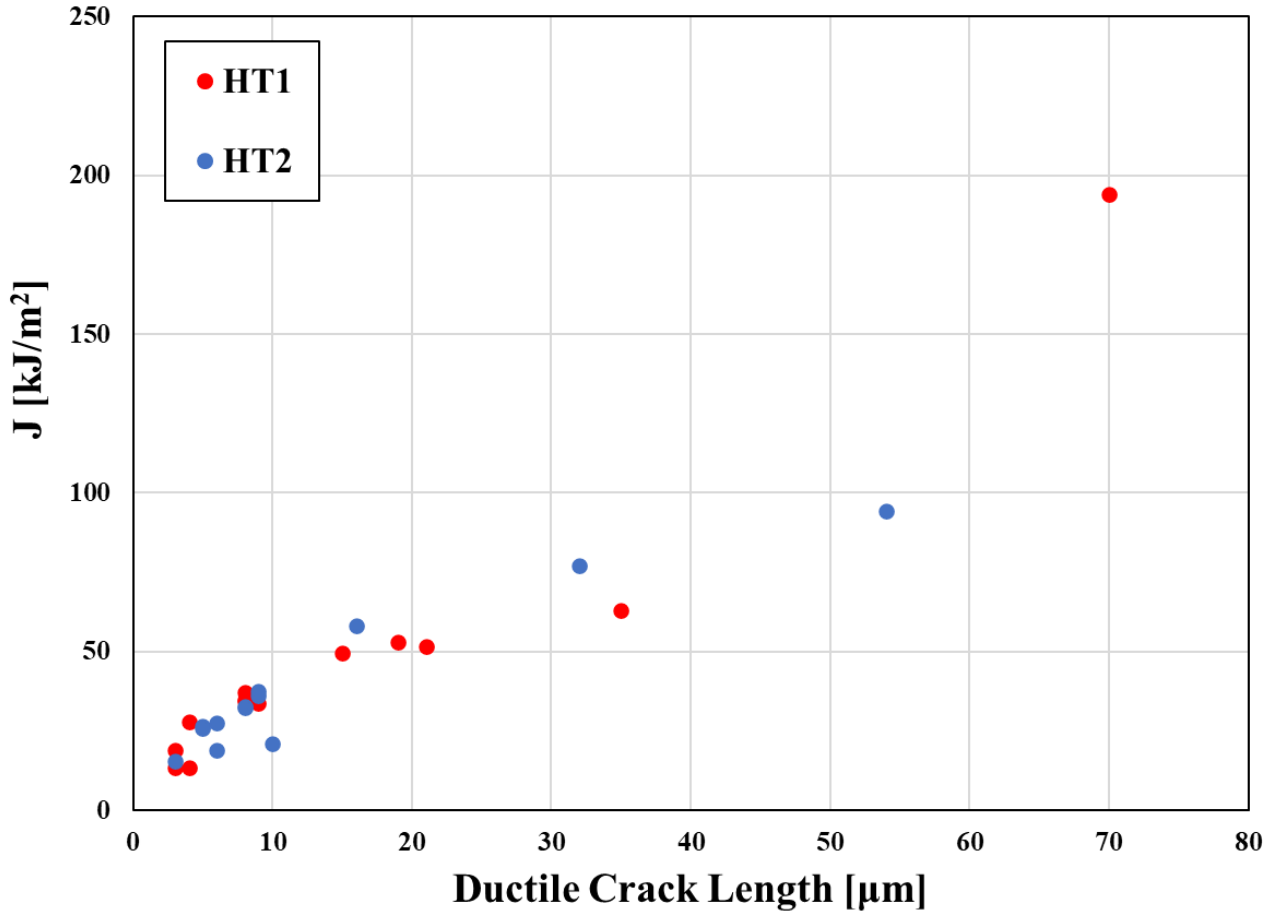

Figure 4.91 Plots of J_c values versus ductile crack growth length of Fracture Toughness tests for HT1 and HT2 conditions.

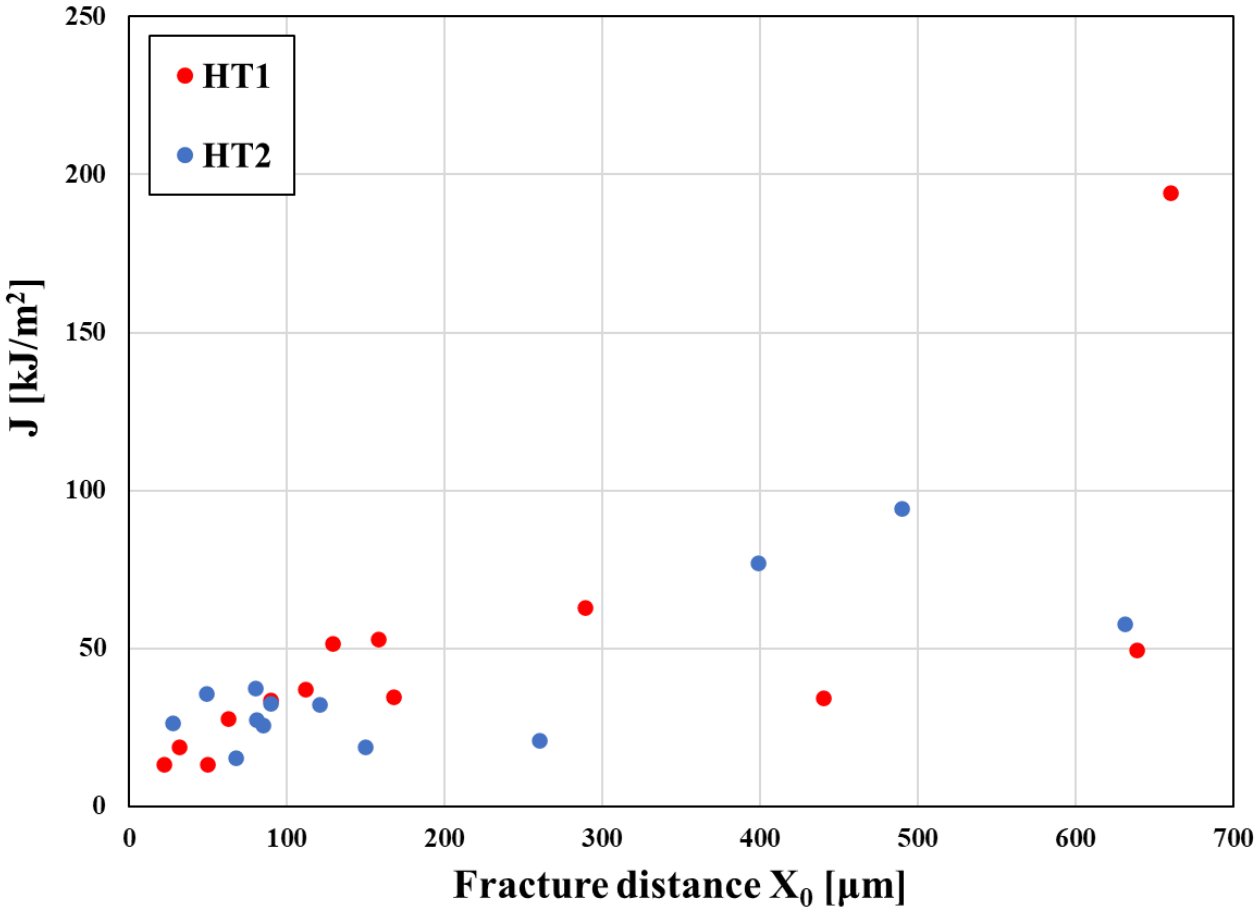

Figure 4.92 Plots of J_c values versus fracture distance of Fracture Toughness tests for HT1 and HT2 conditions.

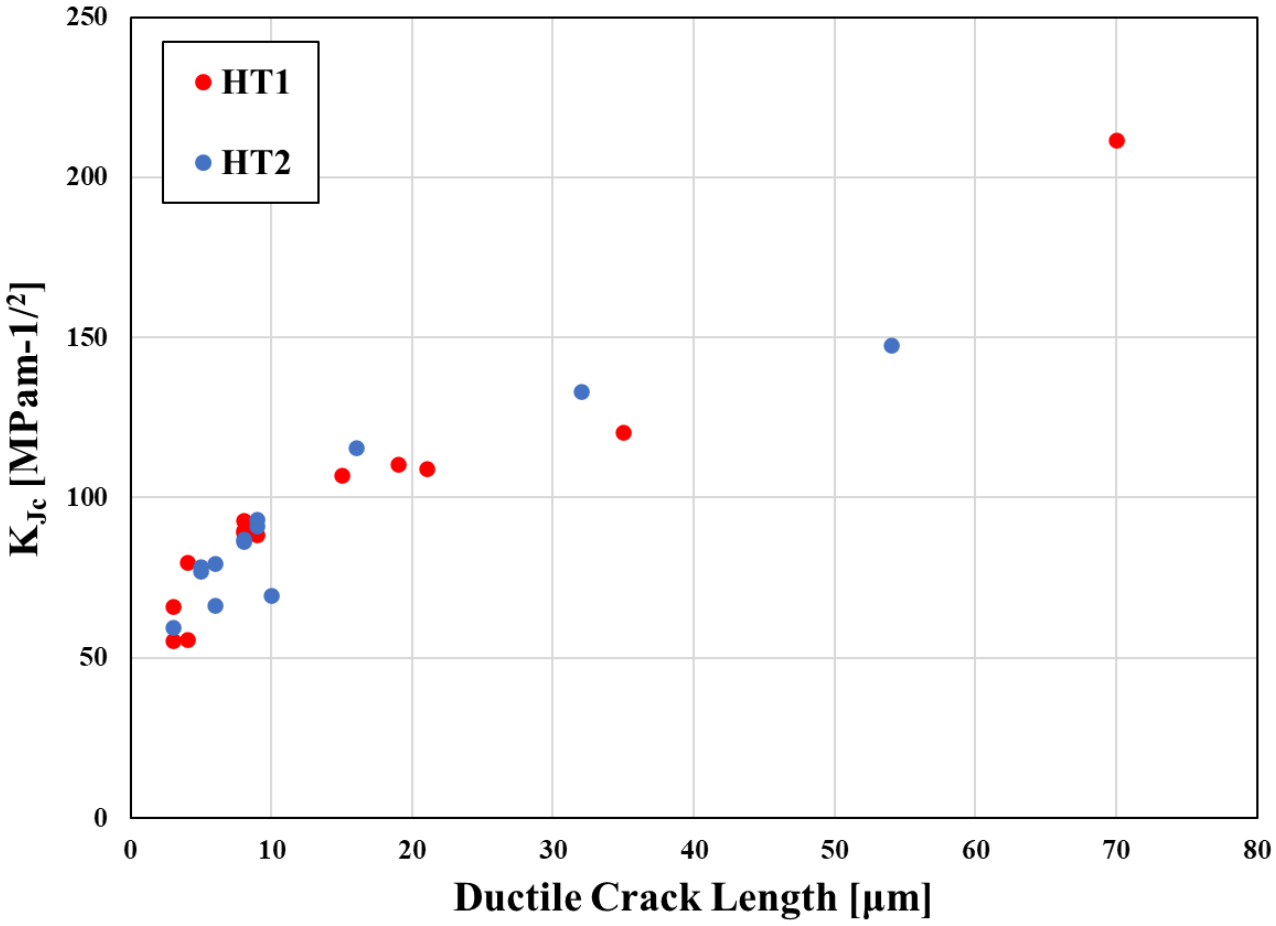

Figure 4.93 Plots of K_{Jc} values versus ductile crack growth length of Fracture Toughness tests for HT1 and HT2 conditions.

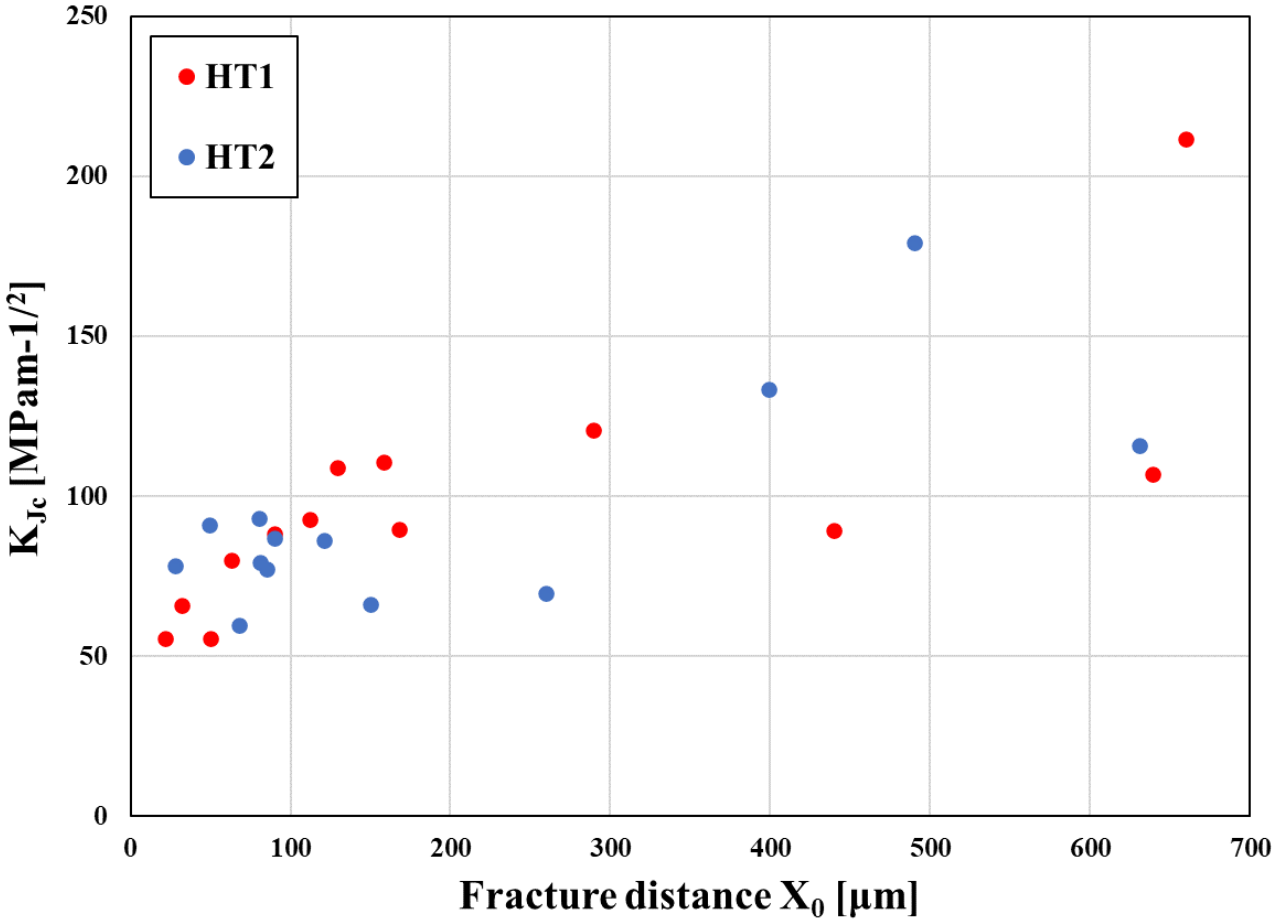

Figure 4.94 Plots of K_{Jc} values versus fracture distance of Fracture Toughness tests for HT1 and HT2 conditions.

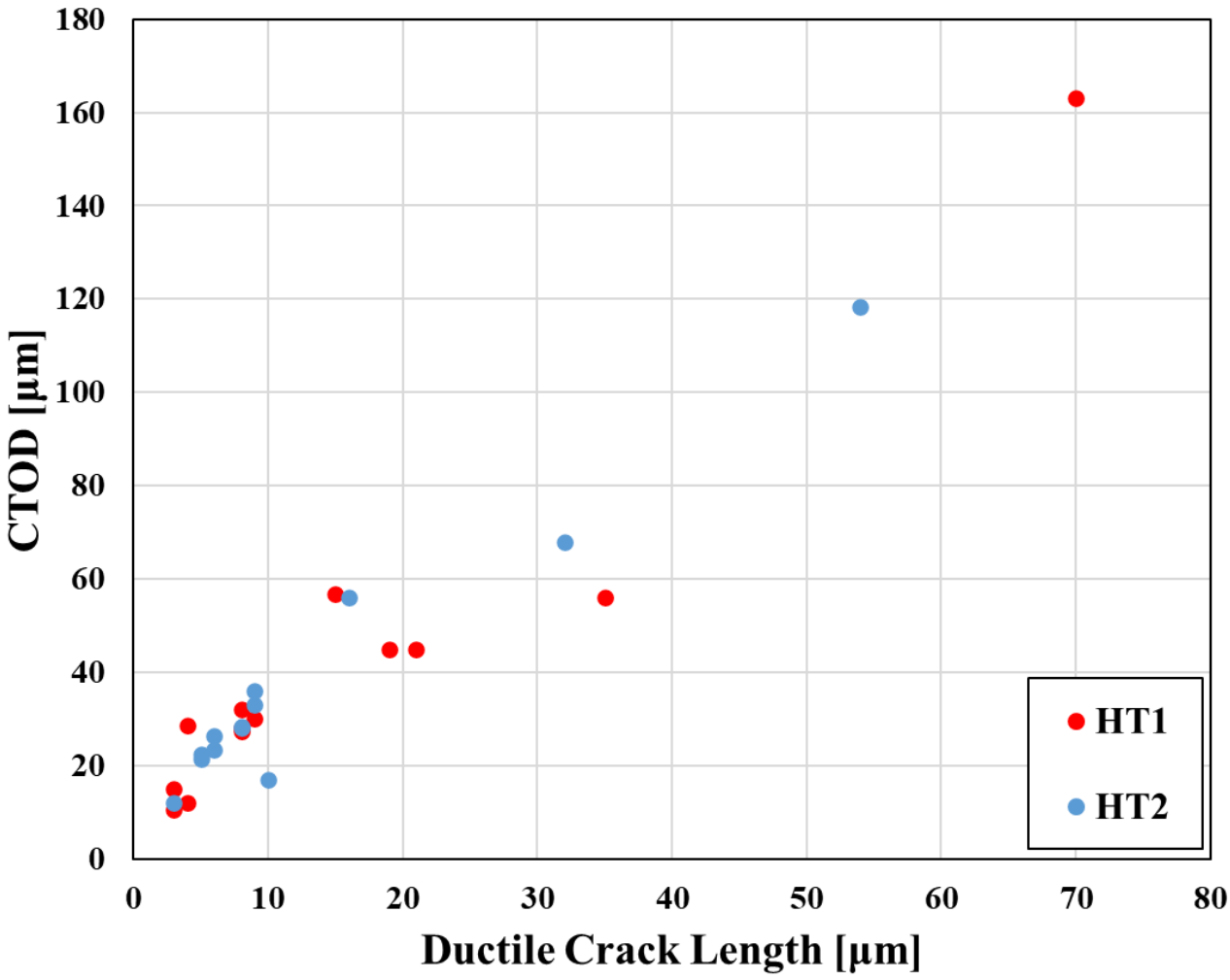

Figure 4.95 Plots of CTOD values versus ductile crack growth length of Fracture Toughness tests for HT1 and HT2 conditions.

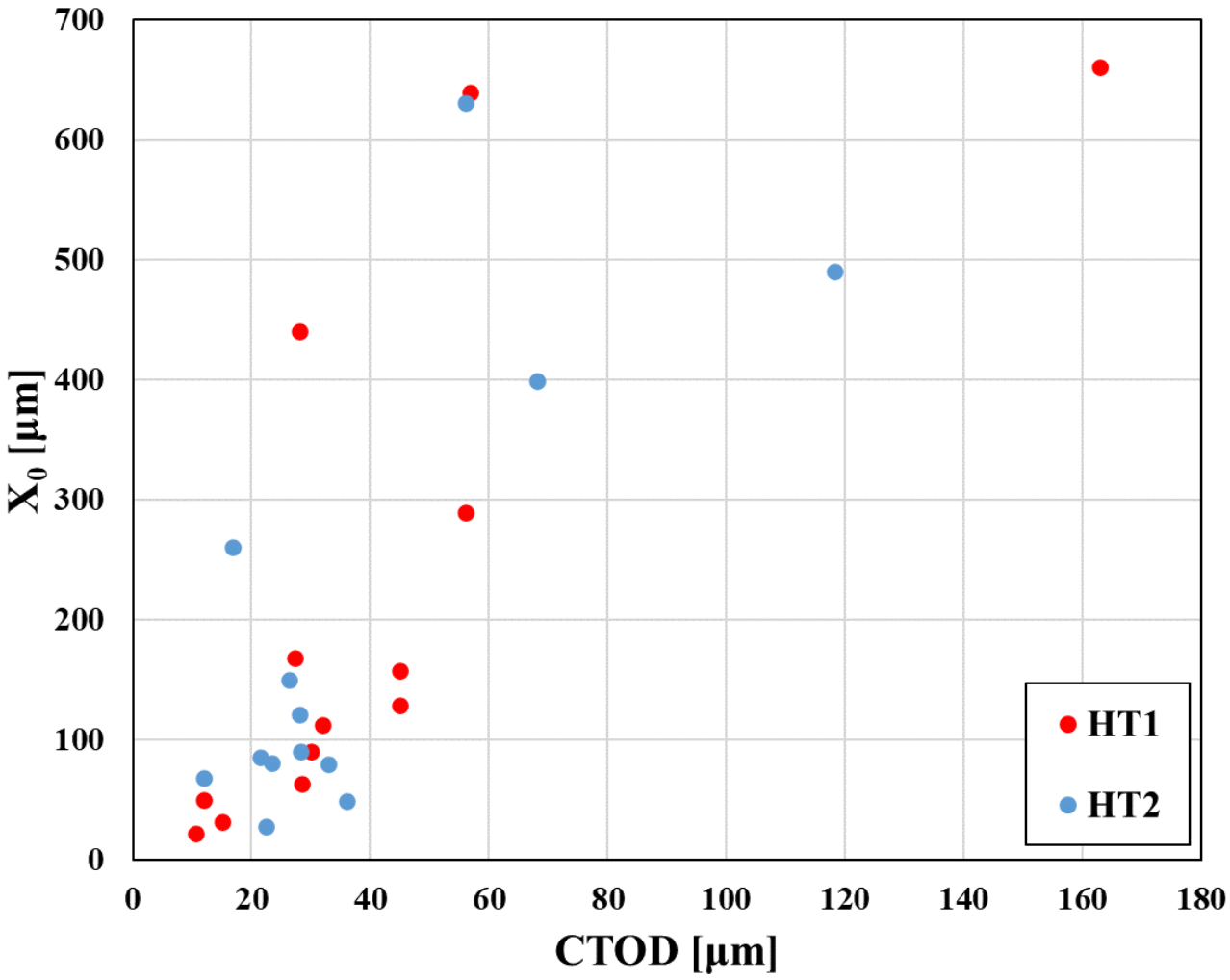

Figure 4.96 Plots of CTOD values versus fracture distance of Fracture Toughness tests for HT1 and HT2 conditions.

(a)

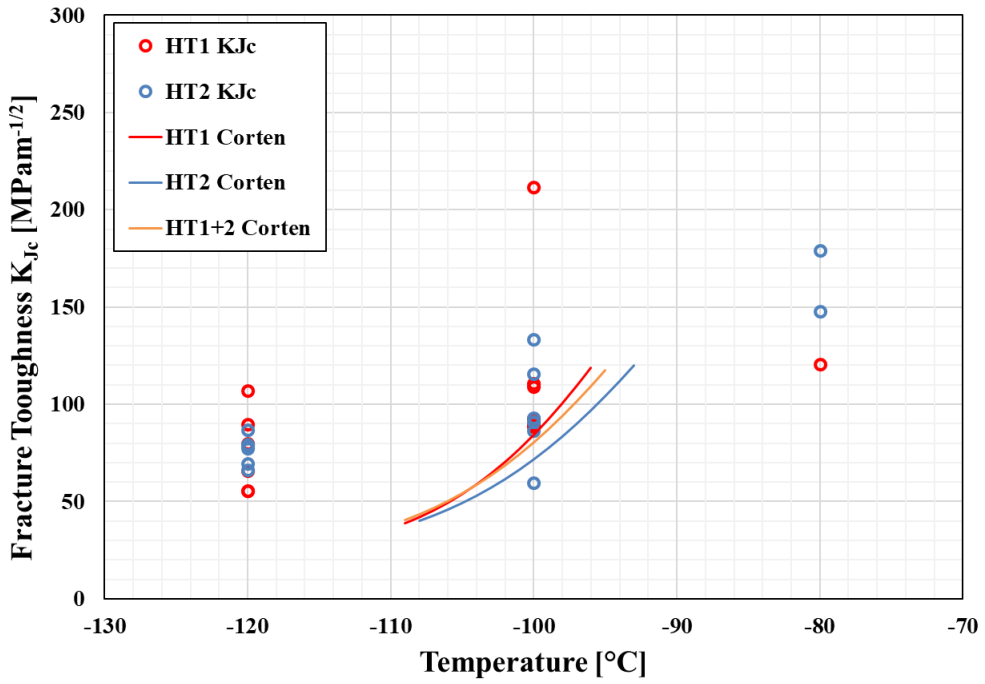

(b)

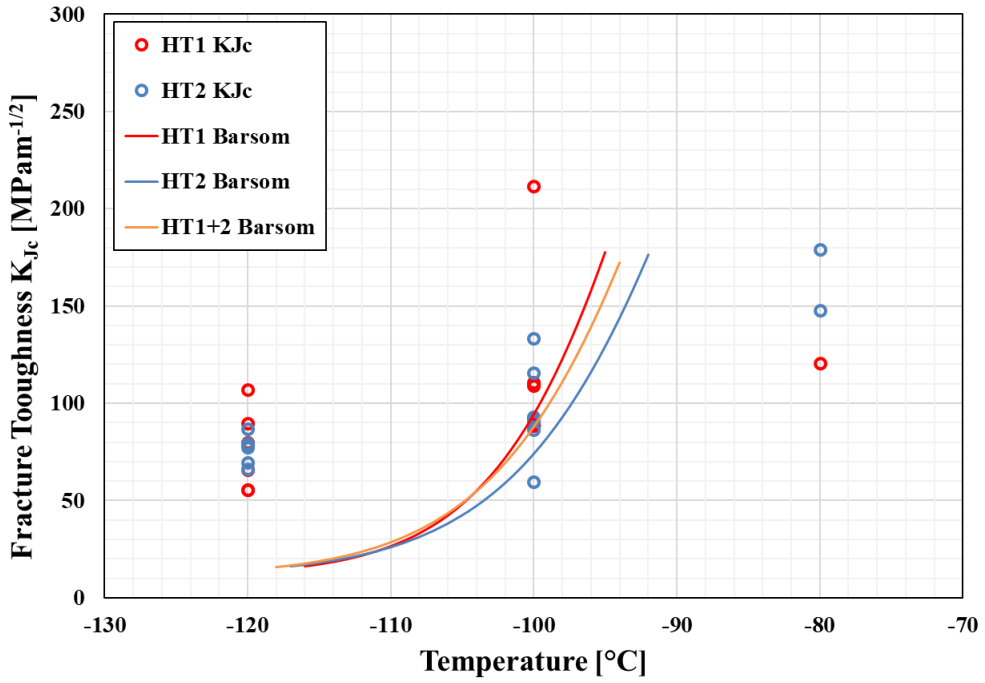

Figure 4.97 The curves of four different correlations for HT1, HT2 and combination of HT1+2 conditions and fracture toughness results calculated from tests, (a) Corten and Sailors, (b) Barsom and Rolfe, (c) Marandet and Sanz and (d) Roberts and Newton.

(c)

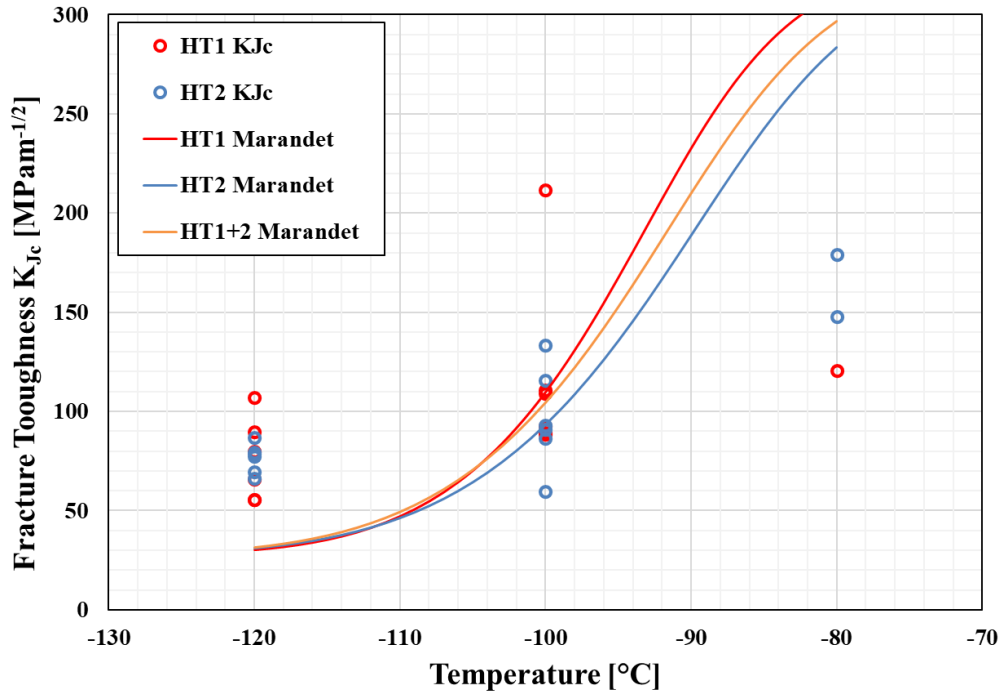

(d)

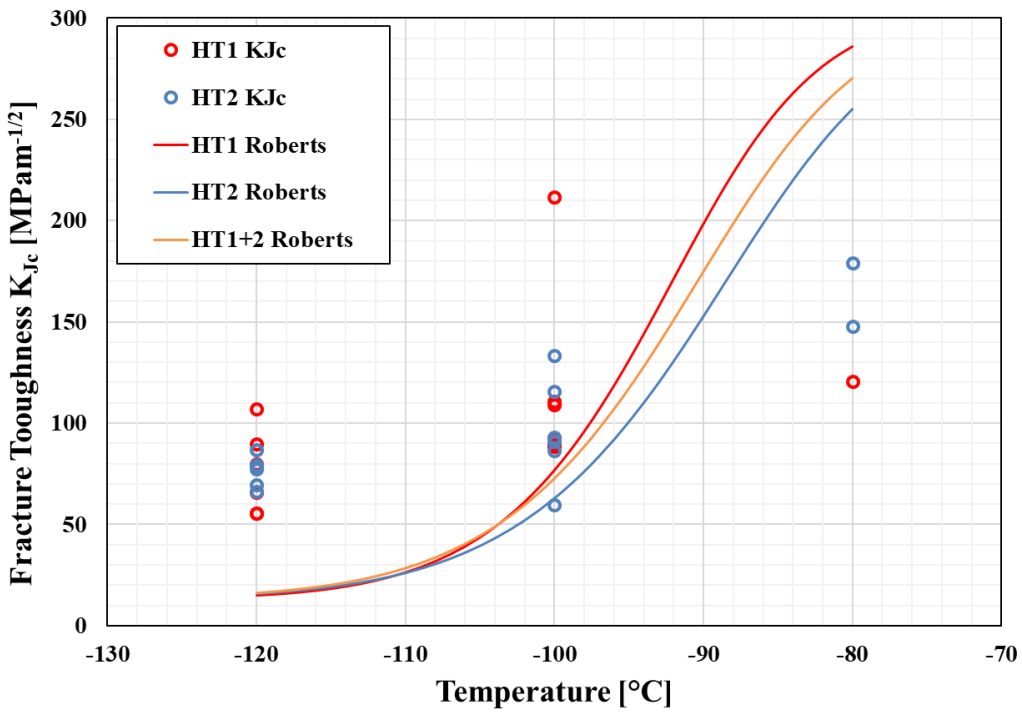

(c) Marandet and Sanz, (d) Roberts and Newton.

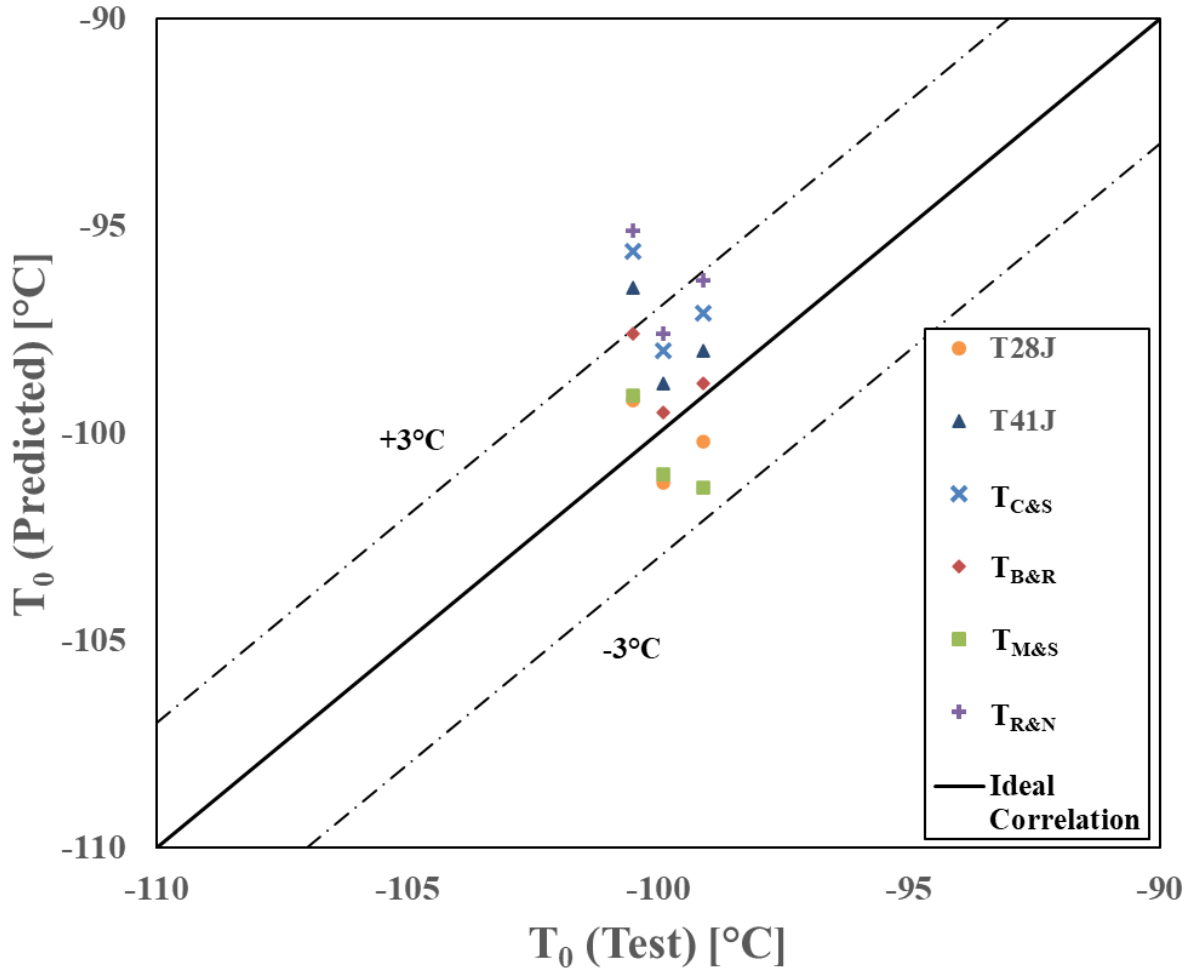

Figure 4.98 Comparisons of the results of four different correlations for HT1, HT2 and combination of HT1+2 conditions and master curve results from tests.

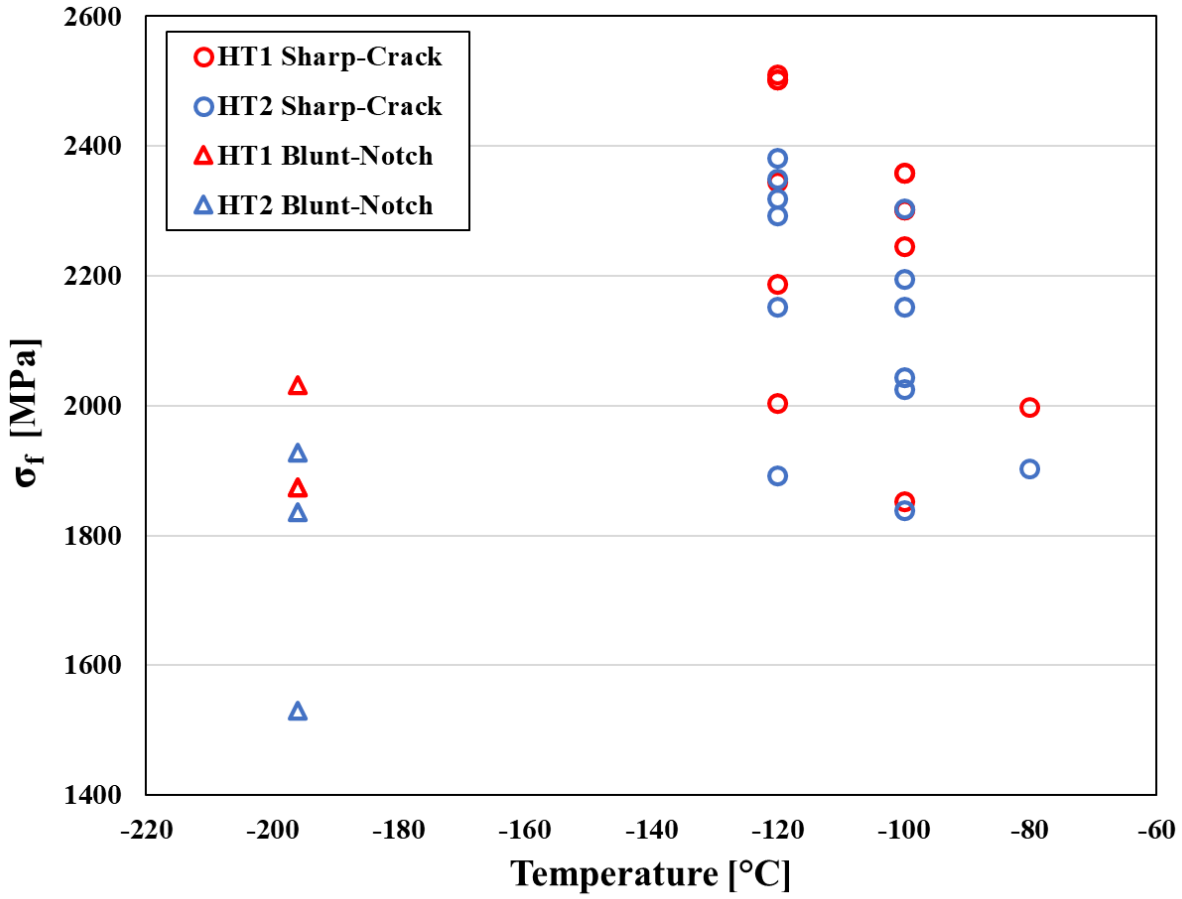

Figure 4.99 Comparisons of local cleavage fracture stress σ_f at various temperatures between Fracture Stress (Blunt-Notch) and Fracture Toughness (Sharp-Crack) tests for HT1 and HT2 conditions.

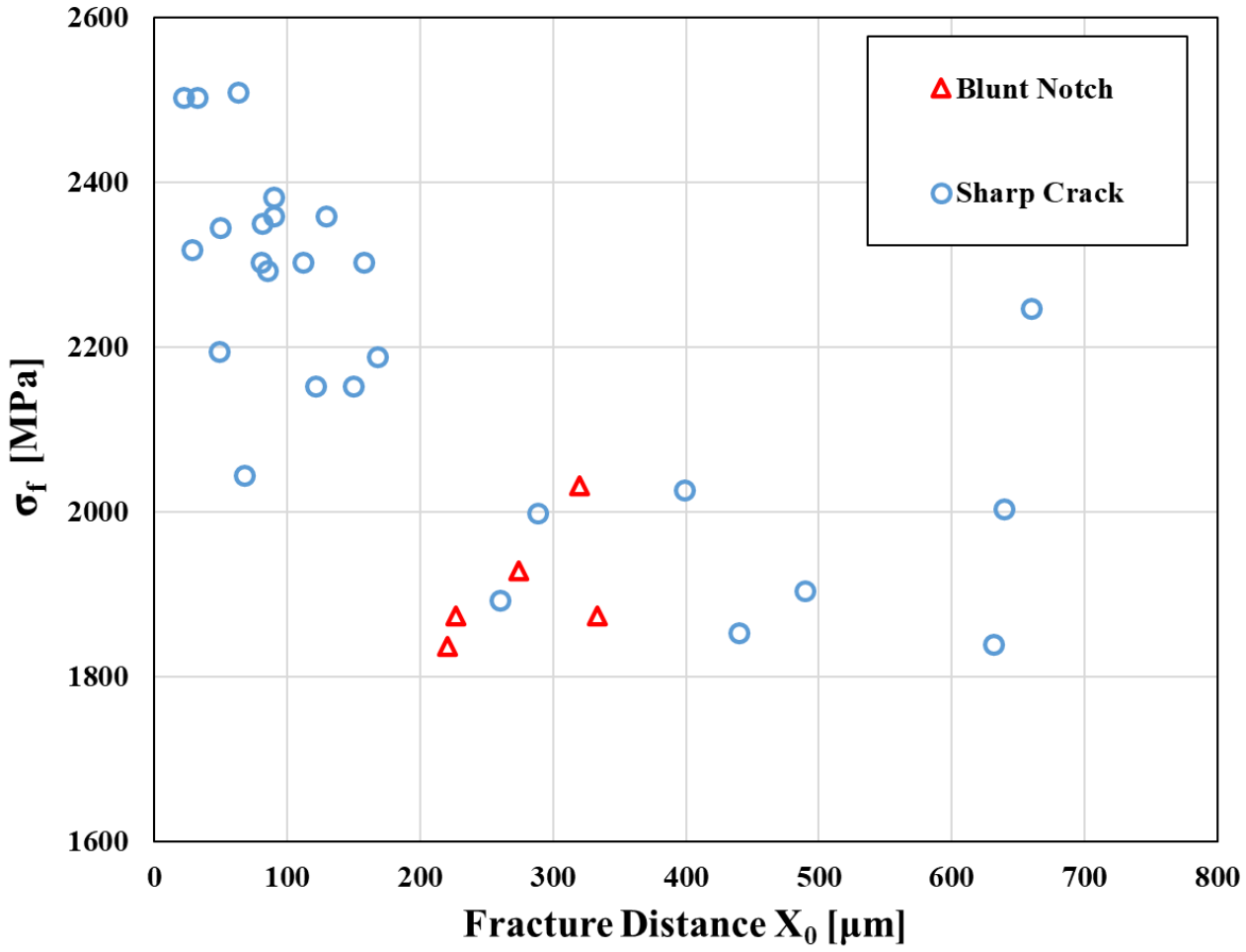

Figure 4.100 Plots of local cleavage fracture stress versus fracture distance between the Blunt-notched specimens and Sharp-cracked specimens.

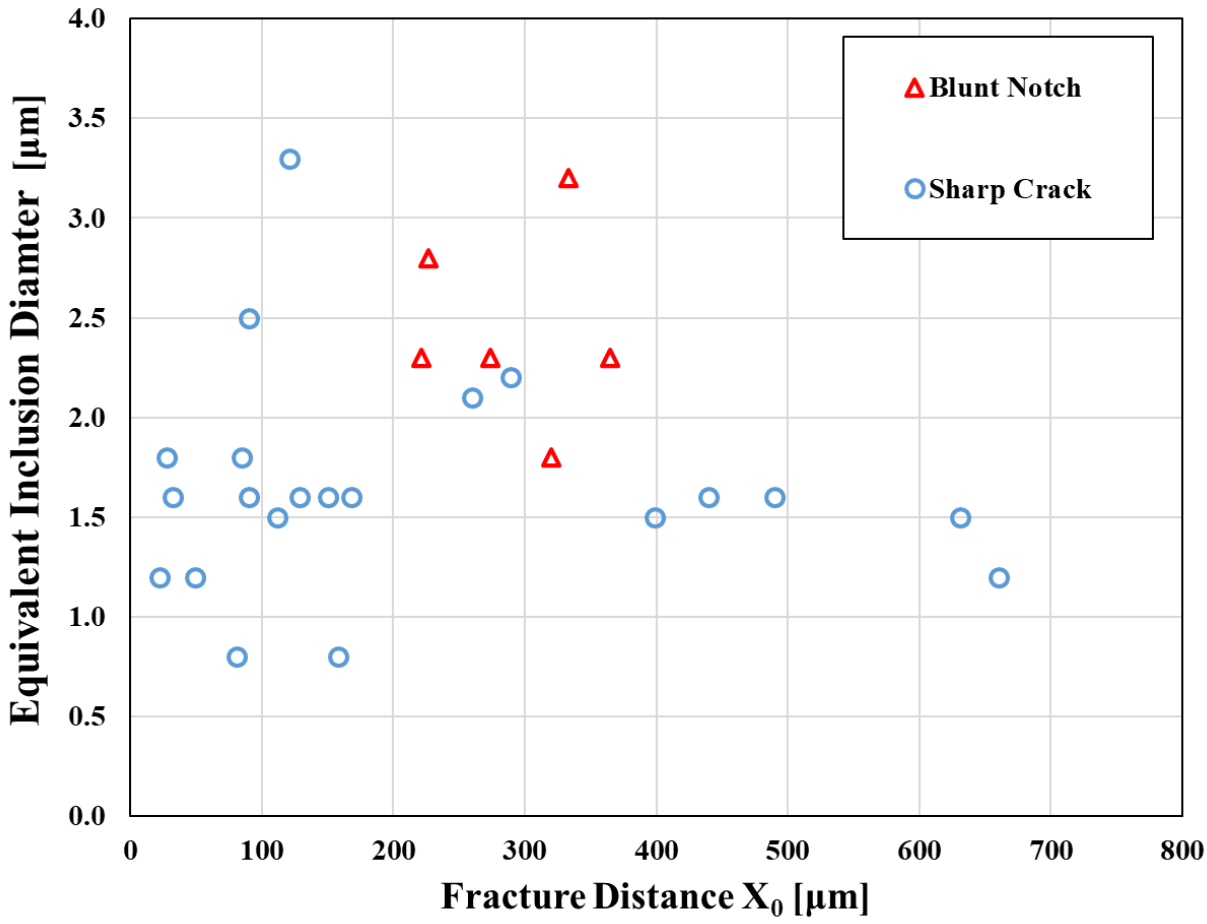

Figure 4.101 Plots of equivalent inclusion diameter versus fracture distance between the Blunt-notched specimens and Sharp-cracked specimens.

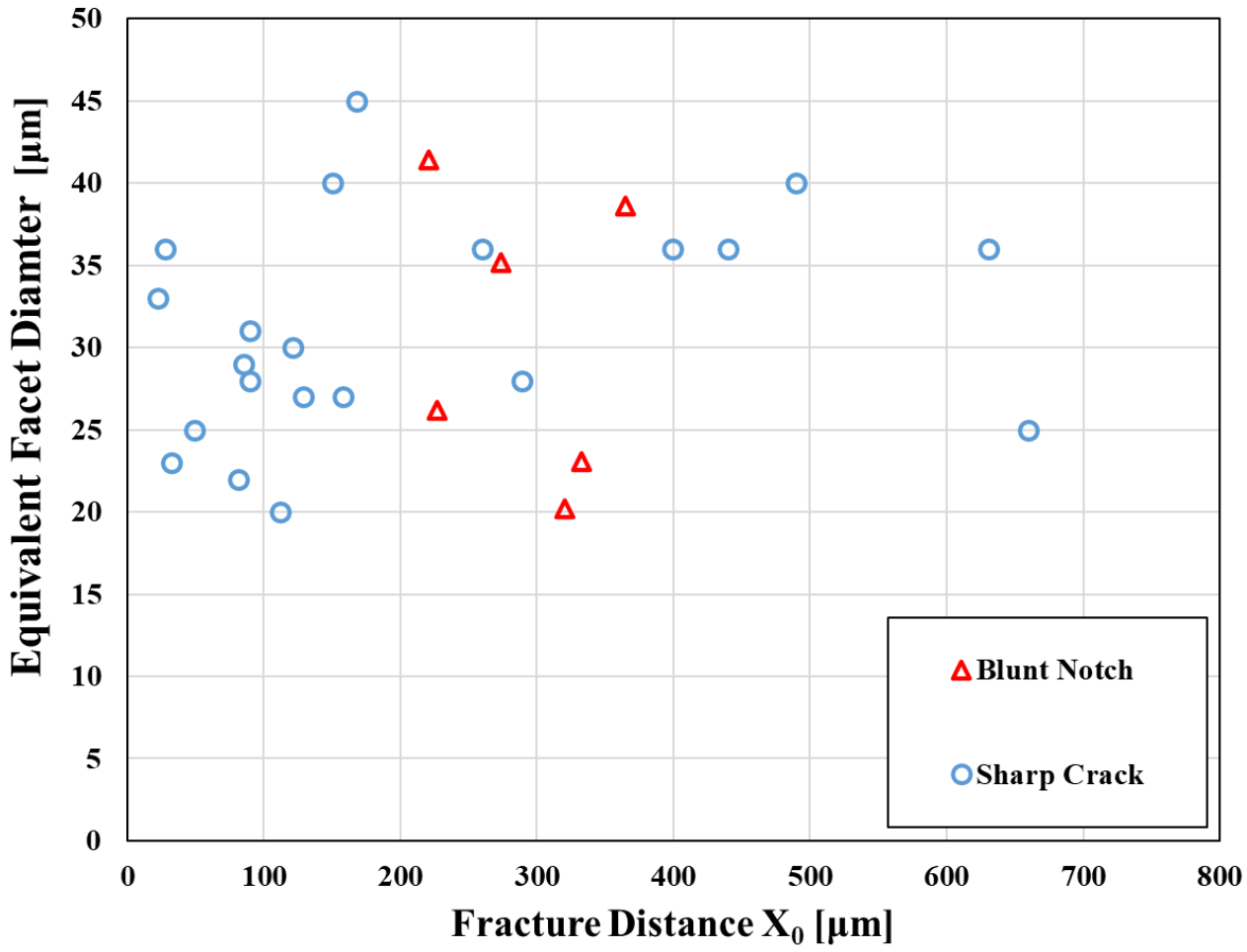

Figure 4.102 Plots of equivalent facet diameter versus fracture distance between the Blunt-notched specimens and Sharp-cracked specimens.

Table 7.1 Hardness results for 9% and 7% Nickel steels.

Distance to start point [mm]	9% Nickel			7% Nickel		
	Diagonal 1 [µm]	Diagonal 2 [µm]	HV 5	Diagonal 1 [µm]	Diagonal 2 [µm]	HV 5 [kg/mm^2]
0	190	190	256	193	193	249
1	195	196	242	187	187	265
2	190	191	256	193	192	251
3	189	191	257	190	191	256
4	191	192	252	189	191	257
5	193	193	249	191	198	245
6	192	192	251	194	197	243
7	194	196	244	192	190	252
8	193	193	250	190	190	253
9	191	191	254	188	189	255
Average	192	192	251	191	192	253

Table 7.2 Summary of tensile testing results for 9% Ni specimens at different temperatures.

Specimen Number	Test Temperature	Yield Stress (0.2% Offset)	Ultimate Tensile Strength	Strain		Work Hardening Exponent n
				Uniform	Total	
	[°C]	[MPa]	[MPa]	[%]		
9Ni-01	-196	970	1176	21.5	34.8	0.14
9Ni-02		966	1176	21.2	34.9	0.14
9Ni-13	-170	904	1095	15.6	32.8	0.15
9Ni-14		897	1066	17.0	30.1	0.12
9Ni-11	-150	846	1051	19.2	33.1	0.14
9Ni-12		846	1017	15.8	29.8	0.12
9Ni-09	-130	811	1006	17.3	32.5	0.13
9Ni-10		812	1012	16.5	33.0	0.17

Table 7.3 Summary of tensile testing results for 7% Ni specimens at different temperatures.

Specimen Number	Test Temperature	Lower Yield Stress	Yield Stress (0.2% Offset)	Ultimate Tensile Strength	Strain		Work Hardening Exponent n
					Uniform	Total	
	[°C]	[MPa]	[MPa]	[MPa]	[%]		
7Ni-09	-196	1049	1068	1090	14.9	27.3	0.08
7Ni-10		1053	1085	1096	15.8	29.2	0.09
7Ni-01	-170	971	998	1016	12.6	25.7	0.08
7Ni-02		966	990	1012	13.7	26.7	0.08
7Ni-03	-150	910	930	962	12.6	27.0	0.08
7Ni-04		916	931	971	12.9	27.5	0.08
7Ni-05	-130	879	900	932	12.8	26.7	0.08
7Ni-06		879	899	932	12.1	26.6	0.08

Table 7.4 Charpy impact test results of 9% Nickel steel.

Specimen Number	Test Temperature	Absorbed Impact Energy	Average Absorbed Energy
	[°C]	[J]	[J]
9Ni-13	**-196**	**242**	**260**
9Ni-14		**252**	
9Ni-15		**278**	
9Ni-16		**270**	
9Ni-17		**260**	
9Ni-18		**256**	

Table 7.5 Charpy impact test results of 7% Nickel steel.

Specimen Number	Test Temperature	Absorbed Impact Energy	Lateral Expansion	Cleavage Area Percentage
	[°C]	[J]	[mm]	%
1	-196	38.0	0.49	78.86
2		55.0	0.59	73.45
3		44.0	0.40	84.43
13	-180	62.0	0.55	71.77
14	-170	78.0	0.92	56.80
8		72.0	0.80	56.20
10		123.0	1.30	43.23
9	-160	186.0	2.03	18.45
15		186.0	2.05	17.69
7	-150	180.0	2.14	23.47
12	-140	223.0	2.24	7.77
11	-130	235.0	2.07	3.69
5	-100	233.0	2.14	3.37
6		238.0	2.64	2.24
4	-80	233.0	2.41	4.62

Table 7.6 Results of fracture stress tests for 9% Ni steel including the maximum fracture load, nominal stress, the ratios of σ_{nom}/σ_{YS} and L/L_{GY}, stress intensification factor.

Specimen Number	**Temperature**	**Yield Stress**	**Maximum Load**	**Nominal Stress**	**σ_{nom}/σ_{YS}**	**L/L_{GY}**	**Stress Intensification (Griffiths)**
	T [°C]	**σ_{YS} [MPa]**	**P [kN]**	**σ_{nom} [MPa]**	**(max 2.292)**	**(max 1.065)**	**$R_{griffiths}$ (max 2.62)**
9Ni-FS-01	-196	968	79.3	3316	3.426	1.593	3.09
9Ni-FS-02			76.1	3182	3.287	1.529	3.04
7Ni-FS-01	-196	1052	101.7	4251	4.043	1.880	3.30
7Ni-FS-02			102.6	4290	4.078	1.896	3.31

Table 7.7 Measurements of crack lengths including the optical microscope measured lengths and the compliance method estimated lengths.

Specimen Number	Original Crack Length [mm]			$0.15a_p$ [mm]	Final Crack Length [mm]			$0.03b_0$ [mm]	Stable Ductile Crack growth Δa [mm]
	Actual (a_0)	Compliance ($a_{0predicted}$)	Difference		Actual (a_f)	Compliance ($a_{fpredicted}$)	Difference		
9Ni -05	14.74	14.97	0.23	2.21	15.70	16.06	0.35	0.52	1.09
9Ni -06	14.92	15.17	0.25	2.24	16.20	16.59	0.39	0.51	1.42
9Ni -07	14.55	14.57	0.02	2.18	15.65	15.81	0.15	0.52	1.24
9Ni -10	14.51	14.73	0.22	2.18	15.54	15.64	0.11	0.52	0.91
9Ni -11	14.33	14.62	0.29	2.15	15.75	15.93	0.18	0.53	1.31
7Ni -02	14.70	14.83	0.13	2.20	16.55	16.74	0.18	0.52	1.91

Table 7.8 Results of the fracture toughness tests for both 9% and 7% Ni steels at -163 °C.

Specimen Number	P_{max}	J_C	Average J_C	K_{Jc}	Average K_{Jc}	J_{Ic}	K_{JIc}	CTOD δ
	[kN]	[kJ/m^2]	[kJ/m^2]	[MPam$^{1/2}$]	[MPam$^{1/2}$]	[kJ/m^2]	[MPam$^{1/2}$]	[mm]
9Ni-05	53.3	852	967	186	190	/	/	0.49
9Ni-06	52.1	1122		186		851	443	0.64
9Ni-07	59.9	1090		204		772	422	0.63
9Ni-10	52.9	816		184		/	/	0.46
9Ni-11	54.4	956		188		772	422	0.54
7Ni-02	50.7	995	995	156	156	663	391	0.62

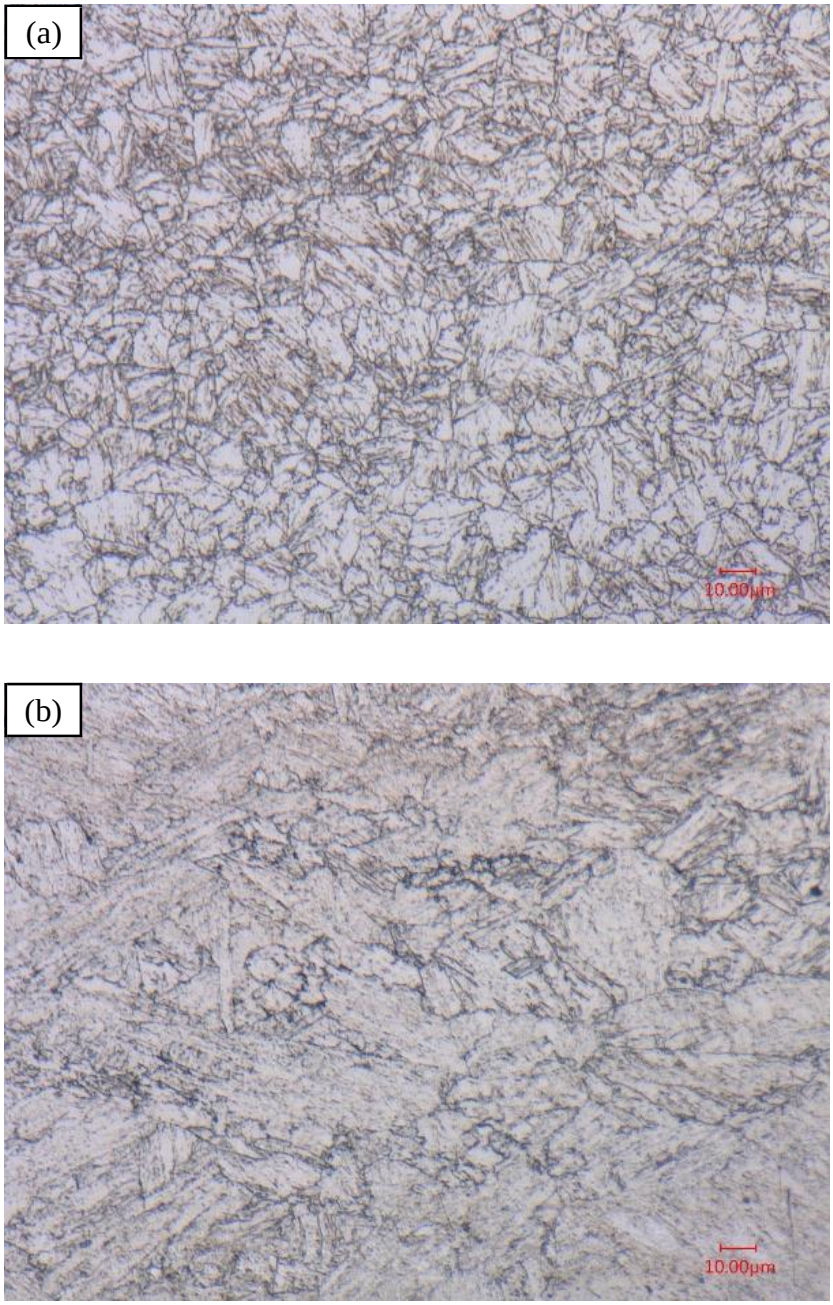

Figure 7.1 Microstructure of (a) 9% and (b) 7% Nickel steel under optical microscope.

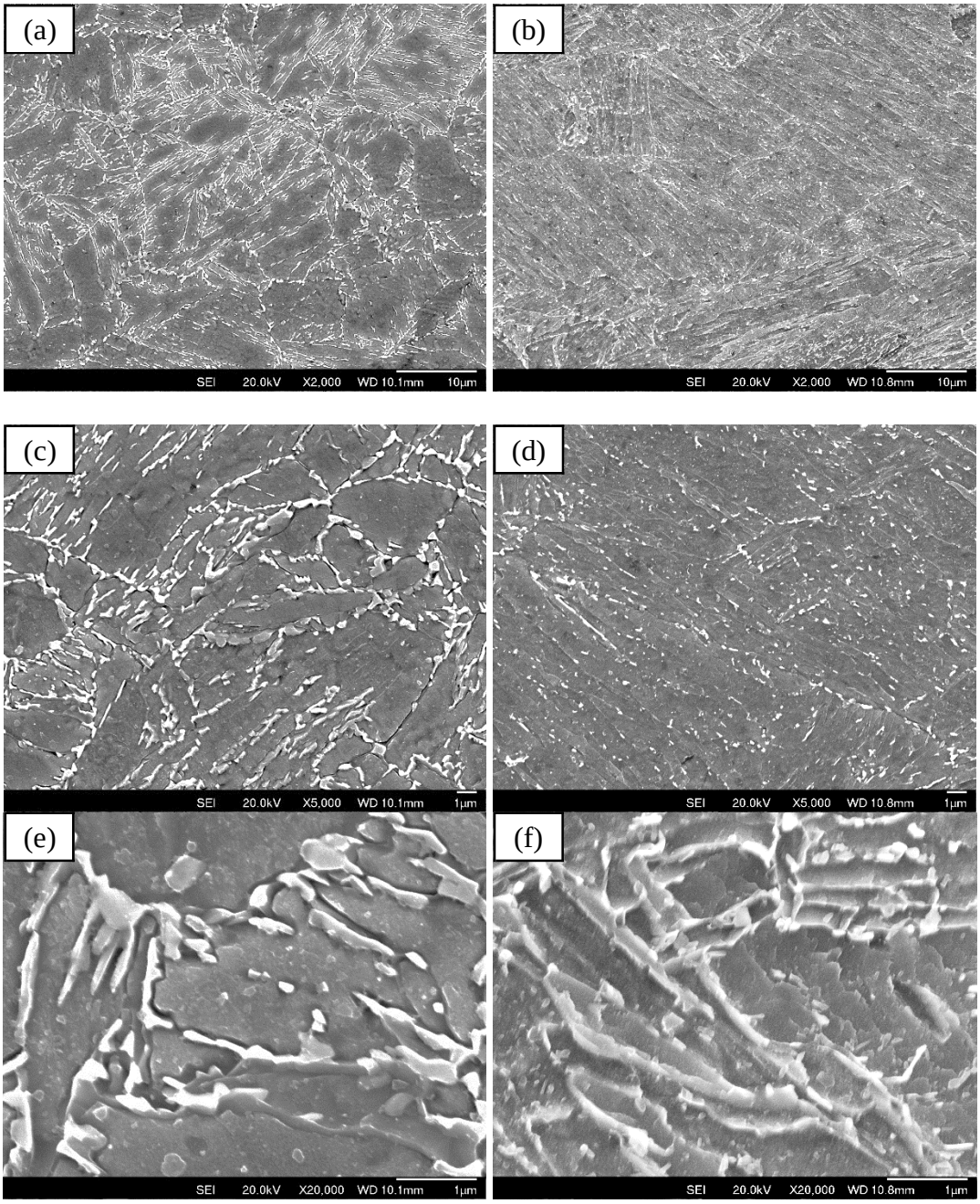

Figure 7.2 A sequence of SEM images of increasing magnification for the microstructure of 9% (left) and 7% (right) Nickel steel: (a) and (b) 2,000×; (c) and (d) 5,000×; (e) and (f) 20,000×.

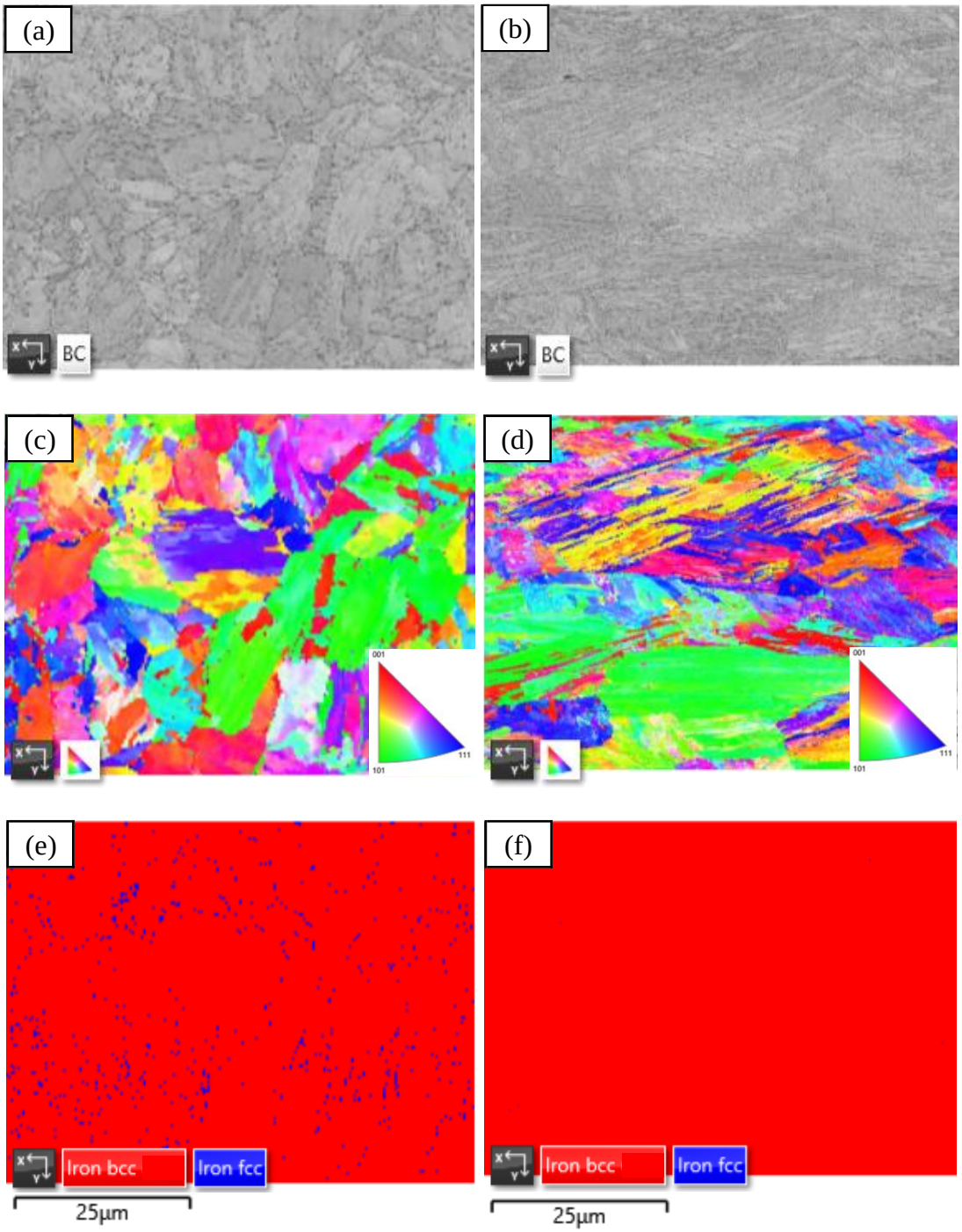

Figure 7.3 EBSD analysis for 9% (left) and 7% (right) Nickel steel: (a) and (b) are the SEM images; (c) and (d) are the EBSD mappings from the same regions as SEM images; (e) and (f) are their phase distributions in the regions, where red represents BCC and blue represents FCC phases.

(a)

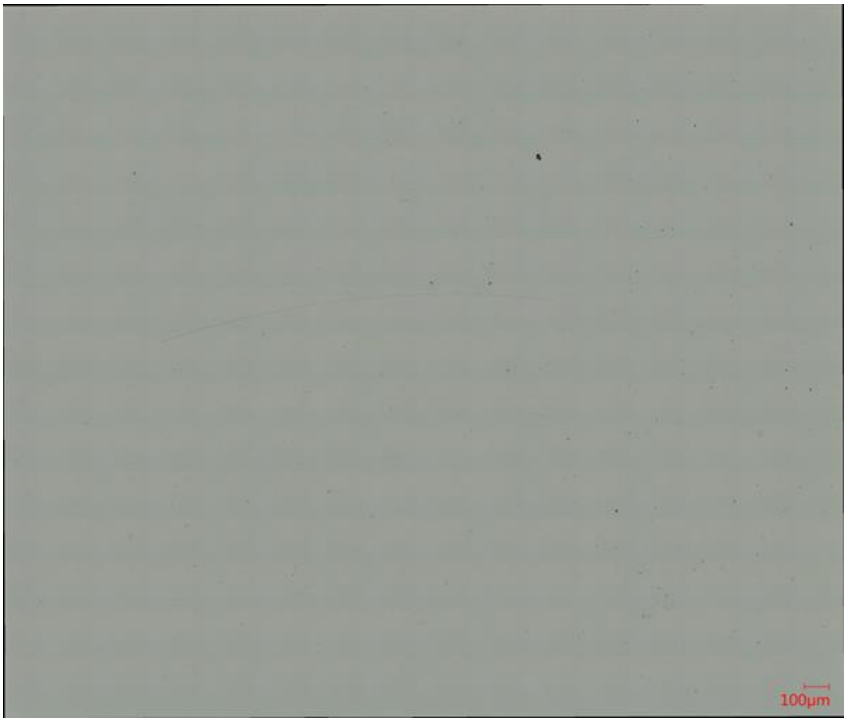

(b)

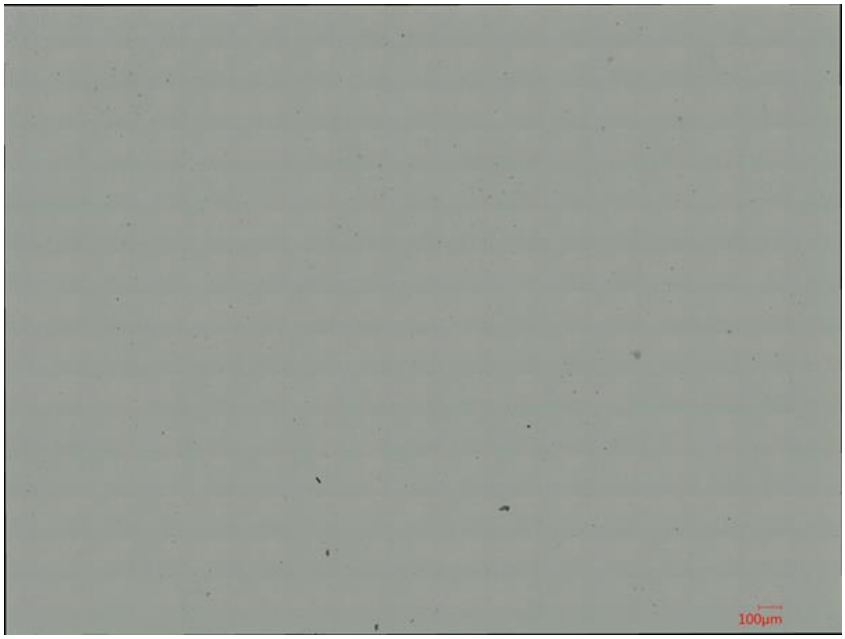

Figure 7.4 Backscattered mode images of polished surfaces from (a) 9% and (b) 7% Nickel steels.

(a)

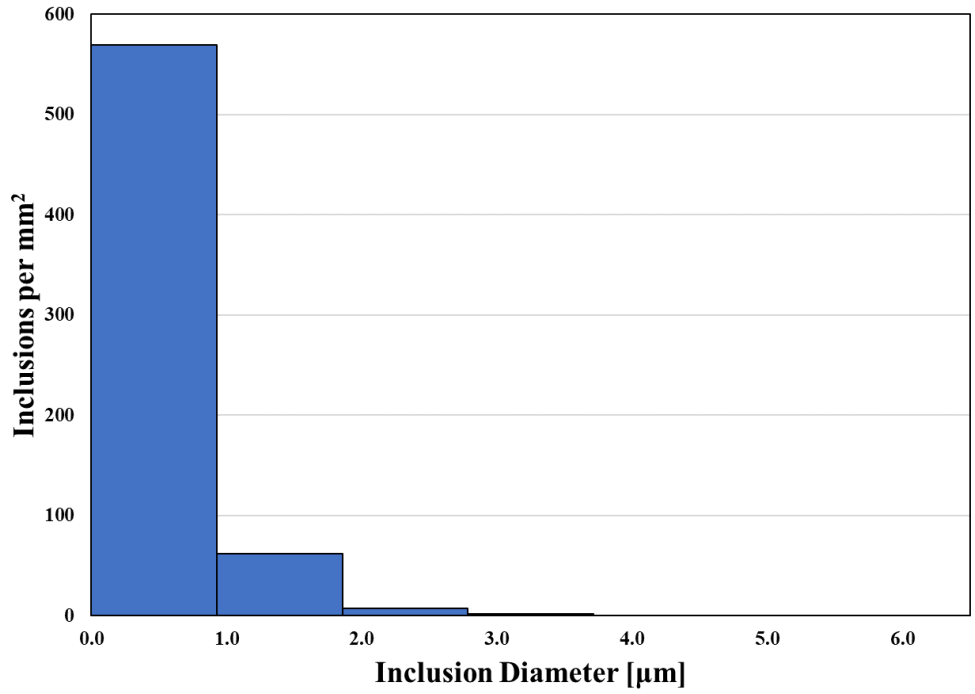

(b)

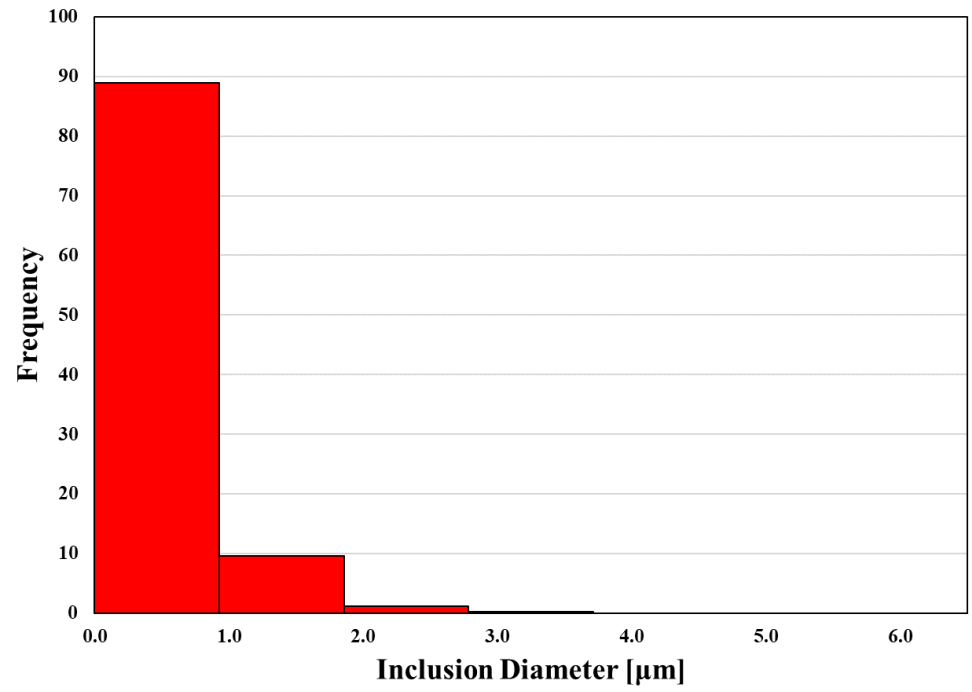

Figure 7.5 Results of inclusion analysis for 9% Nickel steel, (a) inclusion number per mm^2; (b) inclusion frequency.

(a)

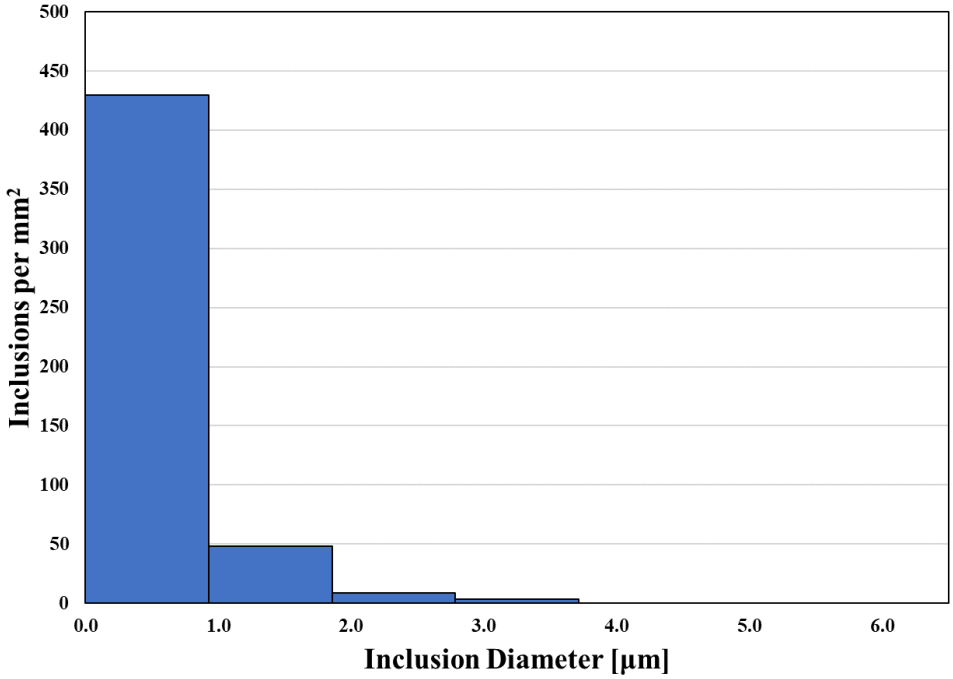

(b)

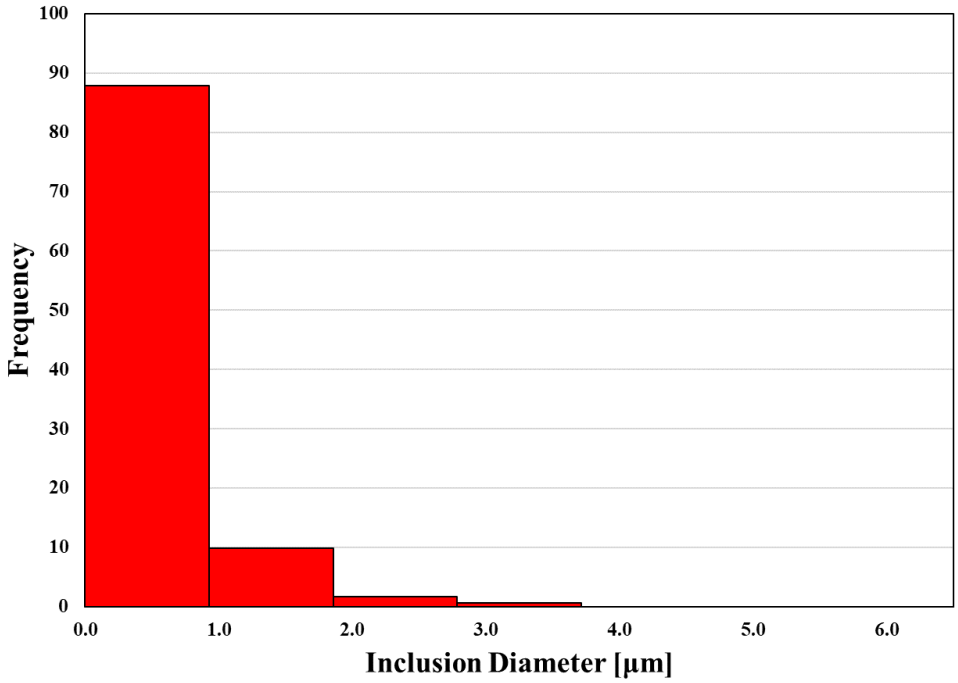

Figure 7.6 Results of inclusion analysis for 7% Nickel steel, (a) inclusion number per mm^2; (b) inclusion frequency.

(a)

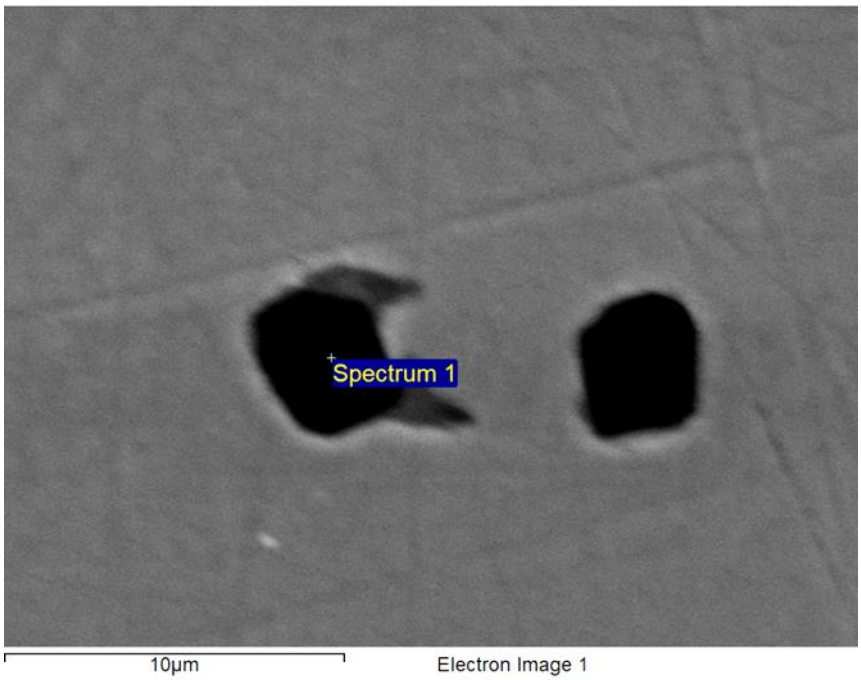

(b)

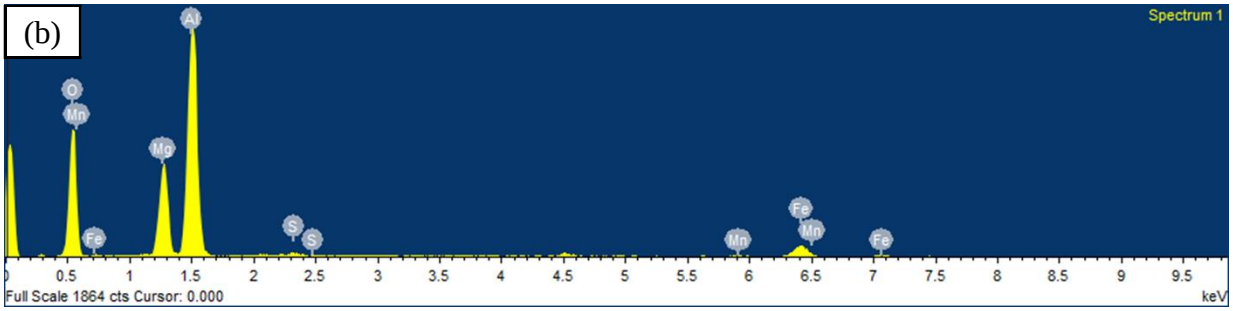

Figure 7.7 Typical inclusion of 9% Nickel steel, (a) SEM image; (b) EDX spectrum.

(a)

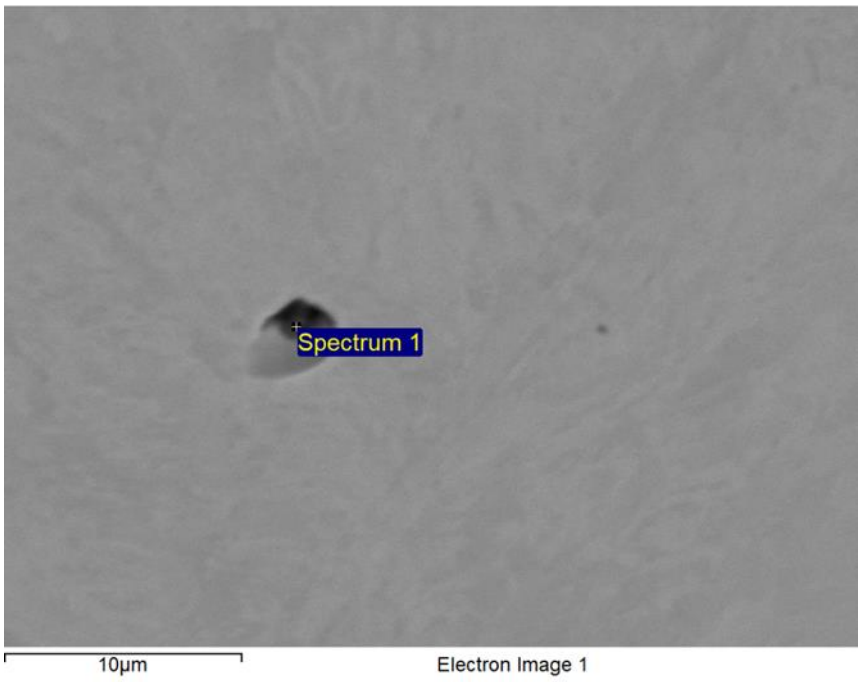

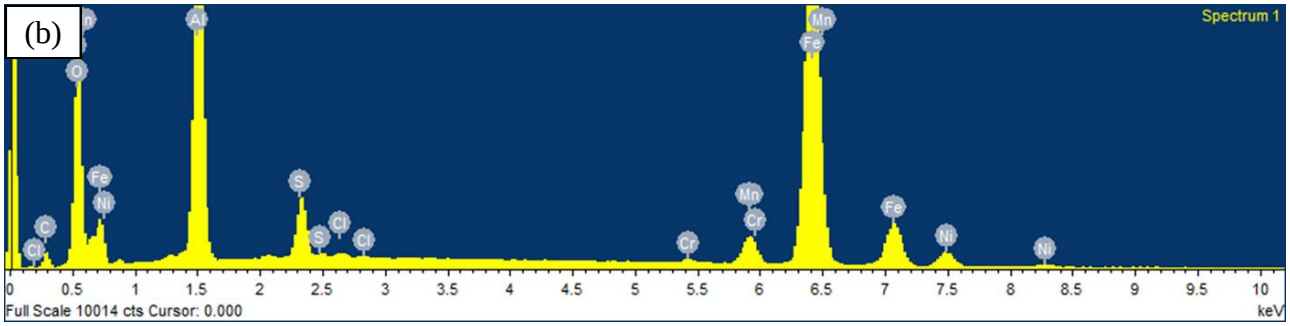

Figure 7.8 Typical inclusion of 7% Nickel steel, (a) SEM image; (b) EDX spectrum.

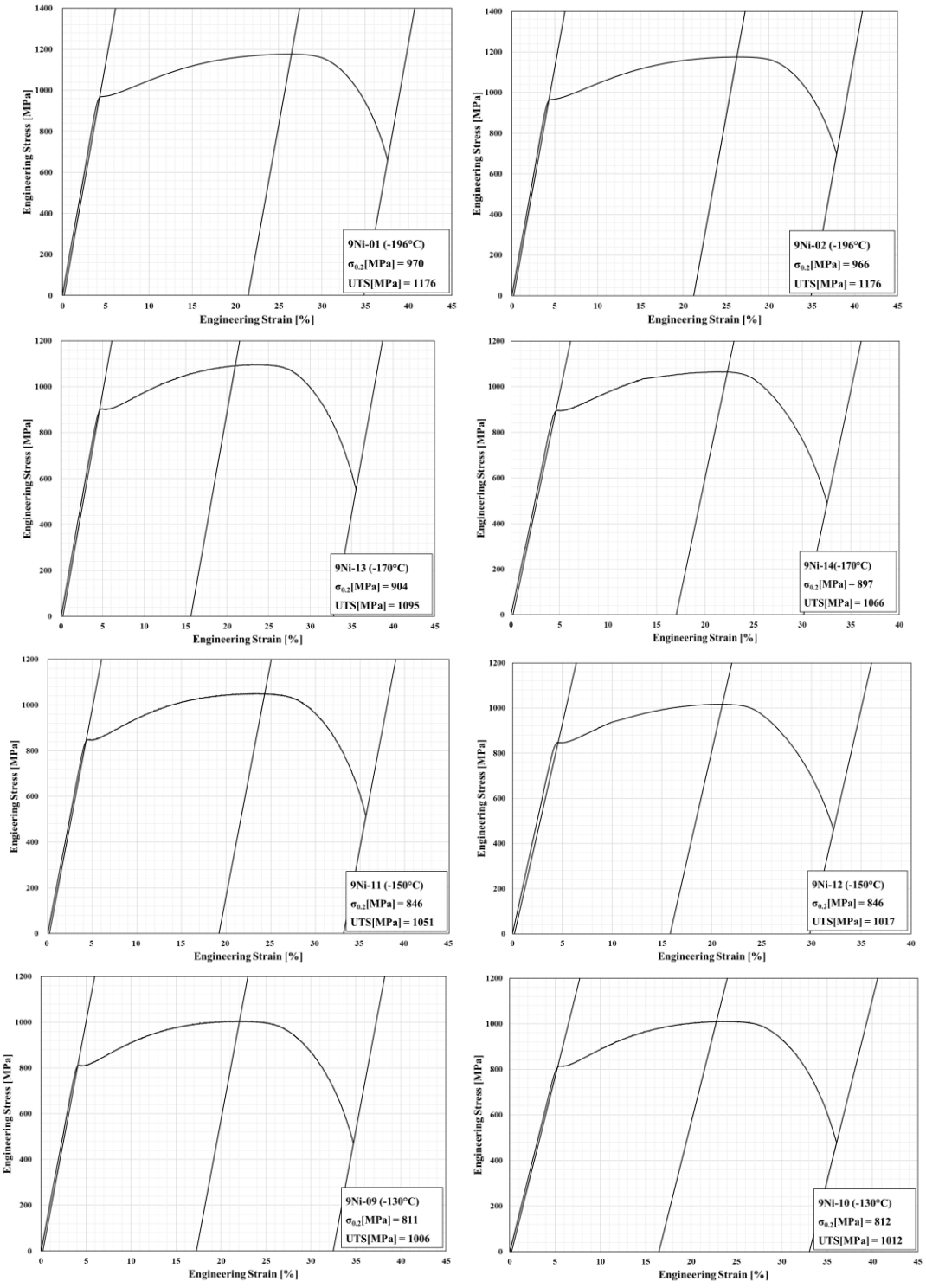

Figure 7.9 Engineering stress-strain curves of 9% Ni specimens at different temperatures.

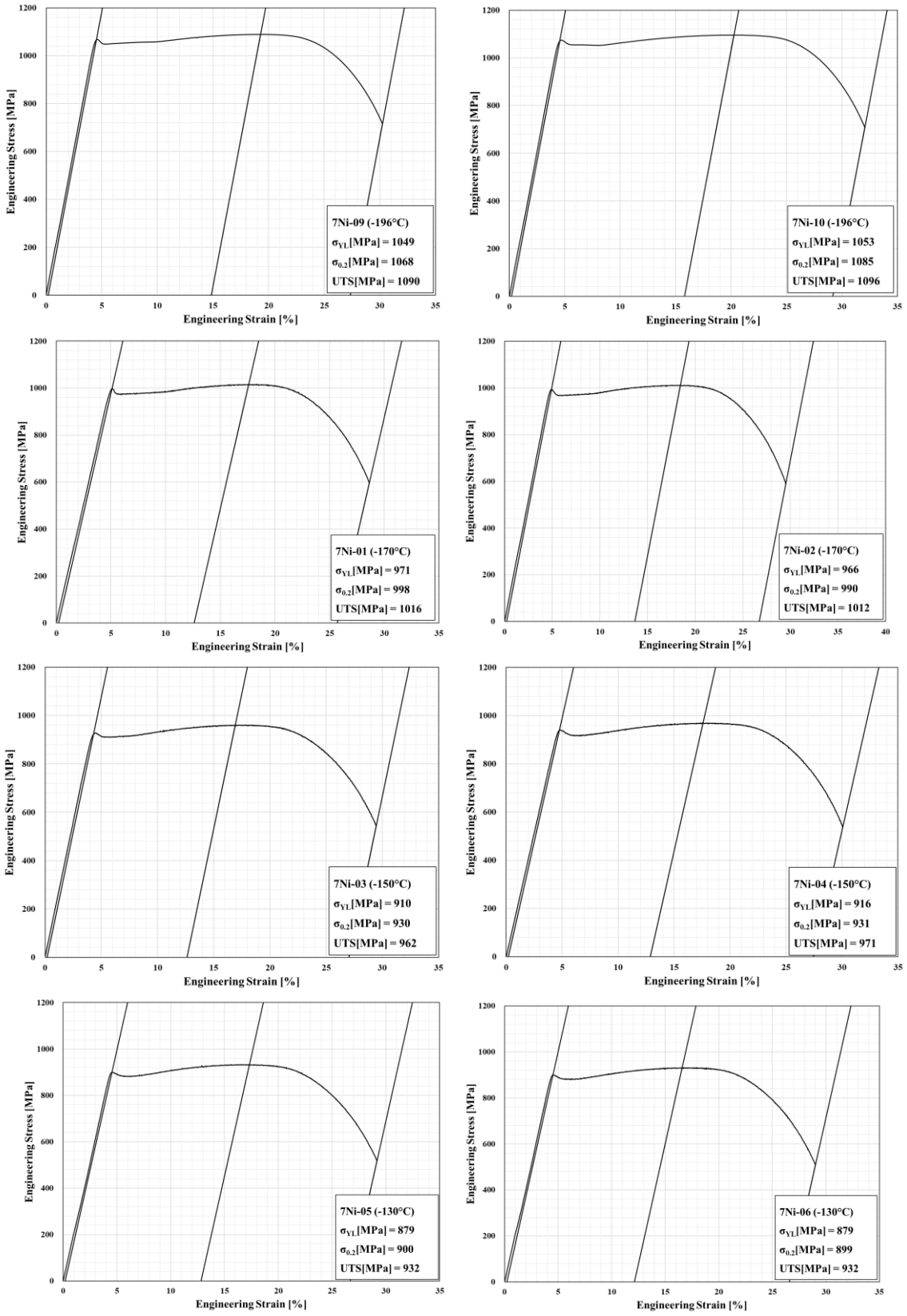

Figure 7.10 Engineering stress-strain curves of 7% Ni specimens at different temperatures.

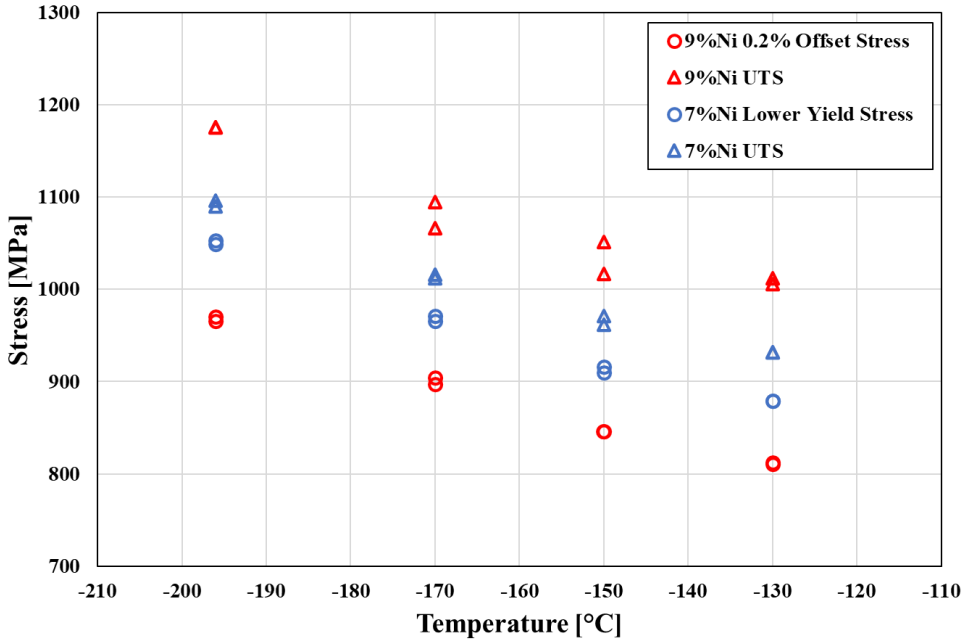

Figure 7.11 Comparisons of yield stress and ultimate tensile strength of 9% and 7% specimens at different temperatures.

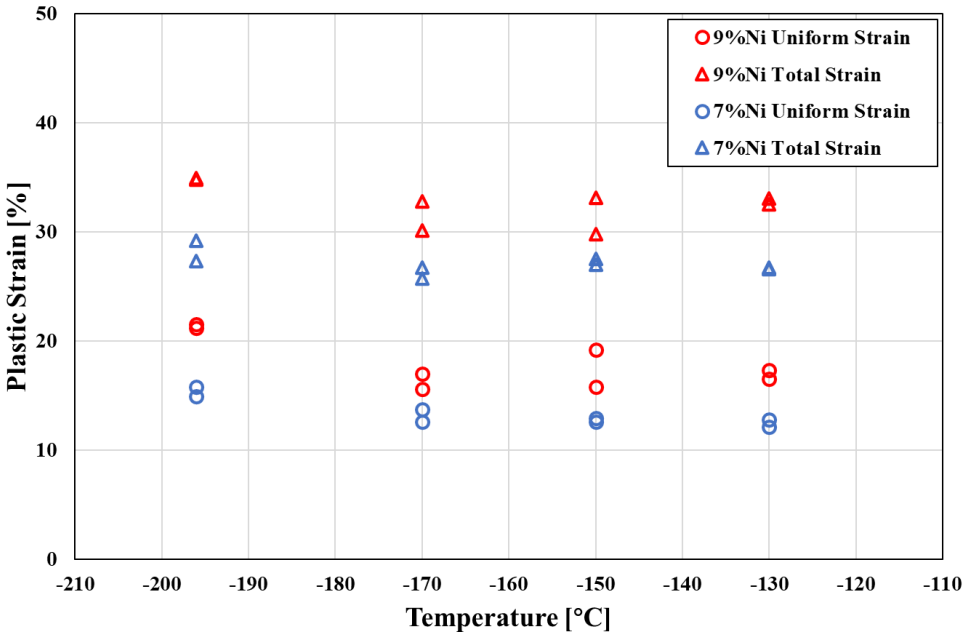

Figure 7.12 Comparisons of uniform strain and total strain of 9% and 7% specimens at different temperatures.

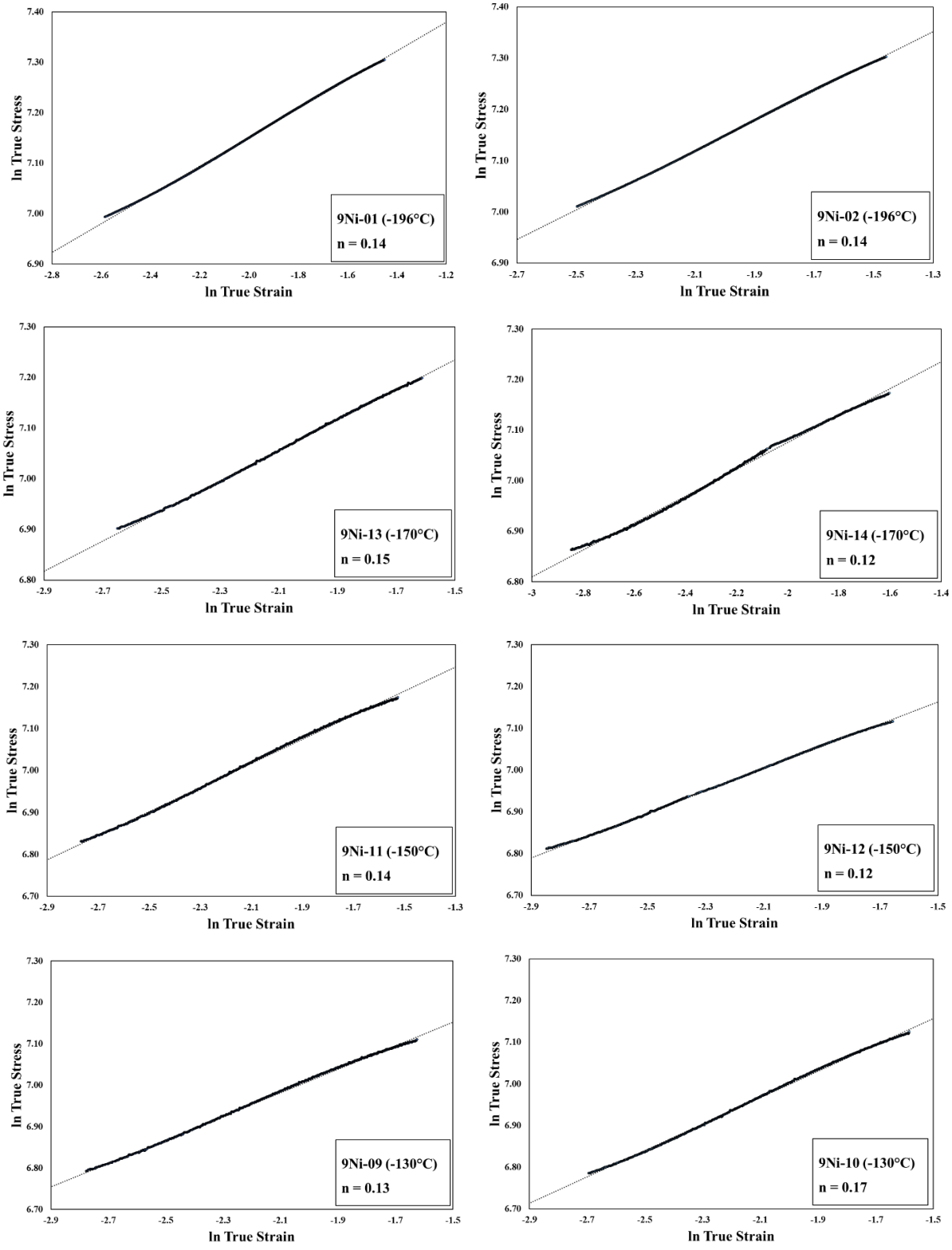

Figure 7.13 Work hardening exponents of 9% Ni specimens at different temperatures.

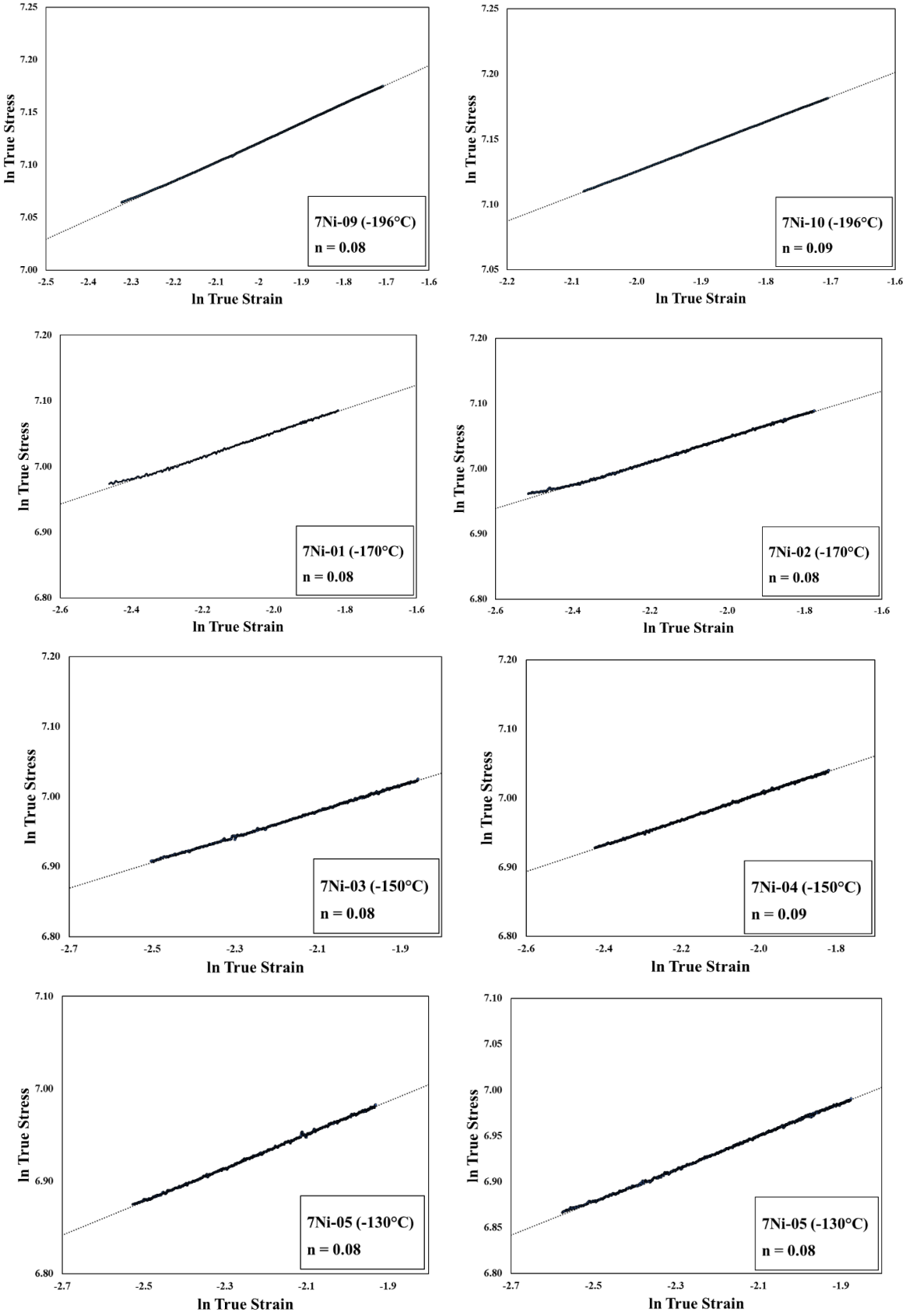

Figure 7.14 Work hardening exponents of 7% Ni specimens at different temperatures.

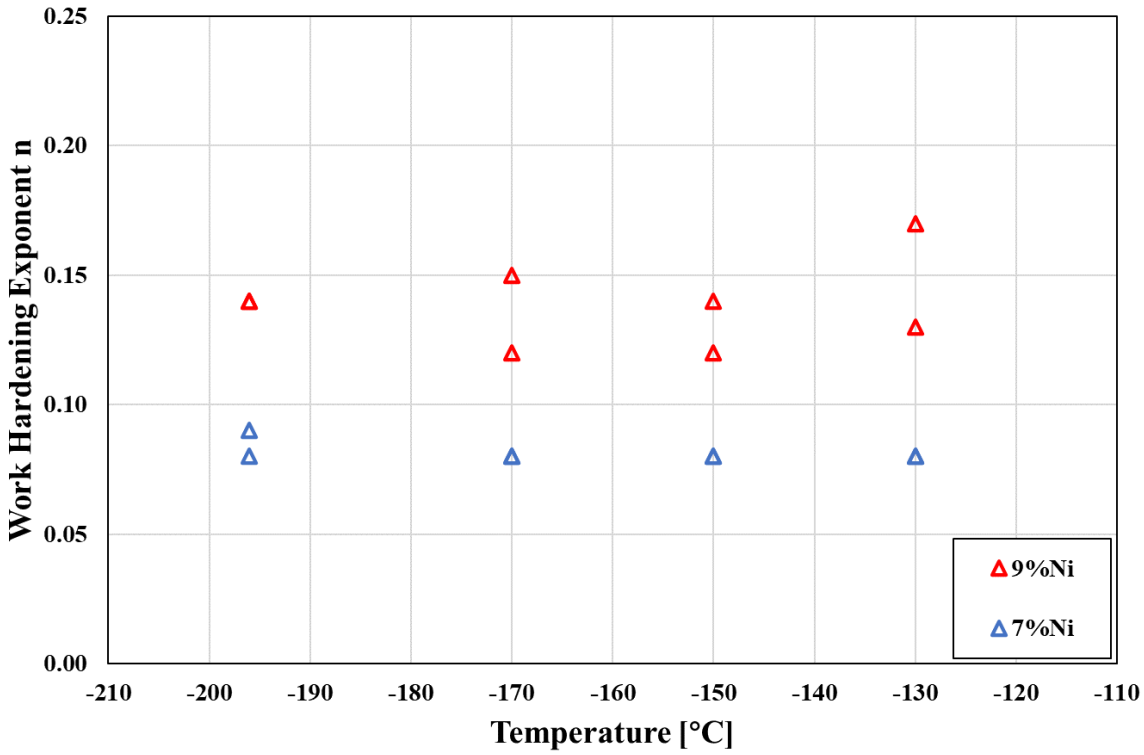

Figure 7.15 Comparison of work hardening exponent of 9% and 7% specimens at different temperatures.

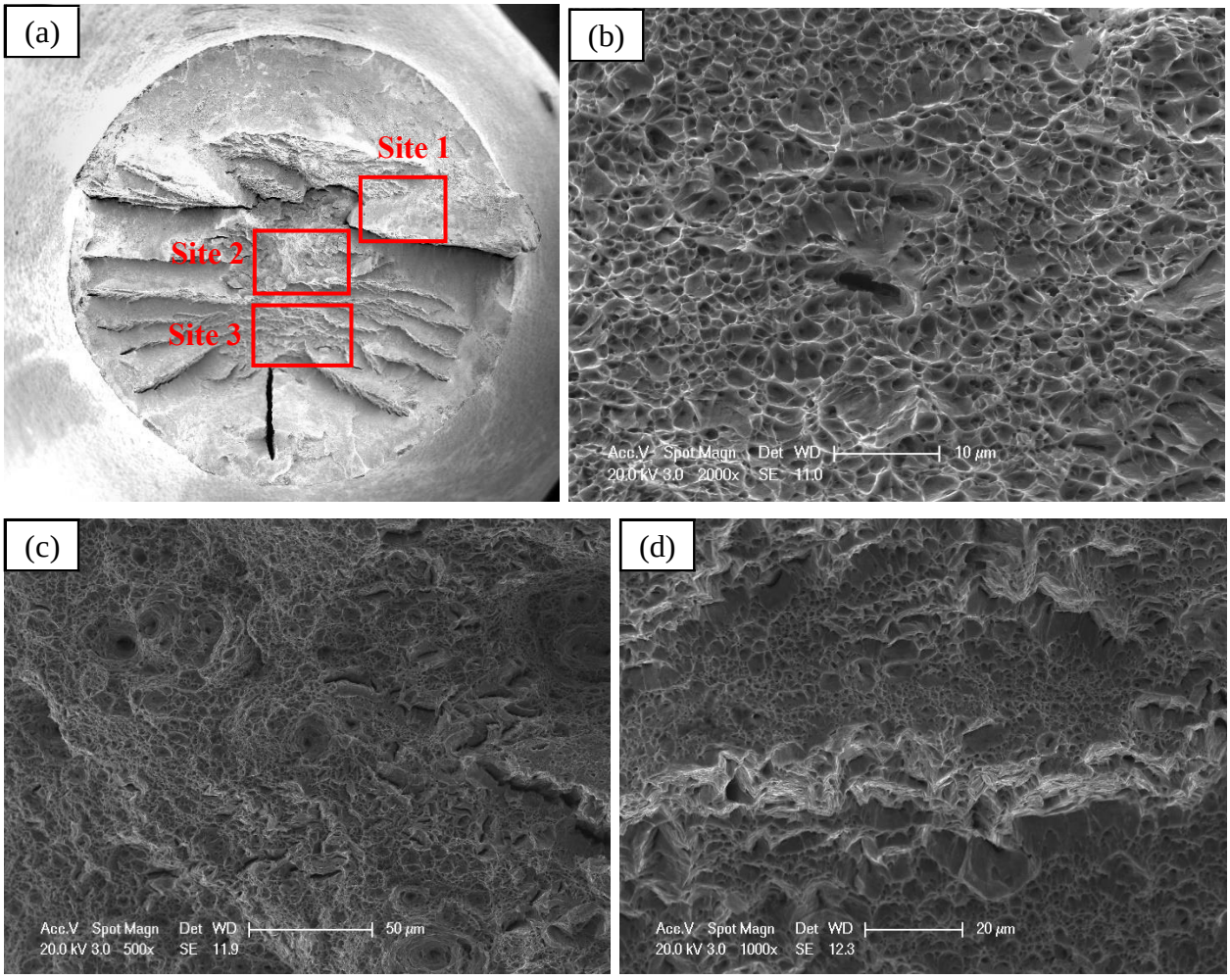

Figure 7.16 Fractography of 9% Ni tensile specimen 9Ni-09 at -130°C, (a) overview of the fracture surface, (b) close view of site 1, (c) close view of site 2, (d) close view of site 3.

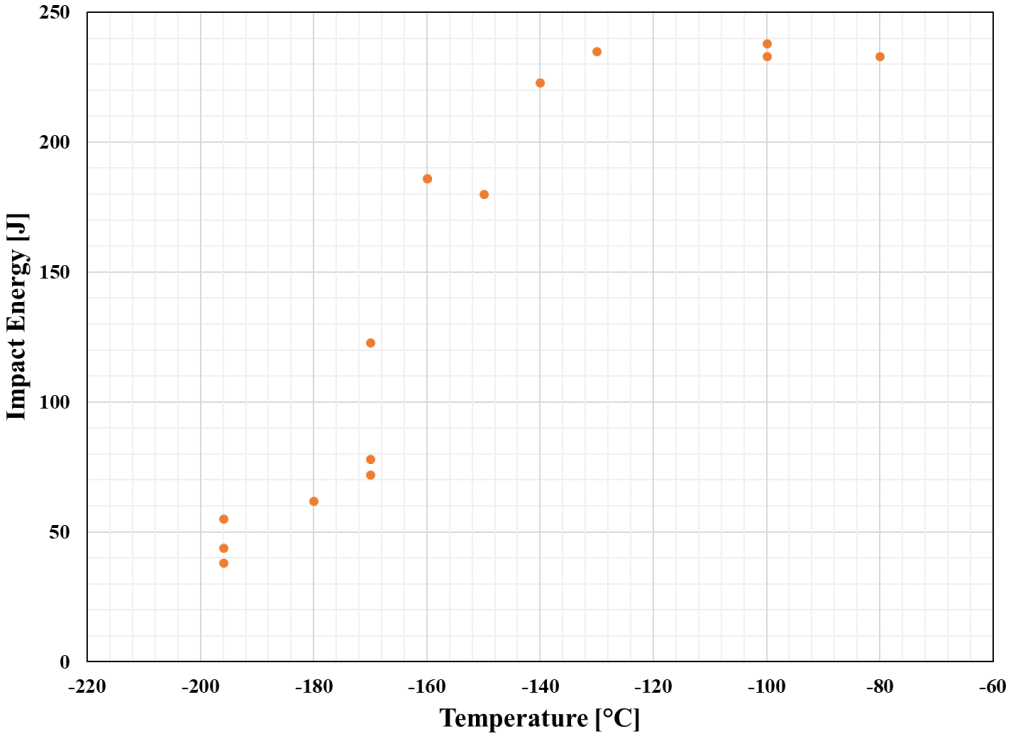

Figure 7.17 Absorbed impact energy of 7% Nickel steel.

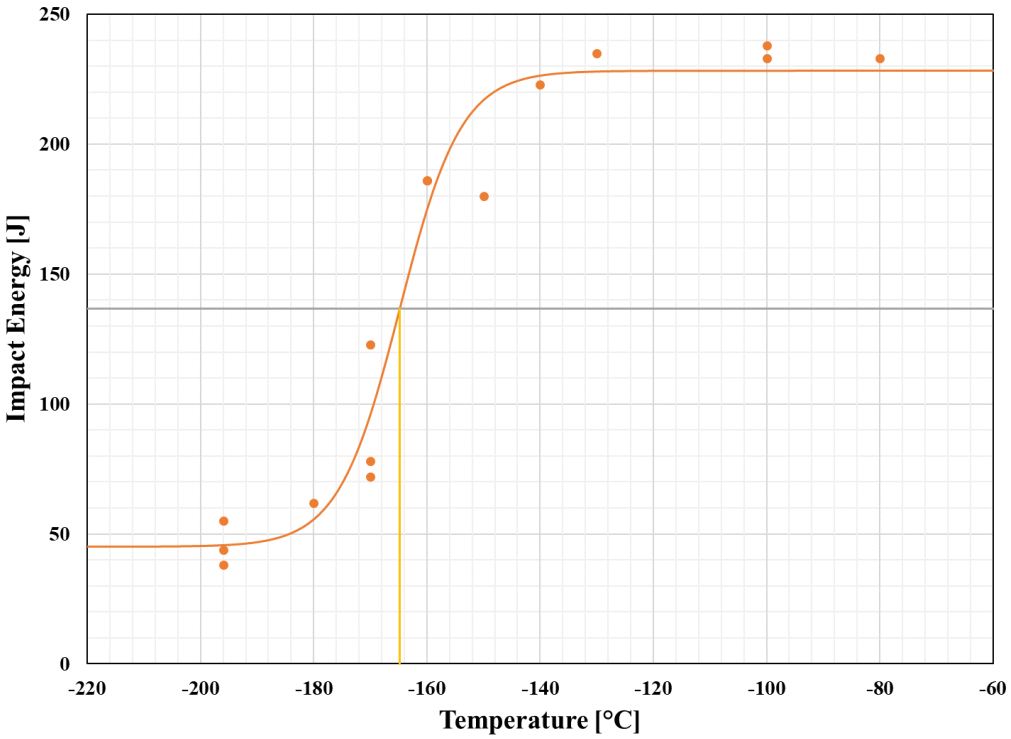

Figure 7.18 Ductile-to-Brittle transition curve of 7% Nickel steel.

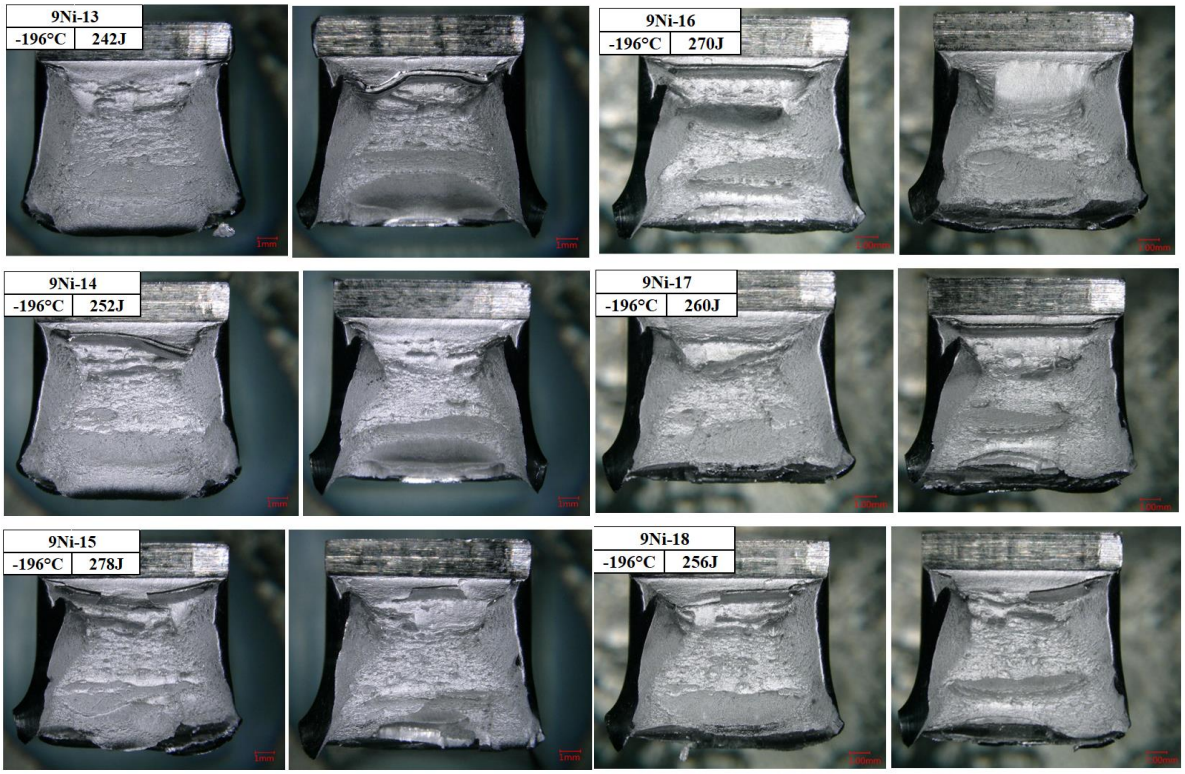

Figure 7.19 Fracture surfaces of 9% Ni steel specimens under optical microscope.

(a)

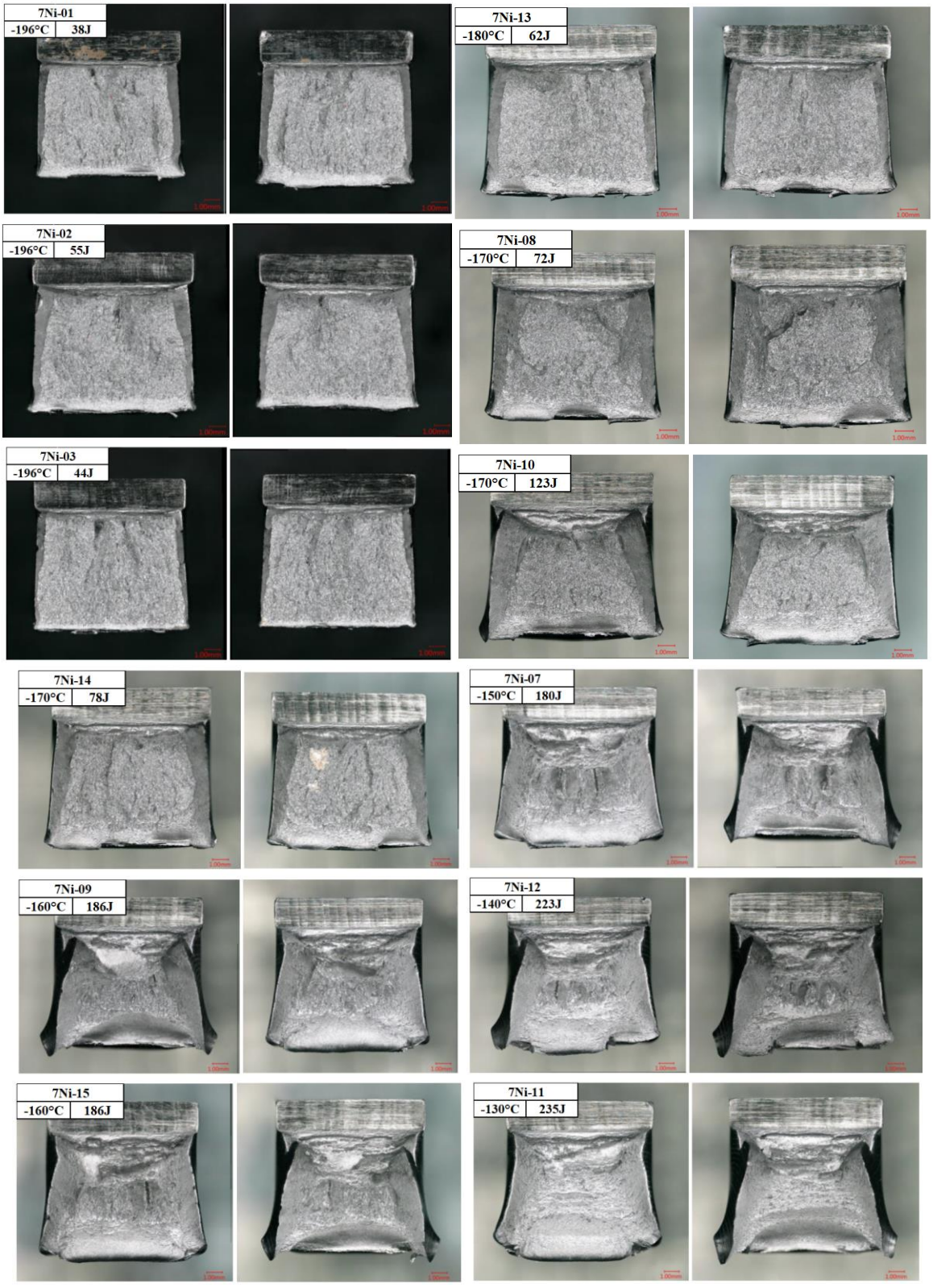

Figure 7.20 Fracture surfaces of 7% Ni steel specimens under optical microscope, (a) -196 to -130 ° C and (b) -100 to -80 °C.

(b)

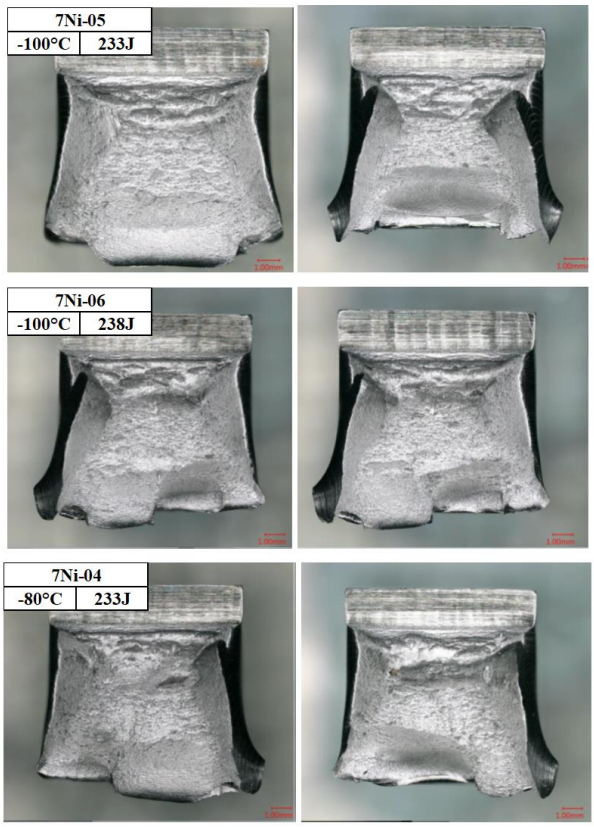

(b) -100 to -80 °C.

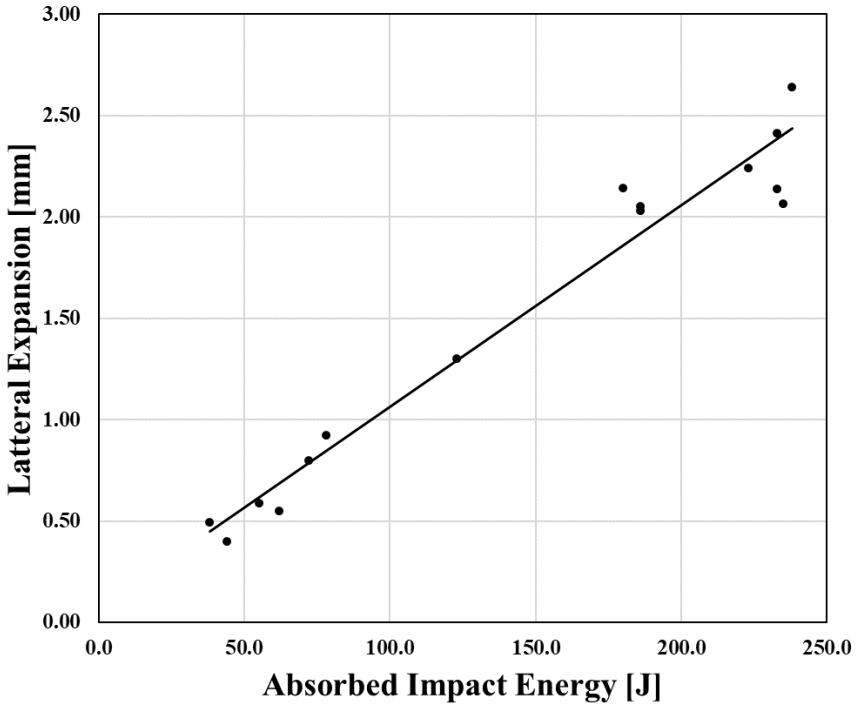

Figure 7.21 Lateral expansion versus absorbed impact energy for 7% Nickel steel.

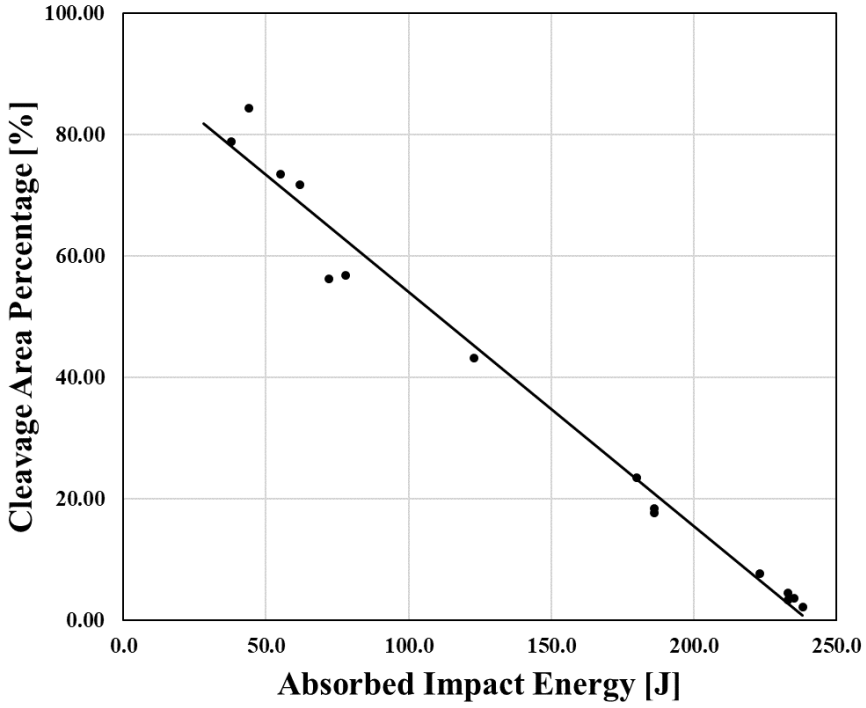

Figure 7.22 Cleavage area percentage versus absorbed impact energy for 7% Nickel steel.

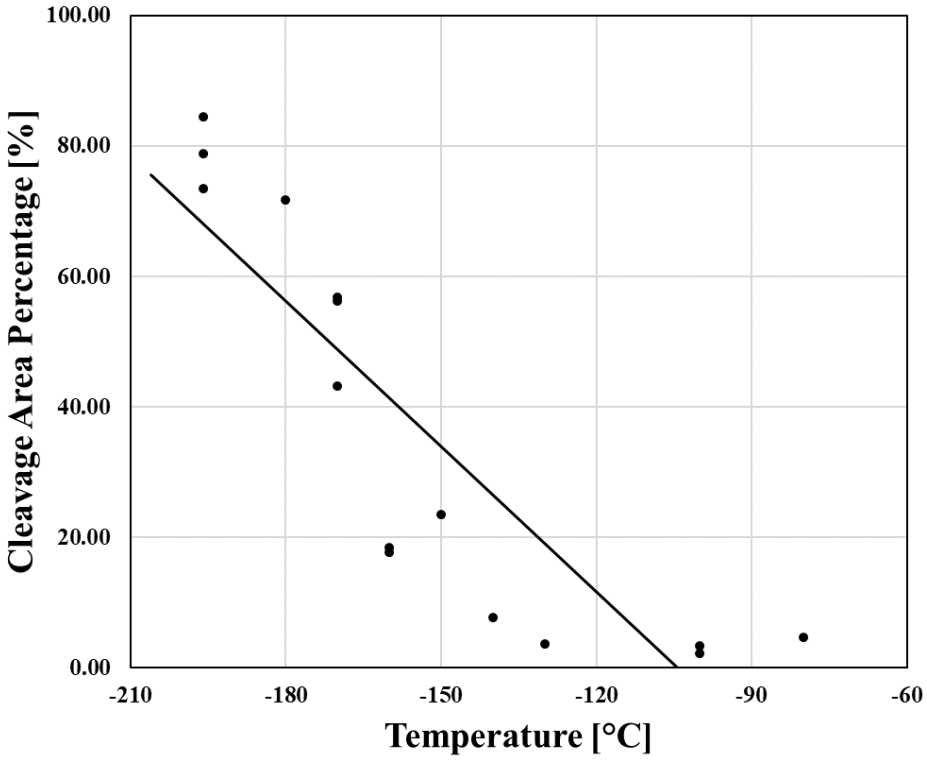

Figure 7.23 Cleavage area percentage versus test temperature for 7% Nickel steel.

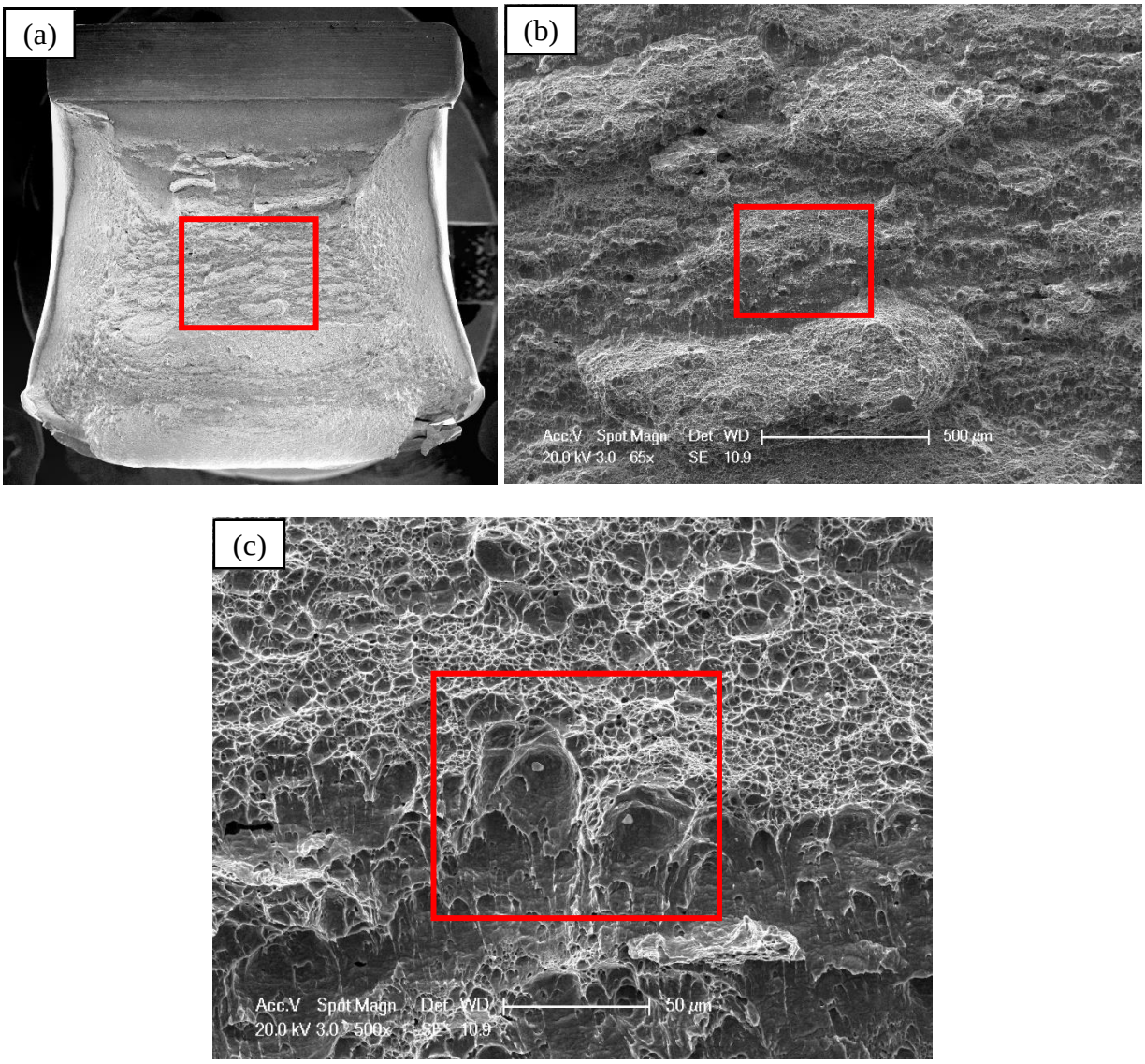

Figure 7.24 Fractography of 9% Ni Charpy impact specimen 9Ni-13 at -196°C, in the sequence of magnification.

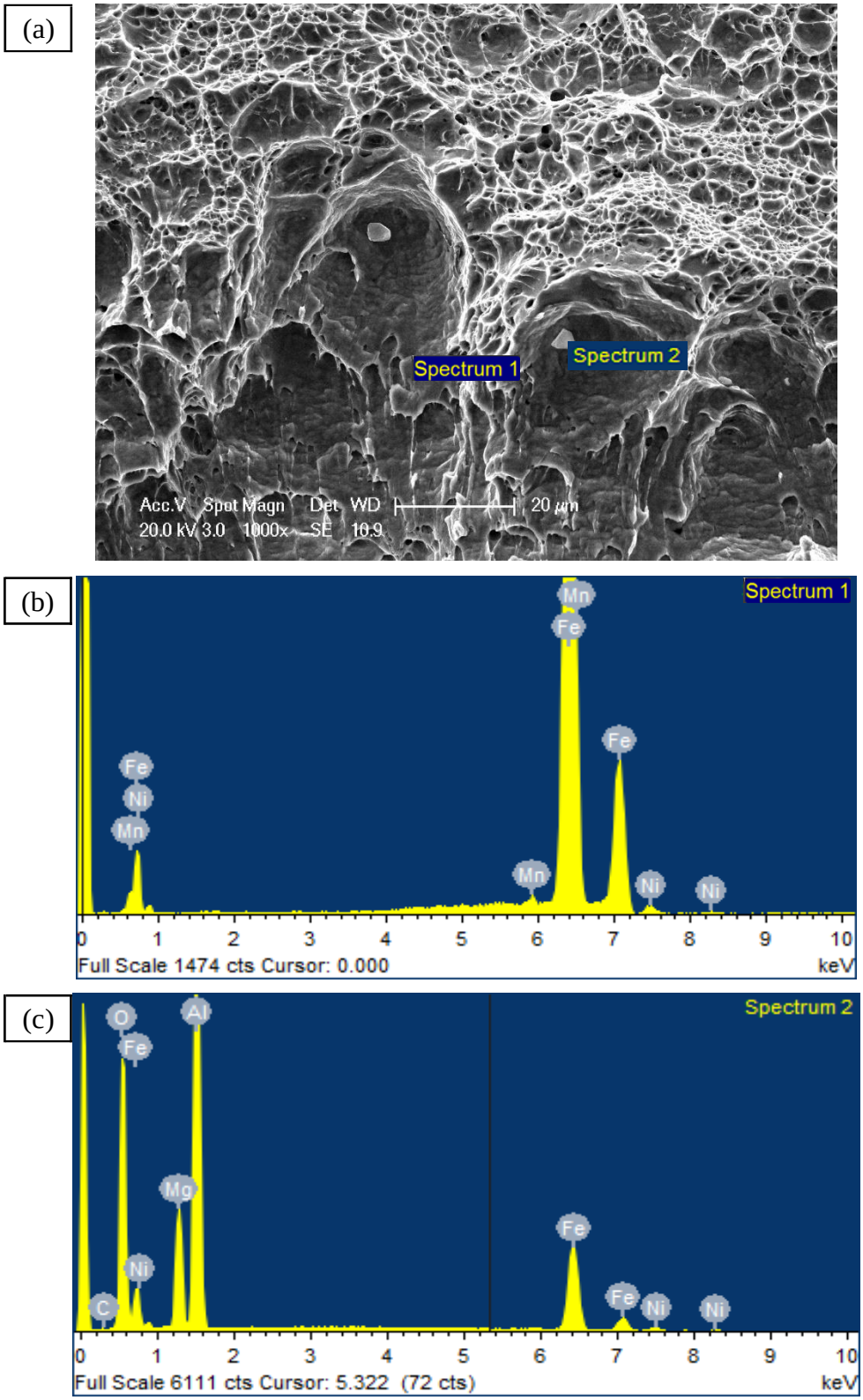

Figure 7.25 EDX analysis for specimen 9Ni-13, (a) sampling locations; (b) chemical composition of the surrounding matrix; (c) chemical composition of inclusion.

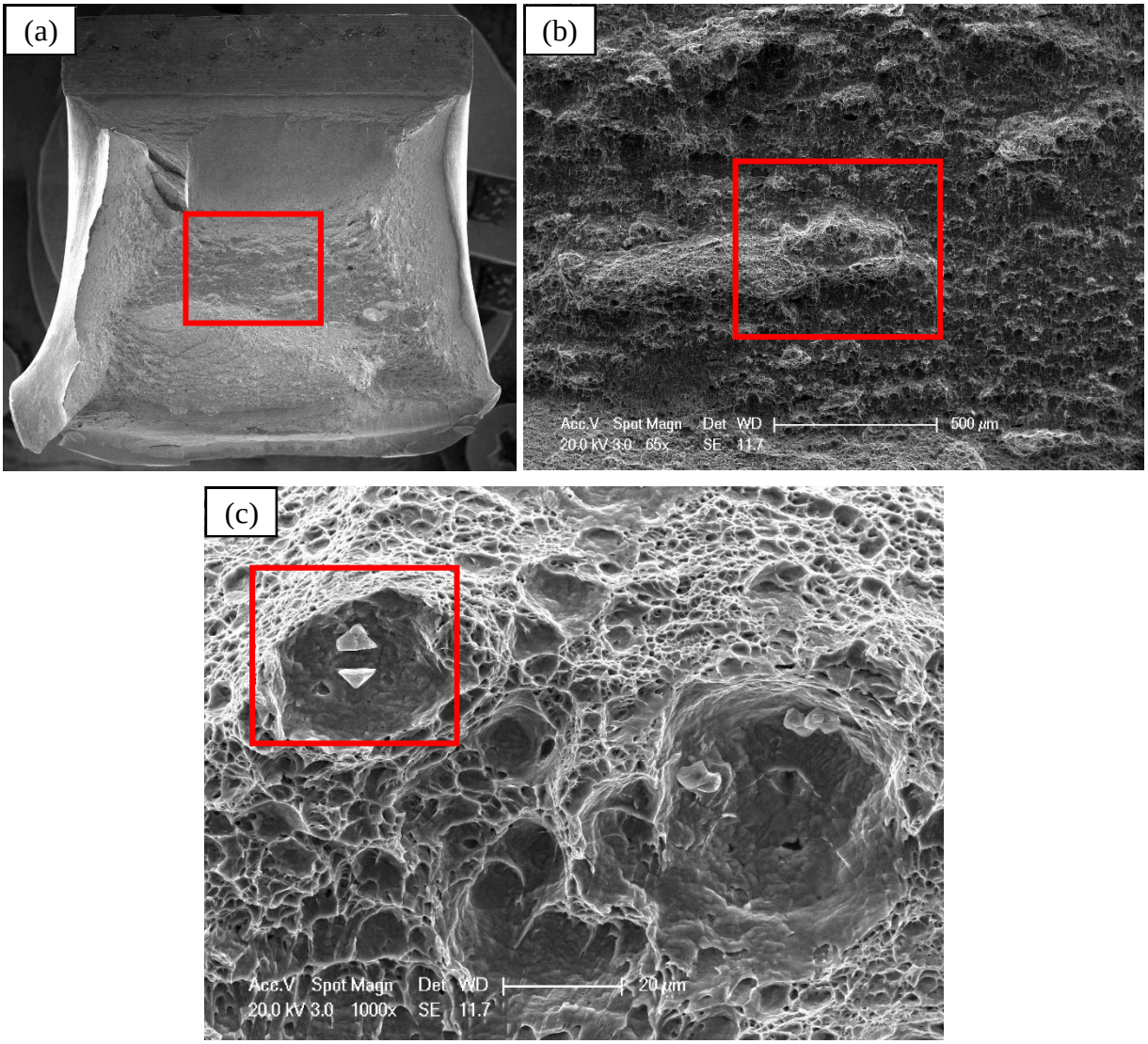

Figure 7.26 Fractography of 9% Ni Charpy impact specimen 9Ni-16 at -196°C, in the sequence of magnification.

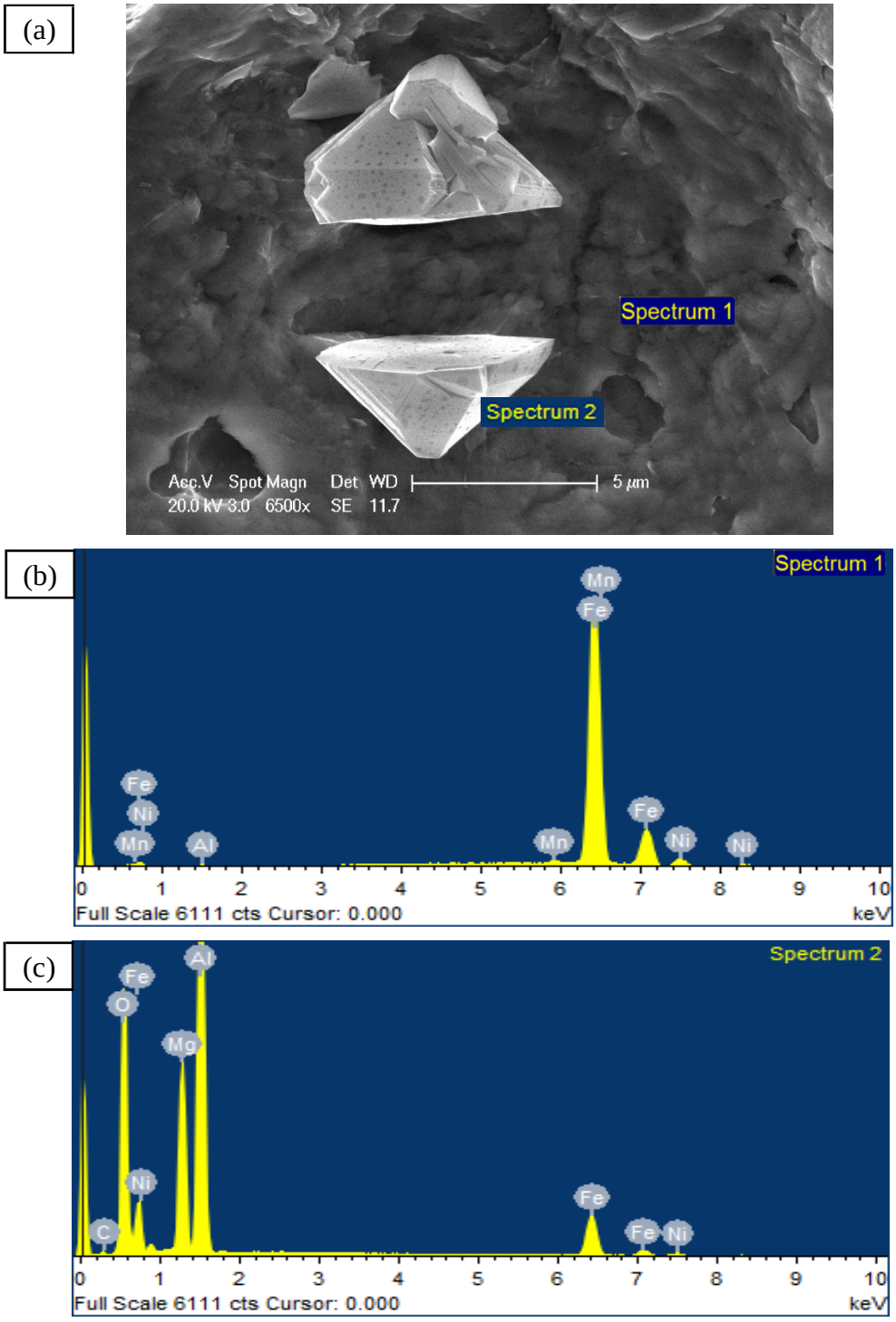

Figure 7.27 EDX analysis for specimen 9Ni-16, (a) sampling locations; (b) chemical composition of the surrounding matrix; (c) chemical composition of inclusion.

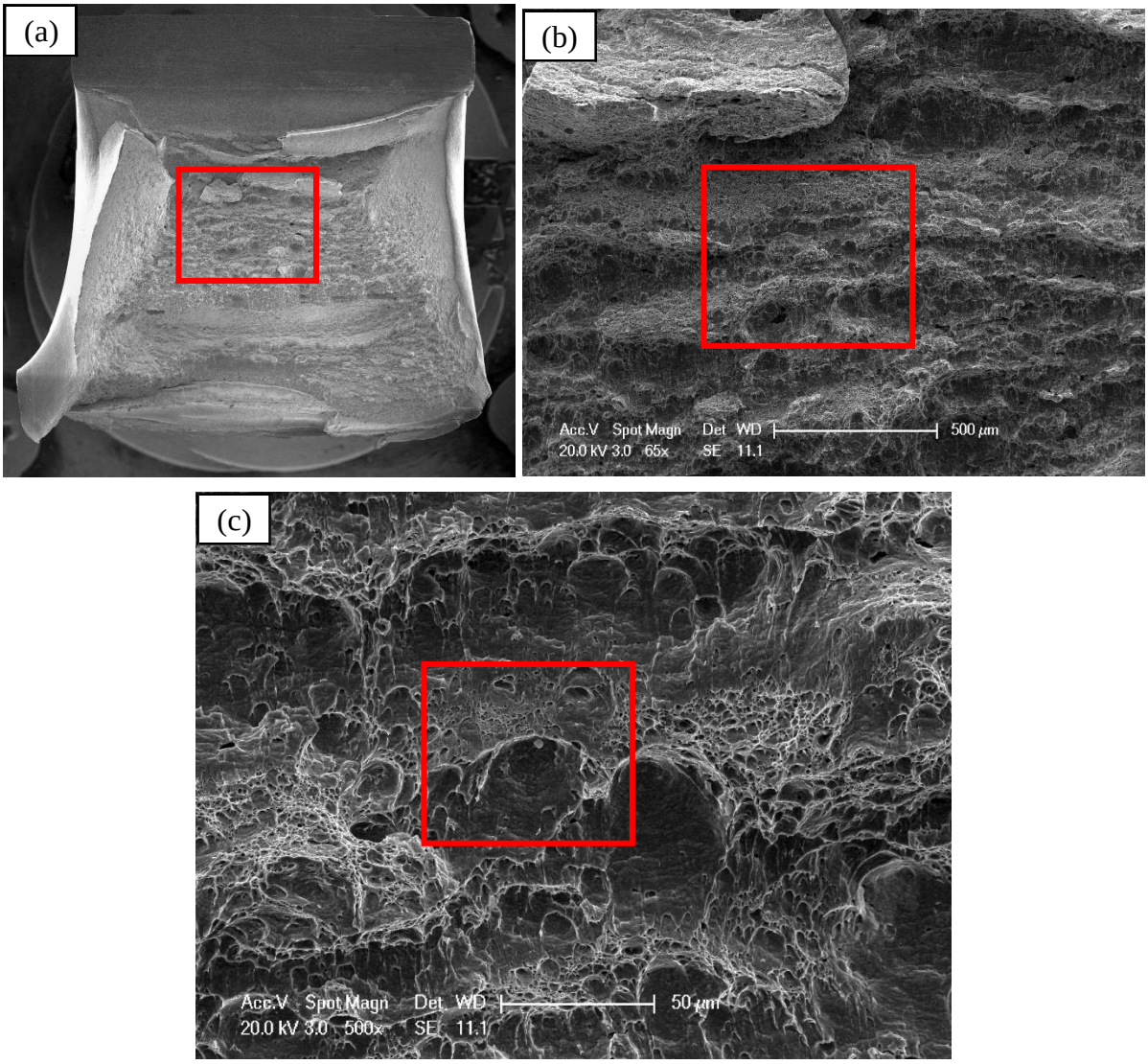

Figure 7.28 Fractography of 9% Ni Charpy impact specimen 9Ni-18 at -196°C, in the sequence of magnification.

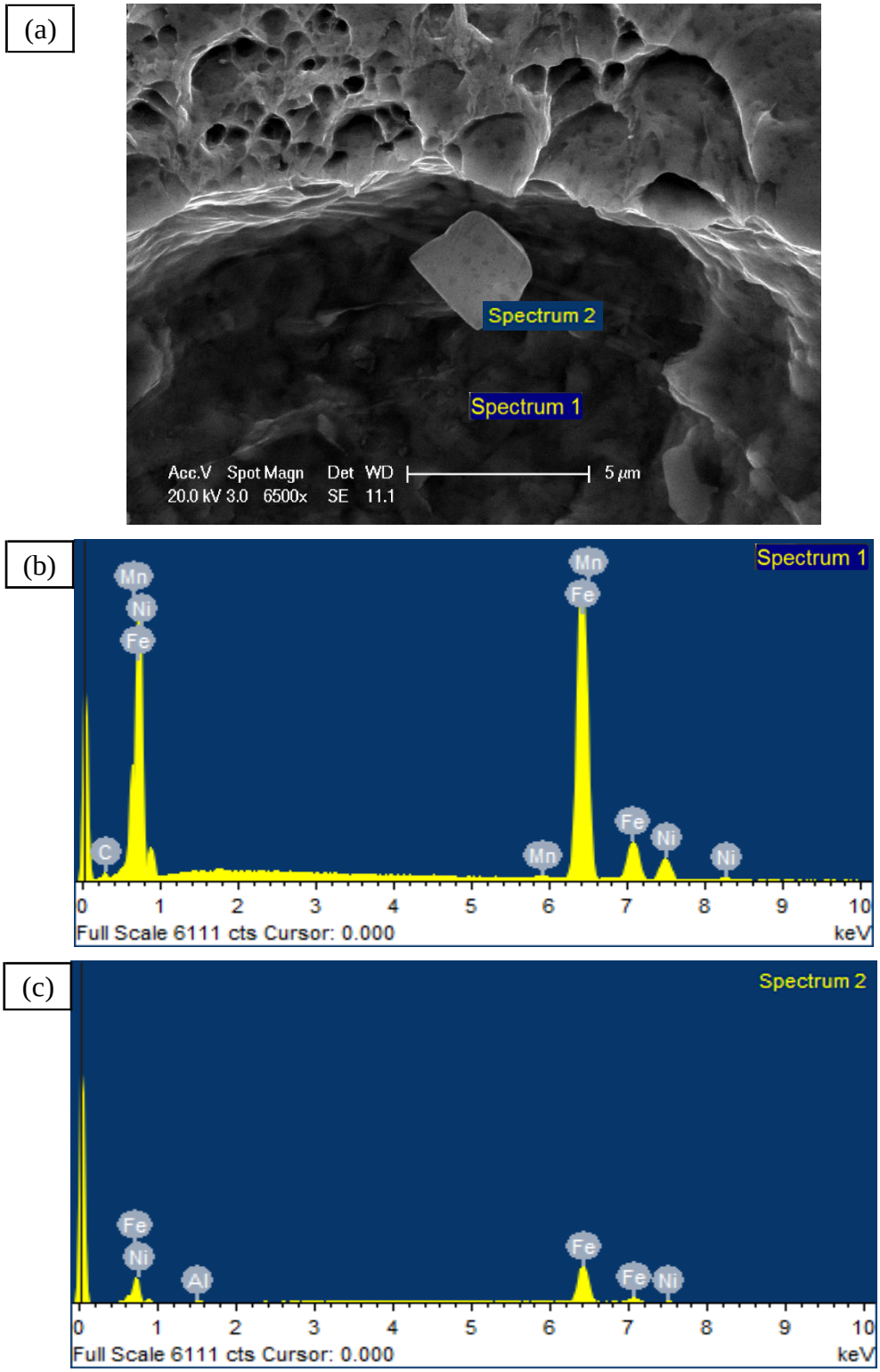

Figure 7.29 EDX analysis for specimen 9Ni-18, (a) sampling locations; (b) chemical composition of the surrounding matrix; (c) chemical composition of inclusion.

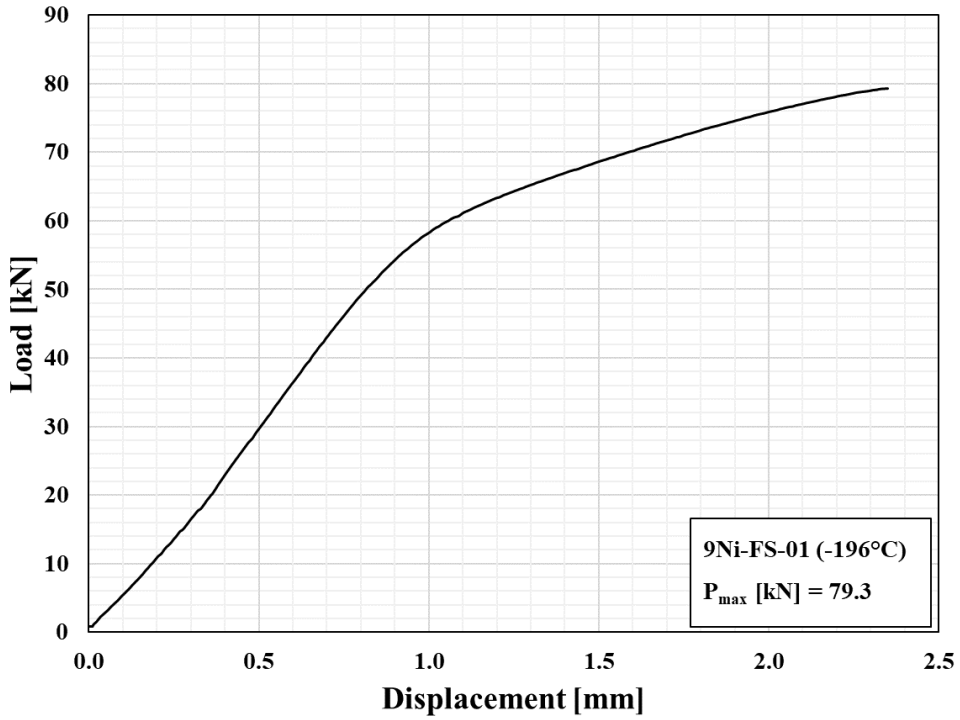

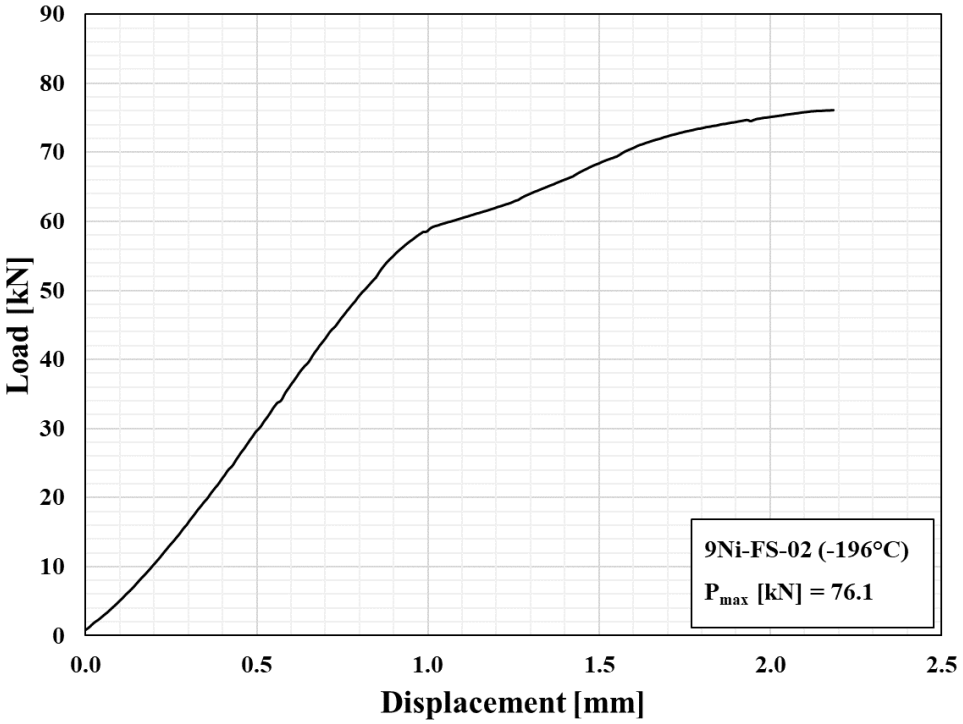

Figure 7.30 Load-displacement curves of fracture stress tests for 9% Ni steel.

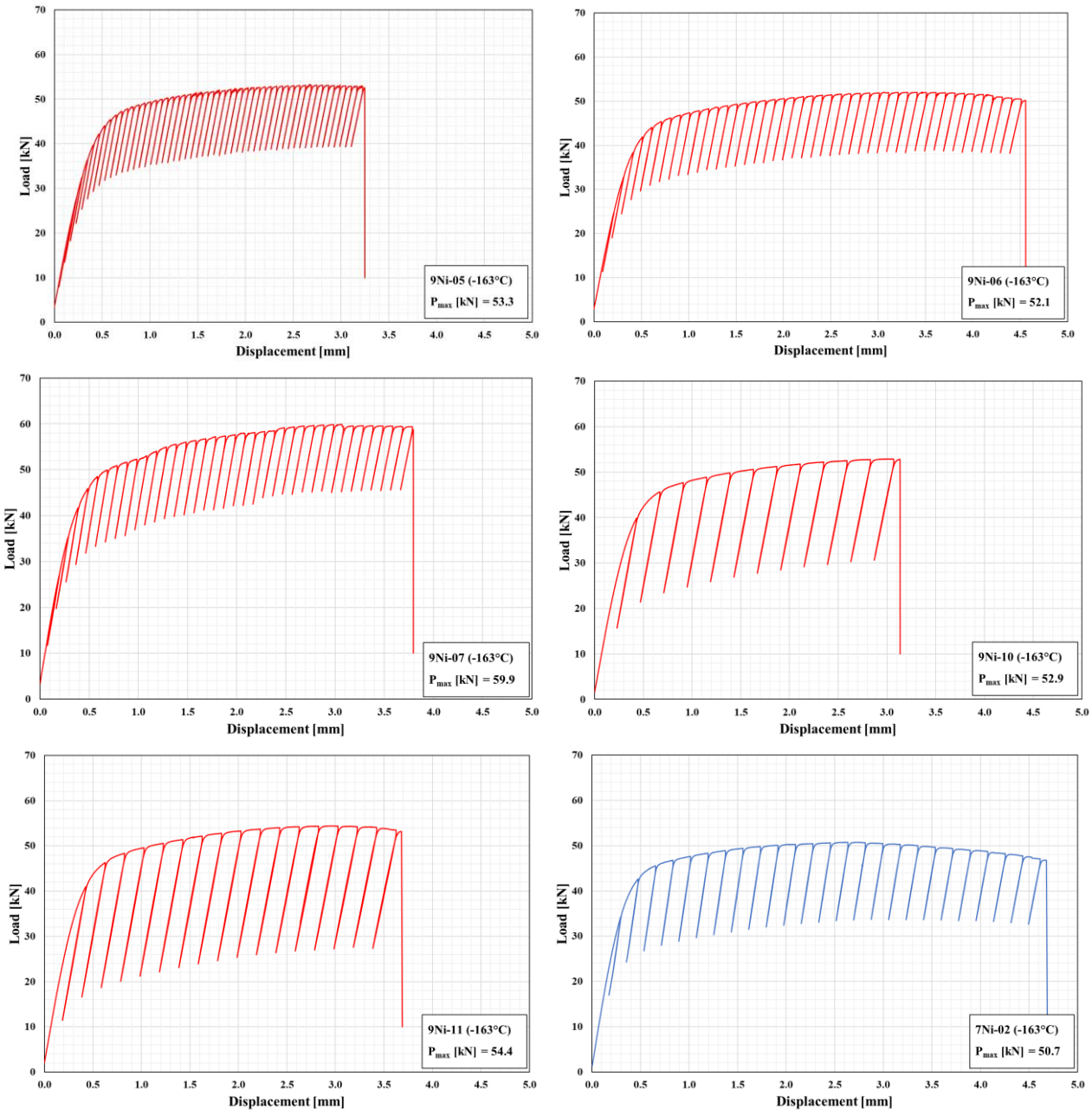

Figure 7.31 Load displacement curve of fracture toughness tests for 9% and 7% Ni steels at -163°C.

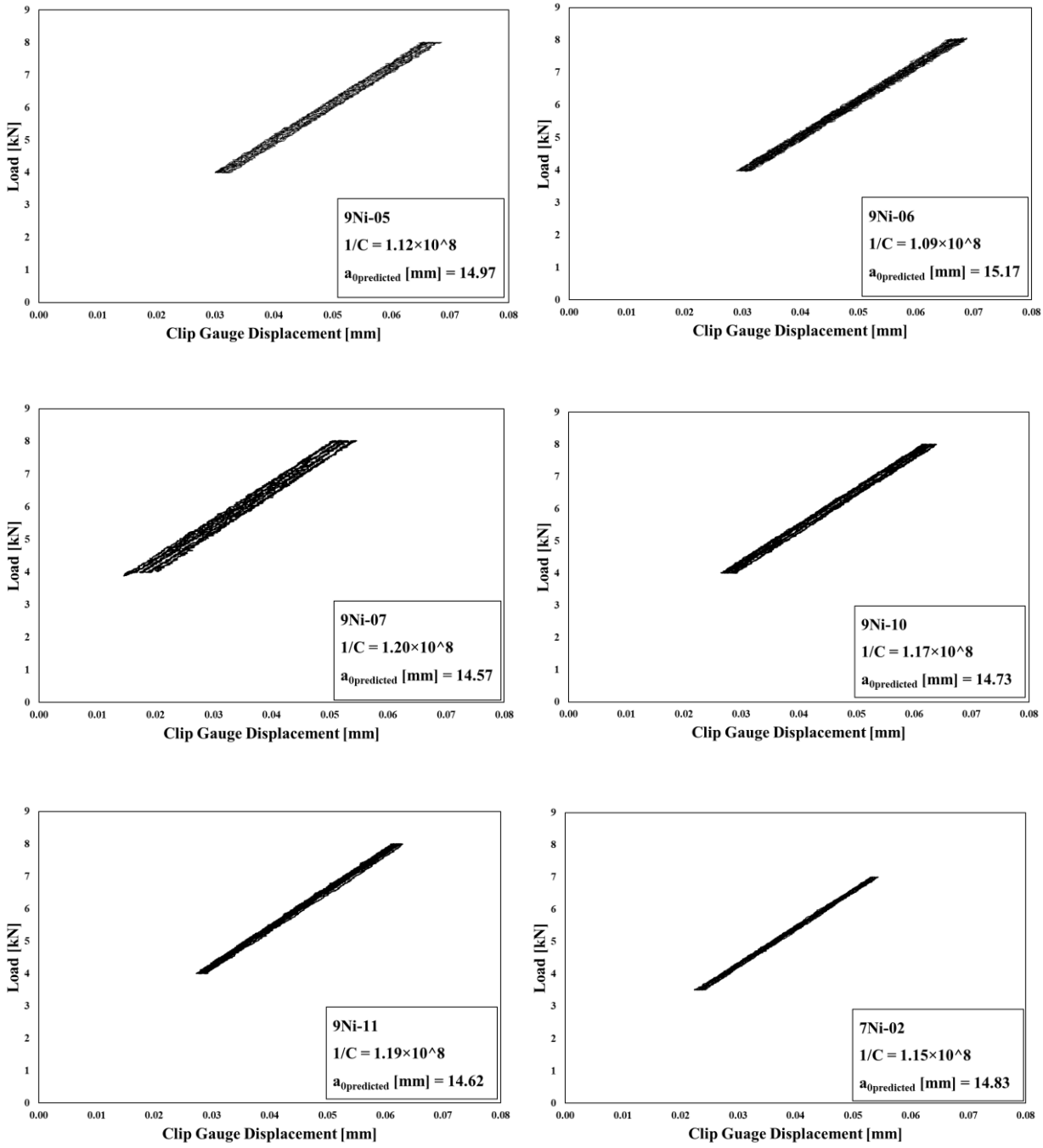

Figure 7.32 Unloading/reloading sequences of the compliance crack estimation for 9% and 7% Ni steels at -163°C.

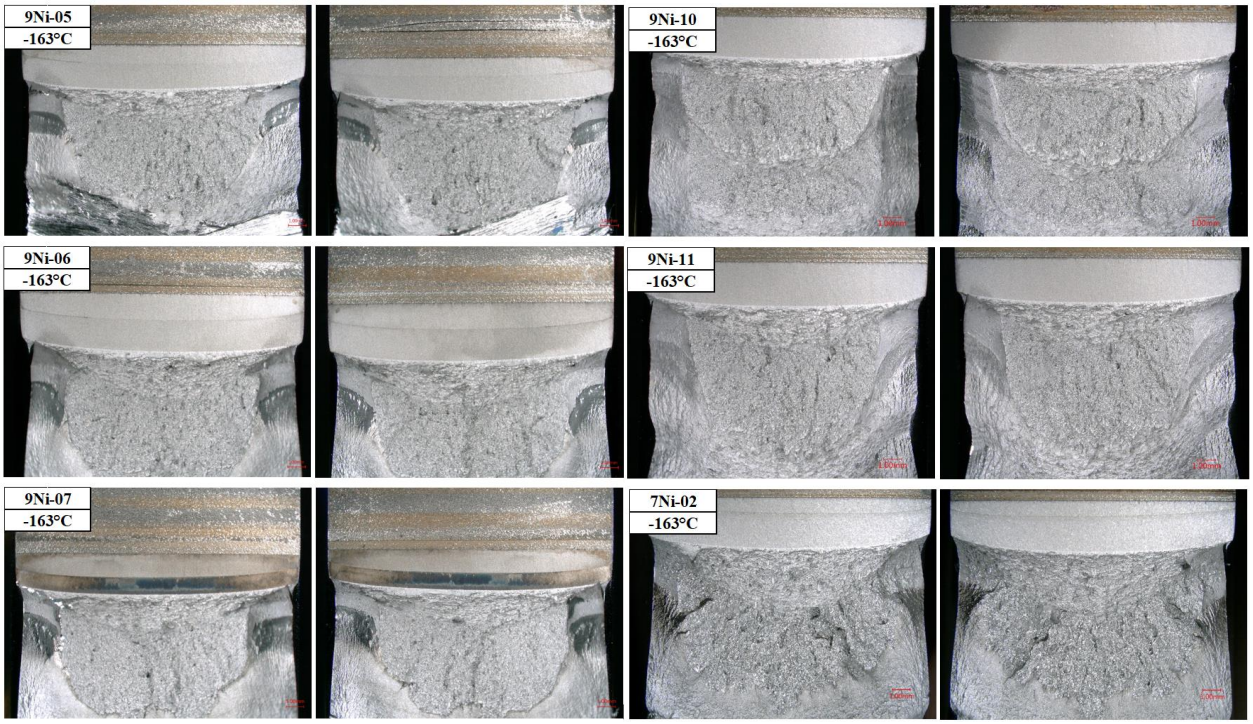

Figure 7.33 Fracture surfaces of fracture toughness specimens for 9% and 7% Ni steels.

(a)

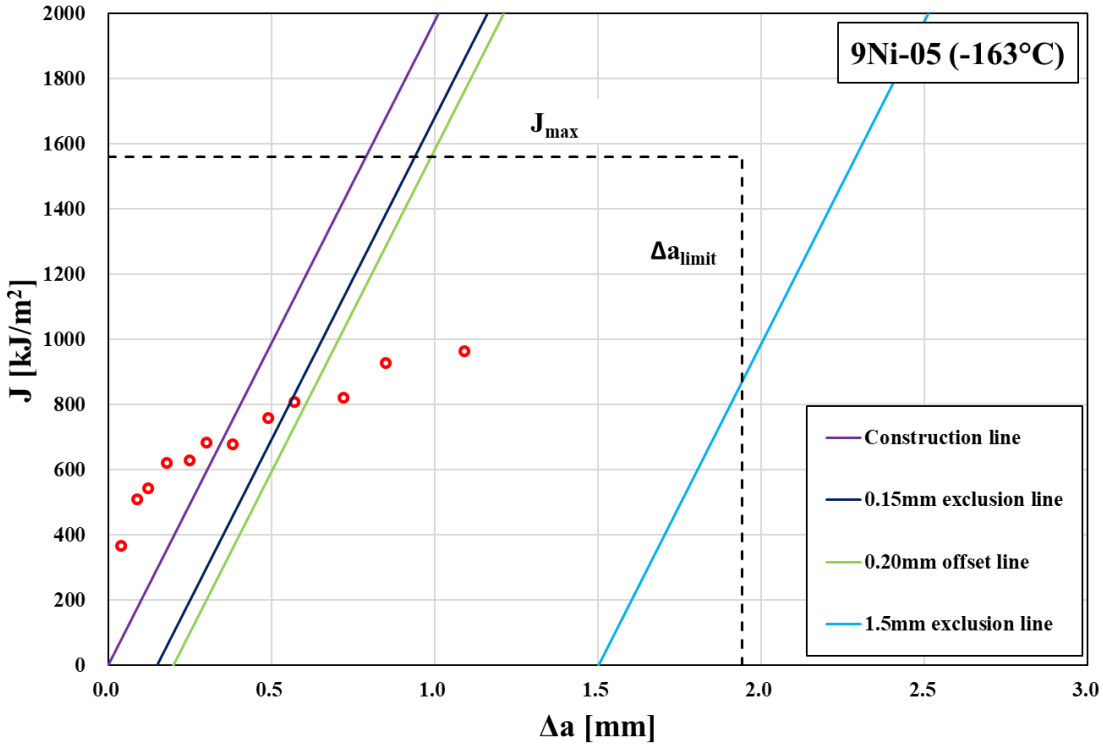

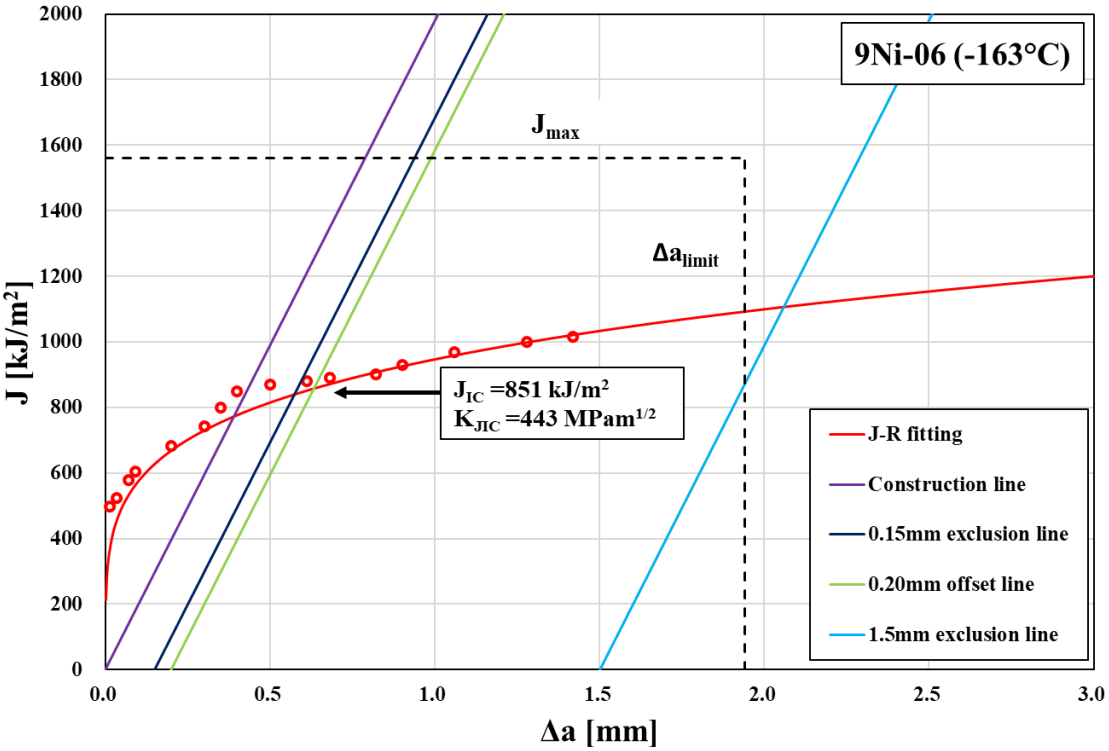

Figure 7.34 *J-R* curves for 9% Ni steel, (a) specimen 9Ni-05 and 9Ni-06 and (b) specimen 9Ni-07 and 9Ni-10.

(b)

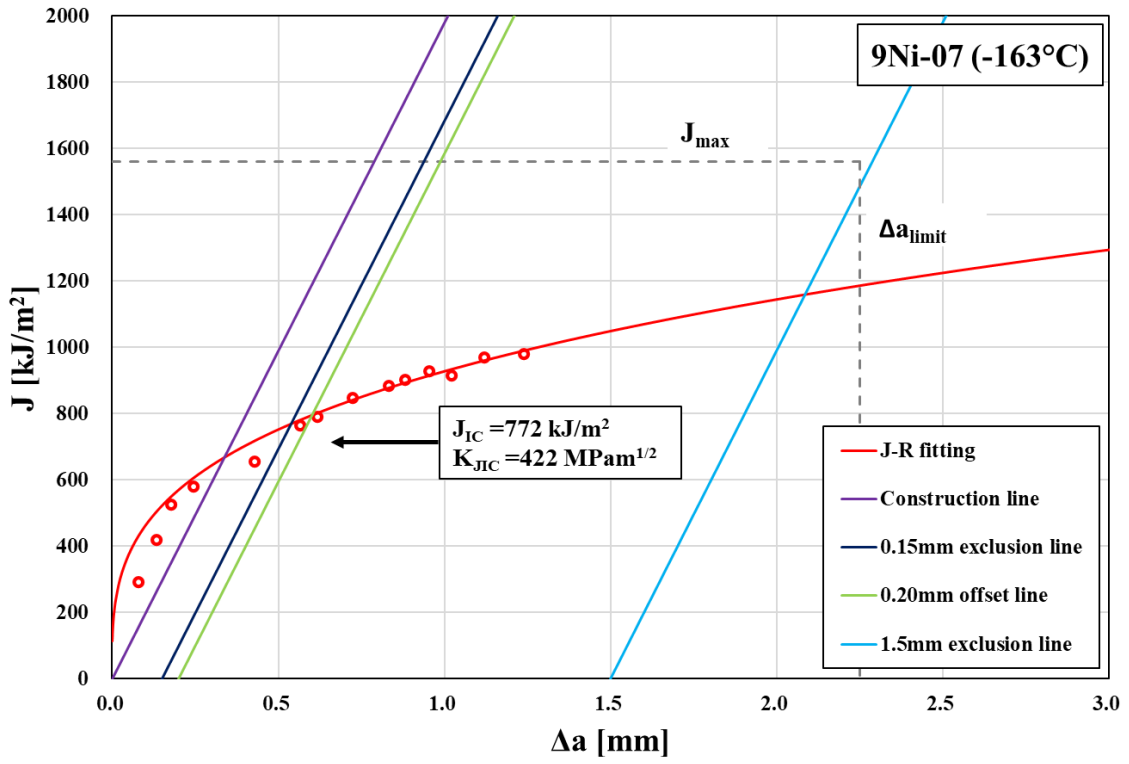

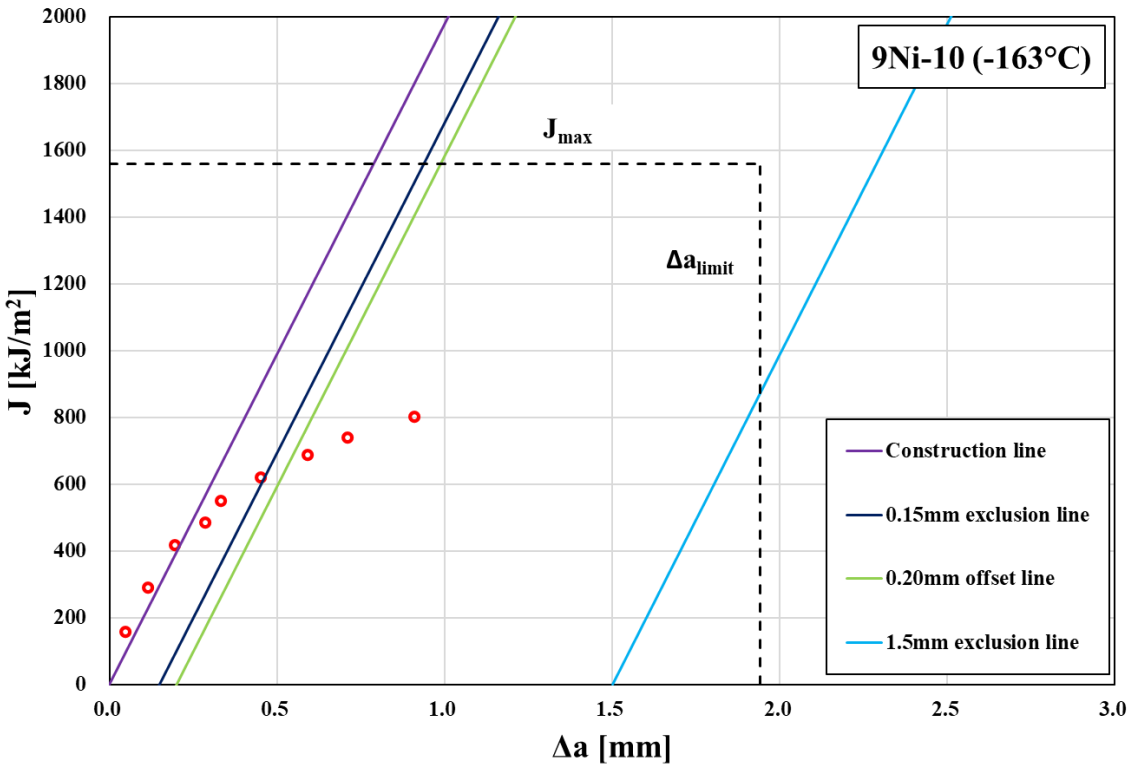

(b) specimen 9Ni-07 and 9Ni-10.

(c)

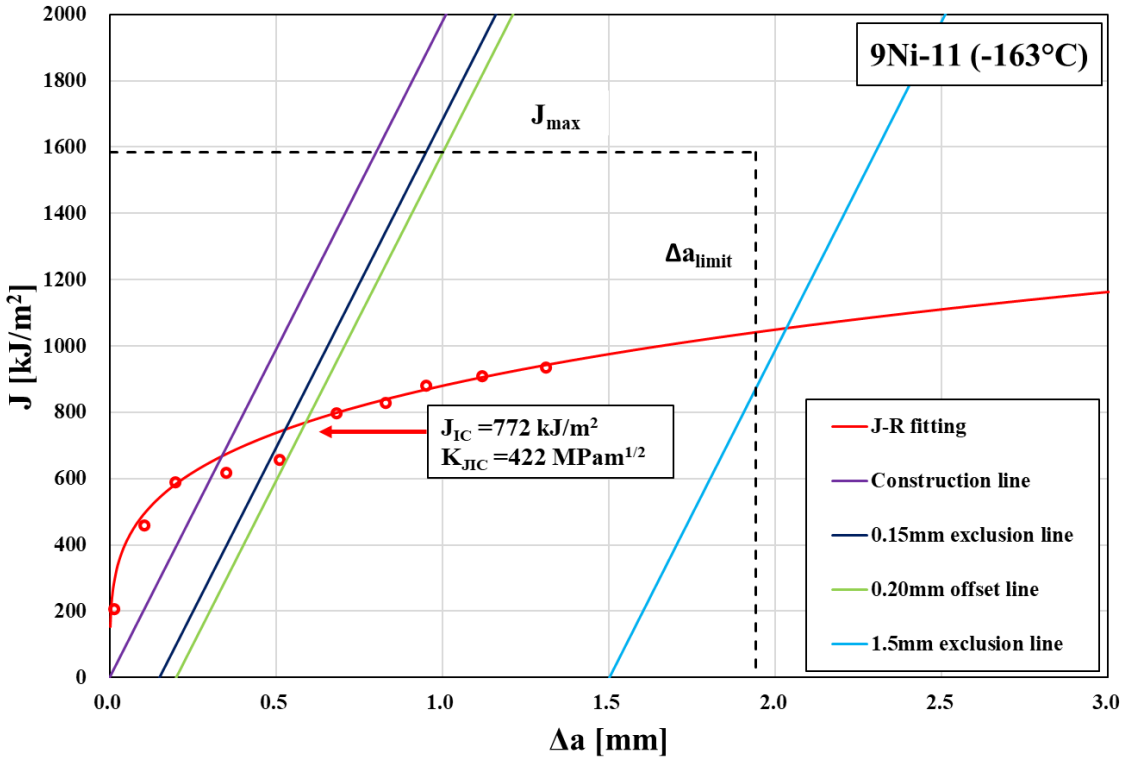

Figure 7.34 *J-R* curves for 9% Ni steel, (c) specimen 9Ni-11.

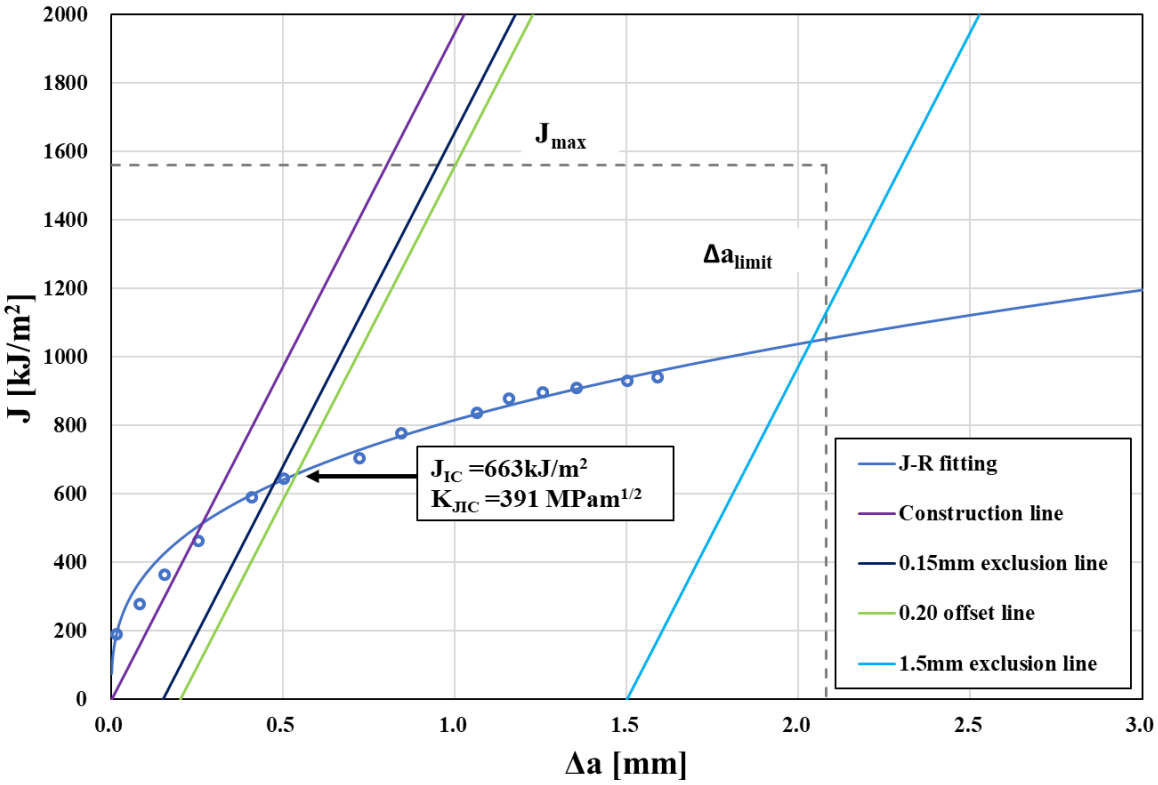

Figure 7.35 *J-R* curve for 7% Ni steel specimen 7Ni-02.

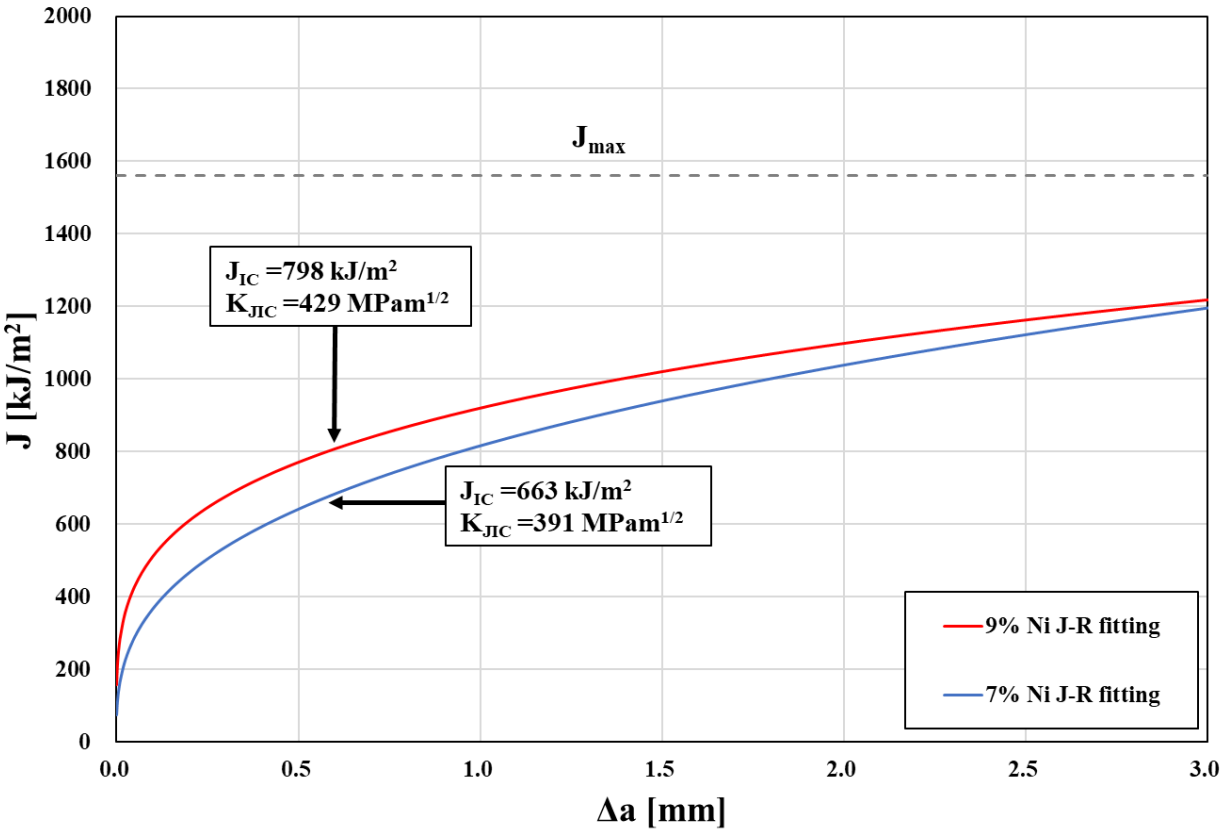

Figure 7.36 Comparison of *J-R* curves for 9% and 7% Ni steels.